KEK Proceedings 96-6
August 1996
A

KEK-PROC--96-6

JP9701021

Proceedings

of

the International Workshop on

Collective Effects and Impedance

for B-Factories

(CEIBA95)

Tsukuba
12 - 17 June, 1995

Editor
Yong Ho Chin

NATIONAL LABORATORY FOR
HIGH ENERGY PHYSICS

Proceedings

of

the International Workshop on

Collective Effects and Impedance

for B-Factories

(CEIBA95)

Tsukuba
12 - 17 June, 1995

Editor
Yong Ho Chin

National Laboratory for High Energy Physics
1 - 1 Oho, Tsukuba-shi, Ibaraki-ken 305, Japan

National Laboratory for High Energy Physics, 1996

KEK Reports are available from:

Technical Information & Library
National Laboratory for High Energy Physics
1-1 Oho, Tsukuba-shi
Ibaraki-ken, 305
JAPAN

Phone: 0298-64-5136
Telex: 3652-534 (Domestic)
(0)3652-534 (International)
Fax: 0298-64-4604
Cable: KEK OHO
E-mail: Library@kekvax.kek.jp (Internet Address)
Internet: http://www.kek.jp

The International Workshop on Collective Effects and Impedance for B-Factories (CEIBA95)
Tsukuba, 12-17 June, 1995

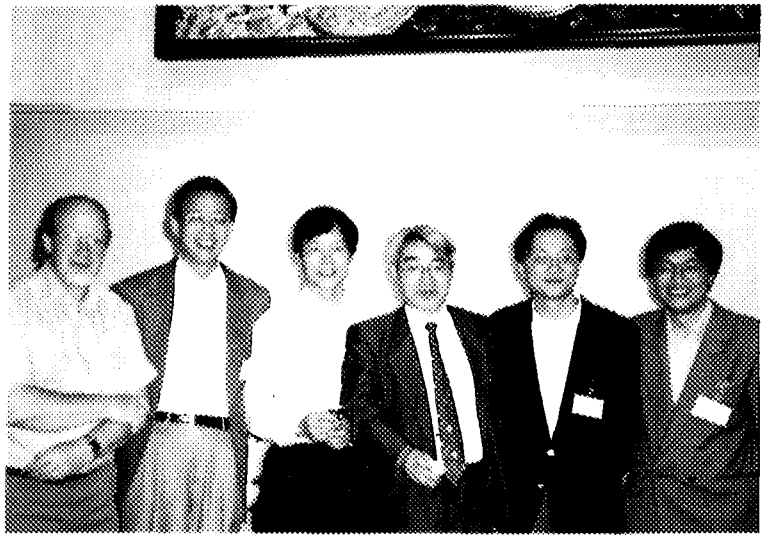

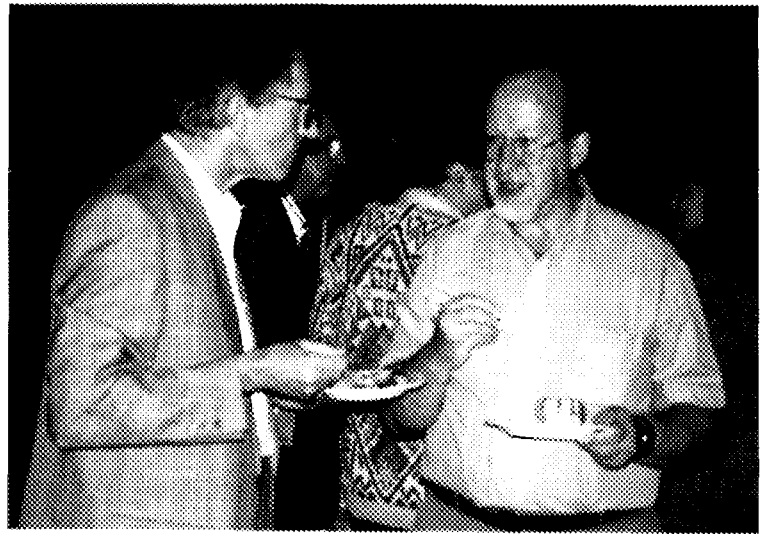

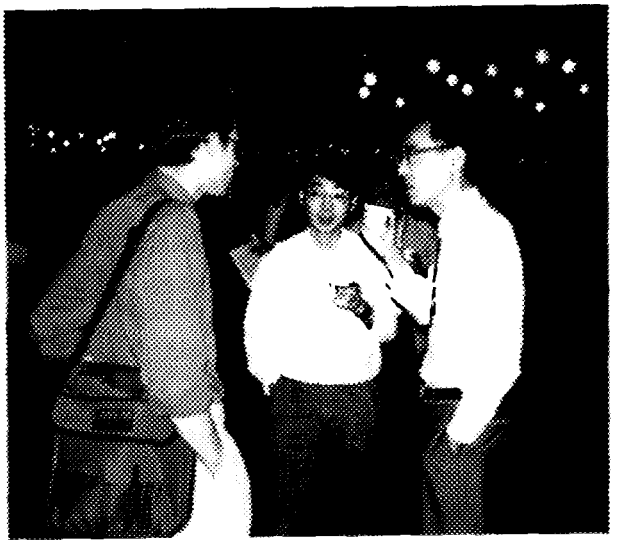

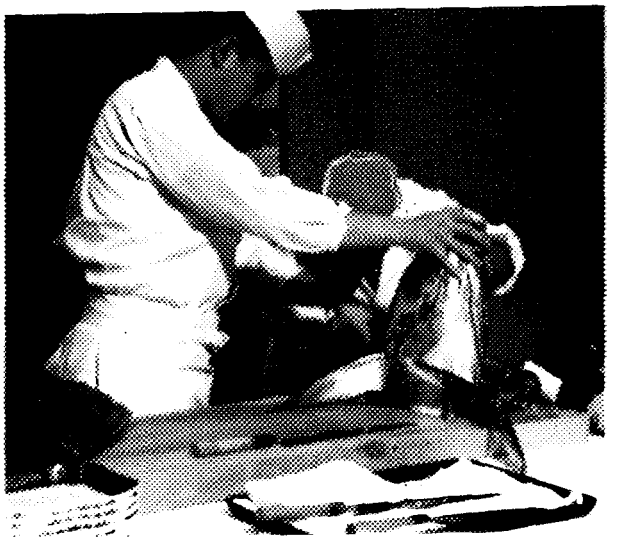

Foreword

The International Workshop on Collective Effects and Impedance for B-Factories (CEIBA95) was held from 12 to 17 June, 1995 in Tsukuba, Japan, hosted by KEK. About 90 participants (30 from the oversees and 60 from KEK) have attended the Workshop.

The aim of the Workshop was to bring experts of single-beam collective effects and impedance issues from all over the world to one place, with the goal of identifying problems in B-factories and finding solutions to them or suggesting future theoretical and experimental studies. These issues include:

- coupled bunch instabilities due to photo-electrons, DIP and cavity HOMs
- bunch lengthening
- ion related instabilities (ion trapping and fast ion instability)
- transverse mode-coupling instability
- damped rf cavities
- feedback systems and kickers
- wake fields and heat deposition from various beamline elements (BPM, bellows, IR masks etc.)
- trapped modes in small discontinuity
- pumping slots and power flow to pumping chamber
- microwave absorbers

Most of findings of the Workshop have provided valuable guidance to the design of other types of high intensity machines as well, such as the Beijing Tau-Charm Factory and DAϕNE Phi-Factory.

The Workshop was started with a half day plenary session, presenting the overall pictures of up-to-date B-factory designs. It was immediately followed by the working session, consisting of three working groups on single-beam collective effects, impedance and RF/Feedback, respectively. The Workshop was concluded by a final plenary session, summarizing the findings of the Workshop.

This proceedings cover most of talks presented in the plenary and working group sessions of the Workshop. There have been great progresses made in these issues since the last B-Factory Workshop in 1992 at KEK. Particularly, the discovery of new types of beam instabilities cast a great enthusiasm among the participants and stimulated people to join the theoretical work or to propose experimental studies to confirm their existence. The editor hopes that the proceedings will encourage more people to join the effort for further development.

Finally, I would like to express my thanks to Prof. Kurokawa for his leadership in the organizing committee of this Workshop.

Yong Ho Chin
Editor

TABLE OF CONTENTS

PLENARY SESSION

IMPEDANCE WORKING GROUP

COLLECTIVE EFFECTS WORKING GROUP

RF - FEEDBACK WORKING GROUP

SUMMARY SESSION

LIST OF PARTICIPANTS

PLENARY SESSION

Impedance and Collective Effects in the KEKB

Yong Ho Chin and Katsunobu Oide

KEK, 1-1 Oho, Tsukuba-shi, Ibaraki-ken, 305, Japan

ABSTRACT

This paper focuses on beam instabilities due to single-beam collective effects, impedances from various beamline elements, ion trapping, photo-electrons, and other issues in the KEKB. We will also discuss the power deposition generated by a beam in the form of the Higher-Order-Mode (HOM) losses by interacting with its surroundings.

1 INTRODUCTION

KEKB is an asymmetric e^+e^- collider at 8x3.5GeV energy for study of B-meson physics[1]. A short bunch σ_z =4 mm and the large beam currents (2.6 A in Low Energy Ring (LER) and 1.1A in the High Energy Ring (HER)) for a very high luminosity of 10^{34} $cm^{-1}s^{-1}$ require serious efforts to minimize the coupling impedance of beamline components in the design stage in order to avoid beam instabilities and to reduce wall heating. In fact, as the result of the successful reduction of the coupling impedance at KEKB, the conventional beam instabilities based on the beam-chamber interaction can now be suppressed by the radiation damping or by the feedback system. The main concern, in turn, is the new types of beam instabilities such as the fast ion instability and the photo-electron instability[1] which are caused by effects of ionized gas and photo-electrons, respectively. Some theoretical investigations have been done. They are discussed in the instability section of this paper.

The short bunch can pick up the impedance at very high frequency ($\approx$ 20 GHz) and thus may create an enormous heat deposition by the HOM. Our estimate shows that the HOM power of about 200 kW will be created in the arc section of LER by various beamline components. Its frequency spectrum has a broad peak around 10GHz. Assuming the energy dissipation only in the chamber wall, the HOM power can run typically for about 300 m along the ring in an e-folding attenuation time. It implies that the HOM power of about 20kW can pass at any point in the ring. The leakage of even a fractional part of this HOM power into beamline components such as bellows may cause a catastrophically large heat deposition in their inner structures. A particular worry is the Interaction Point (IP) where the maximum tolerable heat deposition of the IP chamber is only 200 W. It arises a serious concern whether we should protect these components from the HOM power penetration. Several different types of HOM power absorbers have been studied to protect the beamline components at the arc and the IP chamber, respectively. Their structures and performance are reviewed after the impedance section.

2 IMPEDANCE

In this section, we summarize our estimate of impedances and loss factors of various beamline components. Most of them are small discontinuities in the vacuum chamber wall and

produce inductive impedances. Their wake potentials are almost a derivative of the delta-function, and therefore their loss factors are mostly negligible. Among impedance-generating elements of the rings, the largest contributors are RF cavities, the resistive wall, the IR chamber (including two recombination chambers at both ends), masks at arc, and bellows (because of their large numbers).

2.1 ARES RF Cavities

We proceed our estimate for RF cavity contributions with the assumption that the ARES cavities will be employed in the final design. Then, 20 and 40 cells of the ARES cavities will be needed in the LER and HER, respectively, to compensate the synchrotron radiation and HOM power losses, as well as to satisfy the requirement for the short bunch. A schematic view of ARES cavity is shown in Fig. 1. Using the program ABCI[2], we have estimated that the main body of the ARES cavity produces a loss factor of 0.529 V/pC at bunch length σ_z = 4 mm. Cavities are connected to each other by the vacuum chamber with a diameter of 145 mm through the straight section. They are connected to the beam chamber (diameter=100 mm) only at both ends of the cavity section with 100 mm long tapers. Each taper provides an additional loss factor of 0.363 V/pC.

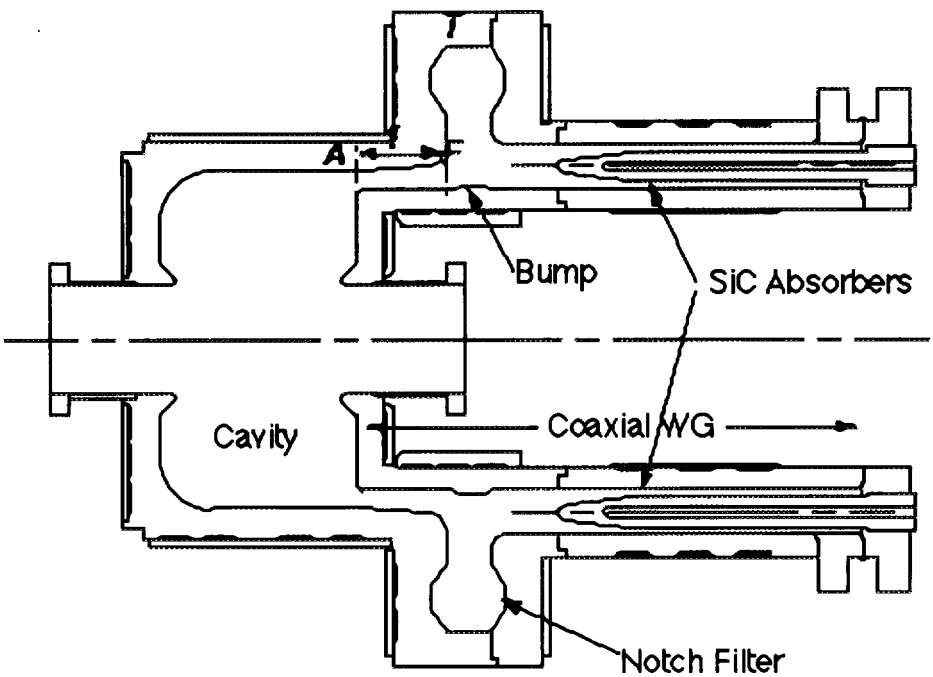

Figure 1: Schematic view of the KEKB HOM-damped cavity.

2.2 Resistive-Wall

The material of the KEKB beam chamber was chosen to be copper because of its low photon-induced gas desorption coefficient, its high thermal conductivity, and its large photon absorption coefficient. Its high electrical conductivity also helps to reduce the resistive-wall impedance. Nevertheless, this is still the dominant source of transverse impedance for the

coupled-bunch instability. The total transverse resistive-wall impedance of the circular pipe with an inner radius b is given by

$$Z_{TRW} = Z_0(\mathrm{sgn}(\omega) - i)\frac{\delta R}{b^3} \tag{1}$$

where $Z_0(\cong 377\Omega)$ is the characteristic impedance of vacuum, δ is the skin depth, R is the average radius of the ring, and $\mathrm{sgn}(\omega)$ denotes the sign of ω. For the LER vacuum chamber ($b \cong 50\,\mathrm{mm}$), Eq. (1) gives the resistive-wall impedance of 0.3MΩ/m at the revolution frequency 100 kHz, while the impedance decreases to 2kΩ/m at the cutoff frequency 2.3 GHz of the chamber. The HER vacuum chamber of racetrack shape may be approximated by a circular one with a radius of 25 mm.

2.3 Masks at Arc

Each bellows has a mask (5 mm high) located in its front to be shielded from the synchrotron radiation from a nearby bending magnet. There are about 1000 bellows (one bellows on both sides of each quadrupole magnet. There will be no mask for BPMs). The cross section of the mask in the medium plane is shown in Fig. 2. For accurate calculations of wake potentials and loss factors, a 3-D program MASK30 has been developed which solves the Maxwell equations directly in time domain. Using this code, we have found that the total longitudinal impedance of 1000 masks is

$$\mathrm{Im}\left[\frac{Z(\omega)}{n}\right] = 2.8\times10^{-3}\Omega \tag{2}$$

where n expresses the frequency ω divided by the revolution frequency ω_0 ($\omega = n\omega_0$). The total loss factor is k_L = 4.6V/pC which corresponds to the total HOM power of 62 kW in the LER.

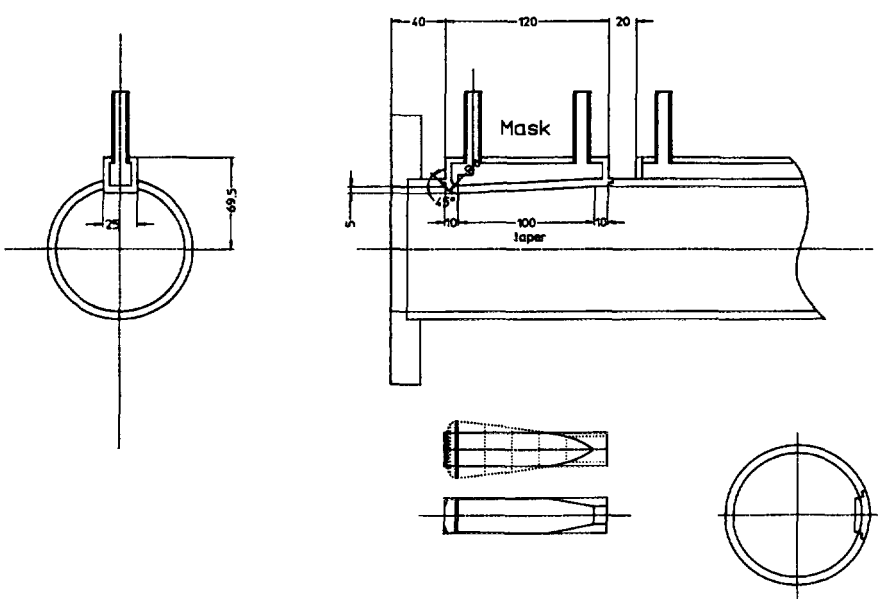

Figure 2: Mask at arc.

2.4 Pumping Slots

The current design of pumping slots adopts the so-called "hidden holes" structure similar to those of HERA and PEP-II. The structure of the LER pumping port and slots are illustrated in Fig. 3. A slot has a rectangular shape with rounded edges, which is long in the beam-axis direction (100 mm long, 4 mm wide). The slot is patched on the pumping chamber side by a rectangular grid. They help to prevent the microwave power generated somewhere else from penetrating through the slots to the pumping chamber and then depositing the energy in the NEG pumps. There are analytic formulae for impedance and loss factor of such a narrow slot with length l and width w by Kurennoy and Chin[3]. The formula for inductive impedance can be written at low frequency (until the wavelength becomes comparable to the slot width) as

$$\mathrm{Im}[Z(\omega)] \approx -0.1334 Z_0 \frac{\omega}{c} \cdot \frac{w^3}{4\pi^2 b^2} \tag{3}$$

where c is the speed of light. The thickness correction to the above formula was studied by Gluckstern[4]. It tends to reduce the impedance by 44% compared with that for zero thickness case. The total impedance of the pumping slots at arc (there are 10 slots per port and there are 1800 ports in total) with thickness correction is

$$\mathrm{Im}\left[\frac{Z(\omega)}{n}\right] = 1.1 \times 10^{-3}\,\Omega \tag{4}$$

The total loss factor was calculated to be 0.37 V/pC. There will be additional contributions from pumping slots in the straight section. Among them, only the ones at the wiggler section have been designed. A rough estimate shows that they will increase the above values for the impedance and the loss factor by about 10%.

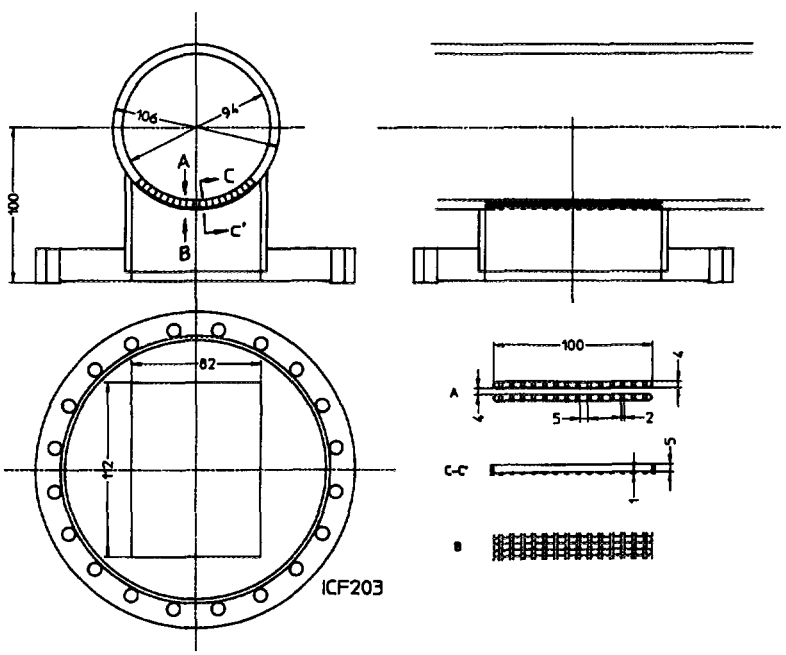

Figure 3: Structure of the LER pumping port and slots.

2.5 BPMs

The annular gap (or groove) in a BPM (see Fig. 4) between the button electrode and the supporting beam chamber can be approximated by a regular octagon. The impedance of a BPM can be thus calculated from the same formula for a narrow slot considering it as a combination of eight narrow slots (two transverse, two longitudinal, and four tilted)[5]. If we neglect small contributions from the longitudinal slots, and consider four tilted slots as two transverse ones, the impedance of the BPM becomes equivalent to that of the four transverse slots. For a transverse slot, the formula (3) is replaced by

$$\mathrm{Im}[Z(\omega)] \approx -Z_0 \frac{\omega}{c} \cdot \frac{\alpha_m}{4\pi^2 b^2} \tag{5}$$

where

$$\alpha_m = \frac{2}{3}\left(\frac{\pi}{4}\right)^2 \frac{a^3}{\ln\frac{2\pi a}{w} + \frac{\pi t}{2w} - \frac{7}{3}} \tag{6}$$

is the longitudinal magnetic polarizability. Other parameters are: a is the radius of the annular gap, w is the width of the gap, and t is the thickness the chamber wall. In our case, they are numerically, $a = 6.5$ mm, w=1 mm, and t =1 mm. For 400 four-button BPMs, the total inductive impedance is

$$\mathrm{Im}\left[\frac{Z(\omega)}{n}\right] = 1.3 \times 10^{-4}\,\Omega \tag{7}$$

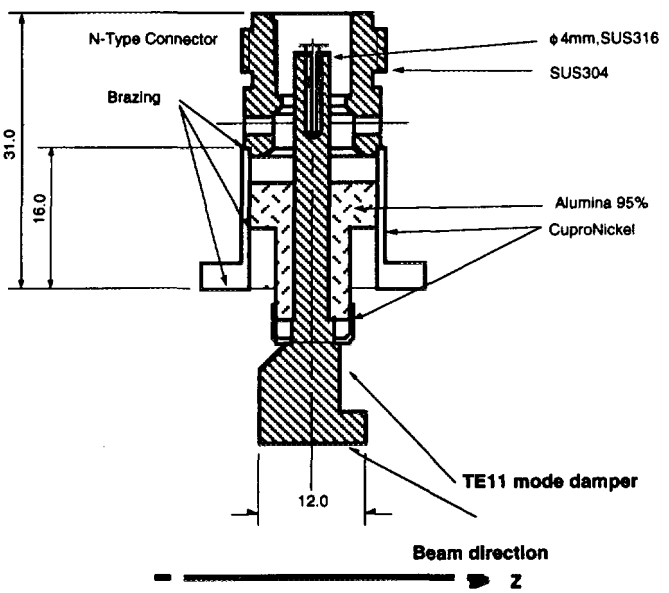

Figure 4: BPM electrode for KEKB.

The total loss factor of BPMs was computed using the T3 code of MAFIA and found to be k_L =0.79V/pC.

There is a theory[6] which predicts that small holes or slots in the beam chamber can create localized trapped modes in their vicinity. These trapped modes can give rise to sharply peaked impedances slightly below the cutoff frequencies of the corresponding propagating modes in the beam chamber. These narrow resonances may drive coupled-bunch instabilities. We have found using MAFIA that there is indeed such a trapped TE11 mode localizing around the electrode at 6.5 GHz. But, this mode radiates its power into the beam chamber and decays out quickly. The shunt impedance is only

$$R = 2.9\Omega \tag{8}$$

per BPM with four buttons. The Q-value is about 40. The growth time due to 400 BPMs turns out to be slower than the radiation damping time by a factor of 10.

2.6 Mask at IP

There are four masks (two large and two small) on both side of the beryllium chamber at the interaction point (IP) to shield it from the direct synchrotron radiation. Figure 5 shows their geometry.

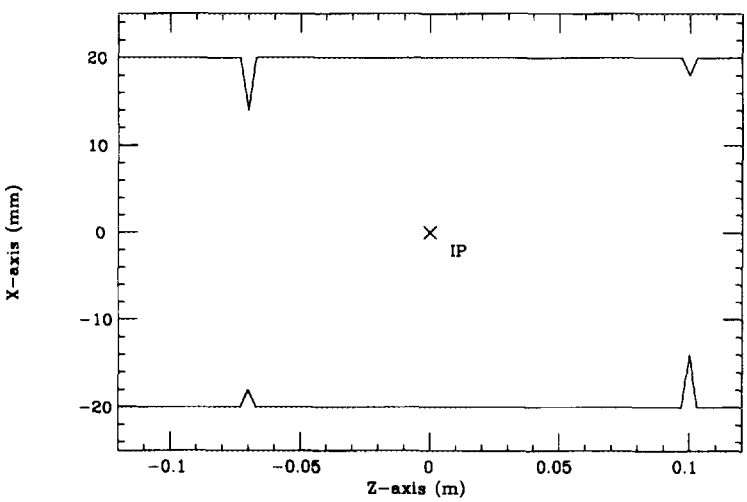

Figure 5: Mask at the IP.

The loss factor due to these masks has been calculated using the code MASK30 and was found to be k_L =0.08V/pC. This value is about one-fourth of that obtained by ABCI using the axi-symmetrical model. The ratio of the two loss factors coincides with the ratio of the opening angle of the IP mask from the beam axis (about 90 degree) to that of the entire circle. Based on this observation, we have learned that we can make a rough estimate of the loss factor for a 3-D structure by multiplying the opening angle ratio to results for its axis-symmetrical model.

Not all of the power generated at the IP will be deposited there. It depends on Q-values of modes excited between the masks. The beam chamber at the IP has the cutoff frequency at 6.36 GHz, and the tips of the taller masks creates another cutoff frequency at 8.20 GHz. It was estimated using the MASK30 code that if the wake fields between these two frequencies are trapped, the deposited power by two (an electron and a positron) bunches at the IP will be 240W, which is 20% more than the design tolerance of 200 W for the beryllium chamber. However, a careful examination with use of an axis-symmetrical model for the IP masks showed that actual Q-values of the modes between 6.36 - 8.20 GHz are at most 70, which is much smaller than $Q \approx 1.4\times10^4$ determined by the finite conductivity of the beryllium chamber. This is because the radius of the beam chamber remains the same inside and outside of the IP region separated by the masks, and thus the modes can escape to the outside region by making a bridge over the masks. Consequently, less than 0.5% ($=70/1.4\times10^4$) of the HOM power created at the IP is deposited there ($P \le 1.2$W). Even if these modes are resonant with the bunch spacing causing a build-up of wake fields, the maximum enhancement factor for a mode on the resonance is only

$$D_{max} = \frac{4Qc}{\omega_m s_b} \approx 3.5 \tag{9}$$

where ω_m is a typical mode frequency and s_b is the bunch spacing. Therefore, the maximum power deposition is $D_{max}P \le 4.2$W. The actual 3-D masks at the IP has a more open structure than the axis-symmetrical model, and thus the power deposition might be even smaller.

A more serious problem may be a dissipation of the HOM power generated at other parts of the IR chamber and propagating to the IP region. As will be seen in the next two subsections, the HOM power of about 7 kW will be created in the entire IR region. Even a 3% deposition out of 7kW exceeds the tolerable power of beryllium IP chamber (200W). It implies that we may need HOM absorbers to stop the flow of HOM power to the IP. We are going to discuss about such a HOM absorber scheme in the section 4.

2.7 IR Chamber

The experimental chamber at the IR makes two large shallow tapers. Its layout is sketched in Fig. 6. Its impedance has been calculated using ABCI and found to be mostly inductive. It is

$$\mathrm{Im}\left[\frac{Z(\omega)}{n}\right] = 1.0\times10^{-3}\Omega \tag{10}$$

The loss factor without the contribution from the IP masks is $k_L = 0.29$V/pC which corresponds to the HOM power loss of 4 kW. This power deposition as well as the power generated at the recombination chambers must be taken care of by e.g., putting an absorber in the chambers.

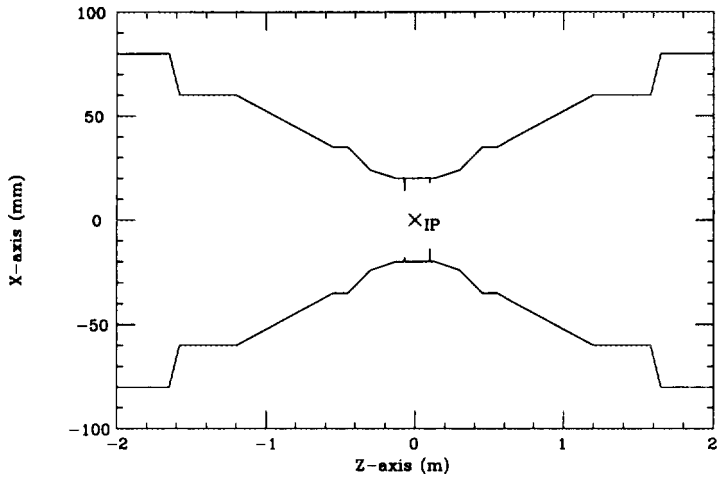

Figure 6: Layout of the IR chamber.

2.8 Y-shaped Recombination Chambers

The LER and HER chambers are combined to a single chamber on both sides of the IP (about 3 m away). The impedance and loss factors of two recombination chambers were computed using MAFIA. Their combined loss factor is 0.22 V/pC, which corresponds to the HOM power loss of 3 kW due to the low energy beam.

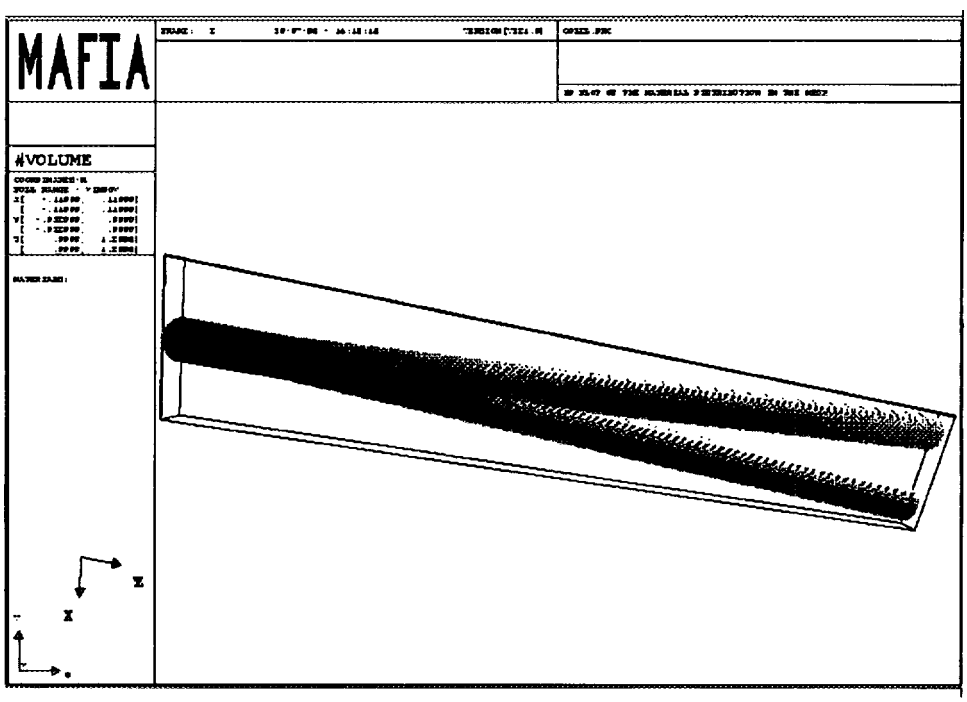

Figure 7: Layout of the recombination chambers.

2.9 Bellows

As explained in the subsection for the masks at arc, there are about 1000 shielded bellows in both rings (one bellows on both sides of every quadrupole). We have adopted the so called sliding-finger structure for bellows. Their layout in the LER is sketched in Fig. 8. The bellows in the HER have a similar structure. These bellows produce predominantly inductive impedance. Their impedance has been calculated with use of ABCI. The imaginary part of the total impedance for 1000 bellows in the LER ring are

$$\mathrm{Im}\left[\frac{Z(\omega)}{n}\right] = 4.23\times10^{-3}\Omega \qquad (11)$$

and the total loss factor is k_L =2.5V/pC. They are $\mathrm{Im}[Z/n] = 0.8\times10^{-2}\Omega$ and k_L =5.0V/pC in the HER.

Additional impedance is generated by the slits between the sliding fingers of the bellows. Using the same formula for a narrow slot, we found that their contributions are negligible.

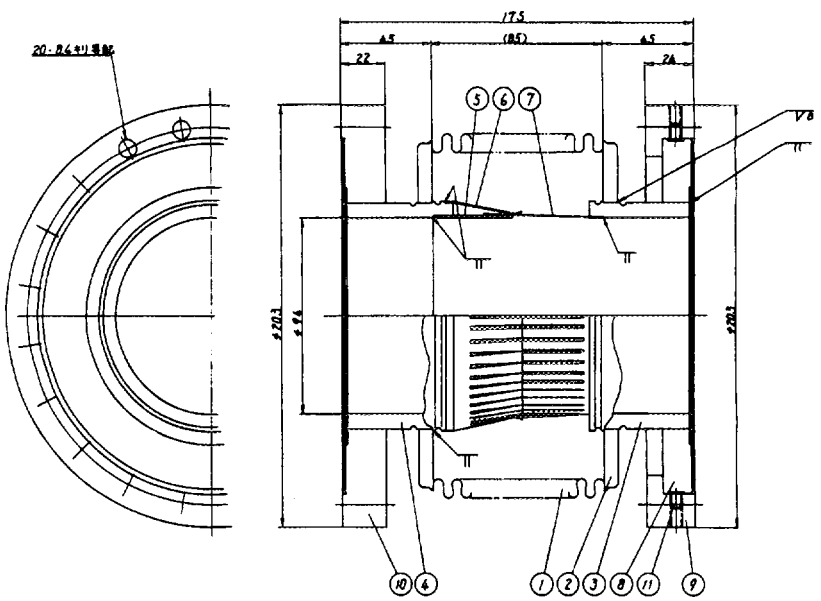

Figure 8: A schematic drawing of a Type-B LER bellows.

2.10 Summary of Impedance Section

The inductive impedances and the loss factors of the individual elements in the LER are tabulated in Table 1. The total HOM power deposition in the LER is P= 327 kW. In the HER, the total inductive impedance would be comparable to that of the LER. The total loss factor in the HER is larger than that of the LER 11.3 V/pC due to additional 20 RF cavities, leading to 35.5 V/pC. The corresponding total HOM power deposition is 90 kW.

Table 1: LER impedance budget and HOM power loss budget.

Components	Number	Inductive impedance Z/n (Ω)	Loss factor (V/pC)	HOM power (kW)
Cavities	20		11.3	153
Resistive-wall	3016 m	5.2×10^{-3} at 2.4GHz	4.0	54
Masks at arc	1000 (5mm)	2.8×10^{-3}	4.6	62
Pumping slots	10×1800	1.1×10^{-4}	0.37	5.5
BPMs	4×400	1.3×10^{-4}	0.79	10.7
Mask at IP	1	≅0.0	0.08	1.1
IR chamber	1	1.0×10^{-3}	0.29	4
Y-shaped chambers	2	-8.0×10^{-4}	0.22	3
Bellows (1mm)	1000	4.23×10^{-3}	2.5	34
Total		0.015	24.2	327

3 HOM ABSORBERS

The Higher-Order-Mode (HOM) power deposition is one of most crucial problems in the KEK B-factory. As stated in the introduction, the HOM power can run typically for about 300 m along the ring in an e-folding attenuation time. This means that the HOM power of about 20kW can pass at any point in the ring. Two crotches in the IR and the IR chamber itself create HOM powers of 3kW and 4kW, respectively. Most of them can drift through the double-walled beryllium IP chamber. It is difficult to estimate how much power will be deposited in the IP chamber, but even a 3% deposition out of 7kW exceeds the tolerable power of beryllium IP chamber (200W) determined by the thermal stress at the Si detectors. In addition, there will be more power flow from the nearby arc section to the IP. Since the IR chamber has the largest aperture at the crotches, some HOM modes may be trapped and become a cause of coupled-bunch instabilities.

Two and one types of HOM power absorbers have been studied for the arc sections and the IR, respectively. It is not yet decided whether HOM absorbers will be implemented at the entire are section, since no beamline components have been found so far in which the heat deposition due to the HOM power leakage amounts to an intolerable level. It is, however, strongly expected to put two HOM absorbers in the IR between the crotches and the IP, and several HOM absorbers in the adjacent straight sections on both sides of IR to stop the HOM power flow from the arc sections to the IP. We will review these absorbers below.

3.1 HOM Absorbers at Arc

There are three basic requirements for the performance of HOM absorbers:

1. high absorption efficiency
2. small loss factor
3. "self-cleaning function" (i.e., to leave a little or no HOM power created by itself inside the chamber).

The requirements (1) and (2) tend to conflict to each other and it is necessary to find an optimal point between them. Assuming that several absorbers are installed at every 300 m (corresponding to about one-tenth of the ring) at the arc, an absorption efficiency of 10-20% makes the total HOM power absorbed by the absorbers comparable to that lost on the chamber wall. From the outgassing point of view, the absorption efficiency of 30-40% would be the maximum. A typical loss factor per absorber in mind is around 0.1V/pC, which increases the total HOM power by about 50% if several tens of absorbers are installed into the LER.

3.1.1 Radial Line + Coaxial Pipe Type

This type of HOM absorber has been studied by the KEK RF group to be used for choke-mode cavities[1]. Figure 9 shows its schematic view. A radial line is inserted into a disconnected vacuum chamber and then bended to guide fields to an attached coaxial pipe where an absorbing material is housed. Merits of this type are (1) there is no cutoff frequency for electromagnetic fields to be absorbed out (2) the absorbing material is not directly exposed to a beam and thus its fragments or dust when cracked will not disturb the beam. It is, however, foreseen that the absorbing efficiency will be limited to an order of 10% due to a mismatching of impedance at the entrance of the radial line. A larger gap size at the entrance will improve the matching at the cost of a larger loss factor.

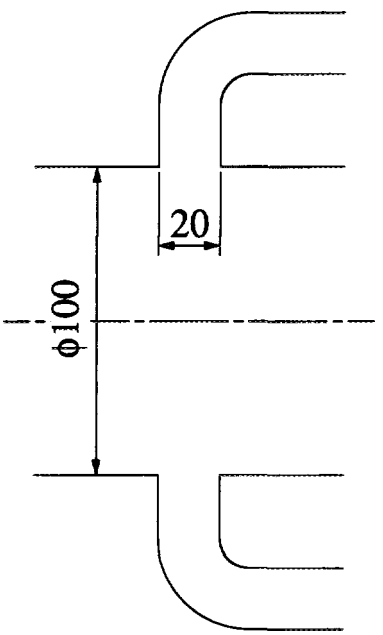

Figure 9: Schematic view of the radial line + coaxial pipe type.

The absorbing efficiency has been computed as a function of frequency up to 20 GHz using the HFSS code. The HOM power is assumed to propagate inside the radial line as either TEM, TM01, or TM02 modes. The result is shown in Fig.10. It can be seen that a good absorbing efficiency in a range of 15% is obtained in the wide range of frequency. The loss factor was calculated using ABCI and found to be 0.2V/pC.

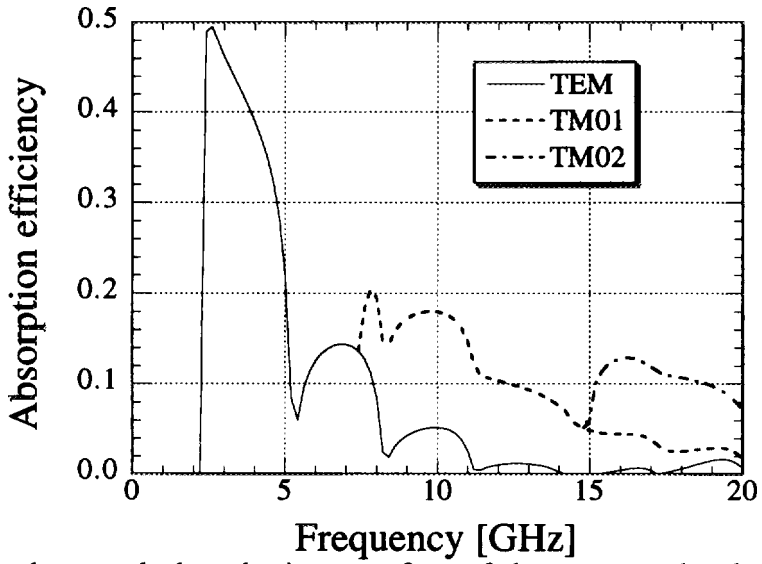

Figure 10: Absorption efficiency of the radial line + coaxial pipe type.

3.1.2 Tilted Slots Type

A conventional (hollow) cylindrical absorber attached to the inner surface of the vacuum chamber can offer a large power absorption, while tending to have a large loss factor as well. A too large absorption efficiency (50-100%) is not desirable in the present case, since it may allow a power deposition in a single absorber more than the maximum tolerance and may cause the heat breakdown and the outgas problems. A way to control both the absorption efficiency and the loss factor is to partially screen the surface of the cylinder by the copper coating so that the absorbing material is exposed to a beam only through tilted slots placed azimuthally along the vacuum chamber. See Fig. 11.

The tilting angle should be determined for an optimal coupling with both TM and TE modes (30-45 degrees are found to be a good angles). The geometrical parameters assumed for computational study are: a 94mm inner diameter with 10 slots tilted by 45 degrees, each of which is 5cm long and 1cm wide. CERASIC-B (a brandname of SiC) is assumed as an absorbing material. We have computed the absorption efficiency for TE11 and TM01 modes at 3 and 8 GHz using the MAFIA code. The results are summarized in Table 2.
From plots of the power distribution on the absorbing material, which are not shown here, we have found that the power is almost uniformly deposited along the beam axis in the TE11 mode. On the other hand, the power deposition of TM01 mode takes place mainly in the upstream of the absorber (the side closer to the source of the power). The loss factor was computed by MAFIA and found to be 0.16V/pC.

The absorption efficiency for the TE11 mode may be improved by decreasing the tilting angle, say, to 30 degrees, at the cost of reducing that for the TM01 mode. The loss factor can be also reduced (the analytical estimate[3] for the 30 degrees tilting case gives the loss factor to be 0.1 V/pC).

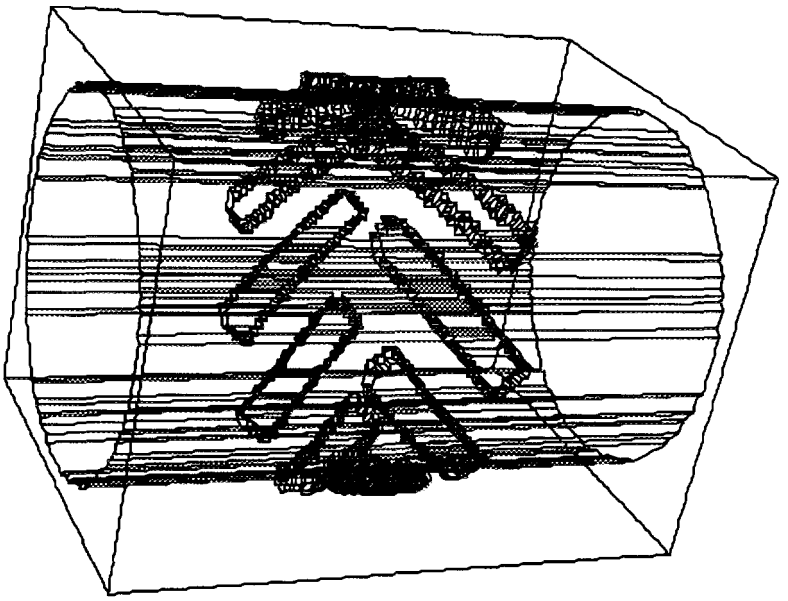

Figure 11: Illustration of the tilted slots type.

Table 2: Absorption efficiency of the tilted slots type for TE11 and TM01 modes.

Frequency (GHz)	*Absorption TE11*	*efficiency (%) TM01*
3	8	13
8	6	13

3.2 HOM Absorber at IR

As stated in the impedance section, the HOM power of about 3kW will be produced by two crotches on the both sides of IR. The tapered IR chamber itself will create another 4kW. In order to stop the power flow to the IP chamber and reduce Q-values of trapped modes near the crotches, a HOM power absorber is planned to be installed on each side of the IR between the crotches and the IP chamber. In contrast to the HOM absorbers at the arc, a large absorption efficiency (70-100%) is required even at the cost of a large loss factor to stop the power flow as much as possible. Our solution is a simple SiC cylinder attached to the inner surface of the copper chamber. Water channels run through the outer surface of the copper chamber for cooling. A proto-type of the absorber has been fabricated by the RF group and was installed to the Tristan Accumulation Ring (AR) in April, 1996, in the upstream of the ARES cavities for a beam test. Its schematic view is illustrated in Fig. 12.

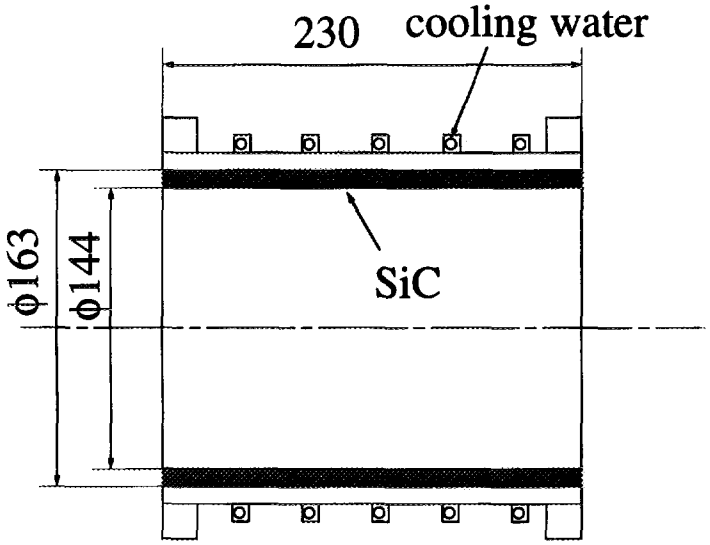

Figure 12: Illustration of the HOM power absorber at IR.

Although the ferrite has a similar power absorption performance as SiC, SiC is preferable for a larger heat conductivity (CERASIC-B: 100W/mK, ferrite: 6.3W/mK) and a smaller outgas rate by an order of magnitude.

The absorption rate was calculated using the HFSS code for the structure with the diameter of 100 mm and the length of 100 mm for different SiC thickness. The results are plotted in Fig. 13. It can be seen that the absorption rate is rather insensitive to the SiC thickness and remains around 70% in the frequency range of 5-15GHz. The loss factor was calculated to be 0.5V/pC per absorber using the analytical formula. This corresponds to an additional 7kW×2=14kW power. It leads that the total HOM power to be taken care by the two absorbers hikes to 21kW (or 10kW by each).

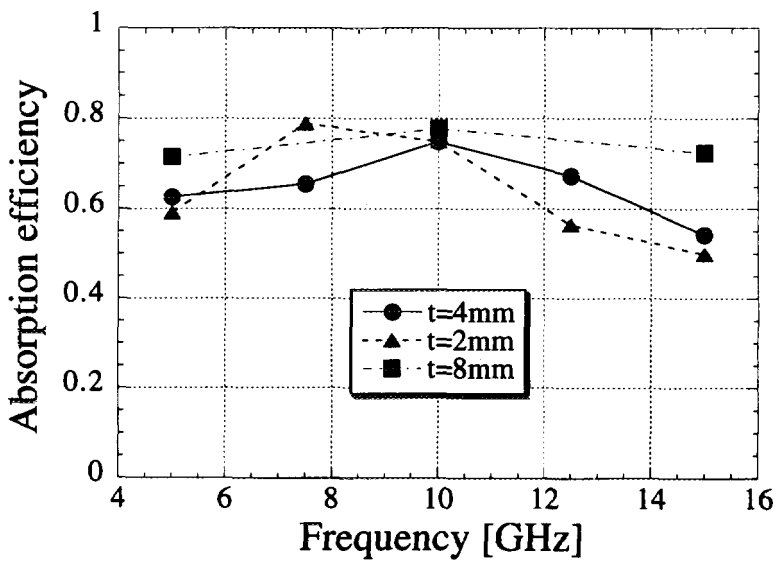

Figure 13: Absorption efficiency of the cylindrical HOM absorber at the IR.

We have also calculated the temperature rise in the SiC surface relative to the cooling water temperature for various absorbed power. The heating is assumed to take place uniformly inside the SiC plate and the copper conductor. We have found that the relative temperature rise is about 30 degrees for the power absorption of 10kW. Therefore, the temperature rise and the resulting outgas from the SiC should cause no problem.

3.3 Conclusions of HOM Absorbers Section

We have studied two types of HOM absorbers for the arc sections of KEKB ring. The calculation results using the HFSS and MAFIA codes demonstrate the proof of principle that they can fulfill our requirements. Namely, both of them offer relatively good absorption efficiencies of 10-15% in the wide range of frequency (5-15 GHz). The loss factors are found to be around 0.1-0.2V/pC per absorber. These values are slightly larger than the design goal, but, still stays in the acceptable range. The optimization of their geometry are in progress. RF power test of full size models should be conducted at the AR in a near future.

The design of HOM absorber at the IR is more straightforward. A conventional cylindrical SiC absorber fits our demands and the computer simulation results show that it can handle the HOM power more than required, while the outgas rate is well under control. Its proto-type was installed into the AR next to the ARES cavities and a series of beam tests are under way.

4 CONVENTIONAL BEAM INSTABILITIES

In this section, we review our predictions of conventional singe-bunch instabilities and coupled-bunch instabilities due to the beam-chamber interaction. As mentioned in the beginning, the single-bunch instabilities are expected to impose no fundamental limitation on the stored current, since the bunch current is relatively low compared with other large electron rings. However, the requirement of the short bunch (σ_z =4 mm) demands a careful attention at any possible causes for deviation from the nominal value. The transient ion problem and coupled-bunch instabilities due to photo-electrons will be discussed separately in the sections 5.

4.1 Bunch Lengthening

There are two mechanisms to alter the bunch length from the nominal value. One is the potential-well distortion of the stationary bunch distribution due to the longitudinal wake potential. The deformed bunch distribution can be calculated by solving the Haissinski equation. The bunch can be either lengthened or shortened depending on the type of the wake potential. Another mechanism is the microwave instability and has a clear threshold current for the onset of the instability.

Oide and Yokoya have developed a theory to include both the potential-well distortion effect and the microwave instability[7]. A program is now available to compute the bunch length according to their theory. Figure 14 shows the calculated bunch length in the LER as a function of the number of particles in a bunch, N_p. As can be seen, there is a constant bunch lengthening due to the potential-well distortion and the microwave instability takes off at $N_p=1.5\times10^{11}$, which is about four times larger than the proposed number of particles per bunch. At the design intensity, the bunch is lengthened only by 10%.

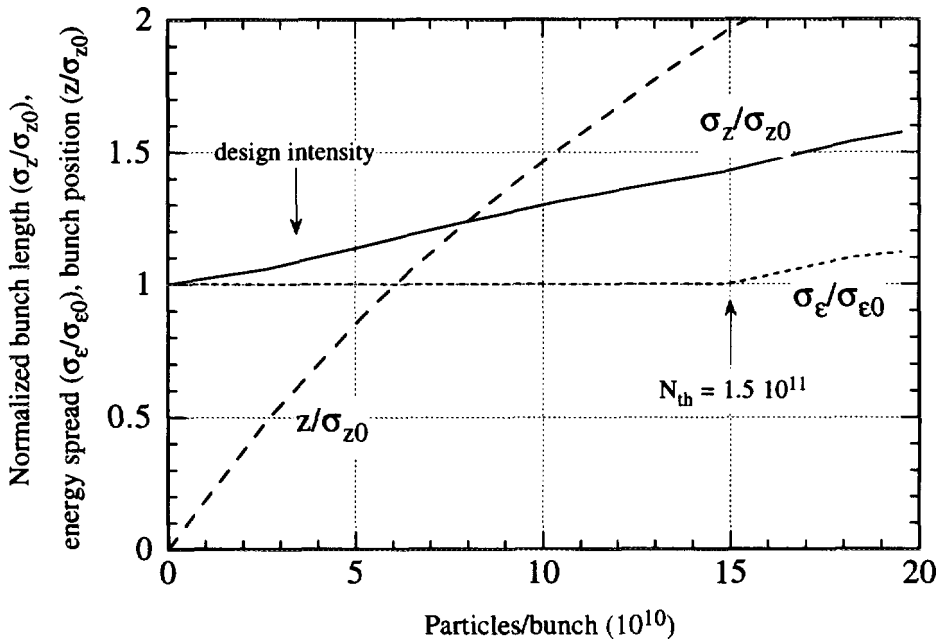

Figure 14: Bunch length and energy spread in the LER.

4.2 Transverse Mode-Coupling Instability

The transverse mode-couplinginstabilityis known to be responsible for limitingthe single-bunch current in large electron rings such as PEP[8] and LEP. This instability takes place when two head-tail modes (m=0 and m=-1 modes in most cases) share the same coherent frequencies. In a short bunch regime where the KEKB will be operated, the coherent frequency of the m=-1 mode keeps almost constant as a function of the bunch current, while that of the m=0 mode keeps descending until it meets with the m=-1 mode. Using the estimatedtransverse wake potentialand the averagedbeta function of10 m, we found that the coherent tune shift of the m=0 dipole mode is only ≈0.0002 at the design bunch current. This value is much smaller than the design value of the synchrotron tune (≈0.017). Thus, the transverse mode-coupling instability will not impose a serious threat on performance of the KEKB.

4.3 Conventional Coupled-Bunch Instabilities

The coupled-bunch instabilities due to high-Q structures such as RF cavities and the resistive-wall beam pipes are expected to be serious in the KEKB rings because of the unusually large beam current. We have adopted the so-called damped-cavity-structure to sufficiently lower the Q-valuesof higher-order parasitic modes, typically less than 100. As a result, the longitudinal growth due to RF cavities were reduced to a manageable level. Even the most unstable mode hasthe growth time (60 msec) longer than the radiation damping time of 20 msec in the LER with wiggler. Transversely, however, the growth time of the resistive-wall instability(≈5 msec) is far shorter than the radiationdamping time of 40 msec. This can be damped by our transverse feedback system which is capable to damp instabilities with growth time as short as 1 msec.

5 NEW TYPES OF BEAM INSTABILITIES

In the course of study on possible beam instabilities at KEKB, two new types of beam instabilities have been discovered by computer simulations. They are based on the interaction of a beam with either ionized gas or photo-electrons in the ring created by the synchrotron radiation. Simulation results predict that they have very short growth time and thus will impose the most serious limitation on the beam current.

5.1 Photo-Electron Instability

The vertical coupled-bunch instability has been observed in the PF at KEK for years when operated in a positron multi-bunch beam mode. This instability has a rather low threshold current and causes an increase of the vertical beam size. The spectrum of the betatron sideband shows a broadband distribution and suggests that this instability does not attribute to the HOM of the RF cavity or the vacuum components. A partial filling of a positron beam has little effect to suppress the instability [9].

A large number of photo-electrons are produced when the synchrotron radiation hits the inner wall of the beam tube. Typically, one photo-electron is created out of ten photons at PF. The following physical model has been proposed to explain the mysterious instability observed at PF in terms of the "beam-photo-electron interaction" [10]: photo-electrons created by the passage of a bunch receive attractive forces from the successive bunches and forms a crowd around the beam axis. While photo-electrons are constantly produced by passages of bunches, some of them hit the tube surface and get lost. After a while, the numbers of newly-born and died photo-electrons reach the equilibrium, and the distribution of photo-electrons becomes stationary when there is no coherent motion of bunches. That stationary distribution at the LER is shown in Fig. 15.

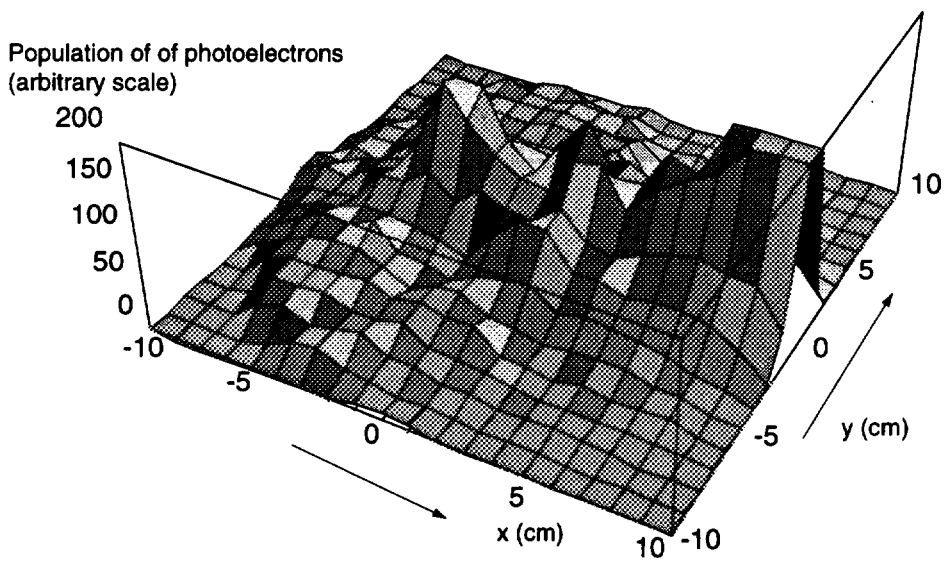

Figure 15: Stationary distribution of photo-electrons.

If a bunch passes through the stationary photo-electron distribution with an offset from the beam axis, the distribution is disturbed and affects the transverse motion of the following bunches. The coherent interaction between bunches and the crowd of photo-electrons can be formulated in the same manner as for the conventional beam instabilities using the concept of wake potential. One can accordingly derive a dispersion relation, the mode number and its frequency. The growth rate of the instability can be estimated from the imaginary part of the frequency shift. Figure 16 shows the vertical wake force simulated for beam current of 2.6A for different beam offsets in the LER. By using the wake force described in Fig. 16, the growth rate of the PEI can be calculated, as shown in Fig. 17. The maximum PEI growth rate of 2500 s^{-1} is much larger than the SR damping rate of 50 s^{-1}.

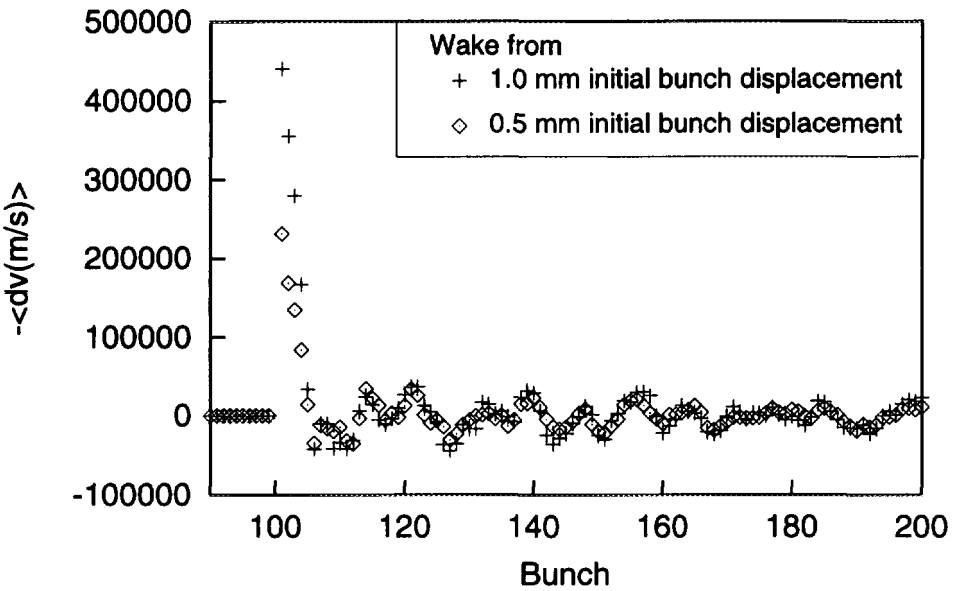

Figure 16: Vertical wake potential due to photo-electrons.

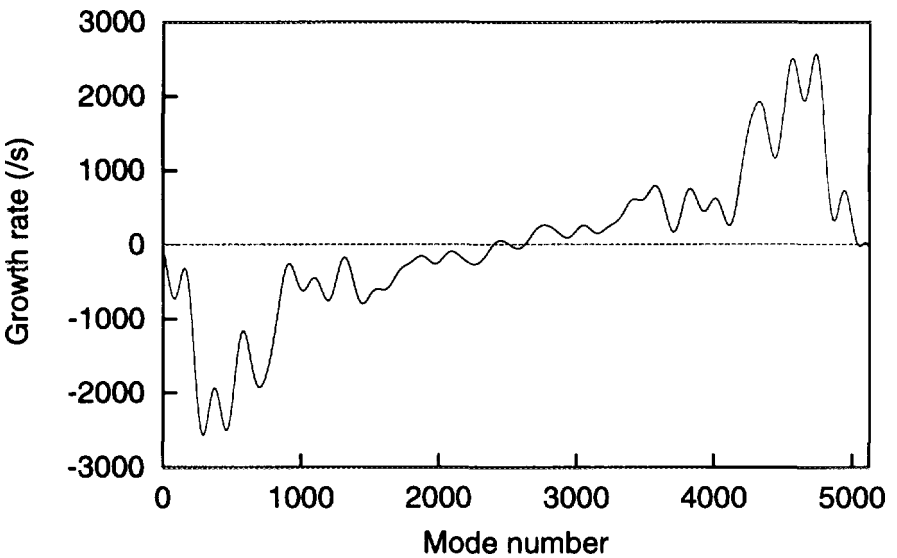

Figure 17: Growth rate of the vertical photo-electron instabilities versus the mode number.

So far, effects of the space charge among the photo-electrons and the image charge induced on the beam chamber are not included. The space charge force dissipates the photo-electrons to prevent their concentration in the vicinity of the beam axis. The image charge force tends to attract the photo-electrons back to the beam chamber to cut the flow of photo-electrons to the beam axis. Figures 18 and 19 show the distributions of photo-electrons without and with the effects of the space charge and the image charge, respectively. Contrary to the case without these effects, photo-electrons are mostly populated near the beam chamber where they are produced when these effects are included. Figure 20 shows the growth rate of PEI with the effects of the space charge and the image charge. The maximum growth rate is now reduced a little bit below 800 s^{-1} which can be damped by the transverse feed-back system.

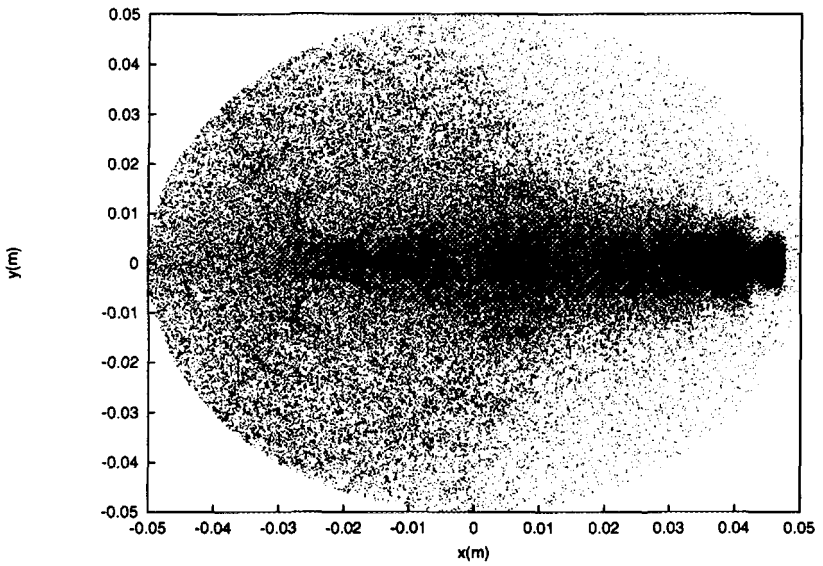

Figure 18: Distribution of photo-electrons inside the beam chamber when the effects of the space charge and the image charge are not included.

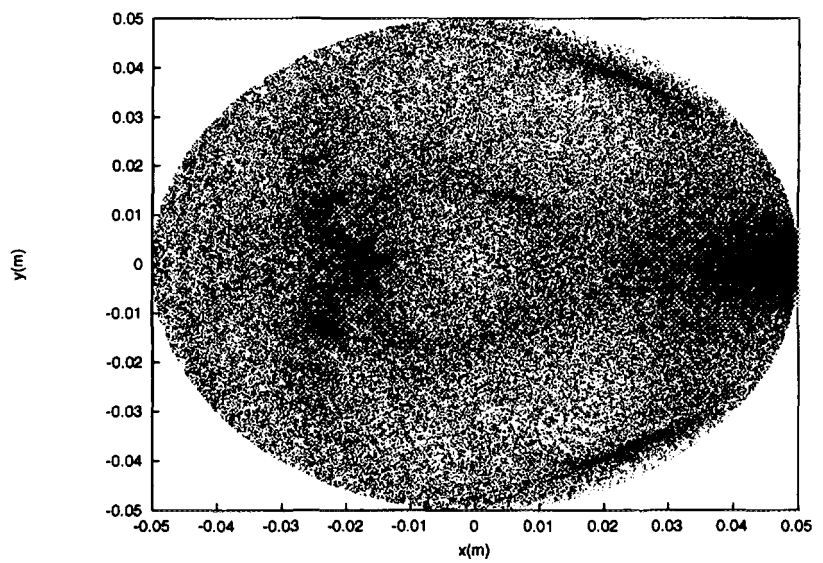

Figure 19: Distribution of photo-electrons inside the beam chamber when the effects of the space charge and the image charge are included.

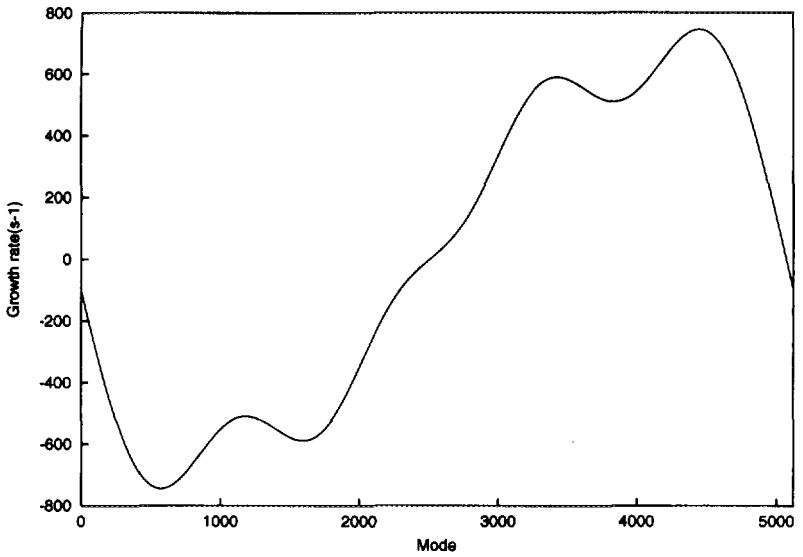

Figure 20: Growth rate of the vertical photo-electrons instabilities versus the mode number when the effects of the space charge and the image charge are included.

5.2 Fast Ion Instability

In any circular machines, the beam produces ions via ionization of residual gas molecules and through other processes. At an electron ring which stores many bunches, these positive ions are attracted towards the beam. After several turns the ions are concentrated near the beam orbit, and they can disturb the beam motion. This phenomenon, called ion trapping, has been studied for many years. One possible cure for this problem is a partial fill, i.e., to create a contiguous group of empty RF buckets that are unoccupied by the beam, and to let the ions drift away during this gap.

Recently it has been pointed out that a somewhat different process can also degrade the beam. This effect may be called transient ion trapping. With high intensity and low emittance beams, even if the ions eventually disappear in the bunch gap, they may cause a serious effect before disappearing through the following mechanism. While each bunch ionizes the residual gas, if a bunch is displaced from the design orbit, the ions left in space will be also displaced. Such ions execute off-centered oscillations in subsequent electron bunches, and they act as an amplifier for the electron oscillation.

Since the vertical emittance is much smaller than the horizontal one, the effect is more serious in the vertical plane. We assume that n_b electron bunches are followed by a gap which is long enough to sweep out the ions. This bunch pattern of n_b bunches plus a gap may be repeated several times over the ring. The first bunch of each train travels in a fresh residual gas without ions.

The linear theory has been developed to study the effect of ions. The amplitude blowup factor G according to the linear theory for the HER is plotted in Fig. 21 as a function of the number of turns for n_t various values of the number of electron bunches n_b. The residual gas is assumed to be CO with the pressure of 10^{-9} Torr. The e-folding time of the amplitude is about 70 turns for n_b =500 ($\propto n_b^2$) although the growth with respect to n_t is not exponential.

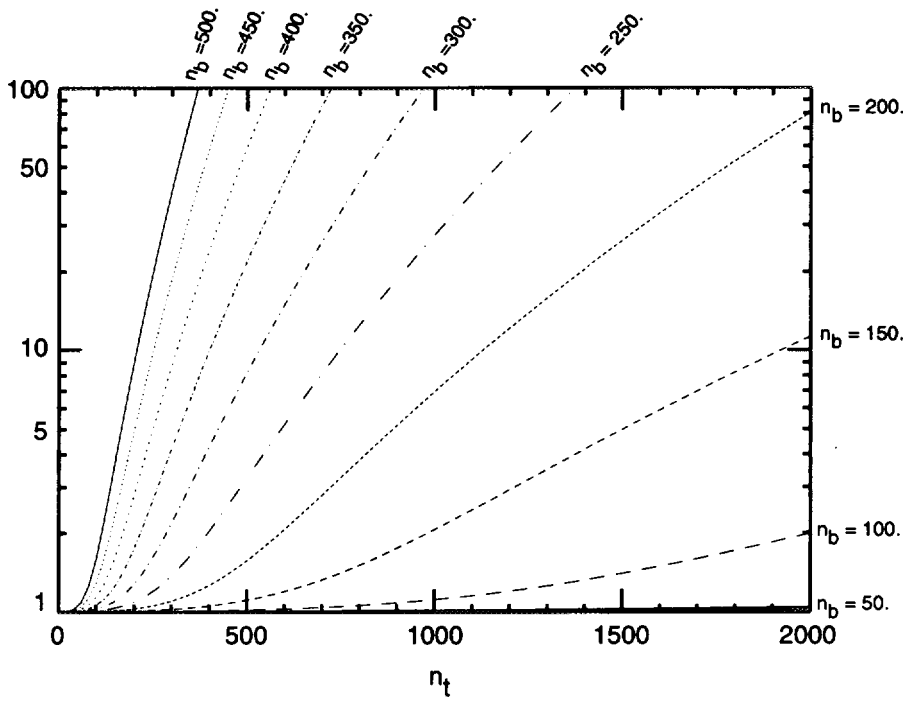

Figure 21: Amplitude blowup factor G for CO^+ of 10^{-9} Torr.

The linear theory is valid only for small amplitude oscillations. It does not predict the emittance growth, either. In order to take into account those effects that are ignored in the linear theory, computer simulation is being conducted. The results of the simulation up to now can be summarized as follows.

- As long as the center-of-mass amplitude is small ≈0.5 standard deviations), the linear theory can describe the phenomena reasonably well.
- The center-of-mass amplitude saturates at about $1\sigma_y$.
- In order to study the effects of the bunch gaps, the electron bunch structures like 256+[25]+256, 256+[50]+256, 128+[25]+128+[25]+128+[25]+128, etc. (the number in [\ ] is the number of missing bunches) have been simulated and compared with continuous 512 bunches. It turned out that the effect of the missing bunches up to 50 does not considerably improve the situation.
- The growth rate with 256 bunches (followed by long enough gap) is much smaller than that with 512 bunches as the linear theory predicts. However, the repetition of 256 bunches plus a gap of much more than 50 missing bunches will not be acceptable because of the luminosity reduction.
- The emittance growth is about 30%.

Thus, in order to damp the growth with 512 successive bunches, a feedback system as fast as 50 to 100 turns (0.5 to 1 msec) is needed, if the gas pressure is 10^{-9} Torr. The fastest bunch mode will be about 50 bunches per cycle.

ACKNOWLEDGEMENTS

The authors would like to thank Drs. N. Akasaka, K, Kanazawa, K. Ohmi, Y. Suetsugu, K. Tajima, Y. Takeuchi, and Prof. K. Yokoya for providing useful information at the time of writing this paper.

REFERENCES

[1] KEKB B-Factory Design Report', KEK Report 95-7, August 1995.

[2] Y. H. Chin, *User's Guide for ABCI Version 8.8*, CERN SL/94-02 (AP) and LBL-35258 (1994).

[3] S. S Kurennoy and Y. H. Chin, KEK Report 96-169, 1995 and to be published in Particle Accelerators.

[4] R. L. Gluckstern, Phys. Rev. A, **46**, 1106 (1992).

[5] S. S. Kurennoy, Part. Accelerators, **39**, 1 (1992).

[6] G. V. Stupakov and S. S. Kurennoy, Phys. Rev. E, **49**, 794 (1994).

[7] K. Oide and K. Yokoya, KEK Preprint 90-10 (1990).

[8] M. S. Zisman et. al., *Study of Collective Effects for the PEP Low-Emittance Optics*, LBL-25582 and SSRL ACD Note-59 (1988).

[9] M.Izawa et. al., Phy. Rev. Let., **74**, 25, 1995.

[10] K. Ohmi, KEK Preprint 94-198 (1994).

Impedance Study for the PEP-II B-factory*

S. Heifets, K. Ko, C. Ng, X. Lin, A. Chao, G. Stupakov,

M. Zolotarev, J. Seeman, U. Wienands, (SLAC)

E. Henestroza, G. Lambertson, J. Corlett, J. Byrd, M. Zisman (LBL),

T. Weiland (Darmstadt), W. Stoeffl, C. Bolser (Livermore),

C. Perkins, M. Nordby, E. Daly, N. Kurita, D. Wright (SLAC).

Abstract

The paper summarizes results on the impedance study of the components of the PEP-II B-factory[1].

* Work supported by Department of Energy contract DE-AC03-76SF00515

Table 1. Parameters of the PEP-II B-factory

parameter		HER/LER	
energy	E	9.0/3.1	GeV
average radius	R	350.03	m
rf frequency	f_{rf}	476.0	MHz
harmonic number	h	3492	
revolution frequency	f_0	136.3	kHz
dc beam current	I_B	0.986/2.14	A
number of bunches	n_b	1658	
particles per bunch	N_B	$(2.72/5.91)\,10^{10}$	
gap	$n_g; l_g$	88; $0.05{*}2\pi R$	
bunch spacing	s_B	1.26	m
momentum comp.	α	$(2.41/1.31)\,10^{-3}$	
energy spread	δ	$(6.1/8.1)\,10^{-4}$	
bunch length	σ_B	1	cm
damping time	τ_x	(36.8/40.4)	ms
z-Partition number	J_E	1.9969/2.0116	
number of cavities	n_{cav}	24/8	
loss/turn	U_0	3.57/0.87	MeV
synchrotron tune	Q_s	0.0516/0.033	
voltage/cavity	V_{rf}	0.77/0.64	MV
cavity shunt imped.	R_s	3.5	MΩ
average beta-x	β_x	(14.5/10.84)	m
average beta-y	β_y	(13.84/9.95)	m

Introduction

There is no need to emphasize how important it is to minimize the beam impedance for a lepton machine with the beam current of several amperes and a large number of bunches. This paper summarizes the results of the impedance studies of the components of the B factory[1]. The prime goal of this activity was to support the design of the vacuum chamber and, at the same time, to get a reasonable model of the machine impedance that can be used later for detailed studies of the collective effects. The work combined analytic approach and extensive simulations with available numerical codes such as MAFIA and ABCI.

The main parameters of the B factory relevant to the paper are given in Table 1.

In this paper we, first, discuss limitations on the impedance given by the beam dynamics. Next, we list the impedance-generating elements in the electron high-energy ring (HER) and mention the difference with the positron low-energy ring (LER). The analysis of the impedance of each element follows. At the end, we summarize results giving the parameters of the impedance of the HER.

Constraints on the impedance

Impedances should be minimized to reduce the wakefields excited by the beam, which may make the beam unstable. Coherent effects impose certain limitations on the magnitude of the impedance.

The longitudinal wakefield modifies the rf potential well and, as a result, changes the bunch shape $\rho(s)$. For a purely inductive impedance L, a single bunch self-consistent potential is

$$U = \frac{s^2}{2\sigma_B^2} + \Lambda L \rho(s) \tag{1}$$

where $\int \rho(s) ds = 1$, and dimensionless

$$\Lambda = \frac{N_B r_e}{2\pi\gamma\alpha\delta^2 R}, \quad r_e = \frac{e^2}{mc^2}, \quad \gamma = \frac{E}{mc^2}. \tag{2}$$

For small s,

$$U = [1 - \frac{\Lambda L}{\sigma_B\sqrt{2\pi}}]\frac{s^2}{2\sigma_B^2}. \tag{3}$$

For the HER at the nominal $I_B = 1\ A$, $\Lambda/\sqrt{2\pi} = 0.88510^{-3}$, and 10% bunch lengthening may be expected for

$$L = 225\ nH, \quad \text{or} \quad Z/n = 0.2\ \Omega. \tag{4}$$

Microwave longitudinal instability sets the limit on the effective impedance $(Z/n)_{eff}$, defined as Z/n averaged with the bunch spectrum

$$(\frac{Z}{n})_{eff} < \frac{2\pi\alpha(E/e)\delta^2}{I_{peak}}, \tag{5}$$

where, for a Gaussian bunch, the peak bunch current is $I_{peak} = I^{av}_{bunch}\sqrt{2\pi}R/\sigma_B$. For the nominal CDR[1], Table 1, the limit is $(\frac{Z}{n})_{eff} < 0.97$ Ohms for the HER and $(\frac{Z}{n})_{eff} < 0.14$ Ohms for the LER. Sometimes SPEAR scaling $(\frac{Z}{n})_{eff} = (\frac{Z}{n})(\sigma_B/b)^{1.68}$ is used to relate effective and machine impedances. For the average $< b >= 3.3$ cm machine impedance is 7.4 times larger than effective impedance, giving $(Z/n) = 7.2$ Ohms for the HER, and $(Z/n) = 1.03$ Ohms for the LER. However, SPEAR scaling may not necessarily be valid for PEP-II. Note that a purely inductive impedance does not lead to microwave instability.

Transverse microwave (transverse fast blow-up) instability limits effective broadband impedance for a given average bunch current;

$$|Z_\perp| < \frac{4Q_s(E/e)b}{I^{av}_{bunch} < \beta_\perp > R}, \tag{6}$$

where Q_s is the synchrotron tune, and $< \beta >$ is the average transverse beta function. At nominal CDR currents, an average $< \beta_\perp >= 10$ m, and a beam aperture $b = 2.5$ cm, the criterion limits impedance to $|Z_\perp| = 21$ MΩ/m for the HER, and $|Z_\perp| = 2.3$ MΩ/m for the LER.

Transverse mode-coupling instability limits the imaginary part of effective transverse impedance

$$ImZ_\perp < \frac{4Q_s(E/e)b}{I^{av}_{bunch} < \beta_\perp > R}\frac{4\sqrt{\pi}}{3}\frac{\sigma_B}{b}, \tag{7}$$

and gives essentially the same constraints for PEP-II as fast blow-up instability.

Slow head-tail instability sets a loose limit on the chromaticity of the ring and is not important for this note.

Transverse impedance also causes closed-orbit distortion and changes the betatron tune; however, these effects are small. They may be enhanced by a factor $Q_L c/(\pi f_m s_B)$ proportional to the loaded Q_L factor of a higher-order mode (HOM) excited by a train of bunches if the frequency of a mode f_m of the narrow-band impedance is in resonance with the bunch spacing $f_m s_B/c = integer + 1/4$, or with the frequency of a coherent coupled-bunch mode of the train.

The maximum kick from a single mode to a bunch centroid with the offset r is

$$\theta = \frac{\Delta p_\perp}{p} = \frac{4\pi N_B r_e}{Z_0 \gamma}(\frac{2r}{s_B})\frac{R}{Q}Q_L, \qquad r_e = \frac{e^2}{mc^2}, \tag{8}$$

provided that the mode frequency is in resonance with the bunch spacing.

For example, one of the strongest rf cavity dipole HOM, with parameters $f = 1674.2\ MHz$, $R/Q = 0.31\ k\Omega/m$, and loaded $Q_L = 2134$, gives the maximum transverse impedance $Z_\perp = (R/Q)Q_L = 0.66\ M\Omega/m$. Take $N_B = 6 \times 10^{10}$, offset $r = 1$ cm, $\gamma = E/mc^2 = 6 \times 10^3$, $r_e = e^2/mc^2 = 2.8 \times 10^{-13} cm$. Then $\theta = 1.0 \times 10^{-5}$ is much smaller than the divergence angle within a beam. The HOM of a cavity with length l is equivalent to a quad with the focusing length $F = l/\theta$. The betatron tune shift given by the mode is $\Delta Q_\perp = -\beta_\perp/(4\pi F)$ and, for $l = 10$ cm, $\beta_\perp = 11$ m, $\Delta Q_\perp = 4. \times 10^{-4}$. Hence, under the resonance condition the maximum tune shift due to the strongest HOM of the 8 rf cavities $\Delta Q_\perp = 0.6 \times 10^{-3}$ in the LER is still much smaller than the beam-beam tune shift ($\xi = 0.03$).

More limitations derive from coupled bunch instabilities.

In the longitudinal case, the growth rate for n_b equally spaced bunches

$$\frac{1}{\tau_n} = \frac{I_B \alpha}{4\pi (E/e) Q_s} \sum_{p=-\infty}^{\infty} \omega_{pn} e^{-(\omega_{pn}\sigma_B)^2} Re Z_l(\omega_{pn})$$

where $\omega_{pn} = \omega_{rev}[pn_b + n + Q_s]$, should be compared to the damping time $\tau_l = 20$ ms. (This conservative approach ignores additional possible Landau damping and

head-tail effect). That limits the impedance at any resonance frequency $f = \omega_{pn}/2\pi$. For the CDR parameters of the rings:

$$(\frac{f}{GHz})(\frac{ReZ}{k\Omega})e^{-(2\pi f\sigma_B/c)^2} < 19.5\ (HER); \quad < 4.1\ (LER). \tag{9}$$

Similarly, comparison of the growth rate of the transverse coupled-bunch instability

$$\frac{1}{\tau_{\perp,n}} = \frac{I_B f_{rev}\beta_\perp}{(E/e)} \sum_{p=-\infty}^{\infty} e^{-(\omega_{pn}\sigma_B)^2} ReZ_\perp(\omega_{pn}), \tag{10}$$

where $\omega_{pn} = \omega_{rev}[pn_b + n + Q_\perp]$, with damping time $\tau_\perp = 40$ ms, limits the transverse impedance at any resonance frequency f_{pn} to

$$\frac{ReZ_\perp}{K\Omega/m}e^{-(\omega\sigma_B/c)^2} < 119.8\ (HER); \qquad < 26.6\ (LER). \tag{11}$$

The longitudinal loss factor gives the energy loss of a beam and defines the power deposited in the beam pipe by an uncorrelated train of bunches

$$P = \Delta E f_0 = \frac{Z_0 I_B^2 \kappa_l s_B}{4\pi}, \tag{12}$$

where $Z_0 = 120\pi\ \Omega$ is the impedance of the vacuum. For a 1 A current and $s_B = 1.26$ m, a loss factor of $\kappa_l = 1$ V/pC corresponds to $P = 4.16$ kW of microwave power.

In summary, the main limitations to impedance come from bunch lengthening, power deposition, and multibunch stability. Single-bunch stability does not seem to be a strong limiting factor.

Table 2. Impedance generating elements, HER PEP-II B factory

RF Cavities	RF cavities	24
	RF cavities tapers	48
Arcs	Copper chamber(m)	1440
	Dipole screens	192
	BPM	198
	Arc bellows module	198
	Collimators	2
	Dipole offsets	384
	Quad pump slots	198
	Arc flex jonts	198
	Flange/gap rings	398
	Early x-ray mask	6
Straights	SS 304L pipe (m)	760
	BPM	92
	Collimators	6
	Pump ports	92
	Sliding joints	92
	Flex joints	92
	Flange/gap rings	184
	Gate valves	16
	Tapers octag./round	12

IR	IR Be chamber	1
	IR masks	
	Q2 septum	2
	Collimators	4
	IR pump ports	2
	Special BPMs	2
	High power dumps	2
Feedback	Feedback pickups	4
	Longitud. kicker	1
	Transverse kicker	1
Inject/Abort	Injection port	1
	Kicker ceramic	3
	Abort dump port	1
Arcs Diagnos.	Synch. light monitor	2
	SSRL xray port	2
Str. Diagnos.	BB curent monitors	1
	DC current transf.	1
	Tune monitor	1
	Profile monitor	1
IR Diagnos.	Luminosity monitor	1
Other	Pulsed separator	4
	PPS stopper	1

Impedances of the components

The list of impedance-generating elements in the HER (including interaction region (IR)) is given in Table 2. The LER is different in only a few aspects. First, the LER has an Al vacuum chamber in the arcs and, because LER dipoles are short, an ante-chamber with discrete pumps is used instead of HER distributed ion pumps (DIPs). In the LER, the impedance of the antechamber "replaces" the impedance of the dipole screens of the HER. Secondly, wigglers give an additional contribution to the LER impedance budget.

RF cavities

The dominant contribution to the impedance comes, of course, from the damped rf cavities (see Fig. 1).

The loaded Q_L factor of the HOMs for a damped cavity is relatively low and the width of a HOM is large compared to the revolution frequency. For this reason, the variation of the HOM frequency in the non-identical cavities (HOM detuning) is not important and the total impedance of the cavities is proportional to the number of cavities.

Table 3 summarizes the main longitudinal monopole and transverse dipole modes found numerically with the code URMEL and those measured on a prototype cavity[1].

The total narrow-band loss factor of a cavity is $\kappa_l = 0.26$ V/pC. This is the sum of the loss-factors of the monopole HOMs below the 2.5 GHz cut-off frequency of the beam pipe with $b = 4.76$ cm radius. The loss factor of the fundamental mode adds 0.167 V/pC. The total loss factor of a cavity calculated by ABCI from the wake field excited by a bunch going through the cavity is $k_l = 0.55$ V/pC; hence, the broad-band loss from the modes above the cut-off frequency is 0.12 V/pC.

The longitudinal wake-field of a rf cavity is depicted in Fig. 2 and for dipole HOMs in Fig. 3. The real part of rf cavity longitudinal broad-band impedances is depicted in Fig. 4. The beam-pipe radius is $b = 4.49$ cm.

Table 3. Single RF Cavity Monopole HOMs

	freq (MHz)	R/Q	$R_s(M\Omega)$	Q_L(num/mes)	$(R/Q)Q_L(k\Omega)$
1	489.6	108.8	5.036	/31926	3472.28
2	769.8	44.97	1.782	26/28	1.26
3	1015.4	0.006	0.0002	169/246	0.001
4	1291.0	7.68	0.692	66/	not visible
5	1295.6	6.57	0.265	/907	5.96
6	1585.5	5.06	0.216	/178	0.90
7	1711.6	4.75	0.404	not visible	
8	1821.9	0.06	0.006	/295	/0.018
9	1891.0	1.68	0.075	not visible	
10	2103.4	3.52	0.235	/233	0.82
11	2161.9	0.02	0.002	/201	0.004
12	2252.2	1.21	0.068	/500	0.61

Table 4. Main RF cavity Dipole HOMs, $r_0 = 4.7625$ cm

	f (MHz)	R/Q (Ω)	Q_L(calc/meas)	$(R/Q)(Q_L/kr_0^2\,(k\Omega/m)$
1	679.6	0.001	35/-	not visible
2	795.5	9.876	121/122	31.86
3	1064.8	31.990	38/-	not visible
4	1133.2	0.320	76/112	0.65
5	1208.2	0.385	2266/1588	10.3
6	1313.2	10.336	/498	80.1
7	1429.0	5.999	/3955	342.0
8	1541.0	2.065	/59	1.62
9	1586.2	5.262	/178	12.1
10	1674.2	14.732	/2134	385.0
11	1704.4	0.285	/444	1.52
12	1761.9	0.330	/7129	27.3

Eight cavities in the LER with the nominal beam current would generate 16.6 kW of power, see Eq. (12), propagating downstream from the cavities and absorbed in the walls. For TM modes in the round pipe with the radius $r = b$, the power absorbed in the wall within the distance $l = 1/\alpha_P$ is $P(z) \propto e^{-\alpha_P z}$, where

$$\alpha_P = \frac{k}{k_z}\frac{\delta}{b}.$$

Here, $k = \omega/c$, $k_z = \sqrt{k^2 - k_m^2}$, and k_m is the cut-off frequency of the m-th propagating mode. The bunch spectrum starts to roll off above frequencies $k\sigma \simeq 1$. For a $\sigma_B = 1$ cm bunch, the roll off starts at the frequency $f \simeq 4.77$ GHz. For such a frequency the skin depth is $\delta \simeq 1\mu m$ and the absorbtion length in the beam pipe with radius $b = 4.76$ cm is of the order of $l \simeq 500$ m. Hence, the wall power deposition from the cavities is $29.0\,W/m$. The broad-band transverse kick-factor of a rf cavity $k_\perp = 5.266$ V/pC/m at $b = 4.49$ cm.

The maximum narrow-band (NB) impedance of a single cavity $(R/Q)Q_L = 5.96\,\mathrm{k}\Omega$ at $f = 1.296$ GHz is larger than the $3.4\mathrm{k}\Omega$ limit set by Eq. (9) for the LER, see Table 3. The coherent stability of PEP-II therefore requires a feedback system. Optimization of the vacuum chamber should be considered, in this context, as an attempt to minimize requirements on the feedback system.

The same is true for the dipole modes. The dipole modes $f = 1.429$ GHz and $f = 1.674$ GHz have maximum impedances much higher than allowed by Eq. (11), see Table 4. Transverse stability depends again on the bunch-by-bunch transverse feedback system.

Resistive wall

The longitudinal resistive-wall impedance is given by[2]

$$\frac{Z_l}{n} = Z_0\frac{(1-i)}{2}\frac{\delta}{b}\frac{L}{2\pi R}F(a/b), \tag{13}$$

where

$$\delta = \sqrt{\frac{2c}{Z_0\sigma\omega}}$$

is the skin depth, $F = 1$ for a circular pipe with radius b, and $F(a/b) = 0.97$ for a

rectangular beam pipe with a ratio of height-to-width of $b/a = 2.4/4.6 = 0.52$.

The transverse resistive-wall impedance for a circular pipe is

$$Z_\perp = \frac{2R}{b^2}\frac{Z_l}{n}. \tag{14}$$

The transverse impedance of a rectangular pipe can be estimated from the impedance of two parallel planes separated by a distance $2b$[3]:

$$Z_\perp = BZ_0\frac{(1-i)}{2}\frac{2R}{b^2}\frac{\delta}{b}\frac{L}{2\pi R}, \tag{15}$$

$B = \pi^2/24$ or $B = \pi^2/12$ for motion parallel or perpendicular to the planes, respectively.

For the 1300 m copper beam pipe of the HER arcs with a conductivity $1/\sigma = 17.7\ \mathrm{n}\Omega - m$, the longitudinal and transverse impedances are $Z_l = 0.823(1-i)\sqrt{n}\Omega$, $Z_x = 0.435/\sqrt{n}\ \mathrm{M}\Omega/m$, and $Z_y = 0.87/\sqrt{n}\ \mathrm{M}\Omega/m$. The 900 m straight, circular stainless-steel pumps with $b = 4.6$ cm and $1/\sigma = 900\ \mathrm{n}\Omega - m$ give $Z_l = 2.16(1-i)\sqrt{n}$ Ω and $Z_\perp = 0.74/\sqrt{n}\ \mathrm{M}\Omega/m$.

Combining the two contributions, the total resistive wall impedances are

$Z_l = 2.98(1-i)\sqrt{n}\ \Omega$, $Z_x = 1.175/\sqrt{n}\ \mathrm{M}\Omega/m$, $Z_y = 1.61/\sqrt{n}\ \mathrm{M}\Omega/m$.

The longitudinal impedance at the roll-off frequency of the bunch $k\sigma_B = 1$, or $n = 3.5\times10^4$, is 0.56 kΩ, still within the limit of Eq. (9). Transverse impedance gives the dominant contribution to the total impedance at low frequencies and is higher than the limit set by Eq. (11). Again, stability of the beam relies on a transverse feedback system.

The loss factor and the power deposition per unit length due to the resistive wall (RW) impedance in a circular beam pipe are

$$\frac{dk_l}{ds} = \frac{1}{2\pi b}\sqrt{\frac{2}{Z_0\sigma}}\frac{\Gamma(\frac{3}{4})}{\sigma_B^{3/2}}, \qquad \frac{dP}{ds} = \frac{e^2}{2\pi b}\frac{n_b N_B^2 f_0}{\sigma_B^{3/2}}\sqrt{\frac{2}{Z_0\sigma}}\Gamma(\frac{3}{4}), \tag{16}$$

where n_b is the number of bunches per ring, N_B is the number of particles per bunch, and f_0 is revolution frequency.

The copper coating on the stainless steel (SS) beam pipe may be used to reduce impedance and heating due to synchrotron radiation from upstream dipoles. The impedance depends on the thickness t of the coating: it decreases exponentially from the value for the SS pipe for $t = 0$ to the value of the copper pipe for $t \simeq \delta_{Cu}$ [4]

$$\frac{Z_l}{n} = Z_0 \frac{(1-i)}{2} \frac{\delta}{b} \frac{L}{2\pi R} \zeta(t/\delta) \qquad (17),$$

where

$$\zeta(x) = \frac{1+\lambda+(1-\lambda)F(x)}{1+\lambda-(1-\lambda)F(x)}, \quad \lambda = \sqrt{\frac{\sigma_{SS}}{\sigma_{Cu}}}, \quad F(x) = e^{-2(1-i)x}. \qquad (18)$$

The factor ζ goes to 1 for a thickness of the order of the skin depth of the coating.

The wall conductance at the transitions between arcs and straight sections has a jump. The impedance generated by such a jump in the conductivity may be estimated as the impedance of a step with a width equal to the difference of the skin depths and is negligible.

HER DIP screen

The screen separates the beam pipe and DIPs in the HER dipole vacuum chamber. We considered several possible screen designs. The issues here were the screen vacuum conductance, beam impedance, crosstalk between the plasma in the DIP and the beam, screening the beam from dust particles that may be produced in the DIP chamber, and screening the DIPs from scattered synchrotron radiation and from penetration of TE modes, which may be generated by an offset beam or by TM/TE mode conversion in the beam pipe. The impedance issue includes broad-band impedance as well as narrow-band impedance produced by the interference of waves generated by openings in the screen or by trapped modes.

The final screen design is based on T. Weiland's old idea of using continuous, narrow longitudinal grooves cut halfway through the screen with small holes cut through another half of the screen thickness (see Figs. 5a,b). Grooves with height w and depth d attenuate the beam field at the slot opening by a factor $e^{-\pi d/w}$ for frequencies $\omega/c < \pi/w$. For $w = 3$ mm, chosen for the grooves, this condition is true

for all frequencies within the $\sigma_B = 1$ cm bunch spectrum. For $w = d$, the attenuation factor is $e^{-\pi} = 0.043$, and the broad-band impedance is reduced by the square of this factor, i.e. by a factor 500.

Narrow grooves also preclude the DIP plasma discharge affecting the beam. Continuous grooves reduce broad-band impedance and eliminate complications of narrow band impedance. Tilted grooves make efficient screening of the beam from dust particles and screening of the DIPs from scattered synchrotron radiation.

Small 3 mm diameter holes give large enough vacuum conductance while simultaneously preventing penetration of TE modes through the screen. A hole acts as an antenna for an incoming TE mode with a dipole moment proportional to r^3. The ratio of radiated power to incoming power of a TE wave generated in the beam pipe with radius b by a bunch with rms length σ_B may be estimated as (see Eq. A1-37)

$$\frac{\Delta U_{rad}}{\Delta U_{in}} \simeq 0.3(\frac{r^3}{b\sigma_B^2})^2. \tag{19}$$

Hence, the penetration length of a TE mode scales with the hole radius as $(1/r)^6$ and, for 3 mm holes, is larger then the absorbtion length of such modes in the beam-pipe walls. The hole separation is chosen large enough to make gap impedance small. This prevents a significant crosstalk between holes, which could result in the adding-up of their dipole moments. The mesh reduces total vacuum conductance by less than 4%. There will be 192 screens, 5.6 m long, with 6 grooves and 8400 holes per screen.

Each hole has an inductance $L = 3.5 \times 10^{-5}$ nH, giving $L = 56.5$ nH for all holes of the 192 screens. Attenuation in the grooves reduces the total inductance of the holes to $L = 0.1$ nH. The holes make the tolerance on the tilt of the grooves very loose in respect to the beam direction.

The total transverse impedance of the HER DIP screens is $Z_\perp = -i\,0.06\ k\Omega/m$.

The resistive part of the impedance and the loss factor for frequencies within the bunch spectrum are negligible small: $k_l = 5.5 \times 10^{-5}$ V/pC.

LER Antechamber

The LER antechamber replaces the DIP vacuum chamber of the HER and is similar to the antechamber of the ALS, see Figs. 6a,b. Impedance of the ALS antechamber was measured and modeled with MAFIA[5]. Broad-band impedance is generated mostly by the discontinuity of the antechamber slot at the ends. Narrow-band impedance would correspond to modes trapped in the antechamber. Simulations and theory show that the dependence of the impedance on the length of the slot saturates when it becomes several times the rms bunch length at several σ_B (several cm). Excitation of the modes of the antechamber by the beam may be attenuated significantly if the slot of the ante-chamber is narrow and long: it works exactly in the same way as to the grooves in the DIP screen. Fig. 7 shows the field pattern at the slot opening that confirms this statement. The attenuation factor found with MAFIA agrees with the simple formula $e^{-\pi d/w}$. However, the opening of the slot has to be large to accommodate the vertical size and the position jitter of the beam. Calculations were carried out with slot heights of 1.8, 1.4, and 1.0 cm. In all cases, the wake field is inductive and small, with maximum values of 0.04, 0.12, and 0.31 mV/pC, respectively, for a slot 40 cm long and 1 cm deep (see Fig. 8). Dependence on the depth c of the antechamber slot was compared for $c = 1$, 12, and 26 cm: the difference is negligible. The calculated inductive $Z/n = 0.5$ $\mu\Omega$ or $L = 5.7 \times 10^{-4}$ nH is quite small and agrees with measurements. No trapped modes were found.

Abort system

The beam abort system requires a long vacuum chamber 3 cm wide and 12 cm deep (from the beam to the bottom) under the beam terminated with the dump[6]as shown in Figs. 9a, 9b. To minimize the impedance the chamber is screened with two shallow rf tapers (down and back up to the beam pipe). The taper going down may be very long and gives negligible impedance. The aborted beam goes through the taper going up. The angle α of this taper is limited by the energy deposition, which depends on radiation length X_0, and thickness t of the screen: $\alpha > t/X_0$. MAFIA calculations for a 3 m long structure with two (up and down) tapers 8.5 cm high and angle $\alpha = 0.048$, give an inductive wake field with $L = 0.23$ nH. The loss factor is

$k_l = 4.5 \times 10^{-3}$ V/pC. No narrow-band trapped modes were found.

Interaction Region

The interaction region (IR) is a complicated 3-D set of masks and tapers as shown in Fig. 10a, and 10b. It was modeled as a whole structure using MAFIA. The broad-band wakefield is approximately inductive with $L = 5$ nH (see Fig. 11). The loss factor of the total structure is $k_l = 0.12$ V/pC. Most of the power lost due to the broad-band impedance propagates downstream and is absorbed outside the IR.

The main issue for the IR is heating. Heating in the IR results mostly from modes trapped in the central Be pipe ± 20 cm around the IP, 3 watts of ohmic losses in the Be pipe, and, to a much smaller extent, from losses in upstream components of the beam pipe, mainly from the IR septum. Broad-band impedance has maximum $ReZ = 0.46\,\mathrm{k}\Omega$ at 6 GHz as a result of averaging of the trapped modes.

The $l = 40$ cm Be pipe with radius $b = 2.5$ cm and adjacent masks with circular openings on both sides was modeled separately. The loss factor of this section is $k_l = 0.012$ V/pC. A number of the trapped modes are confined in the 40 cm Be pipe, due to the adjacent masks (see Fig. 12). Frequencies of the modes range from 4.6 GHz to 5.92 GHz. The frequency interval at the low-frequency end is about 50 MHz. Spacing increases to 150 MHz at the upper frequency end. Trapped modes are, basically, TM_{01} modes of the pill-box cavity with frequencies

$$\frac{\omega}{c} = \sqrt{(\frac{\nu}{b})^2 + (\frac{n\pi}{l})^2}. \tag{20}$$

The lowest radial number $\nu = 2.4$ and the number of the half waves n along the structure range from $n = 1$ to $n = 12$.

Both beams excite the modes simultaneously. For a symmetric structure, the amplitude A of the even modes ($n = 2m$) excited by a bunch is proportional to $(N_+ + N_-)\sin(kl/2)$, and for odd modes ($n = 2m + 1$), $A \propto (N_+ - N_-)\cos(kl/2)$ where $N_\pm$ is the number of particles per bunch in each beam. Therefore, the power deposited in even modes scales as $P \propto (N_+ + N_-)^2$. For an IP placed asymmetrically

at a distance l_1 from one end of the pipe, the amplitude of the even and odd modes is

$$A_{\pm} \propto (N_+ + N_-)[\sin(kl_1) \pm \sin(kl_2)] + (N_+ - N_-)[\cos(kl_1) \mp \cos(kl_2)], \qquad (21)$$

and odd modes can be excited even for equal number of particles in both beams. The power deposition within the Be pipe depends on the Q factor of the modes.

Resistive $Q \simeq 1.25\,10^4$ is very large in our case. Loaded Q_L depends on the coupling of trapped modes to propagating modes in the beam pipe on the other side of the masks, where the beam pipe radius is much larger than that for the Be pipe. We estimate for round openings in the masks that

$$Q_{ext} \simeq (\frac{\pi f_m l}{c})(\frac{b}{a_0})^2 \frac{1}{W_t}, \qquad (22)$$

where a_0 is the radius at the neck of the masks, and W_t is the probability of tunneling through the mask for a mode with frequency f_m:

$$W_t = |e^{-\int dz|q(z)|}|^2, \qquad |q(z)| = \sqrt{(\frac{\nu}{a(z)})^2 - (\frac{2\pi f_m}{c})^2}. \qquad (23)$$

The integral may be estimated as

$$\int dz|q(z)| \simeq \frac{2\sqrt{2}}{3}\Delta^{3/2}\frac{\nu}{a'} \qquad \Delta = \frac{\nu c}{\omega_m a_0} - 1, \qquad (23)$$

where $a' = |da/dz|$ is the slope of the mask.

For our case, this approach gives $Q_{ext} = 1200$ for a typical $f_m = 5.7$ GHz, and $a_0 = 1.5$ cm. In this case, only 10% of power loss goes to the Be pipe wall.

In principal, detuning from a resonance can be done by heating Be pipe. Temperature dependence of the mode frequency

$$\frac{\Delta f}{f} \simeq \frac{(\Delta l/l)}{1 + (\frac{\nu l}{\pi n b})^2} \qquad (25)$$

is different for different n: the coefficient is equal to 1/50 for $n = 1$, and 1/2 for $n = 12$. For $(\Delta l/l) \simeq 10^{-5}\Delta T$, and $\Delta T \simeq 100^o$ the frequency shift for the mode $n = 12$ is small but comparable to the width of the resonance.

The power loss to an even mode with the loss factor κ_m and loaded Q_m^L is

$$P = P_0 D, \qquad P_0 = I_\Sigma^2 \kappa_m \frac{s_B}{c}, \tag{26}$$

where $P_0 = 480\,\mathrm{W}$ is the power loss of uncorrelated bunches, and $I_\Sigma = I_+ + I_-$. The enhancement factor D for a train of bunches with bunch spacing s_B

$$D = (\frac{c}{\omega_m s_B}) \frac{1/Q_m^L}{(\Delta\omega_m/\omega_m)^2 + (1/2Q_m^L)^2} \tag{27}$$

depends on detuning the mode frequency from the resonance frequency ω_r, $\omega_r s_B/(2\pi c) = integer$. Far away from the resonance $\Delta\omega_m/\omega_m >> 1/2Q_m$ and we get the factor $D << 1$. At the resonance

$$D_{max} = \frac{4Q_m^L c}{\omega_m s_B}, \tag{28}$$

and, for $s_B = 120$ cm and $f_m \simeq 6$ GHz, $D_{max} >> 1$ provided that $Q >> 70$. For $Q_m = 1200$, the enhancement $D_{max} = 16$, and $D_{min} = 4.4 \times 10^{-3}$. If only three out of twelve trapped modes are resonant, power loss is $P = 3 \times (1/12) \times 480W \times D_{max} = 1.92$ kW. Power dissipated into the wall itself is $P_{wall} = 192$ W in this case.

The frequency spectrum of a train of bunches also has frequencies at multiples of the revolution frequency ω_0. The number of independent coherent modes is equal to the number of bunches n_B. If the amplitude of the coherent mode is A_l, the power loss of a particle due to this mode is (Eq. A3-17)

$$P \simeq 2I_{av}^2 (\frac{A_l \omega_l}{2c})^2 (R/Q)_l Q_L^l. \tag{29}$$

The rms amplitude of the coherent modes is on the order of $A_l \simeq 2\sigma_B/\sqrt{n_B}$, and power loss due to single coherent mode is $2I_{av}^2(\sigma_B\omega_l/c)^2(Q_L/n_B)(R/Q)_l$. The number of such modes within the resonance width $\omega_l/(Q_L)$ is $\omega_l/(2Q_L\omega_0)$. Total loss of coherent modes

$$(2/\pi)(\sigma_B\omega_l/c)^2 P_0$$

is independent of Q_L and is smaller than the uncorrelated power loss P_0.

Hence, the wall-power loss is acceptable provided the pipe and adjacent masks are carefully designed to avoid resonances with bunch spacing.

Injection port, kicker ceramic

The injection port generates impedance due to a 2 × 12 cm slot in the tapered beam-pipe wall, with the average pipe radius $b = 3.8$ cm (see Fig. 13 a,b). Broad-band impedances, both of the slot and the taper, calculated with MAFIA, are mostly inductive. The slot gives an inductance $L = 0.025$ nH and a loss factor $k_l = 1.5 \times 10^{-3}$ V/pC. The contribution of the taper is larger: $L = 0.15$ nH and $k_l = 5.4 \times 10^{-3}$. Including both contributions, the injection port gives $L = 0.17$ nH and $k_l = 6.9 \times 10^{-3}$ V/pC. No indication of trapped modes was found.

Kicker ceramic section ($\epsilon = 9 >> 1$, thickness $\Delta b = 4$ mm, tube radius $b = 2.75$ cm) for the injection kicker (length $l = 1.25$ m) have a thin titanium coating (resistivity $\rho_{coat} = 43\ \mu\Omega - \text{cm}$). The wakefield generated by the ceramic section depends[7] on the parameter

$$V = \frac{\sigma_B \rho_{coat}}{Z_0 (\Delta b) t}, \tag{30}$$

where $t = 0.75 \mu m$ is the thickness of the coating. For this coating thickness, $V << 1$ and the wake

$$W(s) = \frac{2l}{tb} \frac{\rho_{coat}}{Z_0} \rho(s) \tag{31}$$

is mostly resistive, Eq. Appendix 1-22,

$$R_\Omega = \frac{l \rho_{coat}}{2\pi b t}. \tag{32}$$

For $l = 1.25$ m, the resistive part of the impedance $R_\Omega = 5.7\ \Omega$; the loss factor $k_l = 0.04$ V/pC. The inductive impedance corresponds to $L = 0.5\, 10^{-3}$ nH.

BPM

The HER has 290 sets of four-button BPMs (see Fig. 14). A BPM should have high sensitivity within the bandwidth 1 GHz, but at the same time must have low power going to the cables, low beam impedance, and low heating inside the BPM structure. We compared several designs of a BPM.

A 2 cm diameter round button is reasonably sensitive but the impedance is resonant at 6 GHz with relatively high shunt impedance. The problem may be avoided by making the button asymmetric. In particular, a narrow bridge across the gap eliminates the resonance but makes power to the cable too high. Measurements confirmed the results of MAFIA simulations quite well (see Figs. 15a,b).

The final version of the BPM uses a round button with $a = 1.5$ cm diameter. Such a design (see Fig. 16) satisfies requirements for sensitivity, heating, and power output to the cables.

For a four-button BPM and $N_B = 3 \times 10^{10}$, the sensitivity[9]is defined by the impedance 0.5Ω at 1 GHz.

The impedance of a single button is generated by a $w = 2$ mm round slot. Impedance of a slot can be esimated as the difference of the impedances of two round holes with radii a and $a + w$, giving polarizability $\alpha_e + \alpha_m = 2wa^2$ and

$$L = \frac{2wa^2}{\pi b^2},$$

or $L = 5.7 \times 10^{-3}$ nH per button, $L = 6.8$ nH for 300 four-button BPMs. The Kurennoy[8]estimate is smaller: $\alpha_e + \alpha_m = wa^2/8$. MAFIA[9]gives $L = 3.7 \times 10^{-2}11$ nH and a loss factor of $k_l = 2.7 \times 10^{-3}$ V/pC for a four-button BPM; $L = 11$ nH, and $k_l = 1$ V/pC for 300 BPMs.

Hence, the power loss by the beam is $P = 126$ W per BPM at the current 3A. Power output to a cable is found by direct calculations of the fields at the port and is 9 W per cable. The 1 cm beam offset in the direction to a button can increase power to the cable by a factor of 2 because the frequency harmonic of the field depends on the distance as $1/r$.

Transverse broad-band impedance of 300 BPMs found in simulations[9]is $Z_x = 6.7\, k\Omega/m$, and $Z_y = 5.5\, k\Omega/m$. One mode of the narrow-band longitudinal impedance has a total shunt impedance 6.5 $k\Omega$ at $f = 6.8$ GHz for 300 BPMs. The field pattern of the mode indicates that this mode is a TE_{11} mode (in respect to the button axis).

Transverse narrow-band impedance Z_x has a mode with the total $R_s = 90\,k\Omega/m$ at $f = 6.8$ GHz, and $Z_y = 120\,k\Omega/m$ at $f = 6.2$ GHz.

The impedance is only slightly more than required by the conservative estimate of Eq. (9) and may increase the power of the feedback amplifier by not more than 5%.

Ceramic in the BPM has $\epsilon = 10$ and loss tangent of the ceramic is $\delta_c = 0.0007$. The power deposited by a propagating wave into ceramic with thickness $h = 3$ mm,

$$\frac{P}{P_{in}} = (\frac{\omega}{c})\frac{h}{2}\epsilon\delta_c, \tag{33}$$

is $P = 12$ mW per button for the loss $P_{in} = 126$ W per BPM at $f = 7.5$ GHz.

The power absorbed in the thin Ni layer at the edge of the ceramic in a coax with characteristic impedance $Z_W = (Z_0/2\pi)\ln(b/a)$ and radii a, b is

$$\frac{P}{P_{in}} = (\frac{\omega}{c})\frac{\mu\delta h}{d_{eff}}, \tag{34}$$

where for TEM wave

$$1/d_{eff} = \frac{(a+b)}{2ab\ln(b/a)}, \tag{35}$$

and δ is the skin depth of Ni. Note that $\mu\delta$ scales as $\sqrt{\mu}$. The permeability μ of Ni rolls off at high frequencies very rapidly and at 7 GHz is of the order $\mu = 3$ (see Fig. 17) reducing power loss to Ni to $P = 46.8mW$ per button for the loss $P_{in} = 126$ W per BPM.

The fraction of power absorbed in the resistive walls is on the order of the ratio of the length of a button $l = 1.9$ cm to the absorption length

$$\frac{P}{P_{in}} = (\frac{\omega}{c})\frac{\delta l}{d_{eff}} \tag{36}$$

and is very small.

The Q factor given by these losses is $Q_0 = 534$. The loaded Q_L, determined by MAFIA and confirmed in wire measurements on a BPM prototype, is much smaller: $Q_L \simeq 60$. It is too low to enhance the power loss in a train of bunches.

It is worthwhile to compare the loss factor $k_l = (\omega/2)(R/Q_0)$ of the longitudinal mode $f = 6.8$ GHz with the broad-band loss $k_l = 2.7 \times 10^{-3}$. Taking $Q_0 = Q_L$ and $R_s = 22\,\Omega$ per BPM, we get $k_l = 0.46/Q_L$ per BPM. This figure is larger than the broad-band loss factor for $Q_L = 100$. This argument indicates again that the loaded Q_L should be much less than Q_0 and has to be dominated by the radiation back to the beam pipe.

The relevant parameter for heating is the wall loss factor of a propagating wave multiplied by the number of passes of a wave, $Q_L c/\omega l \simeq 36$ for $Q_L = 60$. That gives absorbed power 2.5 W and heating of button at normal conditions should not be a problem.

If a button cable is accidentally disconnected, the situation may be different. First, reflection from the open unmatched end can produce a standing mode within the BPM. Consider a button as a transmission line. The currents and voltages at both ends of the line are related by the characteristic impedance of the line Z_L and the impedance of a termination Z_t:

$$V_{in} = V_t[\cos\psi + i\frac{Z_L}{Z_t}\sin\psi], \quad I_{in} = I_t[\cos\psi + i\frac{Z_t}{Z_L}\sin\psi].$$

Under normal conditions, the characteristic impedance of the line is matched to the impedance of the cable, and the voltage and current at both ends of the button are the same, except for a phase $\psi = ql$ where q is the propagating constant and l is the length of the line. For a disconnected cable, the current at the output port of the button is zero. The current at the input port is related to the density of the image current induced by the beam and, therefore, is the same as at the normal operation. Hence, voltage at the input port increases by a factor $\cot\psi$ compared to the normal operation. For a TEM wave with frequency ω, the phase ψ is $\psi = \omega l/c$. From a reciprocity theorem it follows that the voltage induced at the beam current and,

hence, the energy loss by the beam and heating are also increased by the same factor $\cot\psi$, or by a factor 6.25 for $f = 7.5$ GHz and $l = 1.9$ cm. Radiation to the beam pipe is also increased due to the reflected TEM mode. Simulations with MAFIA confirmed appearence of the new resonances in the beam impedance with a disconnected cable.

The same design of BPMs with flat buttons will be used in the arcs and straight sections. In the straight sections, a flat button will be flush with the round beam pipe only at the center, making small cavities at the edges. The effect was simulated with MAFIA and changes the broad band impedance only by a few percents.

To screen BPMs from halo electrons, buttons will be recessed by 0.5 mm (including tolerance for installation). Other factors such as direct or secondary synchrotron radiation, or electrons emitted from the chamber walls are not affected by the small recess under consideration. For a beam pipe gap $b = 2.5$ cm and a betatron wavelength $\lambda_\beta \simeq 50$ m the incident angle of a halo electron is $\theta = 4b/\lambda_\beta$, and the recess $\Delta \simeq 2r\theta = 0.75 \times 10^{-3}$ cm would be large enough for the button with radius $r = 0.75$ cm. This number is very small, and practically recess is defined by the tolerances of the BPM installation. Excessive recess may, however, produce trapped modes. The decay length of the trapped mode

$$q = \zeta \frac{k_c^2 V_b}{2S}$$

depends on the parameter ζ. For a round pipe $\zeta = 1$, and for a rectangular beam pipe

$$\zeta = \frac{4a^2 \sin^2(\pi x_b/a)}{a^2 + b^2} = \frac{2a^2}{a^2 + b^2}. \tag{38}$$

The lowest TM mode in a rectangular beam pipe with dimensions $a \times b$, $a > b$ is

$$H_x = \frac{A}{b} \sin\frac{\pi x}{a} \cos\frac{\pi y}{b}, \quad H_y = -\frac{A}{a} \cos\frac{\pi x}{a} \sin\frac{\pi y}{b} \tag{37}$$

and has the cut-off frequency $(\omega_c/c)^2 = (\pi/a)^2 + (\pi/b)^2$. For four buttons with radius r located at $x = x_b = a/4$, $y = 0$ or $y = b$ and recessed by Δ, the total volume of

bulging is $V_b = 4\pi r^2\Delta$, and the decay length of the trapped mode

$$q = \zeta \frac{k_c^2 V_b}{2S}$$

is given by the parameter

$$\zeta = \frac{4a^2 \sin^2(\pi x_b/a)}{a^2+b^2} = \frac{2a^2}{a^2+b^2}. \tag{38}$$

The frequency shift of a mode is

$$\frac{\Delta\omega}{\omega} = \frac{(2\pi)^4 r^4 \Delta^2}{2b^4(a^2+b^2)}. \tag{39}$$

Resistive wall gives in this case

$$(\frac{\Delta\omega}{\omega})_{RW} = \frac{\delta}{ab}\frac{a^3+b^3}{a^2+b^2}. \tag{40}$$

Recess is small if it gives a small frequency shift compared to the shift due to resistive wall:

$$\Delta < (\frac{b}{2\pi r})^2 \sqrt{\frac{2\delta}{ab}(a^3+b^3)}. \tag{41}$$

Take $a = 9.0$ cm, $b = 4.8$ cm, $r = 0.75$ cm, $\delta = 1\mu m$. Then $\Delta < 0.64mm$ has to be taken as the maximum acceptable recess of a button in the arcs. The resistive wall frequency shift in the round pipe of the straights is

$$(\frac{\Delta\omega}{\omega})_{RW} = \frac{\delta}{2b}. \tag{42}$$

The acceptable button recess for four-button BPM in the beam pipe with radius b is

$$\Delta < \frac{b^3}{2\nu r^2}\sqrt{\frac{\delta}{b}}, \tag{43}$$

and larger than that in the arcs: $\Delta < 1.6$ mm for $b = 4.5$ cm, and $r = 0.75$ cm. The estimate of the acceptable recess is conservative and does not take into account losses to a BPM cable.

Bellows, quad/dipole offset, rf seals

We compared several designs for a bellows module. The final design uses fingers outside of the beam pipe and does not use large synchrotron radiation masks. Instead, the beam pipes are offset horizontally by a few mm and the transitions are tapered to produce sufficient protection from th synchrotron radiation (see Figs. 18 a,b).

Impedance of the quadrupole/dipole transition with the tapered beam pipe offset of 5 mm was modeled with MAFIA. The loss factor of the transition is $k_l = 4.5\,10^{-4}$ V/pC. No trapped modes were found either by considering propagation of the rf Gaussian bunch or in the S-matrix calculations.

The impedance of the bellows module is generated by finger slots, slots in the bellows corners, small tapers of the synchrotron radiation masks, and the RF seals. All contributions are small and correspond to an inductive impedance.

Impedances of the tapers of the bellow module were modeled as independent axi-symmetric structures with radii equal to the distances from the beam line to the corresponding taper. The results were then averaged proportional to the azimuthal filling factors, giving an inductance $L = 0.044$ nH and a loss factor $k_l = 3.3 \times 10^{-3}$ V/pC per bellows. For 300 bellows the total inductive impedance is only $L = 13$ nH and $k_l = 1$ V/pC. Due to the larger distance of the taper from the beam and the small vertical size of the vacuum chamber, the taper with the large 20^o angle gives only a small contribution after averaging.

Impedance of the 50 finger slots with length 1.25 cm, and width 0.76 mm is $L = 1.5 \times 10^{-4}$ nH for 50 fingers per bellows. Eight slots in the corners are wider ($w = 4$ mm) and, although they are farther away from the beam, give $L = 7.6 \times 10^{-4}$ nH per bellow, more than the finger slots. The total inductance of the slots is $L = 0.27$ nH per 300 bellows. The difference in the dimensions of the beam pipe in the arcs and straights is of no significance here.

The rf seals in a bellows module are designed to give a small 1 mm high and 0.5 mm wide recess in the beam pipe. The exact height of the recess cannot be known but the rf seal should not look like a groove that may generate trapped modes. Impedance

of the rf seal is inductive[10]

$$L = \frac{4\Delta^2}{b}. \tag{44}$$

To be conservative, we take $\Delta = 1$ mm, $< 1/b >= 0.33\,cm^{-1}$. Then $L = 1.6 \times 10^{-2}$ nH per rf seal. The code ABCI gives the same $L = 1.07 \times 10^{-2}$ nH and the loss factor $k_l = 1.1 \times 10^{-4}$. Neglecting again the difference between dimensions of the bellows in the straights and arcs, we get $L = 0.47$ nH or $Z/n = 0.4 \times 10^{-3}\ \Omega$ for the 290 rf bellows seals in the ring. (Note, that this is an overestimate of the actual impedance).

The estimate of the impedance of the rf bellows seals is valid also for the flange/gap rings. These give an additional $L = 0.47$ nH per ring. Clearly, the main issue for the bellows is not beam impedance but heating and operational reliability of the fingers.

Heating, in particular, may be produced by radiation through the slots, and by coupling of the beam to the modes of the cavity between fingers and bellow convolutions.

Radiation of the slots is dipole radiation with dipole moment induced by the field of a bunch or by the field of a TM HOM generated somewhere upstream from the bellows. The first mechanism gives the average radiated power due to the beam

$$P_{beam} = \frac{Z_0 I_{av}^2}{2\pi^{3/2}}\left(\frac{s_B}{\sigma_B}\right)\left(\frac{lw^2}{32b\sigma_B^2}\right)^2. \tag{45}$$

For $I_{av} = 3$ A, $\sigma_B = 1$ cm, and $b = 3.3$ cm that gives $P = 0.45$ W/bellows from eight corner slots. Fifty finger slots, being narrower, give less by a factor of 123.

Consider now the TM modes generated by the beam somewhere upstream at the components with a total broad-band loss factor of k_l. That defines the power of the incoming HOM modes averaged over frequencies within the bunch spectrum $P_{TM} = I_{av}^2 k_l s_B/c$. Power P_{TM} radiated from a slot due to incoming TM mode may then be compared then with power radiated by the beam P_{beam}:

$$P_{TM} = 2\sqrt{\pi} k_l \sigma_B P_{beam} \tag{46}$$

and, for the total loss factor $k_l \simeq 3$V/pC, can be larger than P_{beam} by a factor of 10.6.

Radiated power becomes on the order of 5 W per bellows module. This estimate does not take into account local variation of power in TM HOM-s.

Radiation from the finger slots induced by a TE mode is 1290 times larger than radiation due to regular TM modes mostly due to the factor $(l/w)^4$. Taking into account the difference in the number of finger and corner slots, we get the power $P = 312.8$ W per bellows module, provided that the power of the incoming TE and TM modes are the same. However, beam does not couple with the TE modes: they can be produced by transformation of the TM-modes or due to decay of modes in asymmetric structures with hybrid modes. In both cases a small factor makes the power of the TE modes on the order of a few percent of the average power of the TM HOMs reducing the radiation power due to TE HOMs to a few watts per bellows module.

Another mechanism that may be important for heating is resonance excitation of eigen modes in the cavity between fingers and bellow convolutions if their frequencies are in resonance with bunch spacing $\omega s_B/c = 2\pi n$. The enhancement factor of the power deposited by the beam is $D = 4Q_L/(2\pi n)$. For a frequency $f \simeq 1$ GHz, the factor $\omega s_B/c = 8\pi$ and D depends on the loaded Q_L, $D_{max} = Q_l/4\pi$. For a TM HOM corresponding to $k_l = 3$ V/pC, the power $P = 0.02$ W/bellows is still small even for $Q_L = 10^4$, which can be expected with stainless-steel convolutions.

Lumped pumps

Ports of the lumped vacuum pumps are screened with a grid of long and narrow slots. The layout for the straight section of the HER is shown in Fig. 19a, and for the arcs in Fig. 19b. In the arcs, there are 24 slots altogether in the upper and lower decks with length $l = 15.4$ cm and width $w = 2.54$ mm.

Impedance of each slot of the pumping screen in the arcs is $L = 1.1 \times 10^{-4}$, and the total contribution of the 24 pumping slots for all of the 200 ports in the arcs is 0.53 nH. The potential problem here is not broad-band impedance but the possibility of trapped modes.

As an example, consider a $g = 2$ cm long circular cavity with a depth $\Delta = 3$ mm in the $b = 3$ cm radius beam pipe[11]. The broad-band impedance of such a small

cavity is small and mainly inductive (see Eq. (41)). However, MAFIA finds a narrow resonance with shunt impedance $R_s = 7\ k\Omega$ and $Q = 2.7 \times 10^4$. Such a mode can be considered as a modified propagating mode with a frequency close to the cutoff frequency $\omega_m/c = \nu_0/b$ where $\nu_0 = 2.405$ is the first root of the Bessel function $J_0(\nu_0) = 0$. A small bulge of the beam pipe changes the frequency of the mode, shifting it below cutoff and making a trapped mode. The situation is analogous to the frequency shift of a mode in a cavity due to a small perturbation of the boundary. The mechanism is described in the original paper by Stupakov and Kurennoy[12]. The paper also gives a numerical example quite similar to the one described above.

The theory[12]predicts a trapped mode at the grid of the vacuum port in the arcs with shunt impedance[13] $R_s = 644.\Omega$, Q factor on the order of 3.5×10^4, and localization length $L = 35$ cm. The shunt impedance of a trapped mode at the vacuum ports of the straight sections is smaller, $R_s = 85.\Omega$. MAFIA confirms that slots cut in the circular beam pipe produce a trapped mode with parameters given by the total magnetic polarizability of the slots, Fig. 20a,b.

The frequency shift of the trapped mode is larger than the width given by the resistivity of the wall. Radiation from a narrow slot outside the thick beam-pipe is suppressed at a frequency close to the cut-off. Radiation into the beam pipe is possible only in the TE_{11} mode, which has a cut-off frequency lower than the cut-off for the TM_{01} mode. However, the width due to this process is very small. For a symmetric placement of the slots, radiation is additionally suppressed.

To eliminate trapping, the beam pipe at the vacuum port may be recessed with the recess volume equal to or slightly larger than the polarizability of the slots. Numerical simulations with MAFIA confirmed this statement[13].

A bow-like recess of the slots in the arcs has to have saggita $\Delta > 0.27$ mm and, practically, will be set to be larger than the fabrication tolerances. A mesh of small holes on the pump side should be used to prevent propagation of TE modes to the pumps.

Tapers

The circular beam pipe of the straight sections ($b = 4.5$ cm) and the rectangular

beam pipe of the arcs (2.5 × 4.5 cm) are connected with tapers (see Fig. 21). The 2D modeling of a 10^o taper connecting two circular beam pipes with radii of 2.5 and 4.5 cm gives a conservative estimate of $k_l = 5.1 \times 10^{-3}$ V/pC and $L = 0.3$ nH per taper (see Fig. 22). The wake is inductive. The real part of the impedance is $ReZ < 0.5\,\Omega$ per taper for frequencies below 5 GHz.

Collimators

A simple model of a collimator as a pair of tapers with a height of 4.5 cm and a taper angle of 10^o gives a loss factor of $k_l = 2 \times 10^{-2}$ V/pC. The wake is inductive and corresponds to $L = 1.57$ nH per collimator (see Fig. 23).

Feedback kickers

Longitudinal and transverse kickers for PEP-II are modeled after those designed and measured for the ALS[14](see Fig. 24). The longitudinal beam impedance of the ALS transverse kicker was found to be $Z/n = 0.53\ m\Omega$ and the loss parameter was estimated as $k_l = 0.66$ V/pC. For the longitudinal ALS kicker, $Z/n = 25\ m\Omega$ and the shunt impedance is 300 Ω within the passband 1.25 GHz.

Tolerance on the beam-pipe misalignment

Misaligned beam pipes can generate additional impedance. For a small misalignment δ of two beam pipes with radius b the impedance is inductive[15]

$$L = \frac{4}{3}\frac{\delta^2}{b}. \tag{47}$$

For $\delta = 2$ mm and $b = 2.5$ cm that gives $L = 0.023$ nH. In the worst case 300 misalignments of this kind give $L = 7$ nH, giving the upper bound for the misalignments with rms error 2 mm. We checked this formula with the 2-D code ABCI considering two pipes with radii 4.7 and 4.5 mm. That gives $L = 0.030$ nH, and the loss factor $k_l = 1.4\,10^{-3}$ V/pC. Inductance, after scaling proportional to the azimuthal filling factor 1/2 and ratio of radii is $L = 0.027$ nH in good agreement with the analytic formula.

Impedance of synchrotron radiation

Maximum value of impedance caused by synchrotron radiation

$$max(\frac{Z}{n}) = 300\frac{b}{R}\Omega \tag{48}$$

for $b = 2.5$ cm and the average radius $R = 350$ m is quite large, giving $L_{max} = 25$ nH. However, the maximum value corresponds to the harmonic number $n_{th} \simeq (\pi R/b)^{3/2} = 7.5 \times 10^6$. Such frequencies are much larger than frequencies within the bunch spectrum which, for $\sigma = 1$ cm, rolls-off starting from $n = 3.5 \times 10^4$. Impedance of the synchrotron radiation is suppressed exponentially for frequencies $n < n_{th}$ and contributes negligibly to the PEP-II impedance budget.

Cross-talk

As usual, we neglected the cross-talk between spatially close components in this calculations. An example of a periodic array of irises shows that such an interference tends to reduce the total impedance, but, to our knowledge, no serious studies of the problem are available at this time. We want to make only a few comments.

At high frequencies, a diffractional model can be used to estimate the length of the interaction of the wake with a particle. Consider, for example, a scraper with the inner radius a in a beam pipe with radius b. The angle of diffraction θ for a wave with frequency $\omega = 2\pi f$ is $\theta \simeq c/\omega a$. The elements of the vacuum system can be considered as independent if the distance between is larger than the length of diffraction $L \simeq (b-a)\omega a/c$.

If two recessed elements of the vacuum chamber are close to each other, a mode can be localized between them. However, to have a large Q factor, the mode should not be coupled with propagating modes outside of the elements. This coupling for smooth obstacles with the width w and height of the recess Δ depends exponentially on the parameter

$$\frac{\nu w}{b}\sqrt{\frac{2\Delta}{b}},$$

where b is the beam pipe radius and $\nu = 2.4$ is a root of the Bessel function. The parameter should be much larger than one for a large Q.

This problem was considered for the rf seal and recessed vacuum port. Both are short (in the model the height of each was 1 mm) and are close to each other. The field pattern found in MAFIA simulations confirmed, as was expected, that such a system does not confine a mode (see Fig. 26).

Summary

The main contributions to impedance of PEP-II come from the rf cavities and the resistive wall impedance. Components giving the main contribution to inductive part of the impedance are summarized in Table 6. The contribution of an element is calculated and multiplied by the number of such elements given in Table 2. These elements are mainly inductive but do have a small resistive part, which give a non-zero loss factor of $k_l = 3.1$ V/pC. We can describe this loss by a constant resistivity R_Ω.

Longitudinal impedance is the sum of the narrow-band and the broad-band impedances. The narrow-band impedance is given by the modes of the cavities (see Table. 3), and a few modes in the BPMs, and kickers. Broad-band longitudinal impedance can be parametrized[16][17] by expansion over $\sqrt{\omega}$. For $\omega > 0$ it takes the form:

$$Z_l(\omega) = -iZ_0\frac{L\omega}{4\pi c} + (1-i)R_W\sqrt{\omega} + R_\Omega + (1+i)R_c\sqrt{\frac{\omega_c}{\omega}}\theta(\omega-\omega_c) + ...$$

where $Z_0 = 4\pi/c = 120\pi\ \Omega$, and $\omega_c/2\pi$ is a cutoff frequency. Usually, the impedance can be set to the cutoff frequency of the beam pipe at the rf cavities. Dependence of the total impedance on the choice of ω_c is weak if the number of modes below cutoff taken into account in the narrow-band impedance and the coefficient R_c are chosen consistently.

The first term in the expansion of Z_l over $\sqrt{\omega}$ describes inductive impedance generated by all elements in the ring with eigen-frequencies much higher than frequencies within the bunch spectrum. The inductance L (L in nH, 1 cm=1 nH) defines the low-frequency parameter Z_l/n where $n = \omega/\omega_0$ is the harmonic number, and $\omega_0 = 2\pi f = c/R$ is the revolution frequency.

The inductance L is given by Table 6. The second term describes the resistive wall impedance. The third term describes a constant resistivity. The wake of a bunch in this case is proportional to $\rho(s)$. The last term is a good parametrization of the high-frequency tail of the rf cavities.

Transverse impedance is dominated by the modes of the rf cavities, Table 4, and resistive wall estimated above. The rest of the ring contribures little and, therefore, it may suffice to have an estimate of such a contribution. This estimate can be obtained in a standard way from the results of Table 6.

Table 6. The main contribution to the inductive impedance of PEP-II

		L (nH)	k_l (V/pC)
	Dipole screens	0.10	
	BPM	11.	0.8
	Arc bellow module	13.5	1.41
	Collimators	18.9	0.24
	Pump slots	0.8	
	Flange/gap rings	0.47	0.03
	Tapers oct/round	3.6	0.06
	IR chamber	5.0	0.12
	Feedback kickers	29.8	0.66
	Injection port	0.17	0.004
	Abort dump port	0.23	0.005
Total		83.3	3.4

Figure Caption

Fig. 1. RF cavity shape (without damping ports).

Fig. 2. Broad-band longitudinal wake potential of a rf cavity.

Fig. 3. Dipole wake potential of a rf cavity.

Fig. 4. Real part of the longitudinal broad-band impedance of a rf cavity.

Fig. 5 a,b. Layout of the DIP screen.

Fig. 6 a,b. Layout of the LER antechamber.

Fig. 7. Electric field pattern for the antechamber.

Fig. 8. Longitudinal wakepotential $W(s)$ for different lengths and depths of the antechamber.

Fig. 9 a,b Layout of the abort system and the model used in MAFIA simulations.

Fig. 10a,b. Layout of masks of the IR in horizontal and vertical planes.

Fig. 11. Broad-band impedance of the IR.

Fig. 12. Field pattern of trapped modes of the Be pipe of the IR.

Fig. 13 a,b. Injection port and the model used in MAFIA simulations.

Fig. 14. Layout of a four button BPM.

Fig. 15 a,b. Comparison of MAFIA simulations with wire measurements of a BPM.

Fig. 16. Impedances and wakefields of a 1.5 cm button.

Fig. 17. Dependence on frequenc of the permeability μ.

Fig. 18 a,b. Layout of a bellows, x, z and y, z planes.

Fig. 19 a,b. Layout of the slots of a vacuum port for the straight sections and arcs respectively.

Fig. 20. (a) Dependence of the E_z component of a trapped mode on the

distance from the slot center and (b) the electric field pattern.

Fig. 21. Layout of the taper of a transition from a round to a hexagonal pipe.

Fig. 22. Wake potential of the taper.

Fig. 23. Longitudinal wake potential of a model of a typical collimator.

Fig. 24. Layout of a feedback kicker.

Fig. 25. Layout of a valve.

Fig. 26. Field pattern with two 1 mm high restrictions. The beam pipe is closed at the ends. The wide restriction confines the mode but a small one has no effect. In a real system, the mode would propagate to the left.

REFERENCES

1. PEP-II, An Asymmetric B Factory, CDR, LBL PUB-5379, SLAC-418, June 1993.

2. R. L. Gluckstern, J. van Zeijts, B. Zotter. Coupling Impedance of Beam Pipes of General Cross Section, CERN SL/AP 92-25, June 1992.

3. J. Byrd, G. Lambertson. Resistive wall impedance of the B Factory, PEP-II AP Note 9-93, March 1993.

4. J.D. Jackson, SSC Central Design Group Report, SSC-N-110 (1986), E. D. Courant, M. Month, BNL-50875, 1978.

5. E. Henestroza, S. Heifets, M. Zolotarev Trapped Modes in the PEP-II B Factory Interaction Region, PAC, Washington, 1995.

6. A. Kulikov, J. Seeman, M. Zolotarev. PEP-II Abort System Specifications, PEP-II Note 61, 10/1994.

7. A. Piwinsky, IEEE Nucl. Sci., 24, No. 3, 1364, 1977.

8. S. Kurennoy, Beam-Coupling Impedance of Holes in Vacuum-Chamber Walls, IHEP 92-84, UNK, 1992.

9. N. Kurita, D. Martin, C.-K Ng, S. Smith, and T. Weiland. Simulation of PEP-II Beam Position Monitor, PEP-II Note 87, March 1995.

10. K. Bane. The Calculated Longitudinal Impedance of the SLC Damping Ring, SLAC-PUB-4618, 1988.

11. Cho K. Ng and T. Weiland. Impedance analysis of the PEP-II Vacuum Chamber, SLAC report, unpublished, 1994.

12. G. V. Stupakov, S. S. Kurennoy. Trapped EM Modes in a Waveguide with a Small Discontinuity, SSCL-Preprint-459, June 1993.

13. S. Heifets, G. Stupakov. Study of the Trapped Modes at the Vacuum Ports, PEP-II Note No. 80, January 1995.

14. J. Corlett, J. Johnson, G. Lambertson, F. Voelker. Longitudinal and Transverse Feedback Kickers for the ALS, LBL-34955, UC-410, 1994.

15. J.F. Crawford. The electro-Magnetic Properties of Vacuum Chambers, TM-12-90-04, Paul Scherrer Institute, November 1991.

16. S. Heifets Broad band Impedance of the B Factory, SLAC/AP-93, February 1992.

17. S. Bartalucci, M. Serio, B. Sparato, M. Zobov, L. Palumbo. Broad-band model impedance for DAPHNE Main Rings, Nucl Inst. and Methods, A337, 1994.

18. R. L. Gluckstern. Preprint CERN SL/92-05 (AP), Geneva, 1992.

19. M. Sands. Preprint PEP-253, SLAC 1977.

20. K. Bane, P.B. Wilson, and T. Weiland. Wakefields and Wakefield Acceleration, SLAC-PUB-3528, 1984.

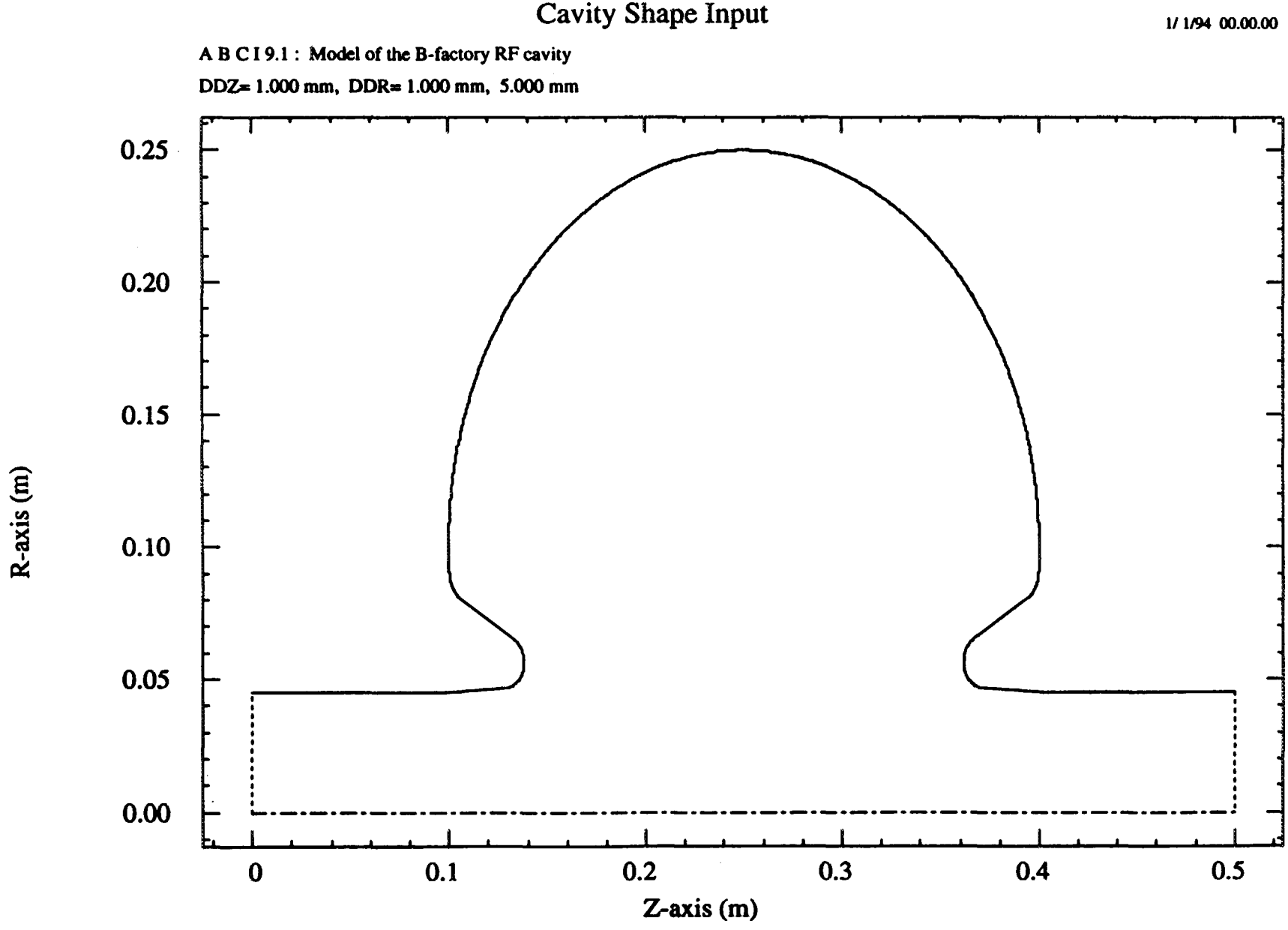
Cavity Shape Input
1/ 1/94 00.00.00
A B C I 9.1 : Model of the B-factory RF cavity
DDZ= 1.000 mm, DDR= 1.000 mm, 5.000 mm
R-axis (m)
0.25
0.20
0.15
0.10
0.05
0.00
0
0.1
0.2
0.3
0.4
0.5
Z-axis (m)

Fig. 1

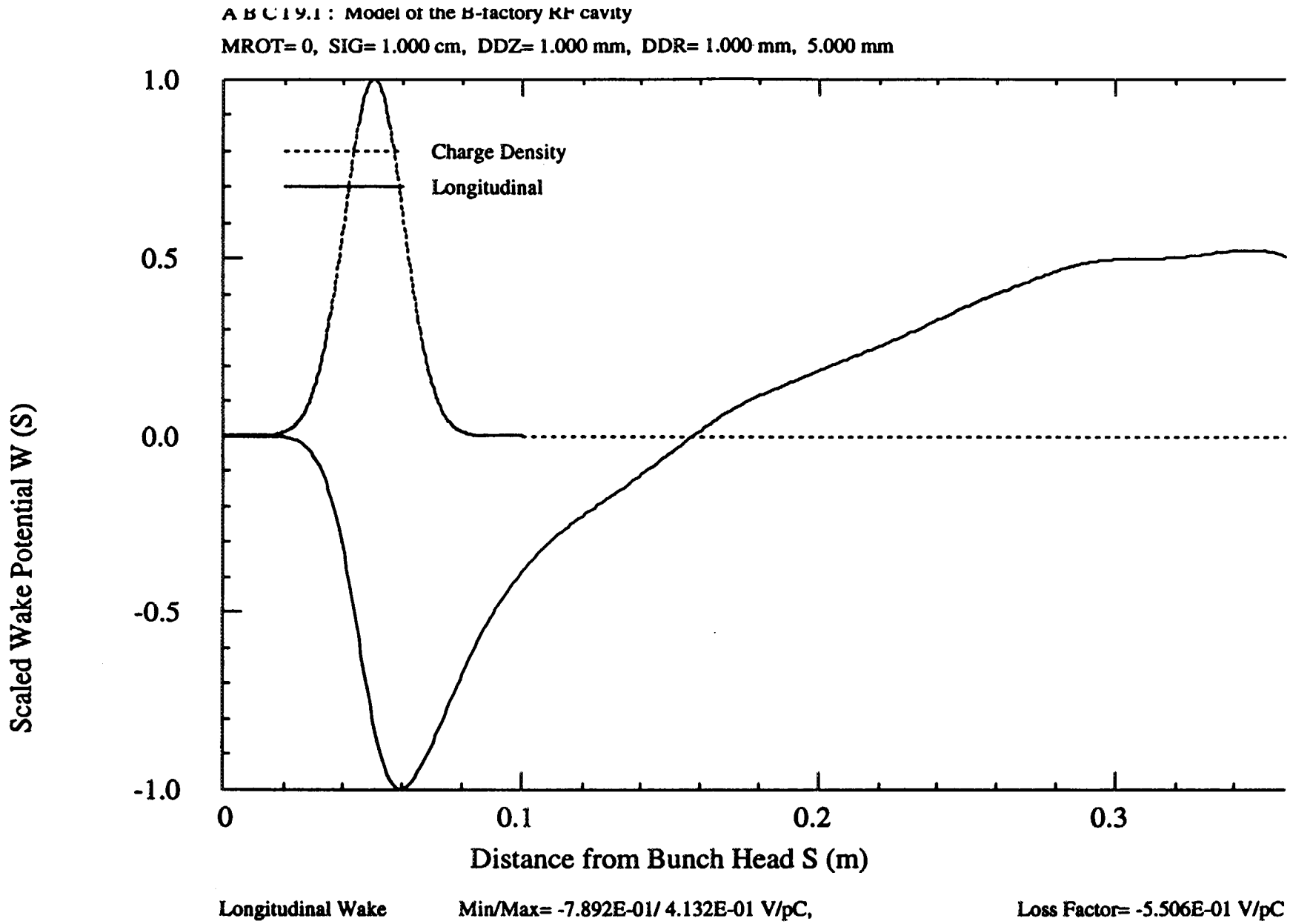
A B C 19.1 : Model of the B-factory RF cavity
MROT= 0, SIG= 1.000 cm, DDZ= 1.000 mm, DDR= 1.000 mm, 5.000 mm
1.0
0.5
0.0
-0.5
-1.0
Charge Density
Longitudinal
Scaled Wake Potential W (S)
0
0.1
0.2
0.3
Distance from Bunch Head S (m)
Longitudinal Wake
Min/Max= -7.892E-01/ 4.132E-01 V/pC,
Loss Factor= -5.506E-01 V/pC

Fig. 2

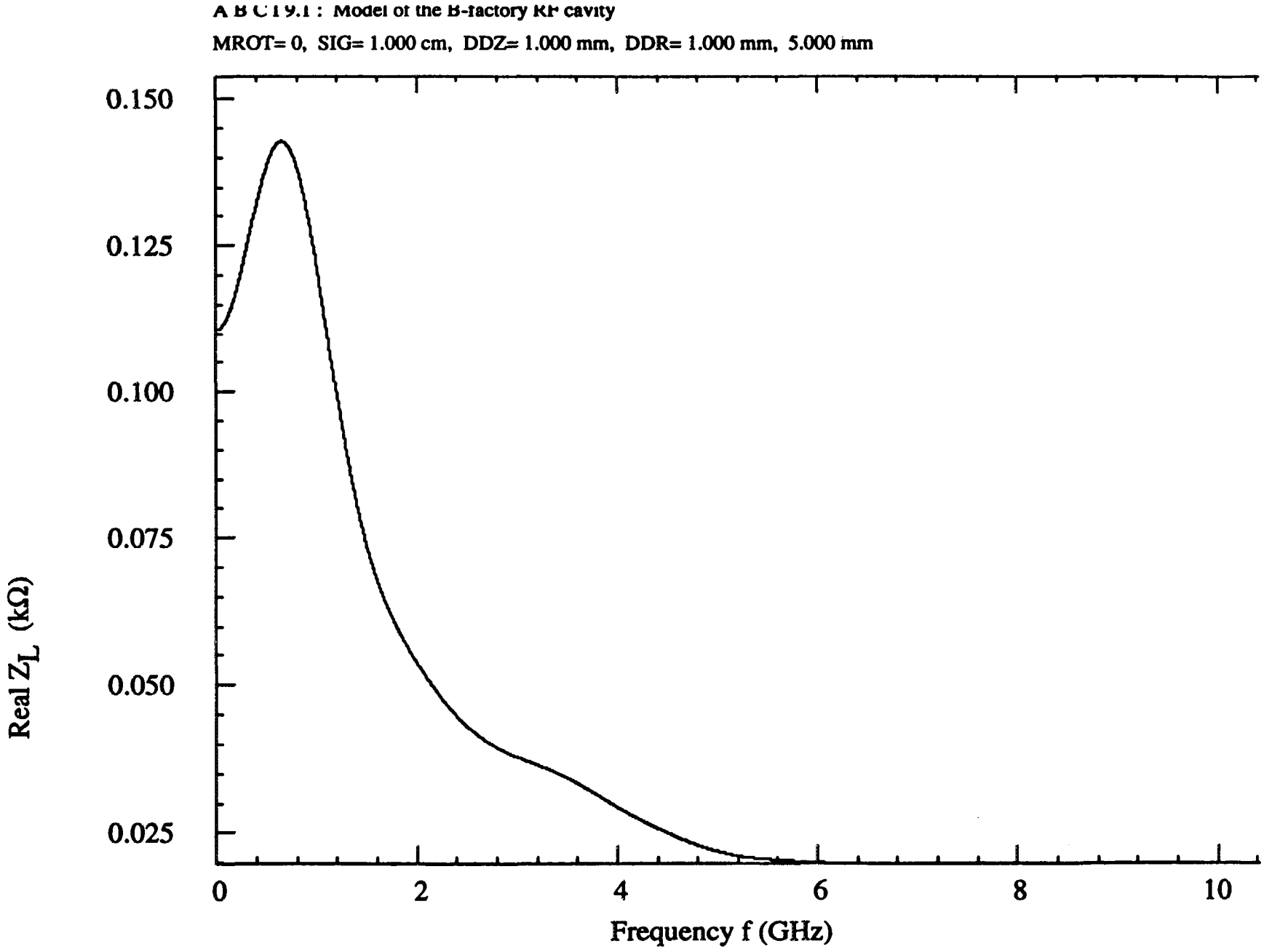
A B C 19.1 : Model of the B-factory RF cavity
MROT= 0, SIG= 1.000 cm, DDZ= 1.000 mm, DDR= 1.000 mm, 5.000 mm
0.150
0.125
0.100
0.075
0.050
0.025
Real Z_L (kΩ)
0
2
4
6
8
10
Frequency f (GHz)

Fig. 3

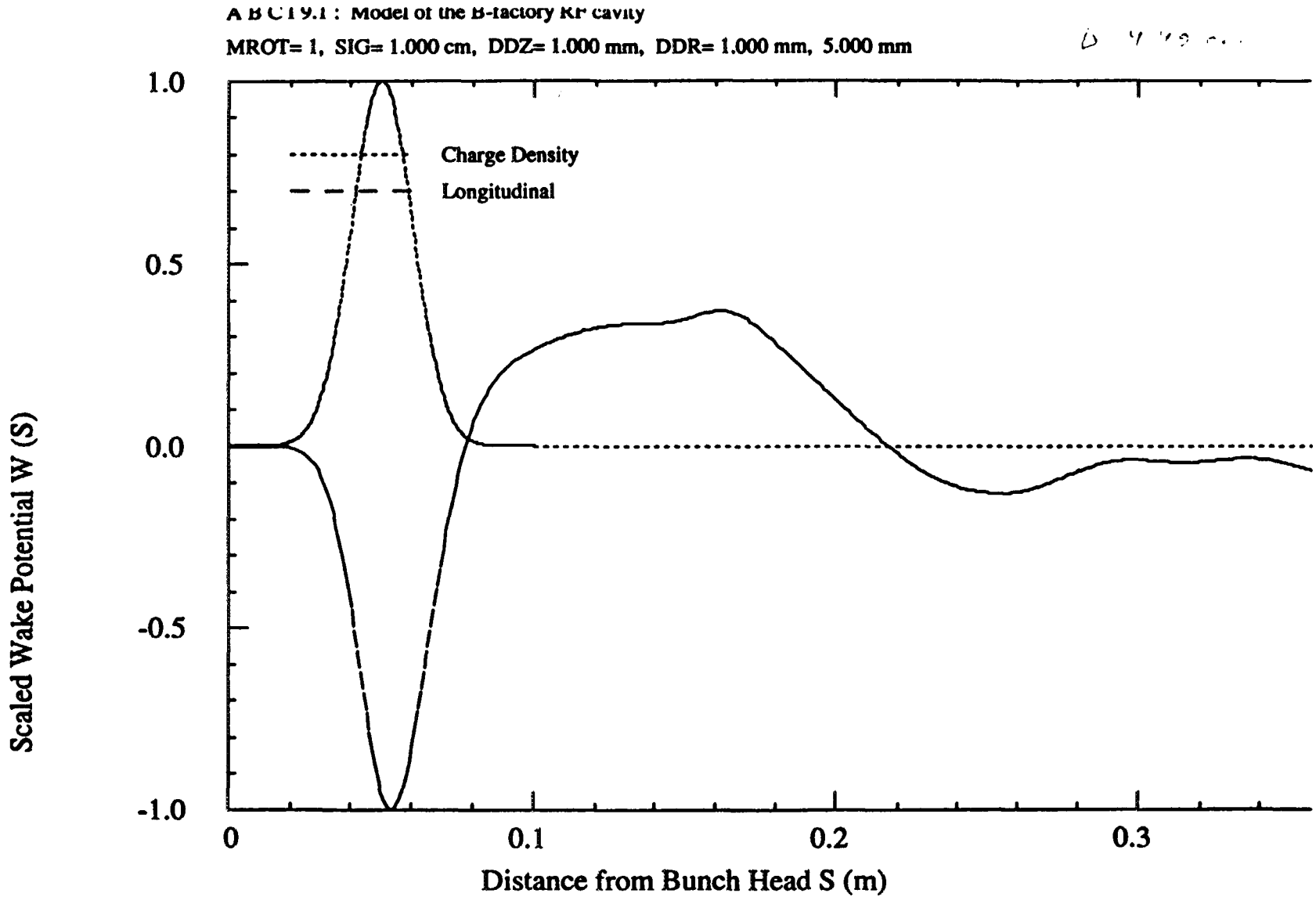
A B C 19.1 : Model of the B-factory RF cavity
MROT= 1, SIG= 1.000 cm, DDZ= 1.000 mm, DDR= 1.000 mm, 5.000 mm
Charge Density
Longitudinal
Scaled Wake Potential W (S)
1.0
0.5
0.0
-0.5
-1.0
0
0.1
0.2
0.3
Distance from Bunch Head S (m)
Azimuthal Wake Min/Max= -1.263E+01/ 4.633E+00 V/pC/m, Loss Factor= -5.278E+00 V/pC
Transverse Wake Min/Max= -4.633E+00/ 1.263E+01 V/pC/m, Loss Factor= 5.266E+00 V/pC
Longitudinal Wake Min/Max= -4.868E+02/ 1.804E+02 V/pC/m², Loss Factor= -3.451E+02 V/pC

Fig. 4.

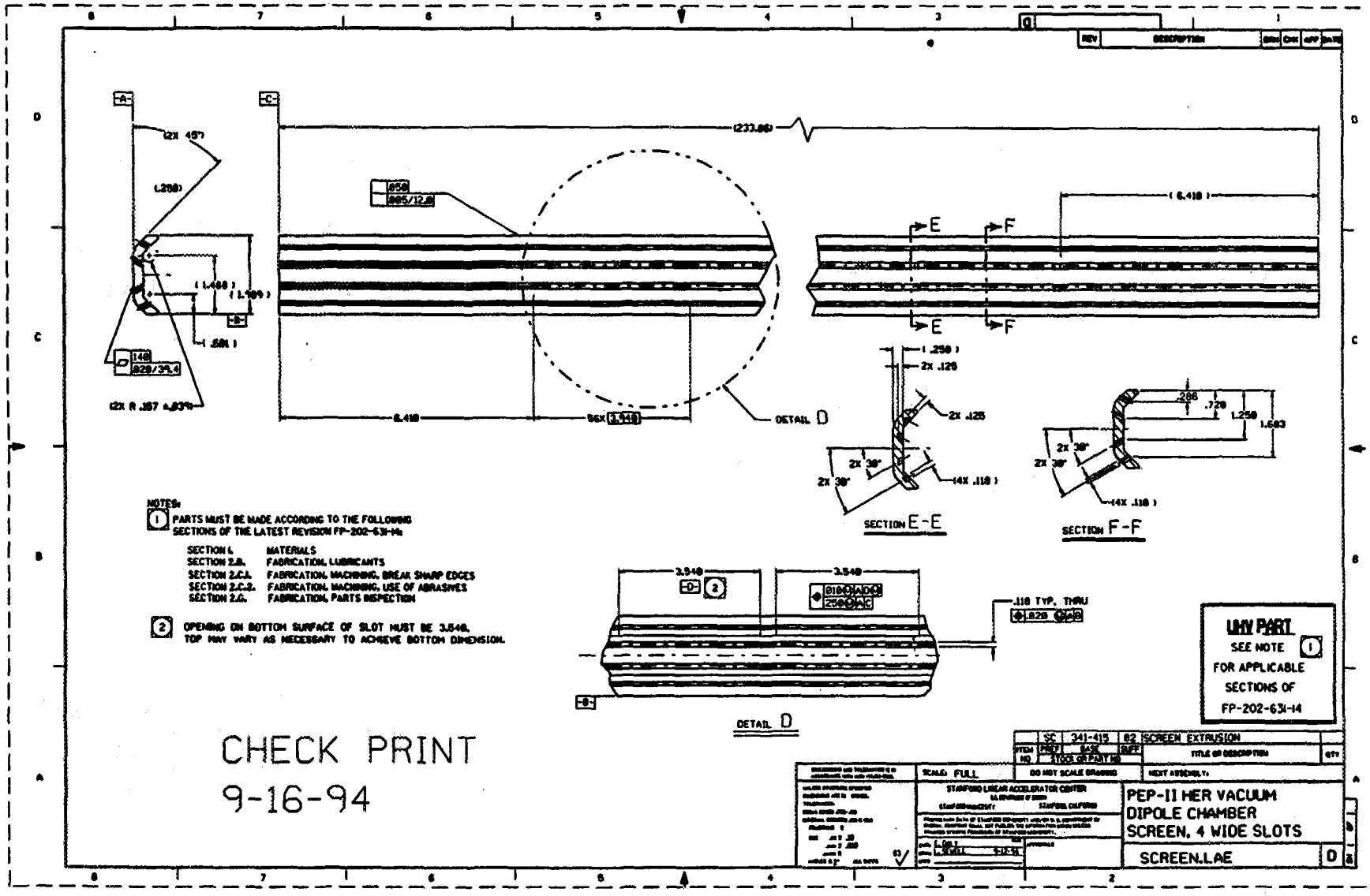
CHECK PRINT
9-16-94
NOTES:
1 PARTS MUST BE MADE ACCORDING TO THE FOLLOWING SECTIONS OF THE LATEST REVISION FP-202-631-14:
SECTION 4. MATERIALS
SECTION 2.B. FABRICATION, LUBRICANTS
SECTION 2.C.1. FABRICATION, MACHINING, BREAK SHARP EDGES
SECTION 2.C.2. FABRICATION, MACHINING, USE OF ABRASIVES
SECTION 2.G. FABRICATION, PARTS INSPECTION
2 OPENING ON BOTTOM SURFACE OF SLOT MUST BE 3.548. TOP MAY VARY AS NECESSARY TO ACHIEVE BOTTOM DIMENSION.
SECTION E-E
SECTION F-F
DETAIL D
DETAIL D
UHV PART
SEE NOTE 1
FOR APPLICABLE
SECTIONS OF
FP-202-631-14
PEP-II HER VACUUM
DIPOLE CHAMBER
SCREEN, 4 WIDE SLOTS
SCREEN.LAE
STANFORD LINEAR ACCELERATOR CENTER
SCALE: FULL
DO NOT SCALE DRAWING

Fig. 5a

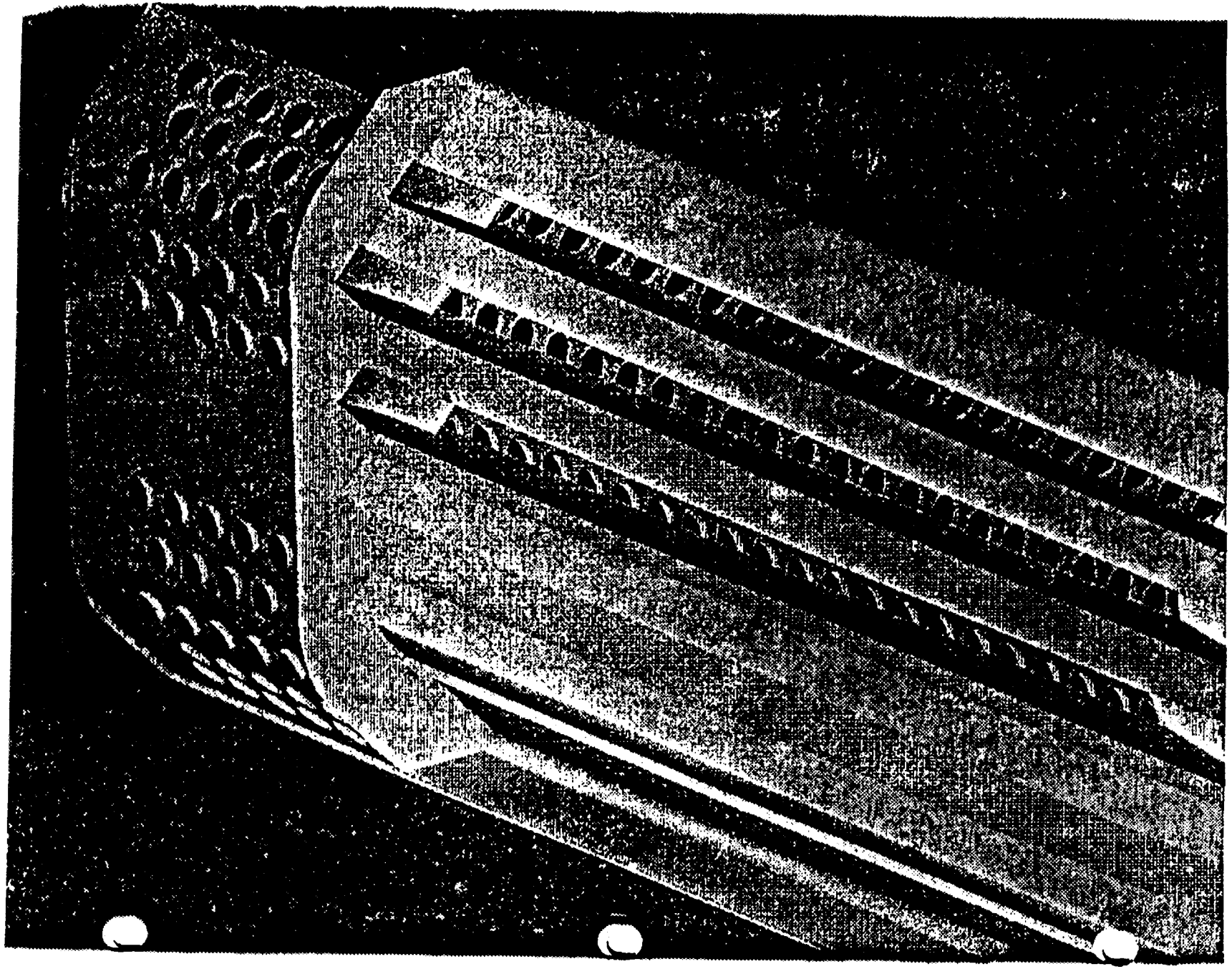

Fig. 5b

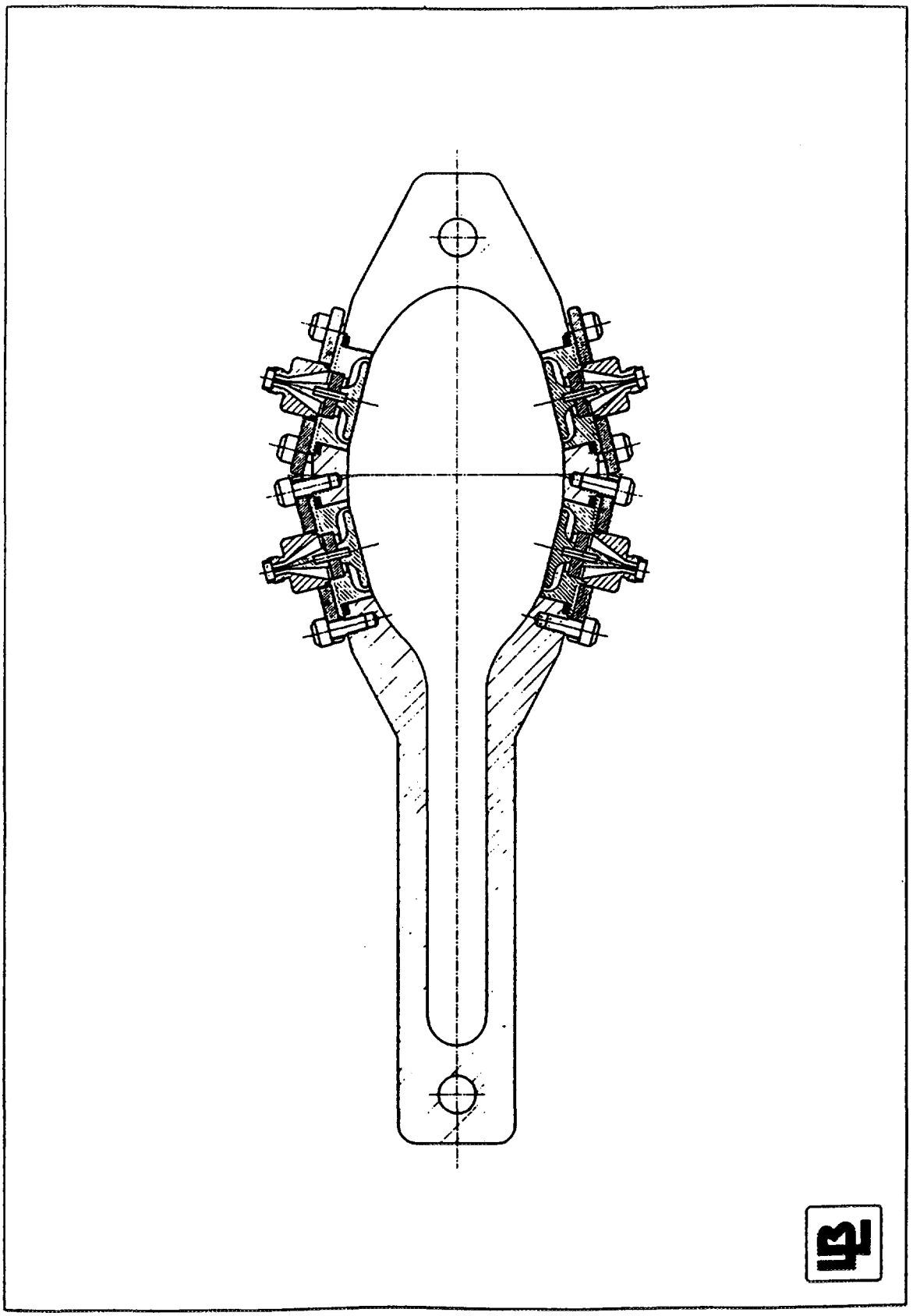

Fig. 9a

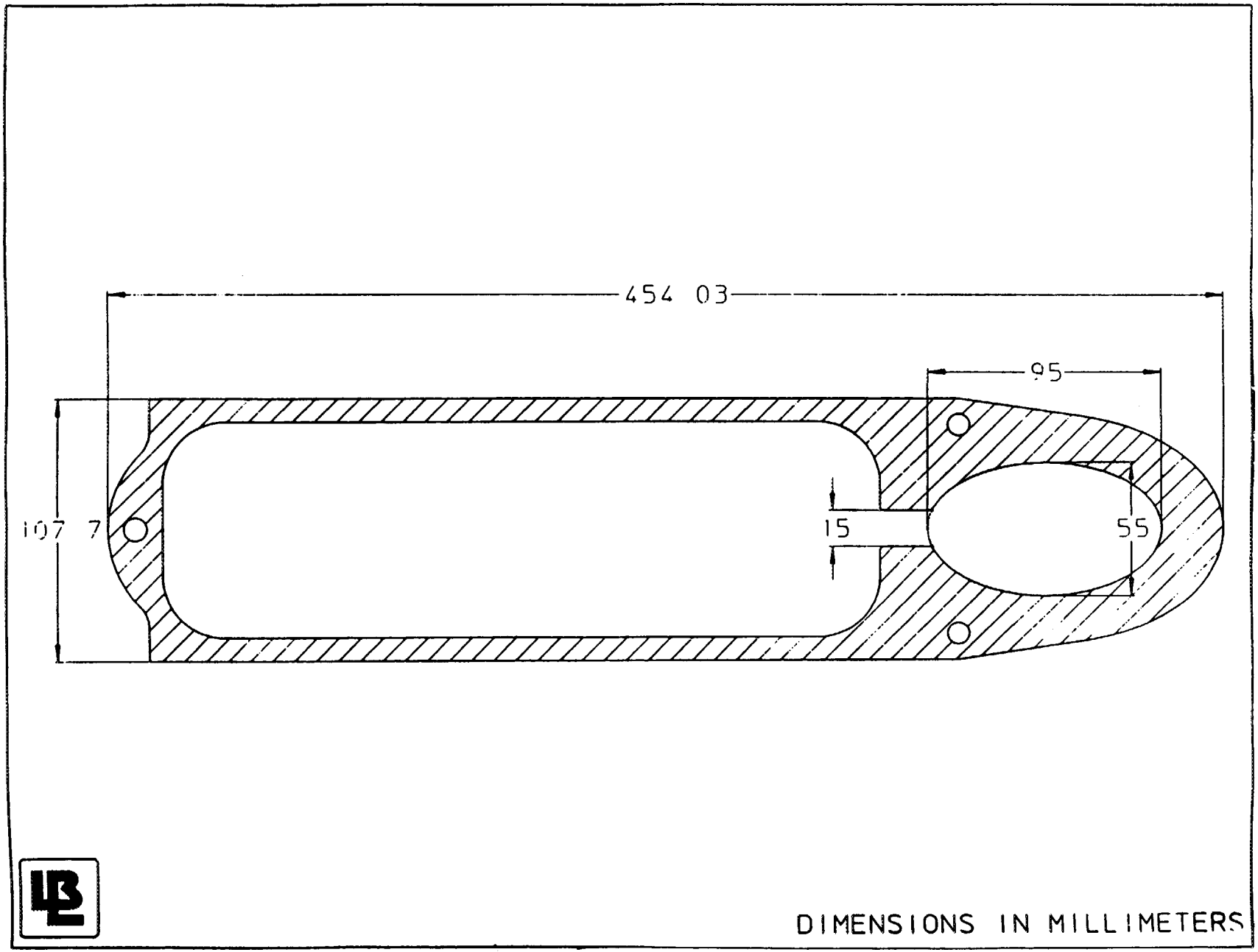

Fig. 6b

E Henestroza

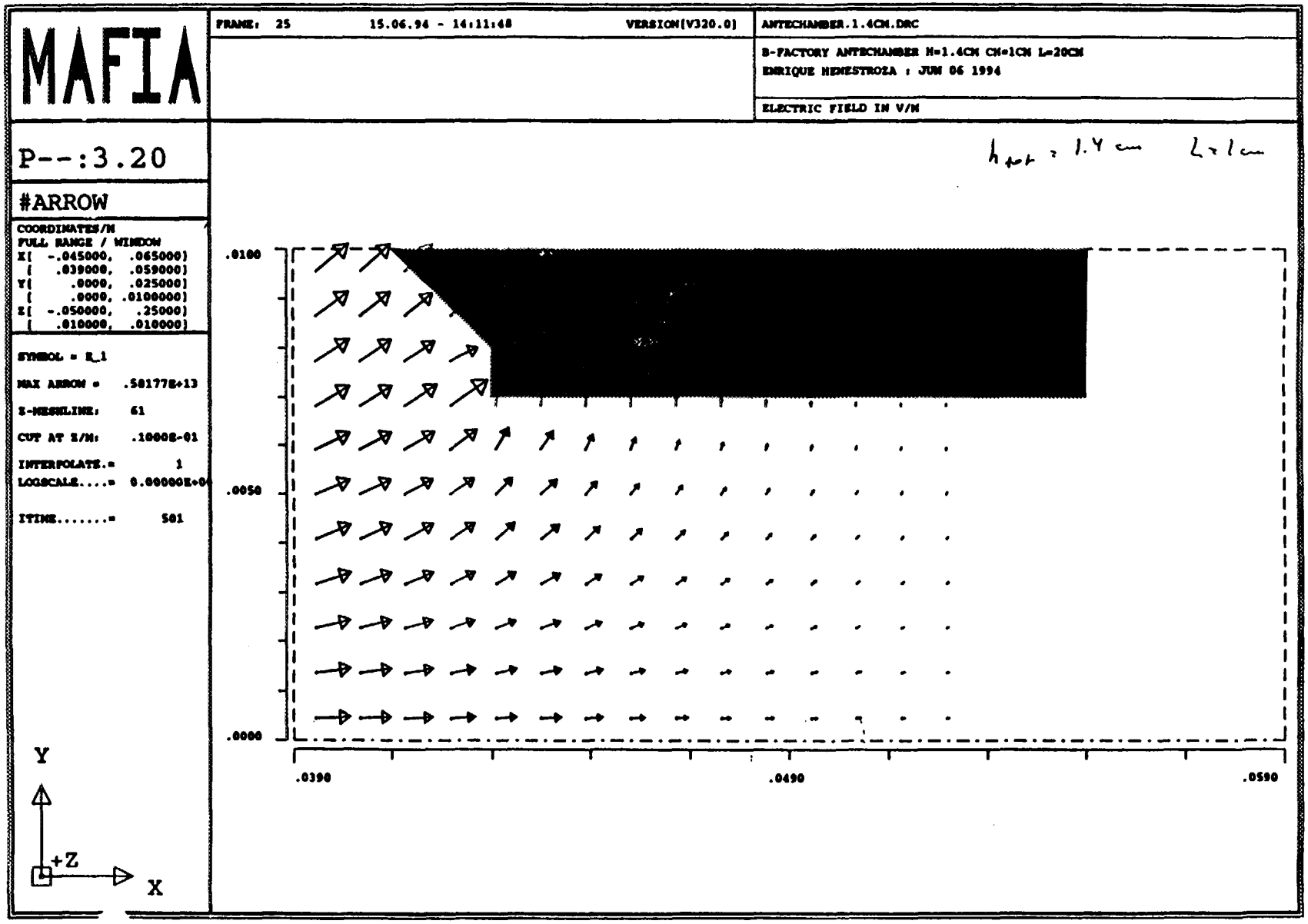

Fig. 7

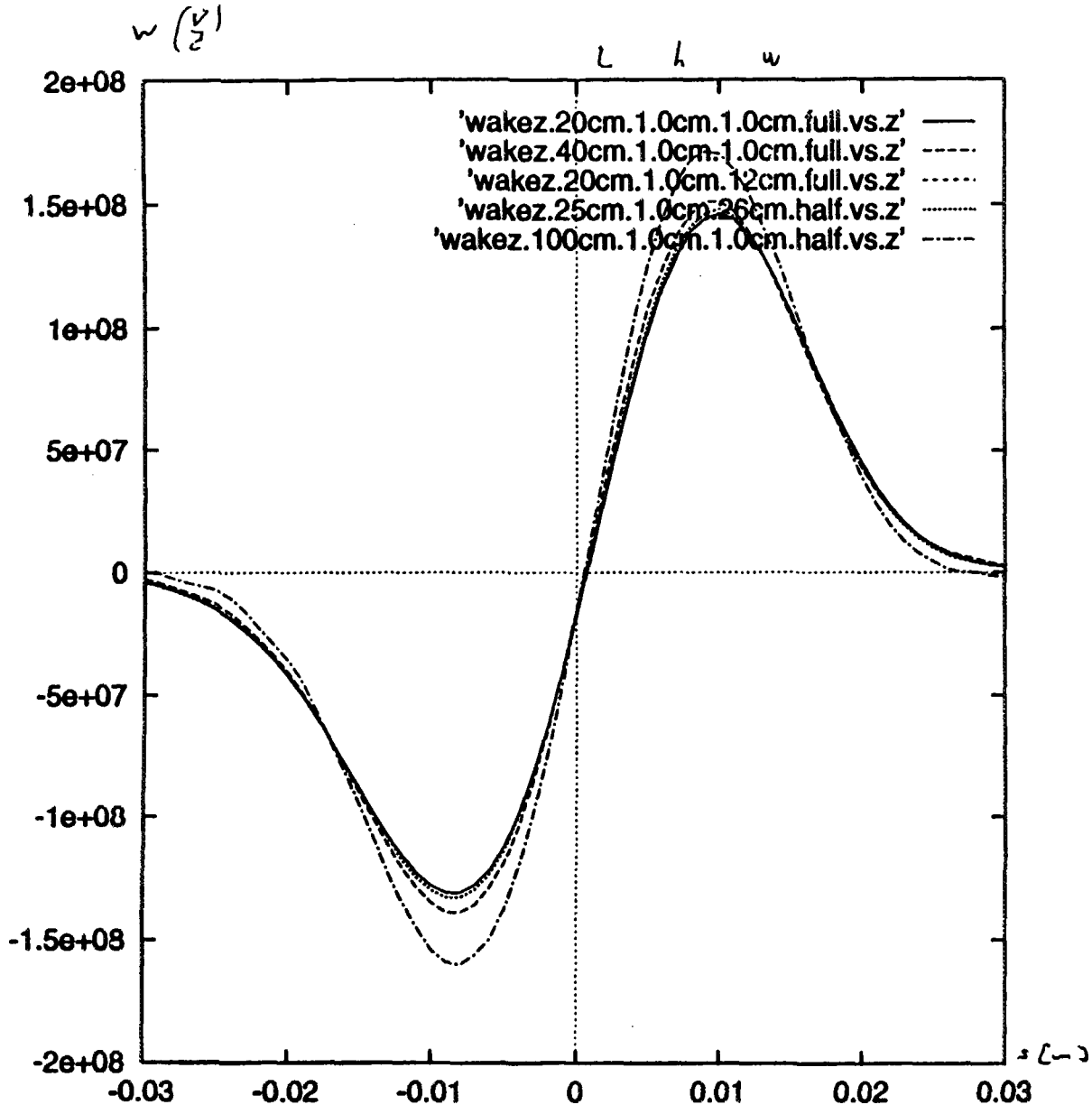
w (V/2)
L h w
'wakez.20cm.1.0cm.1.0cm.full.vs.z'
'wakez.40cm.1.0cm.1.0cm.full.vs.z'
'wakez.20cm.1.0cm.1.2cm.full.vs.z'
'wakez.25cm.1.0cm.2.6cm.half.vs.z'
'wakez.100cm.1.0cm.1.0cm.half.vs.z'
2e+08
1.5e+08
1e+08
5e+07
0
-5e+07
-1e+08
-1.5e+08
-2e+08
-0.03
-0.02
-0.01
0
0.01
0.02
0.03
z (m)

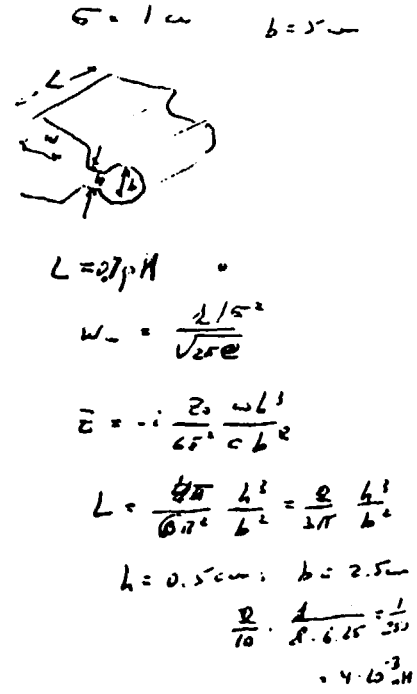
σ = 1 cm
b = 5 cm
L = 0.7 μH
$w_- = \frac{1.15^2}{\sqrt{2\pi e}}$
$\bar{L} = -i \frac{Z_0}{4\pi^2} \frac{\omega L^3}{c\, b^2}$
$L = \frac{4\pi}{(0.1)^2} \frac{L^3}{b^2} = \frac{2}{3\pi} \frac{L^3}{b^2}$
L = 0.5 cm ; b = 2.5 cm
$\frac{2}{10} \cdot \frac{1}{8 \cdot 6.25} = \frac{1}{250}$
$\approx 4 \cdot 10^{-3}$ H

Fig. 8

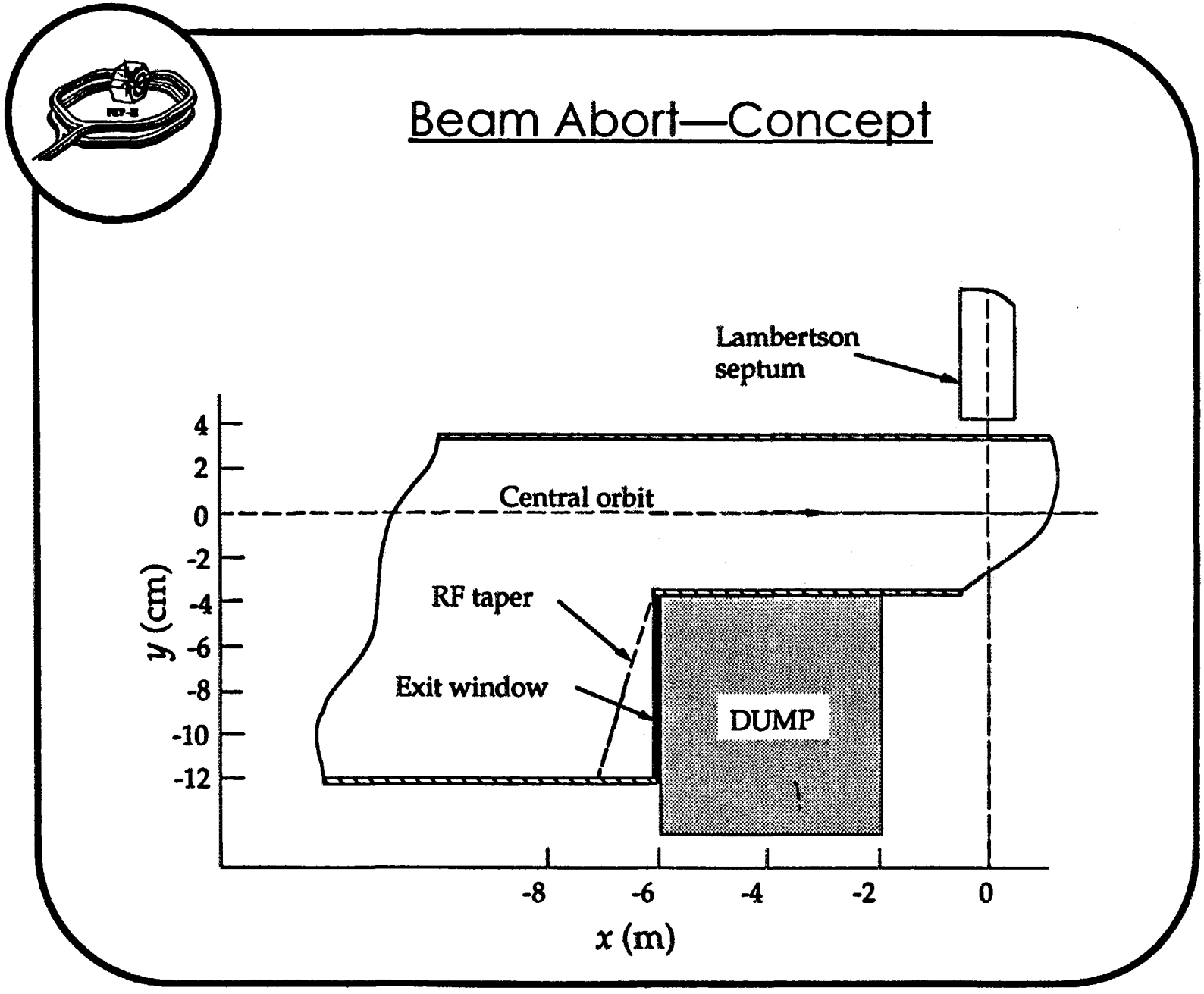
Beam Abort—Concept
Lambertson
septum
Central orbit
RF taper
Exit window
DUMP
y (cm)
4
2
0
-2
-4
-6
-8
-10
-12
-8
-6
-4
-2
0
x (m)
12/2/94 12:35
Beam Abort concept.cnv

Fig. 9a

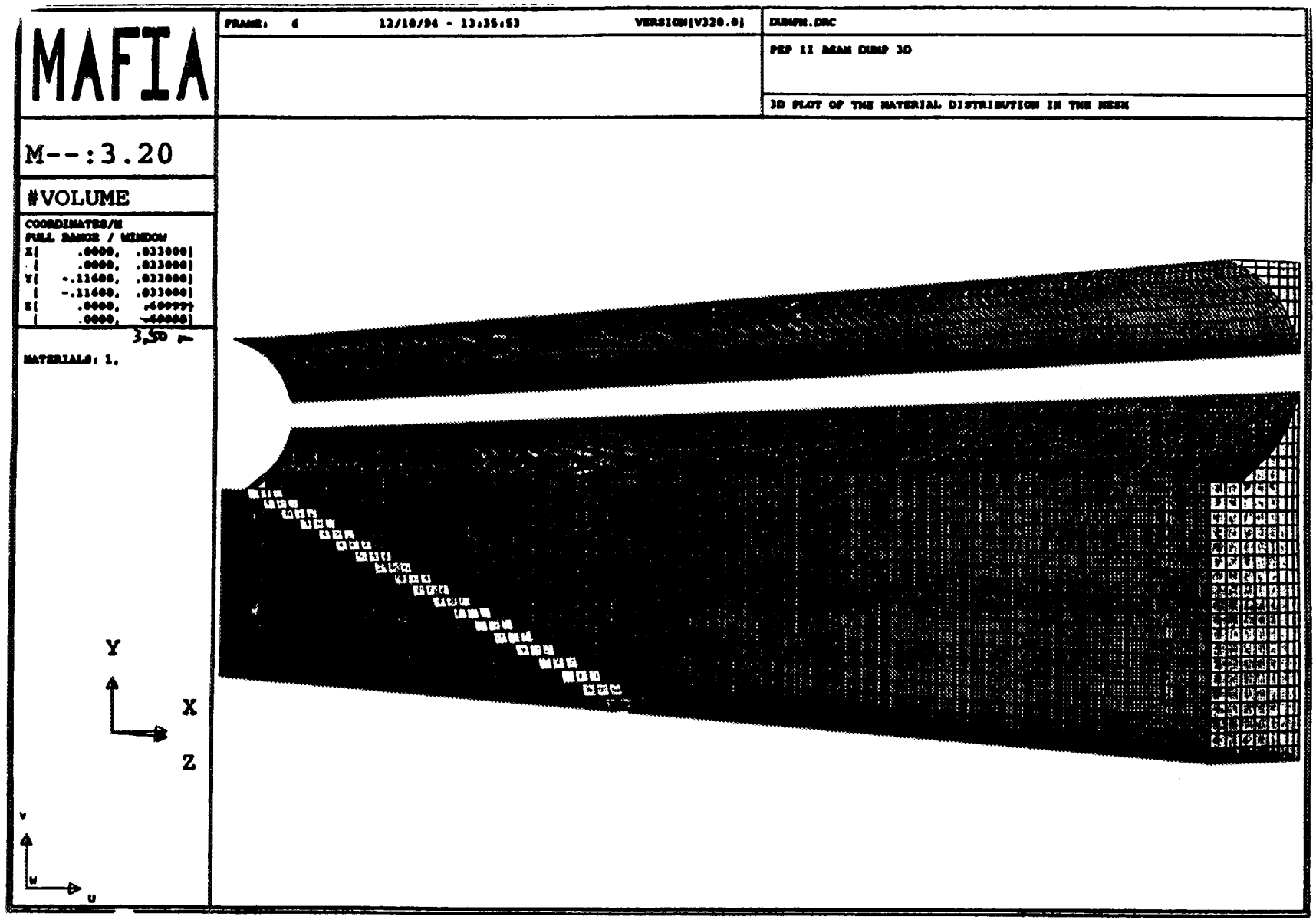
MAFIA
FRAME: 6 12/10/94 - 13:35:53 VERSION(V320.0)
DUMPH.DRC
PEP II BEAM DUMP 3D
3D PLOT OF THE MATERIAL DISTRIBUTION IN THE MESH
M--:3.20
#VOLUME
COORDINATES/M
FULL RANGE / WINDOW
X(.0000, .033000)
(.0000, .033000)
Y(-.11600, .033000)
(-.11600, .033000)
Z(.0000, .609999)
(.0000, .609999)
3.50 pm
MATERIALS: 1.
Y
X
Z
V
U

Fig. 9b

M. Sullivan

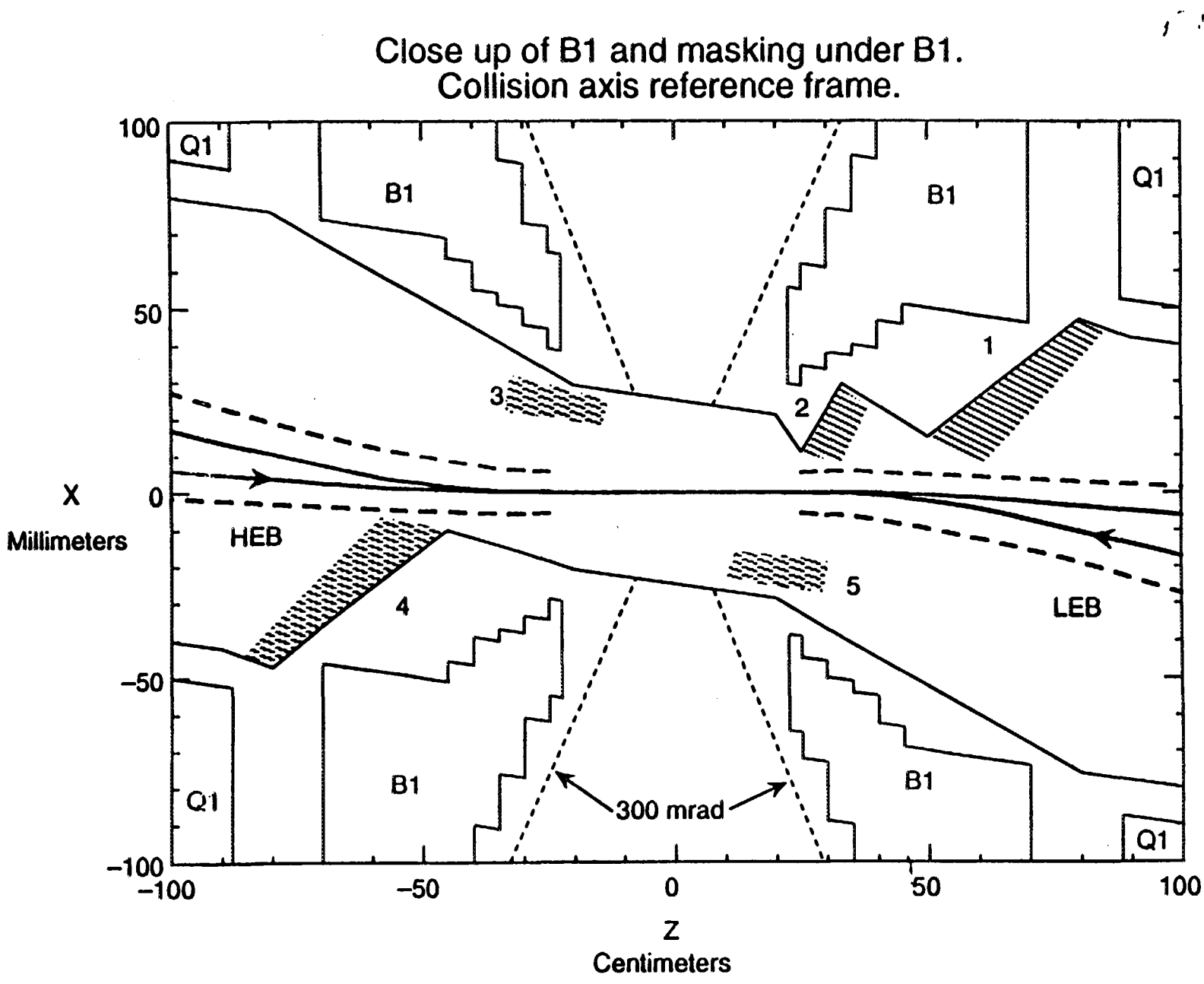

Fig. 10b

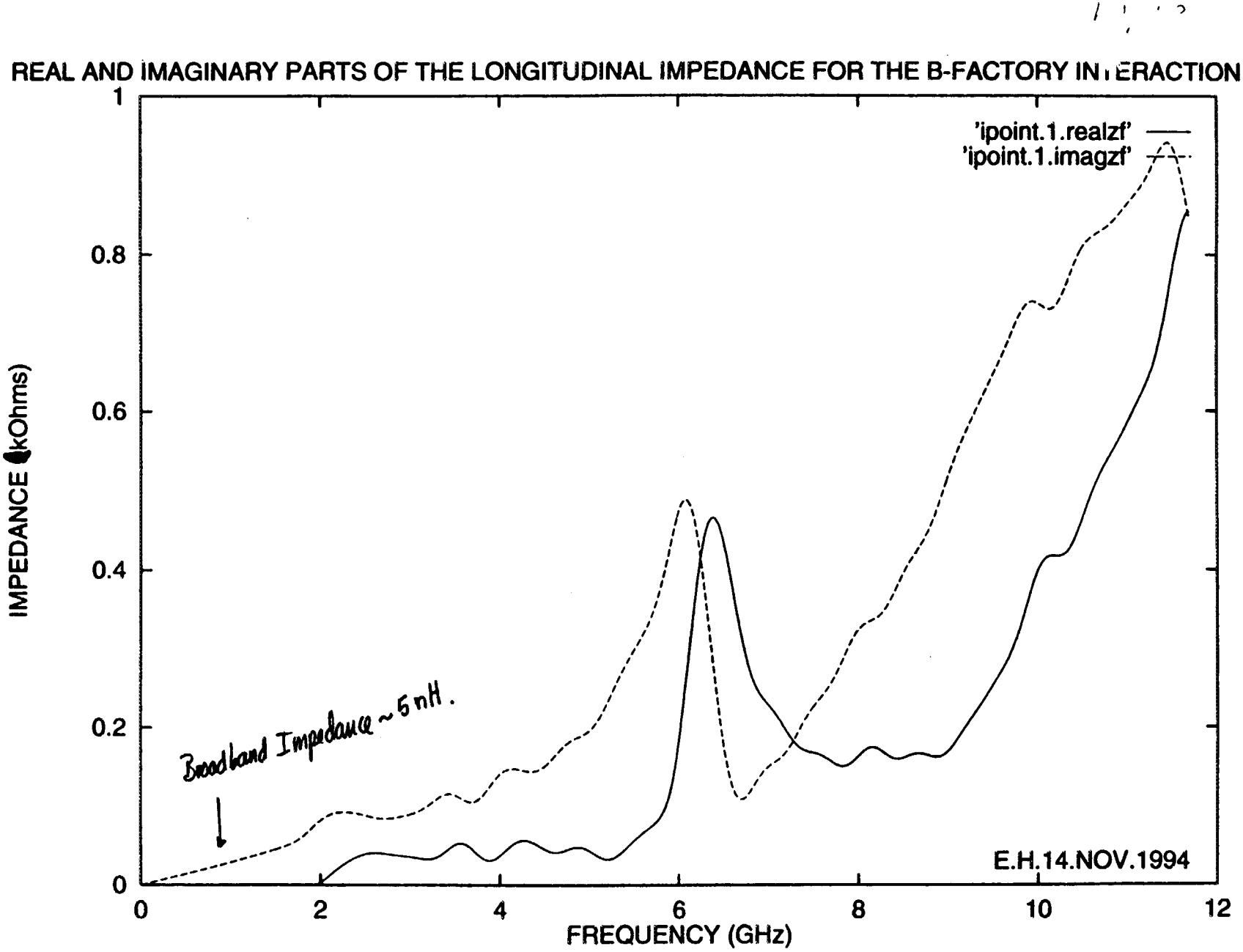
REAL AND IMAGINARY PARTS OF THE LONGITUDINAL IMPEDANCE FOR THE B-FACTORY INTERACTION R
'ipoint.1.realzf'
'ipoint.1.imagzf'
IMPEDANCE (kOhms)
FREQUENCY (GHz)
Broadband Impedance ~ 5nH.
E.H.14.NOV.1994
0
0.2
0.4
0.6
0.8
1
0
2
4
6
8
10
12

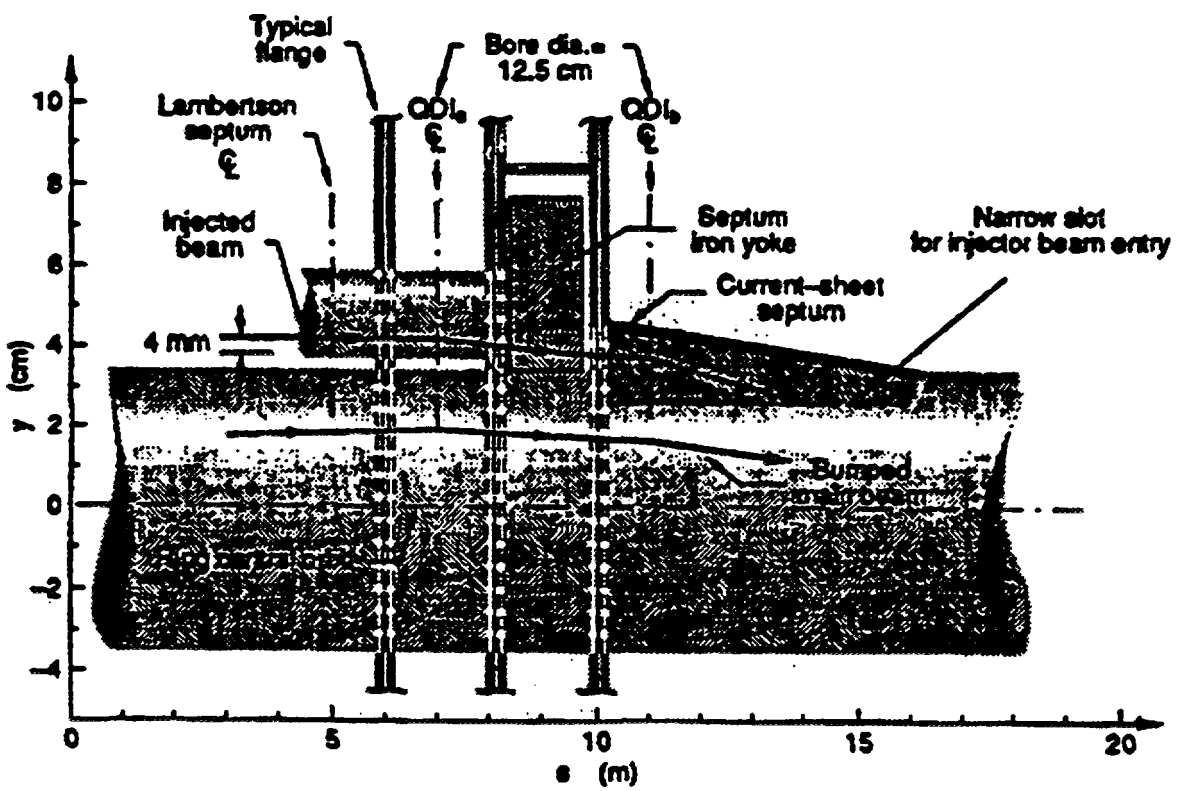
Typical flange
Bore dia.= 12.5 cm
Lambertson septum
Injected beam
4 mm
Septum iron yoke
Narrow slot for injector beam entry
Current-sheet septum
Bumped
y (cm)
s (m)
10
8
6
4
2
0
-2
-4
0
5
10
15
20

Fig. 13a

E. Lyno

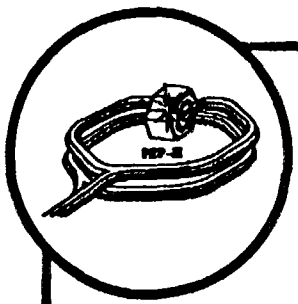

Injection Slot Geometry

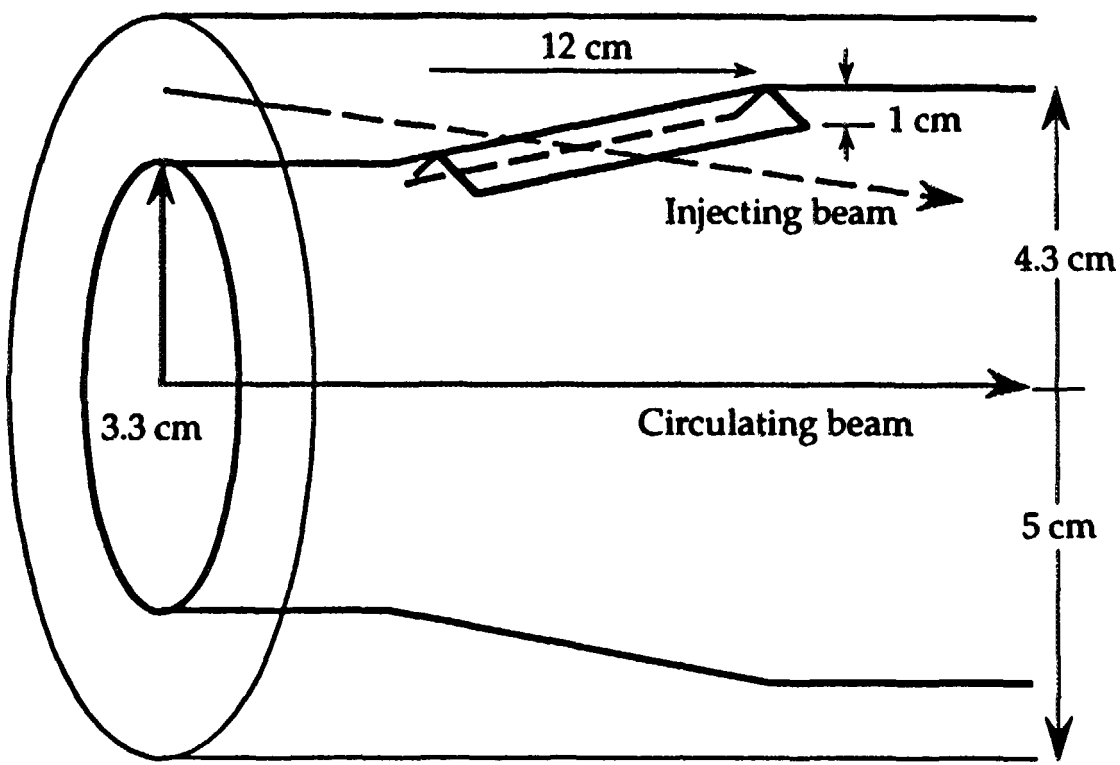

11-94

12/2/94 11:16 injection slot.cnv

Fig. 13b

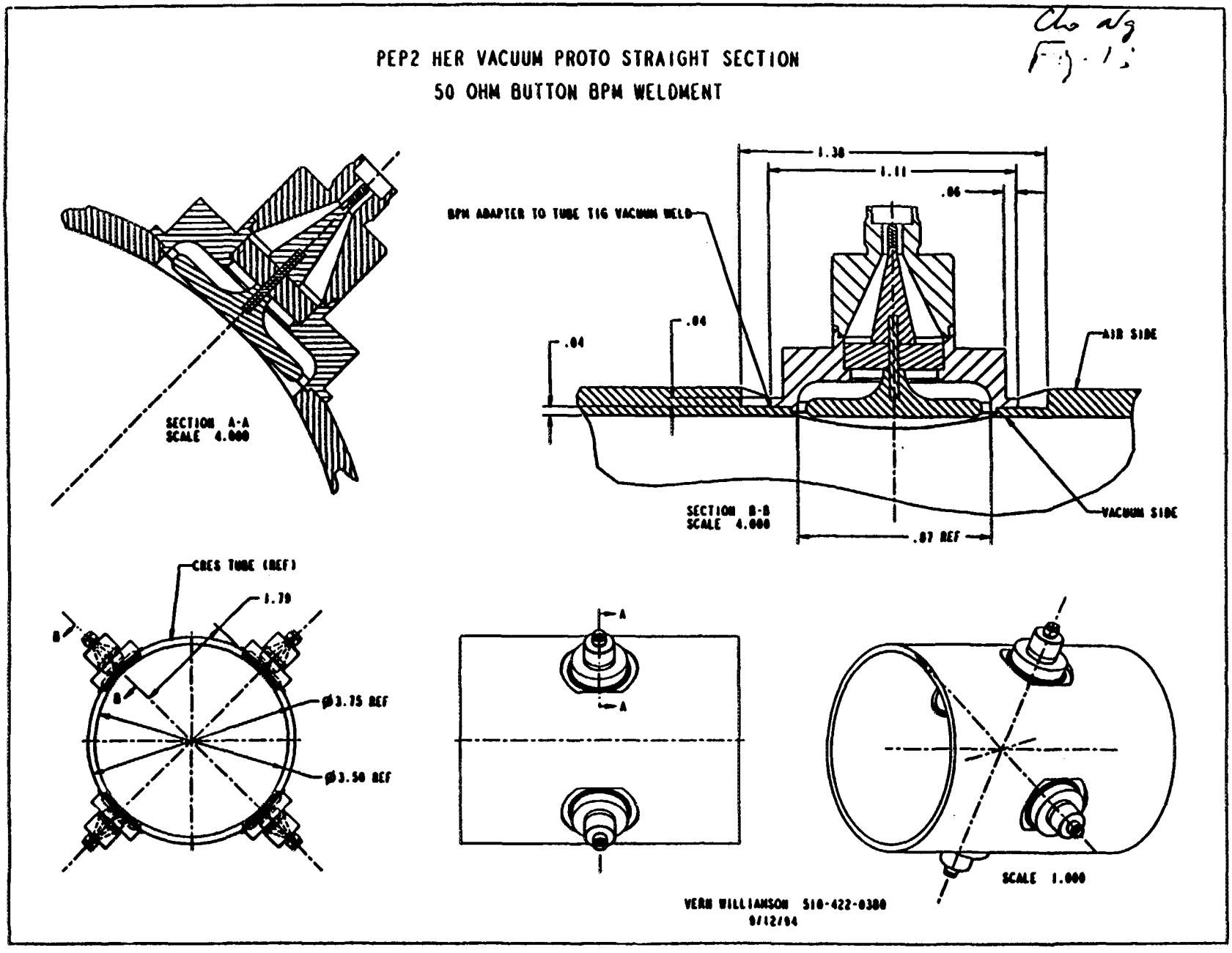
PEP2 HER VACUUM PROTO STRAIGHT SECTION
50 OHM BUTTON BPM WELDMENT
SECTION A-A
SCALE 4.000
BPM ADAPTER TO TUBE TIG VACUUM WELD
1.38
1.11
.06
.04
.04
AIR SIDE
VACUUM SIDE
SECTION B-B
SCALE 4.000
.87 REF
CRES TUBE (REF)
1.70
B
B
ø3.75 REF
ø3.50 REF
A
A
SCALE 1.000
VERN WILLIAMSON 510-422-0380
9/12/94

Fig. 14

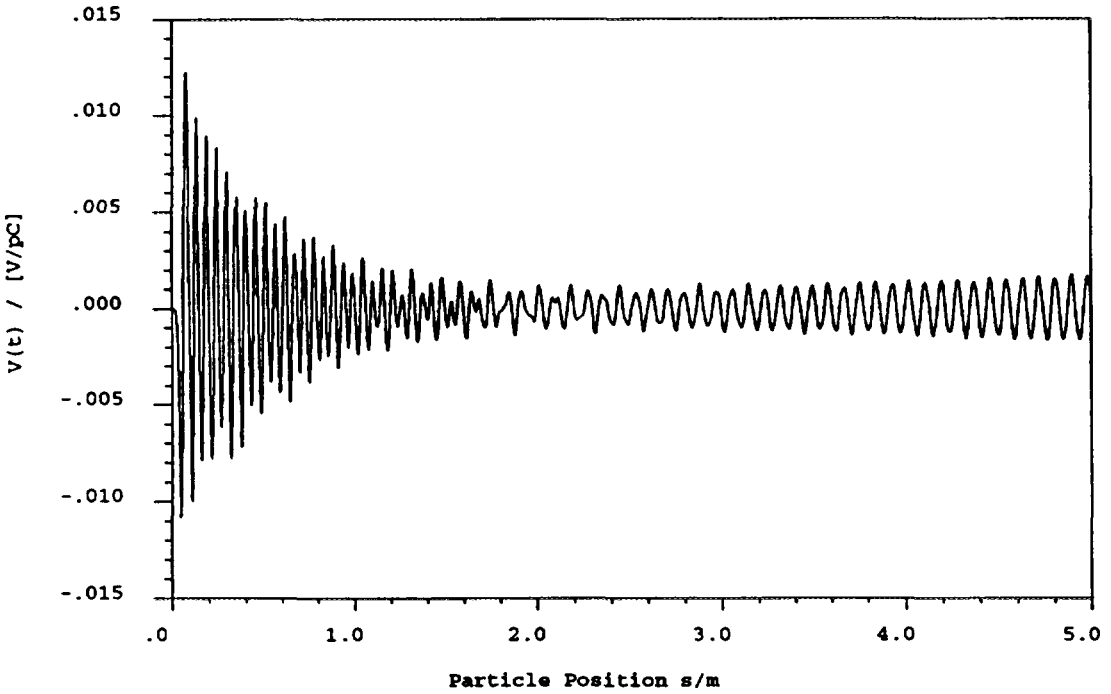

Figure 3: Longitudinal wakefield of the 2-cm BPM as a function of the particle position for a Gaussian bunch with $\sigma_z = 1$ cm.

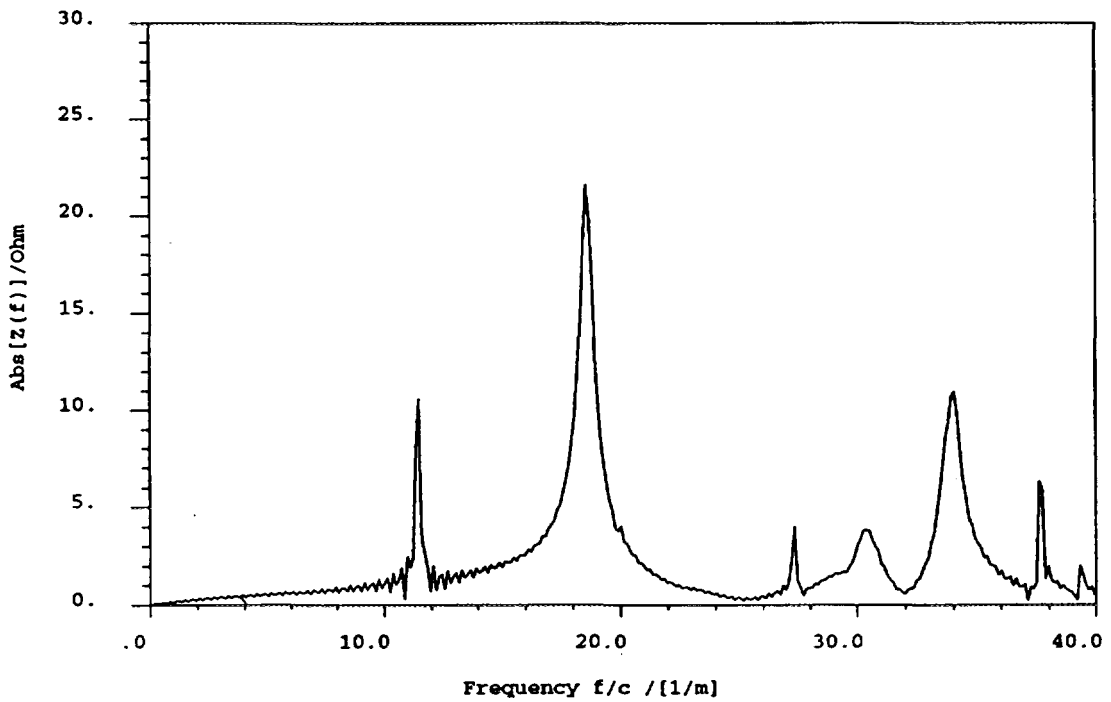

Figure 4: Longitudinal impedance spectrum of the 2-cm BPM as a function of the inverse wavelength for a Gaussian bunch with $\sigma_z = 1$ cm.

Fig. 15a

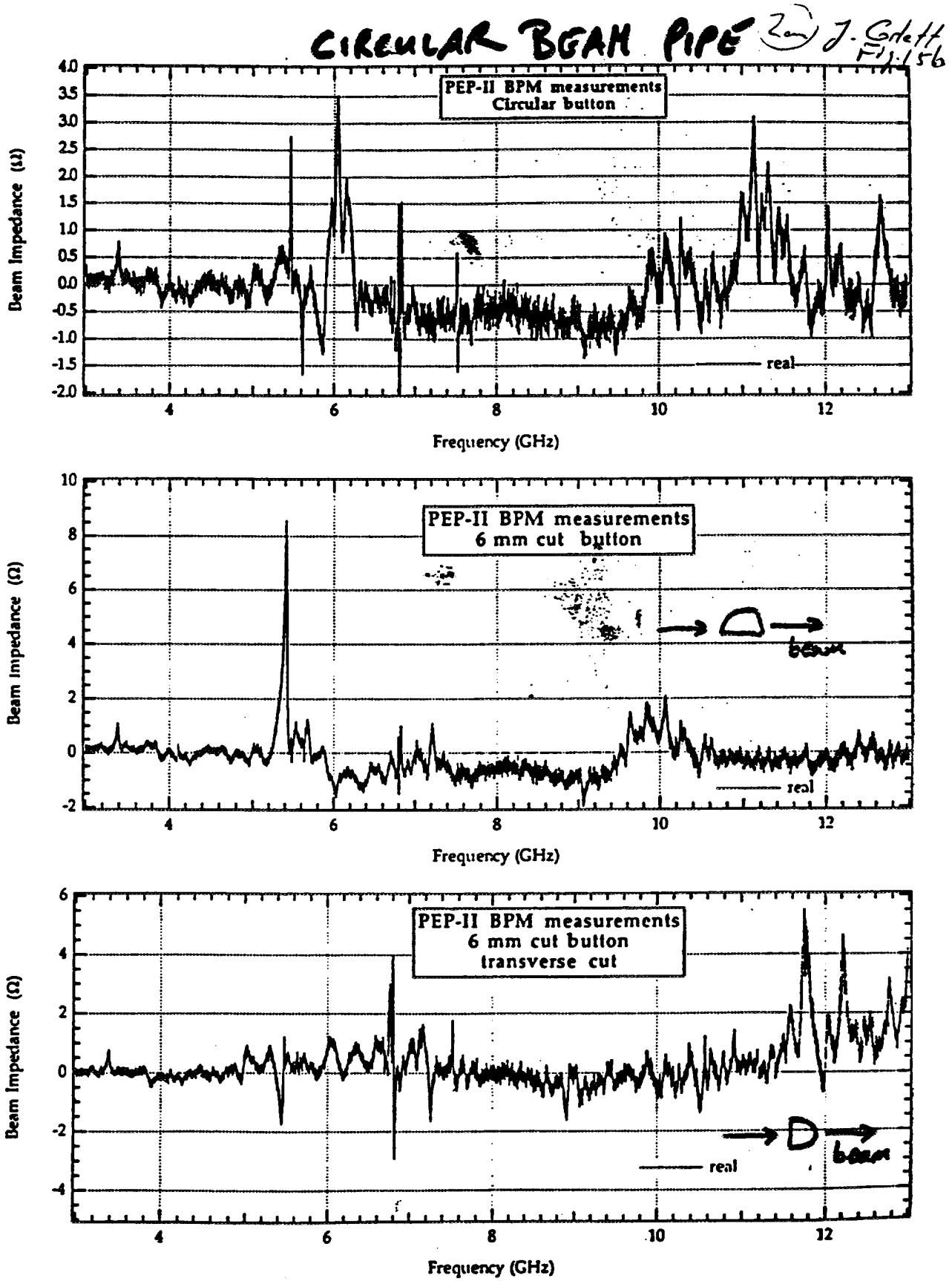
CIRCULAR BEAM PIPE
J. Gratt
FJ-156
PEP-II BPM measurements
Circular button
Beam Impedance (Ω)
real
Frequency (GHz)
PEP-II BPM measurements
6 mm cut button
beam
real
Frequency (GHz)
PEP-II BPM measurements
6 mm cut button
transverse cut
beam
real
Frequency (GHz)

Fig. 15b

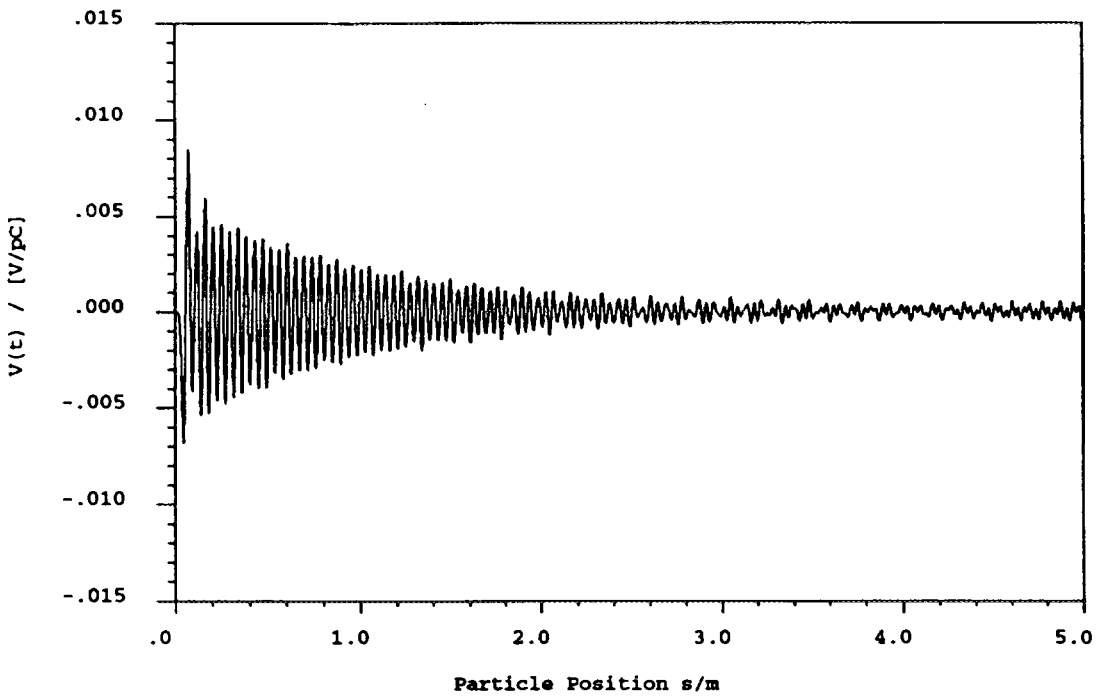

Figure 12: Longitudinal wakefield of the 1.5-cm BPM as a function of the particle position for a Gaussian bunch with $\sigma_z = 1$ cm.

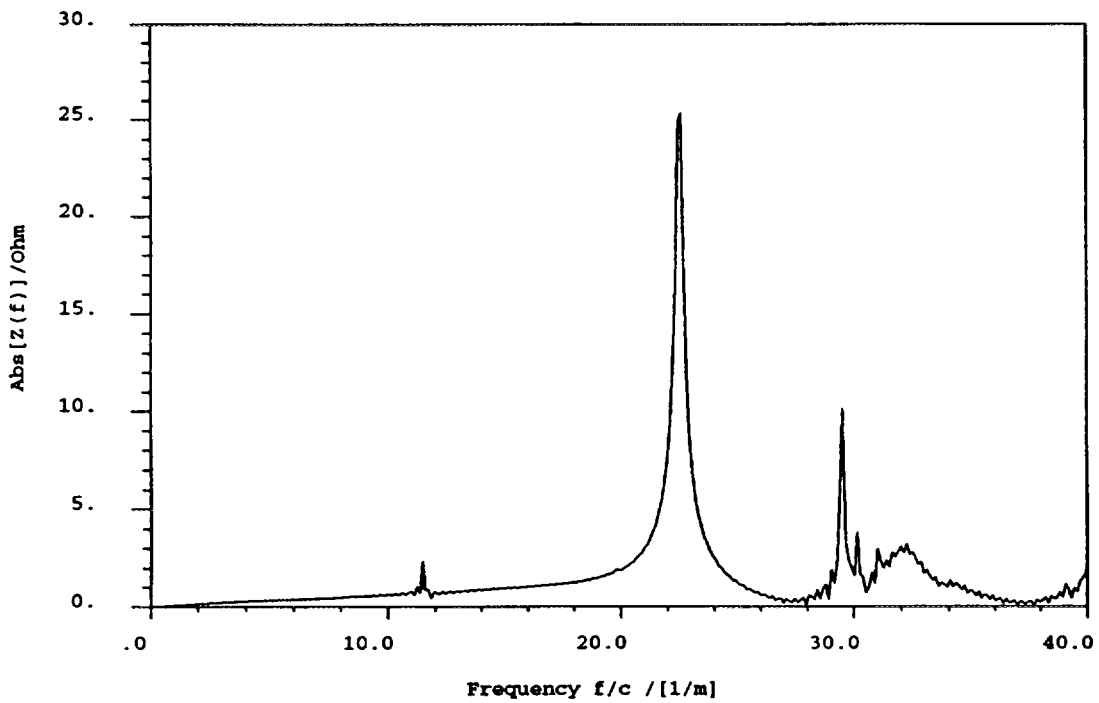

Figure 13: Longitudinal impedance spectrum of the 1.5-cm BPM as a function of the inverse wavelength for a Gaussian bunch with $\sigma_z = 1$ cm.

Fig. 16

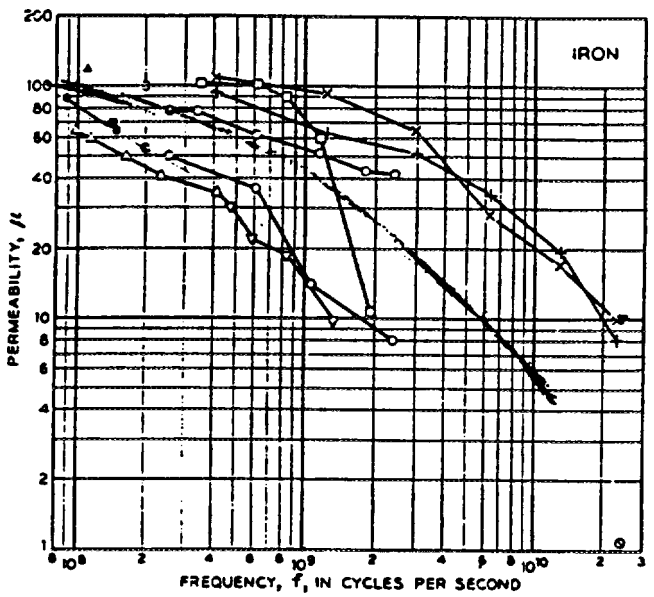

FIG. 17-23. Collection of data on the permeability of iron at high frequencies. Sources: ○, Sänger [34S7]; + and ×, Arkadiew [19A1]; △, Hoag and Gottlieb [39H3]; ▽, Hoag and Jones [32H4]; □, Lindman; ●, Möhring [39M3]; ▲, Schwarz [32S8]; ⊘, Maxwell [46M1]; ■, Procopiu and d'Albon [37P2]; ⊖, Johnson, Rado and Maloof [47J1]; ⊙, Glathart [39G5].

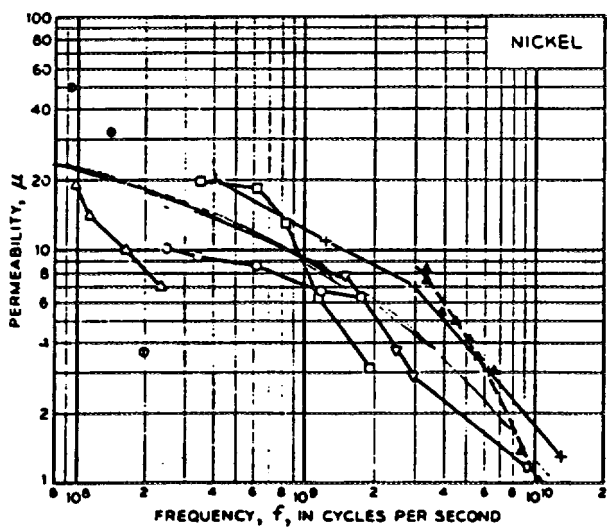

FIG. 17-24. Collection of data on the permeability of nickel at high frequencies. Sources: +, Arkadiew [19A1]; △, Hoag and Gottlieb [39H3]; □, Lindman [38L2]; ▽, Simon [46S1]; ●, Möhring [39M3]; ⊙, Glathart [39G5]; ○, Potapenko and Sänger ([33P1] and private communication to C. Kittel); ▲, Hodsman *et al.* [49H2].

Fig. 17

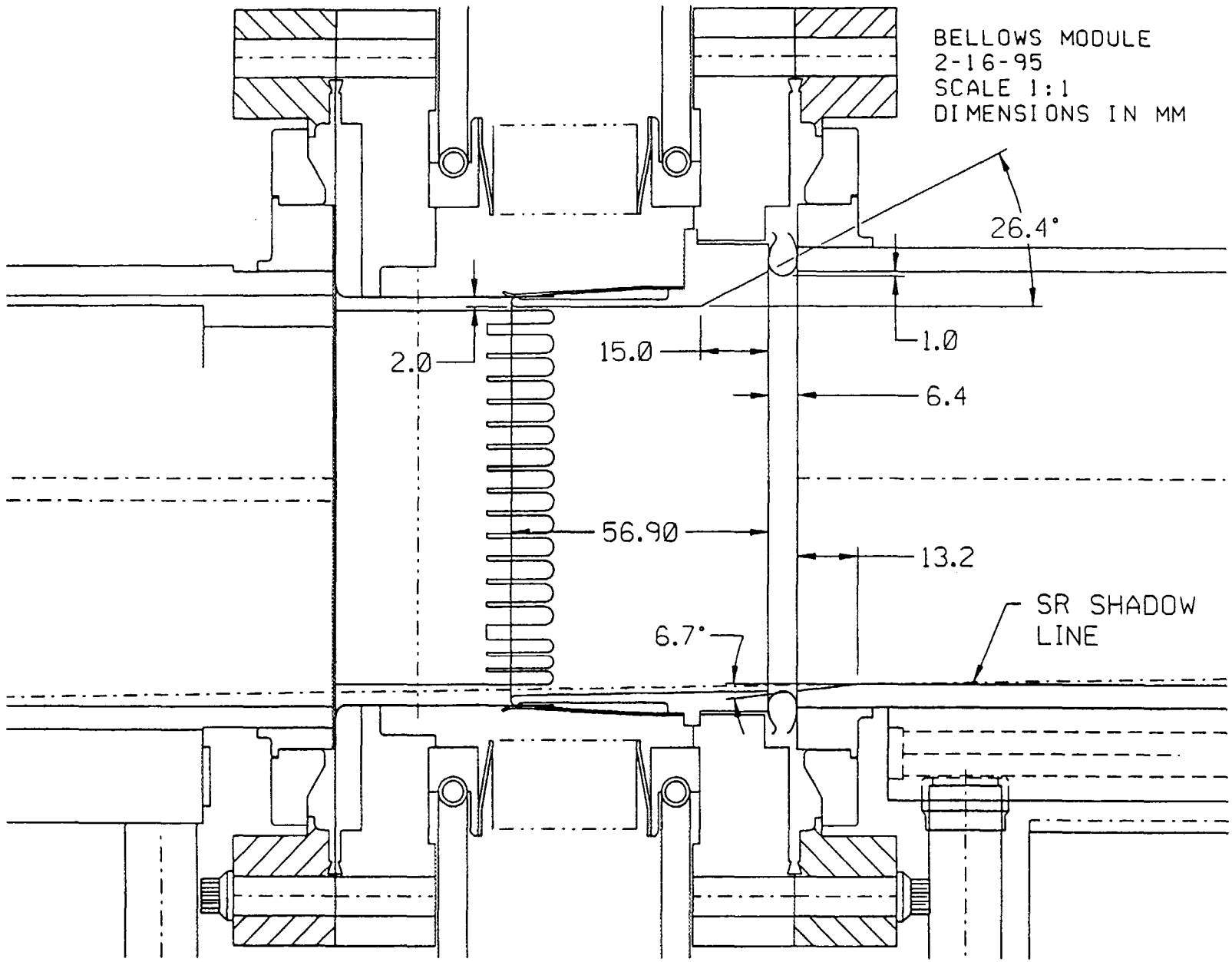
BELLOWS MODULE
2-16-95
SCALE 1:1
DIMENSIONS IN MM
26.4°
1.0
2.0
15.0
6.4
56.90
13.2
SR SHADOW
LINE
6.7°

Fig. 18a

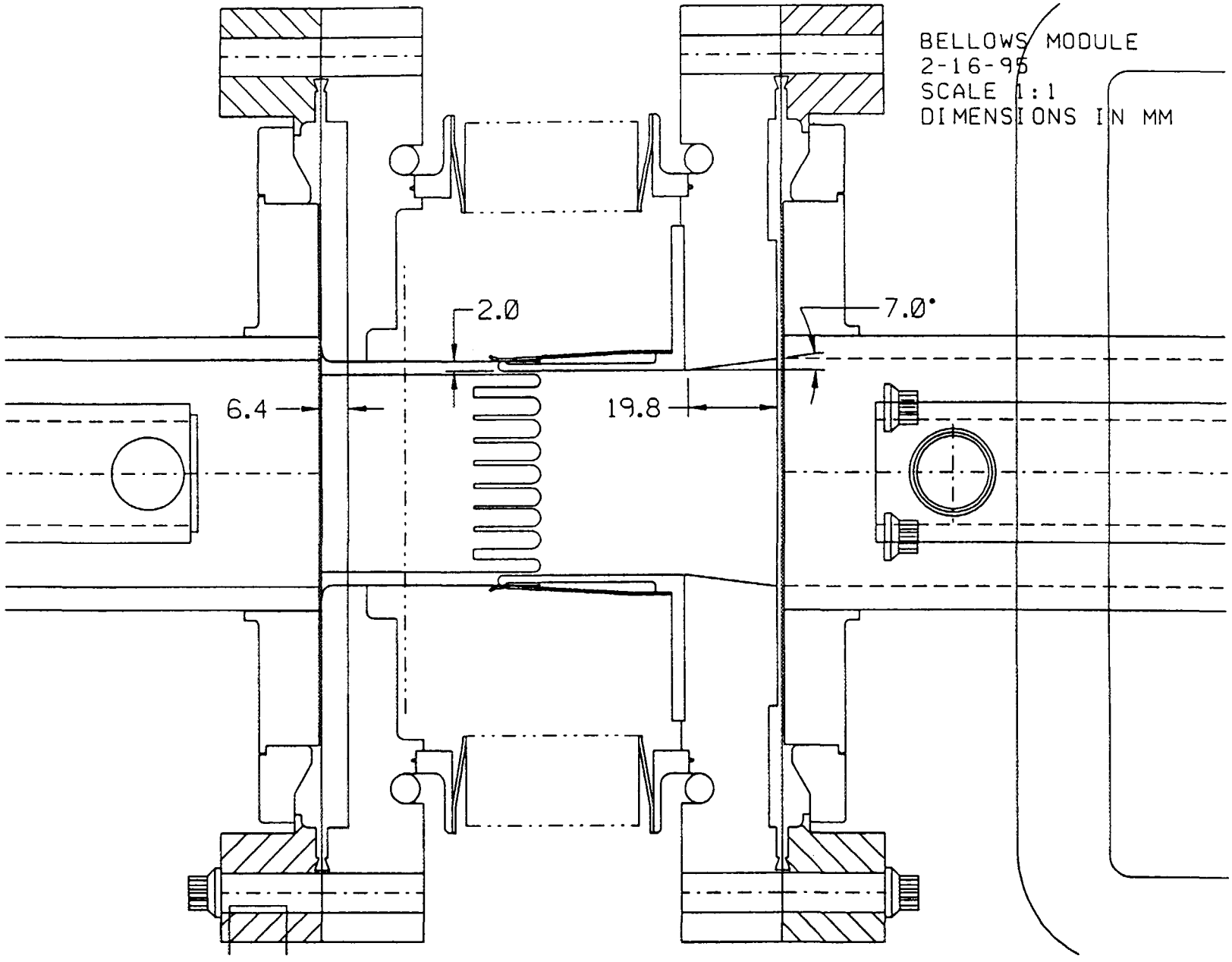

Fig. 18b

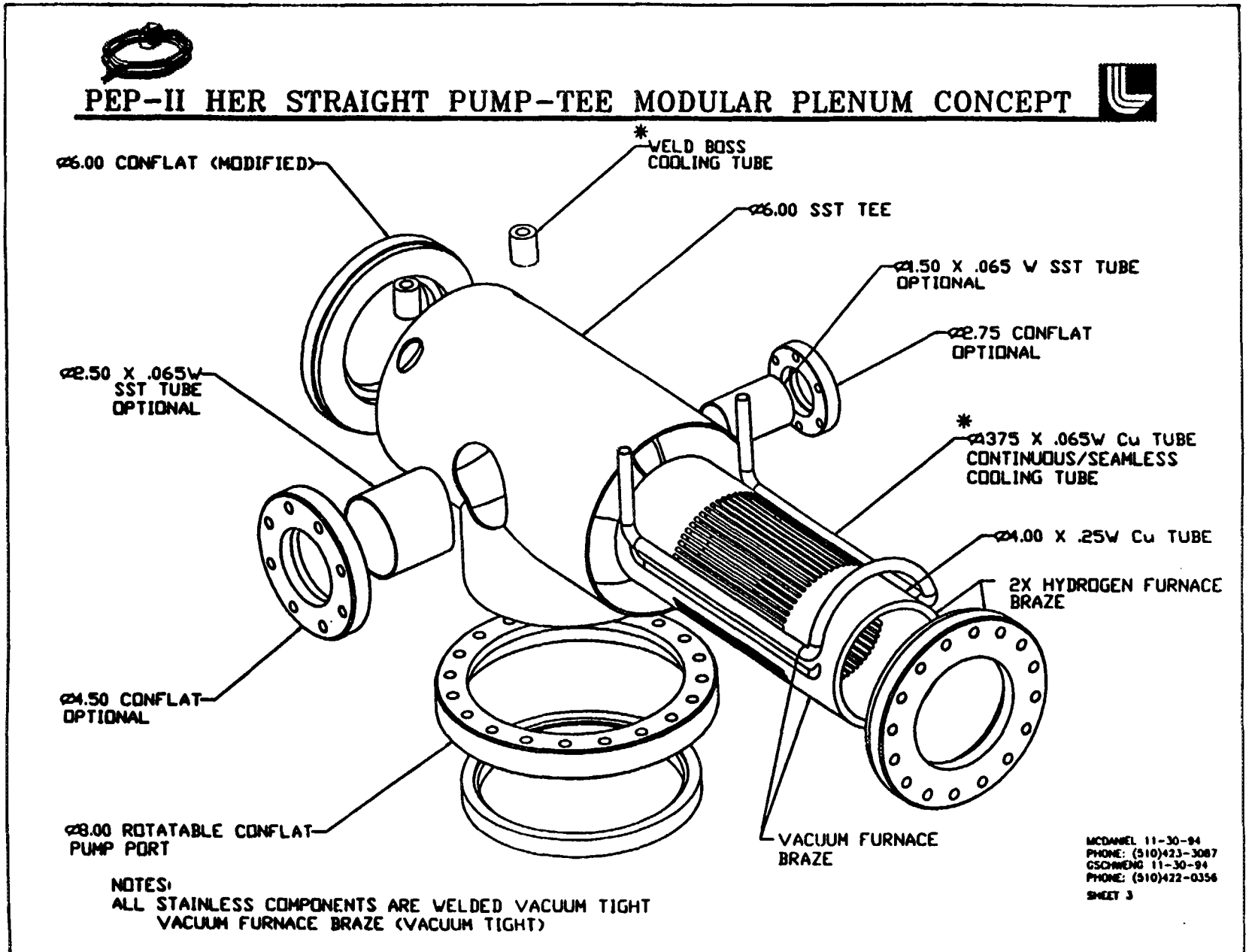
PEP-II HER STRAIGHT PUMP-TEE MODULAR PLENUM CONCEPT
*WELD BOSS COOLING TUBE
Ø6.00 CONFLAT (MODIFIED)
Ø6.00 SST TEE
Ø1.50 X .065 W SST TUBE OPTIONAL
Ø2.75 CONFLAT OPTIONAL
Ø2.50 X .065W SST TUBE OPTIONAL
*Ø.375 X .065W Cu TUBE CONTINUOUS/SEAMLESS COOLING TUBE
Ø4.00 X .25W Cu TUBE
2X HYDROGEN FURNACE BRAZE
Ø4.50 CONFLAT OPTIONAL
Ø8.00 ROTATABLE CONFLAT PUMP PORT
VACUUM FURNACE BRAZE
NOTES:
ALL STAINLESS COMPONENTS ARE WELDED VACUUM TIGHT
VACUUM FURNACE BRAZE (VACUUM TIGHT)
MCDANIEL 11-30-94
PHONE: (510)423-3087
GSCHMENG 11-30-94
PHONE: (510)422-0356
SHEET 3

Fig. 19a

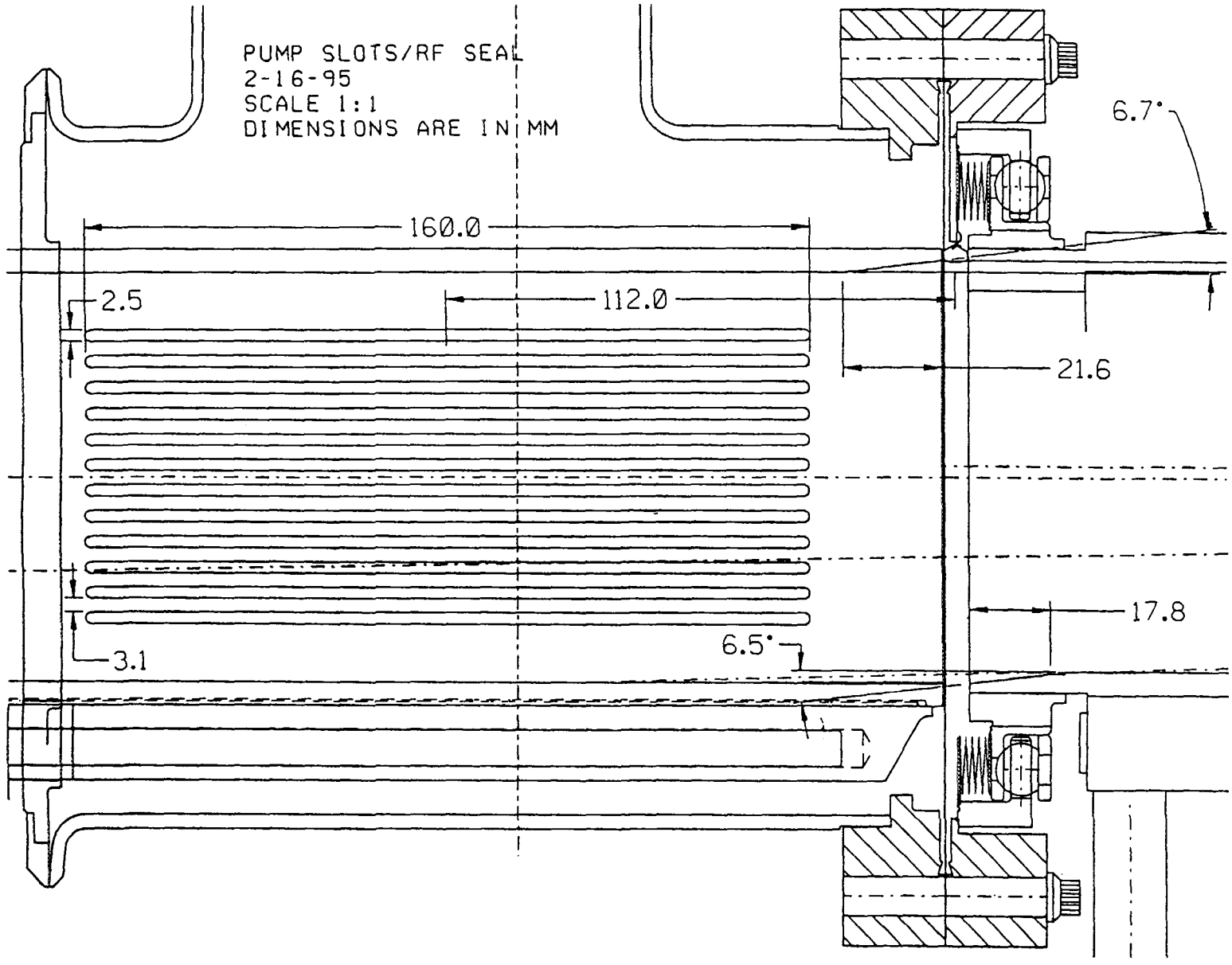
PUMP SLOTS/RF SEAL
2-16-95
SCALE 1:1
DIMENSIONS ARE IN MM
160.0
2.5
112.0
21.6
6.7°
17.8
6.5°
3.1

Fig. 19b

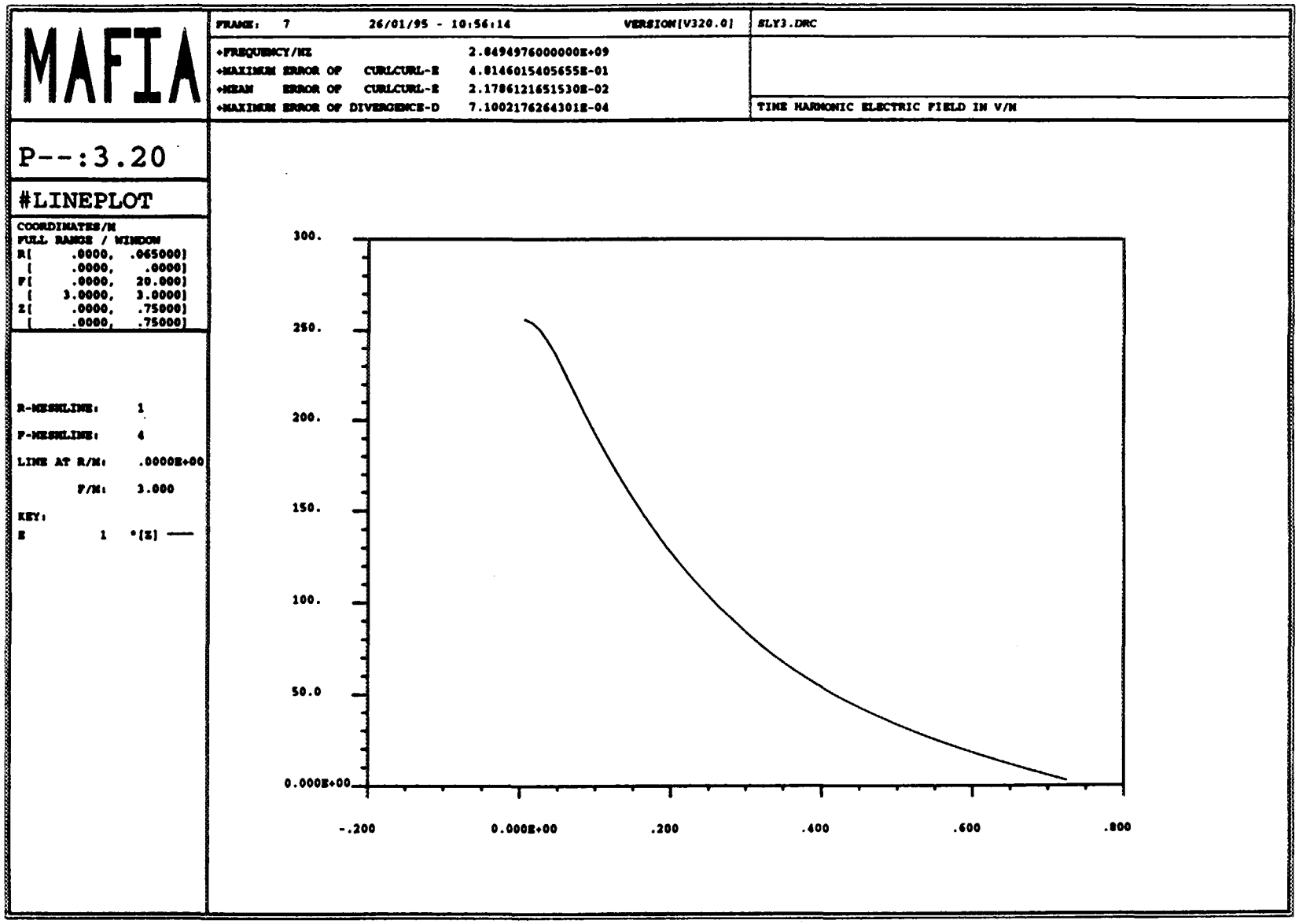
MAFIA
FRAME: 7 26/01/95 - 10:56:14 VERSION[V320.0]
SLY3.DRC
+FREQUENCY/HZ 2.8494976000000E+09
+MAXIMUM ERROR OF CURLCURL-E 4.8146015405655E-01
+MEAN ERROR OF CURLCURL-E 2.1786121651530E-02
+MAXIMUM ERROR OF DIVERGENCE-D 7.1002176264301E-04
TIME HARMONIC ELECTRIC FIELD IN V/M
P--:3.20
#LINEPLOT
COORDINATES/M
FULL RANGE / WINDOW
R[.0000, .065000]
[.0000, .0000]
F[.0000, 20.000]
[3.0000, 3.0000]
Z[.0000, .75000]
[.0000, .75000]
R-MESHLINE: 1
F-MESHLINE: 4
LINE AT R/M: .0000E+00
F/M: 3.000
KEY:
E 1 *[E]
300.
250.
200.
150.
100.
50.0
0.000E+00
-.200
0.000E+00
.200
.400
.600
.800

Fig. 20a

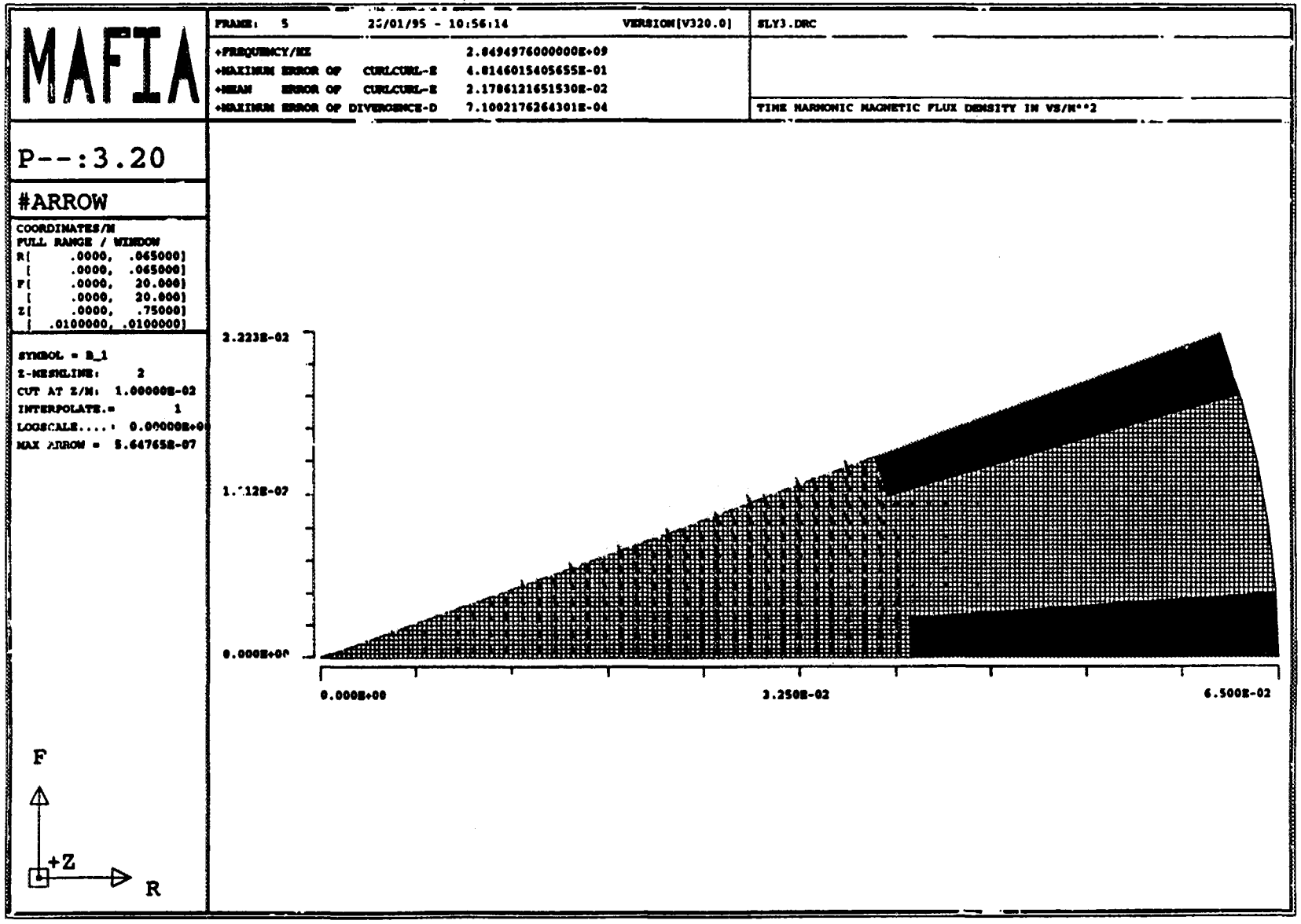
MAFIA
FRAME: 5
25/01/95 - 10:56:14
VERSION[V320.0]
SLY3.DRC
+FREQUENCY/HZ 2.8494976000000E+09
+MAXIMUM ERROR OF CURLCURL-E 4.8146015405655E-01
+MEAN ERROR OF CURLCURL-E 2.1786121651530E-02
+MAXIMUM ERROR OF DIVERGENCE-D 7.1002176264301E-04
TIME HARMONIC MAGNETIC FLUX DENSITY IN VS/M**2
P--:3.20
#ARROW
COORDINATES/M
FULL RANGE / WINDOW
R[.0000, .065000]
[.0000, .065000]
F[.0000, 20.000]
[.0000, 20.000]
Z[.0000, .75000]
[.0100000, .0100000]
SYMBOL = B_1
Z-MESHLINE: 2
CUT AT Z/M: 1.00000E-02
INTERPOLATE.= 1
LOGSCALE....: 0.00000E+0
MAX ARROW = 5.64765E-07
2.223E-02
1.112E-02
0.000E+00
0.000E+00
3.250E-02
6.500E-02
F
+Z
R

Fig. 20b

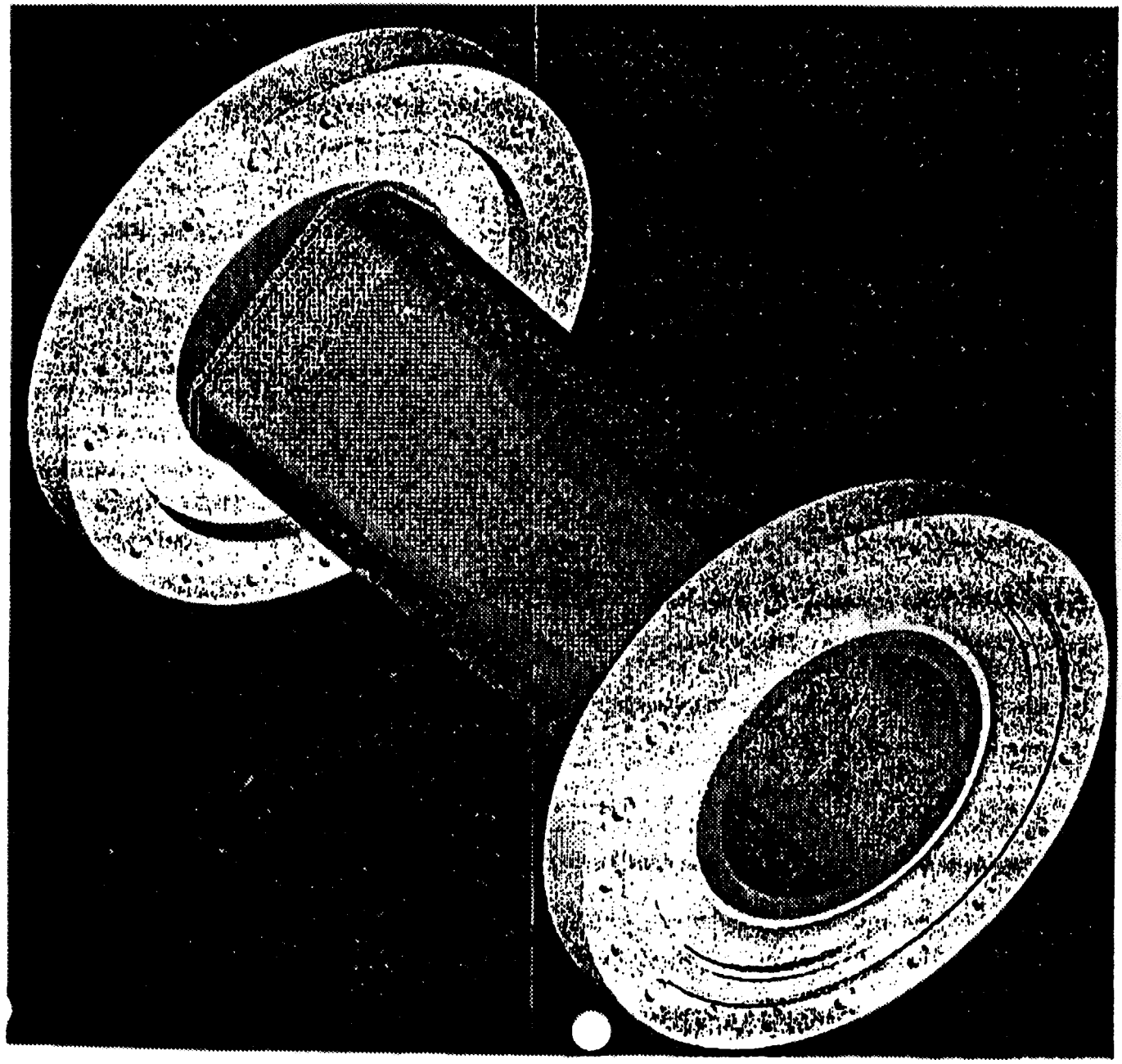

C. Daly

Fig. 21

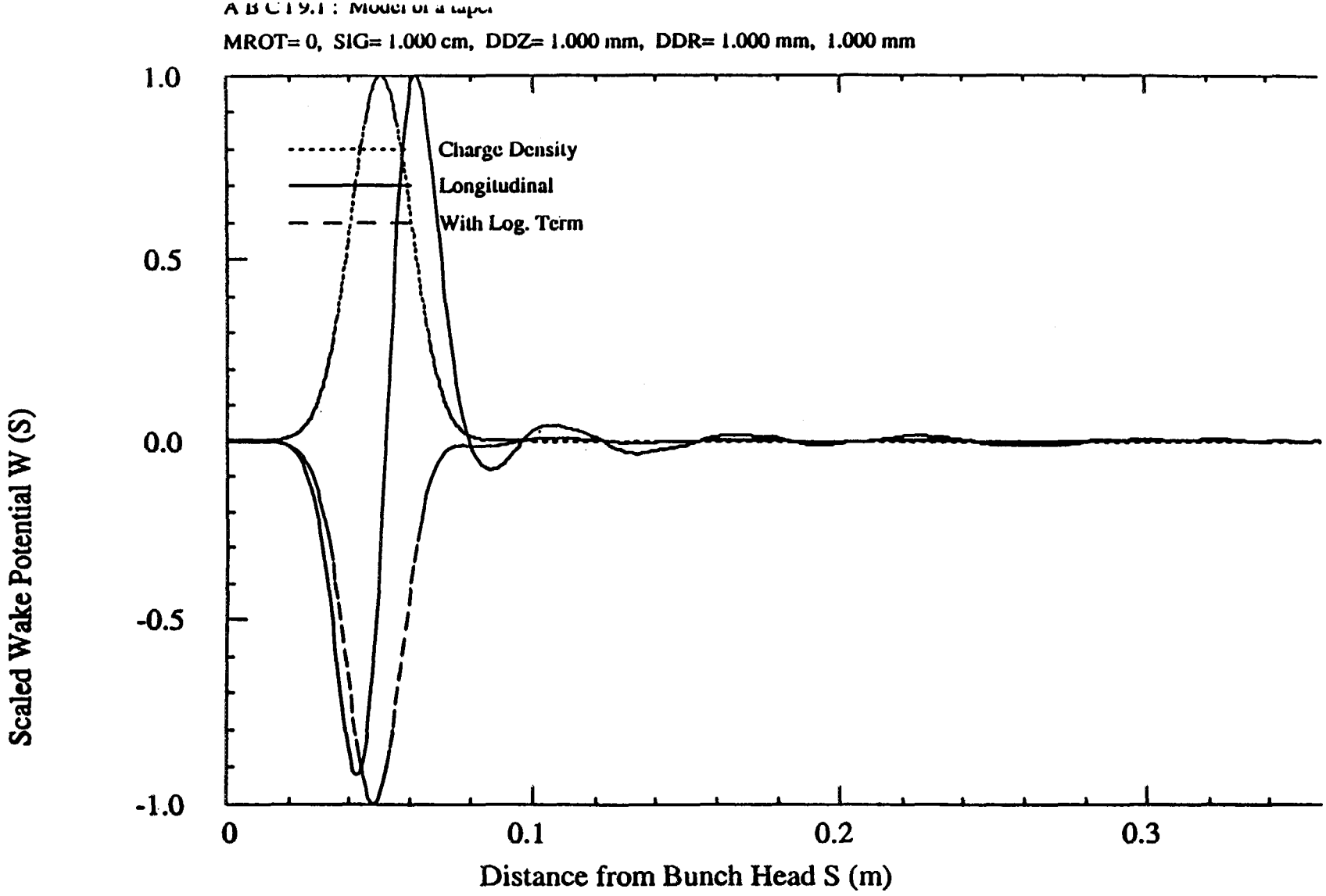
A B C 19.1 : Model of a taper
MROT= 0, SIG= 1.000 cm, DDZ= 1.000 mm, DDR= 1.000 mm, 1.000 mm
Charge Density
Longitudinal
With Log. Term
Scaled Wake Potential W (S)
1.0
0.5
0.0
-0.5
-1.0
0
0.1
0.2
0.3
Distance from Bunch Head S (m)
Longitudinal Wake Min/Max= -7.056E-02/ 7.634E-02 V/pC, Loss Factor= -5.097E-03 V/pC
With Log. Term Min/Max= -4.546E-01/ 3.287E-03 V/pC, Loss Factor= -3.031E-01 V/pC

Fig. 22

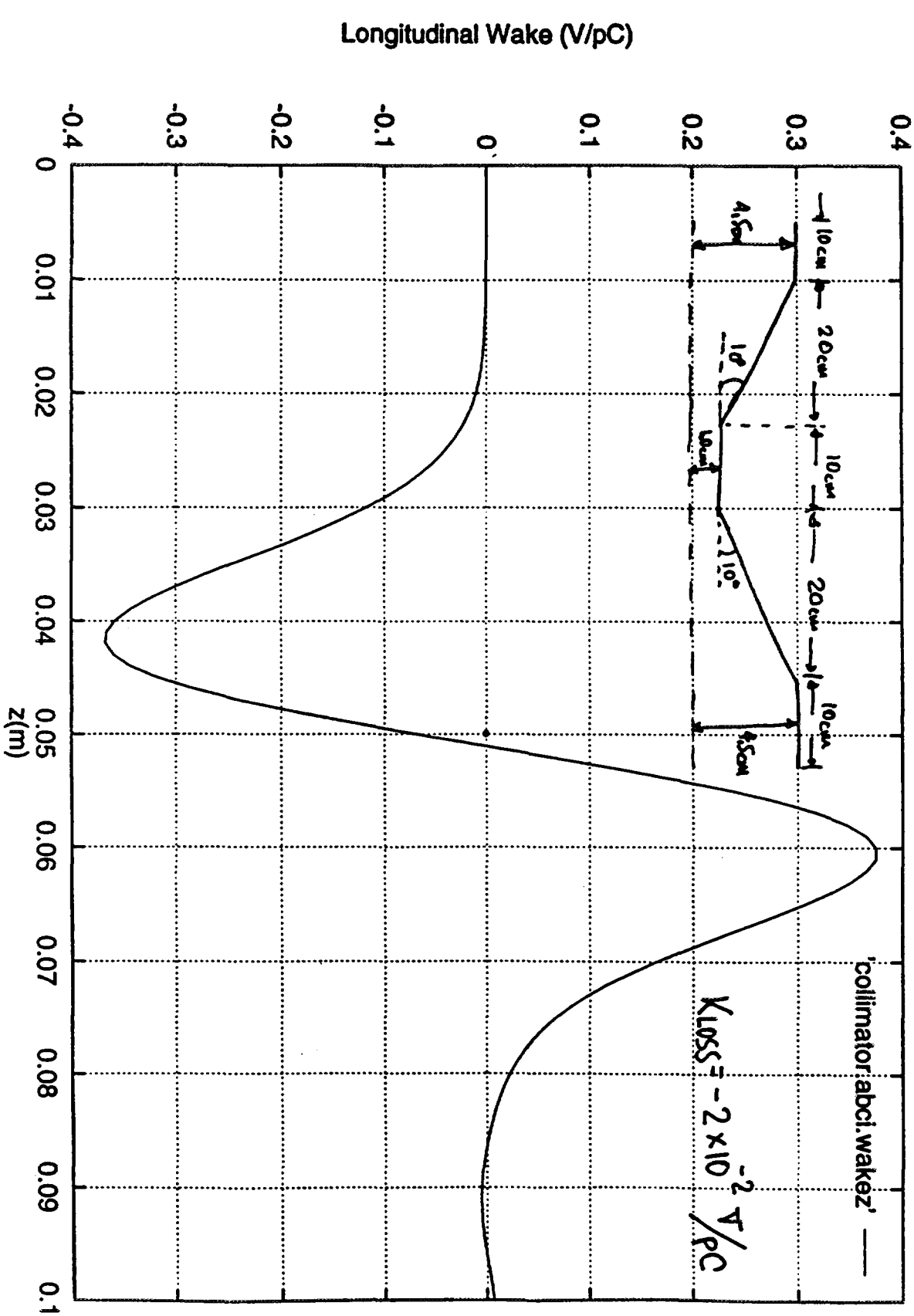
Longitudinal Wake (V/pC)
GENERIC COLLIMATOR FOR B-FACTORY : E.H.14.NOV.94
'collimator.abci.wake2' ——
KLOSS = -2×10⁻² V/pC
10cm
20cm
10cm
20cm
10cm
4.5cm
10°
10mm
-10°
4.5cm
0.4
0.3
0.2
0.1
0
-0.1
-0.2
-0.3
-0.4
0
0.01
0.02
0.03
0.04
0.05
0.06
0.07
0.08
0.09
0.1
z(m)

Fig. 23

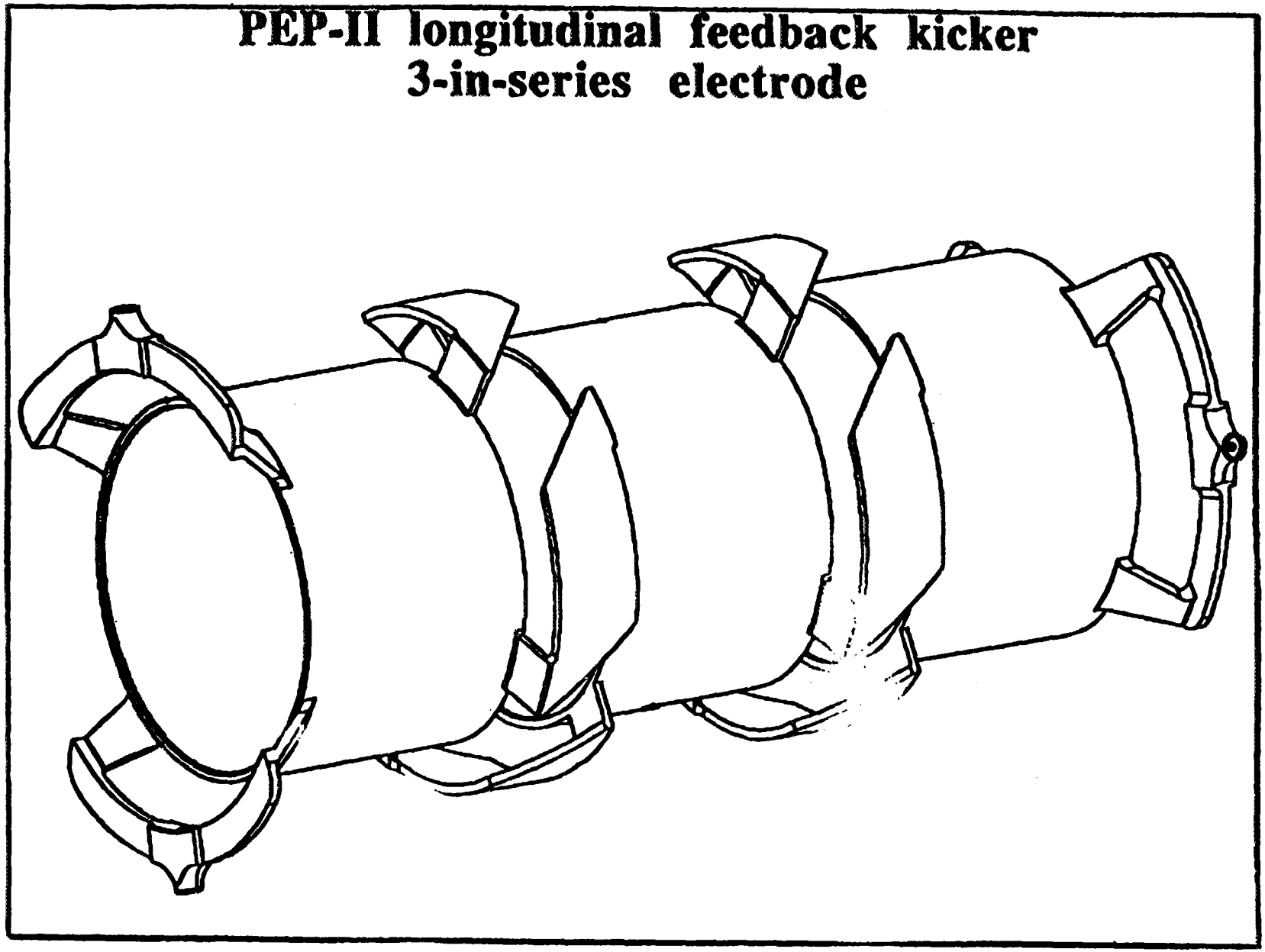

Fig. 24

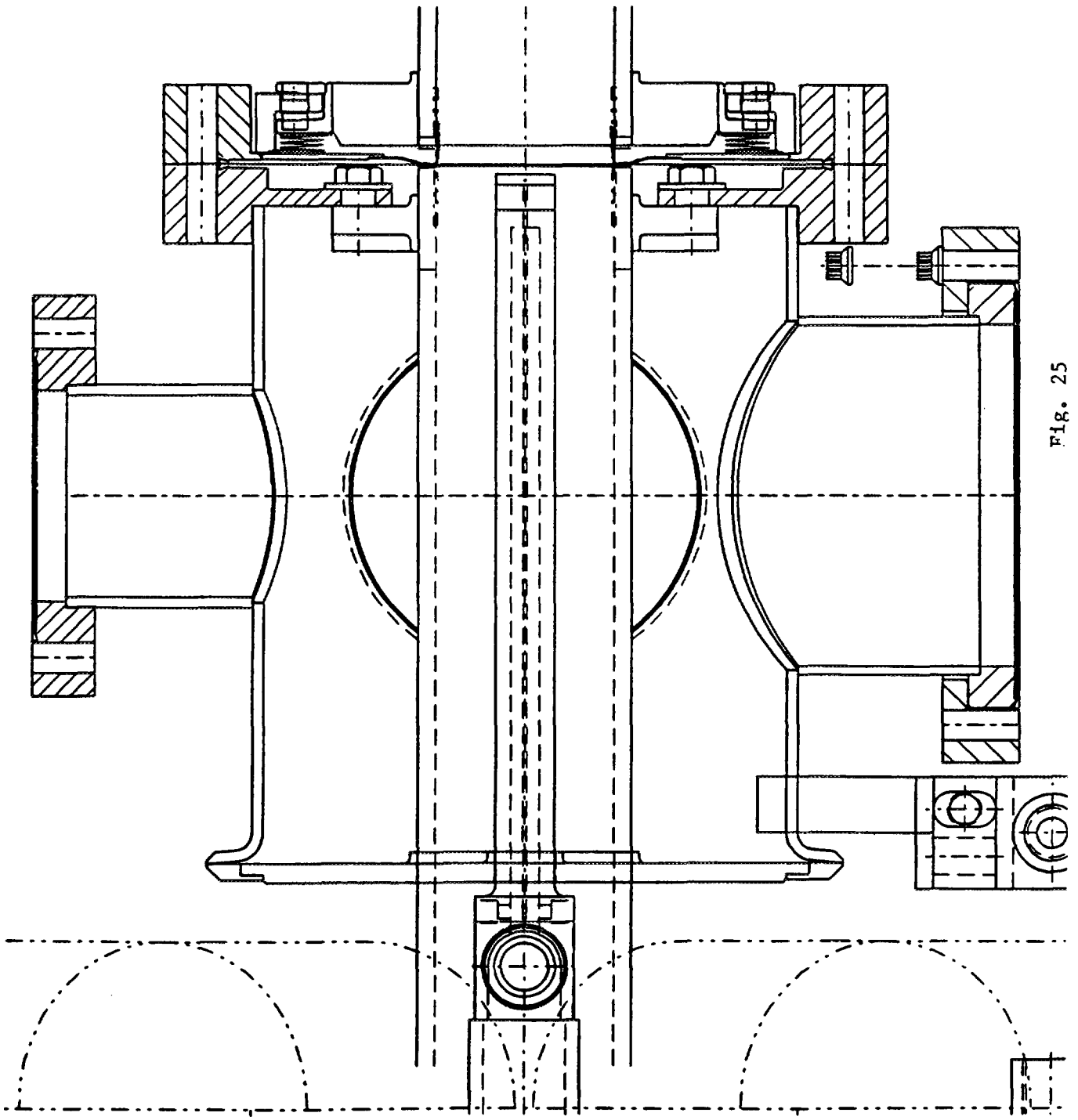

Fig. 25

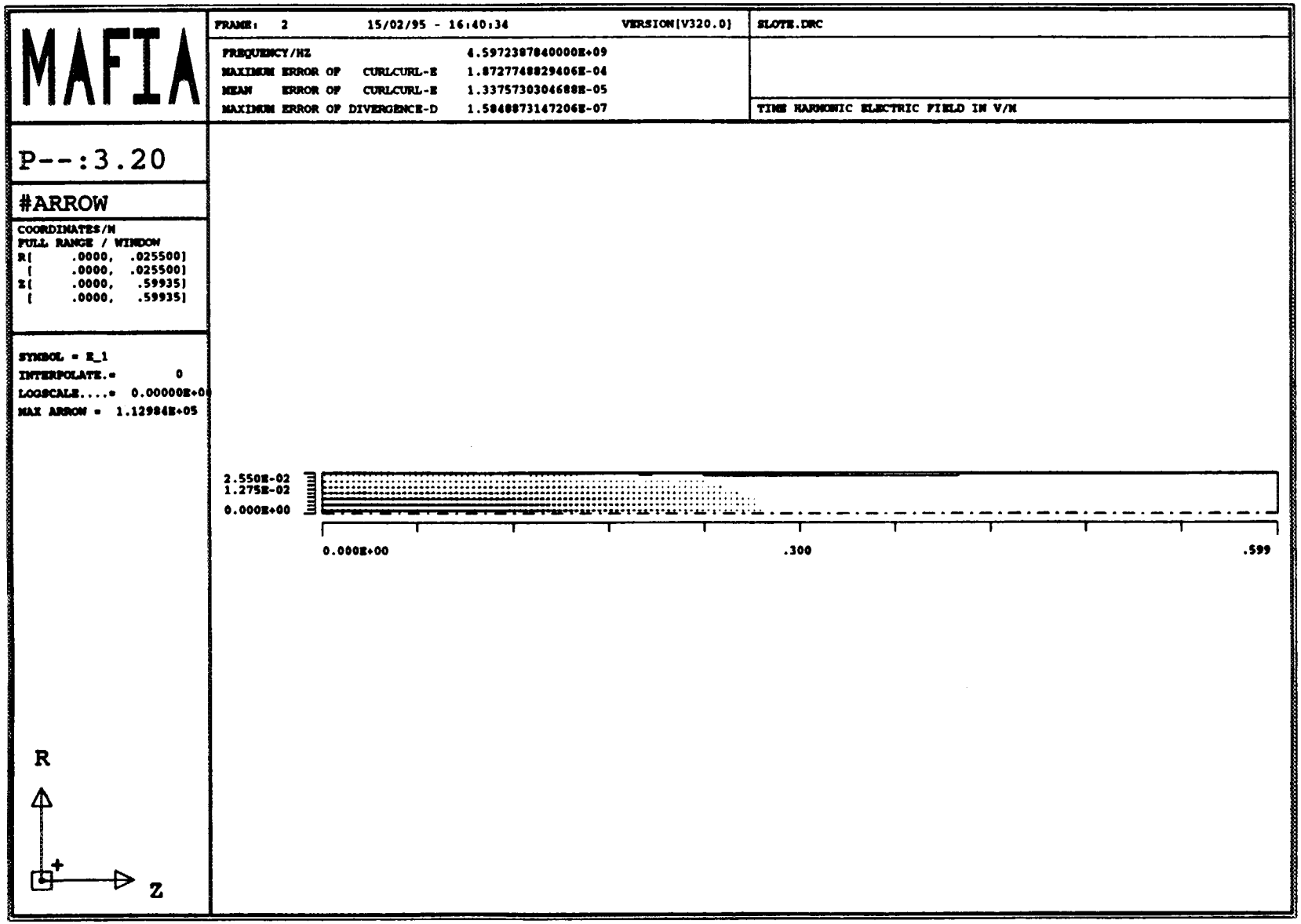
MAFIA
FRAME: 2 15/02/95 - 16:40:34 VERSION[V320.0]
SLOTE.DRC
FREQUENCY/HZ 4.5972387840000E+09
MAXIMUM ERROR OF CURLCURL-E 1.8727748829406E-04
MEAN ERROR OF CURLCURL-E 1.3375730304688E-05
MAXIMUM ERROR OF DIVERGENCE-D 1.5848873147206E-07
TIME HARMONIC ELECTRIC FIELD IN V/M
P--:3.20
#ARROW
COORDINATES/M
FULL RANGE / WINDOW
R[.0000, .025500]
[.0000, .025500]
Z[.0000, .59935]
[.0000, .59935]
SYMBOL = E_1
INTERPOLATE.= 0
LOGSCALE....= 0.00000E+00
MAX ARROW = 1.12984E+05
2.550E-02
1.275E-02
0.000E+00
0.000E+00
.300
.599
R
Z

Fig. 26

The LEP Impedance Model

Bruno Zotter *

CERN, Geneva 23, Switzerland

Abstract

This report describes a number of measurements and computations of the impedance of the Large Electron Positron collider LEP at CERN. The work has been performed over several years, together with D. Brandt, K. Cornelis, A. Hofmann, G.Sabbi and many others. The agreement between measurements of single bunch instabilities on the machine and computer simulations is in general excellent and gives confidence in the impedance model used.

1 Current Limitations by Collective Effects in LEP

Contrary to smaller machines like B-factories, where in general longitudinal effects such as bunch lengthening or energy loss dominate, the main limitations in large storage rings - and LEP is by far the largest one in existence - are usually in one of the transverse planes, mostly the vertical one. This can be understood by the fact that the transverse impedance increases with average machine radius R as shown by the approximate relation

$$Z_\perp \approx \frac{2R}{b^2}\frac{Z_\parallel}{n} \tag{1}$$

where b is the chamber radius or half height, and $Z_\parallel/n$ the longitudinal impedance divided by the mode number. The main limitation of single bunch current in LEP is the transverse mode coupling (TMC) instability, whose threshold is inversely proportional to the sum over the products of all transverse impedances $Z_{\perp i}$ (or the transverse loss factor $k_\perp$) and the beta functions β_i at their locations

$$I_{th} = \frac{2\pi\nu_s E/e}{\sum \beta_i Z_{\perp i}} f(\sigma) \approx \frac{8 f_s E/e}{\sum_i \beta_i k_{\perp i}(\sigma)}. \tag{2}$$

For bunch lengths above a fraction of a mm, the form factor $f(\sigma) \sim \sigma$ (or $k_\perp \sim 1/\sigma$). Hence bunch lengthening is beneficial to stabilise the bunches, whose natural length is of the order of a few mm, depending on the momentum compaction of the particular lattice used. At injection energy (20 GeV), the bunches need to be lengthened even more (typically to 10 - 20 mm) in order to reach sufficiently high currents. This is usually achieved by powering one or more wigglers which have been installed in LEP originally for other purposes (damping, emittance control, polarization). At operating energy, presently 45 GeV, these wigglers are no longer effective and thus are switched off, but the natural bunch length is anyhow 10 - 15 mm. Since β^* is typically 4-5 cm, there is still no loss of luminosity due to the "hour-glass effect".

* Talk given at the workshop on collective effects in B-factories CEIBA 95, Tsukuba, Japan, July 1995

The main longitudinal collective effect encountered during commissioning of LEP was an irregular phase motion of the bunches, which could however be cured by installing a dedicated feedback system. Furthermore, synchro-betatron resonances need to be avoided by careful adjustment of the working point, in particular during accumulation of current. More recently, another longitudinal problem appeared: power dissipation in sensitive equipment related to the superconducting (SC) cavities - in particular HOM couplers, bellows and tapers - which are being installed for operation at 90 GeV (LEP2), and which had to be minimized by design changes.

2 Design of Low-Impedance LEP Components

The largest impedance in LEP is caused by 128 five-cell 352 MHZ copper cavities. (Eight of these have been removed and replaced by 1 GHZ feedback cavities, hence the impedance has not much changed.) At bunch lengths between 10 and 15 mm, each cavity cell has a transverse loss factor of nearly 5 V/pC, hence the total is about 3000 V/pC. For LEP2, 192 four-cell SC cavities will be added - but presently only a few have been installed. Due to their much larger beam pipe radius (12 vs 5 cm), their transverse loss factor $k_\perp$ is much lower than that of the copper cavities, a full SC cavity has only about half the value of a single copper cell. Nevertheless, unless at least some copper cavities are removed, the TMC threshold will be somewhat reduced.

The second most important element for determining the TMC threshold of short bunches in LEP are the bellows, of which a large number (nearly 3000) are required for accommodating the thermal expansion (over 30 mm) of each vacuum chamber. Since the chambers are slightly curved, also a transverse displacement of up to 3 mm should be allowed. A number of solutions were investigated:

- "Inner bellows" - as used e.g. in SPEAR at SLAC - i.e. very thin-walled bellows with shallow corrugations, were found to break during testing, and still had a too high transverse impedance.
- An enlarged vacuum chamber, sliding directly on the standard one over a spring contact - as used e.g. in PETRA at DESY - also was found to have a too high transverse impedance. In addition, this design was considered unreliable since a minimum contact pressure is not guaranteed.
- Specifically for LEP, long Be-Cu fingers were proposed, sliding on the outside of a thin SS extension of the oval vacuum chamber. An outer spiral spring keeps the contact pressure always above the minimum required. These RF screens are tricky to assemble, but in 5 years of operation, only a single finger was found to stick inside the chamber, and they have performed very well at the current levels of LEP.

In ESRF, a reduced version of similar design has been used for some time without any problems for multi-bunch operation. However, recent operation with a few and strong bunches led to pressure increases due to overheating and arcing.

- For machines with even higher currents - such as B or Phi factories - screens without sliding contacts may be preferable. Such a design, consisting of a flexible inner sleeve bulging to the outside during compression - essentially a single convolution inner bellows - had been proposed for Spring8 some time ago. It has not been adopted there for impedance reasons, and a re-evaluation may be indicated.

All other components in the LEP vacuum chamber, such as electro-static separators (of which there are now over 50), collimators, pick-up electrodes, large unshielded bellows (over 200) etc. still present rather small contributions to the total impedance (see Figs.1 and 2). This may change when a substantial number of copper cavities are

removed.

Longitudinal motion of bunches was limiting the performance of LEP before the installation of a dedicated feedback system. However, for several reasons it is not probable that it is caused by a coupled-bunch instability: it has occurred even when only a single bunch was present in LEP - with almost 27 km circumference. When several bunches are in the machine, they tend to move in phase (" zero mode") rather than in one of the more unstable modes with finite phase shift between bunches. Exact analysis of thresholds of the coupled bunch instability is not possible in the presence of such a large number of cavity cells - over 600 - each of which has in addition many resonances. Their frequencies may be slightly different due to fabrication tolerances or different tuner positions, and even change with time due to temperature variations: their total impedance thus may vary widely. For the same detuning factor, the thresholds for transverse coupled bunch instabilities are much lower - but these have not been observed. A similar longitudinal bunch motion was recently seen at DESY, where it was explained as loss of Landau damping rather than a real instability.

3 Impedance Measurements on the Machine

The reactive part of the transverse impedance can be deduced from the slope of the coherent betatron tunes with bunch current:

$$\frac{dQ}{dI} = \frac{eR}{2\pi\sigma E}\sum_i \beta_i Z_{\perp_i}^{eff} \tag{3}$$

where the sum extends over all significant impedances. The effective impedance is defined as the integral (or sum) over the product of the bunch spectrum and the imaginary part of the (transverse) impedance. For a Gaussian distribution, the result can be expressed with complex error functions. For very short bunches - compared to the resonant wavelength - this can be approximated by

$$Z_\perp{}^{eff} \approx 2\frac{R}{Q}(\omega_r\sigma)^2 \tag{4}$$

while it becomes simply R/Q for $\omega_r\sigma \geq 1$. Note that both approximations may be needed for bunches of a given length in the presence of different resonators.

Many measurements of the tune slopes have been made in LEP over the years. The values depend somewhat on bunch length - typically 60-70 A^{-1} in the horizontal and 100-130 A^{-1} in the vertical plane (see Fig.7). A measurement only two weeks ago gave similar values, indicating that the recent installation of more SC cavities and separators has not yet strongly increased $Z_\perp$.

4 Measurements of the Distribution of Impedances

4.1 The distribution of transverse impedance around LEP

The pick-ups in LEP - over 500 in total - have a "1000-turn memory". This permits determination of the phase of the betatron oscillation around the whole machine circumference. The bunch is excited either horizontally of vertically, and the change of phase is determined as function of current by analysis of the measured oscillations. The excitation needs to be weak in order to avoid non-linear effects. The measured changes are very small, and the accuracy of the measurement is limited. Taking only

the results for larger currents ("method I") or using least-square fits ("method II") of all data yields slightly different results, but the average slope is in reasonable agreement with the measurements of total tune shifts (Figs.3 and 4). Only in one or two octants the slope appears locally inverted, which could be a real focussing of the elliptic chamber, or just measurement inaccuracy - therefore a repetition of the measurement with better resolution would be desirable.

4.2 The distribution of the energy loss

The energy loss - proportional to the real part of the longitudinal impedance - can be found my measuring the shift of the closed orbit with bunch current in all pick-ups with finite dispersion. In order to measure the dominant contribution of the RF cavity impedance, one of the 2 RF sectors is switched off, while the other one supplies the required energy. Once there are enough SC cavities installed to replenish the energy loss of the beam, we plan to repeat the experiment with all copper cavities idling.

Since also this measurement is on the limit of sensitivity, the results are averaged over each machine octant (Figs.5 and 6). The loss factors can be found from the relation

$$k_{\perp} = \frac{f_o E}{eD} \frac{\Delta x_{c.o.}}{\Delta I_b} \tag{5}$$

With an average dispersion $D = 0.58$ m in the pick-ups, a total loss factor $k_{||}$ of about 390 V/pC is found, quite near to the computed value of 375 V/pC for a bunch length of 12 mm.

5 Simulation Program TRISIM and Results

Simulation of collective effects for LEP was begun more than a decade ago with a super-particle program SIMTRAC[1]. However, the program was not very fast and the results depend on the number of super-particles used. Also it needs a delta-function wake as input which can only be approximated incompletely.

The next step was a code using an expansion of the particle distribution into Hermite polynomials called HERSIM[2][3]. It was less sensitive to the number of particles, and was faster since it used pre-calculated wake field tables. However, it was limited to polynomials of low (6-th) order, mainly because the wake field tables were produced by successive numerical differentiation which becomes rapidly inaccurate. Due to insufficient convergence, the description of distributions differing strongly from a Gaussian can therefore be rather poor.

These shortcomings are removed by using "linear interpolation functions" - in the shape of shifted triangles (see Fig.7) - in the program TRISIM[4]. A large number of triangles can be used to approximate any distribution quite well. Only a single wake field table is required for triangles of a given base width, which makes the program extremely compact and fast. It is also quite insensitive to the number of super-particles used.

The program TRISIM has been used extensively[5] to simulate current limitations by TMC for various lattice configurations (Fig.8 shows a typical output for an unstable situation), for the operation of LEP2 with many SC cavities, and also for testing a rather complex reactive feedback system using one or more free oscillators which store the information from the pickups. At present, we are also developing a 3-dimensional

version of the program to simulate effects in both transverse planes including betatron coupling.

6 Conclusions

The agreement of measured and computed impedances in LEP is quite satisfactory for single bunch ("short range") effects. For analytic estimates of thresholds and power losses, it was found to be quite important to use the "effective" rather than the low frequency impedance for comparison with experimental results.

The predicted TMC threshold of 0.75 mA/bunch (at the nominal synchrotron tune $Q_s = 0.1$) was based on simple estimates of the transverse impedances of the copper cavities and the shielded bellows. It was found to be only slightly lower in experiments. Since the beam-beam effect limits the bunch currents to about the same values for operation of LEP at 45 GeV, it is presently not required to get to a higher current/bunch. For LEP2, however, which is expected to reach 80-90 GeV where the beam-beam effect is weaker, higher bunch currents would be very desirable to reach high luminosity. In addition to other changes like higher Q_s and/or longer bunches, this could be achieved by keeping the transverse impedance low - e.g. by removal of copper cavities.

For more exact predictions and comparison with experimental data, we now rely mainly on simulation programs such as TRISIM. This program is based on the description of the particle distribution by linear interpolation functions. It gives a rapid and accurate estimate of collective single bunch effects in storage rings - if the impedance model can be trusted. In LEP, the elements with the biggest contributions to the impedances are the copper RF cavities and the shielded bellows, mainly due to their large number. Other elements of smaller importance are the SC cavities, the separators, pick-ups electrodes, collimators, and large bellows. With the wake potentials of these elements as input, the program TRISIM has been found to give excellent agreement with the single bunch effects observed in LEP,

References

[1] D.Brandt, LEP Note 443 (1983)

[2] V.Nys, Divisional Report CERN/LEP-TH/87-35 (1987)

[3] T.Wang, Divisional Report CERN/SL/90-08 (1990)

[4] G.Sabbi, Divisional Report CERN SL/95-25 (1995)

[5] G.Sabbi et al, Proc. EPAC London 1994

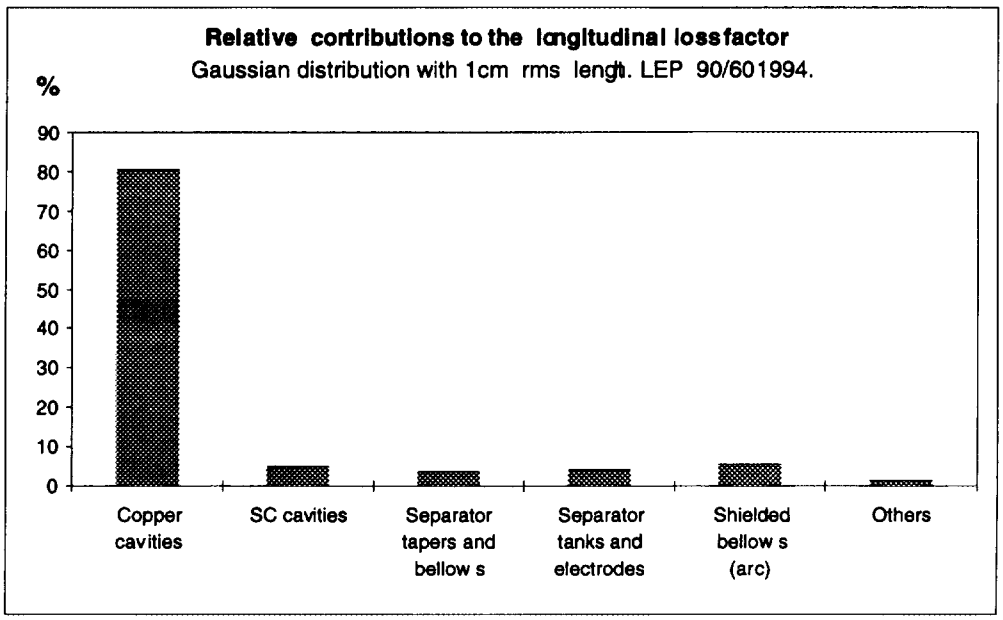

Figure 1: Horizontal Impedances in LEP

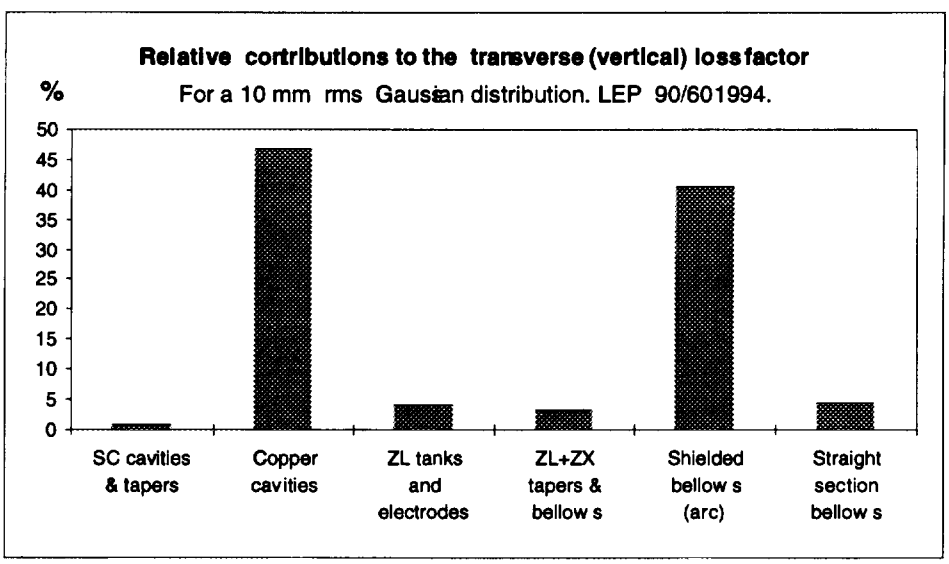

Figure 2: Vertical Impedances in LEP

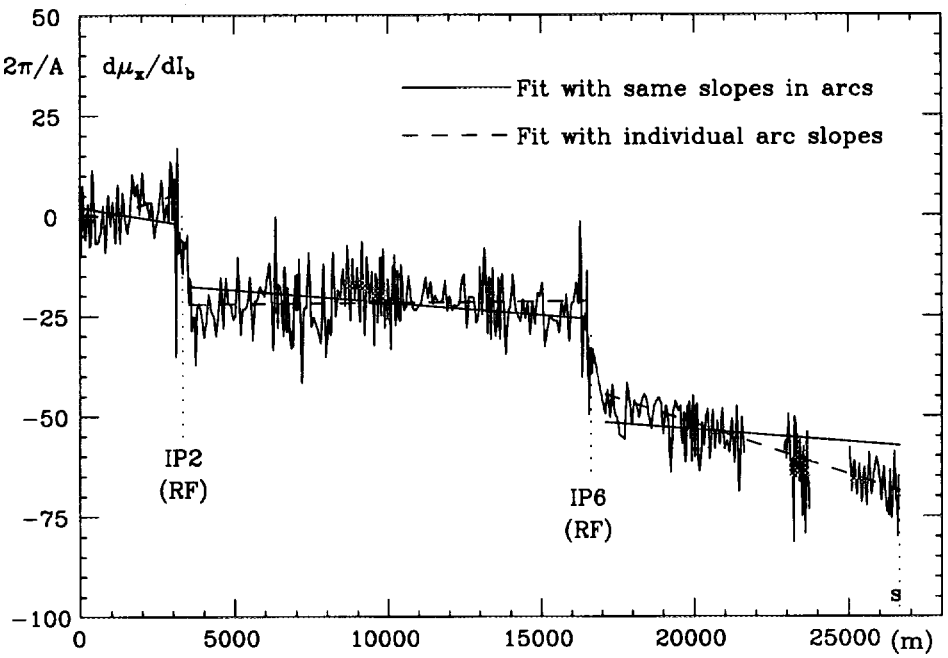

Figure 3: Horizontal Phase Advance with Bunch Current

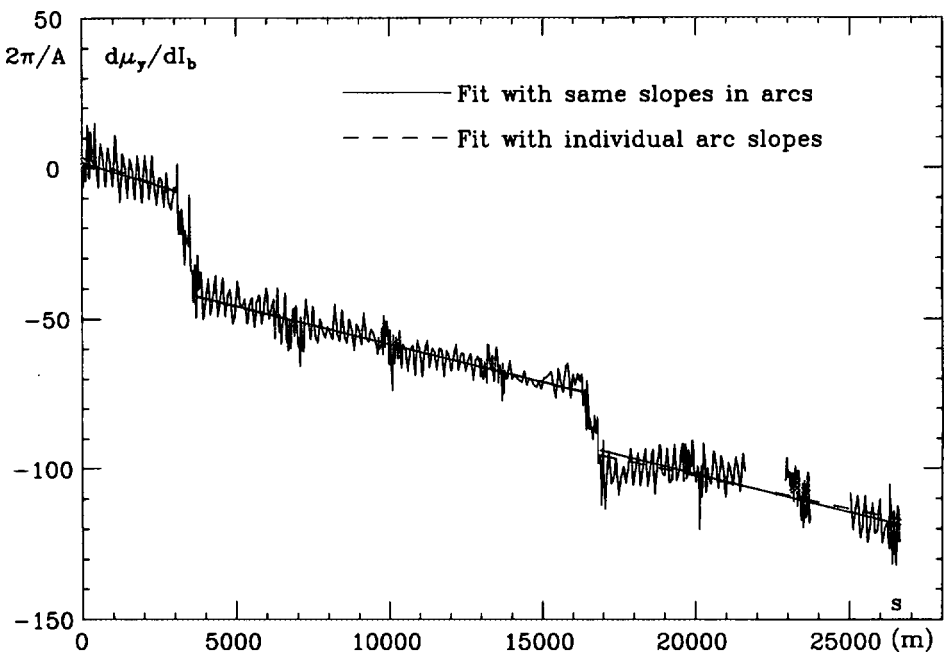

Figure 4: Vertical Phase Advance with Bunch Current

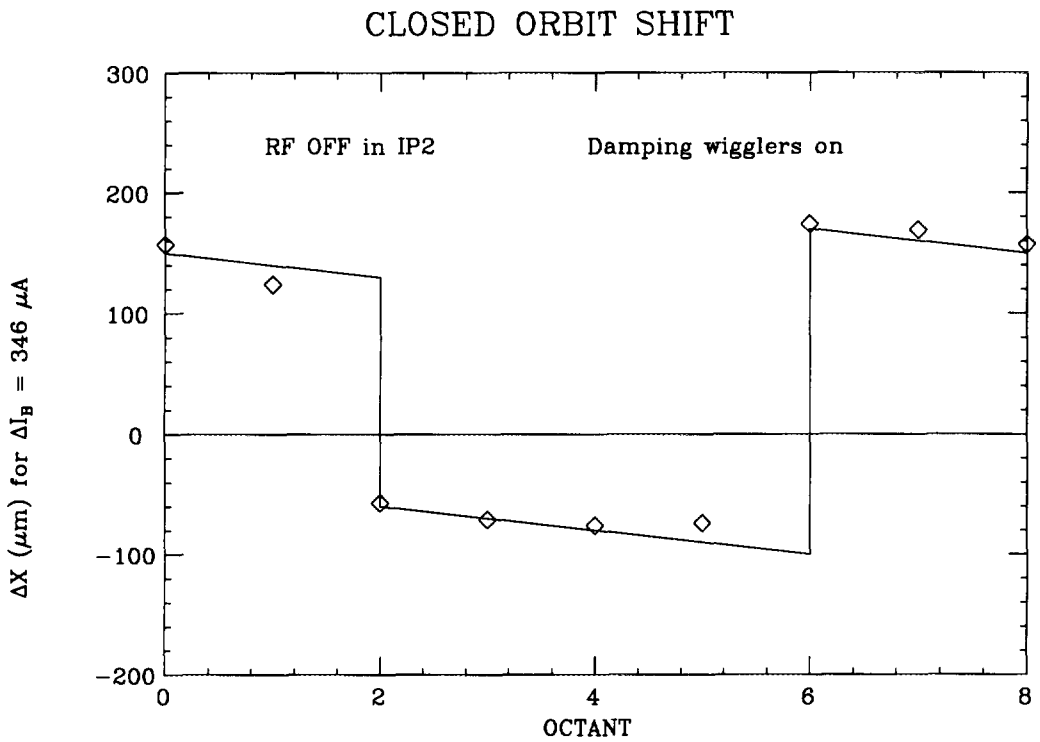

Figure 5: Orbit Displacement with Bunch Current, RF2 off

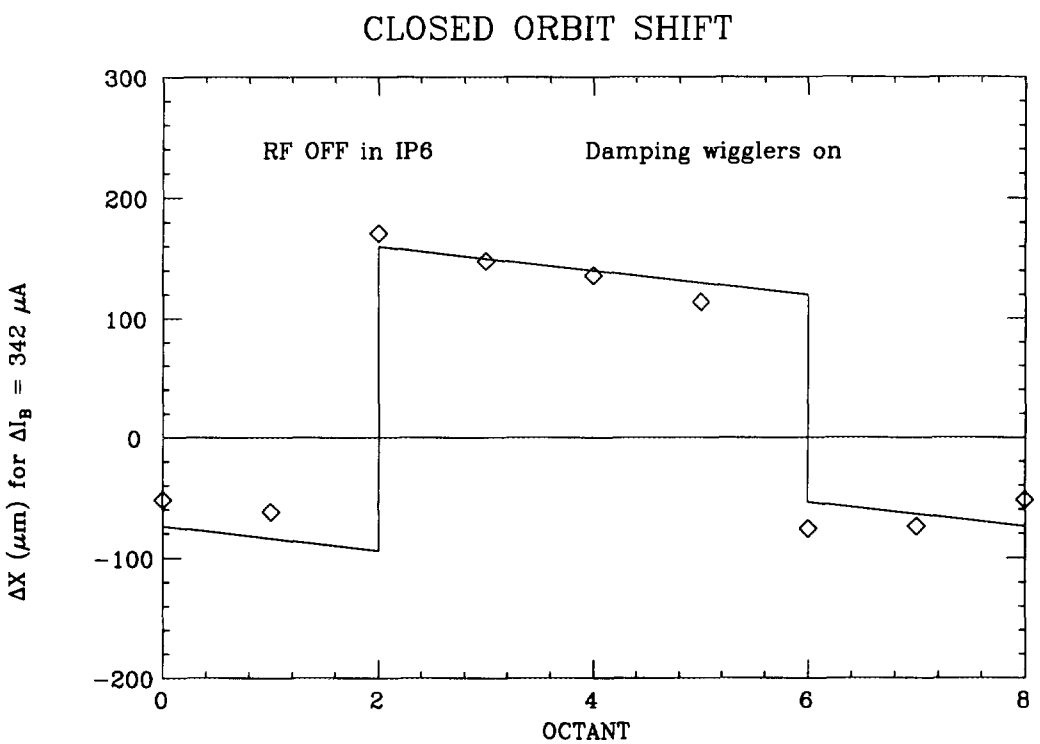

Figure 6: Orbit Displacement with Bunch Current, RF6 off

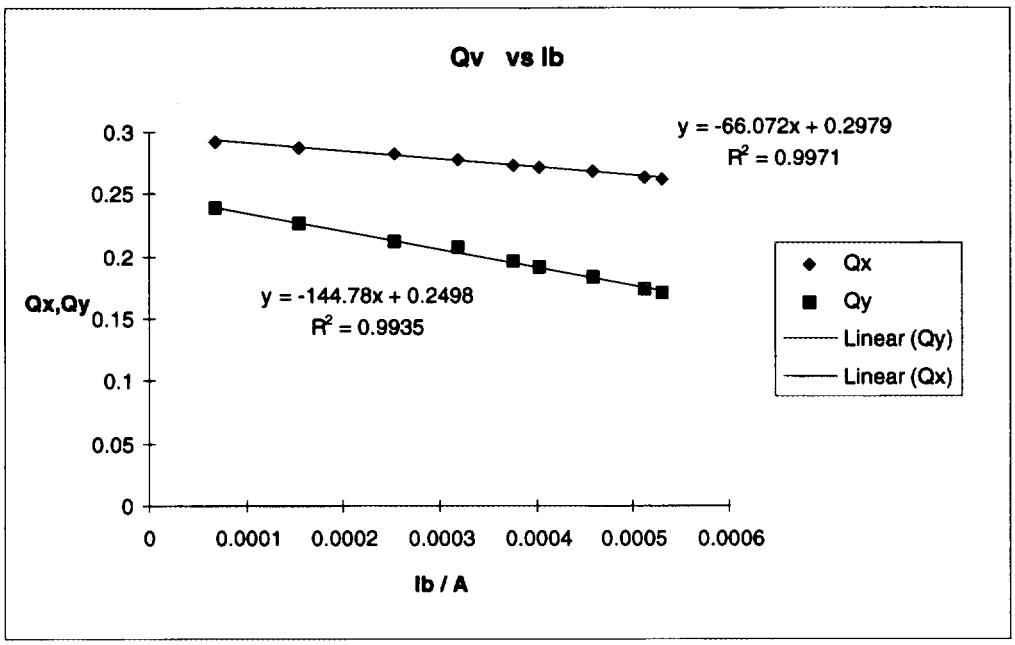

Figure 7: Change of Horizontal and Vertical Tunes with Current

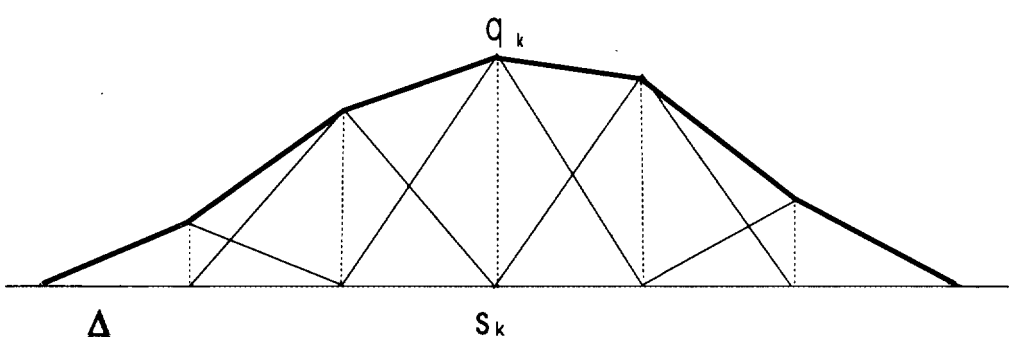

Figure 8: Expansion of Particle Distribution with shifted Triangles.

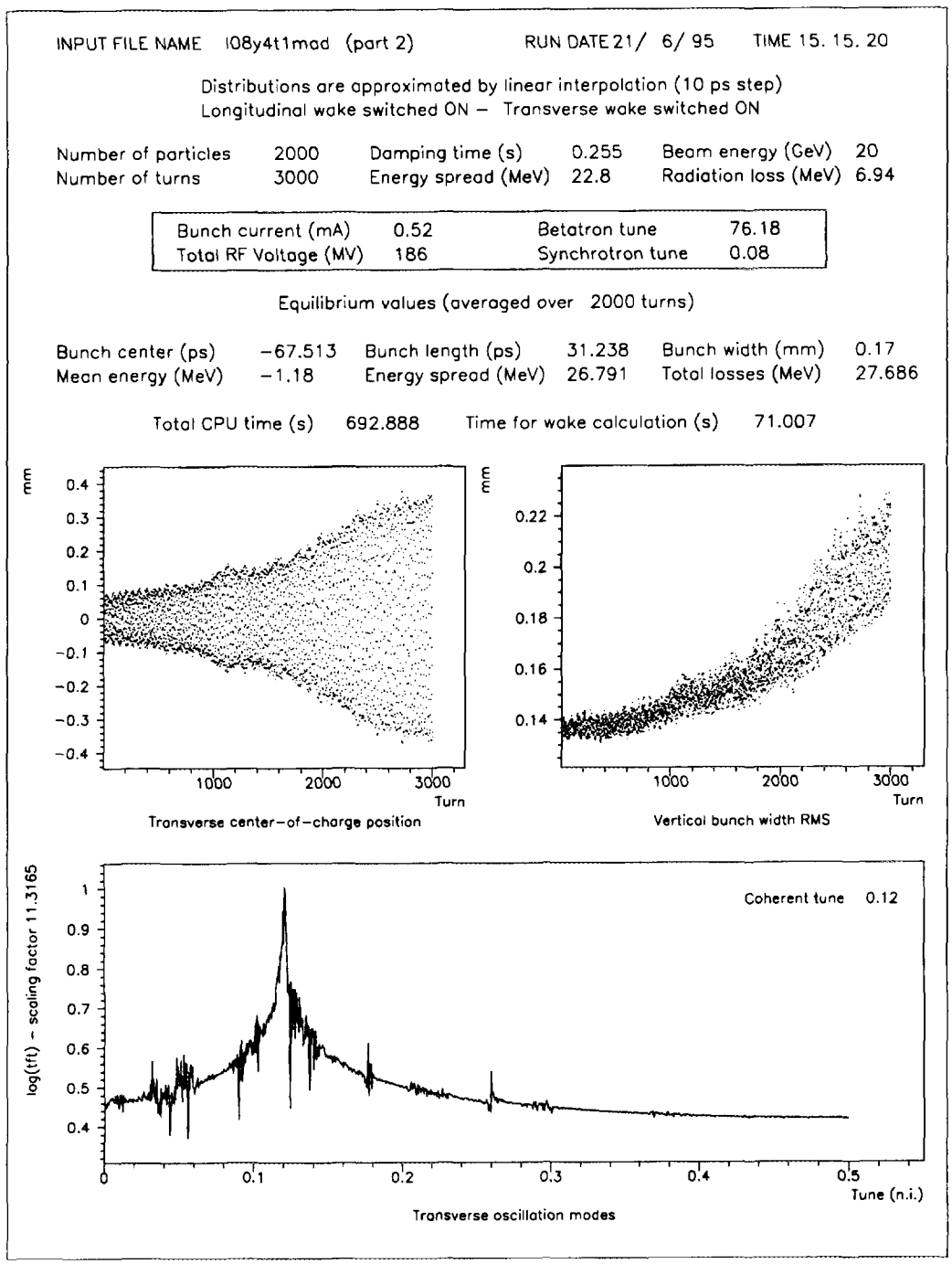

Figure 9: Output of Simulation Program TRISIM

COLLECTIVE EFFECTS AND IMPEDANCE ISSUES FOR THE SOLEIL PROJECT

G. Flynn
LURE-CNRS/CEA/MESR
Centre Universitaire, Bât. 209 D, 91405 Orsay Cedex, France

ABSTRACT

Various issues related to collective effects in the SOLEIL project are adressed. Particular attention is payed to the effects of longitudinal oscillations on undulator brilliance. Preliminary estimates of turbulent bunch lengthening and of the transverse mode coupling threshold are presented.

I. INTRODUCTION AND PROJECT OVERVIEW

SOLEIL is intended to be a very low emittance, medium energy synchrotron radiation storage ring providing radiation in the 10 eV to 20 keV energy range from a large number of undulators and bending magnets as well as from several strong field wigglers. The machine will consist of 16 double bend (DB) lattice cells grouped in 4 super-periods. Four long straight sections (14 m) will be provided for a storage ring free electron laser (FEL), many period undulators and other applications. [1] Several different operating points are possible. The achromatic Chasman-Green (CG) lattice provides a horizontal emittance of 7 nm.rad with zero dispersion in the user occupied straight sections. The minimum emittance of 2.7 nm.rad is obtained with distributed dispersion. The main machine parameters are presented in table 1 for several of the planned operating modes. The machine is designed for a maximum current of 500 mA with total ring filling (560 bunches). An 80 mA, 8 bunch filling pattern is also envisaged for time resolved experiments. Finally an 8 bunch, 1.5 GeV FEL configuration is also planned. The high currents and large number of bunches present many challenging issues, many of which resemble, to some degree, problems encountered in B-Factory projects. The principal collective effects which need to be considered are the following:

-RF induced heating and outgassing
-coupled-bunch longitudinal instabilities
-coupled-bunch transverse instabilities (primarily resistive wall)
-turbulent bunch lengthening (time resolution and FEL experiments)
-transverse mode coupling (single bunch current limit).

The aim of the present paper is to provide a strategic overview of these issues in conjunction with the other design constraints and performance goals of the machine.

II. PERFORMANCE GOALS

Three principal parameters, spectral flux, spectral brilliance and beam life-time determine the "quality" of a synchrotron radiation source from a user point of view. A fourth parameter, bunch length, is of interest to a subset of users (time resolution and FEL operation). Flux, the number of photons per second within a given small energy range integrated in angle depends mainly on the stored current and on the characteristics of the source device (bending magnet, wiggler or undulator). In the discussion that follows, we will consider only undulator emission. Undulator flux is weakly dependent on the emittance (through the effect of angular dispersion on spectral width) and on the effective energy spread. Spectral brilliance, being defined as the number of photons per second per unit solid angle per unit source area (also within a given energy range), is simply the phase space density of photons in the user beam. It is inversely proportional to the convolution of the phase space area of the electron beam with the diffraction limited radiation of a single particle. It is thus a strongly varying function of the emittance. Both flux and brilliance have the advantage of being conserved quantities, they can never be increased by user optics. Few users are interested only by flux as optical apertures and sample sizes are always limited. On the other hand, the number of users requiring extremely high brilliance is expected to increase in the coming years with the advent of more sophisticated optics. Life-time is very important for nearly all users as it determines the integrated flux or brilliance available during the course of a particular experiment.

For these reasons, SOLEIL has been designed to provide a high-current (500 mA), extremely low emittance beam (2 nm.rad) with a greater than ten hour life-time. These requirements lead to the following choices

-distributed horizontal dispersion (to minimize the emittance)
-3 MV of RF (for Touschek life in 8 bunch mode)
-nearly equal filling pattern in multibunch mode (Touschek life).

The need for a small emittance also implies very strong focussing in order to minimize the horizontal beta

function in bending magnets. This in turn leads to large beta values in the quadrupoles and thus to large negative natural chromaticities. It is thus necessary to provide strong sextupoles to correct these chromaticities to zero in order to avoid the head-tail instability. Sufficient additional sextupole strength will be provided to raise the vertical chromaticity to 0.7 in order to raise the transverse mode coupling limit (see section VII.).

These considerations along with the choice of a 500 MHz RF frequency for technological reasons imply the very short natural bunch length of 3.3 mm or 11 psec. While this will be favorable for FEL performance and time resolution users, it may well worsen certain collective effects.

Table 1 : Machine parameters

Circumference [m]	336.		
Straight sections	14.1 m x 4 + 7.4 m x 12		
Revolution frequency, f_0 [kHz]	892.261		
Energy [GeV]	2.15		1.5
Energy loss per turn [keV]	500		118
Natural energy spread	$8.6\ 10^{-4}$		$6.0\ 10^{-4}$
Emittance [nm.rad]	2.7	7	15
Horizontal dispersion in 7 m straight sections [m]	0.18	0.0	-0.1,-0.2
Momentum compaction	$3.8\ 10^{-4}$	$5.5\ 10^{-4}$	$1.3\ 10^{-3}$
Total RF voltage [MV]	2	3	3
Synchrotron tune	$5.439\ 10^{-3}$	$8.0868\ 10^{-3}$	$15.2\ 10^{-3}$
Betatron tunes ν_x, ν_z	18.3, 8.38	18.3, 8.38	19.4, 6.38
Natural bunch length [mm]	3.3	3.1	2.8

III. LONGITUDINAL COUPLED-BUNCH INSTABILITIES

A. Effect on undulator performance

The presence of a non-zero dispersion function in all insertion occupied straight sections renders the performance of the machine extremely sensitive to any increase in the effective energy distribution of the beam as this would increase the horizontal source size and thus reduce the brilliance. A secondary effect of such oscillations is the reduction in spectral flux and brilliance due to undulator line broadening. The most likely source of excess energy dispersion is dipole mode longitudinal coupled bunch (LCB) instability. The effect of such oscillations on the brilliance of a typical undulator has been calculated numerically and the results are shown in figure 1. It is seen that the most important effect is that due to the increase in source dimension. It seems clear from this figure that the amplitude of bunch energy oscillations must be kept to less than about 10^{-3} (corresponding to about a 20 % reduction in brilliance) if an unacceptable degradation of source brilliance is to be avoided. Because of the short bunch length this corresponds to a phase stability of only about 2° or 11 psec. One can see from the figure that if the dispersion function were zero, as is the case in present generation machines, the stability criterion could be substantially relaxed.

B. Instability thresholds

As all similar machines, SOLEIL will be very prone to longitudinal coupled bunch instabilities driven by narrow band higher order mode resonances (HOM's) in

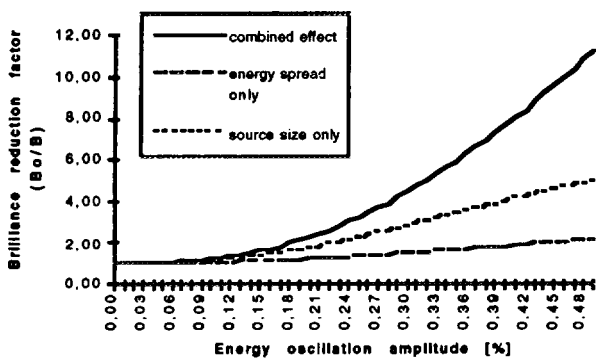

Figure 1: Brilliance reduction due to bunch energy oscillations

the accelerating cavities or other vacuum chamber elements. This can easily be seen from the well-known approximate formula, reproduced here for reference:

$$I_s = \frac{2E_s \nu_s}{\tau_{sr} \alpha} \frac{1}{f_r R_s} \qquad (1)$$

where:

I_S =instability threshold current

E_S=beam energy (in eV)
ν_S=synchrotron tune
τ_{sr}=synchrotron radiation damping time
α =momentum compaction factor
f_r=HOM resonance frequency
R_S=HOM shunt impedance

For a typical cavity HOM (f_r =1000 MHz, R_S=1 MΩ) this formula predicts a threshold current of only 10 mA if the HOM falls directly on a beam harmonic. Formula (1) suggests the use of the following factor, F, as a means of comparing the sensitivities of different machines to LCB instabilities at there nominal operating current:

$$F = \frac{I_{nominal}}{\left(\frac{2E_s\nu_s}{\tau_{sr}\alpha}\right)}$$

The larger the value of F, the lower the HOM strength needed to limit the current below $I_{nominal}$. Values of F for several different B-factory and synchrotron radiation machines are presented in table 2. We see from this table that the machine parameters of SOLEIL render it comparable in sensitivity to the high energy rings of the two current B-factory projects. It is however much less sensitive than the low-energy rings.

Table 2 : Comparison of sensitivities to LCB instability

	KEK-B [2]		PEP-II [3]		ESRF [4]	ELETTRA [5]	ALS [6]	SOLEIL
	HER	LER	HER	LER	(100 mA)	(200mA)	(400 mA)	(500 mA)
$\frac{I_{nominal}}{\left(\frac{2E_s\nu_s}{\tau_{sr}\alpha}\right)}$	1.2	15.8	5.0	21.9	0.14	6.4	24.8	4.8

C. Statistical analysis and HOM displacement

Formula (1) is of course only valid if an HOM falls directly on a beam harmonic. Two questions then come immediately to mind. The first is, what is the probability of the beam current being limited if a realistic distribution of cavity HOM's is assumed? This probability can be estimated rather easily if a few approximate but realistic hypotheses are made. First we observe that the spacing of revolution harmonics in SOLEIL is about 0.9 MHz. Due to manufacturing tolerances, the frequency of a given cavity HOM is only known to a limited precision. Actual experience suggests that for a real cavity equiped with a coupler, pumping holes and other accessories, the uncertainty in HOM frequencies is likely to be considerably greater than 1 MHz. [7] One can then safely assume that HOM position is random with respect to beam harmonics. Formula (1) combined with the Lorentzian line shape of an HOM resonance permits one to deduce the dangerous width of such a resonance with respect to a given design current. The expression is:

$$\Delta f_{danger} = \frac{f_r}{Q}\sqrt{(R_s f_r)F - 1}$$

where Q = quality factor of the resonance.

Finally these assumptions permit one to write the probability of being limited to a current below the nominal current by a particular HOM as:

$$P_{limit} = \frac{\Delta f_{danger}}{f_0}$$

One can then take into account the effect of several HOM's using the binomial distribution. Typical values (f_r =1000 MHz, R_S=1 MΩ, Q=40000, 3 modes per cavity, 5 cavities in the machine) lead to a probability per mode of 15% and a total probability of over 90%. It is thus clear that one cannot rely on luck to avoid instabilities.

The second question one might ask is whether it could be possible, to adjust HOM frequencies dynamically in order to avoid beam harmonics. *A priori*, this seems very difficult given that a typical cavity will contain nearly ten HOM's below the vacuum chamber propagation frequency and that only a quite limited number of parameters are available for adjustment (temperature and tuner position, for example). Recent encouraging results at ELETTRA have however shown that careful temperature control can permit the control of HOM frequencies and lead to at least a great reduction in the amplitude of LCB oscillations. [8] Questions remain however concerning the effects of broadened, nearly propogating, HOM's which cannot be displaced.

C. Cures

The aforementioned considerations having shown that LCB instability is certainly a problem which will have to be dealt with, several possible solutions are currently being considered. The ideal approach would be

to use RF cavities having essentially no narrow band HOM's. Such a "monomode" cavity does in fact exist. It has been developed by Cornell for the high luminosity upgrade of CESR. [9] This cavity has the particularity of being superconducting and some concern exists concerning the long-term reliability of such an RF system. Another approach would be to adopt a system similar to that used at ELETTRA and avoid HOM's by cavity tuning. However it is not yet clear that this alternative will provide a sufficiently stable beam to meet the tolerances presented in (III.A). Finally cavity tuning or partial HOM damping could be combined with a bunch to bunch feedback system. This approach also poses questions concerning beam stability and long-term reliability.

Since none of these potential cures provides a guaranteed solution without concurrent disadvantages, work is currently underway to further elucidate LCB behavior for each of these different systems. Now that quantitative tolerances have been set for longitudinal instability, the next step is to determine LCB saturation amplitudes as a function of HOM impedance. A final decision on the approach to be taken is expected before the end of 1995.

IV. TRANSVERSE COUPLED BUNCH INSTABILITY

A. Resistive wall

The most significant transverse narrow band impedance will most likely be the resistive wall effect. Since the resistive wall impedance is a rapidly decreasing function of frequency, centered around zero, a simple estimate of this effect can be made by considering only the lowest frequency aliases of coupled bunch modes, that is to say, only those frequencies contained between zero and the bunch frequency of 500 MHz. Such a calculation shows that with a stainless steel vacuum chamber, about 50 modes would be unstable. If the chamber were in Aluminum, this number would be reduced to only about 4. It therefore appears that if a stainless steel vacuum chamber is adopted, a transverse feedback system with a bandwidth of about 50 MHz will be necessary.

B. Transverse HOM's

The transverse analog of (1) can be written:

$$I_S = \frac{4\pi E_S \nu_\beta}{\tau_T c} \frac{1}{R_T} \qquad (2)$$

where υ_β represents the lesser of the two betatron tunes. Using this formula, a typical dipole HOM (f_r=1 GHz, R_S=800 kΩ/m, Q=48000) results in a threshold current of about 80 mA. The dangerous width of such a mode would then be on the order of 50 kHz. This implies that the probability of being limited in current by such a mode is much smaller (about 6 %) than that for longitudinal modes. Nonetheless, the presence of such modes in an undamped cavity must be taken into account if mode displacement of longitudinal HOM's is foreseen as they will tend to limit the useable temperature ranges. This effect is all the more dangerous as transverse coupled bunch instabilities, unlike their longitudinal counterparts, typically lead to beam loss.

V. BROAD-BAND IMPEDANCE AND COMPONENT DESIGN

At the present stage of the project, a detailed impedance budget cannot yet be determined as the overall vacuum chamber design has not yet been completed. It is clear that all efforts must be made to build as smooth a vacuum chamber as possible in order to minimize broad-band related collective effects, reduce RF losses per turn and avoid excessive RF induced vacuum chamber heating in the high bunch current mode of operation. For this reason all bellows and pumping holes must be well shielded. In addition vacuum chamber transitions (to cavities for example) must be made as smooth as possible. It is also planned to use special vacuum gaskets which minimize gaps at vacuum chamber connections.

In light of the difficulties which have been encountered with bellows shielding fingers in other laboratories, a program is underway to optimize the design of these shields. Vacuum bellows and there shields must satisfy the following criteria:

i.) provide sufficient transverse and longitudinal flexibility for mounting and thermal dilation during bake-out

ii.) assure a very good and permanent electrical continuity

iii.) minimise the geometric distortion of the electromagnetic boundary conditions seen by the beam

Failure to meet requirements (ii) and (iii) would lead to an increased loss factor and thus to excessive local heating with high bunch currents leading to vacuum degradation. In addition a risk of local multipactoring and electrical discharges due to the induced fields cannot be excluded. Finally excess local heating may lead to additional mechanical deformation leading to additional loss and an unstable cycle. It is also important to note that requirements (i) and (iii) are only relatively compatible. Therefore careful attention should be given to vacuum chamber and support structure mechanical tolerances in order to reduce chamber to chamber discontinuities to a strict minimum.

Since a detailed determination of the expected broad-band impedance does not yet exist for SOLEIL, for the purpose of obtaining a rough preliminary estimate of the importance of various single bunch phenomena, the following values will be used based on a BB resonator fit to a total loss factor curve based on literature values for the individual loss factors of components used in similar machines: [10]

$$\left|\frac{Z_L}{n}\right| = 0.36\,\Omega,\quad f_r = 6.2\ \text{GHz},\quad Q = 1$$

The corresponding transverse broad band impedance, Z_T can then be estimated by the usual approximate formula:

$$|Z_T| = \frac{2R}{b^2}\left|\frac{Z_L}{n}\right| \qquad [11]$$

where R is the average ring radius and b is the vacuum chamber half-height (19 mm), to be about 100 kΩ/m.

It is planned to begin detailed impedance calculations on vacuum chamber elements as soon as an initial vacuum chamber design becomes available. It is hoped to use the 3-D finite element code ANTIGONE [12] for this purpose and work has begun in this direction.

VI. BUNCH LENGTHENING

Using the BB model presented in the last section, the bunch length as a function of current has been calculated using the program BBI [13] with the combined effect of potential well and turbulent bunch lengthening and assuming SPEAR scaling for the impedance. The results are shown in figure 2. We see that for the nominal 8 bunch mode current of 10 mA the bunch has lengthened by more than a factor 3. Nonetheless, because of the extremely short initial bunch length, the nominal current length remains below 1 cm. As for the energy spread, it remains at its natural value for the nominal multibunch current of 0.92 mA but begins to increase between 1 and 2 mA. At the nominal 8 bunch mode current however the energy spread has increased by a factor 4. This implies that in this mode, a significant reduction in undulator brilliance is to be expected for the distributed dispersion optics.

VII. TRANSVERSE MODE COUPLING

Based on the transverse broad-band impedance estimate from section V, the transverse mode coupling thresholds can be estimated using the mode coupling formula:

$$I_{th} = \frac{8(E_s / e)\nu_s}{Z_T\langle\beta_z\rangle R}\sigma_l \qquad [12]$$

to be about 18 mA per bunch. This is larger than the nominal 10 mA/bunch current planned for 8 bunch operation. This estimate must be considered extremely preliminary and further calculations using a more refined impedance model will be performed.

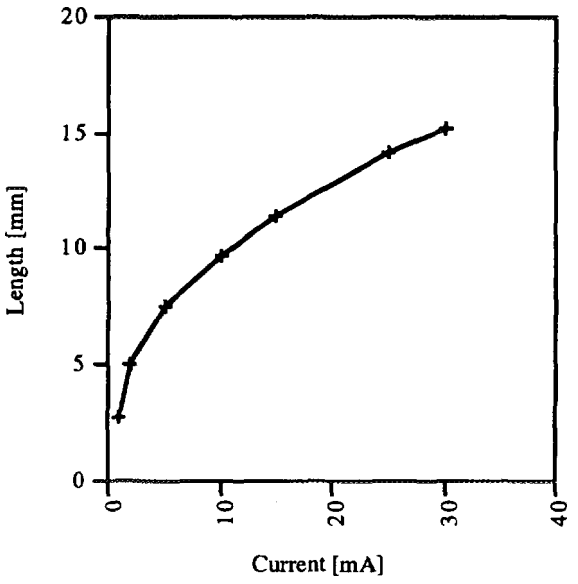

Figure 2 : Bunch lengthening curve (2.7 nm.rad)

VIII. CONCLUSION

This paper has brought to light a certain number of potential difficulties presented by collective effects in achieving some of the performance goals of the SOLEIL project. The fact that at least two machines similar to SOLEIL are currently functioning with good performance is reassuring. Nonetheless a great deal of work remains to be done, in particular, on the LCB instability, transverse mode coupling and vacuum chamber impedance for SOLEIL to fulfill its promise of providing one of the world's most brilliant medium energy synchrotron sources for the beginning of the 21st century.

IX. ACKNOWLEDGEMENTS

I would like to thank M. P. Level and H. Zyngier for their many helpful comments and suggestions.

X. REFERENCES

[1] M. P. Level et. al., "New Specifications for the SOLEIL Project", presented at the *1995 Particle Accelerator Conference and International Conference on High-Energy Accelerators*, Dallas (Texas) USA, May 1995.

[2] S. Kurokawa, "Status of KEKB Project", in Proceedings of the 1994 EPAC Conference, p. 473.

[3] W. Barbetta, et. al., "PEP-II Design Update and R&D Results", in *Proceedings of the 1993 Particle Accelerator Conference*, p. 2010.

[4] ESRF Foundation Phase Report, Grenoble France,1987

[5] ELETTRA Conceptual Design Report, Trieste Italy, 1989

[6] Lawrence Berkeley Laboratory PUB-5172, 31-2 GeV Synchrotron Radiation Source Conceptual Design Report."

[7] M. Svandrlik, private communication.

[8] M. Svandrlik et. al., "The Cure of Multibunch Instabilities in ELETTRA", presented at the *1995 Particle Accelerator Conference and International Conference on High-Energy Accelerators*, Dallas (Texas) USA, May 1995.

[9] H. Padamsee et. al., "Design Challenges for High Current Storage Rings", in *Particle Accelerators*, vol. 40, p. 17-40, 1992

[10] Projet SOLEIL: étude technique, LURE, Orsay France, 1994

[11] J.L. Laclare, "Bunched Beam Coherent Instabilities", CAS Advanced Accelerator Physics, CERN 87-03, 1987

[12] G. LeMeur, F. Touze, "PRIAM/ANTIGONE a 2D/3D Paackage for Accelerator Design," in Proceedings of the 1994 EPAC Conference, p. 1321.

[13] B. Zotter, "BBI-A Program to Compute Bunched Beam Instabilities in High Energy Particle Accelerators and Storage Rings", CERN LEP/TH 89-74, 1989

COLLECTIVE EFFECTS AND IMPEDANCE STUDY FOR THE DAΦNE Φ - FACTORY

M. Zobov, P. Arcioni#, R. Boni, A. Gallo, A. Ghigo, F. Marcellini, M. Migliorati, L. Palumbo°, L. Perregrini#, M. Serio, B. Spataro,

INFN - Laboratori Nazionali di Frascati, P. O. Box 13, I-00044 Frascati (Roma), Italy
(#) Università di Pavia, Via Abbiategrasso 209, Pavia, Italy
(o) INFN-LNF and Università di Roma "La Sapienza", P.le Aldo Moro 2, I-00185 Roma, Italy

Abstract

We describe the design of main impedance generating elements of DAΦNE vacuum chamber and discuss the impact of these elements on single and multibunch beam dynamics.

1. INTRODUCTION

The e^+e^- Φ - factory DAΦNE is presently under construction in Frascati (Italy). It is designed as a double ring system with a maximum number of 120 bunches/beam. The short term luminosity goal is $L = 1.3 \cdot 10^{32} \mathrm{cm}^{-2} \mathrm{sec}^{-1}$ with 30 bunches. The main features of the factory have been described in details elsewhere [1]. Table 1 gives the relevant parameters of the DAΦNE main rings.

The basic design choice of achieving the required luminosity with a large total current, distributed over a large number of bunches, makes the operation very critical with respect to coupled bunch instabilities. These instabilities have been identified since the very beginning of the project as a potentially severe limit on the ultimate achievable luminosity. For this reason, one of the primary goals in the machine design was to reduce to a minimum the number of vacuum chamber elements creating parasitic high order modes (HOMs) capable to drive the multibunch instability and to develop means for damping both the HOMS and the instabilities. This task is accomplished by properly designing the RF cavity and by coupling off the HOMs through loops or wave-guides to extract energy from the resonant fields, thus reducing at the same time the quality factor Q and the shunt impedance R. The residual excitation of beam oscillations is damped by means of a bunch-by-bunch digital feedback system.

The single bunch instabilities are also of great importance for DAΦNE. In order to achieve high luminosity in a short machine the single bunch current must be high. This implies that certain single bunch thresholds must be taken into account. Indeed, for DAΦNE, the approximate criterion on the limit of the microwave longitudinal instability [2]:

$$\left(\frac{Z_L}{n}\right)_{eff} = \frac{\sqrt{2\pi}\alpha(E/e)(\sigma_{\varepsilon 0}/E)^2 \sigma_{z0}}{I_0 R} \qquad (1)$$

gives a small longitudinal impedance limit $(Z_L / n)_{eff} \approx 0.01\Omega$ and the turbulent lengthening (and widening) regime can hardly be avoided. Here σ_{z0} is the natural bunch length (4.82 mm at V_{rf}=250 kV).

The energy spread σ_ε and the bunch length are the key parameters defining Touschek lifetime, parasitic losses, luminosity, multibunch instability rise times etc. This demanded careful analysis of the broad-band impedance of the machine (short range wake fields) and simulation of the bunch lengthening process.

The transverse mode coupling does not seem to be a limiting instability for DAΦNE as it is for large machines, LEP for example [3]. Nevertheless, the instability can be destructive for the beam and its threshold has to be estimated.

The paper is organized in the following way. In Section 2 we discuss the design of the main vacuum chamber elements with analysis of their impedance and possible impact on the beam dynamics. Section 3 describes the results of bunch lengthening simulations and gives estimates for the transverse mode coupling threshold. Section 4 shows the results of the multibunch instability simulations. In the Appendix we summarize formulae which have been used for multibunch instabilities rise time calculations. More details on the subject of the paper can be found in the quoted References.

Table 1. Main DAΦNE Parameters

Energy	E	510.0	Mev
Average radius	R	15.548	m
Emittance	ε_x / ε_y	1/0.01	mm·mrad
Beam-beam tune shift	ξ_x / ξ_y	0.04/0.04	
Betatron tune	ν_x / ν_y	5.13/6.10	
RF frequency	f_{rf}	368.25	MHz
Harmonic number	h	120	
Revolution frequency	f_0	3.0688	MHz
Max. number of bunches	n_b	120	
Minimum bunch separation	s_b	81.4	cm
Bunch average current	I_0	43.7	mA
Particles per bunch	N	$9.0 \cdot 10^{10}$	
Momentum compaction	α	0.0058	
Natural energy spread	$\sigma_{\varepsilon 0} / E$	0.000396	
Bunch length	σ_z	3.0	cm
Synchrotron radiation loss	U_0	9.3	keV/turn
Damping time	τ_ε / τ_x	17.8/36.0	ms
RF voltage	V_{rf}	250	kV
Synchrotron tune	ν_s	0.0078	
Beta functions at IP	β_x^* / β_y^*	450/4.5	cm
Maximum luminosity	L	$5.3 \cdot 10^{32}$	$cm^{-2}s^{-1}$

2. IMPEDANCE GENERATING ELEMENTS

2.1. RF cavity

2.1.1. RF power requirements

DAΦNE is designed to store a maximum current of 5.24 A in 120 bunches per ring at 510 MeV. The RF power per ring, given by the sum of the power delivered to the beam and that dissipated on the cavity walls, is about 100 kW for 120 bunches at 250 kV gap voltage. One 150 kW klystron amplifier per ring will be installed to feed a 368.25 MHz RF cavity.

2.1.2. Shape choice

The choice of the cavity shape has been matter of a long debate. The goal was to reduce both the shunt impedance R and the (R/Q) of the cavity HOMs in order to increase the longitudinal instability thresholds.

The basic ideas to reduce the HOM impedances were to provide large and long tapered cavity beam tubes to let the parasitic modes propagate along them and to couple out the HOM energy by means of waveguides (WG) [4].

The tapered tubes are used as a gradual transition from the cavity iris to the ring vacuum pipe. A careful analysis of the longitudinal wake potentials made with the code TBCI [5] has shown that in a long taper cavity the loss factor of the HOMs is significantly lower than that of a cavity with short tubes [6]. This means that, on the average, the R/Q values of the parasitic modes are reduced.

Two basic cavity shapes, the so called "nose-cone" and "rounded" profiles, were considered. Calculations performed with the computer codes URMEL [7] and OSCAR2D [8] and experimental measurements made on prototypes have shown that the two models are comparable in terms of HOM impedances as illustrated in Table 2. Therefore the rounded cavity was chosen since its mechanical design is much simpler. The cavity shape was then optimized in order to keep the fundamental mode (FM) impedance above 3 MΩ to reduce the dissipated power and make the cooling design easier. Much care was also taken to keep the higher impedance HOM frequencies far away from harmonics of the beam in order to avoid resonant enhancement of the parasitic power losses.

Table 2. Nosecone vs. Rounded

	Nosecone	Rounded		Nosecone	Rounded
Frequency (MHz)	368.3	368.3	*0-MM-1 mode:*		
R/Q (Ω)	69.9	61.7	Frequency (MHz)	704.7	696.8
Q	34000	49000	R/Q (Ω)	4.2	16.0
R_s (MΩ)	2.37	3.04	Q	30000	50000
k_l (V/pC)	0.101	0.129	R_s (kΩ)	128	800
k_0 (V/pC)	0.077	0.068	*0-EM-1 mode:*		
k_{pm} (V/pC)	0.024	0.061	Frequency (MHz)	565.0	532.7
k_t' (V/pC/m)	1.16	1.38	R'/Q (Ω)	30.3	13.7
k_{pm}/k_0	0.31	0.91	Q	42000	54000
k_t'/k_0 *1 mm	0.015	0.02	R_s' (kΩ)	1.28	0.74

2.1.3. HOM damping and measurements on prototype.

HOM damping is obtained by opening rectangular slots onto the cavity surface and applying at those positions rectangular WGs which can convey out of the cavity the fields of the parasitic modes in the TE_{10} WG dominant mode.

The DAΦNE cavity is equipped with five WGs. Three WGs are applied, 120° apart for symmetry considerations, onto the central body. They are 305x40 mm^2 rectangular WGs with TE_{10} cut-off at 495 MHz. Their position allows, on the average, the best coupling with the magnetic field H_Φ of the HOMs. One additional 140x40 mm^2 WG, with cut-off at 1070 MHz, is placed on each tapered tube to couple some high frequency HOMs which penetrate along the pipes and have intense H_Φ at that position.

In order to dissipate the HOM power extracted from the cavity, the rectangular WGs are converted in double ridge WGs with a smooth and wideband tapered section which is finally adapted to 50 Ω by a transition to coaxial. The obtained bandwidth is 0.5-3 GHz and 1.2-3 GHz respectively with standing wave ratio (VSWR) < 2 in the full band. Then, by means of coaxial vacuum feedthroughs, the HOM power can be dissipated onto external 50 Ω loads in air [9]. In this way, the application of dissipating materials in ultra high vacuum (UHV) is avoided. Moreover the HOM power can be sampled with directional couplers.

The broadband transitions have been designed at LNF with the 3D computer code HFSS [10]. They are manufactured in OFHC copper and have been tested on bench in UHV and with RF power [11].

One broadband transition is shown in Fig. 1. It consists of an initial straight 30 cm section followed by an 80 cm tapered double ridge WG terminated with an adapter to a 7/8" coaxial output. The 30 cm straight allows the fundamental cavity mode to vanish before entering the tapered WG. This avoids having high FM field at the coaxial output. The measured VSWR versus frequency response of the WG to coaxial transition is shown in Fig. 2.

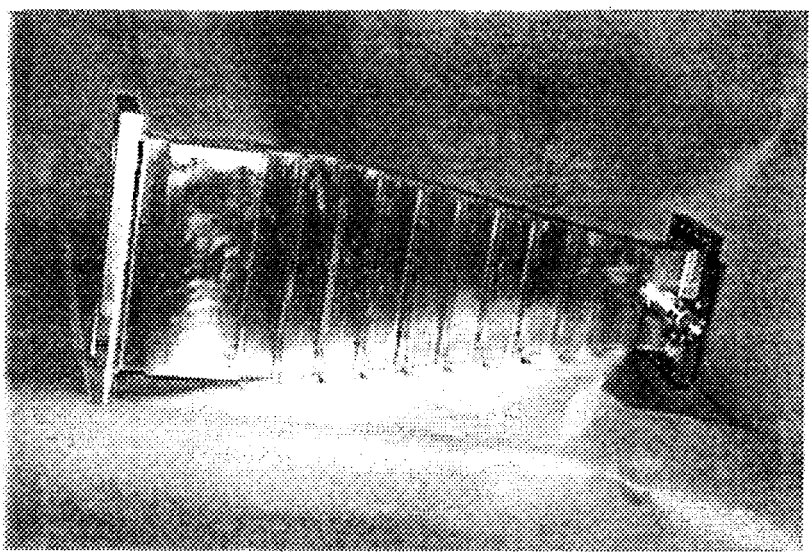

Fig. 1 - Broad band waveguide-to-coaxial transition.

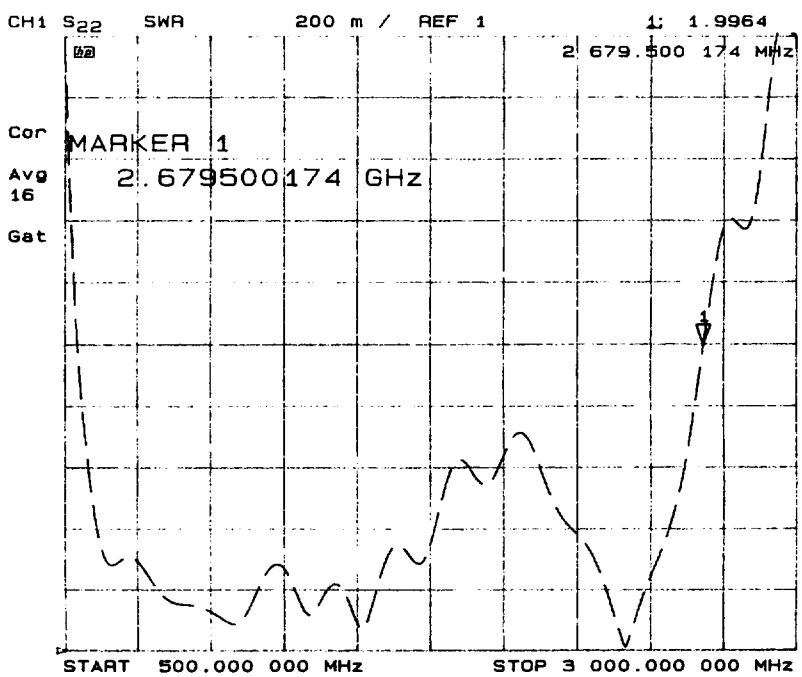

Fig. 2 - Measured VSWR vs. frequency response of waveguide-to-coaxial transition.

With the use of the described damping system, the parasitic mode quality factors Qs of the most dangerous HOMs are reduced, on the average, by two orders of magnitude. In some cases, like for the TM_{011}, the Q damping is even stronger. Frequency and Q of the FM and HOMs have been measured. Also, a careful characterization of the model with the bead perturbation method has been carried out for some longitudinal monopoles to measure their R/Q. Table 3 shows the FM and HOM Qs obtained on a copper cavity prototype equipped with WGs. The last column in Table 3 gives the coupled bunch instability rise time in case of full coupling with the damped HOMs calculated with formulae given in the Appendix. The FM quality factor decreases by 12 % due to the application of WGs.

Table 3. Cavity Prototype Modes

Mode	Freq. (MHz)	R/Q (Ω)	Undamped Q	WG damped Q	τ (ms)
0-EM-1	357.2	61	25000	22000	
0-MM-1	745.7	16	24000	70	1.4
0-EM-2	796.8	0.5	40000	210	14.9
0-MM-2	1023.6	0.9	28000	90	17.5
0-EM-3	1121.1	0.3	12000	300	15.4
0-MM-3	1175.9	0.6	5000	90	25.6
0-EM-4	1201.5	0.2	9000	180	38.4
0-EM-5	1369.0	2.0	5000	170	4.1
0-MM-4	1431.7	1.0	4000	550	2.6
1-MM-1 a	490.0	5.1*	30500	650	3.0
1-MM-1 b	491.3	5.1*	28500	830	2.4
1-EM-1 a	523.5	14.0*	31500	150	4.5
1-EM-1 b	549.7	14.0*	32000	50	13.1

(*) Normalized impedance, URMEL definition.

2.1.4. Simulations.

Simulations of the WG loaded DAΦNE cavity have been carried out using the computer codes POPBCI [12] and HFSS [13] and an analytical method based on the Kirchoff's approximation [14].

The code POPBCI can post-process data from any 3D electromagnetic code to calculate the resonant frequencies and the beam coupling impedances of waveguide loaded resonators. The code considers perfectly matched WGs connected to the cavity body and calculates the longitudinal and transverse mode impedances of the resonator as a function of frequency.

Figures 3 and 4 show $Re[Z_L]$ and $Re[Z_T]$ of the DAΦNE cavity without and with WGs respectively.

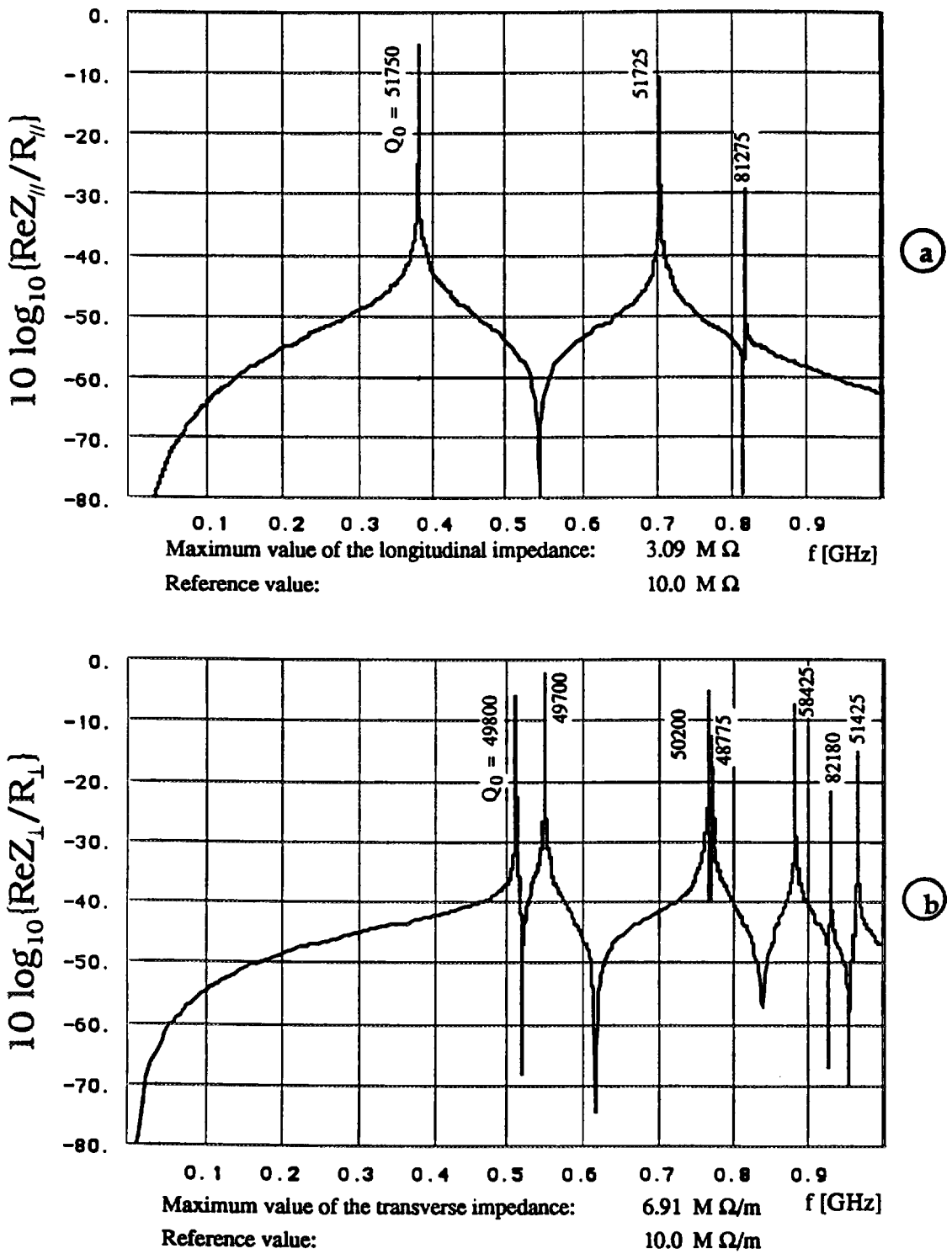

Fig. 3 - Longitudinal and transverse coupling impedances of DAΦNE cavity in the 0 - 1000 MHz frequency band (without waveguide dampers).

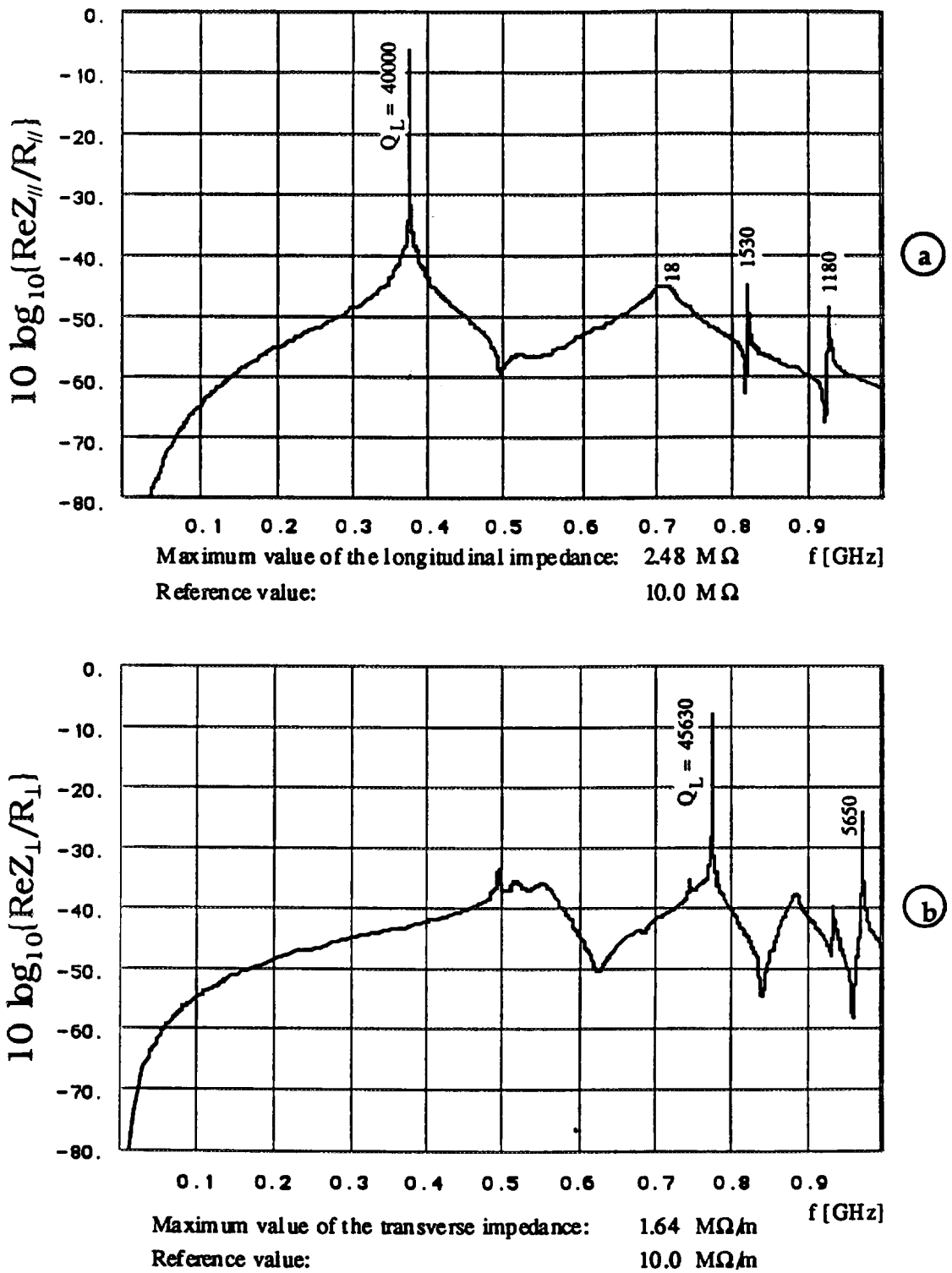

Fig. 4 - Longitudinal and transverse coupling impedances of DAΦNE cavity in the 0 - 1000 MHz frequency band (waveguide terminated with perfectly matched loads).

Similar investigations have been performed using the HFSS code which is based on the finite elements method. HFSS computes the field distribution in the frequency domain inside any passive 3D structure by defining input and output ports. The results are presented in the form of a scattering matrix and the parameters S_{ij} versus frequency are given.

A different simulation method of the DAΦNE cavity with WG loading is based on the so-called Kirchoff's approximation. The fields propagating in the WGs are computed considering the unperturbed magnetic field on the slot surface as the source term for the WG Green's functions. The Q factor of a generic resonance of the loaded cavity (Q_L) is therefore:

$$Q_L = \omega U / \left(P_0 + P_{wg}\right) = 1 / \left(1 / Q_0 + P_{wg} / \omega U\right) \tag{2}$$

where Q_0 is the unloaded quality factor, P_0 is the power dissipated by the cavity walls and U is the energy stored in the cavity. The power P_{wg} absorbed by the WGs is given by the real part of the Poynting vector flux through the rectangular slot.

This method has been applied to the monopolar modes of the DAΦNE cavity and the results of this analytical simulation are presented in [14]. The results obtained with analytical and numerical methods are in rather good agreement.

2.1.5. HOM power loss estimates.

The beam power delivered to the cavity HOMs has been estimated for the 30 bunches initial operation [15] of DAΦNE. The beam current expressed as a Fourier series is:

$$i_b(t) = \sum I_m \exp(jm\omega_0 t) \tag{3}$$

The total HOM power depends on the cavity monopole spectrum and increases when the beam lines I_m overlap the cavity spectrum. The power can finally be derived as follows:

$$P = \sum_{m=0}^{+\infty} \sum_{HOMs} \frac{2(R/Q)QI_m^2}{1 + Q^2\left(\frac{m\omega_0}{\omega_r} - \frac{\omega_r}{m\omega_o}\right)^2} \tag{4}$$

The above expression has been calculated taking into account the beam and cavity spectra. For 30 bunches the HOM power is about 200 W. In the case of full current operation, the HOM losses are below 1 kW per WG.

2.1.6. Present status.

The RF cavity for the DAΦNE main ring is being fabricated by Zanon S.p.A, Schio, Italy. Figure 5 shows a sketch of the resonator equipped with the HOM WGs, the tuning system and the main RF coupler. The cavity central body is obtained from a single forged billet of OFHC copper and is fully manufactured from the inside by an automatic milling machine to avoid large UHV tight weldings. The tapered tubes are made with the same technique. The stainless steel flanges have been welded with the electron beam welding (EBW) technique and the vacuum tightness is ensured by Helicoflex gaskets in the rectangular WG flanges; Be-Cu springs guarantee low RF loss contacts; other flanges are standard Conflat type. The cavity cooling is provided by 10 mm dia. cooling pipes brazed onto the cavity surface with a low temperature alloy. Fig 6 shows a picture of the cavity under construction at Zanon. The RF power tests are scheduled in July 1995.

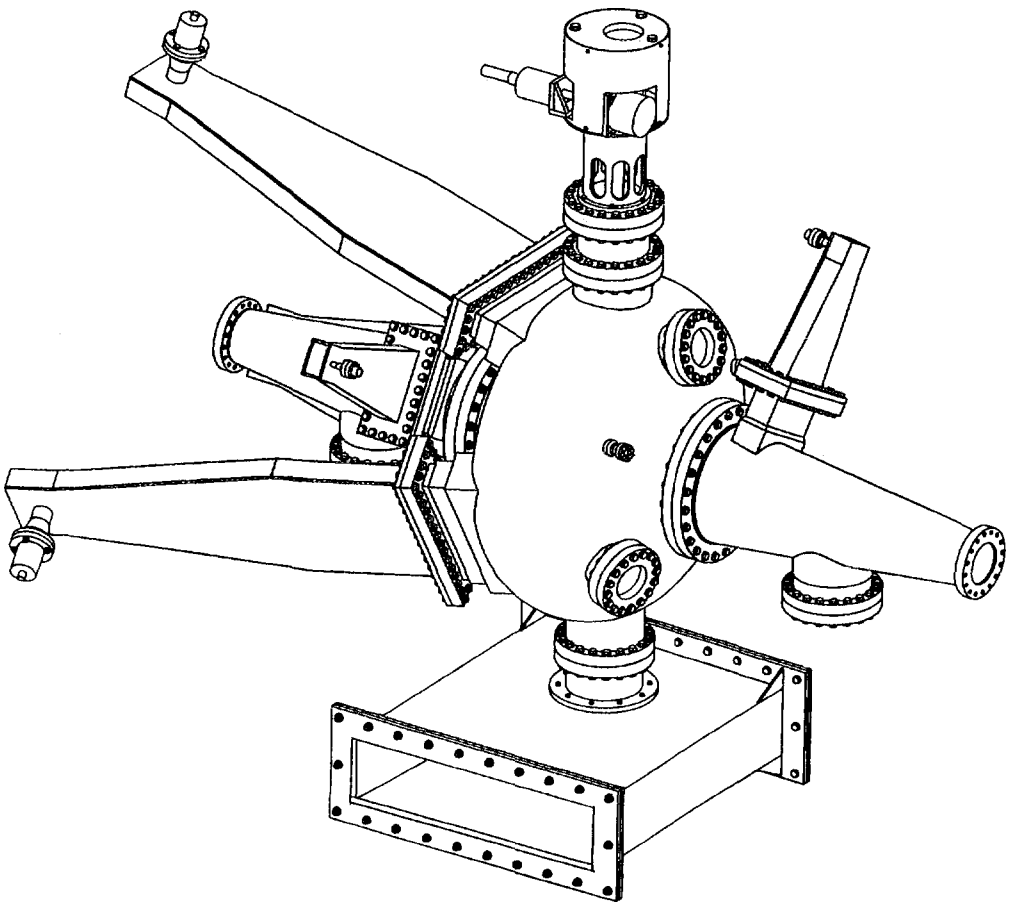

Fig. 5 - Sketch of DAΦNE resonator equipped with HOM waveguides, tuning system and main RF coupler.

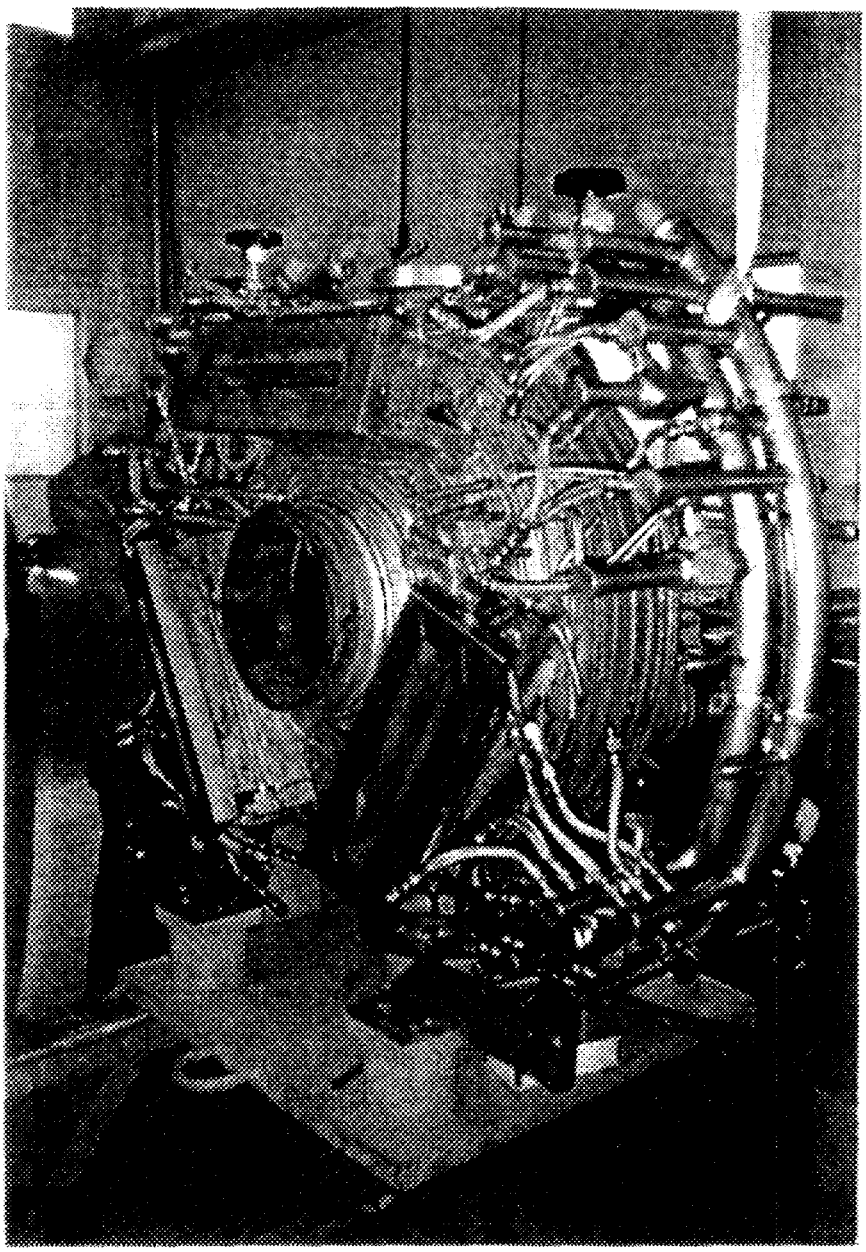

Fig. 6 - DAΦNE cavity under construction at Zanon.

2.2. Longitudinal feedback kicker

Even though the HOMs in the accelerating cavity are heavily damped, the probability for a damped HOM to cross a coupled bunch mode frequency is high and, due to the large total current, the growth rate of unstable modes can be substantially stronger than the natural damping rate (compare the data of Table 3 with radiation damping times given in Table 1).

The required additional damping is provided via a time domain, bunch by bunch feedback system [16] based on digital signal processors (DSPs). The digital section is under construction at SLAC in the framework of a collaboration with the SLAC-LBL PEP-II group on feedback systems for the next generation of factories with intense beams and a large number of bunches. In fact, the design specifications are set to meet the ultimate performance specifications of ALS, PEP-II and DAΦNE. A prototype system with a single board digital section is running at ALS [17].

The maximum power at the kicker is determined by the voltage gain needed to achieve the required damping rate and the maximum synchrotron phase error allowed during injection.

We have some new development with the longitudinal kicker. We have built a prototype with two full coverage striplines broadly resonant at ~ 1.2 GHz, i.e.: 3.25 times the RF frequency, series connected with a $\lambda/2$ line. We have experimented with little surprise how awkward can be proper tuning of this device. Furthermore, according to simulations, the stripline kicker is very rich in HOM content, requiring a careful laboratory characterization.

Therefore, we have explored the possibility to use an RF cavity kicker whose fundamental mode resonates at 3.25 times the RF frequency. Figure 7 shows a cut view of the cavity. The 88 mm diameter beam tube opens into a 200 mm diameter, 72 mm long, pill-box cavity. To obtain the very large bandwidth required (≈ 180 MHz at least, for 120 bunches operation), the cavity is loaded by 6 ridged waveguides followed by broadband transition to 7/8" standard coax, very similar to those in the main RF cavity, except that in this case the coupling is extended to the fundamental mode. The 6 waveguides are placed symmetrically on both sides of the pill box 120° apart from each other. Three WGs are used as input ports and the other three for termination loads. In this way, thanks to the symmetry and since the power dissipated in the external load is much greater than the power dissipated in the cavity walls, the system is perfectly matched.

The kicker cavity does not need to be tuned in operation, being broadband, nor cooled, since almost all the power is dissipated in the external loads. Moreover, the damping waveguides couple out the HOM's as well. The behavior of the device has been completely characterized making use of the HFSS as the fundamental design tool. A cavity kicker prototype has been recently built and measured at LNF. Figure 8 shows the theoretical and experimental transmission frequency response for the fundamental mode and HOMs up to beam pipe cutoff.

A 750 Ω peak shunt impedance, to be compared to the theoretical 400 Ω (measured in a prototype: ≈ 300 Ω) in the stripline, together with a bandwidth larger than 220 MHz have been calculated and measured. The results are shown in Fig. 9.

The mechanical design is now complete and we intend to place an order to industry for two pieces (one per ring) for the initial operation at a reduced number of bunches. According to simulations with realistic values of the HOM impedances, a large bandwidth power amplifier of ~ 200 Watt is enough to damp an initial offset of 100 ps of the injected bunch with the other 29 bunches at the full design current.

Two cavities per ring will eventually be installed for operation at the full nominal current with 3x200 Watt power amplifiers per cavity, each feeding separately a waveguide coupler.

The stripline kicker is a directional device operating in travelling wave mode, and therefore its input downstream ports are almost uncoupled to the beam. On the contrary the cavity kicker is a totally symmetric standing wave structure so that the power released by the beam reaches indifferently all ports. Ferrite circulators are therefore necessary in this case to isolate the output section of the power amplifier feeding the cavity.

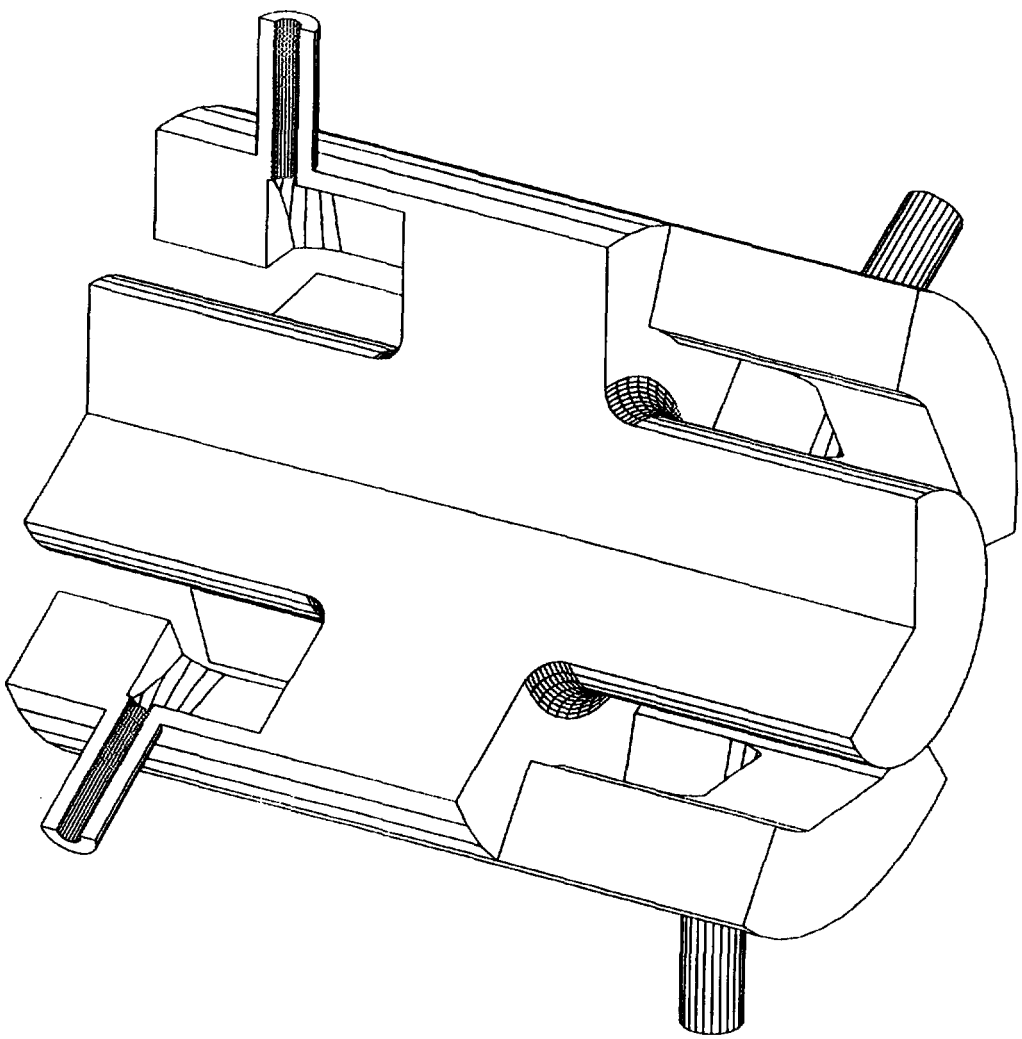

Fig. 7 - Cut view of longitudinal feedback kicker cavity.

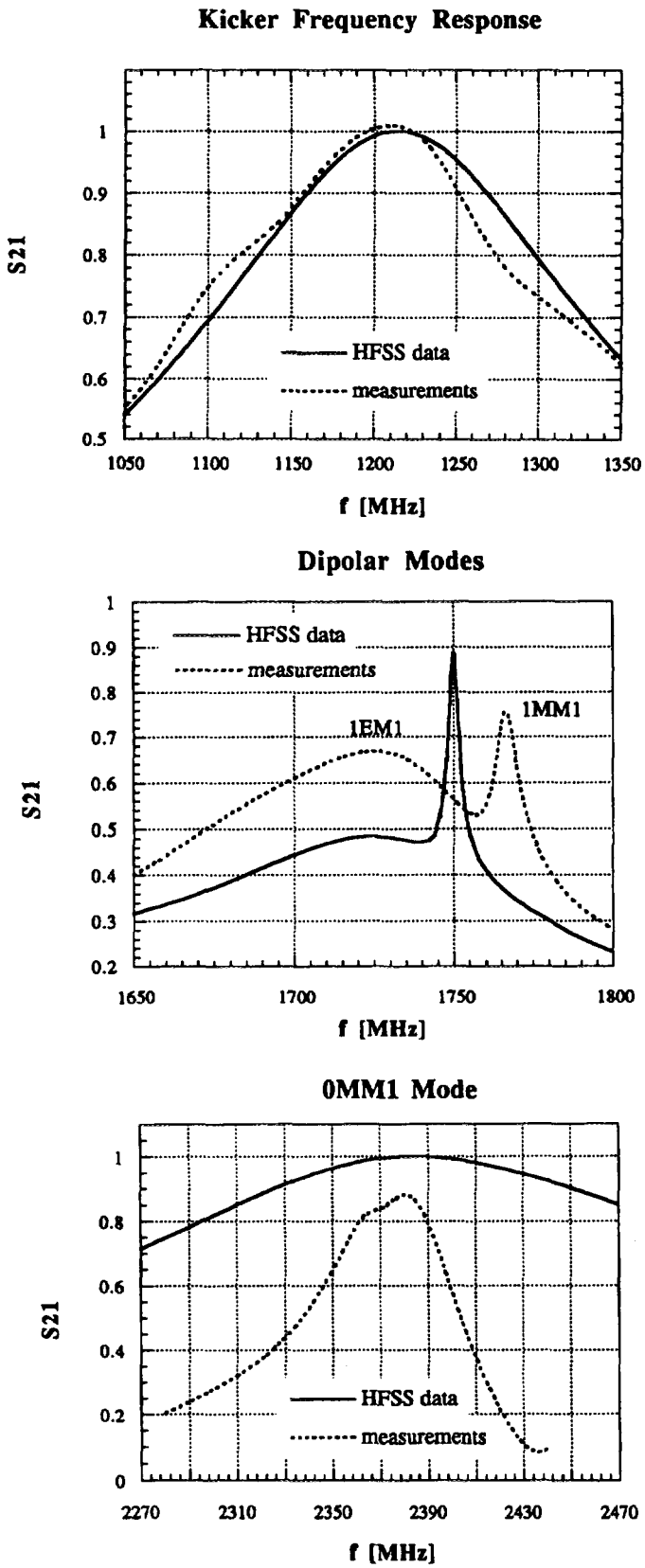

Fig. 8 - Theoretical and experimental WG to WG transmission frequency response of longitudinal feedback kicker cavity.

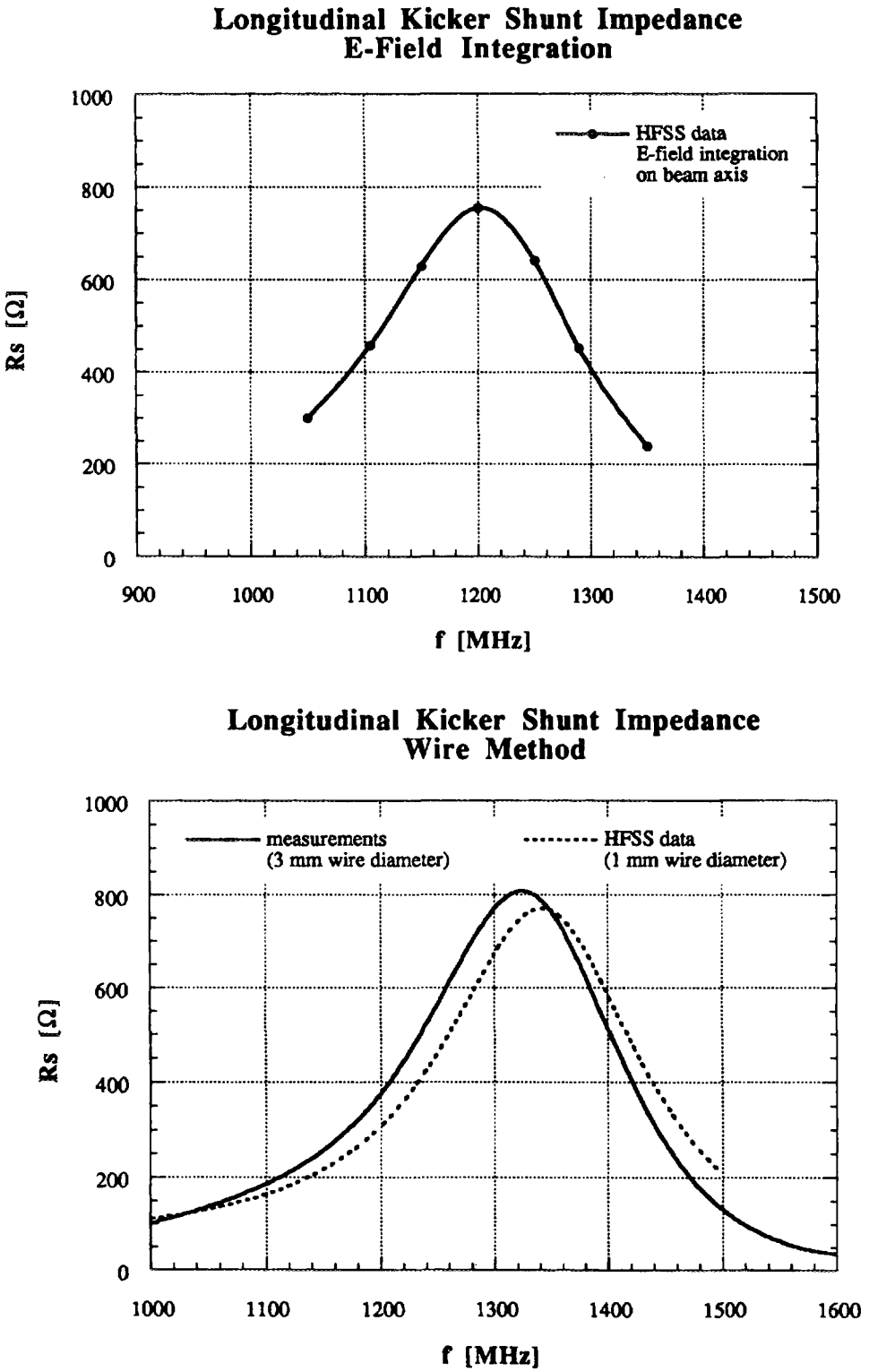

Fig. 9 - Shunt impedance of longitudinal feedback cavity kicker.

2.3. Resistive wall

The resistive wall impedance per unit length is given by [18]:

$$\frac{Z_L}{L} = \frac{\omega}{c}\frac{(1+j)Z_0\delta}{4\pi b}F_0\left(\frac{b}{a}\right)$$

$$\frac{Z_{Tx}}{L} = \frac{(1+j)Z_0\delta}{2\pi b^3}F_{1x}\left(\frac{b}{a}\right) \qquad (5)$$

$$\frac{Z_{Ty}}{L} = \frac{(1+j)Z_0\delta}{2\pi b^3}F_{1y}\left(\frac{b}{a}\right)$$

where

$$\delta = \sqrt{\frac{2c\rho}{\omega Z_0}} \qquad (6)$$

is the skin depth; ρ the material resistivity; Z_0 the free space impedance ($120\pi\ \Omega$). F_0, F_{1x}, F_{1y} are the form factors depending on the geometrical shape of a vacuum chamber cross section, b stands for half the vertical chamber size and a is half the horizontal one.

Almost all the DAΦNE vacuum chamber is made of aluminum, except for a 60 cm long beryllium vacuum pipe in the vicinity of the interaction point and relatively short pieces of stainless steel pipe coated with 40-50 μm copper. The vacuum chamber in the bending magnets is of rectangular shape with cut corners which can be approximated by an ellipse with axes 53×100 mm and $F_0 = 0.95,\ F_{1x} = 0.47, F_{1y} = 0.845$. The beam pipe in the straight sections has a circular cross section with radius b = 44 mm for which $F_0 = F_{1x} = F_{1y} = 1$. The very flat rectangular vacuum chamber inside the wiggler magnets (20×130mm) can be represented in calculations by two infinite parallel plates with $F_0 = 1, F_{1x} = \frac{\pi^2}{24}, F_{1y} = \frac{\pi^2}{12}$.

By summing up the three contributions, the total longitudinal and transverse resistive wall impedances are:

$$Z_L = 0.3(1+j)\sqrt{n}\ \ \Omega\ ,\quad Z_{Tx} = 15.34(1+j)/\sqrt{n}\ \ \frac{k\Omega}{m}\ ,\quad Z_{Ty} = 28.27(1+j)/\sqrt{n}\ \ \frac{k\Omega}{m}$$

Here n is the harmonic number f/f_0.

For a thick wall and not very short bunches the loss factor and the dissipated power per unit length due to the resistive wall impedance are given by:

$$\frac{dk_l}{dz} = \frac{c}{4\pi^2 b \sigma_z^{3/2}} \sqrt{\frac{Z_0 \rho}{2}} \Gamma\left(\frac{3}{4}\right) F_0; \quad \frac{dP}{dz} = \frac{(eN)^2 n_b c}{2\pi R} \frac{dk_l}{dz} \tag{7}$$

where N is the number of particles per bunch and n_b is the number of bunches in the beam.

Then, in the case of 120 bunches, the power deposited in the straight sections is 6.9 W/m, in the bending magnet vacuum chamber 10.9 W/m and in the wiggler vacuum chamber 30.4 W/m. The longitudinal impedance estimated at the bunch spectrum roll-off n = 520 is a rather small value

$$\frac{Z_L}{n} = 0.013(1 + j)\Omega$$

and is not considered to be harmful for the longitudinal single and multibunch beam dynamics while the transverse impedance is dominant at low frequencies and can excite the transverse multibunch instability.

We have evaluated the transverse instability rise time [19] using the well-known expression for the coherent frequency shift [20, 21]. Figure 10 shows the rise time for the first three transverse coherent modes as a function of the machine chromaticity ξ for 30 bunches in the beam.

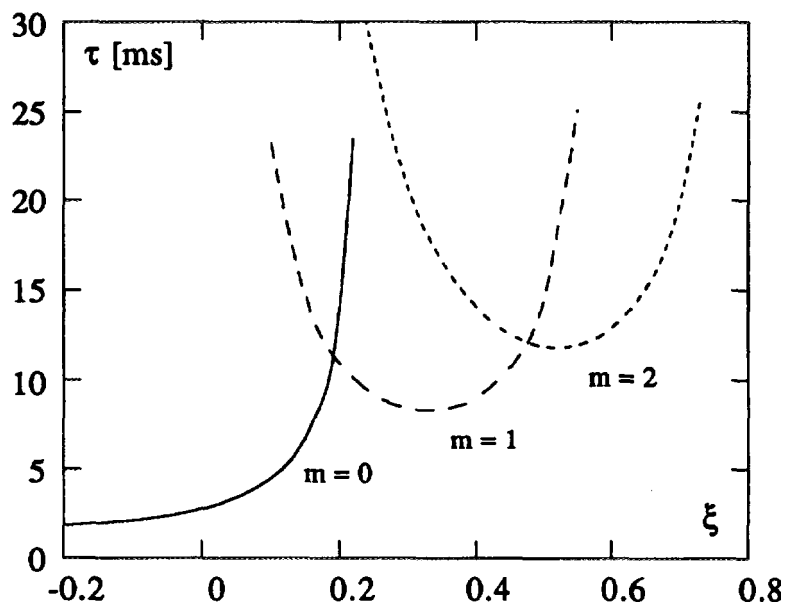

Fig. 10 - Rise times of transverse resistive wall instability for monopole (m = 0), dipole (m = 1) and sextupole (m = 2) modes.

As we can see, the rise time of the monopolar mode (m = 0) for a slightly positive chromaticity is about one order of magnitude faster than the DAΦNE transverse damping time. A transverse feedback system is necessary to damp this instability.

2.4. Transverse feedback kicker

A transverse feedback system is foreseen in order to damp the resistive wall instability and control a large number of transverse coupled bunch modes. The system utilizes two button beam position monitors in order to detect both the horizontal and vertical beam momenta; summing the pick-up signals in proper proportion, the correction signal (in quadrature) at the kicker is produced.

Two transverse kickers will be installed in each ring; these kickers are of stripline pair design (see Fig. 11), with one device per transverse plane. In order to use the stripline as transverse kicker, two voltages of opposite polarity are applied downstream the beam direction at facing ports. The combined magnetic and electric fields give a deflecting Lorentz force in the transverse plane.

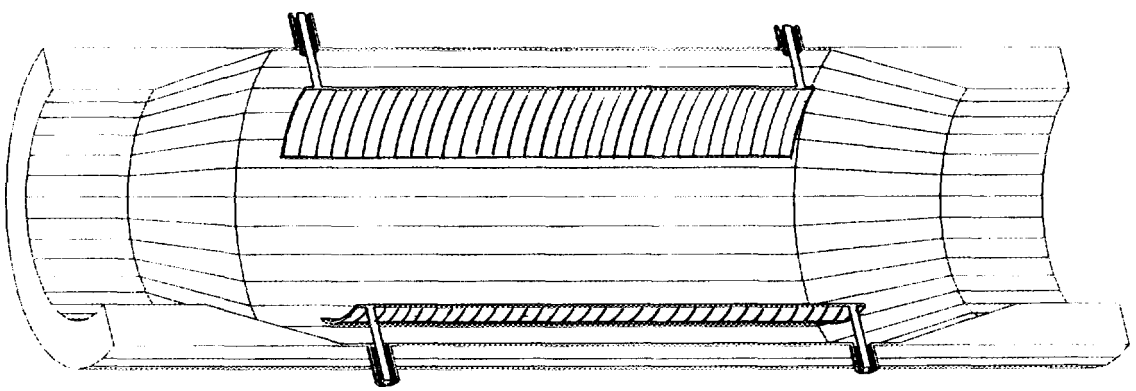

Fig. 11 - Sketch of transverse feedback kicker.

The striplines are chosen to be 20 cm long; the stay clear aperture of the devices is 88 mm (the beam pipe diameter) and the vacuum chamber diameter in this section is 120 mm.

The available space in the machine limits the maximum length of each kicker. Two 50 mm long tapers join the kicker vacuum chamber to the rest of the beam pipe in order to minimize the losses.

The electromagnetic project has been realized with the HFSS computer code optimizing the feedthrough positions, in order to minimize the reflection to the amplifier. The calculated fraction of the input power reflected to the amplifier is less than 2%.

The transverse shunt impedance versus frequency on axis is shown in Fig. 12.

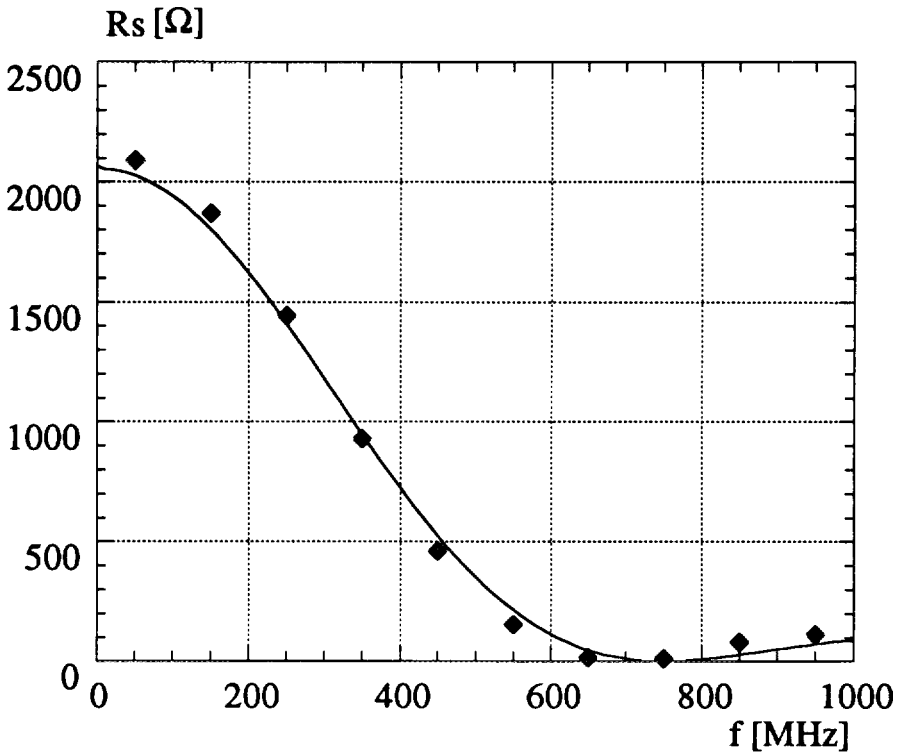

Fig. 12 - Transverse shunt impedance of transverse feedback kicker
(solid line - analytical result; points - HFSS numerical simulation result).

The coupling impedance of the kicker at low frequencies can be evaluated as the impedance of a pair of striplines [22]:

$$Z_L(\omega) = 2Z_s\left(\frac{\phi_0}{2\pi}\right)^2\left(\sin^2\frac{\omega l}{c} + j\sin\frac{\omega l}{c}\cos\frac{\omega l}{c}\right)$$

$$Z_T^{\perp}(\omega) = \frac{c}{b^2}\left(\frac{4}{\phi_0}\right)^2\left(\sin^2\frac{\phi_0}{2}\right)\left[\frac{Z_L}{\omega}\right] \qquad (8)$$

where Z_s is the characteristic impedance of the transmission line formed by a strip and the vacuum chamber wall; l is the stripline length; ϕ_0 the stripline coverage angle; $Z_T^{\perp}$ is the transverse impedance in the direction perpendicular to the striplines.

At frequencies $\omega / 2\pi << c / 4l = 375MHz$ eq. (8) gives for such a kicker:

$$\frac{Z_L}{n} \approx j2Z_s\left(\frac{\phi_0}{2\pi}\right)^2 \frac{l}{R} = j0.064\Omega$$

$$Z_T^{\perp} \approx j\frac{8Z_s l}{\pi^2 b^2}\sin^2\left(\frac{\phi_o}{2}\right) = j1.73\frac{k\Omega}{m} \tag{9}$$

Due to the periodic behavior of (8) these values have to be considered as an upper limit in the low frequency range. The maximum value of the real part of the impedance $\mathrm{Re}\, Z_L / n$ within the low frequency range is 0.04Ω at f = 375 MHz.

Analysis of high frequency kicker behavior with MAFIA and HFSS have shown that some HOMs do not couple to the feedthroughs and remain trapped in the kicker structure. The strongest is the mode at f = 2.303 GHz with Rs = 2.67 kΩ and Q = 1971. The longitudinal coupled bunch instability rise time is about 1 ms at full coupling. If this happens the instability can be damped, in principle, by the longitudinal feedback system. But the power loss due to the mode can be high. Although the mode is at the tail of the bunch spectrum (for 3 cm bunch length), it is close to the spectrum line $25 \cdot (30 f_0)$ = 2.302 GHz in the 30 bunches operation. There is a high probability of full mode coupling with the spectrum line. This would give 1 kW power loss. In order to extract this mode we plan to install an antenna on the kicker taper.

2.5. Interaction region

The interaction region (IR) for the KLOE experiment [23] is 10 m long and is shown in Fig. 13. The low-β permanent quadrupole triplets are 46 cm away from the interaction point (IP) and are confined in a cone of 9° half aperture, leaving a material free solid angle for the apparatus of ~ 99%. It is a requirement of the experiment to have a large (radius 10 cm) aperture vacuum chamber at the IP as transparent as possible to the produced particles.

The outer parts of the IR vacuum chamber are made of stainless steel with a copper coating inside to reduce the ohmic losses. The inner section, bulb-shaped at the IP, is made of 0.5 mm thick pure beryllium, directly brazed onto the stainless steel pipe.

The beryllium bulb-shaped cavity (see Fig. 14 for details) is harmful to the beam dynamics. It traps both monopolar and dipolar HOMs which can result in longitudinal and transverse multibunch instabilities and excess RF power loss [24]. Table 4 shows the parameters of three dangerous monopole modes while Table 5 gives estimated rise times for the dipole mode and quadrupole mode instabilities, τ_1 and τ_2, respectively.

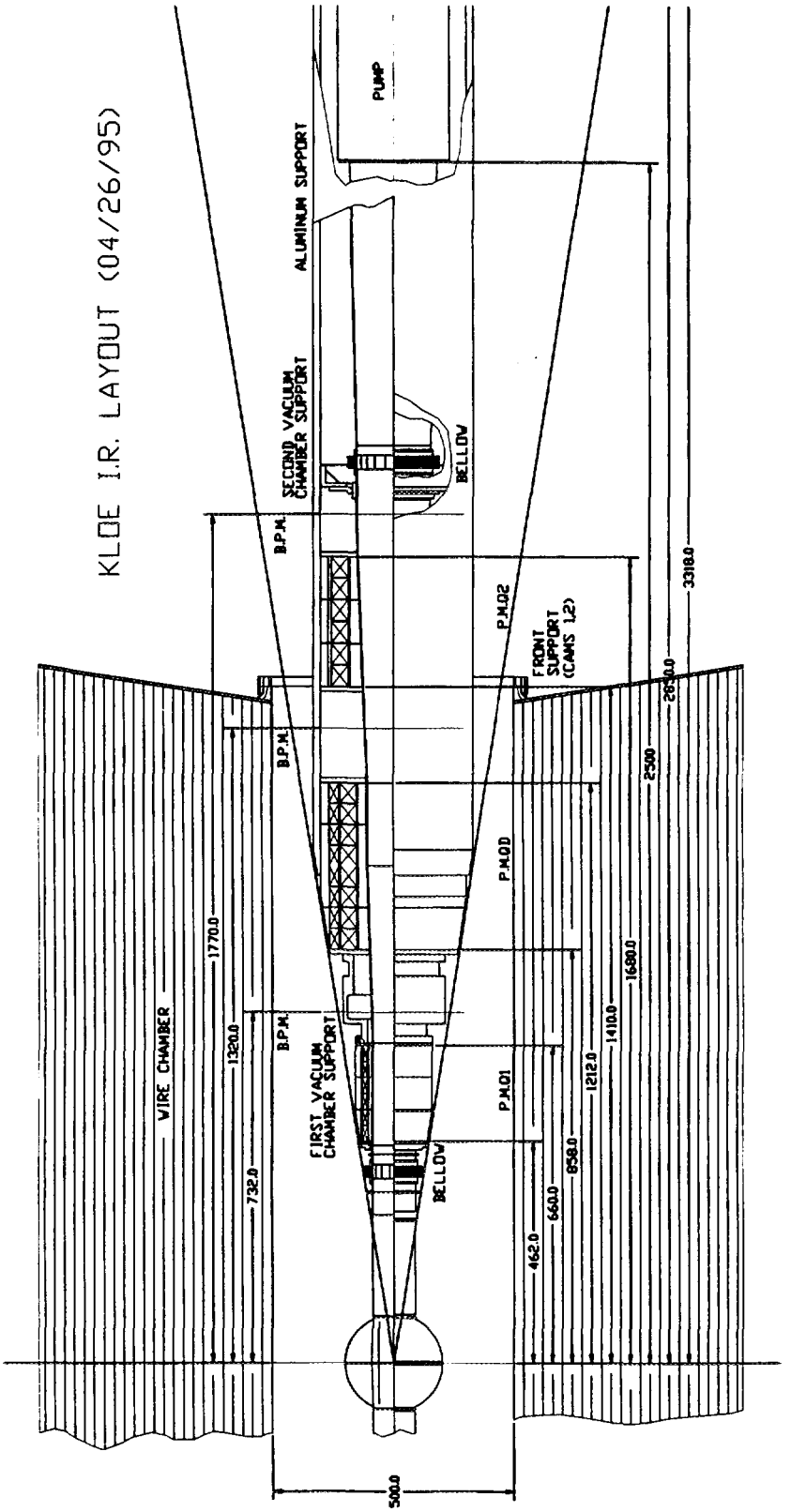

Fig. 13 - KLOE interaction region layout.

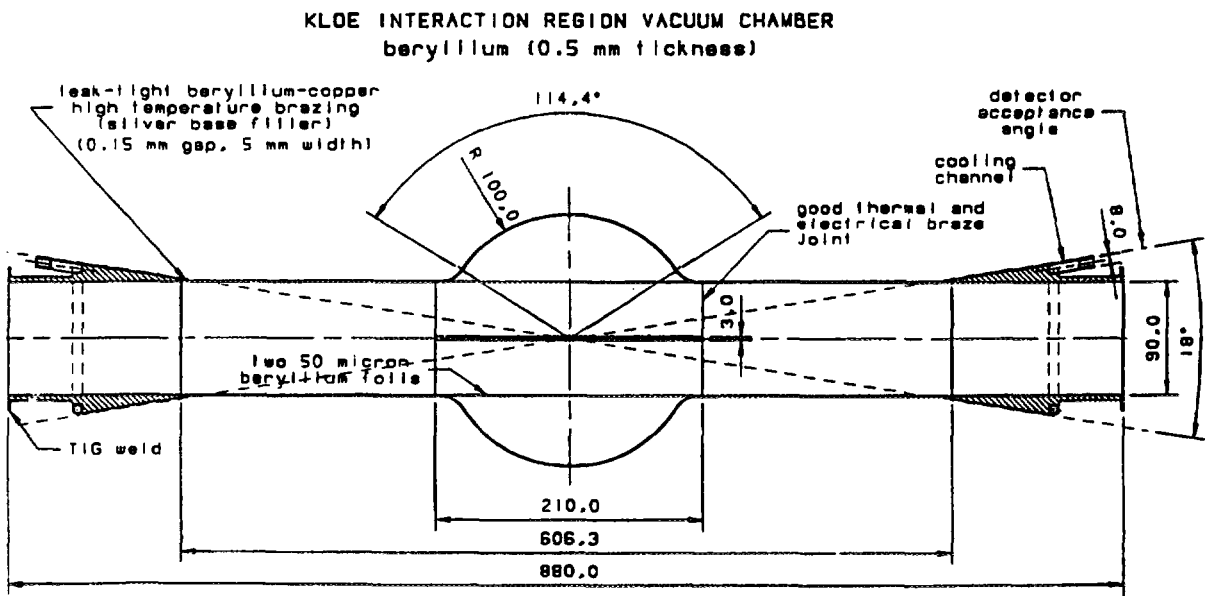

Fig. 14 - Central part of interaction region vacuum chamber.

Table 4. Modes trapped in the spherical part of IR

f [MHz]	R/Q [Ω]	Q
1324.2	15.2	34500
1877.1	14.0	36100
2353.8	7.45	37100

Table 5. Power losses and instability rise times

f [MHz]	τ_1 [ms]	τ_2 [ms]	P_1 [W]
1324.2	0.006	0.012	1109.4
1877.1	0.006	0.008	531.2
2353.8	0.011	0.011	131.1

Note that the dissipated power may be enormous even for a single bunch rotating in the machine when full coupling of the HOM with the closest bunch spectrum line occurs (P_1 in Table 5). This situation has a rather high probability since the spectrum lines are situated at each harmonic of the revolution frequency and due to the temperature drift the HOM can be moved on a spectrum line.

The possibility of using long tapers from the IP to the first quadrupole magnet instead of the beryllium cavity also has been investigated. It was shown that this would not remove the problem of trapped modes completely and, what is even more important, such a thin beryllium structure could collapse under the 1-2 atm. pressure [25].

In order to avoid RF radiation a solution with a thin Be screen of 50-60 μm thickness has been proposed. Its radius is equal to that of the beam pipe and the length ≈20 cm, shielding the bulb-shaped part of the vacuum chamber. This thickness is enough to screen frequencies starting from the first harmonic of the revolution frequency and, on the other hand, transparent for the experiment. The total estimated resistive wall loss in the screen is about 4 W in case of 120 bunches in both electron and positron beams. The synchrotron radiation produces only a small additional heating of the beam pipe (1-2 W) near the IP [26]. The first Be sample prototype has been delivered from K-TEK and is under test at the Frascati Laboratory.

The tapers in the IR are very smooth and give mainly an inductive contribution to the impedance (see below).

The IR for the FINUDA experiment [27] is simpler because the vacuum chamber near the IP is just a cylindrical Be pipe.

2.6. Vacuum port screen

Lumped vacuum ports in the straight sections are screened by a mesh of rounded end 22 mm long and 8 mm wide longitudinal slots. The longitudinal distance between slots is varied randomly within ±10% in order to break the periodicity and destroy possible coherent buildup of the wave radiated by the slots [28].

The low frequency longitudinal and transverse impedance of a slot in a circular vacuum chamber of radius b is calculated analytically [29]:

$$Z_L(\omega) = jZ_o \frac{\omega}{c} \frac{(\alpha_m + \alpha_e)}{4\pi^2 b^2}$$

$$Z_T(\omega) = jZ_o \frac{(\alpha_m + \alpha_e)}{\pi^2 b^4} \vec{a}_s \cos(\varphi_s - \varphi_b) \qquad (10)$$

where α_e and α_m are the electric and magnetic polarizabilities; $\vec{a}_s$ is the unit vector directed onto the slot ; φ_s and φ_b are azimuthal angles of the slot and beam in the vacuum chamber cross section containing the slot.

For slots with rounded ends and $0.1 \le w / l \le 1$, where w is the slot width and l the slot length, α_e and α_m can be found with an accuracy better than 1% by applying the following approximations [30]:

$$\alpha_e \cong -\frac{\pi}{16} w^2 l \left\{ 1 - 0.765 \frac{w}{l} + 0.1894 \left(\frac{w}{l} \right)^2 \right\}$$
$$\alpha_m \cong \frac{\pi}{16} w^2 l \left\{ 1 - 0.0857 \frac{w}{l} - 0.0.0654 \left(\frac{w}{l} \right)^2 \right\} \qquad (11)$$

For a single pump screen containing 90 slots eq. (10)-(11) give:

$$\frac{Z_L}{n} = j1.68 \cdot 10^{-3} \Omega \quad and \quad Z_T = j27.0 \frac{\Omega}{m}$$

In the case of DAΦNE the bunch is longer than the slot sizes and the low frequency formulae (10)-(11) are valid almost for all the bunch spectrum. The real part of a slot impedance is much smaller than the imaginary one and has been calculated in [31]:

$$\mathrm{Re}\, Z_L(\omega) = Z_0 \frac{\left(\alpha_e^2 + \alpha_m^2\right)}{6\pi^3 b^2 c^4} \omega^4 \qquad (12)$$

The corresponding loss factor is :

$$k_l = Z_o \frac{\left(\alpha_e^2 + \alpha_m^2\right) c}{16 \pi^{7/2} \sigma_z^5 b^2} \qquad (13)$$

An estimate for the DAΦNE pump screen gives the negligible value $k_l = 2.8 \cdot 10^{-5} V / pC$.

We should mention that the expressions (12), (13) were obtained for infinitely thin vacuum pipe walls. Due to the finite thickness of the beam screen, which is comparable to the slot width in the DAΦNE case, some additional reduction of the impedances (~ 60%) is expected.

2.7. Antechamber slots

Four 10 m long vessels constitute the vacuum chamber of the bending and wiggler sections of each ring. A continuous 10 m long slot separates the beam channel from an antechamber where the synchrotron radiation absorbers and the pumping stations are situated. The width of the slot very smoothly changes between 20 mm at the absorber location and 10 mm in the wiggler vacuum chamber. Different cross sections along the bending section are shown in Fig. 15. The depth of the slot is always longer than its width. This attenuates beam coupling to the antechamber.

In order to estimate the beam impedance, calculations were carried out with MAFIA (see Fig. 16). Due to the known fact that the dependence of the impedance on the slot length saturates for long slots we assumed for the simulation a 50 cm long slot which, being much longer that the bunch, is adequate to describe the slot impedance. The slot width was taken to be 2 cm and the depth 2.5 cm. The coupling impedance was found by performing the Fourier transform of the long range wake field given by MAFIA.

Figure 17 shows the real and imaginary part of the impedance. As it can be seen, the impedance is small and mainly inductive up to rather high frequencies. The low frequency part of the impedance is less than $Z_L / n = j6.6 \cdot 10^{-5} \Omega$. No dangerous HOM were found in such a structure.

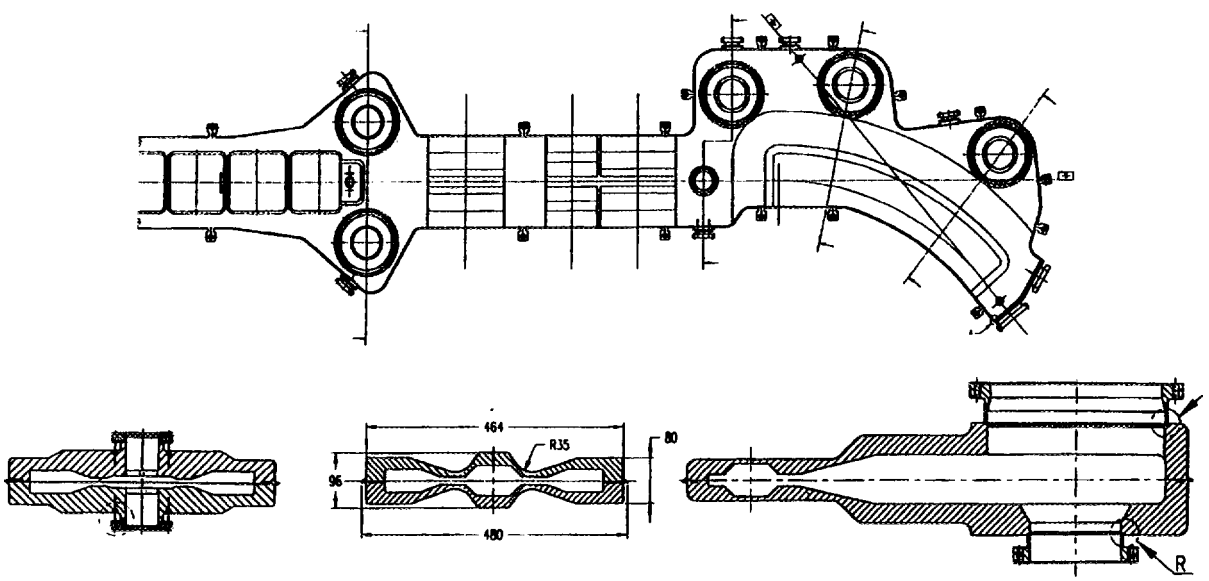

Fig. 15 - Some of arc vacuum chamber cross sections (only half of the arc is shown).

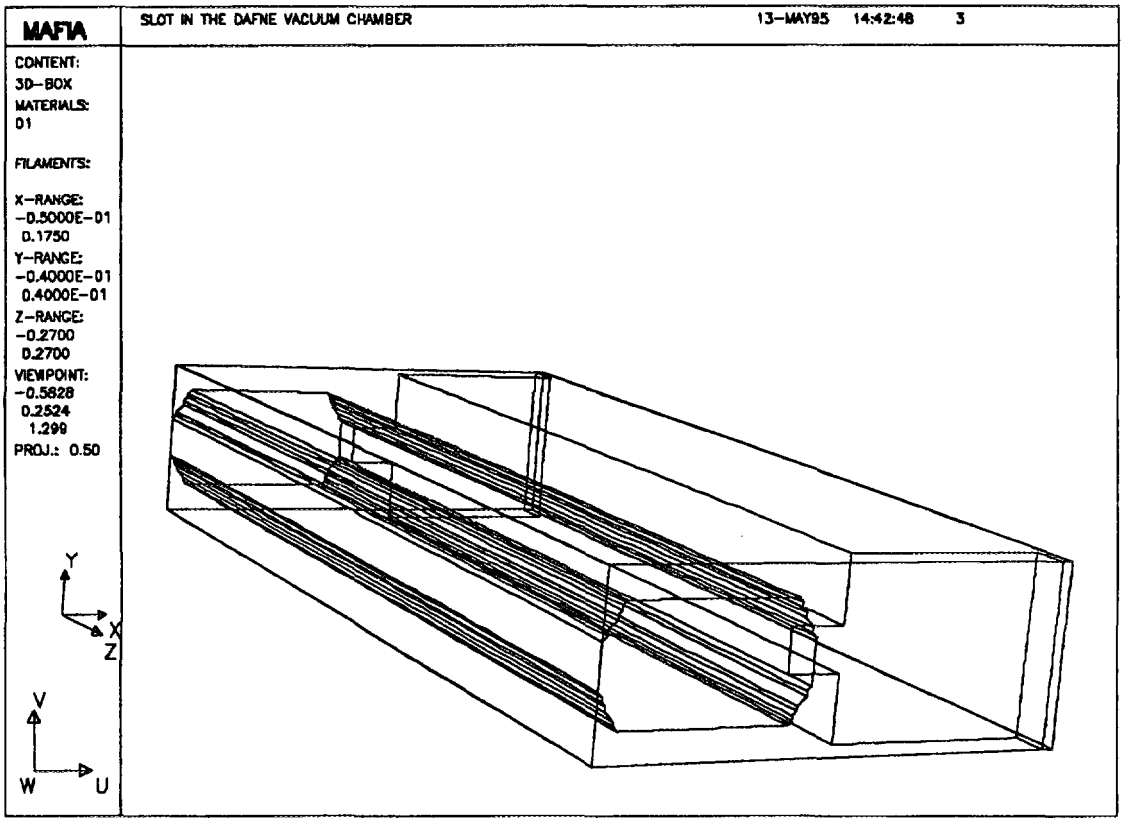

Fig. 16 - MAFIA input for antechamber slot impedance calculations.

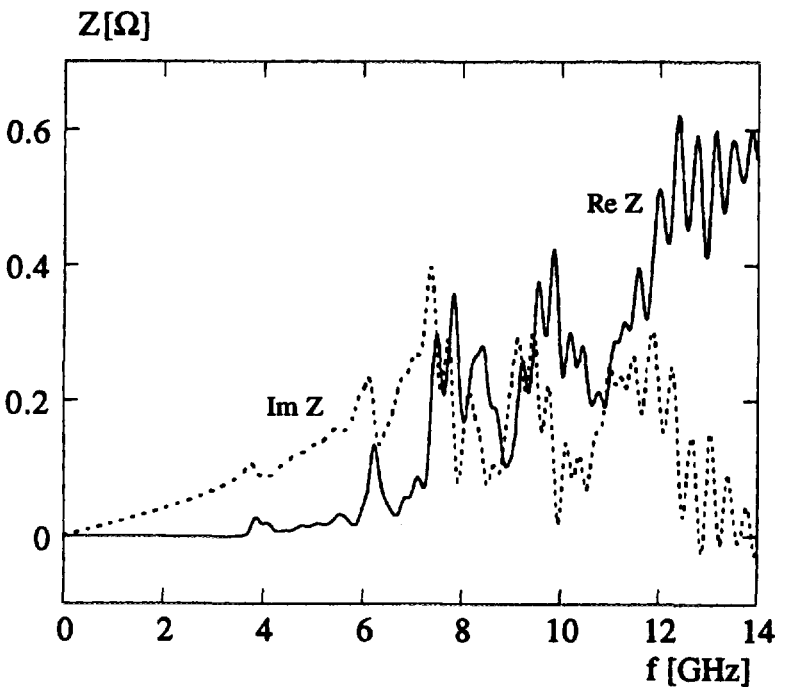

Fig. 17 - Real and imaginary part of the antechamber impedance.

2.8. Beam position monitor (BPM)

The beam position monitor (BPM) system is the primary diagnostic system. We have 41 BPMs in each ring and 12 in the common part of the interaction regions. They consist of four "button" electrodes mounted flush with the vacuum pipe. The design helps maintaining coupling impedance and parasitic losses within acceptably low values in spite of the large number of units.

Since the vacuum chamber cross-section is largely variable along the ring circumference, we have developed six different designs, but in all of them the same type of electrode (SMA 50-MB from Ceramex, France) is used (see Fig. 18).

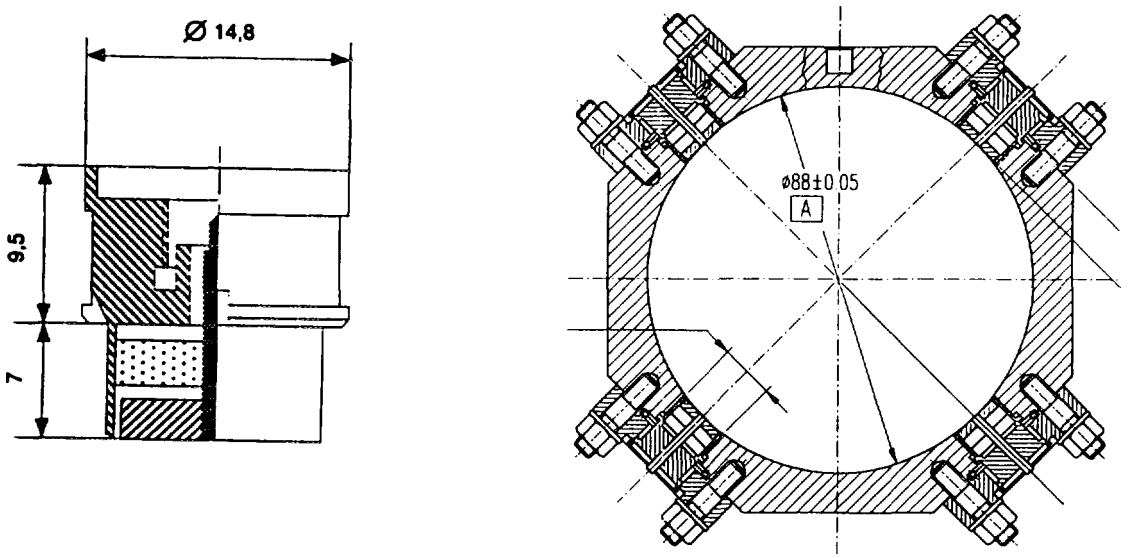

Fig. 18 - Button electrode for DAΦNE BPMs.

The button electrode is mainly sensitive to the beam electric field. The usual equivalent circuit representation of an electrostatic monitor is a current generator of the same value of the image current intercepted fraction, shunted by the electrode capacitance to ground (~ 5pF in our case).

The button is connected to the detector circuit by means of a short run of coaxial cable having characteristic impedance R_0 = 50 Ohm and terminated into an R_0 resistor.

Taking a circular vacuum chamber of radius b as reference, it is useful to write the signal impedance Z_B for a centered beam as:

$$Z_B = F\varphi R_0 \frac{j\omega / \omega_2}{1 + j\omega / \omega_1} \tag{14}$$

where $\omega_1 = 1/R_0C_B$ and $\omega_2 = c/2r$, with C_B the button capacitance to ground, r the button radius, c speed of light, φ the coverage factor = r/4b and F a form factor depending on the chamber geometry and on the electrode position in the chamber (F = 1 for circular geometry).

In this way the signal impedance is written as a frequency-depending part which is a function of the button characteristics (radius and capacitance to ground, equal for all the BPMs) times a constant factor including geometric factors and the termination resistance. In the various BPM designs the values of F range from ~ 0.7 to 1 and the values of φ from ~ 0.03 to 0.125.

Following the arguments of Ref.[32], the low frequency component of the longitudinal coupling impedance (per button) can be written as

$$Z_L(\omega) = \varphi\left(\frac{\omega_1}{\omega_2}\right) Z_B(\omega) \tag{15}$$

and

$$\frac{Z_L}{n} = F\varphi^2 R_0 \left(\frac{\omega_1}{\omega_2}\right) \frac{j\omega_0 / \omega_2}{1 + j\omega / \omega_1} \tag{16}$$

with ω_0 the angular revolution frequency. Note that for a matched electrode $(\omega_1/\omega_2) = 1$.

Taking into account all the BPMs, this gives a fairly small value ($3.3 \cdot 10^{-3}\ \Omega$) for Z/n, with the imaginary part mainly inductive at low frequency and vanishing at high frequency and a maximum of the real part at a frequency $f = \omega_1/2\pi$.

However, this method of evaluation of the coupling impedance is likely to underestimate the result, since it takes into account only that part of fields contributing to the output signal formation. In fact, some modes which do not dissipate their power in the external terminations, have been found with MAFIA. The first one is the mode of TE_{11} type establishing around the electrodes. Since the electric field is maximum at the button circumference and zero at the center connection, no signal is generated outside. The frequency of the mode (~7 GHz) is beyond the bunch spectrum and does not give any substantial contribution to the power loss. Neither it is dangerous for the multibunch stability.

The same is valid for the other modes of that kind at higher frequencies. However, these modes give some additional inductive contribution to the impedance at low frequency. The low frequency impedance of a BPM can be evaluated as the impedance of an annular narrow slot in the vacuum chamber wall. Since the polarizabilities are not known for the slot we calculated the inductive impedance of a single button with MAFIA and applied eq. (10) as a scaling law for different BPM designs taking into account also the geometry of the vacuum chamber and the button position in it. For all BPMs such an estimate gives $Z_L / n < 0.01 \ \Omega$.

2.9 Tapers

In order to reduce the coupling impedance it is necessary to produce a vacuum chamber as smooth as possible. Long tapers, connecting vacuum chamber components, are used in DAΦNE to avoid sharp discontinuities in the vacuum chamber cross section.

The diameter of the beam pipe in the interaction region increases from 88 mm at the interaction point to 200 mm at the gate valve location at a distance of 3.3 m from the IP by means of a system of very gradual azimuthally symmetric tapers, shown in Fig. 13. After the valve, a 1.1 m long taper with the angle less than 4° is used to connect the 200 mm round beam pipe to the 200×54 mm rectangular pipe in front of the splitting magnet. Simulation of such a structure with ABCI gives a low frequency inductive impedance $Z_L / n = j0.033 \ \Omega$ and a loss factor $k_l = 2.58 \cdot 10^{-3} V / pC$ for 3 cm bunch length.

Smooth transitions connect the circular beam pipe of the straight sections (with a diameter of 88 mm) and the rectangular beam pipes after the splitting magnet (88×54 mm). Figure 19 shows an example of such a connection between the rectangular chamber in the splitting magnet and the straight section. The tapers between the rectangular dipole vacuum chamber and the straight section are essentially the same, but steeper (with the angle of 13.9°) due to the limited space allowed. For the taper impedance estimates, in simulations with ABCI, we use an azimuthally symmetric structure and then multiply the results by the azimuthal filling factor. Summing up the contributions from all the tapers of that kind gives $Z_L / n = j0.063 \ \Omega$.

There are other tapers between the rectangular vacuum chamber in the bending sections and the very flat rectangular chamber inside the wiggler magnets (130×20 mm). These tapers are the closest to the beam and to decrease their influence on the beam dynamic the taper angle has to be as small as possible. In the present design the angle is less than 2.5°. The total contribution of the tapers in 4 wiggler section is $Z_L / n = j0.027 \ \Omega$.

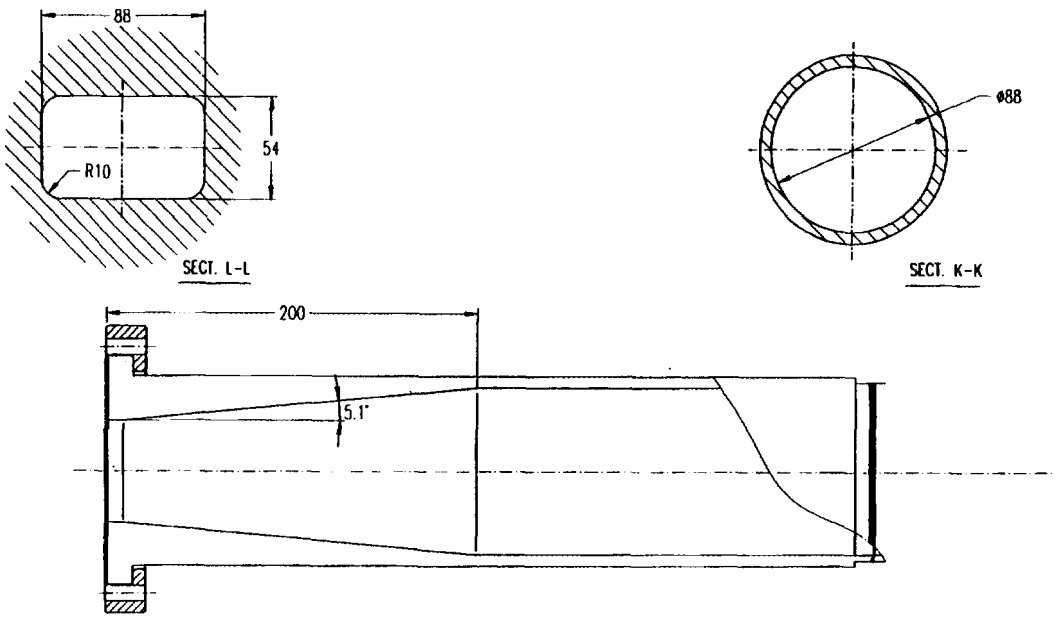

Fig. 19 - Transition between rectangular and round beam pipes.

2.10. Scrapers

A scraper system [33] will be used in DAΦNE to reduce the lost particles background inside the KLOE and FINUDA detectors. It consists of two vertical and two horizontal scrapers in each ring. Fig. 20 shows the horizontal scraper.

The central part of the scraper (target) is made of W and has a thickness of 5 cm to stop almost completely the electromagnetic shower produced by 500 MeV electrons. In order to minimize the contribution of such a discontinuity to the coupling impedance the target joins the neighboring vacuum chamber by means of long tapers in the beam direction which are made of a lighter material.

During machine operation the position of the scraper can be varied to find a compromise between a good life time and an acceptable background in the detectors. At injection the scrapers must be open to exploit the whole available aperture.

The impedance calculations were carried out for the case of maximum target penetration into the vacuum chamber.

Figure 21 shows the real and imaginary part of the impedance calculated as Fourier transform of the wake field given by MAFIA. The impedance remains inductive until ~3 GHz and the low frequency contribution can be estimated as j0.0155 Ω.

The design of the vertical scraper is the same, except that the targets are moved in the vertical direction and the maximum penetration is smaller than the horizontal one.

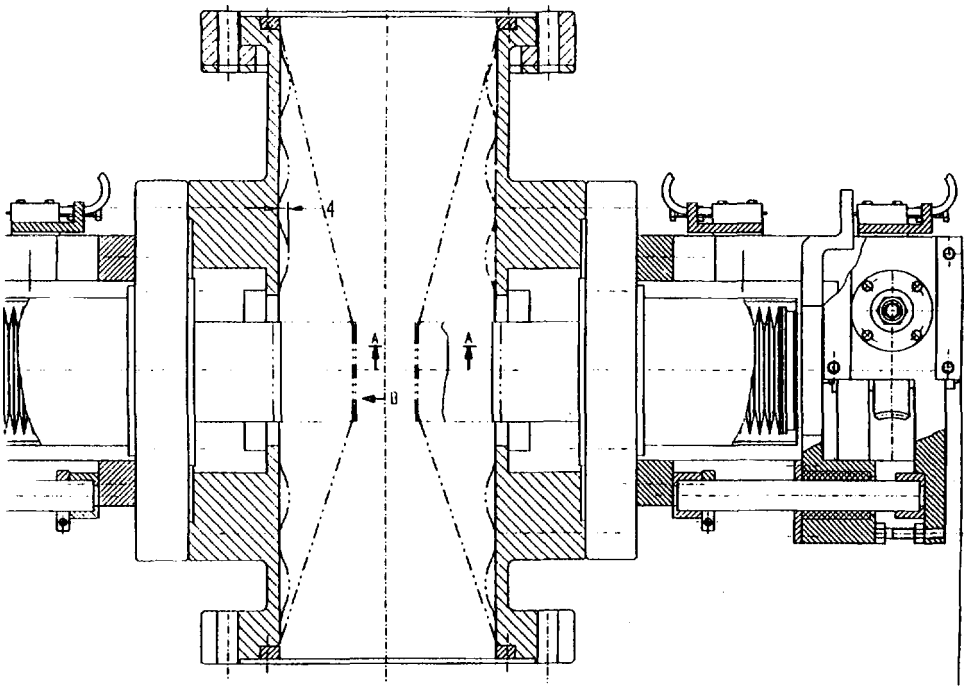

Fig. 20 - Horizontal scraper design.

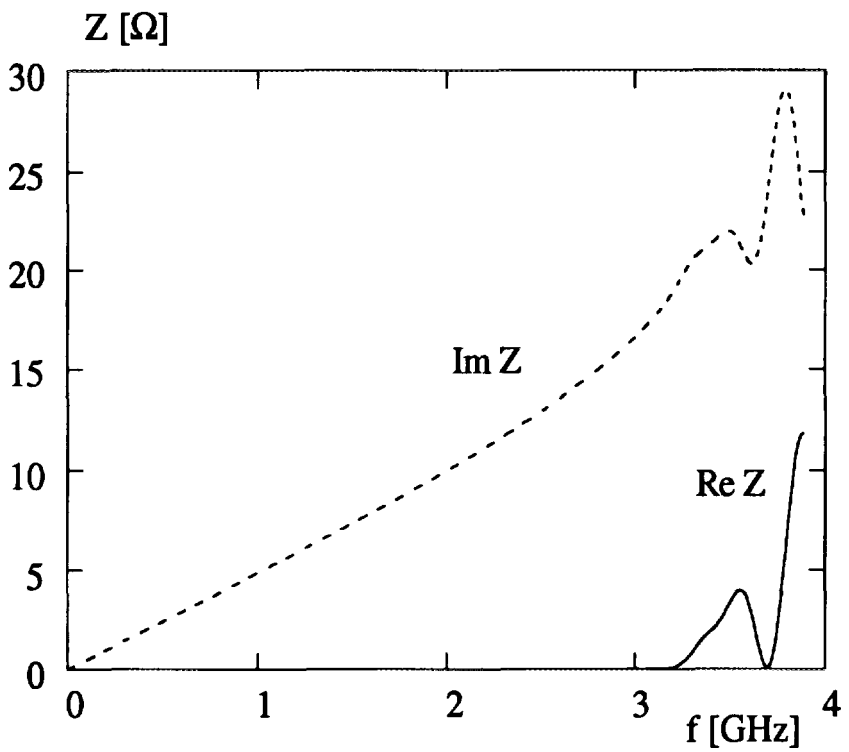

Fig. 21 - Horizontal scraper broad band impedance.

2.11. Bellows

The mainly inductive contribution to the beam impedance is expected from bellows connecting the machine arcs with the straight sections. The bellows have to allow both the longitudinal expansion and the bend in the horizontal plane. It was decided to avoid any sliding contacts in the bellows which can be burned out due to the high current flowing on the bellows screen. Moreover, if, for any reason, there is no contact between the sliding surfaces the capacitance between the sliding contacts can create a resonant circuit with the rest of the bellows. This is a potential danger for the multibunch stability and a source of power losses.

The bellows design proposed for DAΦNE is shown in Fig. 22. The bellows screen is made of thin (0.5 mm) strips oriented in the vertical plane and separated by 4 mm gaps. The width of a strip is 6 mm, i. e. wider than the gap between the strips in order to attenuate radiation outside the screen.

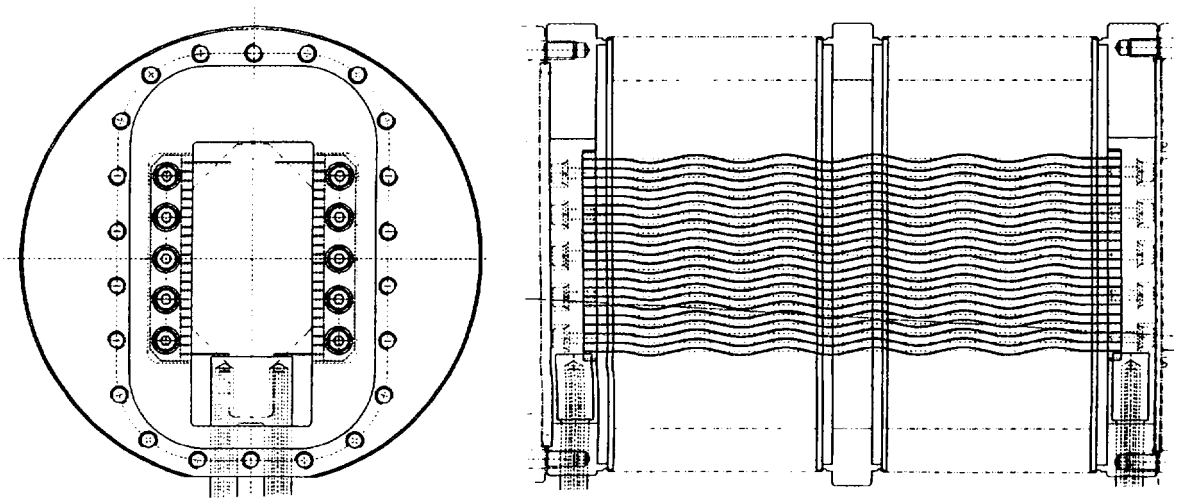

Fig. 22 - Bellows design.

The strips are produced by a hot forming method and have a waved shape. This allows longitudinal expansion. In the working regime the strips are supposed to be almost straight.

Preliminary simulations with MAFIA show that the bellows are inductive at low frequency with a rather small impedance of $Z_L / n = j0.006\Omega$. Simulations in frequency domain indicated a cluster of low shunt impedance low Q HOMs with wave length $\lambda = 2l$, l being the length of the slots between the strips. However, we can not completely rely on the numerical simulation for such a complicated structure which were carried out with a rough mesh due to memory and CPU time limitations. Because of that a bellows prototype was ordered to DOIG SPRING, UK and the coupling impedance will be measured.

2.12. Other inductive elements

There is a large number of small discontinuities in the DAΦNE vacuum chamber, of different kinds, shapes and sizes. These are shallow cavities in flanges and valves, gaps in BPM assembly, slots for the synchrotron radiation monitor etc. Due to the limited space allowed, we do not show the corresponding drawings.

Despite of small sizes, the overall contribution of these elements to the inductive impedance, up to rather high frequencies, can not be neglected. We have used both the analytical expressions of [34] and numerical simulations with ABCI in order to evaluate the contribution. The overall estimated impedance Z_L/n is smaller than j0.1 Ω.

2.13. Space charge impedance, Laslett tune shift

The space charge coupling impedance of a uniform disk beam with transverse size "a" in a smooth round beam pipe of a radius "b" is purely imaginary [35]:

$$\frac{Z_L}{n} = -j\frac{Z_0}{2\gamma^2}\left[1+2\ln\left(\frac{b}{a}\right)\right] \tag{17}$$

$$Z_T = -j\frac{Z_0 R}{\gamma^2}\left(\frac{1}{2a^2}-\frac{1}{b^2}\right) \tag{18}$$

To give an estimate we take $a = <\sigma_y>$, which is the smallest average transverse size and b = 2.65 cm as an average beam pipe radius. This gives:

$$\frac{Z_L}{n} = -j2.1m\Omega \quad and \quad Z_T = -j114.9k\Omega/m$$

The Laslett tune shift [36] for a tri-gaussian bunch can be written in the following form [37]:

$$\Delta\nu_y = -\frac{(N_T/B)\beta_y r_e}{2\pi\beta^2\gamma^3\sigma_y(\sigma_x+\sigma_y)} - \frac{N_T\beta_y r_e}{\pi\gamma}\left\{\frac{1}{\beta^2\gamma^2 B}\frac{\varepsilon_1}{h^2}+\frac{\varepsilon_1}{h^2}+\frac{\varepsilon_2}{g^2}\right\} \tag{19}$$

where N_T is the total number of particles in the ring; $B = \sqrt{2\pi}\sigma_z / s_b$ is the bunching factor with s_b the bunch spacing; h is the half-height of the vacuum chamber; g is the half-height of the magnetic gap. The coefficients ε_1 and ε_2 are the form factors for the vacuum chamber and magnetic gap (can be found, for example, in [38]).

The first term in (19) is a direct space charge term $\Delta\nu_y^{sc}$ and can serve as a measure of the space charge tune spread in a bunch [37]. For DAΦNE it is negligible:

$$\Delta\nu_y^{sc} = -4.4 \cdot 10^{-4} \quad \text{(120 bunches)}$$

i. e. about two orders of magnitude smaller than the beam-beam tune spread.

The second term in (19) is due to induced charges and currents in the vacuum chamber walls and magnet poles. A rough pessimistic estimate gives for DAΦNE:

$$\Delta\nu_y^{ind} = -1.16 \cdot 10^{-2} \quad \text{(120 bunches)}$$

which can be compensated, if necessary, by adjusting the machine linear optics.

Here we have considered only the vertical tune shift because the direct space charge term is much smaller for the horizontal plane due to the larger horizontal beam size and, in turn, the second term gives a slightly smaller value than $\Delta\nu_y^{ind}$ but of the opposite sign.

3. SINGLE BUNCH THRESHOLDS

3.1. Bunch lengthening

In the study of the single bunch dynamics, the wake potential over the bunch length is of main interest. This implies that, in the frequency domain, the bunch does not resolve the details of the actual machine impedance and it rather experiences an average effect. The reduced frequency resolution was the main justification for using different broad-band models, when the machine impedance is substituted by a simple model with a limited number of parameters, extracted from the results of experiments or numerical simulations.

However, when the bunch length changes over a wide range the parameters of the model essentially depend on the bunch length. For example, the wake of an RF cavity can be inductive for long bunches and capacitive for short bunches.

For DAΦNE, where the bunch length changes from a "natural" length of 5-6 mm to the nominal value of 3 cm, it is impossible to characterize the broad-band impedance of a vacuum chamber element by a single value at different bunch lengths. In order to get an idea of the relative contributions of the elements to the total machine impedance, in Table 6 we show the contribution of the main inductive elements (remaining inductive in the foreseen bunch length range), while Table 7 shows the loss factors of the elements contributing to the power loss at the nominal bunch length.

Table 6. Impedance of main inductive elements

Element	Im Z_1/n [Ω]
Tapers	0.156
Transverse feedback kickers (low frequency)	0.128
Scrapers	0.062
Bellows	0.024
Resistive wall (at roll - off frequency)	0.013
BPMs	0.01
Vacuum pump screens	0.02
Injection port	0.0031
Antechamber slots	0.0005
Synchrotron radiation	< 0.015
Space charge	-0.0021
Other inductive elements	0.1
Total	**0.53 Ω**

Table 7. Elements contributing to power losses

Element	$k_l, V / pC$ at σ_z = 3 cm
RF cavity	0.129
Third harmonic cavity	0.157
Longitudinal feedback kicker	0.120
Transverse kickers	0.064
Injection kickers	0.047
IR taper system	0.0026
Scrapers	0.00007
Injection port	0.00004
Total	**0.52**

In order to simulate the bunch lengthening process we undertake a numerical tracking using the wake potential of a short gaussian bunch with σ_z = 2.5 mm (see Fig. 23) as the machine wake function. The computer codes ABCI [39] and MAFIA were used to calculate the wake potential for DAΦNE.

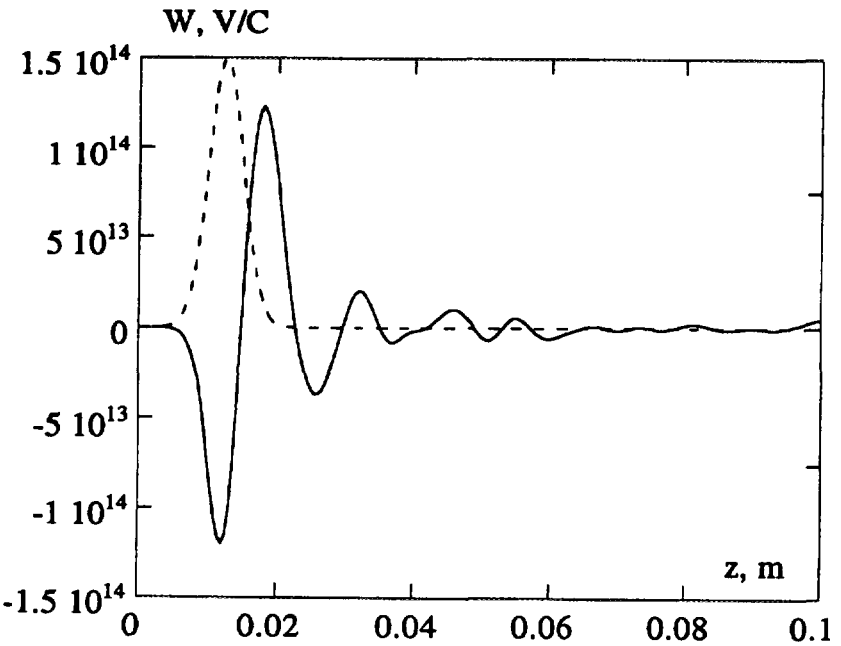

Fig. 23 - Total DAΦNE wake potential for 2.5 mm gaussian bunch.

The tracking method is essentially the same as that successfully used in the bunch lengthening simulations for the SLC damping rings [40, 41], SPEAR [42], PETRA and LEP[43]. The motion of N_s super particles representing the beam is described in the longitudinal phase space by [41]:

$$\varepsilon_i(n) = \varepsilon_i(n-1) - \frac{2T_0}{\tau_\varepsilon}\varepsilon_i(n-1) + 2\sigma_{\varepsilon 0}\sqrt{\frac{T_0}{\tau_\varepsilon}}R_i(n) + V_{rf}' + V_{ind}(z_i)$$

$$z_i(n) = z_i(n-1) + \frac{\alpha c T_0}{E}\varepsilon_i(n) \qquad (20)$$

where $\varepsilon_i(n)$ and $z_i(n)$ are the energy and position coordinates of the i^{th} particle after n revolutions in the storage ring. T_0 is the revolution period; τ_ε the damping time; V_{rf}' the slope of the RF voltage; R_i the random number obtained from a normally distributed set with mean 0 and rms 1.

On each turn all the super particles are distributed in N_{bin} bins and the induced voltage V_{ind} is calculated by [43]:

$$V_{ind}(z_j) = -\frac{Q}{N_s}\sum_{z_i<z_j}^{i=1,N_{bin}} N_b(z_i)w_\delta(z_j - z_i) \qquad (21)$$

Note, that z_j in the expression (21) are the coordinates of the bin centers and the induced voltage at the positions of the super particles is found by a linear interpolation over the $V_{ind}(z_j)$. Here $N_b(z_i)$ is the number of super particles in the bin with the center at z_i and $w_\delta(z)$ is the machine wake function.

For the simulation we have used $V_{rf} = 127\ kV$. This corresponds to the natural bunch length of 6.8 mm. Ns = 200000 particles are tracked over 4 damping times and the average bunch properties, as rms length, rms energy spread, coordinate of the centroid, are calculated by averaging over the last damping time. These bunch characteristics with the bunch distribution are shown in Fig. 24. The bunch distribution gets more bulbous than a gaussian and is tilted forward. Such a distribution corresponds to the inductive - resistive machine broad-band impedance.

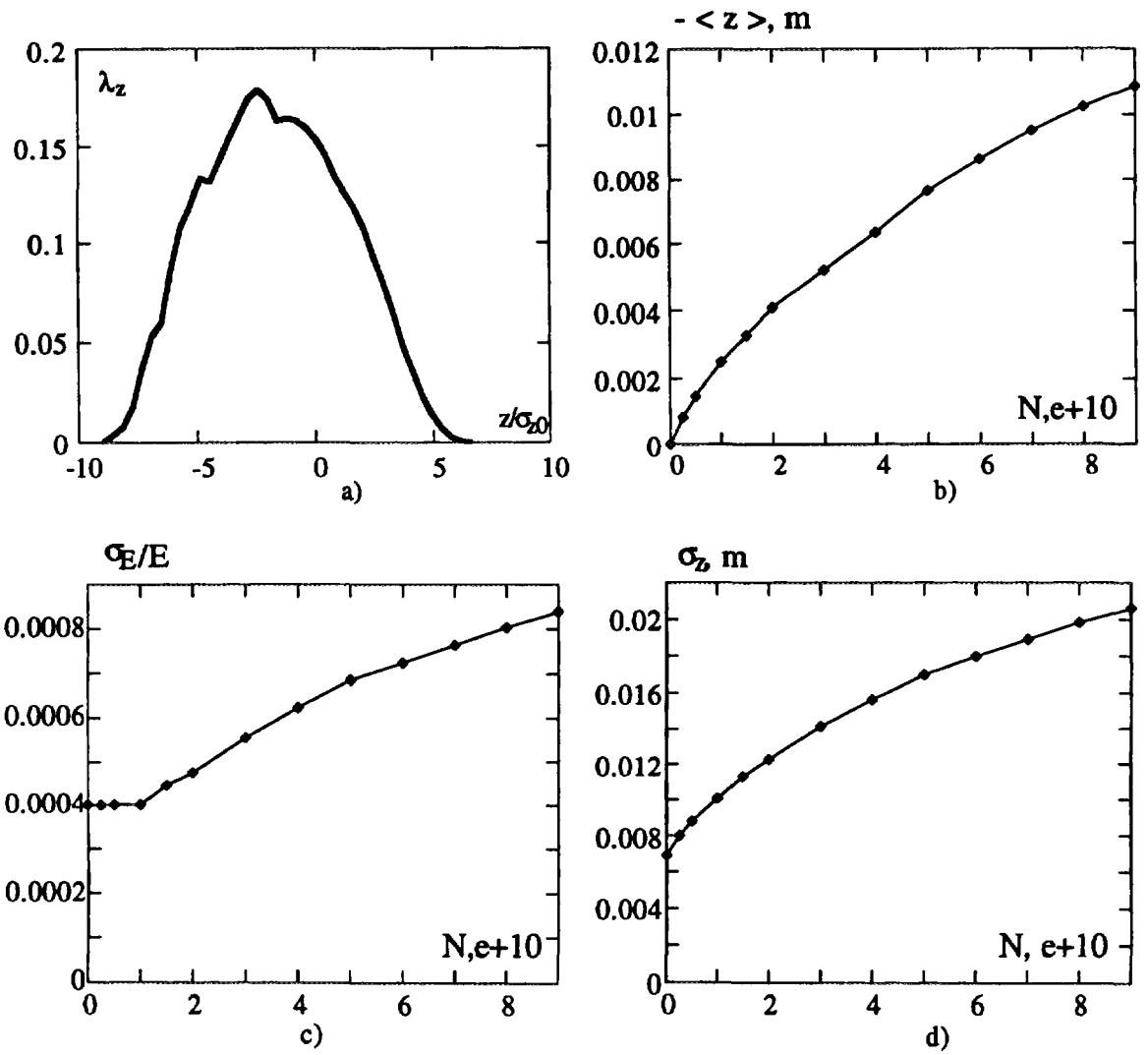

Fig. 24 - Bunch lengthening in DAΦNE at V_{rf} = 127 kV:
a) Bunch shape; b) Bunch centroid coordinate; c) Relative rms energy spread;
d) rms bunch length as intensity function.

As it can be seen in Fig. 24c) the microwave threshold is at $N = 1 \cdot 10^{10}$particles per bunch. Despite such a low threshold the bunch length still does not reach the nominal value of $\sigma_z = 3cm$. We should remark here, that in the simulation we did not included the impedance contribution from the bellows between the machine arcs and straight sections because their final design was not finalized yet. The wake fields due to the bellows give some bunch length increase. Nevertheless, a third harmonic cavity is foreseen for DAΦNE as an additional means for the bunch length control [44, 45].

3.2. Transverse mode coupling threshold

In order to estimate the threshold average current $(I_0)_{th}$ for the transverse mode coupling instability in DAΦNE we use the approximate formula [21] which is valid for the coupling of lowest transverse modes (m = 0 and m = -1):

$$(I_0)_{th} = \frac{4(E/e)\nu_s}{R\sum\{[\mathrm{Im}\, Z_T]\beta_y\}} \frac{4\sqrt{\pi}}{3}\sigma_z \qquad (22)$$

Here the imaginary impedances of vacuum chamber elements must be summed up weighting by the betatron function at their locations.

The bunch arriving from the accumulator ring is expected to be longer than 3 cm and, due to the fact that the synchrotron period is two orders of magnitude shorter than the damping time, the bunch never reaches its "natural" value of 4.8 mm. Numerical simulations of the bunch lengthening show that it never becomes shorter than 1 cm for the nominal bunch current. By substituting DAΦNE parameters in eq. (22) and choosing σ_z = 1 cm we get the impedance limit:

$$\sum\{[\mathrm{Im}\, Z_T]\beta_y\} \le 0.55M\Omega$$

The broad band transverse impedance calculations were carried out with MAFIA and ABCI performing Fourier transform of the short range wake fields. Figure 25 shows the calculated transverse impedance of some main impedance contributing elements (in the case of 1 cm bunch length and Fourier transform over 30 cm wake).

Figure 26 shows the overall contributions to the weighted impedance. As it can be seen the total impedance weighted by the beta function is well below the threshold value 0.55 MΩ in all the frequency range of interest.

Simulations for other bunch lengths have shown that the situation is even safer for longer bunches.

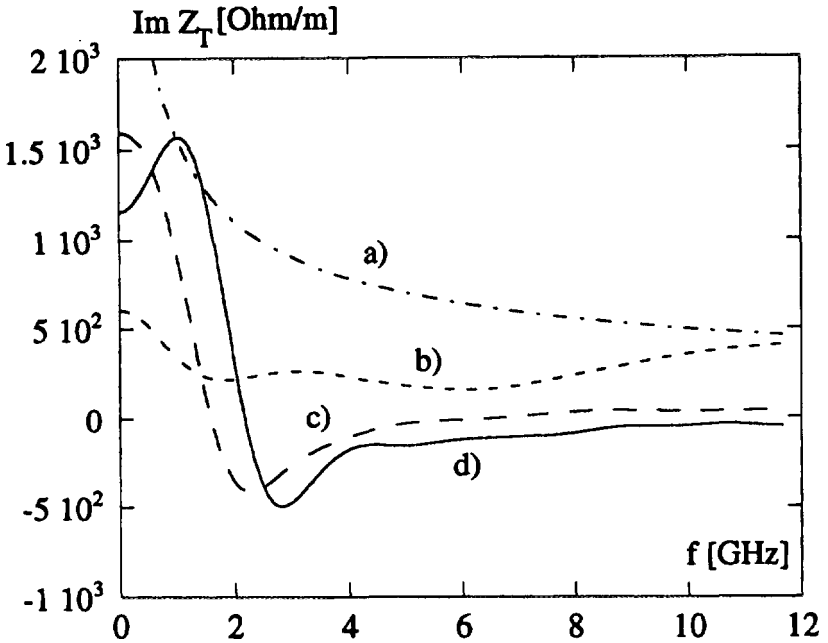

Fig. 25 - Imaginary part of transverse broad band impedance of some vacuum chamber elements: a) resistive wall; b) RF cavity; c) transverse feedback kicker; d) longitudinal feedback kicker.

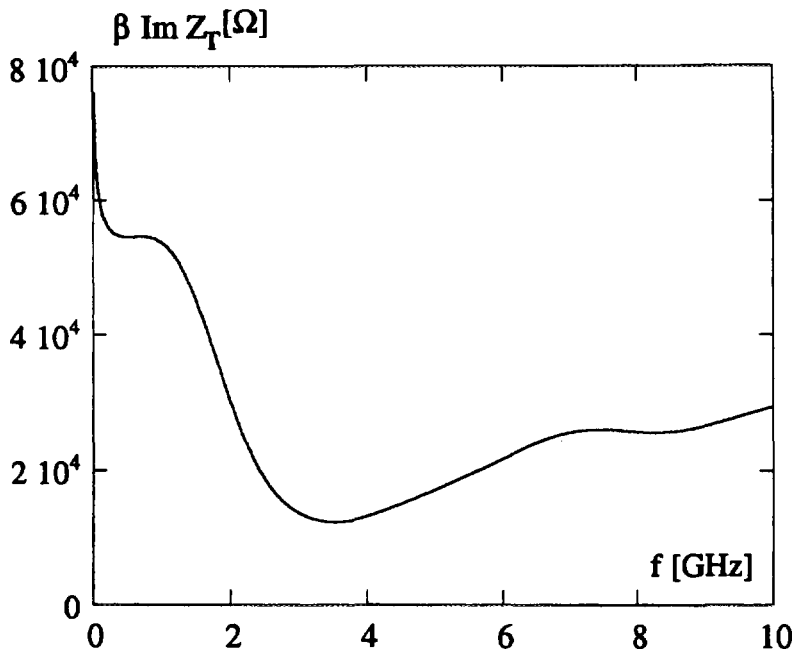

Fig. 26 - Imaginary part of DAΦNE transverse broad band impedance.

4. MULTIBUNCH INSTABILITY SIMULATIONS

A time domain simulation code [4, 46] has been developed in order to investigate the effect of the bunch-by-bunch feedback system on the multibunch dynamics.

We have simulated the instabilities with the feedback off, considering the injection of one bunch (with an error of 100 psec) all the others (29) being in the equilibrium state.

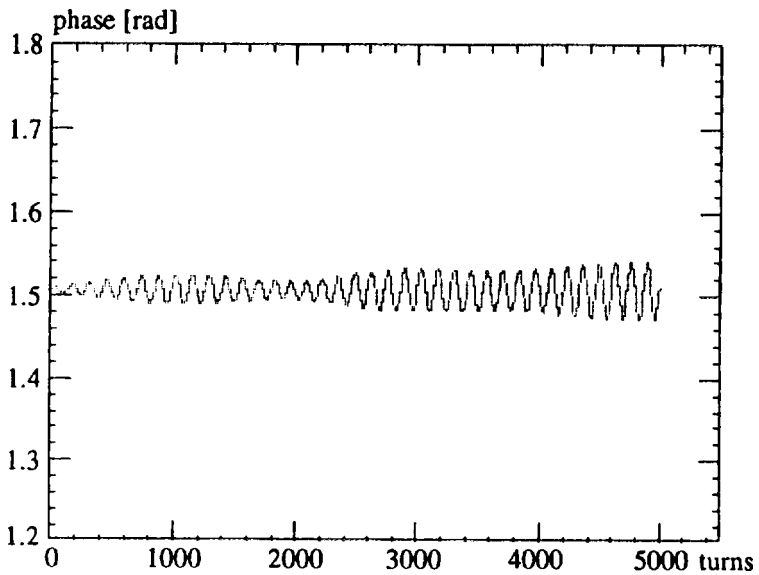

Fig. 27 - Phase oscillations of a perturbed bunch with the feedback off.

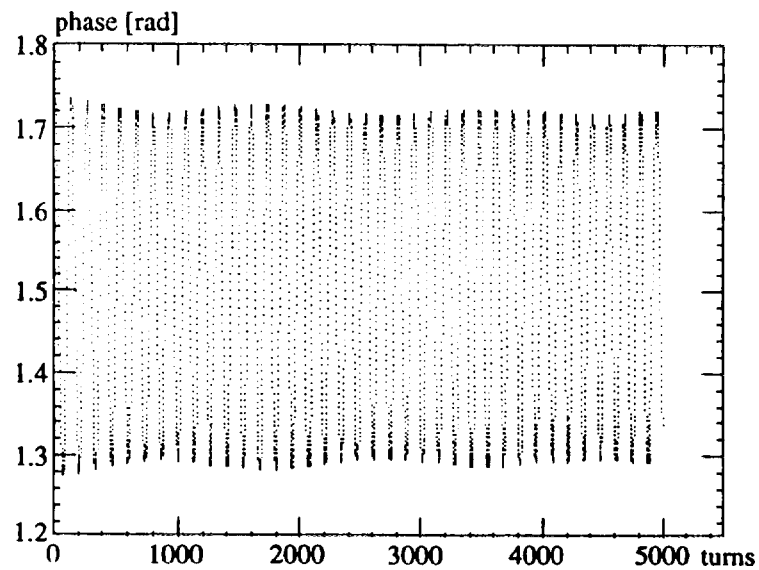

Fig. 28 - Phase oscillations of the injected bunch with the feedback off.

Figures 27, 28 show the oscillations of perturbed and injected bunches during the first 5000 turns. This instability can be easily damped by an ideal kicker with a peak voltage of 400 Volt as shown in Fig. 29. Since the RF cavity kicker has a limited bandwidth, it differs from the ideal case, showing a reduced efficiency of about 20% as shown in Fig. 30.

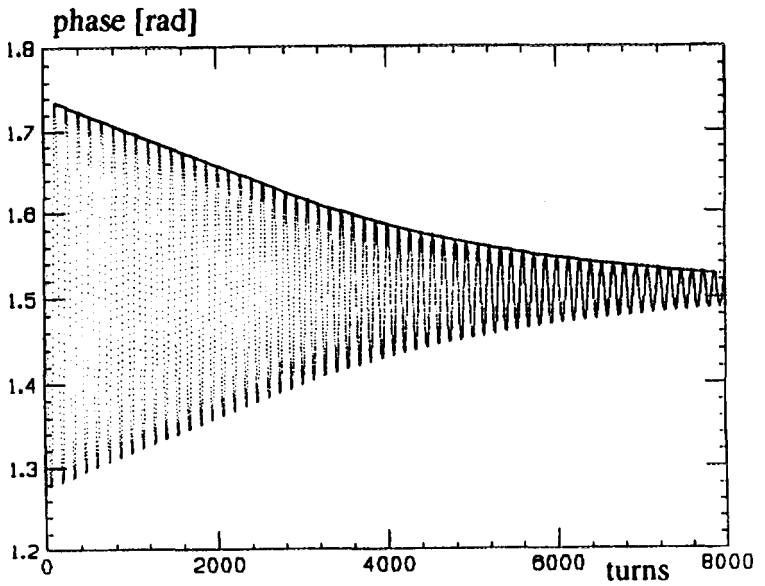

Fig. 29 - Phase oscillations of the injected bunch with an ideal kicker.

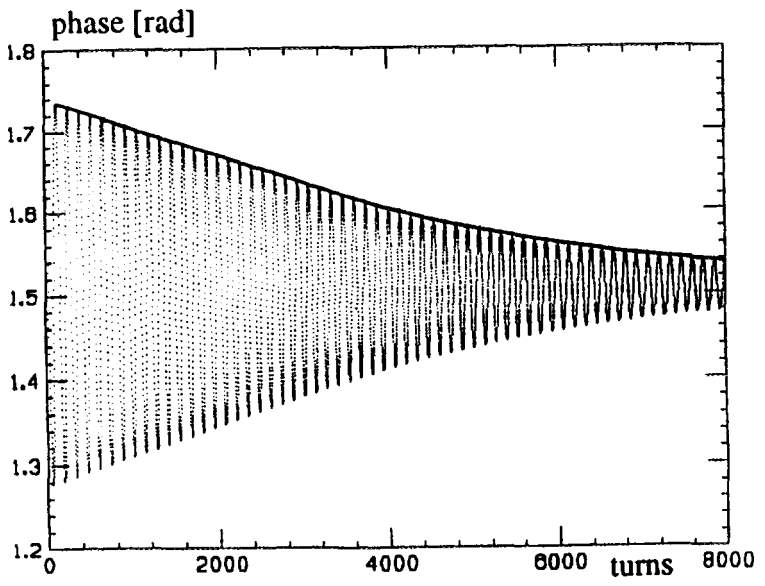

Fig. 30 - Phase oscillations of the injected bunch with the RF cavity kicker.

5. CONCLUSIONS

We have described the design of the main DAΦNE vacuum chamber elements with an analysis of their impedance and impact on the single and multibunch dynamics. The list of presented elements is far from being complete, but enough to demonstrate the design strategy.

Our main concern was the coupled bunch instabilities. Because of that, strong efforts have been undertaken to reduce the number of vacuum chamber elements capable to create dangerous HOMs and to develop techniques for damping the HOMs and the instabilities.

The RF cavity is, certainly, the main contributor to the strongest HOMs which, if not damped, could give a multibunch instability rise time in the order of tens of microseconds. Damping is obtained by strongly coupling HOMs to rectangular waveguides (WG) placed onto the cavity surface. In order to dissipate the extracted power outside the vacuum chamber the rectangular WGs are converted in double ridge WGs by a smooth and wideband tapered section which is adapted to 50 Ω by a transition to coaxial.

Even though the HOMs are heavily damped, the instability growth rate is substantially stronger than the natural damping rate. This demanded the development of feedback systems. A bunch-by-bunch feedback system will be used with an overdamped cavity as a longitudinal feedback kicker. The cavity has about 200 MHz bandwidth with 750 Ω peak shunt impedance. The HOMs of such a cavity are also strongly damped. A transverse feedback system is also foreseen for DAΦNE in order to damp residual transverse oscillations after injection, transverse resistive wall and transverse coupled bunch instability.

Maximum care has been taken to screen possible resonating volumes (bellows, central bulb shape part of the interaction region vacuum chamber etc.).

Numerical tracking has been performed in order to simulate the bunch lengthening process. Broad band wake fields were calculated with numerical codes MAFIA and ABCI. Relative contribution of the inductive elements and loss factors of main lossy elements can be found in Tables 6 and 7, respectively. As expected, the bunch is in the turbulent lengthening regime with the threshold reached at $N \sim 10^{10}$ particles. However, the bunch lengthens to a value (2.1 cm at $V_{rf} = 127$ kV) smaller than the nominal one of 3 cm and additional lengthening may be necessary. A third harmonic cavity is planned for this purpose.

The transverse mode coupling instability does not seem to be the limiting instability for DAΦNE. The estimate has shown that the nominal bunch current is about one order of magnitude lower than the threshold due to the transverse mode coupling.

Ion trapping effects are the subject of a separate paper [47].

6. ACKNOWLEDGMENTS

It is a grateful duty to acknowledge the constant encouragement and guidance by Gaetano Vignola and the ingenuity of many solutions to "impossible" problems provided by Hank Hsieh. Pina Possanza turned many pages by several whimsical hands into a readable form.

7. REFERENCES

[1] The DAΦNE Project Team, "DAΦNE, the Frascati Φ - Factory", in Proceedings of the 1993 Particle Accelerator Conference, Washington D.C., May 17-20, 1993, p. 1993.

[2] D. Boussard, "Observation of Microwave Longitudinal Instabilities in the CPS", CERN-Lab 2/ RF / 75-2 (1975).

[3] A. Hofmann (for the LEP team), "Performance Limitations at LEP", in Proceedings of the 4th EPAC, London, 1994, p.73.

[4] S. Bartalucci et al., "Analysis of Methods for Controlling Multibunch Instabilities in DAΦNE ", Particle Accelerator, Vol. 48, 4 (1995), p. 213.

[5] T. Weiland, Particle Accelerators 15, 245, 292 (1984).

[6] S. Bartalucci et al., "A low loss cavity for the DAΦNE Main Ring", DAΦNE, Technical Note G-6, 1991.

[7] T. Weiland, NIM 216 (1983), pp. 329-348.

[8] P. Fernandes and R. Parodi, IEEE Trans. on Magn., 21(6) (1985) p. 2246.

[9] R. Boni et al., "A Broadband Waveguide to Coaxial Transition for High Order Mode Damping in Particle Accelerator RF Cavities", Particle Accelerator, Vol. 45, 4 (1994), p. 195.

[10] Hewlett Packard Co, "HFSS, The High Frequency Structure Simulator HP85180A™".

[11] R. Boni et al., "Update on the Broadband Waveguide to 50 Ω Coaxial Transition for Parasitic Mode Damping in the DAΦNE RF Cavities", Proceedings of the 4-th EPAC, London, 1994,Vol. 3, p. 2004.

[12] P. Arcioni, "POPBCI - A Post-Processor for Calculating Beam Coupling Impedances in Heavily Damped Accelerating Cavities", SLAC PUB n. 5444, March 1991.

[13] R. Boni et al., "DAΦNE Main Ring Cavity 3D Code Simulations", DAΦNE Technical Note RF-13, July 1994.

[14] R. Boni et al., "Kirchoff's Approximation for Evaluating the Coupling of the DAΦNE RF Cavity with Waveguide Dampers", DAΦNE Technical Note RF-15, October 1994.

[15] R. Boni et al., "Study of the Parasitic Mode Absorbers for the Frascati Φ-Factory RF Cavities", LNF-93/014 (P), April 1993.

[16] G. Oxoby et al., "Bunch by Bunch Longitudinal Feedback System for PEP-II", Proc. of 4th EPAC, London, 1994, p.1616.

[17] J.D. Fox et al.: "Operation and Performance of the PEP-II Prototype Longitudinal Damping System at the ALS", to be published in Proc. of 1995 Particle Accelerator Conference, Dallas, TX, 1995.

[18] R.L. Gluckstern, J. van Zeijts, B. Zotter, "Coupling Impedance of Beam Pipes of General Cross Section", CERN SL/AP, 92-25, June 1992.

[19] M. Migliorati, L. Palumbo, M. Zobov, "Transverse Instabilities in DAΦNE", DAΦNE Technical Note G-25, July 1994.

[20] B. Zotter, F. Sacherer, "Transverse Instabilities of Relativistic Particle Beams in Accelerators and Storage Rings", in Proceedings of the First Course of Int. School of Particle Accelerators, Erice 1976, CERN 77-13, p.175.

[21] M.S. Zisman, S. Chattopadhyay, J. J. Bisognano, "ZAP Users Manual", LBL-21270, UC-28, December 1986.

[22] K.-Y. Ng, "Impedance of Stripline Beam-Position Monitors", Particle Accelerators, 1988, Vol. 23, p. 93.

[23] The KLOE Collaboration, "KLOE, a General Purpose Detector for DAΦNE", Frascati Internal Note LNF-92/019 (IR), April 1992.

[24] S. Bartalucci et. al., "RF Losses in KLOE Interaction Region Vacuum Chamber", DAΦNE Technical Note, G-23, January 1994.

[25] Guido Raffone, private communication.

[26] M.K. Sullivan, "Preliminary Background Calculations for DAΦNE", DAΦNE Technical Note IR-2, March 24, 1993.

[27] The Finuda Collaboration, "Finuda, a Detector for Nuclear Physics at DAΦNE", Frascati Internal Note LNF-93/021, May 1993.

[28] G.V. Stupakov, "Coupling Impedance of a Long Slot and an Array of Slots in a Circular Vacuum Chamber", SLAC-PUB-6698, December 1994 (A).

[29] S.S. Kurennoy, Particle Accelerators 39 (1992), p.1.

[30] S.S. Kurennoy, "Pumping Slots: Coupling Impedance Calculations and Estimates", Report SSCL-636, Dallas (1993).

[31 S.S. Kurennoy, "Beam Coupling Impedance of Holes in Vacuum Chamber Walls", Report IHEP 92-84, Protvino (1992).

[32] R.E. Shafer: "Characteristics of Directional Coupler Beam Position Monitors", IEEE Trans. on Nuclear Science, Vol. NS-32, n.5, p. 1933 (1985).

[33] S. Guiducci, "Background evaluation in DAΦNE", DAΦNE Technical Note IR-6 (1995).

[34] S.S. Kurennoy, G. V. Stupakov, "A New Method for Calculation of Low-Frequency Coupling Impedance", SSC-preprint-332 (1993).

[35] A.W. Chao, "Physics of Collective Beam Instabilities in High Energy Accelerators", New York: Jonh Wiley &Sons, Inc., 1993, p.71.

[36] L.J. Laslett, 'On Intensity Limitations Imposed by Transverse Space Charge Effects in Circular Accelerators", BNL-7534, 1963, p. 324.

[37] M.Furman, P.Morton, "The Laslett Tune Shift for the B Factory", SLAC-ABC-35, July '91.

[38] G. Guignard, "Selection of Formulae Concerning Proton Storage Rings", CERN 77-10, June 1977.

[39] Y.H. Chin, "User's Guide for ABCI Version 8.8 (Azimuthal Beam Cavity Interaction)", LBL-35258, UC-414, February 1994.

[40] K.L.F. Bane, "Bunch lengthening in the SLC Damping Rings", SLAC-PUB-5177, February 1990 (A).

[41] K.L.F. Bane and K. Oide, "Simulations of the Longitudinal Instability in the SLC Damping Rings", in Proceedings of the 1993 Particle Accelerator Conference, Washington, D.C., May 17-20, 1993, p. 3339.

[42] R. Siemann, "Computer Simulation of Bunch Lengthening in SPEAR", Nuclear Instruments and Methods 203 (1982), p. 57.

[43] T. Weiland, "On the Qualitative Prediction of Bunch Lengthening in High Energy Electron Storage Rings", DESY 81-088, December 1981.

[44] S. Bartalucci et. al., "A 3rd Harmonic Cavity for DAΦNE", in Proceedings of the Fourth European Particle Accelerator Conference, London, 27 June-1 July, 1994, p. 1129.

[45] M. Migliorati, L. Palumbo, M. Zobov, "Bunch Length Control in DAΦNE by a higher Harmonic Cavity", Nuclear Instruments and Methods, A 354 (1995), p. 223.

[46] M. Bassetti et al., "A Time Domain Simulation Code of the Longitudinal Multibunch Instabilities", DAΦNE Technical Note G-19, Frascati, June 23, 1993.

[47] C. Vaccarezza, "Ion Trapping Effect and Clearing in the DAΦNE Main Electron Ring", to be published.

APPENDIX

Multibunch longitudinal and transverse instability for high Q resonators (HOMs)

The instability rise time and the coherent frequency shift are obtained by solving the equations (we use the formalism of J. L. Laclare in 'Bunched Beam Coherent Instabilities', CAS Advanced Accelerator Physics, CERN 87-03, p. 264, Vol. I)

$$j(\omega_c - m\omega_s) = -\frac{I_b m\eta}{\omega_s (E/e)} \frac{Z_L(p)}{p} \int_0^\infty \frac{\partial g_o(\hat{\tau})}{\partial \hat{\tau}} J_m^2(p\omega_o \hat{\tau}) d\hat{\tau} \qquad \text{(longitudinal)}$$

$$j(\omega_c - m\omega_s) = -\frac{I_b c}{2(E/e)\nu_{x,y}} Z_T(p) \int_0^\infty \hat{\tau} g_o(\hat{\tau}) J_m^2\left[\left(\left(p + \nu_{x,y}\right)\omega_o - \omega_\xi\right)\hat{\tau}\right] d\hat{\tau} \qquad \text{(transverse)}$$

where ω_c is the coherent synchrotron frequency, m is the mode oscillation number, ω_s is the unperturbed synchrotron frequency, I_b is the beam current, η is the slip factor, E/e is the nominal energy (eV), Z_L is the longitudinal resonator impedance, $g_o(\hat{\tau})$ is the stationary distribution in the phase space, ω_o is the angular revolution frequency, $J_m(x)$ is the Bessel function of the first kind, c is the speed of light, $Z_T(p)$ is the transverse impedance, $\nu_{x,y}$ is the betatron number, $\omega_\xi = \nu_{x,y}\omega_o \xi / \eta$, and ξ is the chromaticity. In case of Gaussian bunch we can solve the integrals analytically and obtain

$$j(\omega_c - m\omega_s) = \frac{I_b m\eta}{\omega_s (E/e) 2\pi\sigma_\tau^2} \exp\left(-p^2\omega_o^2\sigma_\tau^2\right) I_m\left(p^2\omega_o^2\sigma_\tau^2\right) \frac{Z_L(p)}{p} \qquad \text{(longitudinal)}$$

$$j(\omega_c - m\omega_s) = -\frac{I_b c}{4\pi(E/e)\nu_{x,y}} Z_T(p)$$
$$\exp\left[-\sigma_\tau^2\left(\left(p + \nu_{x,y}\right)\omega_o - \omega_\xi\right)^2\right] I_m\left[\sigma_\tau^2\left(\left(p + \nu_{x,y}\right)\omega_o - \omega_\xi\right)^2\right] \qquad \text{(transverse)}$$

where σ_τ is the time bunch length and $I_m(x)$ is the modified Bessel function.

Usually the impedance is computed at the frequency $p\omega_o + m\omega_s$ (longitudinal) or $(p - \nu_{x,y})\omega_o - m\omega_s$ (transverse), obtaining a rise time that in full coupling condition is

$$\frac{1}{\tau_o} = \frac{I_b m\eta}{\omega_s (E/e) 2\pi\sigma_\tau^2} \exp\left(-p^2\omega_o^2\sigma_\tau^2\right) I_m\left(p^2\omega_o^2\sigma_\tau^2\right) \frac{R_s}{p} \qquad \text{(longitudinal)}$$

$$\frac{1}{\tau_o} = \frac{I_b \omega_r}{4\pi (E/e)\nu_{x,y}} R_\perp^{URMEL} \exp\left[-\sigma_\tau^2\left(\left(-p + \nu_{x,y}\right)\omega_o - \omega_\xi\right)^2\right] I_m\left[\sigma_\tau^2\left(\left(-p + \nu_{x,y}\right)\omega_o - \omega_\xi\right)^2\right] \qquad \text{(transverse)}$$

with R_s the longitudinal shunt impedances, ω_r the HOM resonant frequency, and $R_\perp^{URMEL}$ the transverse shunt impedance as given by URMEL code. The impedance should instead be computed at $p\omega_o + \omega_c$ (longitudinal) and $(p - \nu_{x,y})\omega_o - m\omega_c$ (transverse), that is the equations have to be solved self-consistently. In the worst case of full coupling condition, if $\omega_c << \omega_r$, the instability rise time obtained for both longitudinal and transverse case is

$$\tau = \frac{2\tau_f}{\sqrt{1 + 4\frac{\tau_f}{\tau_o}} - 1}$$

with τ_f the HOM filling time.

From the above equation, if $\tau_f << \tau_o$, the rise time coincides with τ_o, but when the cavity HOM filling time is comparable or higher than the instability rise time, the difference can become significant.

Landau damping

To evaluate the effect of the Landau damping on the single HOM multibunch instability, we use the dispersion integral that, in case of Gaussian bunch, can be written as

$$1 = Z_L(p) G^{-1}(y)$$

with h the harmonic number, and

$$G^{-1}(y) = -j \frac{4 I_b \eta p}{\pi (h\omega_s\sigma_\tau)^2} \frac{1}{(p\omega_o\sigma_\tau)^2} \int_0^\infty \frac{\exp(-x) J_m^2\left(p\omega_o\sigma_\tau\sqrt{2x}\right)}{x - y} dx$$

$$y = -\frac{8(\omega_c - m\omega_s)}{m\omega_s h\omega_o^2\sigma_\tau^2}$$

The integral has a principal value and an imaginary part. By imposing $\mathrm{Im}[y] \to 0^+$, the curve of $G(y)$ in the complex plane gives the multibunch instability threshold for a given impedance $Z_L(p)$.

IMPEDANCE AND COLLECTIVE EFFECTS IN THE LHC

Jacques Gareyte

CERN, Geneva 23, Switzerland

Abstract

After a review of the main LHC parameters, and a brief description of the RF and vacuum systems, the coupling impedances of the main machine elements are given, as well as the resulting thresholds for instabilities.

1 Introduction: The LHC parameters

The LHC is a high field, high luminosity hadron collider. Its main role consists in colliding two proton beams at a sufficient center of mass energy and sufficient luminosity to possibly discover and study the Higgs boson. It will also collide heavy ions, in particular lead. At a later stage collisions between protons in LHC and electrons in LEP can be arranged if required.

Since the LHC is to be build in the existing LEP tunnel, its energy is limited to 7 TeV per beam by the maximum bending magnet field of 8.4T technically feasible and economically affordable.

The luminosity in p-p mode is limited by beam-beam effects at $L = 10^{34}\text{cm}^2\text{s}^{-1}$ for a beam intensity of 0.53A. Each beam is made of 2835 bunches of 10^{11} p each, distributed along the ring in a complicated manner (Fig. 1) due to the need to accommodate injection and dump kicker risetimes. The main LHC parameters are displayed in Tables 1 and 2.

The basic layout of the machine (Fig. 2) mirrors that of LEP, with eight straight sections each approximately 540 meters long available for experimental insertions or utilities. The two high luminosity insertions are located at diametrically opposite straight sections, point 1 (ATLAS) and point 5 (CMS). Two more experimental insertions are located at point 2 (ALICE Pb ions) and point 8 (B physics). These straight sections also contain the injection systems. The beams cross from one ring to the other only at these four locations.

The remaining four straight sections do not have beam crossings. Straight sections 3 and 7 contain two beam collimation systems with only classical magnets. Straight section 4 houses the RF systems and section 6 the beam dumping systems.

Two of the LHC systems are particularly important in determining the beam coupling impedance and will be briefly described: these are the RF and vacuum systems. A summary of the LHC coupling impedance and instability thresholds will then be given. A more thorough description of impedances and collective effects in LHC can be found in [1].

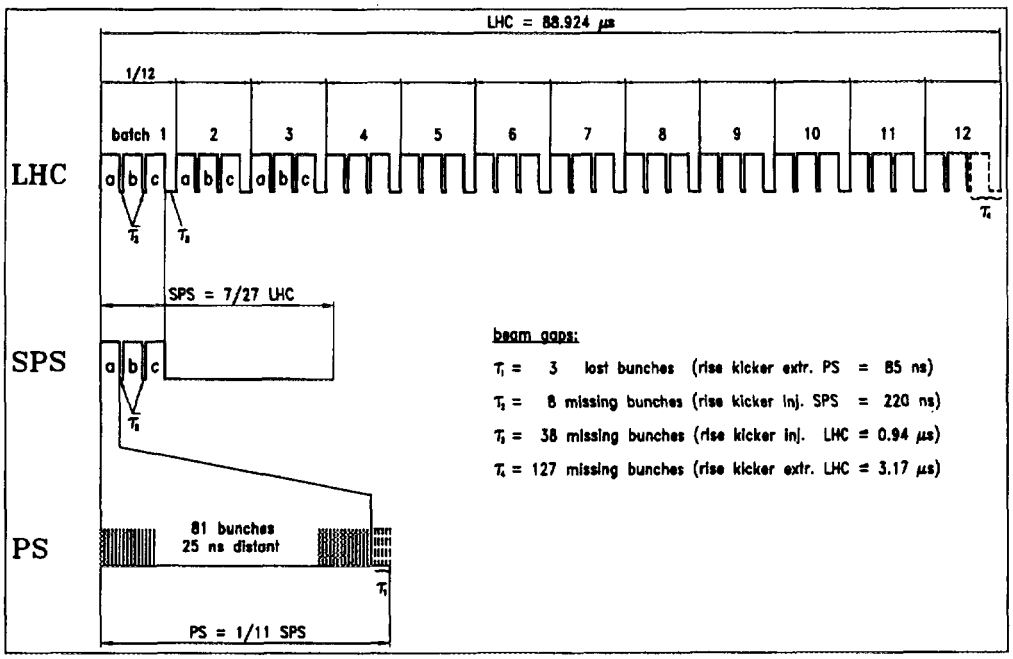

Figure 1: Bunch disposition in LHC and its injectors

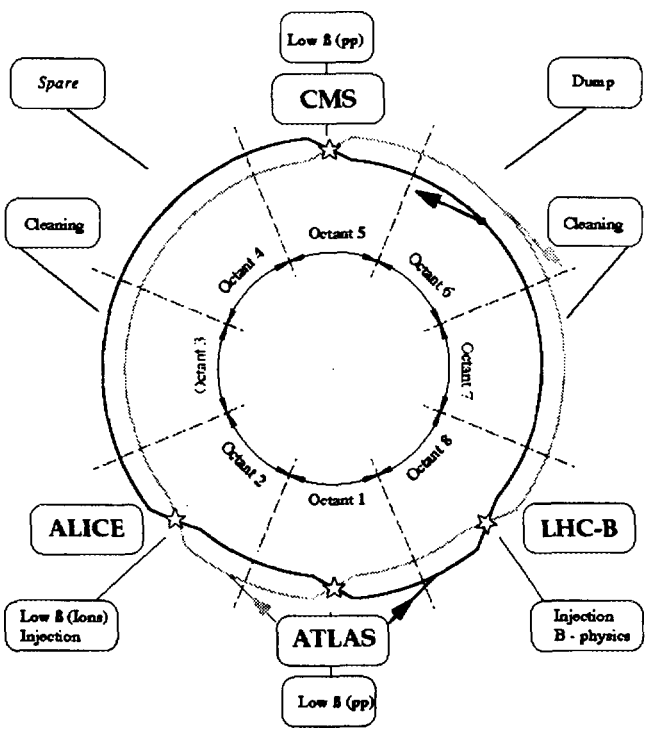

Figure 2: Schematic layout of LHC

Table 1: LHC performance parameters

Energy	E	[TeV]	7.0
Dipole field	B	[T]	8.4
Luminosity	L	[cm^{-2} s^{-1}]	10^{34}
Beam–beam parameter	ξ		0.0034
Total beam–beam tune spread			0.01
Injection energy	E_i	[GeV]	450
Circulating current/beam	I_{beam}	[A]	0.53
Number of bunches	k_b		2835
Harmonic number	h_{rf}		35640
Bunch spacing	τ_b	[ns]	24.95
Particles per bunch	n_b		$1.05\ 10^{11}$
Stored beam energy	E_s	[MJ]	332
Normalized transverse emittance $(\beta\gamma)\sigma^2/\beta$	ε_n	[mrad]	$3.75\ 10^{-6}$
Collisions			
Beta-value at I.P.	β^*	[m]	0.5
r.m.s. beam radius at I.P.	σ^*	[μm]	16
r.m.s. divergence at I.P.	σ'^*	[μrad]	32
Luminosity per bunch collision	L_b	[cm^{-2} s^{-1}]	$3.2\ 10^{26}$
Crossing angle	ϕ	[μrad]	200
Number of events per crossing	n_c		19
Beam lifetime	τ_{beam}	[h]	22
Luminosity lifetime	τ_L	[h]	10

Table 2: LHC parameters related to RF

			Injection	Collision
Intrabean scattering				
Horizontal growth time	τ_h	[h]	45	100
Longitudinal growth time	τ_p	[h]	33	60
Radiofrequency				
RF voltage	V_{rf}	[MV]	8	16
Synchrotron tune	Q_s		$5.5\ 10^{-3}$	$1.9\ 10^{-3}$
Bunch area (2σ)	A_b	[eV.s]	1	2.5
Bucket area	A_{rf}	[eV.s]	1.46	8.7
Bucket half-height	$\Delta p/p$		$1\ 10^{-3}$	$3.6\ 10^{-4}$
r.m.s. bunch length	σ_s	[m]	0.13	0.075
r.m.s. energy spread	σ_e		$4.5\ 10^{-4}$	$1.0\ 10^{-4}$

2 LHC RF and feedback systems

The LHC bunch length must be small enough to keep the unavoidable degradation of luminosity due to the beam crossing angle tolerable. The longitudinal emittance on the other hand must be sufficiently large to reduce the Intra Beam Scattering (IBS) induced growth rate of the transverse emittances, both at injection and in collision. Both conflicting requirements are satisfied with an RF operating at 400 MHz and a bunch longitudinal emittance of 1 eVs at injection and 2.5 eVs at 7 TeV. The RF voltage needed to achieve that is modest (8 MV at injection and 16 MV in collision) and is provided by eight superconducting cavities. These have the advantage of a very low coupling impedance (very large beam pipe diameter) and allow to control the very severe beam loading conditions. The r.m.s. bunch length is 13 cm at injection and 7.5 cm in collision.

Apart from the fundamental mode, two transverse high order modes do not propagate through the large beam pipes in between cavities. These will be damped with tuned antennas close to the cavities. Propagrating modes will be damped by broad band antennas or ferrite rings. In this way RF cavities will not contribute a significant part of the LHC impedance budget.

The feedback systems will also be located in section 4 with the RF. The longitudinal feedback has a bandwidth of $\pm$ 20 MHz (bunch by bunch feedback) centered at 200 MHz. It uses two copper cavities per beam, fed by tetrode amplifiers. Its parameters are dominated by the need to damp injection transients, which are particularly large because of the strong beam loading effects during the injection of the twelve consecutive batches. The high power bandwidth of the amplifier is much smaller that $\pm$ 20 MHz because high power is needed only against injection transients. The transverse feedback is also wide band (bunch by bunch) to damp resistive wall and high order mode induced instabilities. It will be powerful enough at low frequencies (about 1 MHz) to damp large injection errors fast enough to preserve transverse emittance.

3 Vacuum and beam screen

Because of the small diameter (approximately 40 mm) of the beam chamber and the low vacuum pressure needed to preserve beam lifetime, a distributed pumping is mandatory. This is naturally provided by cryogenic pumping on surfaces at a temperature of a few K. However in the LHC a non negligible synchrotron radiation power (3.7 kW per beam) added to the heat load due to beam induced currents in the chamber walls (about 2 kW) must be absorbed at low temperature. It would be excessively expensive to absorb this power at the temperature of the magnet coils, which is 1.9 K. Therefore a second inner chamber is introduced, to shield the vacuum chamber at 1.9 K from both the beam induced currents and the synchrotron radiation. This 'beam screen' is individually cooled at about 20K by helium flowing through small pipes attached to it (Fig. 3)

The beam screen has a large number of small holes to allow the molecules desorbed on its surface by the synchrotron radiation photons to be pumped on the 1.9 K outer vacuum enclosure. These holes cover about 5% of the inner surface of the beam screen. Their dimensions should be small enough to reduce the amount of electromagnetic power generated by the beam which escapes into the coaxial structure between the two chambers. There it propagates at the speed of light and could build up coherently to large values. Elongated slots

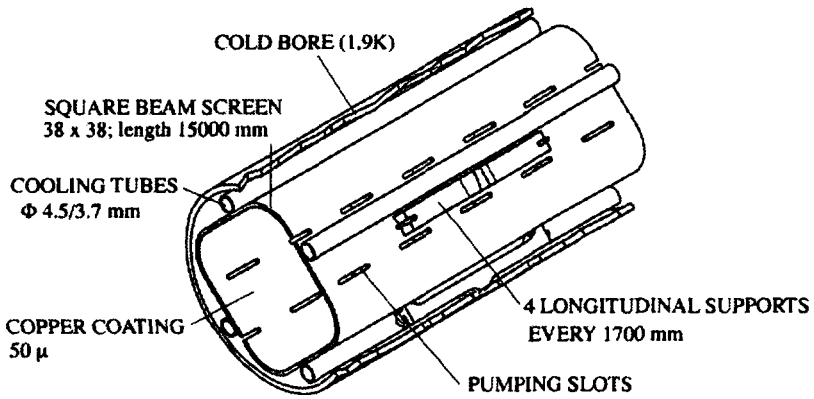

Figure 3: Schematic view of beam screen showing the supports, the cooling pipes and the slots

are preferred because this reduces the coupling impedance presented to the beam compared to round holes for the same total surface. The slots have a width of 1.5 mm and their length varies/in a random fashion around an average of 8 mm to minimize modes trapped below the cut-off frequency of the pipe. The spacing of the slots is also randomized, and RF absorbers are attached to the outside of the screen to avoid synchronism between beam and TEM waves in the coaxial part.

4 LHC effective impedance

Tables 3 and 4 give the effective impedances evaluated respectively at injection energy where the bunch length is 13 cm and at high energy where it is 7.5 cm.

Table 3: LHC effective impedance (in Ω) at 450 GeV.

INJECTION	$\mathrm{Im}(Z_L/n)_{\mathrm{eff}}$	$\beta_{\mathrm{av}}\mathrm{Im}(Z_T)_{\mathrm{eff}} \times 10^{-6}$
Space charge	-0.0058	-442.4
Shielded bellows	0.0815	139.5
Monitor tanks	0.0400	203.0
Pumping slots	0.0156	37.1
Total broad band	0.1313	-62.8
Strip-line monitors	0.127	446.6
Abort kickers	0.007	181.2
SC cavities	0.010	0.4
Total low frequency	0.144	628.2

Table 4: LHC effective impedance (in Ω) at 7 TeV.

TOP ENERGY	$\mathrm{Im}\,(Z_{\mathrm{L}}/n)_{\mathrm{eff}}$	$\beta_{\mathrm{av}}\mathrm{Im}\,(Z_{\mathrm{T}})_{\mathrm{eff}} \times 10^{-6}$
Space charge	-3.3×10^{-5}	-28.6
Shielded bellows	0.0815	139.5
Monitor tanks	0.0400	203.0
Pumping slots	0.0156	37.1
Total broad band	0.1371	351.0
Strip-line monitors	0.073	257.9
Abort kickers	0.004	108.5
SC cavities	0.010	0.4
Total low frequency	0.087	366.8

Table 5: Summary of parasitic losses for LHC at 7 TeV.

Power loss [kW]	FOR A SINGLE BEAM	Power loss per unit length [mW/m]
3.67	Incoherent synchrotron radiation	216
$\ll 0.54$	Coherent synchrotron radiation	$\ll 32$
1.97	Resistive wall (20° K)	74
0.27	Welds	10
0.26	Pumping slots	10
< 0.80	Shielded bellows	< 30
$\ll 1.03$	Leaks in bellows gaps	$\ll 38$
8.54	TOTAL	410

At injection space charge is dominating the transverse impedance. The bellows are shielded in a way similar to the LEP ones, which are well known from field calculations and beam measurements. Table 5 summarizes the parasitic losses at 7 TeV.

5 Single bunch intensity threshold

The longitudinal microwave instability has a threshold of 6.4 10^{12} p at injection and 3.10^{12} at 7 TeV, well above the nominal bunch population of 10^{11} p. Landau damping of longitudinal modes is ensured by RF bucket non linearities for bunch populations smaller than 2.10^{12} p at injection and 2.10^{11} at high energy. In fact, the most dangerous single bunch effect in the LHC is the possible loss of Landau damping for longitudinal modes at 7 TeV.

The transverse mode coupling instability has a threshold of 6.10^{11} p at injection and 1.5 10^{12} p at high energy. Landau damping of transverse modes is provided at the nominal bunch intensity of 10^{11} p by a tune spread in the beam of 10^{-3}, which will either be provided naturally by the machine non-linearities, or otherwise can be supplied by the system of octupolar correctors.

6 Transverse resistive-wall instability

This is a strong instability for machines which have a large total current, especially for very large machines like the LHC. The growth time τ expressed in number of revolution periods T is

$$\frac{\tau}{T} = \frac{2E/e}{\beta Z_T I},$$

where E/e is the energy in electronvolts, I the total beam current and β the betatron function. The transverse impedance Z_T is given by:

$$Z_T = \frac{2c}{b^3}\left(\frac{\rho}{\delta}\right)\frac{R}{\omega},$$

where c is the speed of light, b the beam chamber half-height, ρ the resistivity of the chamber material and δ the skin depth at the lowest betatron frequency ω, and R the average machine radius. Since ρ/δ scales like $\rho^{1/2}R^{-1/2}$, Z_T scales like $\rho^{1/2}R^{1.5}/b^3$. In addition, comparison of existing machine designs shows that β has a tendency to increase like $R^{1/2}$, so that τ/T scales like $b^3/\rho^{1/2}R^2$.

This reveals the problem of resistive-wall instability in high-energy colliders: R is large, and since the beam shrinks at high energy, one is tempted to decrease b in order to reduce cost.

This can only be compensated by reducing ρ, which is achieved by coating the inner side of the LHC beam screen with 50 μm of copper. In this way the growth time, which would be about 3 turns with a stainless steel tube, and therefore unmanageable, is increased to 300 turns.

7 Conclusion

State of the art precautions applied to the design of the LHC elements seen by the beam ensure stability as far as single bunch effects are concerned. In the same way the beam induced heat load to the cryogenic system is kept at a manageable level. Multibunch instabilities with growth times exceeding 100 turns, are damped by feedback.

8 Reference

[1] F. Ruggiero, Single beam collective effects in the LHC, LHC note 313 and proceedings of the workshop on Large Hadron Colliders, Montreux, October 1994.

IMPEDANCE WORKING GROUP

Pumping slot design for KEKB LER

Ken-ichi Kanazawa
KEK National Laboratory for High Energy Physics

In the design of the vacuum system for KEKB, Pumping slots are backed up by mesh to prevent the penetration of beam induced field which causes heat up of pump elements. For the LER the design of the slots looks like a drawing (a) in Figure 1. As shown later the conductance of the structure (a) is same as the structure (b). If finite thickness for a mesh is required, the structure (c) whose conductance is lower than (a) or (b) must be adopted. The purpose of this note is to look for an advise to select a good design to prevent the beam induced field and also to draw an attention to the calculation of the conductance.

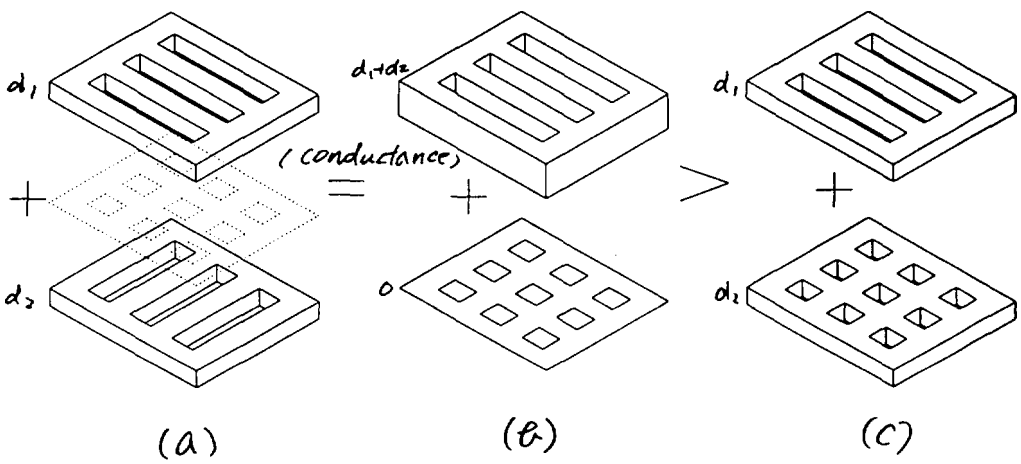

Fig.1 Various possible design of LER slots for a pump port.

The conductance C of a slot as shown in Fig. 2 under the molecular flow condition (the mean free path of a molecule is determined by the geometry of a vacuum chamber and no collision between molecules) is given as the combination of
the conductance of a thin hole : $C_A = \frac{1}{4} vA$, and

the conductance of a long pipe: $C_d = C_A \frac{16\alpha}{3}\frac{A}{F}$

as

$$\frac{1}{C} = \frac{1}{C_A} + \frac{1}{C_d} \qquad (1)$$

where,

A=wl ,the area of the opening

F=2(l+w)d ,the area of the inside wall,

v is an average velocity of gas molecules, and α is a correction factor close to 1 which weakly depends on the ratio of w to l.

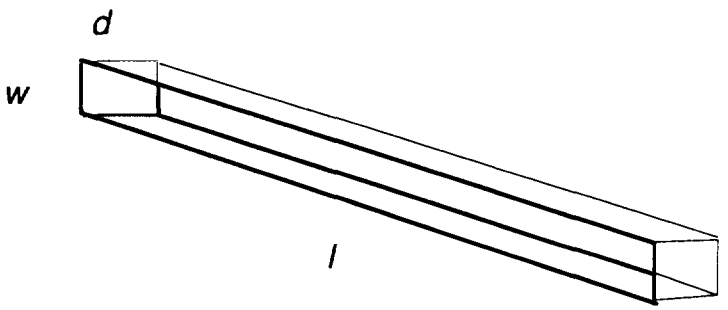

Fig.2 A slot with the aperture of l × w in a wall with the thickness of d.

C can be written as,

$$C = \frac{C_A}{1 + \frac{3}{16\alpha}\frac{F}{A}} \qquad (2)$$

If $\frac{3}{16\alpha}\frac{F}{A} << 1$, C is equal to C_A. And if $\frac{3}{16\alpha}\frac{F}{A} >> 1$: C is equal to C_d

If there are N slots, the combined conductance of slots C_N is given as,

$$C_N = N\,C, \quad \frac{1}{C_N} = \frac{1}{NC_A} + \frac{1}{NC_d} \qquad (3)$$

The conductance C_X for a crossed double slots like the structure (a) is calculated according to the similar combination law as Eq.1. But in this case it must be taken into account that the entrance area to the second slots is A'(sum of square holes) and not equal to NA.

$$\frac{1}{C_X} = \frac{1}{NC_A} + \frac{1}{NC_{d1}} + \frac{1}{C_{A'}}\left(1 - \frac{A'}{NA}\right) + \frac{1}{NC_{d2}} \qquad (4)$$

$$= \frac{1}{C_{A'}} + \frac{1}{NC_{d1}} + \frac{1}{NC_{d2}}$$

$$= \frac{1}{C_{A'}} + \frac{1}{NC_{d1+d2}}$$

The factor $\left(1 - \frac{A'}{NA}\right)$ arises as a correction because A' is not so deferent from NA. Similarly, the inverse of the conductance for the structure (b) is given as,

$$\frac{1}{NC_A} + \frac{1}{NC_{d1+d2}} + \frac{1}{C_{A'}}\left(1 - \frac{A'}{NA}\right)$$

$$= \frac{1}{C_{A'}} + \frac{1}{NC_{d1+d2}}$$

,which is equal to $\frac{1}{C_X}$.

The conductance of the structure (c) can be calculated in the same way as Eq.(4). For the structure (c), the conductance of the thick mesh is smaller than NC_{d2}. Therefore The conductance of structure (c) is lower then (a) and (b).

Reference

H. Kumagai et al, 'Vacuum Science and Engineering', Shokabo, Japan, 1970, in Japanese.

Impedance of the PEP-II DIP Screen*

C.-K. Ng
Stanford Linear Accelerator Center
Stanford University, Stanford, CA 94309, USA

and

T. Weiland
University of Technology
FB18, Schlossgartenstr. 8
D64289, Darmstadt, Germany.

Abstract

The vacuum chamber of a storage ring normally consists of periodically spaced pumping slots. The longitudinal impedance of slots are analyzed in this paper. It is found that although the broad-band impedance is tolerable, the narrow-band impedance, as a consequence of the periodicity of the slots, may exceed the stability limit given by natural damping with no feedback system on. Based on this analysis, the PEP-II distributed-ion-pump (DIP) screen uses long grooves with hidden holes cut halfway to reduce both the broad-band and narrow-band impedances.

*Work supported by Department of Energy, contracts DE-AC03-76SF00515.

1 Introduction

For achieving the required pumping speed, the dipole chamber in the High Energy Ring (HER) of the PEP-II B-Factory was designed with periodically spaced pumping slots on one side of the chamber walls [1]. From the standpoint of beam dynamics, the broad-band and narrow-band longitudinal and transverse impedances should be kept to small values to avoid single-bunch and coupled-bunch instabilities. It turns out the longitudinal broad-band impedance is normally small compared with the impedance budget of the ring, while the longitudinal narrow-band impedance due to the periodicity of the slots may exceed the stability limit given by radiation damping with no feedback system on. It is known that hidden slots can reduce both the broad-band and narrow-band impedances by several orders of magnitude [2]. Furthermore, in the PEP-II DIP screen design, hidden holes are used to prevent possible TE radiation into the pump chamber. Thus, the final design of the DIP screen consists of six continuous grooves of 5.64 m long on one side of the dipole chamber walls, and 3 mm holes with spacing 1 mm are cut halfway in the chamber wall along each groove.

The paper is organized as follows. In the next section, a generic vacuum chamber model used in our analysis is described. Section 3 and section 4 calculate the longitudinal broad-band and narrow-band impedances of the slots, respectively. In section 5, the impedance of the PEP-II DIP screen is evaluated. Section 6 gives a summary of our results. It should be pointed out that here only longitudinal impedance is studied. The analysis of the transverse impedance of slots can be found in Ref. [3].

2 Vacuum Chamber Model

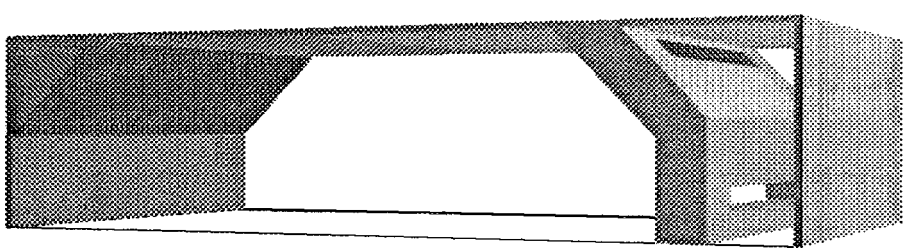

Figure 1: Three dimensional view of a generic vacuum chamber model with four pumping slots connecting the beam chamber with a pump chamber which houses the vacuum pumps. For the purpose of impedance analysis the pumps are replaced by a conducting wall. The inner width is 9 cm, the inner height 5 cm, the slot width 3 mm, and the longitudinal slot spacing 1 cm. The only free parameter is the slot length L_{slot} and the number of slotted sections.

Various models of the vacuum chamber have been analyzed for the PEP-II. However, as the basic physical picture is the same for all the different models, only a generic one is considered here. Fig. 1 shows the three-dimensional view of a generic vacuum chamber with slots on one side. The dimensions have been chosen close to the PEP-II design[1],

but may be considered as a generic chamber layout for electron/positron storage rings. Actually, the vacuum chamber of PEP, PETRA and HERA are almost identical in size. All results presented here are per vacuum chamber slotted section and not for the full length of the final chamber. Thus depending on the slot length one has to multiply the single section results with an appropriate factor. For the PEP-II this factor is approximately $1000/L_{slot}(\mathrm{m})$.

3 Longitudinal Broad-band Impedance

The impedance in general depends on the slot length and it saturates when the length is about several times of its width [4]. The pumping requirements are normally set by the total pumping channel cross section. Thus it is worthwhile to investigate the influence of the length of a slot in order to find an optimum slot length from the impedance point of view. The impedance and wake potentials were computed for slot lengths of 2, 3, 4, 5, 10, 20, 40, 80, 160, 320 and 640 mm. As can be seen from Fig. 2, the wake potential converges quite rapidly with the slot length and no significant increase is observed for a slot length greater than 40 mm. Thus long slots are preferable. Furthermore, the wakefield is found to be purely inductive in nature. From the low frequency spectrum of the wakefield, the inductance is determined and its length dependence is shown in Fig. 3. The inductance converges very quickly to a saturated value of 4.0×10^{-5} nH. The loss parameter has similar variation behavior and its saturated value is 7.9×10^{-7} V/pC. This parameter is a good indication of the effective real part of the impedance weighted with the bunch spectrum. The real part of the impedance is obviously rather small compared to the imaginary part. The inductance of all the slots in the ring is approximately 1 nH.

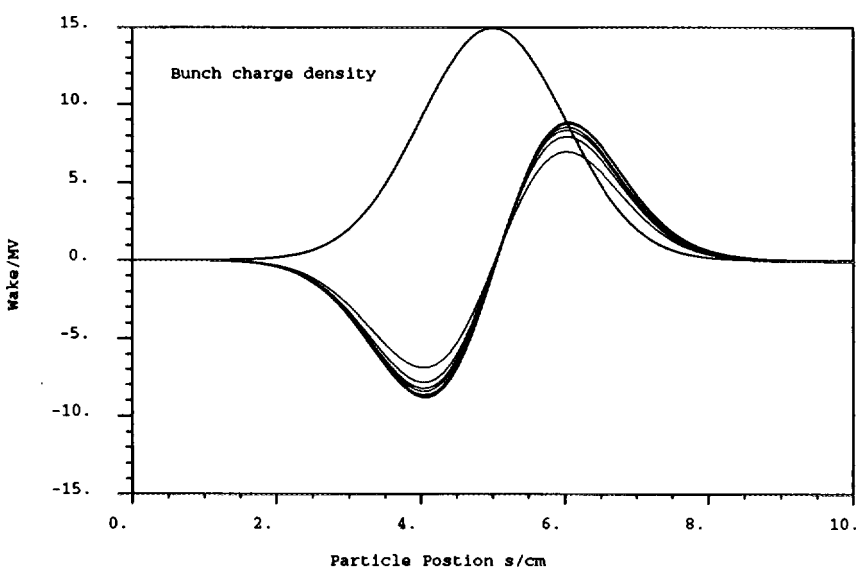

Figure 2: Wake potential as a function of slot length.

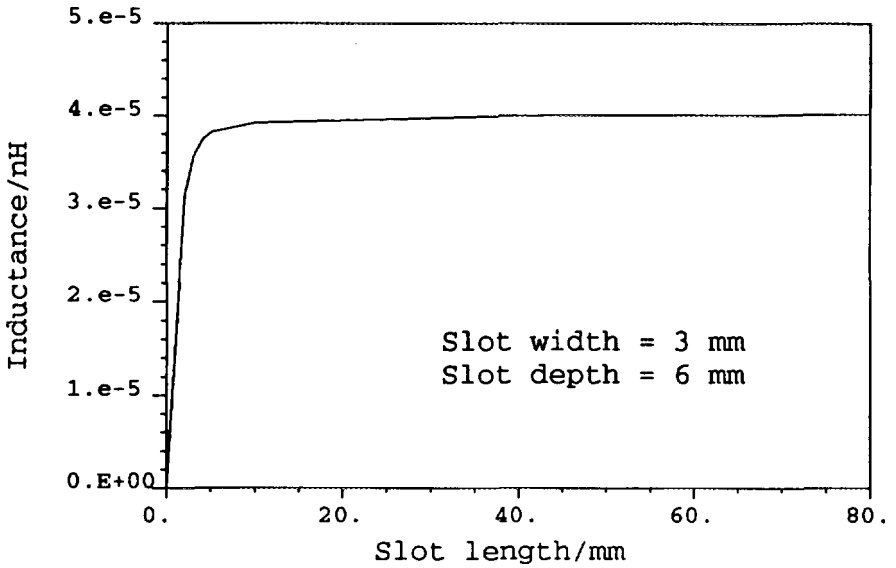

Figure 3: Inductance as a function of slot length.

4 Longitudinal Narrow-band Impedance

Narrow-band impedances are mostly locally confined resonant modes in cavities. A second type of resonant impedance is given by the waveguide character of a vacuum chamber. Basically being a periodic structure, it carries traveling waves with longitudinal and transverse modes just like any traveling wave accelerating structure. There are two possibilities to address this particular impedance, namely frequency and time domain approaches. Strong effects may be found by time domain simulations of a few sections, and weaker effects by modeling the chamber as a periodic structure in frequency domain.

(a) *Section-to-section resonant effects*

In order to identify strong section-to-section effects the wake potentials were computed for pieces consisting of 1,2,4 and 8 sections, with 4 slots per section (see Fig. 1). On the scale where the wake potential is inductive, no significant build-up of a resonant type of impedance has been observed. However, this does not mean that the resonant impedance is negligible but only that it is small compared to the inductive broad-band impedance. Very narrow impedances cannot be found this way but need to be analyzed by frequency domain approaches.

(b) *Traveling Wave Analysis*

As a single mechanical unit, a vacuum chamber is made from 100-200 sections, and an analysis based on infinitely repeating structure is relevant. Thus we can compute traveling waves for any given phase advance per cell. Such a computation results in a Brillouin diagram as one normally finds in linear accelerator designs where similarly long structures (100-200 cavity cells) are used in one unit.

For the vacuum chamber there exist two types of modes. One group shows almost "empty waveguide" mode patterns. A second group shows fields concentrated in the slot

region with almost no field in the center of the vacuum chamber. Examples of these modes for 40 mm slot length are shown in Figs. 4 and 5. In Fig. 6, we show the Brillouin diagram for the structure. The loss parameters, quality factors and shunt impedances for the first seven synchronous waves are listed in Table 2. The mode shown in Fig. 5, a TM_{11}-like mode, has a strong beam coupling. The narrow-band impedance of this mode is about 8 kΩ for the ring, which is roughly a factor of 2 higher than the radiation damping limit at the mode frequency.

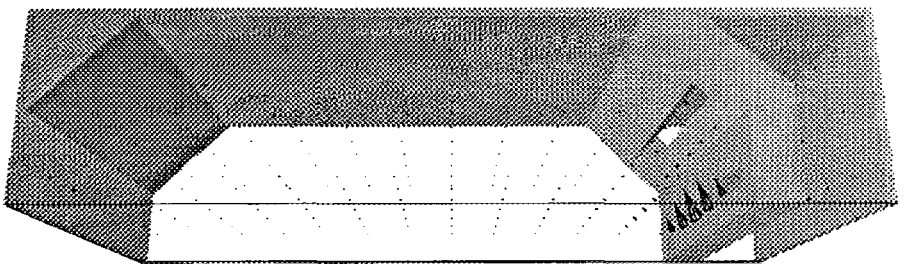

Figure 4: The real part of the electric field of mode 2 with $f = 3.616$ GHz and phase advance 120^{o} per section.

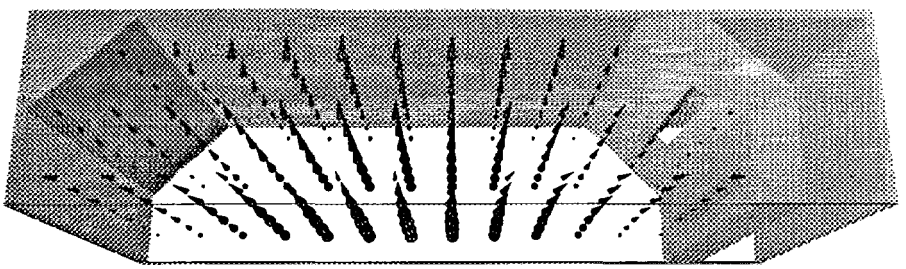

Figure 5: The real part of the electric field of mode 4 with $f = 3.996$ GHz and phase advance 120^{o} per section.

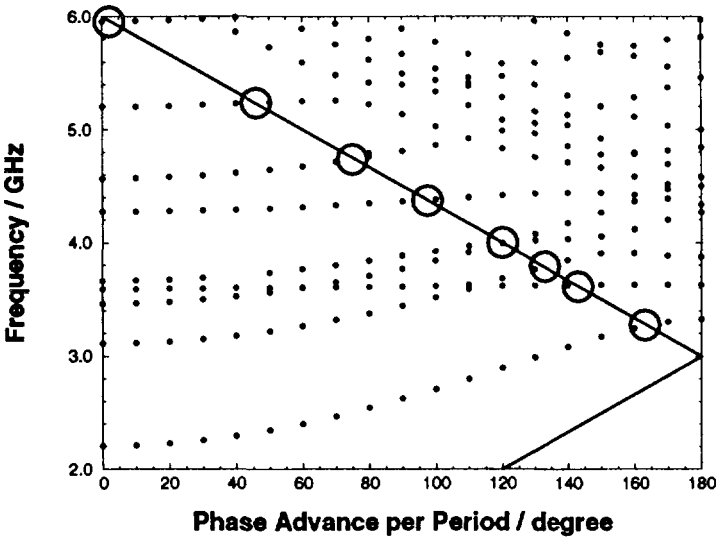

Figure 6: The Brillouin diagram for the vacuum chamber with a slot length of 40 mm and a period of 50 mm. The line light is the solid straight curve. The synchronous modes are marked by circles.

Mode	ϕ /°	f/GHz	k/(V/C)	Q	$R_s/m\Omega$
1	163	3.27	1892	5000	1
2	143	3.63	383	35000	1
3	133	3.80	20170	15000	25
4	120	4.00	148000	27000	318
5	120	4.00	3129	8000	2
6	97	4.37	8129	10000	6
7	75	4.74	23960	37000	60

Table 2. First seven synchronous modes and the associated impedances, quality factors, loss parameters and shunt impedances.

5 PEP-II DIP Screen

From the analysis in the previous two sections, it can be seen that the contribution of the longitudinal broad-band impedance to the total impedance budget of a ring is normally small. The longitudinal narrow-band impedance due to the periodicity of slots may pose problems to coupled-bunched instabilities. The introduction of hidden slots [2] will reduce the broad-band and narrow-band impedances by several orders of magnitude, thus avoiding the complication of randomizing the slots for suppressing the impedance of the resonances excited by the periodic placement of the slots [5].

The final design of the PEP-II DIP screen consists of six continuous grooves of 5.64 m long, 3.75 mm wide and about half the chamber wall thickness located on one side of the dipole chamber walls. Several features of the screen design are in order. First, as seen in section 3, when the length of the groove is greater than a few times of its width, the impedance saturates, and hence the impedance of a 5.64 m long groove along the dipole chamber minimizes the longitudinal broad-band impedance. Second, about half-way deep in the chamber wall, hidden slots are cut along the groove for pumping purposes. Simulations showed that the impedance of a hidden slot is several orders of magnitude smaller than that of a slot of the same length directly cut at the chamber wall. The electromagnetic fields seen by the discontinuities of the hidden slot are suppressed because of the exponential drop-off of the fields into the groove, and consequently the wakefield excitaiton is also reduced exponentially. Third, TE mode traveling waves excited in the ring will radiate into the pump chamber through the slots which may damage the ion pumps. The use of holes instead of slots along the grooves can suppress the TE radiation at the expense of increasing the impedance. In the PEP-II design, 1288 hidden holes each with diameter 3 mm are cut along each groove. Measurements showed that no radiation was observed through the holes [6]. Fourth, the slots are slanted at 45° to protect the distributed ion pumps from single bounce X-rays scattered from the opposite side of the chamber walls.

The impedance of the DIP screen can be separated into two parts: the impedance of the grooves and the impedance of the hidden holes. The impedance of the six grooves

is found to be 1.88×10^{-4} nH. The hidden hole structure is shown in Fig. 7; only half of the structure is modeled because of symmetry. The longitudinal wakefield is shown in Fig. 8, from which the impedance of a column of holes in the six grooves is found to be 4.82×10^{-7} nH. Taking into account of 1288 holes in each groove, the total contribution of all the 192 DIP screens in the HER to the impedance is 0.16 nH, which is less than 1% of the ring impedance budget.

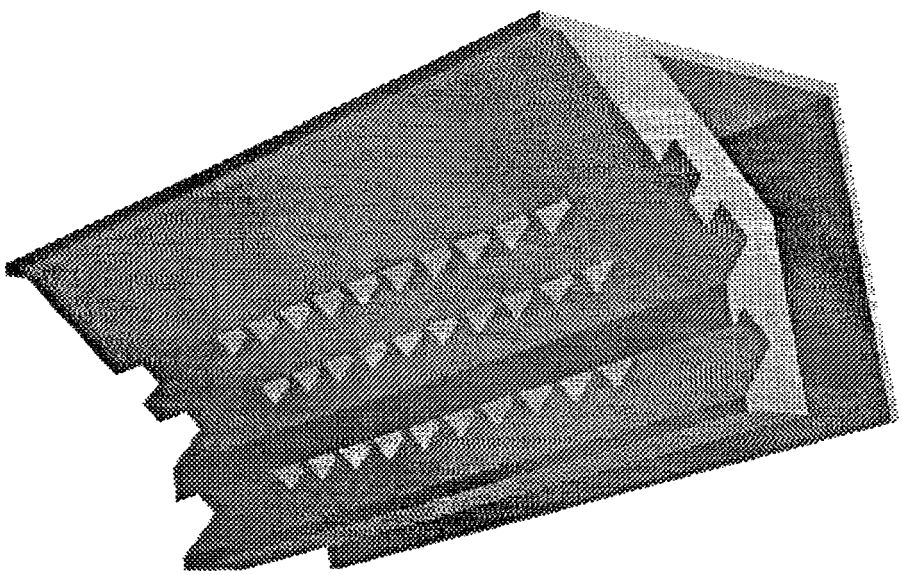

Figure 7: MAFIA model of the PEP-II DIP screen. Ten hidden holes are used in the calculation.

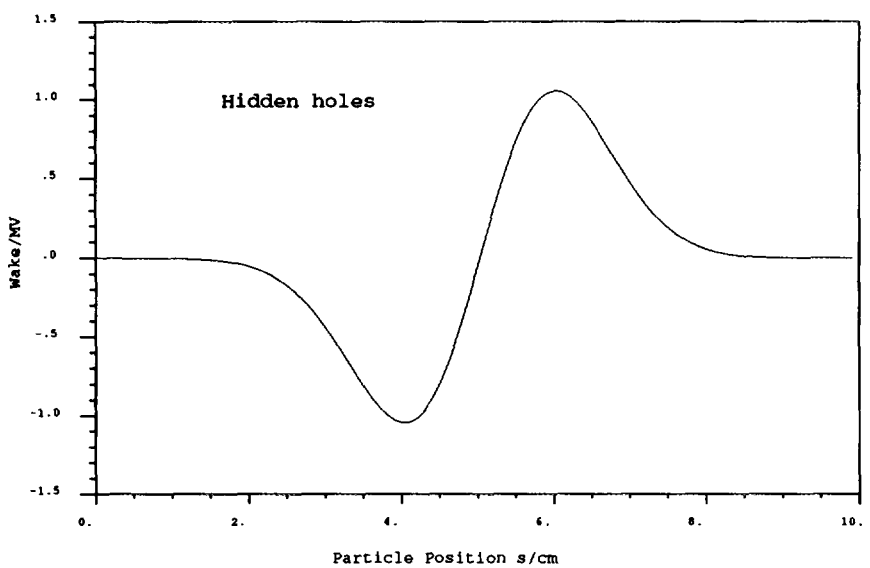

Figure 8: Longitudinal wakefield of the hidden hole structure shown in Fig. 7

6 Summary

The PEP-II DIP screen design uses hidden holes in continuous long grooves which reduces the longitudinal broad-band impedance to very small value, decreases the narrow-band impedance below the limit for coupled-bunch instabilities, and suppresses TE radiation into the pump chambers.

Acknowledgements

We thank A. Chao, E. Daly, S. Heifets, G. Lambertson, M. Nordby and G. Stupakov for useful discussions.

References

[1] An Asymmetric B Factory, Conceptual Design Report, LBL-PUB-5379 or SLAC-418, June 1993.

[2] T. Weiland, Low impedance Vacuum Chambers, PEP-II Technical Note No. 59, 1994.

[3] C.-K. Ng and T. Weiland, Impedance Analysis of the PEP-II Vacuum Chamber, to be published in Proc. of PAC95.

[4] K. L. F. Bane and C.-K. Ng, Impedance Calculations for the Improved SLC Damping Rings, Proc. 1993 PAC, p3432.

[5] G. V. Stupakov, Coupling Impedance of a Long Slot and an Array of Slots in a Circular Vacuum Chamber, SLAC-PUB-6698, 1994.

[6] J. Corlett, private communication.

Pumping Slots: Impedances and Power Losses

Sergey Kurennoy
University of Maryland, Department of Physics,
College Park, MD 20742, USA

Abstract

Contributions of pumping slots to the beam coupling impedances and power losses in a B-factory ring are considered. While their leading contribution is to the inductive impedance, for high-intensity machines with short bunches like e^+e^- B-factories the real part of the impedance and related loss factors are also important.

Using an analytical approach we calculate the coupling impedances and loss factors due to slots in a ring with an arbitrary cross section of the vacuum chamber. Effects of the slot tilt on the beam impedance are also considered, and restrictions on the tilt angle are derived from limitations on the impedance increase. The power leakage through the slots is discussed briefly.

The results are applied to the KEK B-factory.

1 Introduction

A common tendency in design of modern high-intensity accelerators is to minimize beam-chamber coupling impedances to avoid beam instabilities and reduce wall heating. From this viewpoint, narrow slots oriented along the chamber axis are the best choice for pumping holes since they provide the highest ratio of their pumping area to the contribution of slots to the broad-band impedance, e.g., [1]. However, if a long slot has some small tilt with respect to the chamber axis (for example, due to manufacturing errors), its beam impedance can be much higher than that of an untilted slot. In the present paper limitations on the allowed value of the tilt angle are analyzed.

At low frequencies the coupling impedance of slots is mostly inductive. To achieve high luminosity, the e^+e^- B-factory design requires high currents (of the order of or above 1 A) and rather short bunches (with r.m.s. length $\sigma \leq 1$ cm), see [2]. Because of the short bunch length, the beam sees coupling impedances up to very high frequencies, a few tens of GHz, and due to the high currents it can create essential heat deposition via higher-order mode losses. Therefore, it is important to know the coupling impedances of the chamber elements, including the real part, up to rather high frequencies to calculate loss factors and beam power losses.

In Section 2 the analytical approach used is shortly described, and then it is applied to analyze the slot tilt effects. A modification for long slots is also considered. Using these results, an expression for the loss factor of long slots on the vacuum chamber of an arbitrary cross section is derived in Section 3. Specific results for the low (LER) and high energy ring

(HER) of the KEK B-factory are given in Section 4, as well as a discussion of the power leakage through slots.

2 Coupling Impedance of Slots

2.1 Analytical Theory

An analytical theory for calculating coupling impedances of small discontinuities of the vacuum chamber including pumping holes and slots based on the Bethe theory of diffraction on small holes [3] has been developed in Refs. [4, 5, 6].

Let us consider an infinite cylindrical pipe with an arbitrary cross section S and perfectly conducting walls. The z axis is directed along the pipe axis. A slot in the chamber wall has width w and length l, $w \ll l$, and its center is located at the point $(\vec{b}, z = 0)$. We assume that a typical slot size h (i.e., its width w) satisfies $h \ll b$, where b is a typical size of the chamber cross section. Let $\hat{\nu}$ be an outward normal unit vector to the boundary ∂S, $\hat{\tau}$ be a unit vector tangent to ∂S in the chamber cross section S, and $\{\hat{\nu}, \hat{\tau}, \hat{z}\}$ form a right-handed basis.

In the frequency range where the wavelength is large compared to the typical hole size h, and at distances l such that $h \ll l \ll b$, the fields scattered by the hole into the beam pipe are equal to those produced by effective electric P and magnetic M dipoles [3]

$$\begin{aligned} P_\nu &= -\chi\varepsilon_0 E^h_\nu/2; \quad M_\tau = (\psi_{\tau\tau}H^h_\tau + \psi_{\tau z}H^h_z)/2; \\ M_z &= (\psi_{z\tau}H^h_\tau + \psi_{zz}H^h_z)/2 \ , \end{aligned} \tag{1}$$

where superscript 'h' means that the external (beam [4, 5] or corrected, self-consistent [6]) fields are taken at the hole. Then the coupling impedance produced by an arbitrary-shaped hole can be expressed in terms of its electric and magnetic polarizabilities, χ and ψ [4, 5, 6].

These polarizabilities are purely geometrical factors and depend on the hole shape. For example, for a circular hole of radius a in a thin wall $\psi = 8a^3/3$ and $\chi = 4a^3/3$ [3]. In general, ψ is a symmetric 2D-tensor, which can be diagonalized. If the hole is symmetric, and its symmetry axis is parallel to $\hat{z}$, the skew terms vanish, i.e., $\psi_{\tau z} = \psi_{z\tau} = 0$. In a more general case of a non-zero tilt angle α between the major symmetry axis and $\hat{z}$,

$$\begin{aligned} \psi_{\tau\tau} &= \psi_\perp \cos^2\alpha + \psi_{||} \sin^2\alpha \ , \\ \psi_{\tau z} &= \psi_{z\tau} = (\psi_{||} - \psi_\perp)\sin\alpha\cos\alpha \ , \\ \psi_{zz} &= \psi_\perp \sin^2\alpha + \psi_{||} \cos^2\alpha \ , \end{aligned} \tag{2}$$

where $\psi_{||}$ is the longitudinal magnetic polarizability (for the external magnetic field along the major axis), and $\psi_\perp$ is the transverse one (the field is transverse to the major axis of the hole).

The longitudinal impedance at low frequencies is dominated by its inductive imaginary part [7]

$$Z(k) = -\frac{ikZ_0\tilde{e}^2_\nu}{2}(\psi_{\tau\tau} - \chi) \ , \tag{3}$$

where $Z_0 = 120\pi\ \Omega$ is the impedance of free space, $k = \omega/c$, and $\tilde{e}_\nu$ is merely a normalized electrostatic field produced at the hole location by a filament charge placed on the chamber axis.

For a narrow slot with length l and width w such that $w \ll l$, the relation $\psi_{\|} \gg \psi_{\perp}$ holds. If the slot is untilted, i.e., $\alpha = 0$, the only contribution to the magnetic polarizability comes from $\psi_{\perp}$:

$$\psi_{\tau\tau} = \psi_{\perp}; \quad \psi_{\tau z} = 0 \ .$$

The leading terms in χ and $\psi_{\perp}$ for $w \ll l$ are the same:

$$\chi \simeq \psi_{\perp} = Cw^2 l + O(w^3) \ , \tag{4}$$

where the value of coefficient C depends on the slot shape, see in [1]. Due to cancellation of these leading terms in the difference $(\psi_{\tau\tau} - \chi)$, the imaginary part of the impedance Eq. (3) is independent of the slot length for narrow long slots. For example, for a narrow rectangular slots with rounded ends in a thin wall (wall thickness $t \ll w$), $C = \pi/8$ in Eq. (4) and

$$\psi_{\tau\tau} - \chi \simeq 0.267w^3 - 0.1w^4/l \ . \tag{5}$$

For the case of a thick wall, $t \gg w$, coefficient C is smaller, $C = 1/\pi$, and the impedance is also reduced, see in [5].

The function $\tilde{e}_{\nu}^2$ gives the impedance dependence on the slot position in the cross section of the vacuum chamber. For a particular case of a circular pipe of radius b, $\tilde{e}_{\nu} = 1/(2\pi b)$. In the case of the KEKB LER $b = 50$ mm, see Section 4 for a detailed description. For a rectangular chamber of width a and height b with a hole located in the side wall at $x = a, \ y = y_h$

$$\tilde{e}_{\nu} = \frac{1}{b}\Sigma\left(\frac{a}{b}, \frac{y_h}{b}\right) \ , \tag{6}$$

where

$$\Sigma(u, v) = \sum_{l=0}^{\infty} \frac{(-1)^l \sin[\pi(2l+1)v]}{\cosh[\pi(2l+1)u/2]} \tag{7}$$

is a fast converging series; the behavior of $\Sigma(u, v)$ versus v for different values of the aspect ratio u is plotted in [7]. The impedance decreases very fast if the slot is displaced closer to the corners of the chamber, i.e., when $y_h \to b$ or $y_h \to 0$.

For a general cross section one can use a 2D electrostatic code to calculate $\tilde{e}_{\nu}^2$. For example, the KEKB HER chamber has the rectangular cross section 104×50 mm^2 with rounded ends of radius 25 mm. In the NEG part of the chamber the large dimension is the horizontal one, and 6 rounded-end slots 4×100 mm^2 are located symmetrically with respect to the horizontal plane on the rounded part of the chamber in planes inclined to the horizontal one by the angles 4.4°, 13.3°, and 22.1°. In the Q part of the HER chamber the large dimension of the same cross section is oriented vertically, and 6 symmetric slots 4×120 mm^2 are on the flat wall at angles 9.1°, 25.6°, and 38.7° from the horizontal plane. Figure 1 shows the function $\tilde{e}_{\nu}^2$ for the KEKB HER chamber, normalized to that for a circular pipe of radius 50 mm (LER), versus the slot position ($\varphi = 0$ corresponds to the plane of the largest chamber dimension). Note a strong dependence of the slot impedance on the slot position in the cross section of the chamber.

The real part of the slot impedance [6] is non-zero only above the lowest cut-off frequency of the chamber[1]

$$ReZ(k) = \frac{k^3 Z_0 \tilde{e}_{\nu}^2}{8}\left\{\psi_{\tau z}^2 \sum_s^{<} \frac{k_s'^2 \left(h_s^h\right)^2}{k^2 \beta_s'} + \psi_{\tau\tau}^2 \left[\sum_s^{<} \frac{\left(\nabla_{\nu} e_s^h\right)^2}{\beta_s k_s^2} + \sum_s^{<} \frac{\beta_s' \left(\nabla_{\tau} h_s^h\right)^2}{k^2 k_s'^2}\right]\right. \tag{8}$$

[1] As long as the radiation through the slot is neglected, cf. [6]

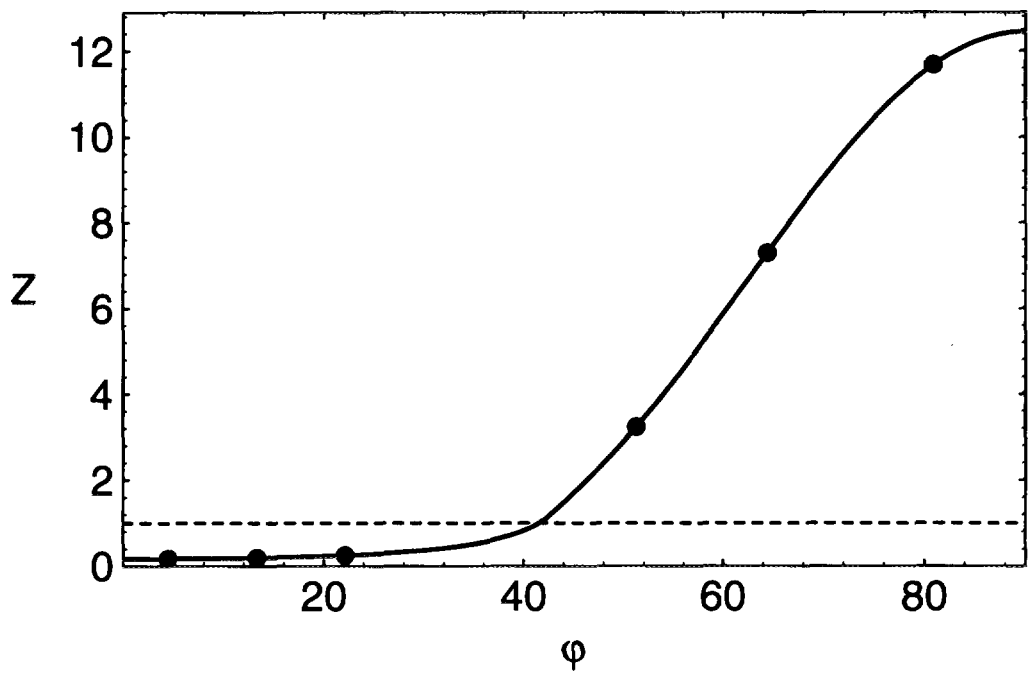

Figure 1: Slot impedance (in units of that for circular pipe of radius 50 mm) versus slot position (φ/degrees) in the HER chamber cross section

$$+ \chi^2 \left[\sum_s^{<} \frac{\beta_s \left(\nabla_\nu e_s^h\right)^2}{k^2 k_s^2} + \sum_s^{<} \frac{\left(\nabla_\tau h_s^h\right)^2}{\beta_s' k_s'^2} \right] \Bigg\} ,$$

where $s = \{nm\}$ is a generalized index, $\beta_s = (k^2 - k_s^2)^{1/2}$, $\beta_s' = (k^2 - k_s'^2)^{1/2}$, and the sums include only a finite number of the eigenmodes propagating in the chamber at a given frequency, i.e., those with $k_s < k$ or $k_s' < k$. Here k_{nm}^2, $e_{nm}(\vec{r})$ are eigenvalues and orthonormalized eigenfunctions (EFs) of the 2D boundary problem in S:

$$\left(\nabla^2 + k_{nm}^2\right) e_{nm} = 0 \; ; \qquad e_{nm}|_{\partial S} = 0 \; , \tag{9}$$

where $\vec{\nabla}$ is the 2D gradient in plane S. Similarly, EFs h_{nm} satisfy the boundary problem (9) with the Neumann boundary condition $\nabla_\nu h_{nm}|_{\partial S} = 0$, and $k_{nm}'^2$ are corresponding eigenvalues.

At frequencies well above the chamber cutoff, the dependence of $Re\, Z$ on frequency can be derived as follows [6]. The average number $n(k)$ of the eigenvalues k_s (or k_s') which are less than k, for $kb \gg 1$, is

$$n(k) \simeq \frac{S}{4\pi} k^2 + O(k) \; , \tag{10}$$

where S is the area of the cross section. Using this property, one can replace sums in the RHS of Eq. (8) by integrals as $\sum_s^< \to \int^k dk \frac{d}{dk} n(k)$. The result is

$$Re\, Z = \frac{Z_0 k^4 \tilde{e}_\nu^2}{12\pi} (\psi_{\tau\tau}^2 + \psi_{\tau z}^2 + \chi^2) \; . \tag{11}$$

The same answer has been obtained [7] simply by calculating the energy radiated by the dipoles into a half-space. The reason is clear: at high frequencies the dipoles radiate into the waveguide the same energy as into an open half-space.

The transverse coupling impedance has the same dependence on the polarizabilities as the longitudinal one, see in [7, 6].

2.2 Modification for Long Slots

Rigorously speaking, Eqs. (8)-(11) are restricted to wavelengths large compared to the slot length. For higher frequencies or longer slots (but still for wavelengths larger then the slot width), one can modify the Bethe approach replacing the slot by a distribution of dipoles and taking into account phase shifts in excitation and radiation of these dipoles depending on their longitudinal position [8]. It does not change the result for the imaginary part, Eq. (3), but modifies $Re\, Z$.

Taking into account that for long slots $\psi \simeq \chi$ ($\simeq w^2 l/\pi$ in a thick wall), we get

$$Re Z(k) = \frac{Z_0 k \tilde{e}_\nu^2 (\psi/l)^2}{4} \left\{ \sum_s^< \frac{\left(\nabla_\nu e_s^h\right)^2}{\beta_s k_s^2} [1 - \cos kl \cos \beta_s l] + \sum_s^< \frac{\left(\nabla_\tau h_s^h\right)^2}{\beta_s' k_s'^2} [1 - \cos kl \cos \beta_s' l] \right\} \; . \tag{12}$$

Figure 2 shows the real part of the slot impedance for the LER as a function of frequency.

2.3 Effects of Slot Tilt on Impedance

2.3.1 Restrictions due to $Im\, Z$

As was discussed above, for an untilted narrow long slot the imaginary part of the impedance (3) is independent of the slot length due to the cancellation of the leading terms in $(\psi_{\tau\tau} - \chi)$, see Eqs. (4). However, if the slot is tilted by some small angle $\alpha \ll 1$, the situation changes drastically since its large longitudinal magnetic polarizability $\psi_{||}$ also contributes, cf. Eqs. (2):

$$\psi_{\tau\tau} = \psi_\perp + (\psi_{||} - \psi_\perp/2)\alpha^2 + O(\alpha^4) \; . \tag{13}$$

The ratio of impedances of the tilted and untilted slot as a function of the tilt angle is

$$\frac{Z(k,\alpha)}{Z(k)} \equiv 1 + \delta(\alpha) \simeq 1 + \alpha^2 \frac{\psi_{||}}{\psi_\perp - \chi} \; . \tag{14}$$

Respectively, if the maximal allowed fraction of the impedance increase δ is given, Eq. (14) gives a restriction on the allowed tilt angle:

$$\alpha < \left(\delta \, \frac{\psi_\perp - \chi}{\psi_{||}} \right)^{1/2} \; . \tag{15}$$

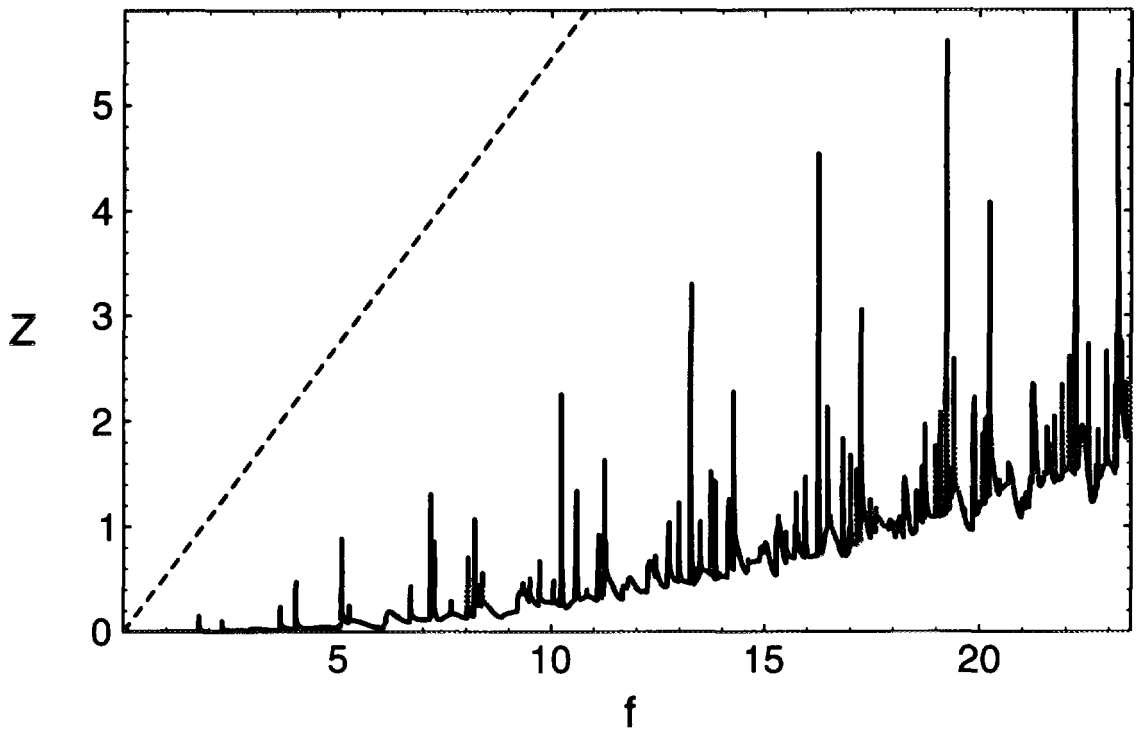

Figure 2: Longitudinal impedance ($Z/\mathrm{m}\Omega$) per slot versus frequency (f/GHz): the real part (solid line) is small compared to the imaginary one (dashed).

For a specific case of a narrow rectangular slots with rounded ends in a thin wall, the polarizabilities in Eq. (14) are

$$\psi_{\|} = \frac{\pi l^3}{12}\left(\ln\frac{8l}{w} - \frac{7}{3}\right)^{-1} \quad ; \qquad \psi_{\perp} - \chi \simeq 0.267 w^3 \ . \tag{16}$$

Then from Eq. (14) follows

$$\delta(\alpha) \simeq \alpha^2 \left(\frac{l}{w}\right)^3 \left(\ln\frac{8l}{w} - \frac{7}{3}\right)^{-1} \ , \tag{17}$$

and restriction (15) takes the form

$$\alpha < \sqrt{\delta}\left(\frac{w}{l}\right)^{3/2}\left(\ln\frac{8l}{w} - \frac{7}{3}\right)^{1/2} \ . \tag{18}$$

Figure 3 shows this restriction for different values of the slot aspect ratio w/l.

2.3.2 Restrictions due to $Re\, Z$

In a similar way, considering an increase of the real part of the impedance due to a small tilt of the slot gives

$$\frac{Re\, Z(k,\alpha)}{Re\, Z(k)} \equiv 1 + \delta_R(\alpha) \simeq 1 + \alpha^2 \frac{\psi_{\|}^2}{\psi_{\perp}^2 + \chi^2} \ . \tag{19}$$

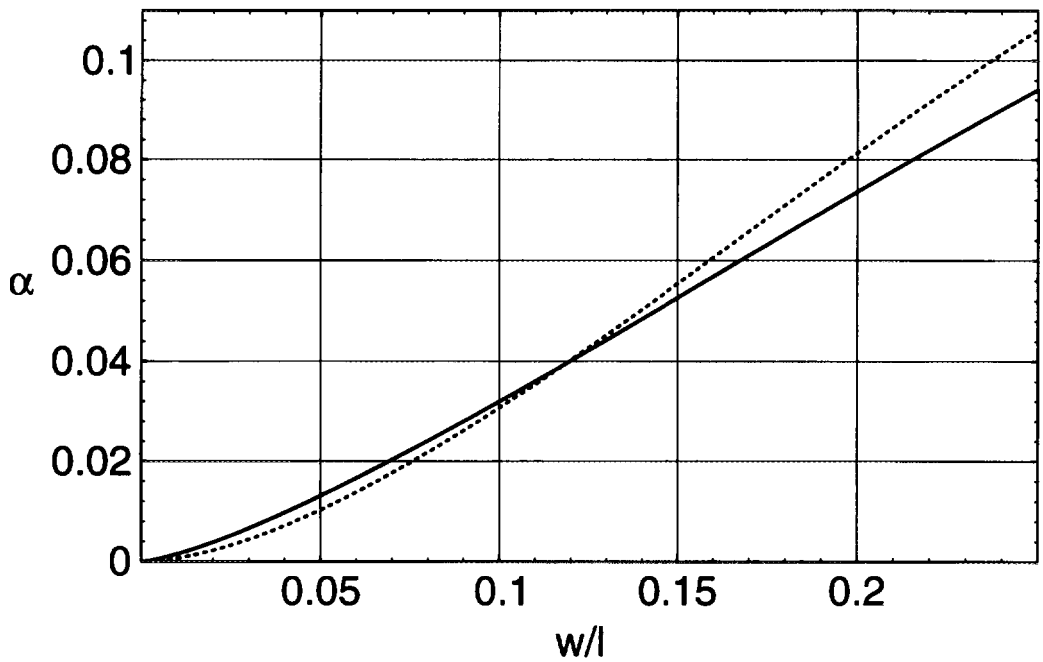

Figure 3: Allowed tilt angle (α/radian) versus slot aspect ratio w/l for $\delta = 0.5$: solid line is due to $Im\, Z$, dotted one is from $Re\, Z$.

For the case of a narrow rounded-end slot, this leads to

$$\delta_R(\alpha) \simeq \frac{2}{9}\alpha^2 \left(\frac{l}{w}\right)^4 \left(\ln\frac{8l}{w} - \frac{7}{3}\right)^{-2} , \tag{20}$$

and the restriction on the tilt takes the form

$$\alpha < 3\sqrt{\delta/2}\, \left(\frac{w}{l}\right)^2 \left(\ln\frac{8l}{w} - \frac{7}{3}\right) . \tag{21}$$

One can see that $Re\, Z$ gives the restrictions on the slot tilt similar to those due to $Im\, Z$, cf. Fig. 3.

2.3.3 Averaged Limitations

One should note that in practice the impedance increase $\delta(\alpha)$ has to be averaged with a corresponding tilt angle distribution. Assuming a Gaussian distribution due to manufacturing errors with average tilt $\bar{\alpha} = 0$ and r.m.s. tilt angle α_0, the average value of the increase $\bar{\delta}$ will be given again by Eq. (17) with substitution $\alpha \to \alpha_0$, since $\delta \propto \alpha^2$. Figure 3 remains valid for this case also, if δ is considered now as an averaged value over the Gaussian distribution with r.m.s. α. Note also that the allowed tilt angle scales as $\sqrt{\delta}$.

The restrictions on the tilt angle of long slots from impedance requirements obtained above are rather tough for very long slots. They are shown in Fig. 3 for the case of a

narrow rectangular slot with rounded ends: the maximal allowed angle for a given impedance increase (taken to be $\delta = 0.5$, i.e., 50%) is plotted versus slot aspect ratio w/l. For the KEKB LER, where the ratio $w/l = 0.04$, it means that the limit on the allowed tilt angle is $\alpha \simeq 0.01$ rad $\simeq 0.6°$ to prevent the slot impedance from increasing more than 50%.

2.4 Near Cutoff: Trapped Modes

It has been demonstrated [9] that a small discontinuity, such as a hole or slot, as well as an enlargement on a smooth waveguide can result in the appearance of trapped electromagnetic modes with frequencies slightly below the waveguide cutoff frequencies. The trapped modes produce narrow resonances of the coupling impedance near the cutoff. For a circular waveguide with many small discontinuities the phenomenon has been studied in [10], and for the case of an arbitrary chamber in [6]. Using results [9, 10], in this section we consider the trapped modes in the LER (in fact, only TM-modes since TE-waves easily leak out through the slots and, therefore, their trapping obviously fails to exist).

There are $M = 8$ pumping slots in one transverse cross section of the LER. With respect to the lowest TM_{01} trapped mode, all M slots in such a group work as a chamber enlargement with "effective" area A in its longitudinal cross section [9]:

$$A = \frac{M\psi_{\tau\tau}}{4\pi b} = \frac{Mw^2 l}{4\pi^2 b} = 6.5 \text{ mm}^2 .$$

The frequency shift down from the TM_{01} cutoff frequency $f_1 \simeq 2.3$ GHz for the trapped mode is

$$\frac{\Delta f}{f_1} = \frac{\mu_1^2}{2}\left(\frac{A}{b^2}\right)^2 \simeq 2 \cdot 10^{-5} , \tag{22}$$

where $\mu_1 \simeq 2.405$ is the first root of Bessel function J_0; i.e., $\Delta f \simeq 45$ kHz. This gap between the trapped mode frequency and the cutoff is rather small, being only marginally larger than the resonance width due to the energy dissipation in the walls

$$\gamma_1/\omega_1 = \delta/(2b) \simeq 1.35 \cdot 10^{-5} ,$$

where δ is skin-depth in the copper.

However, the length of the region which would be occupied by the field of the trapped mode for such a single discontinuity is $l_1 = b^3/(\mu_1^2 A) = 3.3$ m. Since this length is longer than the longitudinal separation $g = 1$ m between the adjacent groups of the pumping slots, the adjacent groups interact each other. According to [10], the number of discontinuities, which work as a single combined one, is $N_{eff} = \sqrt{2l_1/g} \simeq 2.6$, and the new "effective" length of interaction $L = \sqrt{l_1 g/2} = 1.3$ m. Due to this interaction the frequency gap increases $\Delta f \to N_{eff}^2 \Delta f \simeq 0.3$ MHz, which makes it large compared to the resonance width, so that the trapped mode can exist.

Should discontinuities be far separated, $g > l_1$, the total impedance of the ring would be just a sum of contributions $R_1 = Z_0 \mu_1^3 A^3/(\pi \delta b^5)$ from all $N = 2\pi R/g$ discontinuities on the ring (R is the machine radius): $Re\, Z/n = NR_1/n = 2\pi b R_1/(g\mu_1)$. The interaction of discontinuities changes the estimate above by replacements $N \to N/N_{eff}$ and $R_1 \to N_{eff}^3 R_1$

$$\frac{Re\, Z}{n} = N_{eff}^2 \frac{2\pi b}{g\mu_1} R_1 = \frac{4 Z_0 A^2}{\delta b g^2} . \tag{23}$$

It gives $Re\, Z/n \simeq 1\ \Omega$ for the narrow-band impedance produced by the trapped modes in the LER. This value for the narrow-band coupling impedance at such a high frequency does not seem to be dangerous.

In fact, the pumping slots are not quite identical, they have some distribution of areas. It causes a frequency spread of resonances produced by different discontinuities, and can reduce the total narrow-band impedance due to the trapped modes essentially, see [10] for details.

3 Beam Power Losses

The power per unit length of the beam chamber dissipated due to beam fields scattered by the slots is

$$P' = \frac{N_{sl}}{S_b} f_{rev} q_b^2 K \ , \tag{24}$$

where N_{sl} is the total number of slots, S_b is the bunch spacing, $f_{rev} = c/(2\pi R)$ is the revolution frequency, q_b is the bunch charge. The loss factor per slot K is defined as

$$K = \frac{1}{\pi} \int_0^\infty d\omega\, Re\, Z(\omega) \exp\left[-\left(\frac{\omega\sigma}{c}\right)^2 \right] \ , \tag{25}$$

where $\sigma = \sigma_z$ is the r.m.s. bunch length.

Substituting Eq. (12) into Eq. (25), for long slots and short bunches, when $l/\sigma \gg 1$, one can replace fast oscillating functions in the integrand by their average values. Then the integrals are evaluated analytically, which yields a simplified expression for the loss factor

$$K = \frac{Z_0 c\, \tilde{e}_\nu^2 (\psi/l)^2}{8\pi^{1/2}\sigma} \left\{ \sum_s^\infty \frac{\left(\nabla_\nu e_s^h\right)^2}{\beta_s k_s^2} \exp(-k_s^2\sigma^2) + \sum_s^\infty \frac{\left(\nabla_\tau h_s^h\right)^2}{\beta_s' k_s'^2} \exp(-k_s^2\sigma^2) \right\} \ . \tag{26}$$

This expression for the particular case of a circular pipe of radius b becomes

$$K = \frac{Z_0 c (\psi/l)^2}{16\pi^{7/2} b^4 \sigma} \cdot \left\{ \sum_{n=0}^\infty \sum_{m=1}^\infty \frac{1}{1+\delta_{n,0}} \exp\left[-(\mu_{nm}\sigma/b)^2 \right] + \right. \tag{27}$$
$$\left. + \sum_{n=1}^\infty \sum_{m=1}^\infty \frac{n^2}{\mu_{nm}'^2 - n^2} \exp\left[-(\mu_{nm}'\sigma/b)^2 \right] \right\} \ ,$$

where μ_{nm} is mth zero of the Bessel function $J_n(x)$, and μ_{nm}' satisfy $J_n'(\mu_{nm}') = 0$. This result was obtained earlier in [11][2]. Figure 4 shows the loss factor per slot for different values of the r.m.s. bunch length σ for the KEKB LER. The design value for the KEK B-factory is $\sigma = 4$ mm. The numbers in Fig. 4 were checked using a more complicated expression than Eq. (27) including length-dependent terms: the results are very close to those in Fig. 4 for these large values of l/σ.

The dependence $K(\sigma)$ in Fig. 4 can be roughly approximated as $K \propto \sigma^{-3}$, cf. [11]. To check this dependence, we consider a rectangular pipe of cross section $a \times b$, in which case

[2]The overall factor in Ref. [11] was incorrect: it should be multiplied by $1/(4\pi^2)$.

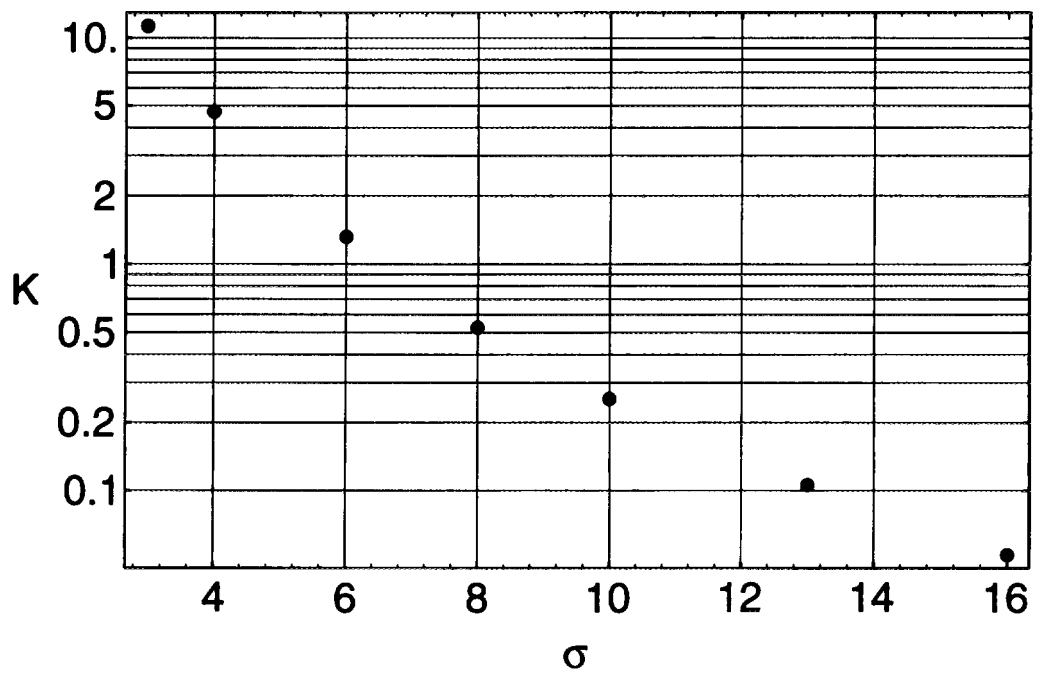

Figure 4: Loss factor per slot $[K/(10^{-6}\mathrm{V/pC})]$ versus r.m.s. bunch length (σ/mm).

the eigenvalues and EFs have simple form, and summation in Eq. (26) for short bunches can be carried out easily. The resulting loss factor is

$$K \simeq \frac{Z_0 c(\psi/l)^2}{16\pi^{3/2}\sigma^3}\tilde{e}_\nu^2 = \frac{Z_0 c(\psi/l)^2}{16\pi^{3/2}b^2\sigma^3}\,\Sigma^2\left(\frac{a}{b},\frac{y_h}{b}\right)\,, \tag{28}$$

where Σ is defined by Eq. (7). In this case, $K \propto \sigma^{-3}$ explicitly. It can be proved also for an arbitrary cross section in the case of long slots, when $l/\sigma \gg 1$ but still $\sigma > w$, using the property (10) of the eigenvalues. Replacing sums in the RHS of Eq. (26) by integrals as $\sum_s^< \to \int^k dk \frac{d}{dk} n(k)$ and performing integrations yields $K \propto \sigma^{-3}$. As follows from Eq. (25), it means that effectively for long slots the averaged behavior of the real part of the impedance is

$$\overline{Re\,Z} \propto k^2\,. \tag{29}$$

For comparison, for holes or short slots $Re\,Z \propto k^4$, see Eq. (11), and according to Eq. (25) the loss factor $K \propto \sigma^{-5}$.

4 Results for KEK B-factory

4.1 KEKB Low Energy Ring

The LER vacuum chamber is a circular pipe with inner radius $b = 50$ mm and wall thickness $t = 6$ mm. The circumference of the ring is 3016 m, and about 1800 m of the beam pipe have long pumping slots to connect it with pumping chambers containing the NEG pumps. The slots are of rectangular shape with rounded ends, with width $w = 4$ mm and length $l = 100$ mm. They are located in groups of 8 parallel slots near the bottom of the beam pipe — 8 slots per meter — with the total number of pumping slots in the LER about 14400.

Another type of slots in the LER vacuum chamber are narrow longitudinal slots 1.2 mm$\times$ 35 mm in RF connectors. The number of slots per connector is 40, with about 100 connectors in the ring.

As was mentioned in Section 2, for a thick wall, the impedance should be multiplied by a thickness correction factor [5]. This factor is about 0.6 for long elliptic holes [5], but it is unknown for the case of a very long slot with rounded ends and parallel sides. For a cautious estimate one can take this factor equal to the ratio of the leading terms of the polarizabilities for an infinitely long slot in a thick and thin wall, namely $8/\pi^2$ [1]. Due to additivity of the impedances at frequencies below the chamber cutoff frequency (2.3 GHz), the analytical results of Section 2 give reliable estimates of the LER total coupling impedances due to slots in this frequency range, see Table 1.

Table 1: Reactive Impedances of LER Slots

Slots	$\lvert Z/n\rvert$/ mΩ	$\lvert Z_\perp\rvert$/ (kΩ/m)
Pumping	0.8	0.6
RF connectors	0.1	0.035

Since the pumping slots in LER are located near the bottom of the chamber, they contribute mostly to the vertical transverse impedance (the value in Table 1), cf. Ref. [7].

The design value of the beam current in the LER is 2.6 A, bunch spacing is 0.6 m, and the number of bunches is 5120. Using results of Section 3, we calculate loss factors and beam power losses due to the beam interaction with the slots in the LER, see Table 2.

Table 2: Power Losses due to LER Slots

Slots	K / (V/pC)	P' / (W/m)
Pumping	$4.6 \cdot 10^{-6}$ per slot	0.3
RF connectors	$1.5 \cdot 10^{-6}$ per conn.	-

One can conclude that the broad-band impedances of the slots are on the level of a few percent of the total estimated impedance budget of the LER, $|Z/n|_{tot} \simeq 15$ mΩ [2], and the power loss is rather small compared to that due to synchrotron radiation.

4.2 KEKB High Energy Ring

The KEKB HER chamber has the rectangular cross section 104×50 mm^2 with rounded ends of radius 25 mm, and the wall thickness is $t = 6$ mm. In the NEG part of the chamber the large dimension is the horizontal one, and 6 rounded-end slots 4×100 mm^2 are located symmetrically with respect to the horizontal plane on the rounded part of the chamber, see description in Section 2.1. In the Q part of the HER chamber the large dimension of the same chamber is oriented vertically, and 6 rounded-end slots 4×120 mm^2 are symmetrically located on the flat wall. The total coupling impedances of the slots are calculated as described in section 2.1, and the results are shown in Table 3. All HER slots contribute only to the horizontal transverse impedance.

Table 3: Reactive Impedances of HER Slots

Slots	$\lvert Z/n\rvert$/ mΩ	$\lvert Z_\perp\rvert$/ (kΩ/m)
NEG	0.4	1.5
Q	0.7	0.8

Due to the lower beam current in the HER (1.1 A instead of 2.6 A in the LER), the power loss due to HER slots a few times lower than that in the LER, see above.

4.3 Power flow through slots to the pumping chamber

A few possible sources of power leakage through the slots to pumping chambers are discussed, and estimates are given for the KEKB LER taken as an example [11].

4.3.1 Power flow due to direct beam fields on the slots

When the beam field illuminates a slot, it produces scattered fields both inside the beam pipe and outside, in the pumping chamber. The energy radiated by these outside fields into the pumping chamber can be calculated in the same way as for the beam pipe. One should only use so-called "external" polarizabilities of slots instead of the "internal" ones which we used above, cf. [5]. For the case of the thick wall (thickness t is larger than the slot width w) these "external" polarizabilities are much smaller than the "internal" ones:

$$(\psi, \chi)^{ext} \simeq \exp(-\pi t/w)\ (\psi, \chi)\ . \tag{30}$$

Since the power loss is proportional to the polarizabilities squared, one can easily realize that the power flow to the pumping chamber due to this source is negligible:

$$P_1' \simeq \exp(-2\pi t/w)\ P_{in}' \simeq 0.03\ \text{mW/m}\ .$$

4.3.2 Power flow from transverse currents due to the beam betatron motion

One should note that the relation (30) works only for the electric and transverse magnetic polarizabilities. The term "transverse" here means that the beam magnetic field is directed

perpendicular to the slot largest dimension, and this is correct for the case of the beam longitudinal motion when there is only the azimuthal component of the beam magnetic field. However, if the transverse motion of the beam is taken into account there is also some longitudinal magnetic field of the beam on the slot. In this case the longitudinal magnetic dipole moment is induced on the slot. It is proportional to the longitudinal magnetic polarizability of the slot, which is equal to [1]

$$\psi_{\|} = \frac{\pi l^3}{12}\left(\ln\frac{8l}{w} + \frac{\pi t}{2w} - \frac{7}{3}\right)^{-1} , \tag{31}$$

and is much larger than the transverse one, $\psi_{\perp} = w^2 l/\pi + O(w^3)$, for long slots. In addition, its "internal" and "external" values are almost equal, because the magnetic field parallel to the slot easily penetrate through it. So, we have to estimate the power flow due to this effect.

Since the power radiated in TE-modes $P'_H \propto Re\, Z \propto M^2$, where $M = \psi H/2$ is the effective magnetic dipole moment induced by the beam magnetic field H on the slot, we will consider the ratio

$$r = \frac{M_z}{M_\varphi} = \frac{\psi_{\|} H_z}{\psi_{\perp} H_\varphi} . \tag{32}$$

The ratio of fields H_z/H_φ can be approximated by the ratio of the beam current components, $j_{\perp}/j \simeq \nu/n$, where $\nu \simeq 45$ is the betatron frequency, and $n = \omega/\omega_0$ is the longitudinal harmonic number, with $\omega_0 = c/R$ being the revolution frequency. Then

$$r = \frac{\pi^2 l^2}{12 w^2}\left(\ln\frac{8l}{w} + \frac{\pi t}{2w} - \frac{7}{3}\right)^{-1} \frac{\nu\omega_0}{\omega} , \tag{33}$$

which is about 0.2 at the beam pipe cutoff frequency. We are interested in frequencies above the chamber cutoff, and because (33) decreases with frequency increase, one can conclude that the power flow into the pumping chamber P'_2 from this source is less than 1/25 of the power radiated in TE-modes into the beam pipe, which is about one half of the total P', i.e., about 0.15 W/m, see Table 2. As a result,

$$P'_2 < 6 \text{ mW/m} .$$

4.3.3 Power flow due to the fields scattered by slots to the beam pipe

It is mentioned above that the total power P' radiated by slots into the beam pipe is divided almost evenly between TM- and TE-modes: $P'_E \simeq P'_H \simeq P'/2 = 0.15$ W/m. These modes propagate in the beam pipe and reach following slots. For TM-waves penetration through the longitudinal slots is exponentially small, see above. However, TE-waves have a longitudinal magnetic field (the wall currents are transverse to the slots), and contribute to the energy flow into the pumping chamber. The minimal (optimistic) estimate for that power flow would be

$$P_3'^{min} = \frac{A_{sl}}{A_{wall}} P'_H \simeq 4 \text{ mW/m} ,$$

where $A_{sl}/A_{wall} = 0.025$ is the fraction of the wall surface occupied by slots. On the other hand, the most pessimistic (maximal) estimate is to assume that the total energy of TE-modes will leak out through slots:

$$P_3'^{max} = P'_H \simeq 0.15 \text{ W/m} .$$

Of course, a part of the energy in TE-modes will be lost in the walls of the beam pipe, so the last number gives the upper estimate.

Concluding this section, one should mention that there is one more source of the power leakage through the slots to the pumping chamber: TE-modes generated in the vacuum chamber by the beam due to its interaction with large elements like RF chambers, etc. Such modes can easily leak out through long slots. This source is believed to be the most dangerous one, however, it is difficult to make estimates for the related power flow. A simple remedy to prevent the power flow to the pumping chamber (due to this or all other sources of HOM) would be placement of thin metallic grids on the outer part of the pumping slots.

5 Summary and Conclusions

The analytical methods are applied to analyze effects of the beam interaction with pumping slots in the vacuum chamber of a B-factory. Using earlier obtained analytical expressions, the slot contributions to the longitudinal and transverse broad-band coupling impedance are calculated for the LER and HER of the KEK B-factory. The existence of the trapped modes due to the slots and their contribution to the narrow-band impedance are considered.

New analytical results include an analysis of the influence of the slot tilt on the coupling impedance and derived restrictions on the tilt angle. Besides that, an expression for the loss factor of long slots for the case of short bunches is derived for an arbitrary cross section of the vacuum chamber. Using this result, the power losses due to the beam interaction with pumping slots in the KEK B-factory are calculated. The power flow through the slots to the pumping chamber is also discussed.

The specific calculations for the KEK B-factory show that the pumping slots contribute a few percent to the total broad-band coupling impedance budget. The trapped modes due to the slots (if any) can produce only a small narrow-band impedance at frequencies near the chamber cutoff. Calculated beam power losses are small compared to those from synchrotron radiation, and the power flow to the pumping chamber is well below the allowed level.

The author would like to thank the KEK for the partial support of his participation in the workshop. This work was also supported in part by the U.S. Department of Energy.

References

[1] S.S. Kurennoy, SSC Lab Report SSCL-636, Dallas, 1993; in *Proceed. of the 4th EPAC*, edited by V. Suller *et al*, (London, 1994), p.1286.

[2] Y.H. Chin, in *these Proceedings.*

[3] H.A. Bethe, Phys. Rev. **66**, 163 (1944).

[4] S.S. Kurennoy, Part. Acc. **39**, 1 (1992).

[5] R.L. Gluckstern, Phys. Rev. A **46**, 1106, 1110 (1992).

[6] S.S. Kurennoy, R.L. Gluckstern, and G.V. Stupakov, in *Proceed. of PAC95* (Dallas, 1995); Phys. Rev. E **52**, No. 4 (to appear in Oct. 1995).

[7] S.S. Kurennoy, in *Proceed. of the 3d EPAC*, edited by H. Henke *et al*, (Berlin, 1992), p.871; more details in Institute for High Energy Physics (Protvino) Report No. IHEP 92-84, 1992 (unpublished).

[8] G.V. Stupakov, Phys. Rev. E **51**, 3515 (1995).

[9] G.V. Stupakov and S.S. Kurennoy, Phys. Rev. E **49**, 794 (1994).

[10] S.S. Kurennoy, Phys. Rev. E **51**, 2498 (1995).

[11] S.S. Kurennoy and Y.H. Chin, KEK Preprint 94-193, Tsukuba, 1995.

Bellows Design and Testing for KEKB

Y.Suetsugu
National Laboratory for High Energy Physics,
1-1 Oho, Tsukuba, Ibaraki 305, Japan

Abstract

A bellows assembly with an RF-shield has been developed for the KEK B-Factory (KEKB). The RF-shield is a usual finger-type but has a special spring-finger to press the contact-finger on to the beam tube without fail. The mechanical workings of the RF-shield is tested using a trial model and no mechanical problem is found except for the dust production. The necessary contact force, 50 g/finger, is obtained experimentally transmitting the 508 MHz microwave up to 80 kW through the trial model.

I. Introduction

In parallel to the general design of vacuum system, the bellows assembly with an RF-shield has been developed and tested for the KEK B-Factory (KEKB)[1]. The RF-shield screens the corrugations of bellows from bunched beams and makes the wall current flow smoothly to reduce the excitation of the higher order mode (HOM) [2-4]. The maximum beam current of the Low Energy Ring (LER) of the KEKB is 2.6 A with 5000 bunches and 4 mm bunch length. The peak current and the RMS current are 156 A and 17 A, respectively. The RF-shield has to keep a good electrical contact while absorbing the thermal expansion and contraction during beam operations or baking.

The usual RF-shield is the finger-type which consists of lots of narrow sliding fingers around the beam tube to bridge the gap of bellows [2,3]. Each finger (we call it as the contact-finger here) should touch the beam tube with a appropriate contact force to keep a sufficient electrical contact. The most important point for the finger-type RF-shield is the strength of the contact force. The larger the force, of course, the better the electrical contact, but the more intense the abrasion (dust generation) during the mechanical workings. There has been, however, no practical data for the contact force so far.

We developed a bellows assembly with a RF-shield of usual finger-type but having the special spring-fingers other than the usual contact-fingers to press surely the contact-fingers on to the beam tube. The mechanical test was performed using a trial

model To find the necessary contact force experimentally, the excess heating was checked transmitting the 508 MHz microwave up to 80 kW through the model. We report here the structure of the bellows assembly and the results of the experiments.

II. Structure

The bellows assembly designed for the KEKB LER is schematically drawn in Fig. 1. The main components of the RF-shield are the inner tube, the contact-finger and the spring-finger. The contact-fingers are pressed on to the inner tube from outside of it by the spring-fingers with an appropriate contact force. The electrical contact is kept at the edge of the inner tube. Since the contact-finger is outside of the inner tube, the impedance of bellows assembly is small sufficiently. For 1 mm thick inner tube, for example, the calculated broad band impedance (Z/n) and the loss factor (k) of a bellows assembly for the LER are 4.23×10^{-6} W and 2.5×10^{-3} V/pC, respectively. Every spring-finger presses one contact finger independently. The contact-finger does not have to provide a spring action and can be made of a thin metal strip. The contact force, therefore, does little change even if the bellows is bent or set with some transverse offsets due to misalignment. For the KEKB, the RF-shield should absorb the expansion/contraction of 20 mm and the offset of 1 mm, but no tilting (shearing). The required lifetime is 10^5 times for the expansion/contraction with 1 mm stroke. The cooling water channels are attached considering the reflected power of the synchrotron radiation (SR), Joule loss and HOM loss at the inner surface.

Figure 2 shows the outlook of a trial model of the bellows assembly (bellows and RF-shield). The model is for the LER and has a circular cross section. The inner diameter is 94 mm and the nominal total length is 160 mm. The contact-finger is 0.2 mm thick Beryllium-Copper (C1720) and has the width of 5.5 mm and the gap of

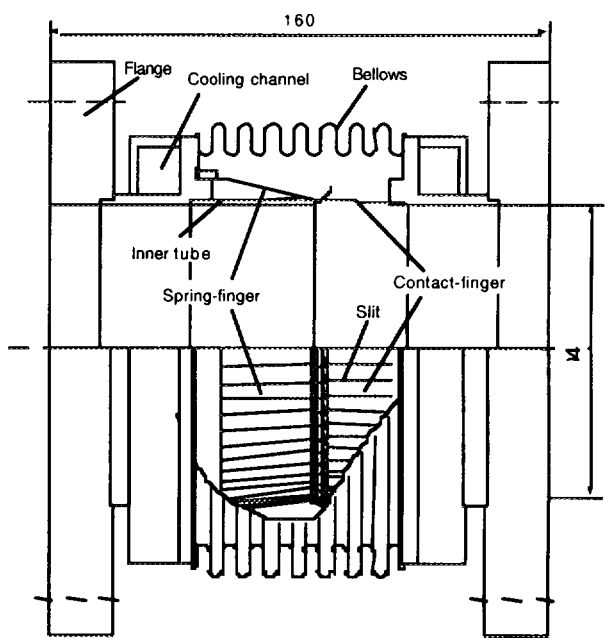

Figure 1. Schematic drawing of the bellows assembly for LER.

0.5 mm. The spring-finger is also 0.3 mm thick Beryllium-Copper (C1720) with the width of 4.6 mm and the gap of 2.4 mm. The tip of the spring-finger, where the spring-finger pushes the contact-finger, has a curvature of 5 mm and is coated with TiN (1 μm thick). Both of the contact-fingers and the spring-fingers received the heat treatment at 315 °C. The inner tube is 1 mm thick Stainless Steel (SS304) and is surrounded by 50 contact-fingers. Other parts of the bellows assembly is also made of Stainless Steel.

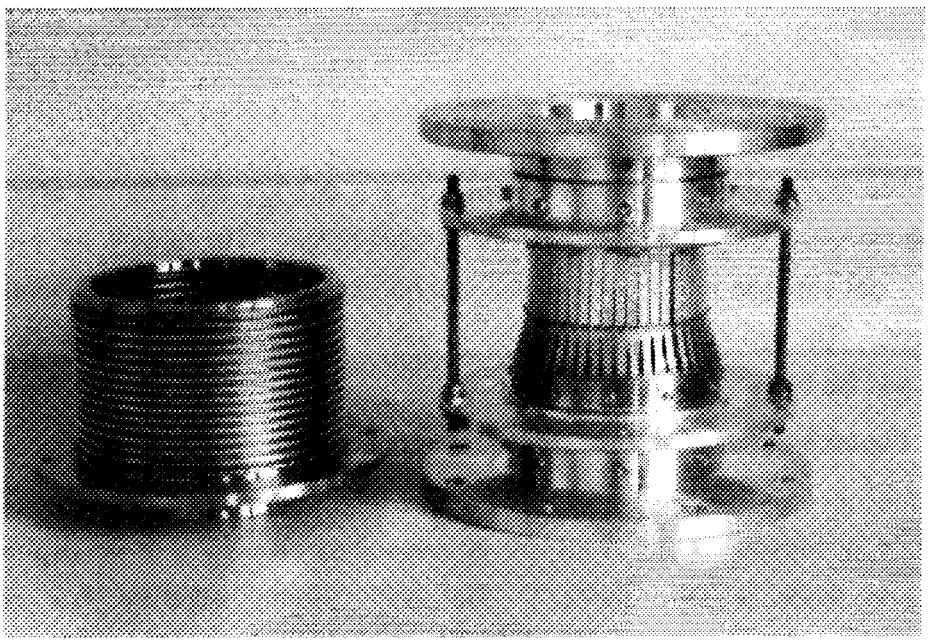

Figure 2. Out look of the bellows (left) and the RF-shield (right).

III. Mechanical Working Test

The mechanical workings of RF-shield was tested using the trial model in atmosphere and under the pressure of 1×10^{-2} Torr. The RF-shield was expanded and contracted for 5000 times with 20 mm stroke in atmosphere. The contact forces were in the range of 150 - 170 g/finger. One stroke took about 10 seconds. We observed no kinking or sticking of contact-fingers and found no mechanical problem.

However, we observed lots of metal dusts generated during the working due to the abrasion between the contact-fingers and the inner tube or the spring-fingers [3]. The mean size of dusts was about 50 μm. The dust generation is a serious problem because the dusts will do harm to the stored beam by shortening the lifetime or broadening the beam size when passing through or trapped to the beam. Actually the dust generation

reduces by several orders in vacuum because most of the dusts are the metal particles oxidized immediately after the detachment from the surface. The dust generation, however, is inevitable for the finger-type RF-shield to some extent. An approach to reduce the particle is to choose appropriate combination of the materials or the coatings for the fingers. We are now undergoing the abrasion test using some practical materials, such as Beryllium-Copper with and without TiN coating, Hastelloy or Inconel. The second effective solution is to choose a sufficient but not excess contact force. We have tried to find the minimum contact force experimentally as described in the following section.

IV. Necessary Contact Force

We transmitted the high-power microwave through the bellows assembly and check the excess heating of it changing the contact force. The microwave was applied because it can simulate more realistic wall current excited by the bunched beam than the DC current. The bellows model is similar to that descried in Sec.2 but has the length of 200 mm and the body of Aluminum alloy.

Figure 3 shows a schematic diagram of the experimental apparatus. The 50 Ω coaxial transmission line was formed by the trial model and an inner rod inside. The 508 MHz CW microwave up to 80 kW is transmitted through it in atmosphere. The transmission mode is TEM mode. The wall current, therefore, has only axial component that is just the same as the real wall current in the beam tube. The microwave was supplied from a 10 MW klystron used for the RF cavity of the TRISTAN Main Ring.

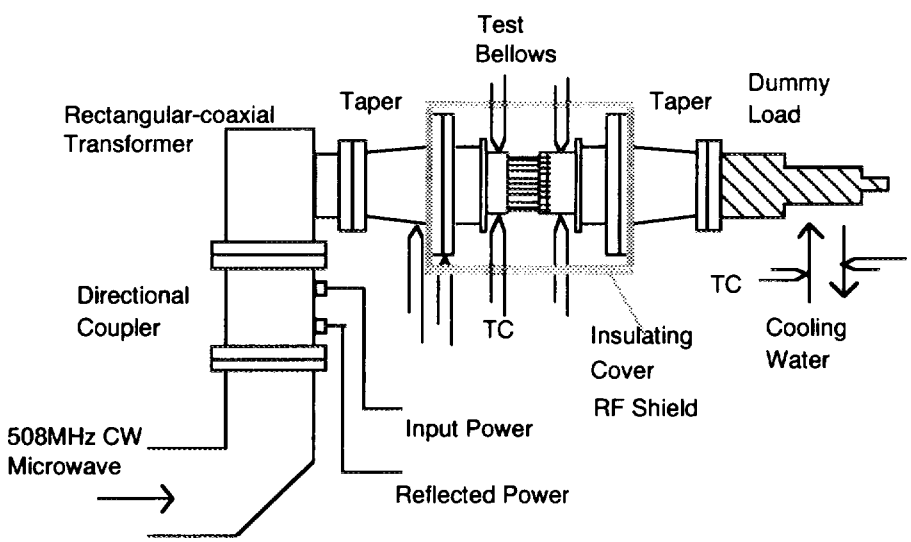

Figure 3. Set up for the test to find necessary contact force using 508 MHz microwave.

The input power was stepped up by 10 or 20 kW and kept for about 10 minutes at each power level. About 14 kW microwave power serves the same RMS wall current with the 2.6 A operation at the LER. The bellows assembly was insulated thermally and the increase of temperatures of the RF-shield (spring fingers, contact fingers and beam tubes just near the fingers) was measured at every step. The power losses at the bellows assembly for several contact forces were estimated from the surface resistance, the specific heat and the increase of temperature.

The power losses per 10 kW input are plotted against the contact forces in Fig.4. For the average contact forces less than 50 g/finger the excess heating was observed. In this case the color change due to the high temperature and also the arcing spots were found on the contact-fingers after the experiment. The dotted line in the figure is the result for the case of the minimum power loss, that is, calculated without any contact resistance.

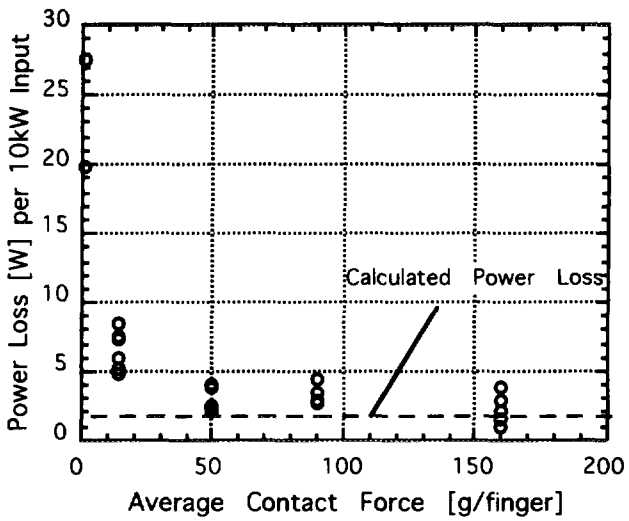

Figure 4. The power loss at the bellows assembly per 10 kW input of 508 MHz microwave for several contact forces. The dotted line is the calculated power loss.

The results indicate that the contact force larger than 50 g/finger is necessary. Considering the manufacturing or setting error, however, the spring finger should be designed to provide the contact force of 100 g/finger at least. This value is much less than that in the mechanical working test (about 170 g/finger), and the problem associated with metal particles may be reduced. Attention should be paid, however, that the experiment was performed in atmosphere, where the water vapor in the air will work as a lubricant.. Furthermore, the frequency of wall current in the experiments is far low compared to those in the real beam tube. The test using 2856 MHz microwave to check the arcing in vacuum is now in preparation.

V. Summary

The bellows assembly with the RF-shield is developed for the KEKB. The RF-shield is a finger-type but has the special spring-finger to press the contact-finger without fail. The minimum contact force was surveyed experimentally transmitting the

microwave up to 80 kW through the bellows assembly in atmosphere. The contact force larger than 50 g/finger was found to be necessary to avoid the excess heating. The test to check the arcing in vacuum is now in preparation. The test to find the best combination of finger materials to reduce the dust generation is also undergoing.

Acknowledgments

The authors would like to thank the members of TRISTAN Vacuum Group in KEK for their useful discussions. The authors also express their deep appreciation to H.Nakanishi of TRISTAN RF Group for their lots of valuable suggestions and kind instructions on RF experiments.

References

[1] H.Hisamatsu, H.Ishimaru, K.Kanazawa, S.Kato, M.Nakagawa, M.sato, M.Shimamoto, Y.Suetsugu and N.Terunuma, To be published in *Proc. 13th Int. Vac. Conf. & 9th Int. Conf. Slid Surface*, Yokohama (1995).

[2] R.Ballion, J.Boster, W.Giesske, H.Hartwig, D.Jagnow, R.Kose, J.Kouptsidis, G.Schumann and M.Schwartz, *Vacuum*, Vol.41, 1887 (1990).

[3] U.Wienands, E.Daly, S.A.Heifets, A.Kulikov, N.Kurita, M.Nordby, C.Perkins, E.Reuter, J.T.Seeman, F.C.Belser, J.Berg, F.R.Holdmer, J.A.Kerns, M.R.McDaniel and W.Stoeffle, To be published in *Proc. 1995 US PAC*, Dallas (1995).

[4] E.Ihloff, A.Averill, J.Flanz, K.Jacobs, S.Sobczynski, D.Wang and A.Zolfaghari, *Proc. 1993 US PAC*, p.3851, Washington, D.C. (1993).

DAMPED BUTTON ELECTRODE FOR B-FACTORY BPM SYSTEM

T. Shintake, N. Akasaka, T. Obina and Y. H. Chin
KEK:National Laboratory for High Energy Physics,
Oho 1-1, Tsukuba-shi, Ibaraki 305 Japan

Abstract

A new concept of damping of resonances in a button electrode has been proposed and tested in the BPM system for the B-Factory project at KEK (KEKB). Since a very high current beam has to be stored in the machine, even a small resonance in the ring will result in losing a beam due to multi-bunch instabilities. In a conventional button electrode used in BPMs, a TE110 mode resonance can be trapped in the gap between the electrode and the vacuum chamber. In order to damp this mode, the diameter of the electrode has been chosen to be small to increase the resonance frequency and to radiate the power into the beam pipe. In addition, an asymmetric structure is applied to extract the EM energy of the TE110 mode into the coaxial cable as the propagating TEM mode which has no cut-off frequency. Results of the computer simulations and tests with cold models are reported. The quality factor of the TE110 mode was small enough due to the radiation into the beam pipe even in the conventional electrode and the mode coupling effect due to the asymmetric shape was significant on a cavity-like TE111 mode.

I. Introduction

In the KEKB accelerator, the beam current will be of several amperes. Since the number of BPMs amounts to about 400 per ring, possible resonances in the gap is of serious concern to avoid coupled bunch instabilities. On the other hand, it is not necessary to take care very much of VSWR in a wide frequency range, since only 1 GHz component of the beam is detected for the beam position measurements. The resonances in the BPMs can be classified into two categories; one due to a button electrode and another due to a ceramic part that is used for a vacuum seal.

II. BPM Structure

We adopted the N-type vacuum feedthrough because it has an advantage of high power rating and the enough mechanical strength compared to that of the SMA type. Connectors will be brazed to the block of copper chamber.

The small button size has an advantage that can enhance the damping of the TE110 mode due to the radiation into the beam chamber. On the other hand, the minimum size of the button is limited to accomplish the required precision of the position measurements, i.e., better than 80 dB in the signal-to-noise ratio at the beam current of 10 mA. We determined the diameter of the button electrode to be 12 mm. The gap distance was determined to be 1 mm to avoid the multipactering discharge.

The structure of the asymmetric BPM is shown in Fig. 1. Three faces of the button are cut out to enhance its asymmetry, and are connected to the center conductor with a taper.

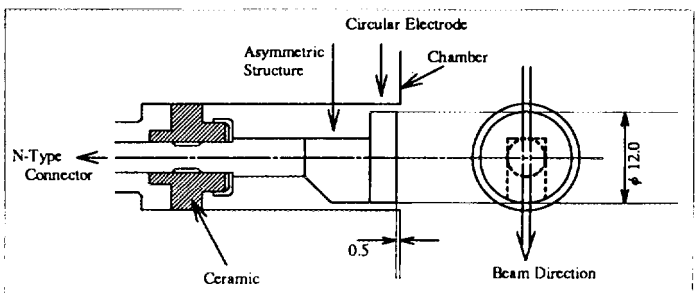

Figure. 1. Illustration of the damped BPM. The diameter of the disk is φ 12 mm and the gap size is 1 mm. The distance between the electrode surface and the wall is determined to be 0.5 mm to prevent the synchrotron radiation.

III. Computer Simulations

The damping efficiency of the asymmetric structure has been simulated with the computer code MAFIA. Resonance frequencies and mode patterns (monopole or dipole) are tabulated in Table I. The field pattern of the TE110 mode at 7.3 GHz is shown in Fig. 2. In this model, the BPM is not placed at the chamber wall but at the cylinder that has a magnetic-short boundary at the end.

Table I
Resonance frequency calculated with MAFIA.

frequency[GHz]	mode pattern	location (label in Fig. 5)
1.88	Monopole	
3.96	Monopole	
5.82	Dipole	ceramic (C1)
6.21	Monopole	coaxial (Coax)
7.30	Dipole	button (B1)
7.89	Dipole	ceramic (C2)
8.88	Monopole	

Among these modes, EM energy of the monopole modes are extracted to the outside of the BPM and have negligible effects on the beam instabilities. The dipole modes under cutoff frequency of the coaxial lines, however, are trapped inside the BPM. The electric field of the dipole mode at 5.8 GHz is localized at the ceramic, so that the

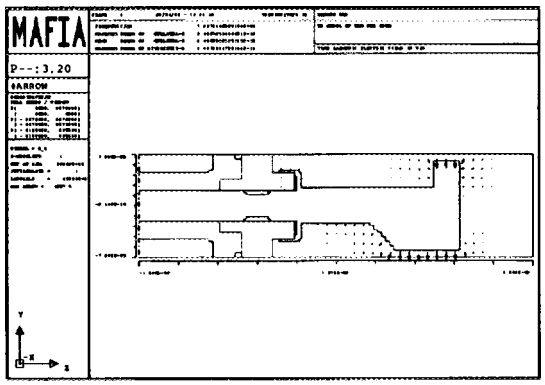

Figure. 2. Electric field pattern of the TE110 mode. EM energy is concentrated at the button electrode.

coupling between this mode and the beam is small. As shown in Fig. 2, the TE110 mode at 7.3 GHz is not effectively converted to TEM modes. The coupling between the two modes can be enhanced by increasing the length of the asymmetric structure. However, this method has a disadvantage of the dipole mode at the ceramic penetrating into the beam chamber.

The longitudinal wake potential was calculated for LER with MAFIA T3 assuming the bunch length of 4 mm. The diameter of the beam chamber is 147 mm. The result

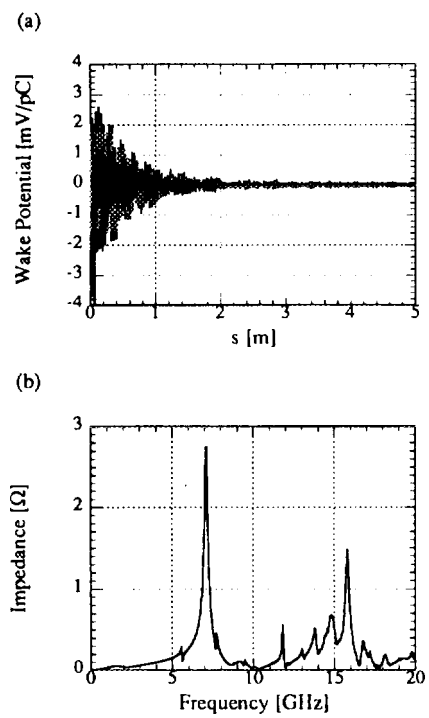

Figure. 3. Calculation of longitudinal wake field with MAFIA T3: (a) wake potentioal and (b) impedance. The bunch length is 4 mm.

is shown in Fig. 3(a). The loss parameter is 2.0 mv/pC. Fig. 3(b) is the absolute value of the impedance calculated from Fig. 3(a) by Fourier transformation. Two large peaks at 7.1 and 15.8 GHz are clearly seen. The least square fitting of these peaks gives their peak values and Q. The result is summarized in TableII.

Table II
Characteristics of the two peaks in Fig. 3(b).

frequency[GHz]	Impedance[Ω]	Q
7.1	2.9	43
15.8	1.4	82

IV. Experiments and Results

We measured at first the transmission characteristics (S_{21}) of the electrode with a setup shown in Fig. 4. The

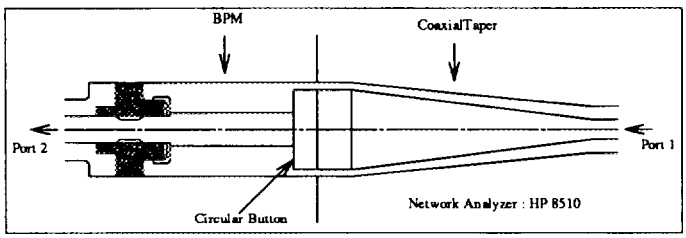

Figure. 4. The setup to measure the transmission characteristics of BPM.

TEM-mode signals are fed to the electrode through a taper. Figure 5 shows the S_{21} response of a conventional circular electrode. There are two sharp peaks at 6.2 GHz

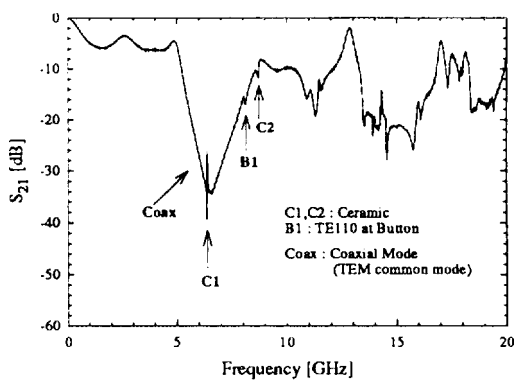

Figure. 5. S_{21} measurement of circular BPM.(Network Analyzer HP 8510)

and 8.8 GHz, which are labeled as C1 and C2 in the figure. We measured the S_{21} response without ceramic and found that these peaks are resonances in the ceramic. The difference between the calculation with MAFIA and the measurement is explained by two reasons: one is that the resonance frequency listed in the Table I is the calculation for the damped BPM, and the other is that the measured BPM is not brazed. The peak around 8 GHz, labeled as

B1, appears when the button electrode is placed at the off-center position. The broad peak labeled as Coax denotes the resonance of the whole coaxial structure. In this setup, it is difficult to measure the quality factor of the TE110 mode resonance because only the coaxial mode can be excited.

Next, we excited the TE110 mode directly with the setup shown in Fig. 6. Two probes inserted through $\phi 2$ mm

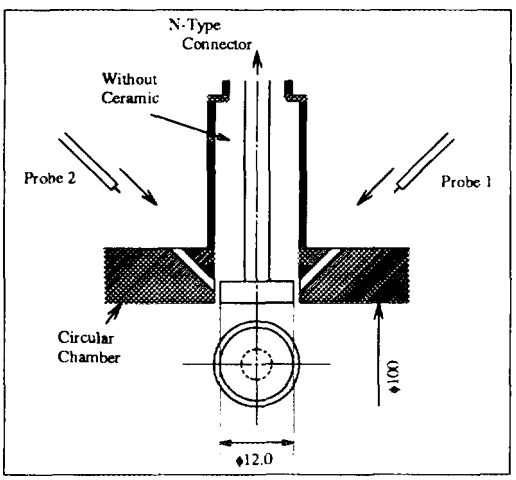

Figure. 6. Experimental setup of the TE110 measurement. Two semi-rigid cable is used as an antenna to excite the TE110 mode at the disk. The BPM was mounted on $\phi 100$ mm circular beampipe, at those ends absorbers were loaded.

holes excite the TE110 mode at the button electrode, while the N-type connector is connected to the matched load. To avoid ceramic resonances, we did not attach the ceramic part during this measurement.

Figure 7 shows the S_{21} spectrum of the circular electrode, where three large peaks are recognized. The first

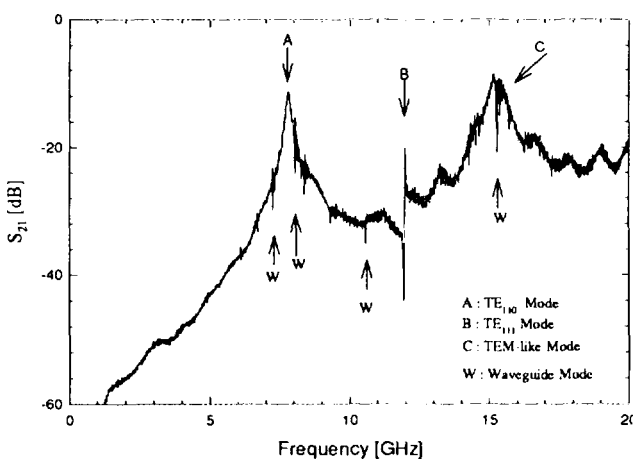

Figure. 7. Dipole mode resonance of the circular BPM.

peak around 7.8 GHz, marked as A, is TE110 mode at the electrode. This resonance frequency is consistent with the numerical results of MAFIA. The quality factor of the mode was estimated to be 40. Another measurement with an asymmetric electrode showed a small decrease of the quality factor.

The second peak marked as B in the figure is identified as the TE111 cavity mode inside the BPM. This mode is trapped in a coaxial volume behind the button. The resonance frequency of this mode is given by $k = \sqrt{k_z^2 + k_c^2}$, where k is the wave number of the resonance frequency, $\lambda_z (= 2\pi/k_z)$ the wavelength determined by the length of the electrode axis, k_c the cutoff wave number. The quality factor is about 300 with the circular electrode and about 50 with the damped electrode. Since this measurement did not include the ceramic part, the resonance frequency and the quality factor may be different from those of the actual BPM. We will investigate the coupling of this mode to the beam in near future.

The third peak marked as C is the TEM common-mode resonance. This mode is harmless because of its low quality factor and high coupling to the external circuit. There are several sharp peaks marked as W. These frequencies are identified as cutoff frequencies of TM_{nm} modes in a $\phi 100$ mm circular chamber.

V. Discussion

The beam current spectrum and the power spectrum of the KEKB are shown in Fig. 8, for a natural bunch length σ_z of 4 mm. This figure shows that we should avoid resonances in the frequency range below about 15 GHz.

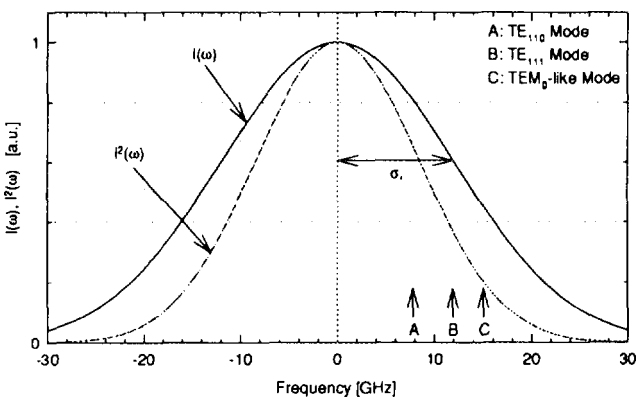

Figure. 8. The beam spectrum of KEKB for the natural bunch length $\sigma_z = 4$ mm. The solid line shows the beam current spectrum $I(\omega)$ and the dotted line shows the power spectrum $P(\omega) \propto I^2(\omega)$.

We estimate the growth time of the instability due to the TE110 mode. The R/Q is calculated from the loss factor k calculated with MAFIA and from the relationship [1]

$$k = \frac{\omega_r}{2}\left(\frac{R}{Q}\right) e^{-\omega_r^2 \sigma_t^2}, \qquad (1)$$

where ω_r is the resonance frequency and σ_t is the bunch length in units of time. The experimental results show the Q value of the TE110 mode is about 40, leading the peak impedance $R = 2.9\ \Omega$ per one BPM (4 buttons).

The growth rate of longitudinal coupled bunch instability is given by [2]

$$\tau^{-1} = \frac{\alpha N e^2}{2ET_0^2\omega_s} \sum_{p=-\infty}^{\infty} (p\omega_0 + \omega_s)\mathrm{Re}\left[Z(p\omega_0 + \omega_s)\right] \epsilon^{-\omega_r^2\sigma_t^2}, \tag{2}$$

where N is the number of electrons (positrons) in the ring and E is the beam energy. The calculated growth time of the instability is 48 ms in the LER and 58 ms in the HER, which are sufficiently larger than the radiation damping time of 43 ms in the LER and 23 ms in the HER. The calculation is made for the worst case, i.e. we take into account only one resonance of BPMs. Therefore, if we only think of the TE110 mode, we may adopt the circular button in the final design of the KEKB position monitors.

The TE111 mode exists only inside the BPM and it may affect little on the beam impedance, however, the coupling has not been estimated yet. Since the asymmetric structure have good damping effect on the mode, there is still some possibility of using the structure.

At last, we mention about the resonance in the ceramic briefly. Since it is difficult to damp these modes, we will optimize the thickness of the ceramic to detune the resonance from the RF harmonics.

Fabrication tests on brazing the electrode to the copper chamber is in progress. There still remain technical problems in the ceramic feedthrough, i.e., some of the feedthrough had vacuum leakage troubles after the brazing process. We are trying to optimize the detailed structure of ceramic part and sealing metal parts to meet both requirement of the brazing process and the RF impedance issues.

Acknowledgment

The authors wish to thank Dr. Y. Suetsugu who had designed and supported to manufacture the test chamber.

References

[1] P. B. Wilson, SLAC-PUB-2884, (1987)
[2] A. W. Chao, AIP Conf. Proc. 105(1983) p.353

Numerical Simulation of the PEP-II Beam Position Monitor*

N. Kurita, D. Martin, C.-K. Ng, S. Smith
Stanford Linear Accelerator Center
Stanford University, Stanford, CA 94309, USA

and

T. Weiland
University of Technology
FB18, Schlossgartenstr. 8
D64289, Darmstadt, Germany.

Abstract

We use MAFIA to analyze the PEP-II button-type beam position monitor (BPM). Employing proper termination of the BPM into a coaxial cable, the output signal at the BPM is determined. Thus the issues of signal sensitivity and power output can be addressed quantitatively, including all transient effects and wakefields. Besides this first quantitative analysis of a true BPM 3D structure, we find that internal resonant modes are a major source of high value narrow-band impedances. The effects of these resonances on coupled-bunch instabilities are discussed. An estimate of the power dissipation in the ceramic vacuum seal under high current operation is given.

*Work supported by Department of Energy, contracts DE-AC03-76SF00515.

1 Introduction

There are several issues of concern for the button-type BPMs in the PEP-II [1] vacuum chamber. First, the presence of BPMs in the vacuum chamber contributes significant impedances, broad-band and narrow-band. For broad-band impedance, the contribution of all the BPMs to the total impedance budget can be readily calculated. Narrow-band impedances arise from the formation of resonances or trapped modes in the BPM, which may have detrimental effects on the beams because of coupled-bunch instabilities, and which may produce heating effects above tolerable levels. Second, the power coming out of the cable connected to the BPM should not be too high such that it is within the handling capability of the diagnostic electronics, but not at the expense of losing the signal sensitivity at the processing frequency of 952 MHz. Third, the power carried by the trapped modes and by the signal, especially when the beam is offset, may produce considerable heating in the ceramic and metallic walls of the BPM. These issues are closely related to each other, thus increasing the complexity of designing the BPM. In view of these electrical and mechanical requirements, BPMs with 1.5-cm diameter buttons have been selected for the PEP-II.

The paper is organized as follows. In the next section, we describe the essential features of the MAFIA modeling of the BPM. The calculations are carried out in the time domain to obtain the wakefield and other relevant information. In section 3, we present the main results of the numerical simulation. The longitudinal broad-band and narrow-band impedances, the signal sensitivity and power output at the coaxial cable are calculated. We estimate the power dissipation in the ceramic vacuum seal in section 4. A summary of the results is given in section 5. In this paper, we are mainly concerned with the electrical properties of the BPM. The mechanical design of the BPM can be found in Ref. [2].

2 MAFIA Modeling

The detailed layout of the BPM in the arcs of the PEP-II High Energy Ring (HER) is shown in Fig. 1. Each BPM consists of four buttons, located symmetrically at the top and at the bottom of the vacuum chamber. The HER arc sections have totally 198 BPMs. There are 92 BPMs in the straight sections of the HER, and the four buttons are located symmetrically at 90° from each other at the circumference of the circular pipe. The BPM button is tapered in such a way that the impedance matches that of a 50 Ω coaxial line. A ceramic ring for vacuum insulation is located near the button region. It has a dielectric constant of about 9.5. The inner radius of the ceramic vacuum seal needs to be adjusted for optimum matching.

The 3D MAFIA model of the BPM is shown in Fig. 2. Because of symmetry, only one quarter of the structure is simulated. One button of the BPM is situated on the top of the vacuum chamber, and it tapers gradually to a coaxial line above. The simulation is done in the time domain, which consists of two kinds of calculations, namely wakefield and

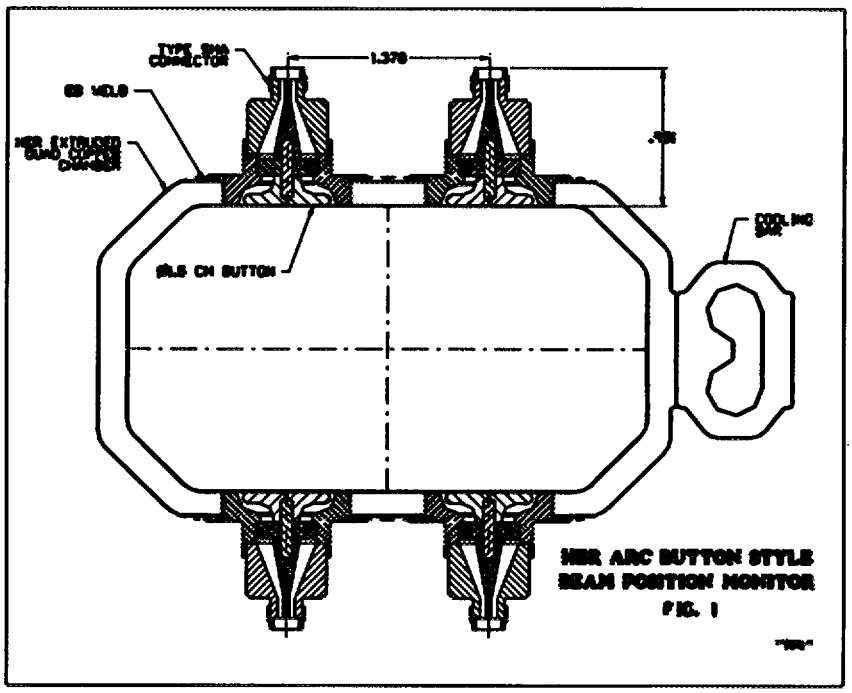

Figure 1: Layout of the 4 buttons of a BPM in the arcs of the HER vacuum chamber.

port transmission calculations. For wakefield calculation, a rigid beam comes in along the z-direction. It excites electromagnetic fields at the BPM, which in turn act back on the beam. The boundary conditions at the beam entrance and exit planes are set to waveguide boundary conditions so that electromagnetic waves traveling to these boundaries are not reflected. At the top boundary of the coaxial line, it is treated as an outgoing waveguide port, where the transmission of the signal is determined. A two-dimensional eigenvalue problem is first solved to determine the propagating and evanescent modes of the coaxial line. These modes are then loaded at the port in the 3D time domain calculation. Since the beam excites a broad frequency spectrum, a broad-band boundary has to be implemented at the waveguide port.

The impedance of a BPM can be evaluated from the wakefield or its Fourier transform. From the Fourier transform of the wakefield, we can identify potential resonant modes excited by the beam in the BPM. Since the resolution of narrow resonances in the impedance spectrum depends on the number of sampling points in the wakefield calculation, we evaluate the wakefield up to a long distance of $s = 5$ m, where s is the bunch coordinate. The transmission calculation at the port gives us the value of the outgoing voltage at the end of the coaxial line as a function of time, which corresponds to the signal picked up by the BPM as the beam passes through this region of the vacuum chamber.

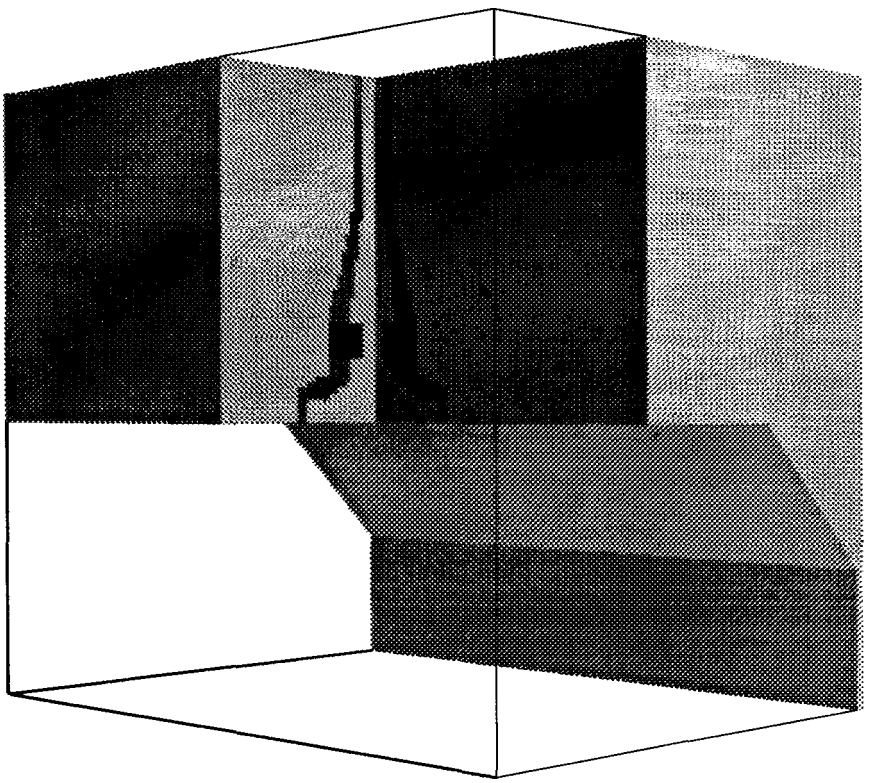

Figure 2: 1/4 MAFIA geometry of the BPM in the vacuum chamber. The button region is cut out for viewing purposes.

3 Longitudinal Impedances

The high beam current in the PEP-II B-Factory poses stringent requirements on impedances and power deposition. BPMs can generate considerable broad-band and narrow-band impedances. To avoid single-bunch instabilities, the accepted limit of the total broad-band effective impedance for the prescribed PEP-II current is $|Z/n|_{eff} = 0.5\ \Omega$ [1], where $n = \omega/\omega_{rev}$ is the harmonic number. It is desirable that BPMs contribute a small fraction to the total broad-band impedance budget. Narrow-band impedances can also be generated as a result of the excitation of trapped modes in the BPMs. Their values have to be controlled below some limits so that coupled-bunch instabilities will not occur. The most serious higher-order mode excited by the beam is the TE_{11} mode with respect to the button axis. Its frequency increases with a decrease in the diameter of the button. The acceptable limit of the narrow-band impedance for avoiding coupled-bunch instabilities is a function of the frequency $f = \omega/2\pi$ of the resonant mode and is given by [3]:

$$(\frac{Re[Z]}{k\Omega}) < 3.0(\frac{GHz}{f})e^{(\omega\sigma_z/c)^2}, \tag{1}$$

where σ_z is the bunch length. It should be noted that the above limit is a conservative

estimate since it takes into account of only radiation damping. Other damping mechanisms such as feedback will help suppress the narrow-band resonance. The numerical factor is given for the Low Energy Ring (LER) with a current of 3 A, and the limit is inversely proportional to the current. The exponential factor indicates the decay of the beam spectrum at high frequencies.

In the following, we present the numerical results from MAFIA simulations. In our simulations, a Gaussian bunch with $\sigma_z = 1$ cm is used and the total bunch length is 10σ's. For the coaxial port, at the range of frequency of interest, only the TEM mode propagates. Thus for the output signal at the coaxial line, we only need to consider this mode. The MAFIA results shown in the following figures are normalized to a bunch charge of 1 pC. The numerical results for impedance, power and other relevant quantities for the case with 3 A current (8.3×10^{10} per bunch) are listed in Table 1.

Energy loss by beam		126 W
Power out of one cable		9 W (37 W)*
Transfer impedance at 952 MHz		0.65 Ω
Broad-band impedance, $\|Z/n\|$		0.008 Ω (11 nH)
Narrow-band impedance:	MAFIA	6.5 kΩ at ~ 6.8 GHz
	accepted	3.4 kΩ

Table 1: Impedance and power of the 1.5-cm BPM. The beam current is 3 A. The impedances are for all the BPMs in the ring. *The power in the parentheses is that out of the cable which is closest to the beam when it is 1 cm offset from the axis.

In Fig. 3, we show the longitudinal wakefield as a function of the beam coordinate s. It can be seen that, for $0 \lesssim s \lesssim 10\sigma$, the wakefield is roughly inductive. The inductance of each BPM is estimated to be 0.04 nH or $|Z/n| = 3.4 \times 10^{-5}\Omega$. The total contribution of all the BPMs is 11 nH or $|Z/n| = 0.008\,\Omega$. The total broad-band impedance budget for all the ring elements is estimated to be 0.31Ω [4], and therefore the BPMs contribute a quite small fraction of it. By integrating the wakefield, the loss parameter of a BPM is found to be 2.7×10^{-3} V/pC. For $N = 8.3 \times 10^{10}$ and a bunch spacing of 1.2 m, this gives a power loss of 126 W by the beam. In Fig. 4, we show the impedance spectrum as a function of frequency. A sharp peak of 25 Ω is seen at around 6.8 GHz, which should be compared with the TE_{11} cutoff frequency of 6.4 GHz of an ideal coaxial waveguide with the button dimensions. The frequency and impedance of the TE_{11} mode are in satisfactory agreement with measurements [5]. The total impedance of all BPMs due to this resonant mode is 6.5 kΩ, which is about twice the accepted value calculated by Eq. 1. This resonance can be suppressed to a small value by introducing asymmetry [6, 7] at the button at the cost of increased mechanical complexity. Since the narrow-band impedance is small compared with the feedback power (~ 100 kΩ) used for damping the RF cavity higher-order modes, we rely on the feedback system to suppress this resonance.

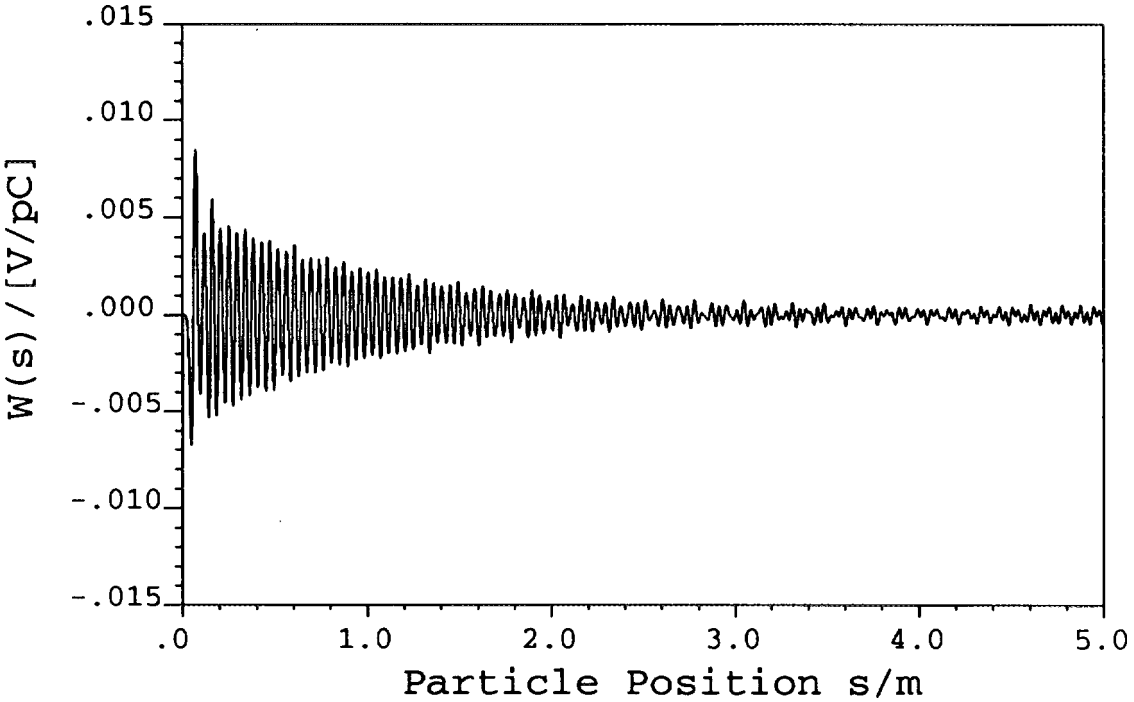

Figure 3: Longitudinal wakefield of the 1.5-cm BPM as a function of the particle position for a Gaussian bunch with $\sigma_z = 1$ cm.

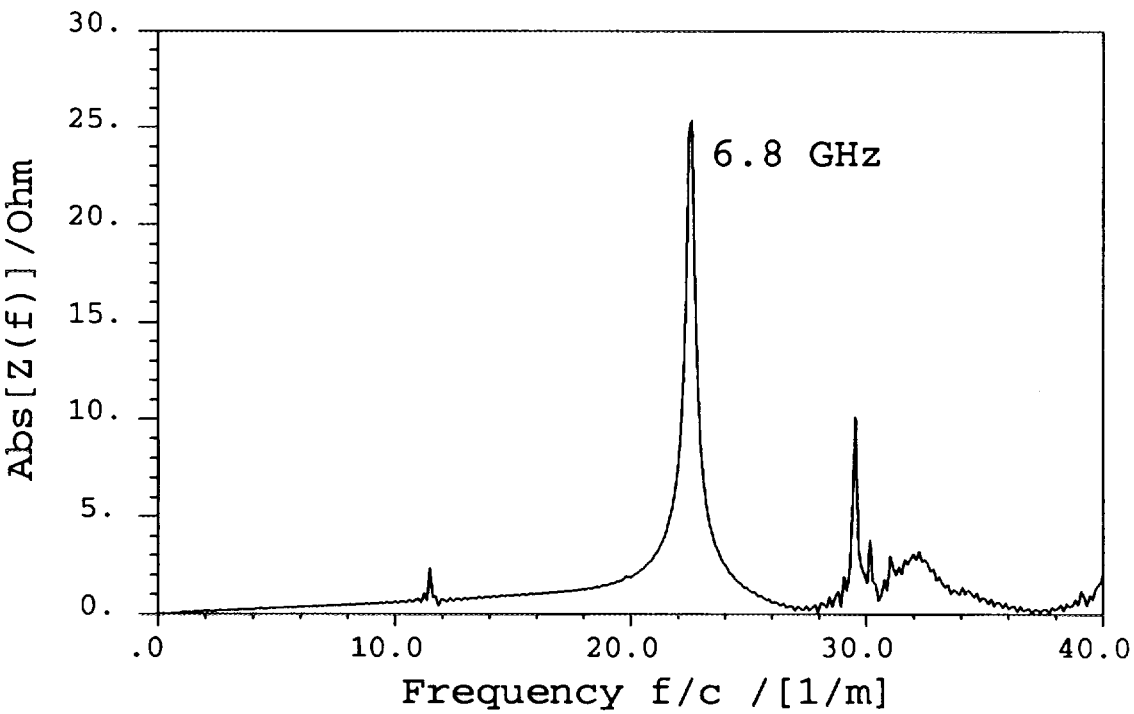

Figure 4: Longitudinal impedance spectrum of the 1.5-cm BPM as a function of the inverse wavelength for a Gaussian bunch with $\sigma_z = 1$ cm.

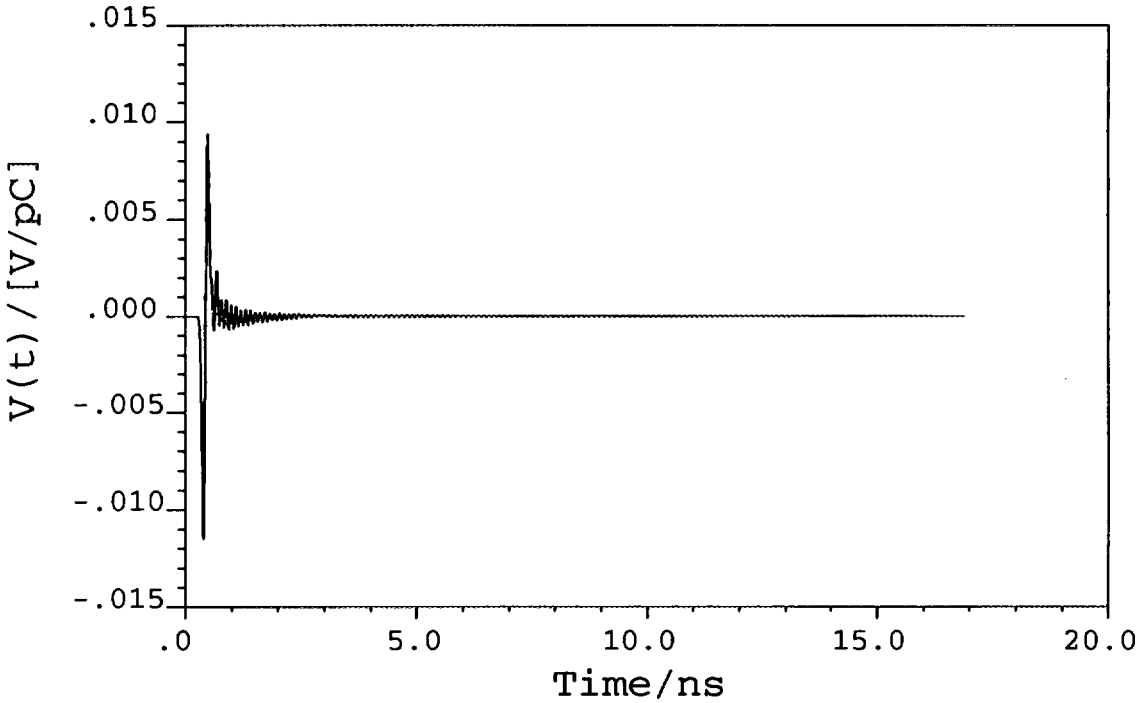

Figure 5: Voltage output of the 1.5-cm BPM at the coaxial line as a function of time.

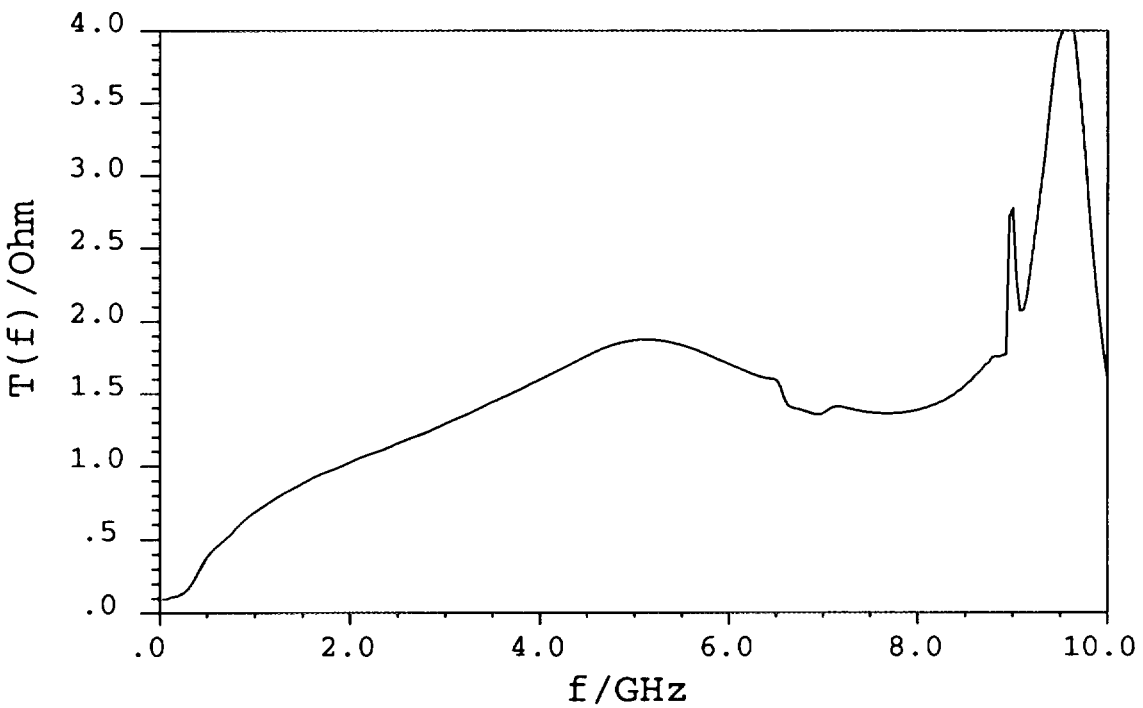

Figure 6: Beam-to-signal transfer function of the 1.5-cm BPM at the coaxial line as a function of frequency.

4 Signal and Power Output

In Fig. 5, we show the output signal of the TEM mode at the coaxial line as a function of time. The signal dies off rapidly after the transient excitation during the passage of the beam. The power output can be evaluated by integrating the signal voltage over time. When the beam is offset from the center of the chamber, the monitor closest to the beam will transmit the highest power. The power carried by the signal for this monitor for an 1 cm offset beam is 37 W, which can be handled by the diagnostic electronics. Fig. 6 shows the Fourier transform of the output signal divided by the beam current spectrum. The frequency content of the signal is quite broad-band and there is no evidence of high narrow peaks up to 10 GHz. In particular, at 952 MHz, the transfer impedance is 0.65 Ω, which is above our minimum requirement of 0.5 Ω.

The sensitivity of a BPM is generally determined by the signals picked up by the different monitors when the beam is off center. We define the sensitivity function as:

$$S_i = \frac{1}{d_i}\left(\frac{A-B}{A+B}\right), \tag{2}$$

where i can be either x or y. For S_x, d_x is the offset in the x-direction, and A and B are the signals picked up by the top right and top left monitors respectively. For S_y, d_y is the offset in the y-direction, and A and B are the signals picked up by the right top and right bottom monitors respectively. Fig. 7 shows the sensitivity functions S_x and S_y as functions of frequency. It can be seen that the frequency dependences of S_x and S_y are similar and are extremely flat up to about 5 GHz. Their values at 952 MHz satisfy our position resolution requirements.

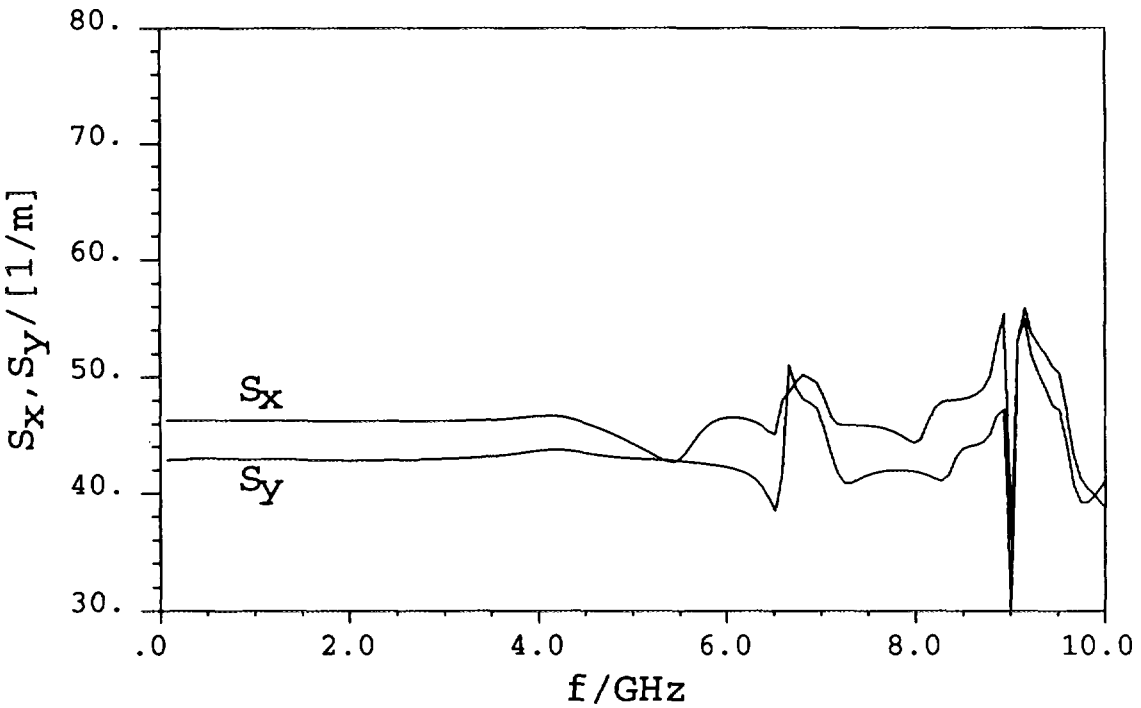

Figure 7: Sensitivity functions of the 1.5-cm BPM as functions of frequency.

5 Power Dissipation

The high power throughput of the signal and the presence of HOMs in the BPM may generate considerable heating effects. Due to the transient behavior of the problem, the calculations of the power loss in the ceramic and in the metallic walls are carried out by fourier-transforming the time evolutions of the electromagnetic fields in the BPM. The energy dissipation in the ceramic during a single bunch crossing is given by:

$$P = \int \omega \epsilon_i(\omega) |\vec{E}_\omega(\vec{x})|^2 \frac{d\omega}{2\pi} d\vec{x}, \tag{3}$$

where

$$\vec{E}_\omega(\vec{x}) = \int \vec{E}(\vec{x}, t) e^{i\omega t} dt, \tag{4}$$

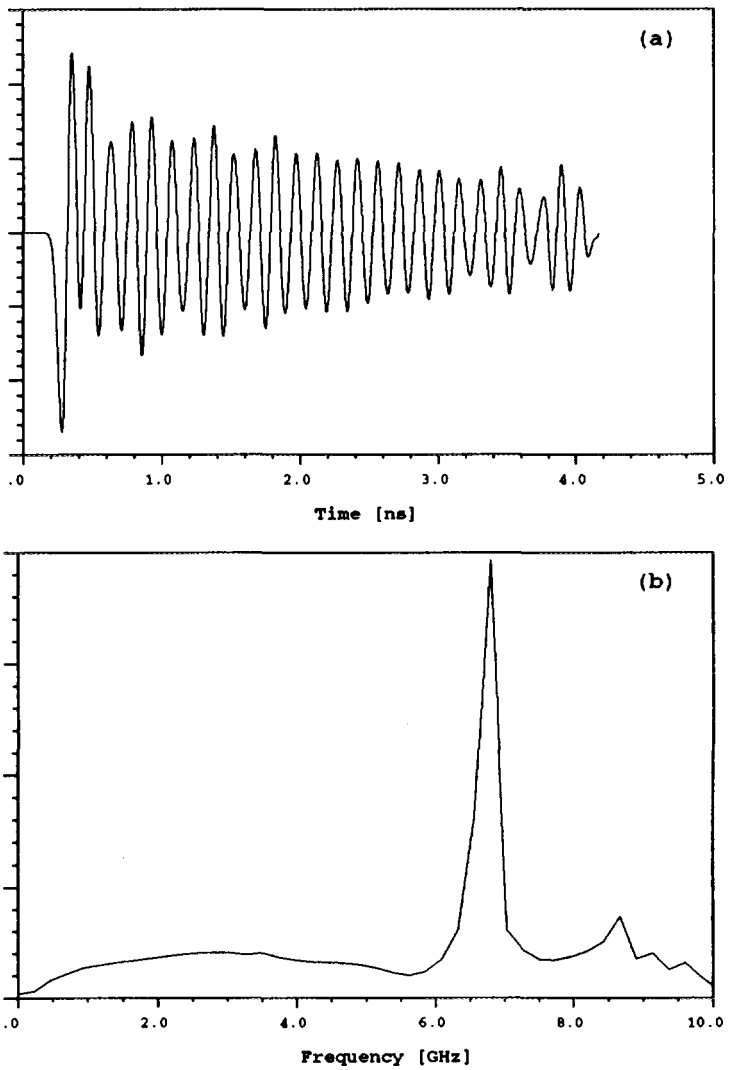

Figure 8: (a) The time history of the electric field and (b) its Fourier transform for a typical location in the ceramic vacuum seal.

and ϵ_i is the imaginary part of the dielectric constant. The time dependence of the electric field and its Fourier transform at a typical location in the ceramic vacuum seal is shown in Fig. 8. A resonant peak appears in the Fourier spectrum, corresponding to the trapped TE mode in the BPM. Since the Q value of the resonance is about 100, we do not expect heating enhancement due to multi-bunch effects. Therefore it is sufficient to use the above formulas to determine the power dissipation. Assuming the ceramic has a dielectric constant of 9.5 and a loss tangent of 0.0007, we find that the ceramic loss is $\sim$ 0.35 W when the beam is offset by 1 cm at 3 A. At the junction of the ceramic and inner molybdenum center pin where heating effects are of more concern than the outer wall, the power loss is found to be $\sim$ 0.007 W, assuming copper conductivity. The introduction of other material such as nickel on the surface of the center pin will increase the power dissipation roughly by an order of magnitude. ANSYS were used to estimate the thermal and structural stabilities of the BPM under these conditions with an additional heat source of 0.25 W/cm^2 from scattered synchrotron radiation. A maximum temperature of 110°C was found on the button and a temperature gradient of about 30°C in the ceramic. ANSYS simulations showed that the temperature and stress distributions are acceptable [2].

6 Summary

We simulated the PEP-II BPM using MAFIA and showed that the 1.5-cm button type BPM has the required transfer impedance and signal sensitivity. The broad-band impedance is a small fraction of the ring impedance, and the narrow-band impedance can be suppressed by the feedback system. The power dissipated in the ceramic vacuum seal was estimated, and temperature and stress distributions were found to be acceptable from ANSYS simulations.

Acknowledgements

We would like to thank J. Corlett, S. Heifets, K. Ko, G. Lambertson, M. Nordby, J. Seeman and T. Shintake for many useful discussions.

References

[1] An Asymmetric B Factory, Conceptual Design Report, LBL-PUB-5379 or SLAC-418, June 1993.
[2] N. Kurita et. al., Design of the Button Beam Position Monitor for PEP-II, to be published in Proc. of PAC95.
[3] S. Heifets, Estimate of the Wakefield Tolerances, AP-99 (1994).
[4] S. Heifets, Broad Band Impedance of the B-Factory, SLAC/AP-93 (1992).
[5] J. Corlett, these proceedings.
[6] T. Shintake et. al., these proceedings.
[7] N. Kurita et. al., Simulation of PEP-II Beam Position Monitors, PEP-II Technical Note No: 87, 1995.

Impedance of a Slotted-pipe Kicker

Zhou Feng

Institute of High Energy Physics, Academia Sinica
P.O.Box 918(9), Beijing, P.R.China, 100039
E-mail: zhouf@bepc3.ihep.ac.cn

Abstract

This paper introduces the principle of a new slotted kicker simply, which is made by using vacuum pipe itself with proper slits as current conductors, and then, presents a rough estimation of its longitudinal and transverse impedance , respectively. Calculation shows that its impedance is reduced significantly compared to our present air-coil kicker.

1. Introduction

For further luminosity upgrading of BEPC (Beijing Electron Positron Collider), several approches were proposed, among which mini-β insertion was the most promising. However, the crucial factor for the BEPC mini-β scheme is the reduction of bunch length from present 6-7 cm to about 3 cm. Hence, finding an approach to shorten the bunch length becomes a very important issue. In BEPC, the bunch lengthens according to following scaling low:[1]

$$\sigma_l(cm) = 0.404(\frac{I\alpha_p}{E\nu_s^2})^{\frac{1}{2.6}} \tag{1}$$

Where I is the bunch current, α_p the momentum compaction factor, ν_s the synchrotron tune and E the beam energy. Therefore, for the purpose of it, the coupling impedance should be decreased from present about 4.0 Ω to 1.6 Ω. Measurements show that the most contribution to the impedance comes from 4 kickers and 40 bellows. Based on this motive, we are developing a slotted-pipe kicker model which has low impedance, and then replace the present kickers by the new kicker.

In this paper, we will brifely introduce the principle of a new slotted-pipe kicker, and then emphase to presents the formulas for calculating impedance of the kicker.

2. Principle of Slotted-pipe Kicker

Before introducing the new kicker, we would like to simply describe the structure of the present kickers in BEPC. The present kickers are air-coil magnets which has two current

metal plates surrounded by a large vacuum tank, as shown in Fig.1. For this kicker, there are some sources of impedance, such as larger tapers. According to the measurements[2], the longitudinal impedance of the kicker (Z/n) is about 0.25 Ω. So it is necessary to design a new kicker to replace the old one. However, in accordance with our present situation, we had better improve it on the basis of present kickers. This new slotted-pipe kicker is principally based on the design of G.Blokesch [5], which use the vacuum pipe wall itself with properly arranged slits as current conductors. The schematic diagram and cross section of the slotted kicker are shown in Fig.2. These two parallel conductors on both sides of the beam axis form an inductive loop, and the six slits between the conductors are connected to ground which is one of the most important features different from the current kicker. Due to our racetrack pipe, the central metal plates are the nearest to the beam. So these plates carry away most of image currents travelling with the beam along the beam pipe, and thus through qualitative analysis, the impedance is reduced greatly.

In designing a new kicker, the first is to meet the requirements of magnetic field, such as field strength, good field region and so on. The second is to make the impedance as small as possible. Hence the relation between field requirements and low impedance needs to be compromised. In BEPC, the parameters of kicker for injection are as follows:
•kicker magnet field strength $\int Bdl = 200Gs.m$,
•good field region $x = \pm 22mm$,
•field error=±2%.
For the purpose of meeting the field listed above, 8 slots such as 3, 4, 5, 6, and 7, 8, 9, 10 are made. Note that the width of slots, w, should be as narrow as possible, since the imaginary impedance is almost proportional to w^3[4]. In order to form an inductance on the basis of above 8 slots, transverse slots must be cut, such as 1 and 2 shown in fig.2. Impedance study[6] shows that the tranverse slots contribute to more impedance than the longitudinal slots, since these transverse slots cut field lines. Whereas, we should also make the width of tranverse slots as small as possible.

3. Calculation of longitudianl impedance for new kicker

At frequency below cutoff, the cross talk among the slots is neglected. So the impedance of this kicker is the summation of these slots, including 8 longitudinal slots and 2 transverse slots. In order to solve question conveiently, we approximate the racetrack pipe into circular pipe, i.e., its radius of circular pipe is the short semiaxises. And thus the upper estimation of impedance for this racetrack structure is given. Applying to Bethe theory[3], S.Kurennoy derived formulas for calculating impedance of slots whose width w and length l are smaller than radius of beam pipe b as follows:[4]

$$Z(\omega) = -iZ_0 \frac{\omega}{c} \frac{(\alpha_{mag} + \alpha_{el})}{4\pi^2 b^2} \tag{2}$$

where $\alpha_{mag}, \alpha_{el}$ are the electric and magnetic polarizabilities of the slots, respectively. However, for our new slotted kicker, the width is smaller than b, but its length is larger than b. So our case violate the condition of equation (2). Fortunately, Stupakov[7] extends the theory to the limit l≥b (w is still smaller than b). He thought that the impedance of these slots comes only from the ends of the slots, i.e., the impedance of long slots is independent

of their length. So, the impedance of long slots is the same as that of short slots given in equation (2).
For a rectangular-end slot oriented in the beam,

$$\alpha_{el} = -\frac{\pi}{16} w^2 l (1 - 0.5663\frac{w}{l} + 0.1398(\frac{w}{l})^2) \tag{3}$$

$$\alpha_{m\perp} = \frac{\pi}{16} w^2 l (1 + 0.3577\frac{w}{l} - 0.0356(\frac{w}{l})^2) \tag{4}$$

$$\alpha_{m\parallel} = 0 \tag{5}$$

For a round-end slots oriented in the beam,

$$\alpha_{el} = -\frac{\pi}{16} w^2 l (1 - 0.765\frac{w}{l} + 0.1894(\frac{w}{l})^2) \tag{6}$$

$$\alpha_{m\perp} = \frac{\pi}{16} w^2 l (1 - 0.0857\frac{w}{l} - 0.0654(\frac{w}{l})^2) \tag{7}$$

$$\alpha_{m\parallel} = 0 \tag{8}$$

Therefore, for a rectangular slots:

$$\alpha_m + \alpha_e = w^3 (0.1814 - 0.0344\frac{w}{l}) \tag{9}$$

For a round-end slots:

$$\alpha_m + \alpha_e = w^3 (0.1334 - 0.05\frac{w}{l}). \tag{10}$$

Considering the impedance value and the effect of high volts, we should make the slots with rounded-end. Now substituting equation (10) into (2), one can obtain the impedance of a slot oriented in the beam:

$$Z(\omega) = -iZ_0 \frac{\omega}{c} \frac{w^3 (0.1334 - 0.05\frac{w}{l})}{4\pi^2 b^2} \tag{11}$$

In the 8 longitudinal slots of our slotted kicker, there are four slots whose width is 7 mm, and another four slots whose width is 9 mm. Here, note that the thickness of the wall is smaller than the width of slots. So their impedance is calculated directly using the equation (11): The impedance of the slots with the width of 7 mm is,$Z(\omega)/\mathrm{n} = i0.2 \times 10^{-5}$, and also for the 9mm wide slots, $Z(\omega)/\mathrm{n} = i0.43 \times 10^{-5}\Omega$. Totally, the 8 longitudinal slots contribute to the impedance of about $i2.5 \times 10^{-5}\Omega$.
The impedance of transverse slots can be estimated approximately as follows:

$$\alpha_{m\parallel} = \frac{\pi l^3}{24(ln(\frac{8l}{w}) + \frac{\pi t}{2w} - \frac{7}{3})}, \tag{12}$$

Since, for narrow transverse slots, the electric polarizability α_e is smaller than the longitudinal magnetic polarizability $\alpha_{m\parallel}$ by an order of magnitude and can be neglected in calculating impedances. Hence,

$$\alpha_m + \alpha_e = \frac{\pi l^3}{24(ln(\frac{8l}{w}) + \frac{\pi t}{2w} - \frac{7}{3})}. \tag{13}$$

Generally speaking, one can replace the circle by regular octagon with side a=π b/4[5]. For our transverse slots of slotted kicker, one can estimate the impedance of four transverse slots with length a and width w. Applying to equation (13), one can obtain:

$$\alpha_e + \alpha_m = \frac{2}{3}(\frac{\pi}{4})^2 \frac{b^3}{(ln\frac{2\pi b}{w} + \frac{\pi t}{2w} - \frac{7}{3})}; \tag{14}$$

Substituting the equation (14) into (2), the impedance due to transverse cut with the width 7 mm and the thickness 3 mm is Z(ω)/n=i3.0$\times 10^{-4}\Omega$. Now one can easily find that the transverse slots made more contribution to impedance than longitudinal slots. The total longitudinal impedance of this slottd kicker is Z/n=$i3.25 \times 10^{-4}\Omega$.

4. Transverse impedance of slotted kicker

The dipole transverse impedance is defined as

$$Z_\perp(\omega) = -\frac{i}{qr}\int_{-\infty}^{+\infty} dz e^{-ikz}[\vec{E} + Z_0\vec{\beta} \times \vec{H}]_\perp. \tag{15}$$

The transverse impedance of longitudinal slots reduces to[7]

$$Z_{\perp 1} = i\frac{Z_0 w^3}{2\pi^2 b^4}(0.1334 - 0.05\frac{w}{l}), \tag{16}$$

and likewise, its formula of transverse slots can be obtained:

$$Z_{\perp 2} = i\frac{Z_0}{48b}\frac{1}{(ln(\frac{2\pi b}{w}) + \frac{\pi t}{2w} - \frac{7}{3})} \tag{17}$$

After substituting parameters into equation (16) and (17), the total transverse impedance is very little.

5. Conclusion and Future work

At the frenquency below cutoff, the real part impedance of this kicker is zero, and the imaginary part is about 10^{-4} magnitude. Therefore, through analysis, the slotted kicker has very low impedance. Of course, further work is to simulate this kicker using 3-D MAFIA to confirm our results given above.

Acknowledgements

The author would like to express his thanks to Prof.Wang shuhong, Drs.Zhao zhentang and Hao Yaodou for their help, and special thanks to Prof. M.Tigner for his fruitful suggestion. Also we thank others from injection group for their kind help.

References

1. Q.Qing et al., proceedings of 1995 International Acc.Conf..Dallas,USA.
2. G.W.Wang, Ph.D. desertation
3. H.A.Bethe, Phys.Rev.1944
4. S.S.Kurennoy, IHEP 92-84, UNK
5. G.Blokesch, et al.,NIM A338(1994)
6. V.Thiagarajan, et al., SSCL-650
7. G.V.Stupakov, Phys.Rev.E, Vol.51,1995

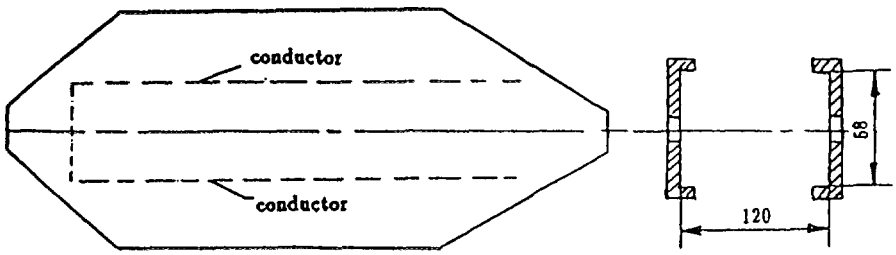

Fig.1 Schematic map of the present kicker

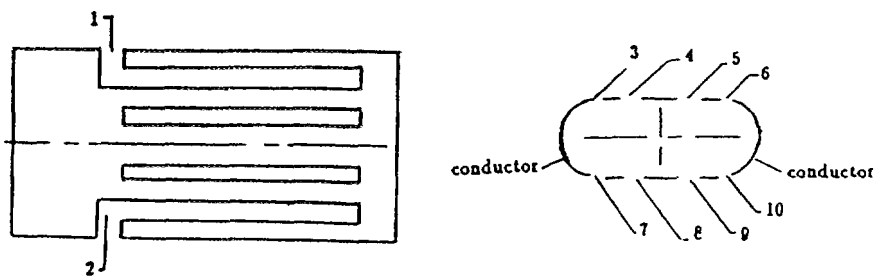

Fig.2 Structure of a slotted-pipe kicker

Debye Potentials, Electromagnetic Reciprocity and Impedance Boundary Conditions for Efficient Analytic Approximation of Coupling Impedances in Complex Heterogeneous Accelerator Pipes

Stefania Petracca
Dip. Fisica Teorica e S.M.S.A. Universita' di Salerno,
and I.N.F.N. Salerno, Italy.

Abstract

Debye potentials, the Lorentz reciprocity theorem, and (extended) Leontóvich boundary conditions can be used to obtain simple and accurate analytic estimates of the longitudinal and transverse coupling impedances of (piecewise longitudinally uniform) multi-layered pipes with non simple transverse geometry and/or (spatially inhomogeneous) boundary conditions.

1 Introduction

The interaction of relativistic charged particle beams with the sorrounding chamber is often conveniently described in terms of coupling impedances. There is a wide Literature concerning coupling impedance properties and computation (see [1] - [9], and references quoted therein), but only few analytic solutions are available, for those simple cases where both the Laplacian is separable in the transverse coordinates and the boundary conditions are simple (e.g. perfect conductors).

In most practical situations, where the cross sectional pipe geometry is not simple (e.g., a square with rounded corners, as in the proposed LHC liner design), and several electrically different wall materials are used, one has to resort to numerical solutions.

As compared to extensive numerical simulations, however, analytic solutions, though approximate, may give an immediate insight into the relative role of the machine parameters, thus providing valuable design hints.

In this paper we rely on some popular methods from classical Electromagnetics to obtain general (though approximate) formulas for computing beam coupling

impedances (and related quantities, e.g., the parasitic loss) in complex pipes with non simple transverse geometry, consisting of several co-axial tubes, possibly made of different materials. In representative cases (e.g. the circular cross section chamber with resistive wall) our method reproduces the known exact solution. Most of the above results have been developed by the Author in connection with the LHC study at CERN.

The paper is organized as follows. In *Sect. 2* we introduce as a preliminary tool the Debye potential formalism for accelerator pipes [11]; in *Sect. 3* we present some general formulae obtained by applying the Lorentz reciprocity theorem, connecting the coupling impedances of a (piecewise longitudinally uniform) pipe with complicated transverse geometry and/or boundary conditions to those of a simple one, assumed known, whereof the non-simple pipe differs by suitably *small* perturbations [12]. Under the same section we also discuss the accuracy of the approximations involved, and compute the pertinent parasitic losses. In *Sect. 4* we use the equivalence between plane TEM waves in stratified media and voltage waves through cascaded transmission lines to obtain *equivalent* impedance boundary conditions at the internal surface of a pipe whose wall may consist of several (circumferentially inhomogeneous) lossy layers with different electrical and magnetic properties, possibly intermingled by non conducting (e.g., vacuum) gaps. In *Sect. 5* a simple impedance boundary condition describing a (perfectly conducting) perforated wall is introduced. Conclusions follow under *Sect. 6*. The reciprocity theorem, transmission line equations, and the computation of the interaction constant for (plane, regular) dipole lattices are summarized in *Appendix A, B* and *C*. MKSA units are used throughout.

2 Electromagnetic Fields in Piecewise Uniform Pipes from Debye Potentials

In this section we sketch a general and systematic framework for computing the electromagnetic fields generated by a relativistic beam in longitudinally uniform pipes consisting of several co-axial shells made of different materials [11]. Anisotropic, non perfectly conducting, corrugated or slotted walls are allowed, in principle. The Reader will find similarities with the approach formulated by Schwinger and Marcuvitz to solve Maxwell equations in waveguides [13]. The formalism provides an alternative derivation of Chao's results [14] for cylindrical pipes, and is entirely phrased in vector form.

Starting from Maxwell equations, where $\vec{e}$, $\vec{h}$ are the electric and magnetic fields, $\vec{d}$, $\vec{b}$ the inductions, ρ, $\vec{j}$ the charge and current densities, and using the obvious decompositions:

$$\nabla = \nabla_t + \partial_z \vec{u}_z, \qquad \vec{f} = \vec{f}_t + f_z \vec{u}_z, \tag{1}$$

where $\vec{f}$ is *any* of the functions $\vec{e}$, $\vec{h}$, $\vec{b}$, $\vec{d}$, and the suffix t stays for transverse, we obtain, separating transverse and longitudinal terms:

$$\begin{cases} (\nabla_t \times \vec{e}_t) = -\partial_t\, b_z \vec{u}_z, \\ (\nabla_t \times \vec{h}_t) = (\partial_t\, d_z + j_z)\vec{u}_z, \\ \vec{u}_z \times (\partial_z \vec{e}_t - \nabla_t e_z) = -\partial_t \vec{b}_t, \\ \vec{u}_z \times (\partial_z \vec{h}_t - \nabla_t h_z) = \partial_t \vec{d}_t, \\ \nabla_t \cdot \vec{d}_t = -\partial_z d_z + \rho, \\ \nabla_t \cdot \vec{b}_t = -\partial_z b_z. \end{cases} \tag{2}$$

If the source-term is a transverse sheet[1] of charge traveling in the (positive) z-direction with constant velocity v_0:

$$\begin{aligned} &\rho(x,y,z,t) = \rho_S(x,y)\delta(z - v_0 t), \\ &\vec{j} = v_0 \rho\ \vec{u}_z, \end{aligned} \tag{3}$$

ρ_S being a surface charge density, we expect the same z,t dependance for all functions involved. Thus we switch to the spectral representation:

$$\vec{f}(x,y,z,t) = \frac{1}{2\pi} \int_{-\infty}^{\infty} \vec{F}(x,y,k)\ \exp[-jk(z - v_0 t)]\ dk. \tag{4}$$

Furthermore, assuming the medium described by material constitutive relationships of the following form[2]:

$$\vec{d}(\vec{r},t) = \int_{-\infty}^{\infty} \epsilon(\tau)\ \vec{e}(\vec{r}, t-\tau)\ d\tau, \quad \vec{b}(\vec{r},t) = \int_{-\infty}^{\infty} \mu(\tau)\ \vec{h}(\vec{r}, t-\tau)\ d\tau, \tag{5}$$

the following spectral material equations are obtained:

$$\vec{D}(x,y,k) = \widetilde{\epsilon}\ (kv_0)\ \vec{E}(x,y,k), \quad \vec{B}(x,y,k) = \widetilde{\mu}\ (kv_0)\ \vec{H}(x,y,k), \tag{6}$$

where $\widetilde{\epsilon}$, $\widetilde{\mu}$ denote the frequency-dependent complex permittivity and permeability

[1] More general (undeformable) charge profiles can be represented, using $z-$convolution, viz.: $\rho(x,y,z - v_0 t) = \rho(x,y,z) * \delta(z - v_0 t)$.

[2] These are rather general, allowing for dielectric (magnetic) losses as well. The only restrictions are: isotropy (which could be removed at the expense of some complication), homogeneity and time-invariance.

(Fourier transforms) of the material medium. Using eq.s (3) to (6), into (2), one gets:

$$\begin{cases} (\nabla_t \times \vec{E}_t) = -jkv_0\, \widetilde{\mu}\,(kv_0)\, H_z \vec{u}_z, \\ (\nabla_t \times \vec{H}_t) = (jkv_0\, \widetilde{\epsilon}\,(kv_0)\, E_z + \rho_S v_0)\vec{u}_z, \\ \vec{u}_z \times (-jk\, \vec{E}_t - \nabla_t E_z) = -jkv_0\, \widetilde{\mu}\,(kv_0)\, \vec{H}_t, \\ \vec{u}_z \times (-jk\, \vec{H}_t - \nabla_t H_z) = jkv_0\, \widetilde{\epsilon}\,(kv_0)\, \vec{E}_t, \\ \nabla_t \cdot \vec{E}_t = jk\, E_z + \rho_S / \widetilde{\epsilon}\,(kv_0), \\ \nabla_t \cdot \vec{H}_t = jk\, H_z. \end{cases} \tag{7}$$

The next step involves resolving the (transverse) field vectors into their irrotational and solenoidal parts [15]:

$$\vec{F}_t = \vec{F}_t^{(sol.)} + \vec{F}_t^{(irr.)}. \tag{8}$$

Using eq.s (8) into (7), one easily obtains from the first and last pair of equations:

$$\begin{cases} (\nabla_t \times \vec{E}_t^{(sol.)}) = -v_0\, \widetilde{\mu}\,(kv_0)\, (\nabla_t \cdot \vec{H}_t^{(irr.)})\, \vec{u}_z, \\ (\nabla_t \times \vec{H}_t^{(sol.)}) = v_0\, \widetilde{\epsilon}\,(kv_0)\, (\nabla_t \cdot \vec{E}_t^{(irr.)})\, \vec{u}_z. \end{cases} \tag{9}$$

The $3rd$ and $4th$ equation in (7), on the other hand can be written as equalities between a solenoidal and irrotational vector, which can be therefore set both to zero. Accordingly, the $3rd$ equation yields:

$$\begin{cases} \vec{u}_z \times \vec{E}_t^{(sol.)} = v_0\, \widetilde{\mu}\,(kv_0)\, \vec{H}_t^{(irr.)}, \\ \vec{u}_z \times \left\{ \vec{E}_t^{(irr.)} - \nabla_t \left[\dfrac{\nabla_t \cdot \vec{E}_t^{(irr.)} - \rho_S / \widetilde{\epsilon}\,(kv_0)}{k^2} \right] \right\} = v_0\, \widetilde{\mu}\,(kv_0)\, \vec{H}_t^{(sol.)}, \end{cases} \tag{10}$$

while the $4th$ gives:

$$\begin{cases} \vec{u}_z \times \vec{H}_t^{(sol.)} = -v_0\, \widetilde{\epsilon}\,(kv_0)\, \vec{E}_t^{(irr.)}, \\ \vec{u}_z \times \left[\vec{H}_t^{(irr.)} - \dfrac{\nabla_t \nabla_t \cdot \vec{H}_t^{(irr.)}}{k^2} \right] = -v_0\, \widetilde{\epsilon}\,(kv_0)\, \vec{E}_t^{(sol.)}. \end{cases} \tag{11}$$

The first equations in (10) , (11) can be also written:

$$\vec{E}_t^{(sol.)} = -v_0\, \widetilde{\mu}\,(kv_0)\, \vec{u}_z \times \vec{H}_t^{(irr.)}, \quad \vec{H}_t^{(sol.)} = v_0\, \widetilde{\epsilon}\,(kv_0)\, \vec{u}_z \times \vec{E}_t^{(irr.)}, \tag{12}$$

which shows that knowledge of the irrotational parts alone is sufficient to recover the complete (transverse) field. Using the $1st$ (resp. $2nd$) equation in (12) into the $2nd$ equation in (11), (resp., (10)) one gets:

$$\begin{cases} \nabla_t \nabla_t \cdot \vec{H}_t^{(irr.)} - k^2[1 - v_0^2 \, \widetilde{\epsilon}\,(kv_0)\, \widetilde{\mu}\,(kv_0)]\, \vec{H}_t^{(irr.)} = 0, \\ \nabla_t \nabla_t \cdot \vec{E}_t^{(irr.)} - k^2[1 - v_0^2 \, \widetilde{\epsilon}\,(kv_0)\, \widetilde{\mu}\,(kv_0)]\, \vec{E}_t^{(irr.)} = \nabla_t \rho_S / \, \widetilde{\epsilon}\,(kv_0). \end{cases} \tag{13}$$

Next we let:

$$\vec{E}_t^{(irr.)} = -\nabla_t \Phi, \quad \vec{H}_t^{(irr.)} = -\nabla_t \Psi, \tag{14}$$

into eq. (13), thus obtaining:

$$\begin{cases} \nabla_t \nabla_t \Phi - k^2[1 - v_0^2 \, \widetilde{\epsilon}\,(kv_0)\, \widetilde{\mu}\,(kv_0)]\Phi \;=\; -\rho_S / \, \widetilde{\epsilon}\,(kv_0) + C, \\ \nabla_t \nabla_t \Psi - k^2[1 - v_0^2 \, \widetilde{\epsilon}\,(kv_0)\, \widetilde{\mu}\,(kv_0)]\Psi \;=\; C'. \end{cases} \tag{15}$$

Note that if and only if $[1 - v_0^2 \, \widetilde{\epsilon}\,(kv_0)\, \widetilde{\mu}\,(kv_0)] \neq 0$ the (as far undetermined) constants C, C' can be set to zero, via a trivial transformation of the potentials. From the last pair of eq.s in (7) we finally get:

$$\begin{cases} E_z = jk[1 - v_0^2 \, \widetilde{\epsilon}\,(kv_0)\, \widetilde{\mu}\,(kv_0)]\Phi - C/jk, \\ H_z = jk[1 - v_0^2 \, \widetilde{\epsilon}\,(kv_0)\, \widetilde{\mu}\,(kv_0)]\Psi - C'/jk, \end{cases} \tag{16}$$

and hence Φ and Ψ are nothing but the *Debye potentials* of the electromagnetic field [16]. Once the Debye potential have been computed, the *complete* solution of the EM problem is available: eq.s (16) give the longitudinal components E_z, H_z, eq.s (14) furnish the irrotational parts of $\vec{E}_t$, $\vec{H}_t$, and finally eq.s (12) yield the solenoidal parts of $\vec{E}_t$, $\vec{H}_t$.

2.1 Boundary Conditions

Usually, the beam pipe consists of several co-axial shells with different electromagnetic properties ϵ and μ. The boundary conditions to be satisfied by the fields and inductions across the interface between different media are well known: $\hat{n} \times \vec{e}$ and $\hat{n} \times \vec{h}$ must be continuous $\hat{n}$ being the unit vector normal to the interface.[3]

Another class of possible boundary conditions are those of the *impedance* type, viz.:

$$\hat{n} \times \left[\hat{n} \times \vec{E} - \widetilde{Z}_w \, \vec{H}\right] \;=\; 0, \tag{17}$$

[3]It can be readily proved that the further boundary conditions on the inductions, namely that $\hat{n} \cdot \vec{d}$ and $\hat{n} \cdot \vec{b}$ should be continuous across the interface follow automatically from the continuity of $\hat{n} \times \vec{e}$ and $\hat{n} \times \vec{h}$.

where $\tilde{Z}_w$ is the (complex) Fourier transform of the wall surface impedance operator evaluated at $\omega = kv_0$. Conditions of this kind are credited to and named after M.A. Leontóvich [18], and can be conveniently used in a variety of problems (see [17] for a review), including non-perfectly conducting, anisotropic, pierced or corrugated walls.

The standard and impedance boundary conditions can be easily rephrased in terms of the potentials Φ and Ψ.

For the standard b.c., using eq.s (14) and (12) one gets:

$$\begin{cases} \hat{n} \times \vec{E} = (\hat{n} \times \vec{u}_z) \left[jk\, \tilde{\gamma}^{-2}\, \Phi + C/jk \right] + \\ \quad + \hat{n} \times [-\nabla_t \Phi + v_0\, \tilde{\mu}\, (kv_0)\, \vec{u}_z \times \nabla_t \Psi], \\ \\ \hat{n} \times \vec{H} = (\hat{n} \times \vec{u}_z) \left[jk\, \tilde{\gamma}^{-2}\, \Psi + C'/jk \right] + \\ \quad + \hat{n} \times [-\nabla_t \Psi - v_0\, \tilde{\epsilon}\, (kv_0)\, \vec{u}_z \times \nabla_t \Phi], \end{cases} \tag{18}$$

where $\tilde{\gamma} = (1 - v_0^2\, \tilde{\epsilon}\, (kv_0)\, \tilde{\mu}\, (kv_0))^{-1/2}$. It is noted that the $1st$ and $2nd$ term on the $r.h.s$ of eq.s (18) represent the transverse and longitudinal part of $\hat{n} \times \vec{E}$, $\hat{n} \times \vec{H}$, and must be therefore *separately* continuous across the interface between two different media. Equations (18) accordingly yield a total of *four* (component) equations.

Impedance boundary conditions, on the other hand rephrase into:

$$\begin{aligned} &\hat{n} \times \left\{ \left\{ (\hat{n} \times \vec{u}_z)[jk\, \tilde{\gamma}^{-2}\, \Phi + C/jk] - \tilde{Z}_w\, (-\nabla_t \Psi - v_0\, \tilde{\epsilon}\, (kv_0) \vec{u}_z \times \nabla_t \Phi) \right\} + \right. \\ &\left. + \left\{ \hat{n} \times (-\nabla_t \Phi + v_0\, \tilde{\mu}\, (kv_0) \vec{u}_z \times \nabla_t \Psi) - \tilde{Z}_w\, \vec{u}_z [jk\, \tilde{\gamma}^{-2}\, \Psi + C'/jk] \right\} \right\} = 0 \end{aligned} \tag{19}$$

Here the $1st$ and $2nd$ term in the innermost curly brackets represent transverse and longitudinal vectors and must therefore *separately* vanish at the boundary. Equation (19) accordingly splits into a total of *two* (component) equations.

3 Coupling Impedances and Debye Potentials

In a pipe with longitudinally-invariant cross section the force produced by a point charge Q running parallel to the pipe axis, with (constant) velocity $\beta_0 c$ and transverse coordinate $\vec{r}_0$, on another point charge q traveling on a parallel trajectory, with transverse coordinate $\vec{r}_1$ at an (axial) distance s behind, is a function of $\vec{r}_0$, $\vec{r}_1$ and s only, and can be derived from a scalar potential, w, called the wake potential per unit lenght[4]:

$$\vec{F}(\vec{r}_1, \vec{r}_0, -s) = -qQ\, \nabla w(\vec{r}_1, \vec{r}_0, -s). \tag{20}$$

[4]In pipes with longitudinally varying cross section the fields depend *separately* on z, t, and Lorentz force is no more a function of $s = z - \beta_0 ct$. However, one can subdivide the pipe into subsections $L_i \leq z \leq L_{i+1}$ such that:

$$\vec{f}_i = \int_{L_i}^{L_{i+1}} \vec{F} dz = -qQ \nabla\, W_i, \quad i = 1, 2, \ldots$$

where $\nabla = \{\partial_z \vec{u}_z, \nabla_{\vec{r}_1}\}$. The principal parts of the longitudinal and transverse wake force in the limit as $\vec{r}_0, \vec{r}_1 \longrightarrow 0$ are:

$$F_s = -qQ\partial_s \; w(0,0,s), \tag{21}$$

$$\vec{F}_\perp = -qQ\nabla_{\vec{r}_1}\nabla_{\vec{r}_0} \; w(\vec{r}_1,\vec{r}_0,s)|_{\vec{r}_0=\vec{r}_1=0} \cdot \vec{r}_0 \; = \; -qQ\partial_s \; \bar{\bar{w}} \; (s) \cdot \vec{r}_0, \tag{22}$$

where $\bar{\bar{w}}$ (s) is the transverse dyadic wake potential per unit length, obeying the Panofsky-Wentzel theorem:

$$\partial_s \; \bar{\bar{w}} \; (s) \; = \; \nabla_{\vec{r}_1}\nabla_{\vec{r}_0} \; \; w(\vec{r}_1,\vec{r}_0,s)|_{\vec{r}_0=\vec{r}_1=0} \cdot \tag{23}$$

The spectral coupling impedances per unit length are defined as follows [20], [21]:

$$Z_{||} = \frac{1}{\beta_0 c}\mathcal{F}_{s\longrightarrow k}\left(\frac{F_s}{qQ}\right), \qquad \vec{Z}_\perp = \frac{j}{\beta_0 c}\mathcal{F}_{s\longrightarrow k}\left(\frac{\vec{F}_\perp}{qQ}\right), \tag{24}$$

where $\mathcal{F}_{s\longrightarrow}$ denotes the $s \longrightarrow k$ Fourier transform operator, with $k = \omega/\beta_0 c$.

The wake potential per unit length w can be computed from the electric Debye potential ϕ produced by the leading charge Q as follows [12]:

$$w(\vec{r}_1,\vec{r}_0,s) = \frac{(1-\beta_0^2)}{Q} \; \phi(\vec{r}_1,\vec{r}_0,-s), \tag{25}$$

whence, using eqs. (20) to (24):

$$Z_{||}(\omega) = jk\frac{(1-\beta_0^2)}{\beta_0 cQ}\Phi(0,0,k), \tag{26}$$

and[5]:

$$\bar{\bar{Z}}_\perp \; (\omega) = j\frac{(1-\beta_0^2)}{\beta_0 cQ}\nabla_{\vec{r}_0}\nabla_{\vec{r}_1} \; \Phi(\vec{r}_0,\vec{r}_1,k)|_{\vec{r}_0=\vec{r}_1=0} \cdot \tag{27}$$

4 Coupling Impedances in Complex Structures From Reciprocity Formulas

According to eq.s (26), (27), computing impedances requires the explicit knowledge of the (electric) Debye potentials. Unfortunately, eq. (15) can be solved only in a few simple cases, where the pipe geometry and (electromagnetic) material properties are *simple*. In all other cases, impedances must be computed numerically.

---

where W_i is a function of $(\vec{r}, \vec{r}_0, s)$ only, and is called wake funtion [19]. For longitudinally uniform pipes one has $\vec{f}_i = \vec{F}(L_{i+1} - L_i)$, and $w = W_i/(L_{i+1} - L_i)$.

[5]The tensor nature of the transverse impedance first emphasized by Vaccaro [22] and related to the same property of Laslett coefficients [10] is clearly exhibited.

Nonetheless, in many practical istances, the actual pipe geometry and material properties of the pipe can be viewed as perturbations of a simpler pipe, where Helmholtz equation is separable and the wall is a perfect conductore, for which the Debye potentials are known. It turns out [12] that in this case the coupling impedances can be approximately computed in analytic form to a high degree of accuracy, provided the perturbations are not too large, by resorting to Lorentz reciprocity theorem (see *Appendix A*) as follows.

Let $\Phi_0(\vec{r},\vec{r}_0)$ and $\Phi(\vec{r},\vec{r}_1)$ the (k-domain) electrical Debye potentials of the electromagnetic fields produced by the charge densities:

$$\rho_0 \;=\; Q\delta(\vec{r}-\vec{r}_0)\delta(z-\beta_0 ct), \qquad \rho \;=\; Q\delta(\vec{r}-\vec{r}_1)\delta(z-\beta_0 ct) \tag{28}$$

in two vacuum pipes differing by some alterations in the boundary geometry and/or electrical properties. We call the problem described by Φ_0 (assumed known) and Φ (unknown) as *unperturbed* and *perturbed*, respectively. Thus:

$$\nabla_t^2\Phi_0^* - k^2(1-\beta_0^2)\Phi_0^* = -\frac{Q}{\epsilon_0}\delta(\vec{r}-\vec{r}_0), \quad \nabla_t^2\Phi - k^2(1-\beta_0^2)\Phi = -\frac{Q}{\epsilon_0}\delta(\vec{r}-\vec{r}_1), \tag{29}$$

where $\vec{r}$ denotes the transverse position, Q is the electric bunch charge, ∇_t is the transverse gradient, $\beta_0 = v_0/c$, ϵ_0 is the vacuum dielectric constant, and the asterisk means complex conjugation.

Multiplying the first equation in (29) by Φ and the second one by Φ_0^*, subtracting and integrating over the pipe cross section S one gets the following reciprocity formula (see *Appendix A*):

$$\int_S \left(\Phi\nabla_t^2\Phi_0^* - \Phi_0^*\nabla_t^2\Phi\right) dS = \oint_{\partial S}\left(\Phi\frac{\partial\Phi_0^*}{\partial n} - \Phi_0^*\frac{\partial\Phi}{\partial n}\right) d\ell \;=\; \frac{Q}{\epsilon_0}\left[\Phi_0^*(\vec{r}_1,\vec{r}_0) - \Phi(\vec{r}_0,\vec{r}_1)\right], \tag{30}$$

where ∂S is the boundary of S, and Green's theorem has been used to convert the surface integral into a contour one. It is expedient to rephrase the l.h.s. of (30) in terms of fields instead of potentials (16), thus getting:

$$\Phi_0^* = -\frac{E_{0z}^*}{jk(1-\beta_0^2)}, \quad \frac{\partial\Phi_0^*}{\partial n} = \nabla_t\Phi_0^*\cdot\vec{u}_n = -E_{0n}^{*(irr.)}, \quad \frac{\partial\Phi}{\partial n} = \nabla_t\Phi\cdot\vec{u}_n = -E_n^{(irr.)}, \tag{31}$$

$$\Phi|_{\partial S} = \frac{E_z|_{\partial S}}{jk(1-\beta_0^2)} = \frac{Z_{wall}\,H_c|_{\partial S}}{jk(1-\beta_0^2)} = -\frac{Y_0 Z_{wall}}{jk(1-\beta_0^2)}\left(\beta_0 E_n^{(irr.)} + \beta_0^{-1}E_n^{(sol.)}\right)\Big|_{\partial S}, \tag{32}$$

where $Y_0 = Z_0^{-1}$, and $Z_0 = \sqrt{\mu_0/\epsilon_0}$ is the free space wave impedance. The second equality in (32) follows from a Leontóvich boundary condition at the pipe wall

$$\vec{u}_n \times \left[\vec{u}_n \times \vec{E} - Z_{wall}\vec{H}\right]_{\partial S} = 0, \tag{33}$$

where Z_{wall} is the (complex) characteristic impedance of the wall, evaluated at $\omega = kv_0$. The unit vectors $\{\vec{u}_z, \vec{u}_c, \vec{u}_n\}$ are defined in *Fig. 1.*

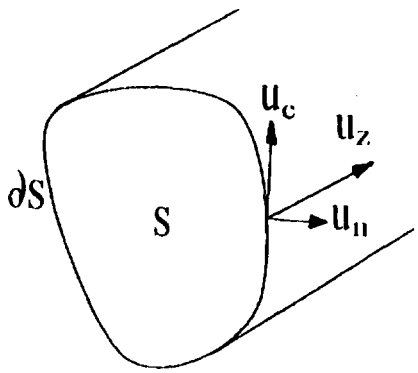

Fig. 1 - Unit vectors relevant to eq.s (32)

Note that the fields E_{0n}, E_{0z} refer to the *unperturbed* situation, and are thus known, while H_c, E_n, E_z refer to the *perturbed* situation, and are unknown. Using (31) and (32) in (30) one obtains the following (exact) relationship:

$$\frac{1}{jk(1-\beta_0^2)}\left\{\oint_{\partial S} Y_0 Z_{wall} E_{0n}^{*(irr.)}(\vec{r},\vec{r}_0)\left(\beta_0 E_n^{(irr.)}(\vec{r},\vec{r}_1)+\beta_0^{-1}E_n^{(sol.)}(\vec{r},\vec{r}_1)\right)d\ell - \right.$$

$$\left. - \oint_{\partial S} E_{0z}^{*}(\vec{r},\vec{r}_0)E_n^{(irr.)}(\vec{r},\vec{r}_1)d\ell\right\} = \frac{1}{\epsilon_0}\left[\Phi_0^{*}(\vec{r}_1,\vec{r}_0)-\Phi(\vec{r}_0,\vec{r}_1)\right]. \qquad (34)$$

From eq.s (34) and (26), letting $\vec{r}_0, \vec{r}_1 \longrightarrow 0$, we get [12]:

$$Z_{\|}(\omega)-Z_{0\|}(\omega) = \frac{\epsilon_0}{\beta_0 c Q^2}\left\{Y_0 \oint_{\partial S} Z_{wall} E_{0n}^{(irr.)*}(\vec{r},0)\left[\beta_0 E_n^{(irr.)}(\vec{r},0)+\beta_0^{-1}E_n^{(sol.)}(\vec{r},0)\right]d\ell - \right.$$

$$\left. - \oint_{\partial S} E_{0z}^{*}(\vec{r},0)\; E_n^{(irr.)}(\vec{r},0)\; d\ell\;\right\}. \qquad (35)$$

where we used the well known fact that the longitudinal impedance of a perfectly conducting pipe (*unperturbed* situation) is a pure reactance [20].

Furthermore, from the dyadic Panofsky-Wentzel theorem (23), applying the dyadic differential operator $\nabla_{\vec{r}_0}\nabla_{\vec{r}_1}$ to both sides of the identity (34), letting $\vec{r}_0, \vec{r}_1 \longrightarrow 0$, and then using (27), we get:

$$\overline{\overline{Z}}_{\perp}(\omega) - \overline{\overline{Z}}_{0\perp}(\omega) = \frac{\epsilon_0}{\beta_0 c Q^2 k}\left\{Y_0 \oint_{\partial S} Z_{wall}\nabla_{\vec{r}_0}E_{0n}^{(irr.)*}(\vec{r},\vec{r}_0)\;\nabla_{\vec{r}_1}\left[\beta_0 E_n^{(irr.)}(\vec{r},\vec{r}_1)+\right.\right.$$

$$\left.\left. +\beta_0^{-1}E_n^{(sol.)}(\vec{r},\vec{r}_1)\right]d\ell - \oint_{\partial S}\nabla_{\vec{r}_0}E_{0z}^{*}\;(\vec{r},\vec{r}_0)\nabla_{\vec{r}_1}E_n^{(irr.)}(\vec{r},\vec{r}_1)\;d\ell\;\right\}\Bigg|_{\vec{r}_0=\vec{r}_1=0}. \qquad (36)$$

Equations (35) and (36) relate the *perturbed* and *unperturbed* coupling impedances[6]. They show the different roles played by the boundary and material perturbations in

[6]The longitudinal and transverse impedances are obviously independent of the total charge, as the fields in (35) and (36) are proportional to Q.

a particularly clear fashion. As a matter of fact, the r.h.s of eq.s (35) and (36) is the sum of two terms: the first is nonzero if and only if Z_{wall} is not identically zero on the boundary ∂S, and accordingly accounts for the effect of the constitutive properties of the (imperfectly conducting) wall[7]. The second integral term on the r.h.s. of eq.s (35) and (36) on the other hand, is non-zero if and only if the *unperturbed* axial field component E_{0z} is not identically zero on ∂S, and thus accounts for the effect of the geometrical perturbation of the boundary. Accordingly the second integral in (35) and (36) effectively spans only the *geometrically perturbed* boundary subset $\partial S - \partial S_0$.

4.1 Approximate (Perturbative) Formulae

Equations (35) and (36) as they stand are *exact* but of little use, since if the fields in the *perturbed* geometry were known, one could compute the coupling impedances directly, using eq.s (24). However, following a standard procedure of microwave engineering [23], we may *approximate* the unknown fields in the *perturbed* geometry by those produced by the same source term in the *unperturbed* geometry, in order to compute the perturbed coupling impedances using (35) and (36). The error introduced in by this substitution can be estimated as follows. Let us denote as:

$$\delta = \mathcal{M}\ (\partial S - \partial S_0), \tag{37}$$

the measure (length) of the difference between the perturbed and unperturbed boundary, and let further:

$$Z_{wall} = \bar{Z}_{wall}\ \Delta, \qquad \bar{Z}_{wall} = \frac{Z_{wall}}{\Delta}\ , \qquad \Delta = max_{\partial S}\ |Z_{wall}|\ , \tag{38}$$

Using the following power expansion for the unknown field:

$$\vec{E} = \vec{E}_0 + \sum_{l,m=0,\infty}^{l+m\geq 1} \vec{E}_{lm}\ \Delta^l\ \delta^m, \tag{39}$$

and similar expansions for the unknown impedances in eqs. (35) and (36), we recognize that the approximate formulae correspond to keeping only the linear terms in the formal development of the impedance perturbations in powers of Δ and δ. Therefore the error made after taking $\vec{E} \sim \vec{E}_0$ is at least of second order in the assumed *small* parameters δ and Δ.

In many instances, the exact coupling impedances depend *linearly* from Δ and/or δ. In those cases, our approximate procedure returns the *exact* solution. This happens, e.g., for the circular pipe of radius b with resistive wall, where eq. (35) becomes:

$$Z_{||} = \frac{Z_{wall}}{2\pi b}. \tag{40}$$

[7]Note that in the *local* spirit of Leontóvich boundary conditions, Z_{wall} can vary from point to point along ∂S, thus describing quite general inhomogeneous cross-section contours, consisting, e.g., of different materials.

In fact, letting

$$\vec{E}(\vec{r},\vec{r}_{0,1}) = \vec{E}_0(\vec{r},\vec{r}_{0,1}) = \frac{Q}{2\pi\epsilon_0}\left\{\frac{\vec{r}-\vec{r}_{0,1}}{|\vec{r}-\vec{r}_{0,1}|^2} - \frac{\vec{r}-\vec{r}_{0,1}(b/r_{0,1})^2}{|\vec{r}-\vec{r}_{0,1}(b/r_{0,1})^2|^2}\right\}, \tag{41}$$

where E_0 is the known exact solution for a circular pipe of radius b with perfectly conducting wall[8] into (35) and (36), taking into account that:

$$\lim_{r_0\to 0}\nabla_{\vec{r}_0}\vec{E}_0(\vec{r},\vec{r}_0) = \lim_{r_1\to 0}\nabla_{\vec{r}_1}\vec{E}_0(\vec{r},\vec{r}_1) = \frac{Q}{\pi\epsilon_0 b^2}\,\frac{\vec{r}}{r}, \tag{42}$$

and using:

$$Z_{wall} = Z_0(1-\frac{j\sigma}{kv_0\epsilon_0})^{-1/2}, \tag{43}$$

where σ is the wall conductivity, we obtain:

$$Z_{\|} = \sqrt{\frac{|\omega|\mu_0}{2\sigma}}\,\frac{[1+j\ sgn(\omega)]}{2\pi b}, \quad (\sigma >> kv_0\epsilon_0), \tag{44}$$

and

$$k\,(\bar{\bar{Z}}_{\perp} - \bar{\bar{Z}}_{0\perp}) = \sqrt{\frac{|\omega|\mu_0}{2\sigma}}\,\frac{[1+j\ sgn(\omega)]}{\pi b^3}(\hat{u}_x\hat{u}_x + \hat{u}_y\hat{u}_y), \quad (\sigma >> kv_0\epsilon_0), \tag{45}$$

in complete agreement with the exact solution reported in [24].

4.2 Parasitic Loss Formula

Once the perturbed longitudinal impedance (35) has been computed, it is possible to calculate the energy lost by the beam due to the finite conductivity of the chamber wall (parasitic loss [25]). The energy lost per unit pipe length ($J\ m^{-1}$) is[9]:

$$\frac{\Delta\mathcal{E}}{L} = \int_{-\infty}^{+\infty} d\omega\ |I(\omega)|^2 Re\left\{Z_{\|}(\omega)\right\}, \tag{46}$$

where $I(\omega)$ is the beam current frequency spectrum. As already emphasized, the space charge term (second term in r.h.s. of (35)) does not contribute to the resistive part of $Z_{\|}$, and the unperturbed impedance $Z_{\|}^{(0)}$ is purely reactive. Hence, from (35):

$$\frac{\Delta\mathcal{E}}{L} = \frac{\epsilon_0\,Y_0}{c\,Q^2}\int_{-\infty}^{+\infty} d\omega\ |I(\omega)|^2 \oint_{\partial S} dl\ Re\left\{Z_{wall}E_{on}^{(irr.)}(E_{on}^{(irr.)} + \beta_0^{-2}E_{on}^{(sol.)})\right\}. \tag{47}$$

[8]The field (41) is produced by the charge Q at $\vec{r}_0$, and its image at $\vec{r}_0(b/r_0)^2$.

[9]As the particle velocity is purely longitudinal transverse forces don't make any work.

5 Computation of Wall Impedance for Multi-Layered Pipes

Accelerator pipes are usually composed of several conducting shells with different electrical properties, possibly separated by non-conducting (e.g., vacuum) layers. In order to compute the electromagnetic field within such structures one has to solve, in principle, Maxwell equation in *each* homogeneous region, enforcing the usual boundary conditions (continuity of the tangential field components) at the interfaces between material media with different properties). In many instances, on the other hand, one is only interested in computing the field in one region S only, e.g., the beam chamber. In this case, impedance boundary conditions, when applicable [17], can substantially improve computational efficiency. Impedance boundary conditions have been assumed to apply in deriving eq.s (35), (36).

In the simplest case, impedance boundary conditions read:

$$\hat{n} \times \left[\hat{n} \times \vec{E} - Z_{wall}\vec{H}\right]_S = 0, \tag{48}$$

where S is the boundary of the problem's domain, Z_{wall} describes the external medium, and $\hat{n}$ the outward unit vector normal to S. The heuristic principle behind them is discussed below.

For a plane wave incident on an optically lossy half-space, the transmitted field wave-vector is normal to the interface plane S, for any angle of incidence. Thus in the lossy half-space including S^+ (the face of S inside the lossy medium) one has in the spectral domain:

$$\hat{n} \cdot \vec{e} = \hat{n} \cdot \vec{H} = 0, \quad \hat{n} \times \vec{E} = Z\ \vec{H}, \quad Z = Z_0 \left(1 - j\frac{\sigma}{\omega\epsilon_0}\right)^{-1/2}, \tag{49}$$

where Z is the characteristic impedance of the lossy material, $Z_0 = 376.7\ ohm$ the free space wave impedance, and $\hat{n}$ unit vector normal to S poynting toward the lossy medium. The tangential field components being continuous across S, equation (48) holds true on S^- (the face of S outside the lossy medium) as well.

The applicability of Leontóvich conditions to more general situations relies on the following heuristic arguments. The plane-wave incident field assumption can be relaxed, provided the medium is sufficiently lossy over all the plane wave spectrum of the incident field. The plane interface assumption, on the other hand, can be relaxed provided S can be viewed as *locally* plane within the first Fresnel zone drawn on the (plane) wavefront tangent to S^+. The radius of the first Fresnel zone goes to zero with the wavelength inside the medium, i.e., as $|n|$ goes to infinity, n being the boundary material refraction index. A sufficient condition which fulfills all requirements above is [17]:

$$\mathcal{I}m(n)\ k\ R \gg 1 \tag{50}$$

throughout the whole $k-$spectrum of the incident field, R being the (local) curvature radius of the boundary surface. Equation (50) is met in a wide variety of practical relevant cases, and Leontóvich conditions are accordingly widespreadly used in microwave engineering.

For multilayered lossy walls, we can capitalize on the well known analogy between transverse electromagnetic (TEM) plane-waves in transversely homogeneous, longitudinally stratified media, and voltage (current) waves in cascaded trasmission lines tracts [26]. The analogy is embodied in the fact that the electric and magnetic field components in a layer with (complex) constitutive parameters ϵ, μ and thickness L, obey the same equations (see *Appendix C*) as the voltage and current waves in a trasmission line tract of lenght L, characteristic impedance $Z_0 = (\mu/\epsilon)^{1/2}$ and wave number $\beta = \omega(\epsilon\mu)^{1/2}$. The distance along the (locally common) normal to the layers corresponds to the transmission line longitudinal coordinate z, the electric and magnetic field components correspond to V and I. In a lossy medium β has a large (negative, frequency dependent) imaginary part $\alpha = (\sigma/\omega\mu)^{1/2}$, whose reciprocal is the so called penetration-depth, $\delta_S = (2\omega\mu\sigma)^{-1/2}$. A layer for which $L \gg \delta_s$ can be thought of as being infinitely thick for all practical purposes.

As an illustration, consider a pipe wall consisting of two lossy layers (see *Fig. 2a*), the outermost one being so thick and lossy as to be considered to extend to infinity.

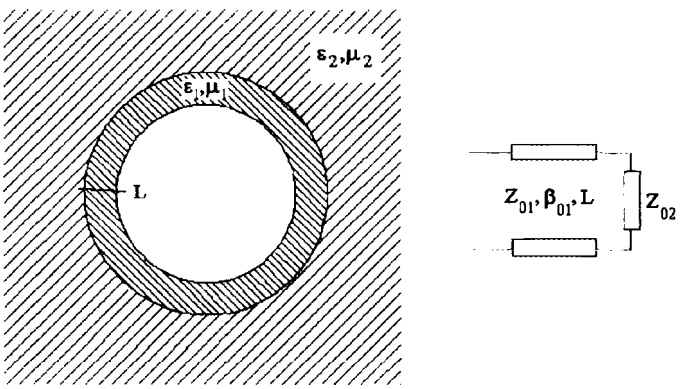

Fig. 2 - Pipe with two-layer wall (a)
and equivalent trasmission line circuit (b)

The equivalent wall impedance Z_{wall} to be used in applying Leontóvich boundary condition (48) at the innermost surface S^-, is the input impedance $Z(z)$ of the transmission line circuit shown in *Fig.2b*, and can be accordingly computed by using the transport formula for the (voltage) reflection coefficient $\Gamma(z)$, viz.:

$$\Gamma(z) = \Gamma(0)e^{2j\beta z}, \tag{51}$$

and the relationship between the reflection coefficient and the impedance[10]:

[10]For the sake of the Reader who might be unfamiliar with transmission line theory, these concepts are reviewed in *Appendix C*.

$$Z(z) = Z_0 \frac{1+\Gamma(z)}{1-\Gamma(z)}. \tag{52}$$

by successively computing the following quantities: $Z(0)=(\mu_2/\epsilon_2)^{1/2} \longrightarrow \Gamma(0) \longrightarrow \Gamma(-L) \longrightarrow Z(-L) = Z_{wall}|_{S^-}$. The whole procedure can be iterated to apply to multi-layered walls.

As a further, perhaps less intuitive example, consider the situation in *Fig. 3.*

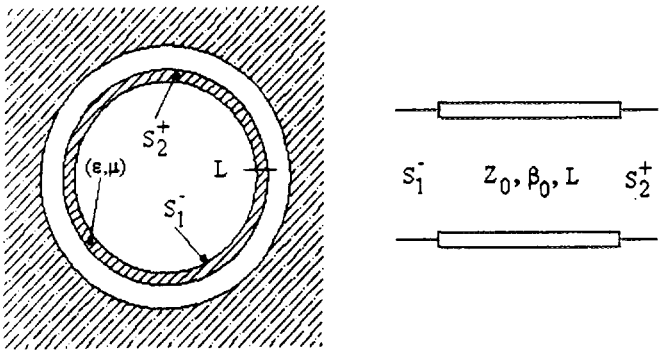

Fig. 3 - Lossy shell separating vacuum chamber from vacuum gap (a) and equivalent trasmission line circuit (b)

In this case, the assumption of (lossy) TEM propagation in the direction (locally) normal to the boundary is *not* justified a priori within the *vacuum* layer. Accordingly, whenever the lossy layer thickness isn't large w.r. to δ_S, one has to solve Maxwell equations *both* in the pipe *and* in the vacuum gap. However, it is *not* necessary to solve Maxwell equations *in* the lossy layer. In the spirit of Leontóvich boundary conditions, it is instead possible to relate the tangential fields at S_2^+ to those at S_1^- via a transmission matrix (see *Appendix B*), viz.:

$$\begin{cases} -\hat{n} \times \vec{E}_{tan}(S_2^+) = \mathcal{A}\, \hat{n} \times \vec{E}_{tan}(S_1^-) + \mathcal{B}\, \vec{H}_{tan}(S_1^-) \\ \vec{H}_{tan}(S_2^+) = \mathcal{C}\, \hat{n} \times \vec{E}_{tan}(S_1^-) + \mathcal{D}\, \vec{H}_{tan}(S_1^-). \end{cases} \tag{53}$$

The reason for using a transmission matrix instead of an impedance or scattering one is that the overall transmission matrix of cascaded transmission line tracts is just the product of the individual transmission matrices, which makes the extension to multilayered lossy shells separating vacuum regions almost immediate.

6 Impedance Boundary Conditions at Perforated Walls

In the proposed LHC design, gas desorption due to synchrotron radiation and subsequent surface deposition on the beam screen limits the efficiency of the beam pipe vacuum system, unless many small perforations are drilled on its surface, allowing for a transfer of the excess gas to a cold bore wall, where the pumping capacity is adequate [27]. Making the holes small enough (in terms of a typical synchrotron wavelenght) is necessary to prevent significant radiation exposure of the cold bore.

The effect of so many ($\sim 10^6\ m^{-1}$) holes on the beam coupling impedances should be carefully investigated, in order to optimize their shape, size, number and distribution. Equations (35) and (36) can still be used to compute approximate coupling impedance values, using suitable local impedance boundary conditions on the perforated wall area.

Extensive work in connection with perforated pipes has been done by Kurennoy [29], Gluckstern [30] and Co-workers, in the frame of Bethe's theory [28] of diffraction from *small* holes[11]. For the longitudinal impedance per unit length of a circular beam pipe with radius b carrying N_λ holes, per unit length, both Authors find [12]:

$$Z_{\|} \;=\; -jZ_0\,k_0\,\frac{(\alpha_e+\alpha_m)}{4\pi^2 b^2}\,N_\lambda \;=\; -j\frac{Z_0\,k_0}{2\pi b}\frac{(\alpha_e+\alpha_m)}{s_t\,s_z}, \tag{54}$$

where $k_0 = \omega/c$ is the free-space wavenumber, c being the vacuum light-velocity, $\alpha_{e,m}$ are the electric and magnetic polarizabilities of each hole, and we assumed these latter to form a regular array with spacings s_t and s_z in the transverse and axial directions of the beam pipe, respectively, so as to let:

$$N_\lambda \;=\; \frac{2\pi b}{s_t s_z}. \tag{55}$$

By comparing eq.s (54) and (40), which applies to a circular pipe, one is led to the heuristic conclusion that the perforated wall can be described by an impedance boundary condition with[13]:

$$Z_{wall} \;=\; -j\,\frac{Z_0 k_0}{s_t s_z}(\alpha_e+\alpha_m). \tag{56}$$

The single hole polarizabilities $\alpha_{e,m}$ depend on the hole shape and size and the wall thickness (see [33], [34] for a list of available results). For the simplest case of circular

[11] A notable result of Kurennoy's analysis, whose interest lies beyond the pumping-hole issue, is related to the occurrence of *trapped modes* in the neighbourhood of pipe discontinuities [31]. On the other hand, Gluckstern improved over Bethe's results by including a nonzero wall thickness [32].

[12] Kurennoy has also computed the (negligible) real correction to (54) resulting from radiation leakage through the holes [36].

[13] The exact solution of the canonical problem of plane wave incidence on a conducting plane bearing a 2–dimensional regular array of holes, and of the corresponding (lowest order) impedance boundary conditions yields twice the value (56) [37].

holes in a thin plane, one has [28] $\alpha_e = -(2/3)r_0^3$, $\alpha_m = (4/3)r_0^3$, r_0 being the hole radius. For holes drilled in a plane with thickness w such that $w/r_0 > 2$ one has with good accuracy[14]:

$$\alpha_{e,m}^{(i)} \approx 0.56\, \alpha_{e,m}^{(0)}, \quad \alpha_{e,m}^{(e)} \approx \alpha_{e,m}^{(0)}\, e^{-\xi_{e,m}(w/r_0)}, \tag{57}$$

where the superfix $(e), (i), (0)$ refers to the external, internal and zero wall thickness polarizability, $\xi_e \approx 2.405$, $\xi_m \approx 1.841$.

It would be desirable to improve eq. (56) by *i*) including the effect of electromagnetic coupling among the holes, and *ii*) taking into account the effect of the imperfectly conducting cold-bore wall.

Electromagnetic coupling among the holes can be accounted by using in (56) the *effective* electric polarizabilities $\alpha'_{e,m}$ of each hole, *in the presence of the others*, viz.:

$$\alpha_{e,m} \longrightarrow \alpha'_{e,m} = \frac{\alpha_{e,m}}{1 - C_{e,m}\alpha_{e,m}}, \tag{58}$$

where the coupling constants depend on the induced dipole orientation. In a relativistic beam pipe, the induced electric dipoles are normal to the perforated wall, while the magnetic ones are tangent, and for circular holes, parallel to the (transverse) magnetic field. Then (see *Appendix C*) [15]:

$$C_e = C_\perp = s^{-3}\left[-\frac{12}{5\pi} + 8\pi\, K_0(2\pi),\right] \tag{59}$$

$$C_m = C_\parallel = s^{-3}\left[\frac{6}{5\pi} - 8\pi\, K_0(2\pi),\right] \tag{60}$$

where K_0 denotes the Bessel function of the $3rd$ kind.

Next we may wish to include the effect of an external, coaxial imperfectly conducting tube (cold-bore). For the special case of a circular liner of radius b surrounded by a coaxial colde-bore tube of radius a, according to [39] one has[16]

$$Z_\parallel = -j\frac{Z_0\, k_0}{4\pi^2 b^2}\left[(\alpha_e + \alpha_m) - \frac{(\alpha_e + \alpha_m)^2}{(\alpha_e + \alpha_m) + j\, s_t s_z \delta_S (1 + b/a)}\right] N_\lambda \tag{61}$$

where δ_S is the field penetration depth into the walls of the coaxial region. If $(\alpha_e + \alpha_m) \ll s_t s_z \delta_S (1 + b/a)$ by comparison with (40) one is led to the following wall impedance:

---

[14]Equations (57) are obtained by regarding the thick hole as a cut-off circular waveguide [32], [35].

[15]Equations (59), (60) imply a quasi static ($s_t, s_z << \lambda$) assumption, which could be removed at the expense of some complications (See *Appendix C*).

[16]In [39] the assumption of one hole per each pipe cross section contour is implicitly made, viz., $s_t = 2\pi b$.

$$Z_{wall} = -j\frac{Z_0 k_0}{s_t s_z}\left[(\alpha_e + \alpha_m) + j\frac{(\alpha_e + \alpha_m)^2}{s_t s_z \delta_S (1 + b/a)}\right] \tag{62}$$

to describe an (imperfectly conducting) perforated tube of radius b surrounded by another imperfectly conducting tube with radius a.

It is interesting to note that eq. (62) is obtained by computing the parallel impedance of (56) and

$$Z_{eq} = Z_m(1 + \frac{b}{a}) \tag{63}$$

which represents the surface impedance at $r = b$ accounting for the losses in *both* walls of the coax region, where Z_m is the characteristic impedance of the walls[17].

It should be noted, however, that the above discussed corrections to (56) should be taken as meaningful only by comparison with terms of higher order in $k \cdot (hole\ size)$, in the expansion of $\alpha_{e,m}$, [40] which are neglected when using Bethe's formulas for $\alpha^{(0)}_{e,m}$.

7 Conclusions

We outlined a simple approach to the analytic computation of beam coupling impedances and related quantities in accelerator pipes with complex geometric and (electromagnetic) constitutive features.

The accuracy could be further improved by including higher order impedance boundary conditions [38], and using the variational form of the reciprocity (reaction) theorem [23]. Work in both directions is currently in progress.

References

[1] T. Weiland, Nucl. Instrum. Meth. **216**, 31, 1983.

[2] K.F.L. Bane et al., SLAC-PUB 3528, 1984.

[3] S. Heifets and S. Kheifets, Rev. of Modern Physics, 1991 and SLAC-PUB-5297, 1990.

[4] S.S. Kurennoy, CERN SL/91-31 (AP), 1991.

[5] K. Yokoya, Part. Acc. **41**, 221, 1993.

[6] S. Heifets, Part. Acc. **42**(3-4), 199, 1993.

[7] B. Zotter and T.S. Wang, CERN Rep. SL, 1991.

[17] This is an obvious consequence of the r^{-1} dependance of the TEM magnetic field in the coaxial region.

[8] R.L. Gluckstern et al., Phys. Rev. E, **47**(1), 656,1993.

[9] M.M. Karliner et al., Budker INP 94-45, 1994.

[10] S. Petracca, CERN Rept. SL/AP 93-13; Part. Acc., **48**, 181, 1994.

[11] S. Petracca, CERN SL Note 94-59 (AP).

[12] S. Petracca, CERN SL/Note 94-78; Particle Accelerators, 1995, in print; IEEE Trans. Nucl. Sci., 1995, in print.

[13] J. Schwinger, J. Appl. Phys. **22**, 806, 1951.

[14] A.W. Chao, *Physics of Collective Beam Instabilities in High Energy Accelerators*, J. Wiley & Sons, 1993, *Sect. 2.1.*

[15] P.M. Morse and H.P. Feshbach, *Methods of Theoretical Physics*, McGrawHill, 1976.

[16] J. Van Bladel, *Electromagnetic Fields*, Hemisphere, 1990.

[17] T.B.A. Senior, IEEE Trans. **AP-29**, 826, 1981.

[18] M.A. Leontóvich, *Issledovanya po Rasprostraneniyu Radiovoln.* USSR Acad. Press, 1948.

[19] A.W. Chao, ibid., *Sect. 2.2.*

[20] P.B. Wilson, SLAC-PUB 4547, 1989.

[21] A.W. Chao, ibid., *Sect. 2.3.*

[22] L. Palumbo et al., CERN CAS 87-03, **1**, 341, 1987.

[23] R.F. Harrington, *Time Harmonic Electromagnetic Fields*, McGraw-Hill, 1961, *Ch. 7.*

[24] A.W. Chao, ibid., *eq.s 2.77.*

[25] A.W. Chao, ibid., *Sect. 2.5.*

[26] J. A. Stratton, *Electromagnetic Theory*, McGraw Hill, New York, 1941.

[27] -CERN LHC Design Study, 1991.

[28] H. Bethe, Phys. Rev. **66**, 163-182, 1944.

[29] S. S. Kurennoy (et al.), CERN SL/91-29(AP) rev.; IHEP 92-84 UNK; Part. Acc., **39**, 1, 1992; SSCL-636, 1993; SSCL-650, 1993; Proc. EPAC, 1265, 1994.

[30] R. L. Gluckstern (et al.), CERN SL/90-113(AP), CERN SL/92-05(AP), CERN SL/92-06(AP), CERN SL/92-18(AP), IEEE Trans. **MTT39**, 274, 1991, IEEE Trans. **MTT38**, 186, 1990; ibid., 1529, (corrections).

[31] S.S. Kurennoy, Phys. Rev. **E49**, 794-799, 1994; ibid. **51**, 1995.

[32] R.L. Gluckstern Phys. Rev. **A46**, 1106, 1992.

[33] S.B. Cohn, Proc. IRE, **39**, 1416-1421, 1951; ibid. **40**, 1069-1071, 1952.

[34] J. van Bladel et al., IEEE Trans., **AP-25**, 198-205, 1977; IEEE Trans., **AP-28**, 703-707, 1980.

[35] N. McDonald, IEEE Trans., **MTT-20**, 689-695, 1972.

[36] S.S. Kurennoy, IHEP Rep. 92-84 - UNK, 1992.

[37] S. Petracca, CERN SL Rept., 1995 in preparation.

[38] T.B.A. Senior and J.L. Volakis, IEEE Trans., **AP-37**, 1566-1572, 1989.

[39] R.E. Gluckstern, CERN SL 92-06 (AP).

[40] J. Van Bladel, Radio Sci. **14**, 319-331, 1979.

[41] A.N. Kolmogorov and V.S. Fomin, *Elements of Functional Analysis*, MIR, 1972.

[42] W.J. Welch, IRE Trans. Antennas Propagat., **8**, 63, 1960.

[43] V.H. Rumsey, Phys. Rev., **94** (2), 1483, 1954.

[44] J. Brown and W. Jackson, Proc. IEE, **B102**, 37-42, 1955.

[45] H.S. Bennett, J. Appl. Phys., **24**, 785-810, 1953.

[46] E.C. Titchmarsh, *The Theory of Functions*, Oxford Un. Press, 1939, p. 443

[47] I.S. Gradshteyn and I.M. Ryzhik, *Table of Integrals Series and Products*, Academic Press, 1980, eq. 3.754.2

[48] R.E. Collin, *Field Theory of Guided Waves*, IEEE Press, 1991, *prob.s 12.7 and 12.8.*

Appendix A - Lorentz Reciprocity Theorem

Reciprocity is a general property of self adjoint (integro-differential) operators [41] defined in a domain U, for which:

$$\langle \mathcal{L} f, g^* \rangle = \langle f, \mathcal{L}^* g^* \rangle , \qquad (A1)$$

where $\langle \cdot, \cdot \rangle$ denotes the (functional) scalar product over any subdomain of U.

The reciprocity theorem is readily established as follows. Let:

$$\mathcal{L}\, f = u, \quad \mathcal{L}\, g = v, \qquad (A2)$$

describe two different situations, where $\mathcal{L}$ is the problem Green operator, the source-terms f and g are in general different, and the two situations *may* also differ in a sub-domain $\Delta U \subset U$, where, e.g., the medium physical properties could have been changed. Taking the product of the complex conjugate of the second equation in $(A2)$ by f, subtracting the first equation multiplied by g^*, and integrating over the problem domain U one gets:

$$\langle f, \mathcal{L}^* g^* \rangle - \langle \mathcal{L} f, g^* \rangle = \langle v^*, f \rangle - \langle g^*, u \rangle . \qquad (A3)$$

In view of (A1), the last identity takes the form:

$$\langle f, \mathcal{L}^* g^* \rangle_{\Delta U} - \langle \mathcal{L} f, g^* \rangle_{\Delta U} = \langle v^*, f \rangle - \langle g^*, u \rangle . \qquad (A4)$$

For the special case where $\Delta U = \emptyset$ one gets the simplest result:

$$\langle v^*, f \rangle = \langle g^*, u \rangle . \qquad (A5)$$

The (functional) scalar products $\langle v^*, f \rangle$ and $\langle v^*, f \rangle$ are technically called *reactions*, and thus the reciprocity theorem in its simplest form states that the reaction of the *source* f on the *field* v^* is equal to the reaction of the *source* g^* on the *field* u.

In isotropic media, the Green function of the Maxwell equations is self-adjoint, and the reciprocity theorem can be accordingly established in full generality [42]. The corresponding formulation in terms of reactions has been thoroughly emphasized by Rumsey [43].

Appendix B - Transmission Line Concepts

Voltage and current waves in uniform transmission lines are described, (in the time harmonic or frequency domain representations), by:

$$V(z) = V^+ e^{-j\beta z} + V^- e^{j\beta z}, \qquad I(z) = Y_0[V^+ e^{-j\beta z} - V^- e^{j\beta z}], \qquad (B1)$$

where V^+, V^- are the complex amplitudes of the forward and backward voltage waves, β, Y_0 are the medium propagation constant and characteristic admittance, respectevely.

The (voltage) reflection coefficient:

$$\Gamma(z) := \frac{V^- e^{j\beta z}}{V^+ e^{-j\beta z}} = \Gamma(0)\, e^{2j\beta z}, \qquad (B2)$$

is the ratio between the complex amplitude of the reflected and incident voltage waves. Using eq. $(B3)$ in $(B1)$ we get:

$$V(z) = V^+ e^{-j\beta z}\,[1+\Gamma(z)], \qquad I(z) = Y_0 V^+ e^{-j\beta z}\,[1-\Gamma(z)]. \qquad (B3)$$

The local impedance on a (uniform) transmission line is defined by:

$$Z(z) := \frac{V(z)}{I(z)} = Z_0\,\frac{1+\Gamma(z)}{1-\Gamma(z)}. \qquad (B4)$$

Equations $(B2)$ and $(B4)$ allow to obtain the input impedance of a homogeneous transmission line tract of length ℓ terminated into a load impedance Z_L. In fact, once $Z(0) = Z_L$ is known, so is $\Gamma(0)$ from $(B5)$. Then eq. $(B3)$ gives $\Gamma(-\ell)$, and from this using again $(B5)$ one gets the input impedance $Z(-\ell)$. Iterating the above reasoning, one can easily compute the input impedance of several cascaded homogeneous transmission line tracts, like in *Fig. 2b*. Equations $(B2)$ and $(B4)$ also show that the input impedance of a transmission line extending to infinity, for which $V^- = 0$, is Z_0 at any z.

To obtain the trasmission matrix of an homogeneous transmission line tract, consider the two port network representing a line tract with propagation constant β and characteristic impedance $Z_0 = 1/Y_0$, where V_2, I_2 and V_1, I_1 are the voltage and current at the output ($z = 0$) and input ($z = -\ell$) ports, respectively. The trasmission matrix relates the output quantities to the input ones as follows:

$$\begin{cases} V_2 = \mathcal{A} V_1 + \mathcal{B} I_1 \\ I_2 = \mathcal{C} V_1 + \mathcal{D} I_1. \end{cases} \qquad (B6)$$

Specializing (B1) at the output and input ports $z = 0, -\ell$ gives:

$$V_2 = V^+ + V^-, \quad I_2 = Y_0[V^+ - V^-], \qquad (B7)$$

$$V_1 = V^+ e^{j\beta\ell} + V^- e^{-j\beta\ell}, \quad I_1 = Y_0[V^+ e^{j\beta\ell} - V^- e^{-j\beta\ell}], \qquad (B8)$$

whence one easily obtains V^+ and V_- as functions of V_1, I_1. Substituting back in (B7) and comparing with (B8) one gets:

$$\mathcal{A} = cos(\beta\ell), \quad \mathcal{C} = Y_0\, cos(\beta\ell) \mathcal{B} = -\,j\, Z_0\, sin(\beta\ell), \quad \mathcal{D} = -\,j\, sin(\beta\ell). \quad (B9)$$

Appendix C - Effective Polarizability in a Plane Regular Array

In this Appendix we summarize the approach developed by Brown [44] and Bennett [45] to compute the effective (electrical or magnetical) polarizability α' of a single hole (possibly noncircular) in a plane regular array. The induced dipole moment f is related to the pertinent field component by:

$$\vec{f} = \alpha(\vec{F}_0 + \vec{F}_{int}), \tag{C1}$$

where α, is the polarizability of a single hole, $\vec{F}_0$, is the incident field, and $\vec{F}_{int}$ is the *interaction* field acting on the each and any hole due to the presence of all other holes. These latter are due to the very existence of the induced dipoles, and can thus be written:

$$\vec{F}_{int} = C\vec{f}, \tag{C2}$$

where C depends only on the dipole orientation and the array geometry, *not* on the type of field (electric or magnetic).
According to eq.s $(C1)$, $(C2)$, the effective polarizability is given by:

$$\alpha' = \frac{\alpha}{1 - \alpha C}, \tag{C3}$$

The interaction constant depends on the direction of the dipoles. It is convenient (superposition) to solve for the simplest cases where each induced dipole f is parallel to one of the co-ordinate axes. For the canonical problem sketched, of a plane regular array of y-directed dipoles placed at $\vec{r}_{nm} = (na)\vec{u}_x + (mb)\vec{u}_y$. the interaction constant will be denoted as C_y.

The general solution of this problem, which implies *no* restriction about the ratio between the dipole spacing and the wavelength has been obtained by Collin [48]. Here we shall confine to the simple case where a quasi-static approximation can be invoked (hole spacing << wavelength), which is appropriate for our present purposes.

The field at $\vec{r} = 0$ (electrostatic or magnetostatic) due to all other dipoles at $\vec{r}_{nm} \neq 0$ can be derived from a scalar potential, viz.:

$$\phi = \vec{u}_y \cdot \sum_{r_{nm} \neq 0} \frac{\vec{r}_{nm}}{4\pi r^3}, \quad F_y = -\partial\phi/\partial y|_{\vec{r}=0}. \tag{C4}$$

Hence, from $(C4)$,

$$C_y = F_y = \frac{1}{4\pi} \sum_{(n,m)\neq(0,0)}^{-\infty,\infty} \frac{2(mb)^2 - (na)^2}{[(mb)^2 + (na)^2]^{5/2}} =$$

$$= \frac{1}{\pi} \sum_{m=1}^{\infty} (mb)^{-3} + \frac{1}{2\pi} \sum_{n=1}^{\infty} \sum_{m=-\infty}^{\infty} \frac{2(mb)^2 - (na)^2}{[(mb)^2 + (na)^2]^{5/2}} =$$

$$= \frac{6}{5\pi b^3} - \frac{2}{\pi b} \sum_{m,n=1}^{\infty} \left(\frac{2m\pi}{b}\right)^2 K_0\left(\frac{2mn\pi a}{b}\right) \sim$$

$$= \frac{6}{5\pi b^3} - \frac{8\pi}{b^3} K_0\left(\frac{2\pi a}{b}\right), \qquad (C5)$$

where the Poisson summation formula [46]

$$\sum_{-\infty}^{\infty} f(\theta m) = \sum_{-\infty}^{\infty} \mathcal{F}[f](2m\pi/\theta), \qquad (C6)$$

$\mathcal{F}$ being the Fourier transform operator has been used together with [47]:

$$\mathcal{F}[(z^2 + a^2)^{-1/2}] = 2K_0(a\omega) \qquad (C7)$$

and the exponentially fast decay to zero of K_0 with increasing argument.

More or less obviously, if the induced dipoles were directed along the $x-$direction, one should interchange a and b in eq. $(C5)$. Hence:

$$C_x \approx \frac{6}{5\pi a^3} - \frac{8\pi}{a^3} K_0\left(\frac{2\pi b}{a}\right). \qquad (C8)$$

Finally, for $z-$directed dipoles the interaction constant can be written:

$$C_z = \frac{1}{4\pi} \sum_{(n,m)\neq(0,0)}^{-\infty,\infty} \frac{(mb)^2 + (na)^2}{[(mb)^2 + (na)^2]^{5/2}} =$$

$$= -\frac{1}{4\pi} \sum_{(n,m)\neq(0,0)}^{-\infty,\infty} \left\{ \frac{2(mb)^2 - (na)^2}{[(mb)^2 + (na)^2]^{5/2}} + \frac{2(na)^2 - (mb)^2}{[(na)^2 + (mb)^2]^{5/2}} \right\} =$$

$$= -(C_y + C_x). \qquad (C9)$$

where the last equality is obtained by comparison with eq.s $(C5)$, $(C6)$.

Observations Involving Broadband Impedance Modelling *

J. Scott Berg
Stanford Linear Accelerator Center, Stanford University, Stanford, CA 94309

Abstract

Results for single- and multi-bunch instabilities can be significantly affected by the precise model that is used for the broadband impedance. This paper discusses three aspects of broadband impedance modelling. The first is an observation of the effect that a seemingly minor change in an impedance model has on the single-bunch mode coupling threshold. The second is a successful attempt to construct a model for the high-frequency tails of an r.f. cavity. The last is a discussion of requirements for the mathematical form of an impedance which follow from the general properties of impedances.

1 Introduction

Computing instability thresholds and growth rates requires good models for broadband and narrow-band impedances.

In some cases seemingly minor changes in the broadband impedance model can cause significant changes in instability thresholds, as shown in section 2. Thus, the broadband impedances in the ring should be modelled more carefully. In section 3, this is done for the high-frequency tails of the r.f. cavities in the PEP-II B factory. Section 4 of this paper describes some of the mathematical properties that an impedance is required to satisfy, and some of the resulting constraints that these properties place on the form of a broadband impedance model.

2 Effect of Impedance Cutoff

The various small objects in the PEP-II ring have been modelled to have an impedance that is primarily inductive [1]. The impedance should be cut off so that the transverse impedance goes to zero at infinity. This can be done by writing the transverse inductive impedance as

$$\frac{-iL}{(1-i\omega/\omega_C)^{3/2}}, \tag{1}$$

where L is the low-frequency inductance, and ω_C is a cutoff frequency. The choice of $3/2$ in the exponent is based on the assumption that the high-frequency tail of the impedance consists of a large number of resonances that give a roll-off similar to a single cavity [2].

The choice of the cutoff frequency ω_C has a strong effect on where transverse single-bunch mode coupling occurs, as shown in Fig. 1. The characteristic frequency cutoff of the bunch distribution $\beta_0 c/2\pi\sigma_\ell$ for this example is 4.77 GHz. Notice that there is a strong variation in the mode coupling threshold even for values of the ω_C well above this frequency.

This result demonstrates that seemingly minor details of the impedance model can have significant effects on the resulting analysis of coherent instabilities.

An important qualification to this example is that this analysis only included the $m = 0$ and $m = 1$ transverse modes (see [3, 4, 5]). As demonstrated in [6, 7, 8], when one includes impedances that have a high-frequency component, as we do here (the real part of (1) peaks at $\tan(\pi/5) \approx .727$ times the cutoff frequency), higher order modes should be included for a complete picture. As can be seen from the definition of K_k in [3, 4, 5], K_k peaks at $k\beta_0 c/4\pi\sigma_\ell$. Thus, m should be at least high enough so that K_{2k} (the diagonal term for row k in our eigenvalue system) has its peak at higher frequencies than any significant impedances for $k > m$. It is not clear whether m should be twice that value, so that even off-diagonal terms with significant overlap are considered even if their corresponding diagonal terms are negligible.

*Work supported by Department of Energy contract DE–AC03–76SF00515.

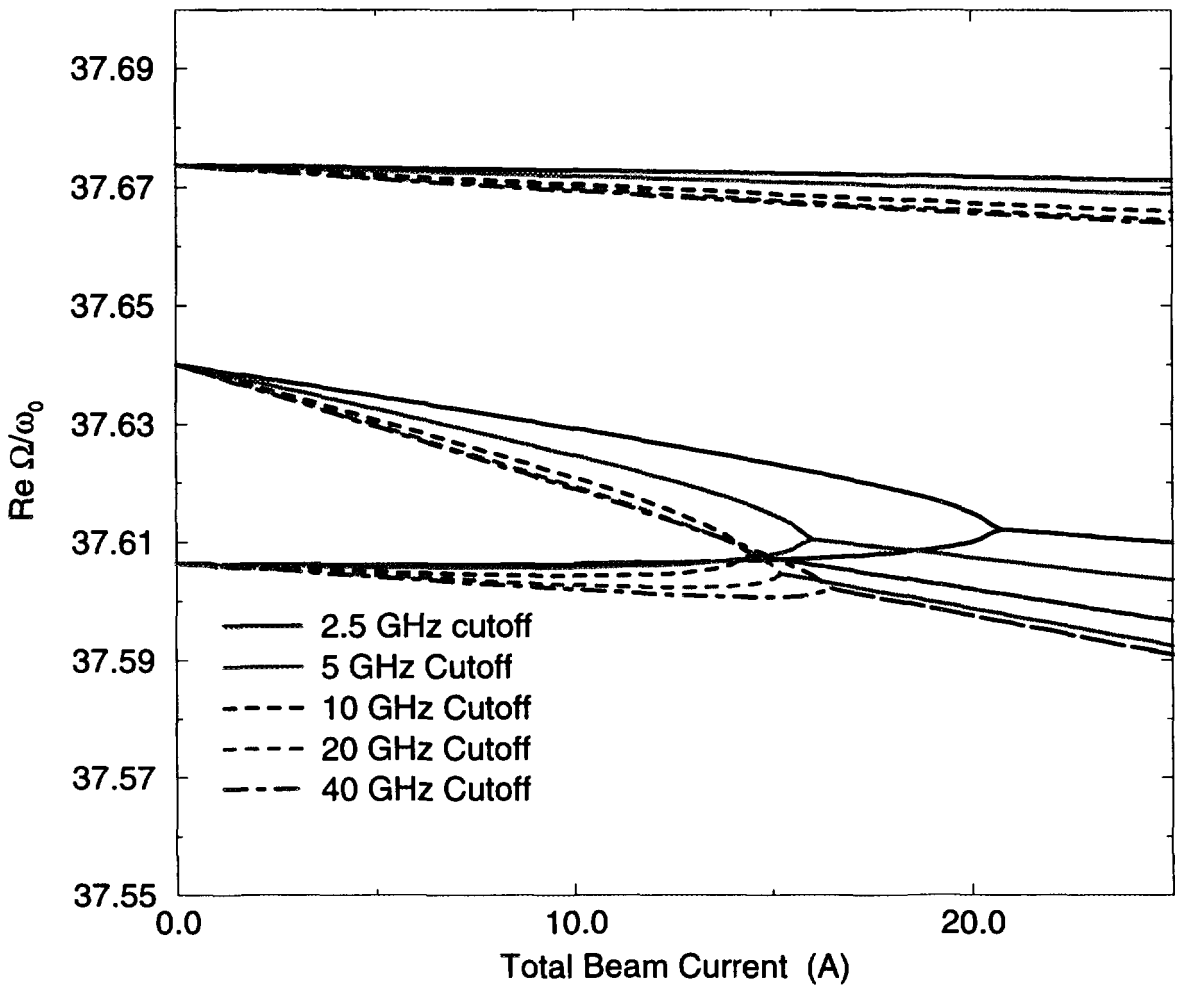

FIGURE 1: Real parts of mode frequencies for a single bunch, plotted versus total beam current. The parameters for the PEP-II B factory are used. The beam becomes unstable at the point where two mode frequencies coincide. Different sets of lines represent different values of inductance cutoff ω_C as described in the text. The impedance is otherwise the model used in [3].

3 Model of High-Frequency Cavity Tails

Section 2 suggests that a good model for the high-frequency impedance behavior is important. An important part of that behavior can come from the high-frequency impedance due to r.f. cavities.

The impedance of the r.f. cavities in PEP-II has been modelled to consist of the known higher-order modes plus a high-frequency tail. The real longitudinal wake of any device must satisfy the following physical considerations [9]:

- It must be real
- It must be causal
- It must be energy-conserving
- It must have no effect on a DC beam.

Since the total wake for the cavity satisfies these properties, then if the higher-order modes used are the real resonant modes of the cavity, it is expected that the remaining wake should also satisfy these properties.

The longitudinal impedance due to a single isolated cavity rolls off as $\omega^{-1/2}$ at high frequencies [10]. Nearly the simplest possible impedance that satisfies the above properties and rolls off as $\omega^{-1/2}$ is

$$iA\left[\left(1+\frac{\omega}{\omega_0+i\alpha}\right)^{-1/2}-\left(1-\frac{\omega}{\omega_0-i\alpha}\right)^{-1/2}\right]. \tag{2}$$

This model is "simple" in the sense that it consists of only a pair of symmetrically placed branch cuts in the lower half plane. The only simpler model would be one where there was a single branch cut along the negative imaginary axis. It turns out that such a model does not have enough freedom to describe the cavity tails.

The model (2) will be used to describe the cavity tails; the parameters A, ω_0, and α will be found based on the actual cavity properties. Other models have been proposed for an impedance with an $\omega^{-1/2}$ roll-off. See [11, 12].

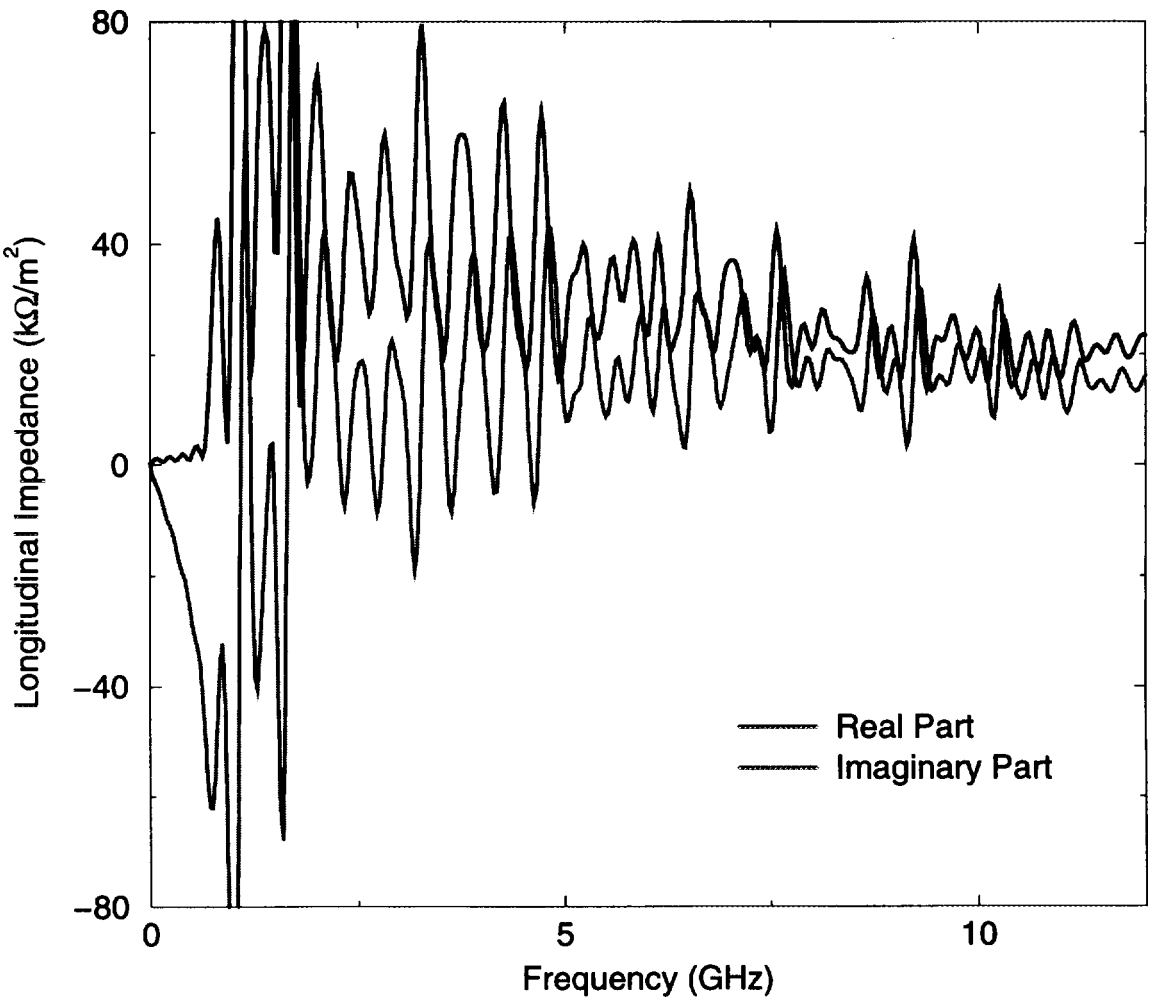

FIGURE 2: Impedance of a PEP-II r.f. cavity model found with ABCI.

The total wake of the cavity is obtained by running a model of the PEP-II r.f. cavity through the program ABCI for $m = 1$ (to get the transverse wake) [1, 13]. The resulting impedance is shown in Fig. 2. The narrow-band impedances from this rough model of the cavity are expected to be similar, but not quite the same, as the known resonant modes of the cavity. Because of this discrepancy in the resonant modes (and the fact that the integration time is relatively short compared to the resonant mode decay times), the impedance of the known cavity modes cannot simply be subtracted from the total cavity impedance. Instead, the wake

due to the known cavity modes is subtracted from the total wake given by ABCI, and the result is Fourier transformed to obtain the impedance. This impedance is shown in Fig. 3.

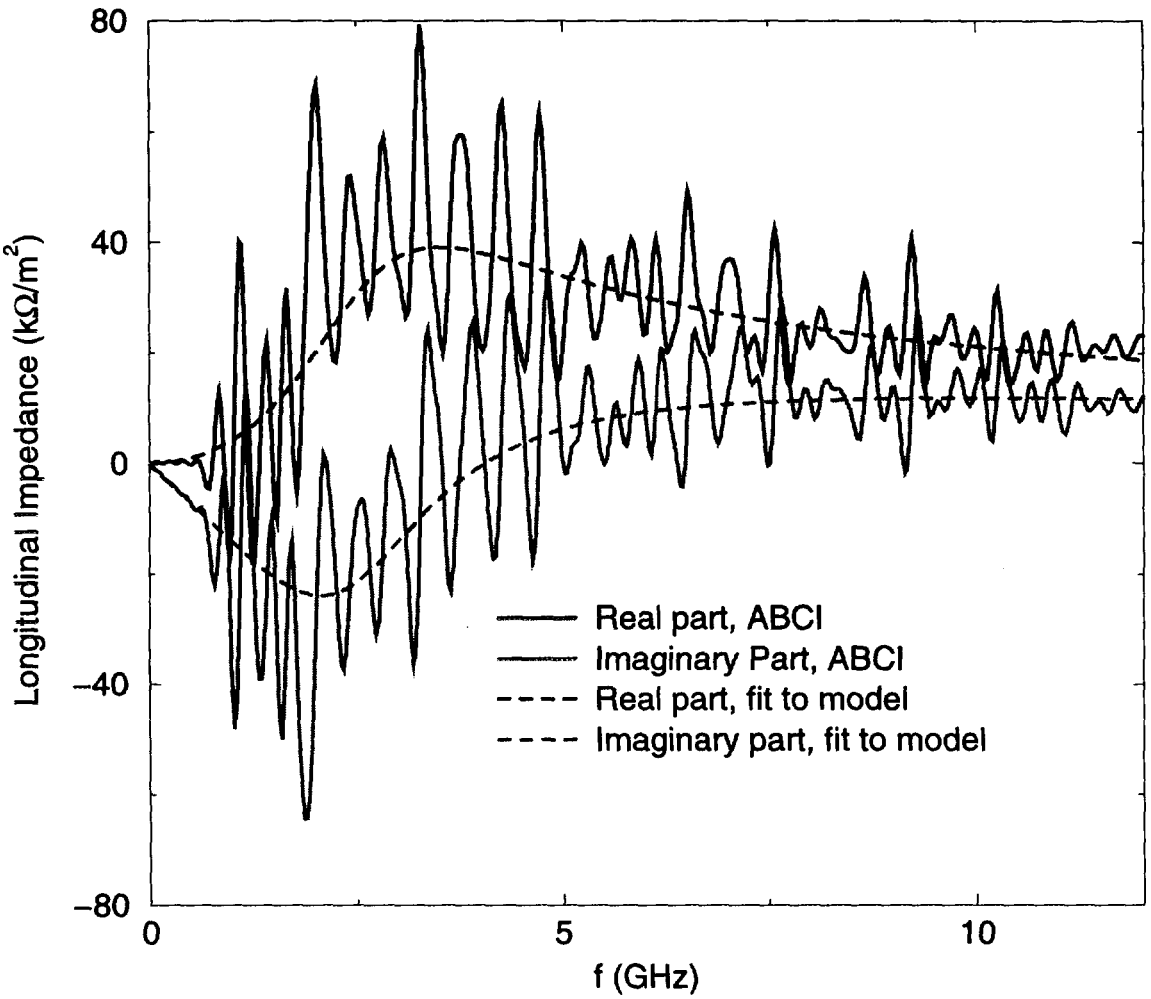

FIGURE 3: Impedance of the PEP-II r.f. cavity with higher-order modes subtracted. Also shown is the model [Eq. (2)] that was fit to this impedance. The parameters of the model are $A = 45.1344$ kΩ/m^2, $\alpha = 1.34722$ GHz, and $\omega_0 = 2.4$ GHz.

The parameters of the model (2) are fit by matching the low-frequency limit of the model to the low frequency limit of the imaginary part of the impedance, and matching the high-frequency limit of the model to the average of the real and imaginary parts of the impedance. The value of ω_0 is fixed for this fit. An initial guess of $\omega_0 = 2$ GHz is made, since this frequency is just above the last of the known cavity modes. The value of ω_0 is adjusted, while maintaining the matching of the low- and high-frequency limits, to give the best fit (as judged by eye). The resulting ω_0 turned out to be 2.4 GHz. A comparison of the fit model and actual impedance (after removal of known higher-order modes) is shown in Fig. 3. The agreement can be seen to be very good.

To obtain the good agreement that was found here, all three parameters in the model were necessary. This is an advantage of this model over the models used in [11, 12], which have fewer degrees of freedom. Note that the cavity tails give a small but non-negligible contribution to the inductance.

This analysis could be improved in the following ways: the value of the parameters could be found by a nonlinear fit instead of fitting one parameter by eye; the wakes could be computed with ABCI for longer times; a better way of subtracting the higher-order modes could be found; and better windowing could be

done on the data (to smooth out the oscillations).

4 General Properties of Impedances

As stated earlier, there are four properties that longitudinal impedances must satisfy [9]:

- The impedance must correspond to a real wakefield. Thus, $[Z(-\omega^*)]^* = Z(\omega)$.
- The impedance must correspond to a causal wake. Thus, it must be analytic in the upper half plane (i.e., no poles or branch cuts).
- The impedance must be energy-conserving. Thus, the real part of $Z(\omega)$ must be non-negative for real ω.
- A DC beam should be unaffected by wakefields. Thus, $Z(\omega)$ must be zero at $\omega = 0$.

This section discusses the constraints that these facts, in particular energy conservation, put on the impedance models that one can construct.

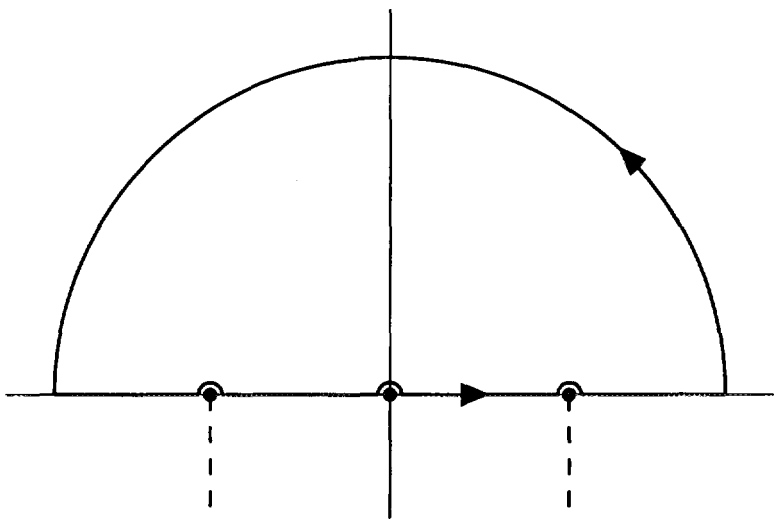

FIGURE 4: Integration contour for $Z'(\omega)/Z(\omega)$. Dashed lines represent branch cuts; the single dot at the origin is a pole of $Z'(\omega)/Z(\omega)$.

Assume that one has an impedance that rolls off like $(-i\omega)^\nu$ as $\omega \longrightarrow \infty$ in the complex plane. Integrate $Z'(\omega)/Z(\omega)$ around the contour shown in Fig. 4. The contour should pass over any zeros or poles of Z on the real axis, or any branch cuts that touch rhe real axis, as shown.

The integral around the contour is

$$i\left(\pi\nu - \pi\sum_{k=0}^{N-1}\alpha_k + \Delta\phi\right), \tag{3}$$

where N zeros, poles, or branch cuts intersect the real axis, each of order α_k respectively (e.g., $\alpha_k = -1$ for a simple pole). The change in phase along the segments on the real axis is $\Delta\phi$. Equation (3) is equal to $2\pi i$ times the number of zeros, including multiplicity, in the upper half plane, n_Z. Note that n_Z must be a nonnegative integer, since no poles or branch cuts can be in the upper half plane for Z. Since the real part of $Z(\omega)$ must be positive along the real axis, the absolute value of the change in phase must be less than or equal to π along any given segment between zeros, poles, or branch cuts. Thus, since there are $N+1$ such segments, $-(N+1)\pi \leq \Delta\phi \leq (N+1)\pi$, resulting in the inequality

$$-(N+1) \leq 2n_Z + \sum_{k=0}^{N-1}\alpha_k - \nu \leq N+1. \tag{4}$$

As an example, say no branch cuts or poles of the impedance touch the real axis. Then the α_k are integers that are greater than or equal to 1. Thus, the sum of the α_k is an integer greater than or equal to N. Since n_Z is a non-negative integer, equation (4) then constrains $\nu \geq -1$, but places no constraints on the upper limit for ν.

5 Conclusion

This paper has shown how in some cases, knowing the details of the broadband impedance of a machine can be important. Because of this, a model of the high-frequency tails of the PEP-II r.f. cavities was constructed. This model gave a good approximation to the behavior due to those tails for a model of the cavity run through the program ABCI. The general properties of impedances place constraints on the model for the broadband impedance that one can use. These constraints contributed to the decision to use the model of equation (2) for the cavity tail impedance.

Much of this work, especially that in sections 2 and 3 is preliminary and requires more research, as indicated in comments in those sections.

Finally, thanks to Sam Heifets for many helpful discussions.

References

[1] S. Heifets, et al. "Impedance Study for the PEP-II B-factory." SLAC/AP-99, Stanford Linear Accelerator Center, Stanford, CA (1995).

[2] S. Heifets. Private communication.

[3] J. S. Berg and R. D. Ruth. "Transverse Multibunch Modes for Non-Rigid Bunches, Including Mode Coupling." In these proceedings.

[4] J. S. Berg and R. D. Ruth. "Transverse instabilities for multiple nonrigid bunches in a storage ring." SLAC-PUB-95-6829, Stanford Linear Accelerator Center, Stanford, CA (1995). To appear in Phys. Rev. E.

[5] J. S. Berg and R. D. Ruth. "Transverse Multibunch Instabilities for Non-Rigid Bunches." SLAC-PUB-95-6830, Stanford Linear Accelerator Center, Stanford, CA (1995). Presented at the 16th IEEE Particle Accelerator Conference (PAC95) and International Conference on High-Energy Accelerators, Dallas, Texas, May 1-5, 1995.

[6] T. Linnecar and E. N. Shaposhnikova. "Analysis of the Transverse Mode Coupling Instability of the Leptons in the SPS." CERN/SL/93-43 (RFS), CERN, Geneva, Switzerland (1993).

[7] T. P. R. Linnecar and E. N. Shaposhnikova. "The Transverse Mode Coupling Instability and Broadband Impedance Model of the CERN SPS." In V. Suller and C. Petit-Jean-Genaz, editors, *Fourth European Particle Accelerator Conference*, Vol. 2, pp. 1093–1095, Singapore (1994). World Scientific.

[8] T. Linnecar and E. N. Shaposhnikova. "Transverse Mode Coupling Instability of the Leptons in the CERN SPS." In these proceedings.

[9] A. W. Chao. *Physics of Collective Beam Instabilities in High Energy Accelerators.* John Wiley & Sons, Inc., New York (1993).

[10] S. A. Heifets and S. A. Kheifets. "High-frequency Limit of the Longitudinal Impedance of an Array of Cavities." Phys. Rev. D, **39**(3), 960–970 (1989).

[11] A. Hofmann and B. Zotter. "Improved Impedance Models for High-Energy Accelerators and Storage Rings." CERN LEP/TH 88-51, CERN, Geneva, Switzerland (1988).

[12] A. Hofmann and B. Zotter. "Analytic Models for the Broad Band Impedance." In F. Bennett and J. Kopta, editors, *Proceedings of the 1989 IEEE Particle Accelerator Conference*, Vol. 2, pp. 1041–1043, New York (1989). IEEE.

[13] Y. H. Chin. "User's Guide for ABCI Version 8.8 (Azimuthal Beam Cavity Interaction)." LBL-35258, Lawrence Berkeley Laboratory, Berkeley, CA (1994).

COLLECTIVE EFFECTS WORKING GROUP

A Fast Beam-Ion Instability

G. V. Stupakov

Stanford Linear Accelerator Center, Stanford University, P.O. Box 4349, Stanford, CA 94309

Abstract

The ionization of residual gas by an electron beam in an accelerator generates ions that can resonantly couple to the beam through a wave propagating in the beam-ion system. Results of the study of a beam-ion instability [1,2] are presented for a multi-bunch train taking into account the decoherence of ion oscillations due to the ion frequency spread and spatial variation of the ion frequency. It is shown that the combination of both effects can substantially reduce the growth rate of the instability.

I. INTRODUCTION

A fast beam-ion instability which is caused by the interaction of a single electron bunch train with the residual gas ions, has been studied recently in Ref. [1,2]. The instability mechanism is the same in both linacs and storage rings assuming that the ions are not trapped from turn-to-turn. The ions generated by the head of the bunch train oscillate in the transverse direction and resonantly interact with the betatron oscillations of the subsequent bunches, causing the growth of the initial perturbation of the beam.

The nature of the instability closely resembles the beam-breakup instability due to transverse wakefields. It differes from instabilities previously studied [3-9], where the ions, usually treated as being in equilibrium, interact with a circular electron or proton beam. The instability we discuss can occur in a transport line, linac, or a storage ring with a clearing gap to prevent ion trapping.

An important element that has to be included into the treatment of the instability is a frequency spread within the ion population. It is known that the frequency spread and associated with it decoherence in an instability problem usually results in Landau damping effect and in some situations can suppress the instability. We show that although the ion frequency spread does not fully suppress the instability, it decreases the growth rate making it in a typical situations two or tree times smaller than that predicted without decoherence effects.

We also consider spatial modulation of the ion frequency due to the variation of the beta and dispersion functions along the beam path. It turns out that combination of this variation with the frequency spread can substantially weaken the instability. This is not a very important effect in a FODO lattice, but it could prove to be much more significant in other lattices such as the TBA or Chasman-Green structures used in many synchrotron light sources.

For the sake of simplicity, we focus on the interaction of an electron beam with ions, although similar effects apply to a positron beam trapping free electrons.

The variation of the ion frequency ω_i included in this paper is caused by two sources. One of them is due to the horizontal beam density profile in a flat beam which causes the local ion frequency to depend on the horizontal position. Another source of spread in ω_i is the nonlinearity of the ion oscillations inside the beam.

For analytical study we adopt a model that treats the bunch train as a continuous beam. This model is applicable if the distance between the bunches l_b is smaller than the betatron wavelength, $l_b \ll c/\omega_\beta$ and the ion oscillation wavelength $l_b \ll c/\omega_i$. This condition is well satisfied for multi-bunch machines such as the PEP-II High Energy Ring [11] or the NLC Damping Ring [12]. We assume a one-dimensional model that treats only vertical linear oscillation of the centroids of the beam and the ions.

The paper is structured as follows. In Section II, the differential equations of motion are derived. Section III discusses averaging of the equations based on different time scales associated with oscillations and growth of the instability. The ion frequency spread and

resulting decoherence of ion oscillations are analyzed in Section IV. Analytical and numerical solutions of the equations for the NLC Damping Ring and PEP-II High Energy Ring are presented in Sections V and VI respectively. They are compared with direct computer simulation of the instability in Section VII. Effects of spatial ion frequency variation are discussed in Sections VIII and IX. The results are summarized in Section X.

II. THE EQUATIONS OF MOTION

We will assume a rigid vertical motion of the beam and define the offset of the centroid at time t and longitudinal position s as $y_b(s,t)$. The distance s is measured from the injection point at $t = 0$. The equation for the beam centroid, including the interaction with the ion background, is

$$\left(\frac{1}{c}\frac{\partial}{\partial t} + \frac{\partial}{\partial s}\right)^2 y_b(s,t) + \frac{\omega_\beta^2}{c^2} y_b(s,t) = \kappa \cdot (ct - s)\left(y_i(s,t) - y_b(s,t)\right) \ . \tag{1}$$

The left hand side of this equation accounts for the free betatron oscillation of a moving beam (we assume $v_{beam} \approx c$). On the right hand side, we included the force acting on the beam from the ions whose centroid is offset by $y_i(s,t)$. In the linear theory, this force is proportional to both the relative displacement between the beam and ions centroids and the ion density. Assuming a continuous electron beam with a uniform density per unit length, the ion density increases due to collisional ionization as $ct - s$ (it is equal to zero before the beam head arrives at the point s at time $t = s/c$). After separating the factor $ct - s$ on the right hand side of Eq. (1), the coefficient κ is

$$\kappa \equiv \frac{4\dot{\lambda}_{ion} r_e}{3\gamma c \sigma_y (\sigma_x + \sigma_y)} \ , \tag{2}$$

where γ denotes the relativistic factor for the beam, r_e is the classical electron radius, $\sigma_{x,y}$ denotes the horizontal and vertical rms-beam size respectively, and $\dot{\lambda}_{ion}$ is the number of ions per meter generated by the beam per unit time. Assuming a cross section for collisional ionization of about 2 Mbarns (corresponding to carbon monoxide at 40 GeV), we have

$$\dot{\lambda}_{ion}[\mathrm{m}^{-1}\mathrm{s}^{-1}] \approx 1.8 \cdot 10^{9} n_e[\mathrm{m}^{-1}] p_{gas}[\mathrm{torr}] \ , \tag{3}$$

where n_e is the number of electrons in the beam per meter, and p_{gas} the residual gas pressure in torr.

To find the equation for ions, we will assume that they perform linear oscillations inside the beam with a frequency ω_i. Furthermore, we will allow a continuous spectrum of ω_i given by a distribution function $f(\omega_i)$ normalized so that

$$\int f(\omega_i)\, d\omega_i = 1 \tag{4}$$

(in Sec. VIII we will consider a more general case when f also depends on s). The spread in ω_i at a given position s (and for a given ion species) is caused by several sources; they are discussed in more detail in Sec. IV. The distribution $f(\omega_i)$ is peaked around the frequency $\omega_i = \omega_{i0}$ corresponding to small vertical oscillations on the axis,

$$.\omega_{i0} \equiv \left[\frac{4 n_e r_p c^2}{3A\sigma_y(\sigma_x + \sigma_y)}\right]^{1/2} , \tag{5}$$

where A designates the atomic mass number of the ions, n_e the number of electrons in the beam per unit length, and r_p the classical proton radius ($r_p \approx 1.5 \cdot 10^{-16} cm$). Typically, the frequency spread $\Delta\omega_i$ is not large; we assume $\Delta\omega_i \ll \omega_{i0}$.

We also have to distinguish between the ions generated at different times t' because they will have an initial offset equal to the beam coordinate $y_b(s,t')$. Let us denote by $\tilde{y}_i(s,t|t',\omega_i)$ the displacement, at time t and position s, of the ions generated at t' ($t' \le t$) and oscillating with the frequency ω_i. We have an oscillator equation for $\tilde{y}_i$

$$\frac{\partial^2}{\partial t^2}\tilde{y}_i(s,t|t',\omega_i) + \omega_i^2\left[\tilde{y}_i(s,t|t',\omega_i) - y_b(s,t)\right] = 0 \ , \tag{6}$$

with initial condition

$$\tilde{y}_i(s,t'|t',\omega_i) = y_b(s,t') \ , \qquad \left.\frac{\partial \tilde{y}_i}{\partial t}\right|_{t=t'} = 0 \ . \tag{7}$$

Finally, averaging displacement of the ions produced at different times t' and having different frequencies ω_i gives the ion centroid $y_i(s,t)$

$$y_i(s,t) = \frac{1}{t-s}\int_s^t dt' \int d\omega_i f(\omega_i)\tilde{y}_i(s,t|t',\omega_i) \ . \tag{8}$$

Equations (1), (6)-(8) constitute a full set of equations governing the development of the instability in the beam-ion interaction.

III. AVERAGING OF THE EQUATIONS

Equation (6) can be easily integrated with the initial conditions (7) yielding

$$\tilde{y}_i(s,t|t',\omega_i) = y_b(s,t) - \int_{t'}^{t} \frac{\partial y_b(s,t'')}{\partial t''} \cos\omega_i(t-t'')\,dt'' \ . \tag{9}$$

Now using Eq. (8), Eq. (1) reduces to an integro-differential equation

$$\left(\frac{1}{c}\frac{\partial}{\partial t} + \frac{\partial}{\partial s}\right)^2 y_b(s,t) + \frac{\omega_\beta^2}{c^2} y_b(s,t) = -\kappa \int_s^t (ct'-s)\frac{\partial y_b(s,t')}{\partial t'} D(t-t')\,dt' \ , \tag{10}$$

where $D(t-t')$ denotes a decoherence function defined as

$$D(t-t') = \int d\omega_i \cos\omega_i(t-t') f(\omega_i) \ . \tag{11}$$

This function represents the oscillation of the centroid of an ensemble of ions with a given frequency distribution $f(\omega_i)$ having an initial unit offset.

Instead of t and s, it is convenient to transform to new independent variables z and s, where $z = ct - s$. The variable z measures the distance from the head of the beam train and for a fixed z the variable s plays a role of time. Denoting

$$y(s,z) \equiv y_b(s, s+z) \ , \tag{12}$$

Eq. (10) takes the form

$$\frac{\partial^2}{\partial s^2} y(s,z) + \frac{\omega_\beta^2}{c^2} y(s,z) = -\kappa \int_0^z z' \frac{\partial y(s,z')}{\partial z'} D(z-z')\,dz' \ . \tag{13}$$

If $D(z) = \cos\omega_i z$ (no frequency spread), Eq. (13) reduces to the equation derived in Ref. 1.

We will assume that the interaction between the beam and the ions is small,

$$c^2\kappa l \ll \omega_{i0}^2,\ \omega_\beta^2\ , \tag{14}$$

where l denotes the length of the bunch train, so that the instability develops on a time scale which is much larger than both the betatron period and the period of ion oscillations. Typically this inequality is easily satisfied. In such a situation, the most unstable solution of Eq. (13) can be represented as a wave propagating in the beam with a slowly varying amplitude and phase,

$$y\,(s,z) = \mathrm{Re}A\,(s,z)\,e^{-i\omega_\beta s/c + i\omega_{i0}z/c}\ , \tag{15}$$

where the complex amplitude $A\,(s,z)$ is a 'slow' function of its variables,

$$\left|\frac{\partial \ln A}{\partial s}\right| \ll \frac{\omega_\beta}{c}\ ,\quad \left|\frac{\partial \ln A}{\partial z}\right| \ll \frac{\omega_{i0}}{c}\ . \tag{16}$$

For a fixed z, the s-dependence of Eq. (15) describes a pure betatron oscillation, while, for a fixed s (that is in the ion frame of rest), the z-dependent part implies oscillations with the frequency ω_{i0}. Hence the wave resonantly couples the ions and the electrons.

Substituting Eq. (15) into Eq. (13) and averaging it over the rapid oscillations with the frequencies ω_{i0} and ω_β, one finds

$$\frac{\partial A\,(s,z)}{\partial s} = \frac{\kappa\omega_{i0}}{4\omega_\beta}\int_0^z z' A\,(s,z')\hat{D}\,(z-z')\,dz'\ , \tag{17}$$

where the function $\hat{D}\,(z)$ is

$$\hat{D}\,(z) = \int d\omega_i f\,(\omega_i)\,e^{i(\omega_i-\omega_{i0})z/c}\ . \tag{18}$$

One of the advantages of the above approach is that it allows a simple scaling of the instability with the vacuum pressure. Indeed, the only place where the pressure p enters Eq. (17) is the parameter κ which is proportional to p (see Eqs. (2) and (3)). By introducing a new variable $s\kappa$ instead of s, we can eliminate κ from the equation. This means that increasing the pressure n times is equivalent to the shrinking the s axis by the same factor. Thus, having solved Eq. (17) for one particular value of pressure, we can use the result for various p by simply rescaling the s variable, $s \propto p^{-1}$.

IV. ION DECOHERENCE

The frequency spread of the ions at a given longitudinal coordinate s stems from several sources. One of them is a variation of the electron density in the beam along the horizontal axis. Since the ion frequency scales as the square root of the electron density, $\omega_i \propto \sqrt{n_e}$, ions located at different coordinates x in a flat beam will have different ω_i. For a Gaussian distribution of electrons in x, $n_e \propto \exp\left(-x^2/2\sigma_x^2\right)$, and we obtain $\omega_i(x) \propto \exp\left(-x^2/4\sigma_x^2\right)$. Hence,

$$\omega_i(x) - \omega_{i0} = \omega_{i0}\left[\exp\left(-x^2/4\sigma_x^2\right) - 1\right], \tag{19}$$

where ω_{i0} is the frequency at $x = 0$.

To find the decoherence function $\hat{D}$, we will utilize a simple one-dimensional model that assumes that the ion frequency of horizontal oscillations is much smaller than the vertical frequency ω_i, and neglects the horizontal ion motion on the time scale of the decoherence. In this model, the ion distribution in x is the same as the electron distribution (because the rate of ionization is proportional to n_e),

$$f_i(x) = \frac{1}{\sqrt{2\pi}\sigma_x}\exp\left(-x^2/2\sigma_x^2\right), \tag{20}$$

and Eq. (18) takes the form

$$\hat{D}(t) = \int_{-\infty}^{\infty} dx f_i(x)\exp\left\{-i\omega_{i0}t\left[1 - \exp\left(-x^2/4\sigma_x^2\right)\right]\right\}. \tag{21}$$

Note that in this model we overestimate the effect of the decoherence. For flat beams, a typical ratio of the horizontal and vertical oscillation frequencies is roughly 3. Thus, the horizontal motion of the ions modulates the vertical oscillation frequency ω_i between ω_{i0} and $\omega_i(x)$ making the average ω_i smaller than $\omega_i(x)$. To fully account for this effect, one has to deal with the two-dimensional ion motion which would make the consideration much more involved.

At this point, we note that Eq. (21) has been defined as the average offset of the ions at a given s. However, the quantity relevant to the electron-ion coupling is the average force

that acts on the electron beam. The force differs from the average displacement because the ion density decreases with x and thus the ion electric field at the beam edges is suppressed relative to that at the bunch center. To account for this effect, we correct $\hat{D}(t)$ by including the electron density n_e in the integrand of Eq. (21)

$$\hat{D}(t) = \text{const} \int_{-\infty}^{\infty} dx f_i(x) n_e(x) \exp\left[-i\omega_{i0} t \left(1 - e^{-x^2/4\sigma_x^2}\right)\right] , \tag{22}$$

where the constant in Eq. (22) must be chosen such that $\hat{D}(0) = 1$. This gives

$$\hat{D}(t) = \frac{1}{\sqrt{\pi}\sigma_x} \int_{-\infty}^{\infty} dx \exp\left[-i\omega_{i0} t \left(1 - e^{-x^2/4\sigma_x^2}\right) - x^2/\sigma_x^2\right] . \tag{23}$$

The plots of the real and imaginary parts of this function are shown in Fig. 1. Asymptotically, for large values of $\omega_{i0}t$,

$$\hat{D}(t) \approx (1 + i\alpha\omega_{i0}t)^{-1/2} , \tag{24}$$

where the numerical factor $\alpha = 1/4$.

Another source of ion decoherence is the nonlinearity of the electron potential. It results in a dependence of ω_i on the amplitude of the oscillation and causes an additional spread in the oscillation frequencies ω_i. We have numerically computed the decoherence function due to nonlinearity in a manner similar to the approach of Ref. 13 ; it is also plotted in Fig. 1. One can show that the decoherence due to nonlinearity has the same asymptotes as Eq. (24) with a somewhat smaller α. In what follows, we will use the simple form given by Eq. (24) for $\hat{D}(t)$ in which we put $\alpha = 3/8$ to account for the additional decoherence due to the nonlinearity.

V. ANALYSIS

Let us for a moment ignore the ion decoherence in Eq. (17) and put $\hat{D}(z) \equiv 1$. In this case, the equation can easily be solved analytically. Differentiation with respect to z, reduces Eq. (17) to the differential equation

$$\frac{\partial^2 A(s,z)}{\partial s \partial z} = \frac{\kappa \omega_{i0}}{4\omega_\beta} z A(s,z) \ . \tag{25}$$

For the initial condition $A(0,z) = 1$, the solution is

$$A(s,z) = I_0\left(z\sqrt{\frac{\kappa\omega_{i0}}{2\omega_\beta}s}\right) \ , \tag{26}$$

where I_0 is the zeroth order Bessel function of imaginary argument. This solution was found in Ref. 1 using a different method. For large values of the argument the asymptotic expansion of the Bessel function yields

$$A(s,z) \approx \left(2\pi z\sqrt{\kappa\omega_{i0}s/2\omega_\beta}\right)^{-1/2} \exp\left(z\sqrt{\kappa\omega_{i0}s/2\omega_\beta}\right) \ , \tag{27}$$

which indicates an instability with a characteristic time $\tau \approx 2\omega_\beta/\kappa\omega_{i0}l^2c$, where l is the length of the bunch train. Note that since $A(s,z) \propto \exp\left(z/l\sqrt{s/c\tau}\right)$, the characteristic time τ does not represent an e-folding time, and the instability develops much slower than it would be in the case of normal exponential growth $\propto \exp(s/c\tau)$.

VI. NUMERICAL RESULTS

To study the effect of the decoherence in more realistic cases, we wrote a computer code that numerically integrates Eq. (17) with $\hat{D}(t)$ given by Eq. (24). The two input parameters for the code are the characteristic time $\tau = 2\omega_\beta/\kappa\omega_{i0}l^2c$, and the train length $\omega_{i0}l/c$.

Simulations have been performed for the NLC Damping Ring and the PEP-II HER. In the NLC Damping Ring (see relevant parameters in Ref. [1]), we assumed a residual gas with a vacuum pressure of $p = 10^{-8}$ Torr and an atomic number of A=28. This corresponds to a characteristic time of $\tau = 45$ ns and a bunch length of $\omega_{i0}l/c = 150$. The results are depicted in Fig. 2 for the initial condition $A(0,z) = 1$; for comparison, in Fig. 3, we plot the solution of Eq. (27) for the same parameters but without the decoherence. The plots show the growth of the beam centroid at 10 positions evenly spaced along the bunch train. Comparing Fig. 2 and 3, shows the decoherence slowing down the instability. To characterize the growth rate of the instability, we defined τ_{growth} as an e-folding time for the

last bunch in the train. Since the instability is not exponential, τ_{growth} varies with time. For the time interval 1 $\mu s < t < 2$ μs, we find that $\tau_{growth} \approx 0.5$ μs without decoherence and $\tau_{growth} \approx 1$ μs with ion decoherence; the decoherence decreases the growth rate by a factor of two.

Figures 2 and 3 illustrate the growth of the instability from an initial condition Eq. (15) which is the most unstable perturbation. In reality, the initial noise in the beam will contain different harmonics of which only one or two, having a spatial period $2\pi c/\omega_{i0}$, are very unstable. Assuming that the number of bunches in the train equals N_b and their displacements are uncorrelated with the rms value of δ, a simple statistical argument shows that the amplitude of harmonics in the bunch will be of the order of $\delta/\sqrt{N_b}$. To illustrate the effect of random initial positions, we integrated Eq. (17) including the effect of the ion decoherence with the initial condition corresponding to uncorrelated displacement with $\delta = 1$ for 90 bunches in the NLC Damping Ring. The result is shown in Fig. 4 for $p = 10^{-9}$ and $p = 10^{-8}$ (as noted in Section III, variation of the pressure simply re-scales the horizontal axis in the plot). The figure shows that the development of the instability is somewhat delayed until the amplitude of the unstable mode with an initial value $\delta/\sqrt{90} \approx 0.1$ reaches the value comparable to 1; for $p = 10^{-8}$, this occurs after roughly $5\mu s$. After this point, the growth proceeds at about the same rate as in Fig. 2.

For the PEP-II High Energy Ring, we assumed a vacuum pressure of $p = 10^{-9}$ Torr and A=28. This corresponds to a characteristic time $\tau = 5.5\mu s$ and a bunch length $\omega_{i0} l/c = 220$. The bunch offsets at 10 positions in the train are shown in Fig. 5 as a function of s for the initial condition $A(0, z) = 1$. From this figure, we estimate that the e- folding growth time, on the time interval 200 $\mu s < t < 400$ μs, is roughly $\tau_{growth} \approx 150$ μs. As noted before, this growth time depends on the interval considered.

VII. COMPUTER SIMULATIONS

Direct macro-particle simulations of the instability have been performed [2] using a computer code described in Ref. 1. In the simulations, each of the bunches is represented by 10,000 macro-particles and they interact with the ions which are represented by roughly 50,000 macro-particles. In this manner, the beam and ion distributions evolve self-consistently as the beam is tracked through the magnet lattice.

The results of a simulation for the NLC Damping Ring with a vacuum pressure of $p = 10^{-8}$ Torr are shown in Fig. 6 where we have plotted the oscillation amplitude, normalized by $\sqrt{N_{macro}}/\sigma_y$; this allows for a direct comparison with Fig. 4. Comparing Fig. 6 with Fig. 4 shows a good agreement for the growth rate of the instability during the initial stage ($t < 6\ \mu s$). At later times, the macro-particle simulation exhibits saturation which is presumably due to the nonlinearity of the beam-ion force as the amplitude of the oscillations become comparable to the rms beam size σ_y; this occurs at a value of 100 in the normalized units of the plot.

VIII. EFFECT OF SPATIAL ION FREQUENCY VARIATION

An inhomogeneity of ω_i has different effect on the instability depending on the typical scale λ_i on which the ion frequency varies. If this scale is much smaller than a half of the wavelength λ_{inst} associated with the instability, $\lambda_{inst} = 2\pi/(\omega_\beta + \omega_i)$, (about 15 m for CO ions in the HER of the PEP-II), $\lambda_i \ll \lambda_{inst}$, fluctuations of ω_i can be considered as an effective frequency spread in the ion population which contributes to Landau damping mechanism. In the opposite limit, $\lambda_i \gg \lambda_{inst}$, one has to deal with the problem where the unstable perturbation propagates in a system which characteristics slowly vary is space.

Here we consider only the effect of long-range variation of the ω_i. They result in breaking the synchronism between the ion and electron oscillations and suppression of the resonant interaction between the species. We will show that this effect may result in a substantial

weakening of the instability.

The governing equation (17) remains valid in the case of slow modulation of the ion frequency if one considers the distribution function $f(s,\omega_i)$ and the decoherence function $\hat{D}(s,z)$ as depending on s. Eq. (18) now takes the form

$$\hat{D}(s,z) = \int d\omega_i f(s,\omega_i)\, e^{i(\omega_i-\omega_{i0})z/c}. \tag{28}$$

We further assume that $f(s,\omega_i)$ is such that

$$f(s,\omega_i) = F(\omega_i - \omega_{i0} - \delta\omega_i(s)), \tag{29}$$

where $\delta\omega_i(s) \ll \omega_{i0}$. This means that moving to a new location s shifts the distribution function in ω_i-space as a whole but does not change its form. Putting Eq. (29) into Eq. (28) yields

$$\hat{D}(s,z) = e^{i\delta\omega_i(s)z/c} D_0(z), \tag{30}$$

where

$$D_0(z) = \int d\omega F(\omega)\, e^{i\omega z/c} \tag{31}$$

is the decoherence function in the homogeneous case given by Eq. (24). We see that inhomogeneity effectively modifies the decoherence function.

IX. NUMERICAL RESULTS AND ANALYSIS

Equation (1) has been integrated numerically for the parameters of the HER of the PEP-II assuming the gas pressure $p = 10^{-9}$ torr of CO (A=28), and

$$\delta\omega_{i0}(s) = a\omega_{i0}\sin(2\pi ns/C,) \tag{32}$$

where C is the circumference of the ring and a is the relative variation of the frequency. Fig. 7 shows the result for 10% variation of ω_{i0}, $a = 0.1$, and $n = 1$. Note the exponential growth of the amplitude with an estimated e-folding time $\tau_e = 400\mu s$ (cf. with 150 μs in

the homogeneous case). Fig. 8 shows the result for $a = 0.3$ and $n = 1$, with the e-folding time about 800 μs.

The exponential nature of the instability and the increase of the growth time can be explained in the following way. Inclusion of the ion frequency variation makes the decoherence function Eq. (30) such that it is effectively localized on a scale that is much smaller than the characteristic distance (in z) on which $A(s,z)$ varies. This allows us to neglect the variation of the $z'A(s,z')$ in the integrand of the right hand side of Eq. (17) and put it in front of the integral,

$$\frac{\partial A(s,z)}{\partial s} \approx \frac{\kappa\omega_{i0}}{4\omega_\beta} z A(s,z) \int_0^z \hat{D}(s, z-z')\, dz' \approx \frac{\kappa\omega_{i0}}{4\omega_\beta} z A(s,z) \int_0^\infty \hat{D}(s,z')\, dz'. \tag{33}$$

Furthermore, since the instability is developing on a large time scale, we can average the function $\hat{D}(s,z)$ over s. This gives

$$\frac{\partial A(s,z)}{\partial s} = \frac{1}{\tau_e c} A(s,z), \tag{34}$$

with the exponential solution

$$A(s,z) = A_0(z) \exp(s/c\tau_e), \tag{35}$$

where

$$\tau_e^{-1} = \frac{\kappa\omega_{i0} c}{4\omega_\beta} z \left\langle \int_0^\infty \hat{D}(s,z')\, dz' \right\rangle, \tag{36}$$

and the angular brackets denote averaging over s. Eq. (36) can be rewritten as

$$\tau_e^{-1} = \frac{1}{2\tau} \frac{z}{l} \left\langle \int_0^\infty \hat{D}(s,z') \frac{dz'}{l} \right\rangle, \tag{37}$$

where $\tau = 2\omega_\beta / \kappa\omega_{i0} c l^2$ is the characteristic time introduced Section V ($\tau = 5.5 \mu s$ for the HER of the PEP-II), and l is the length of the bunch train. Using Eqs. (37), (30) and (24), one finds

$$\tau_e^{-1} = \frac{1}{2\tau} \frac{z}{l} \frac{c}{a l \omega_{i0}} \int_0^\infty \frac{d\xi J_0(\xi)}{(1 + i\alpha\xi/a)^{1/2}}. \tag{38}$$

Numerical integration for the above examples gives $\tau_e = 350\mu s$ for $a = 0.1$, $z = l$, and $\tau_e = 760\mu s$ for $a = 0.3$, $z = l$, in good agreement with the simulations.

Asymptotically, for $a > 0.3$, the integral in Eq. (38) approaches 1, yielding a simple formula for τ_e,

$$\tau_e \approx 2\tau \frac{l}{z} \frac{a l \omega_{i0}}{c}. \tag{39}$$

In order to apply the above analysis to a particular lattice, it is necessary to include many spatial harmonics in Eq. (32). This has not been accomplish yet. To get a rough estimate of the amplitude of the ion frequency variation we plotted in Fig. 9 the ion frequency (CO) in the PEP-II HER as a function of the position in the ring. The plot indicates that one can expect 10-20% variation of ω_i in the ring.

X. DISCUSSION

In this paper, we described a fast beam-ion instability which can develop in a train of bunches with a clearing gap. We have included into consideration the ion frequency variation due to the nonlinearity of the beam-ion force in both the x and y planes. In general, the dependence of ω_i on the horizontal motion is the more important effect and strictly should be described with a two-dimensional treatment of the ion motion. There are other sources of ion frequency spread that we have not considered although they can be included in our formalism in a straightforward manner.

In all cases, the variation of the ion frequency causes Landau damping and slows the instability growth rate. In the two examples that we studied, the growth rate was reduced by roughly a factor of 2. For longer bunch trains, where the factor $\omega_{i0} l/c$ becomes larger, the reduction of the growth rate should be more pronounced. We should also note that we have characterized the instability with an approximate e-folding time τ_{growth}. While this differs from the characteristic time τ that more accurately describes the instability which grows as $\exp(\sqrt{t/\tau})$, it provides a more intuitive estimate of the impact of the instability.

For example in the PEP-II HER, τ_{growth} is roughly 150 μs while $\tau \approx 6$ μs. This growth rate could be decreased further by adding additional clearing gaps in the bunch train [1]. For example, a second gap will increase the instability rise time to roughly $\tau_{growth} \approx 0.6$ ms which is inside the bandwidth of the feedback system.

Our analytical model is confirmed by comparison with a macro-particle computer simulation and shows a good agreement. An important effect which is not included in the model but will also suppress the instability is the tune spread in the electron beam. The tune spread can arise from the beam energy spread and the chromaticity of the optical lattice, the nonlinearity of the lattice, the space charge force due to the ions or the electrons themselves, or the beam-beam collision in a colliding beam storage ring. For example, in the PEP-II High Energy Ring with a beam-beam collision parameter $\xi = 0.03$, the estimated decoherence time for the betatron oscillations is 200 μs and it is comparable with the growth rate of the instability.

We have shown that even slight variation of the ion frequency along the beam path makes the instability truly exponential and, what is more important, further suppresses the growth rate. For synchrotron light sources, where the ion frequency variation is very large, this mechanism can be a strong stabilizing factor for the fast-ion instability.

XI. ACKNOWLEDGMENTS

We would like to thank A. Chao, S. Heifets, T. Raubenheimer and F. Zimmermann for useful discussions. This work was supported by Department of Energy contract DE-AC03-76SF00515.

REFERENCES

[1] T. O. Raubenheimer and F. Zimmermann. "Fast Beam-Ion Instability: I. Linear Theory and Simulations," submitted to *Phys. Rev. E* and SLAC-PUB-95-6740 (1995).

[2] G. V. Supakov, T. O. Raubenheimer, and F. Zimmermann. "Fast Beam-Ion Instability: II. Effect of Ion Decoherence," submitted to *Phys. Rev. E* and SLAC-PUB-95-6805 (1995).

[3] G. Koshkarev and P. Zenkevich, "Resonance of Transverse Coupled Oscillations in Two Circular Beams,", *Part. Accel.*, **3** (1972) 1.

[4] E. Keil and B. Zotter, "Landau Damping of Coupled Electron-Antiproton Oscillations," CERN ISR-TH/71-58 (1971).

[5] L. J. Laslett et al., "Transverse Two-Stream Instability in the Presence of Strong Species-Species and Image Forces," *Nucl. Instr. and Meth.* **A121** (1974) 517.

[6] R. Alves Pires et al., "On the Theory of Coherent Instabilities Due to Coupling Between a Dense Cooled Beam and Charged Particles from the Residual Gas", *Proc. 1989 Part. Accel. Conf.*, Chicago, p.800.

[7] E. Jones et al., " Transverse Instabilities Due to Beam-Trapped Ions and Charged Matter in the CERN Antiproton Accumulator," *Proc. 1985 Part. Accel. Conf.*, Vancouver, p.2218.

[8] A. Poncet, "Ion Trapping and Clearing," *Proc. 1989 CERN Accel. School*, Uppsala, Sweden, CERN 90-04 (1990).

[9] A. Poncet, "Ions and Neutralization," *Frontiers of Particle Beams: Intensity Limitations*, Lecture Notes in Physics: 400 (Springer-Verlag, Berlin, 1990).

[10] D. Sagan and A. Temnykh, "Observations of the Coherent Beam-Ion Interaction in the CESR Storage Ring," *Nucl. Instr. and Meth.*, **A344** (1994) 459.

[11] PEP-II: An Asymmetric B Factory Conceptual Design Report, SLAC-418 (1993).

[12] Parameters for the NLC Damping Ring can be found in: *Proceedings of the 5th Int. Workshop on Next-Generation Linear Colliders*, Stanford, CA, SLAC-436 (1994).

[13] R.E. Meller, et al. "Decoherence of Kicked Beams," SSC-N-360, 1987.

FIGURES

Figure 1. Real (1) and imaginary (2) parts of the function $\hat{D}(t)$ given by Eq. (23), and the asymptotes of Eq. (24) (dashed lines). Curves 3 and 4 shows real and imaginary parts respectively of the decoherence function due to nonlinearity of the ion motion.

Figure 2. Growth of an initial unit offset in the NLC Damping Ring at 10 different points in the train (the line corresponding to the first point is superimposed on the abscissa) with ion decoherence.

Figure 3. Growth of an initial unit offset in the NLC Damping Ring at 10 different points in the train (the line corresponding to the first point is superimposed on the abscissa) without decoherence.

Figure 4. Instability in the NLC Damping Ring with random initial condition and with ion decoherence.

Figure 5. Growth of an initial unit offset in the PEP-II High Energy Ring.

Figure 6. Macro-particle simulation of of the instability in the NLC Damping Ring with a vacuum pressure of 10^{-8} Torr and A=28; the position of every 10th bunch is plotted.

Figure 7. Instability in the PEP-II High Energy Ring for 10% variation of the ion frequency. The vertical scale is logarithmic.

Figure 8. Instability in the PEP-II High Energy Ring for 30% variation of the ion frequency.

Figure 9. The oscillation frequency for CO ions in the PEP-II HER as a function of the position in the ring.

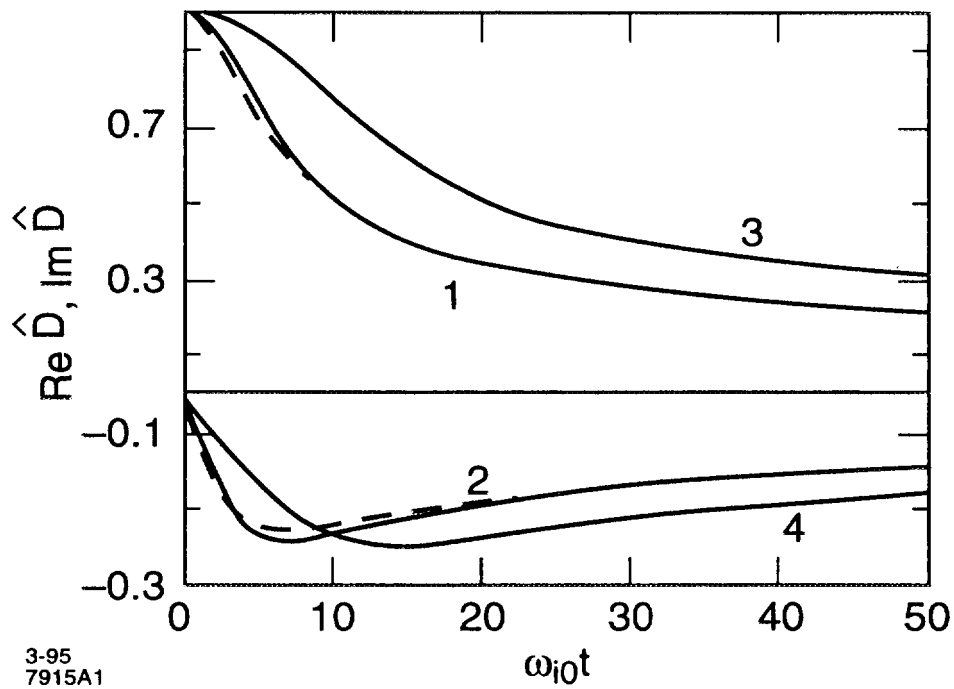

Fig. 1.

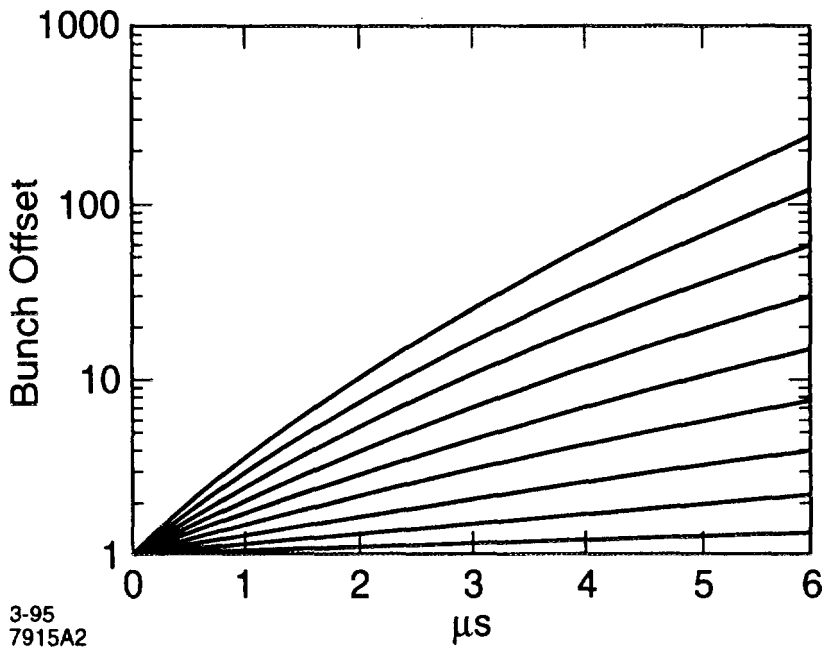

Fig. 2.

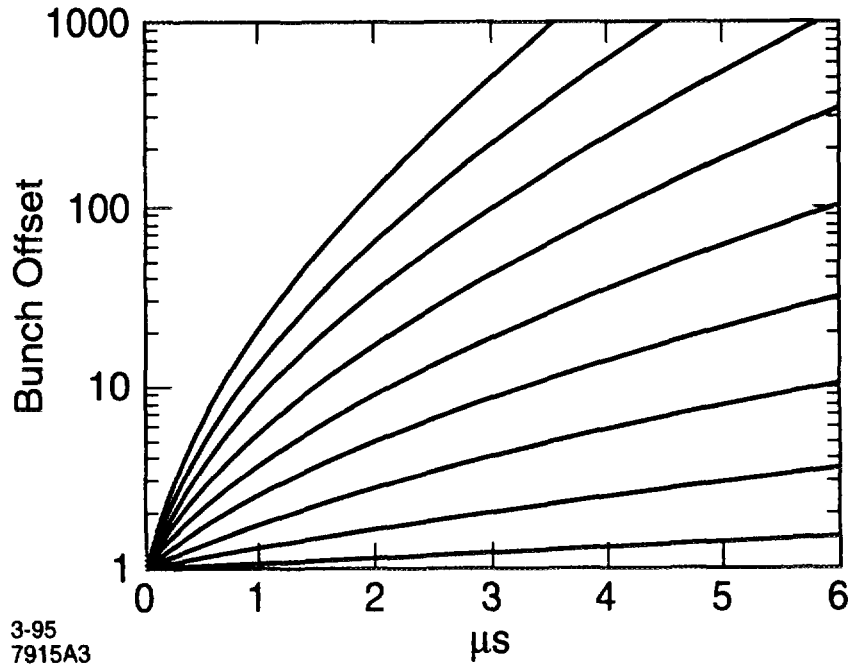

Fig. 3.

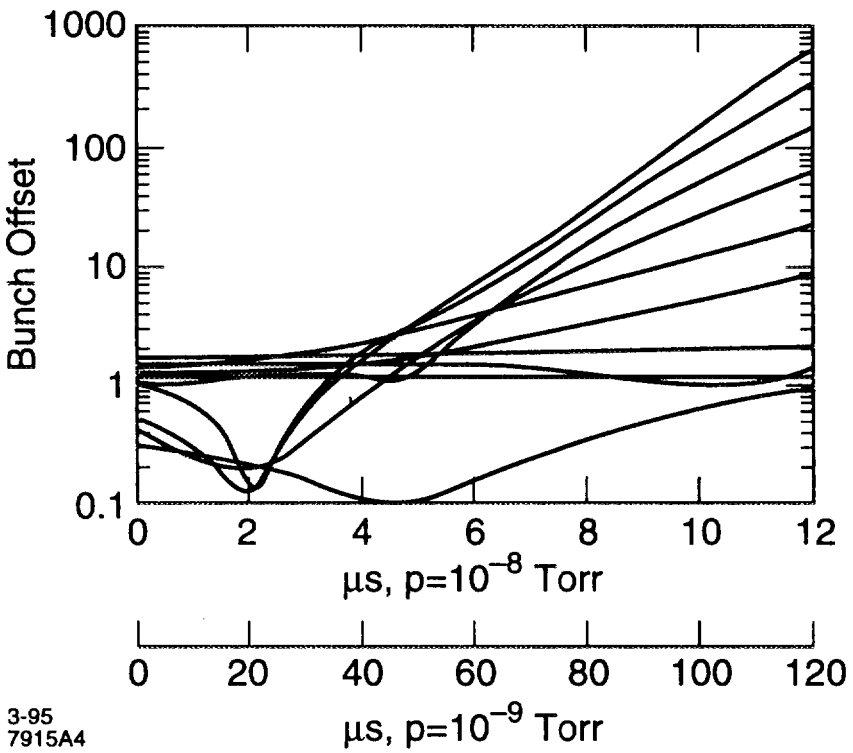
1000
100
10
1
0.1
Bunch Offset
0
2
4
6
8
10
12
μs, p=10^-8 Torr
0
20
40
60
80
100
120
μs, p=10^-9 Torr
3-95
7915A4

Fig. 4.

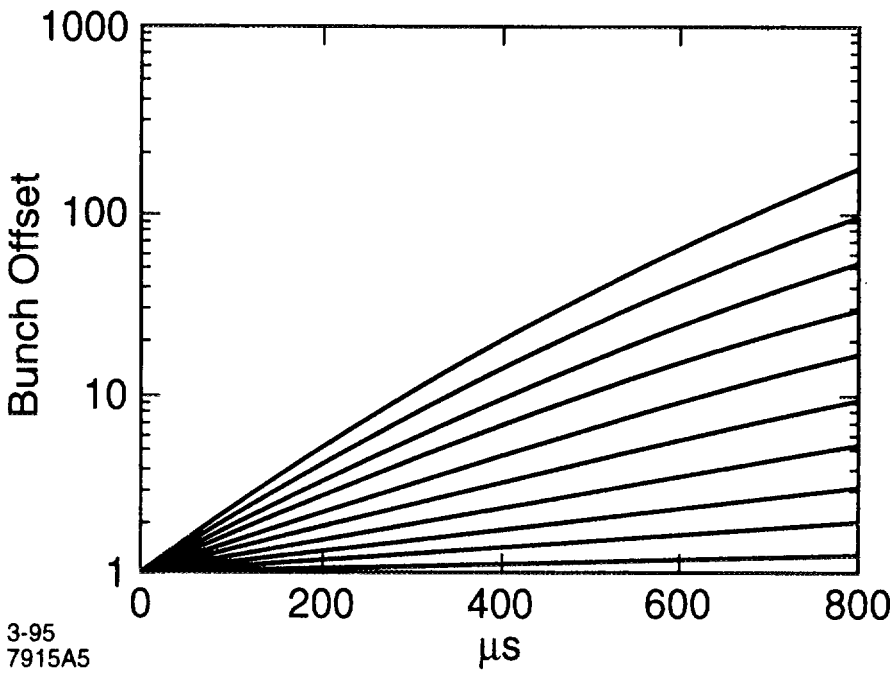

Fig. 5.

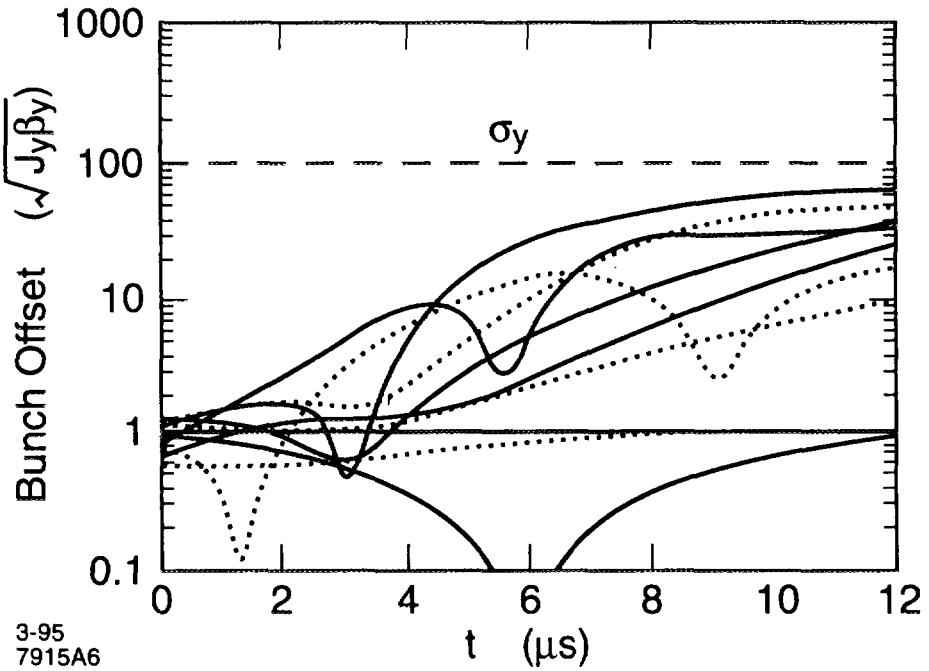
1000
100
10
1
0.1
σ_y
Bunch Offset $(\sqrt{J_y\beta_y})$
0
2
4
6
8
10
12
t (μs)
3-95
7915A6

Fig. 6.

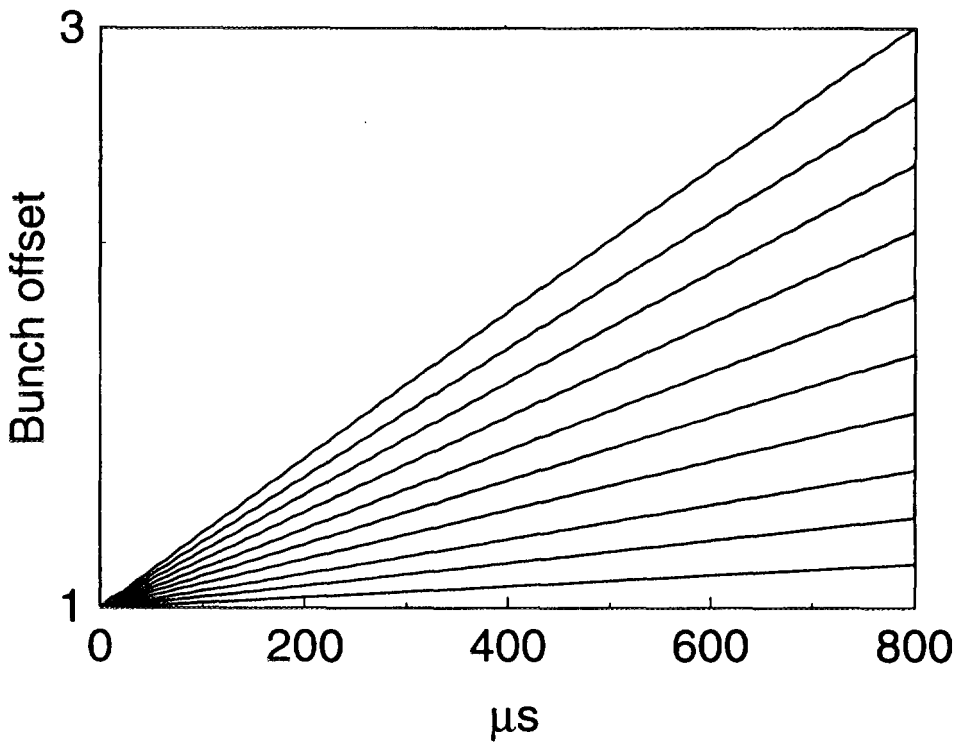

Fig. 7.

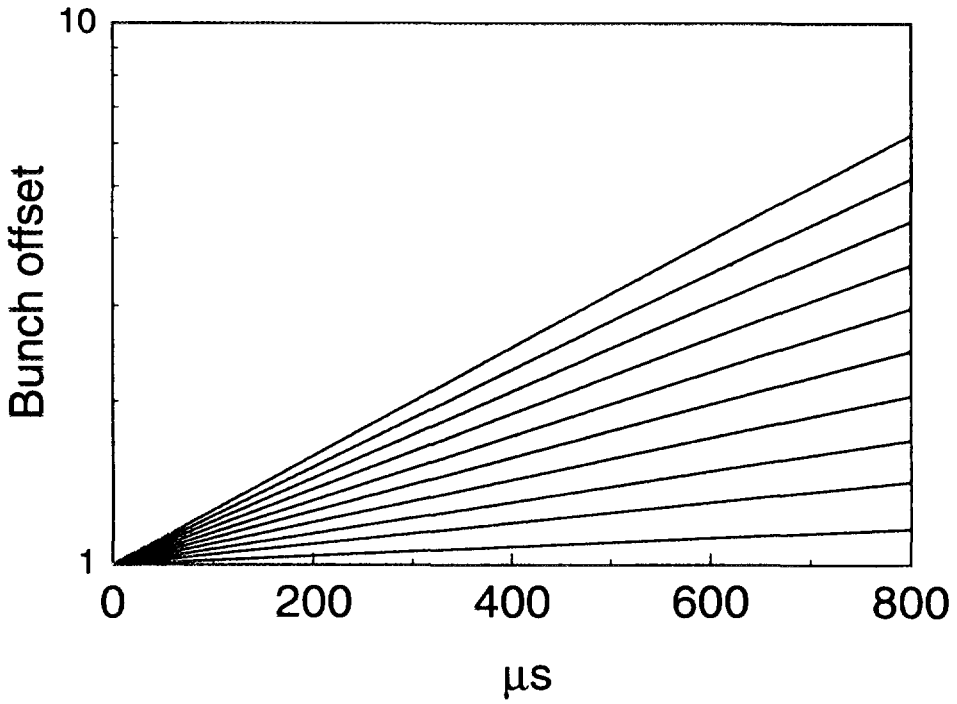

Fig. 8.

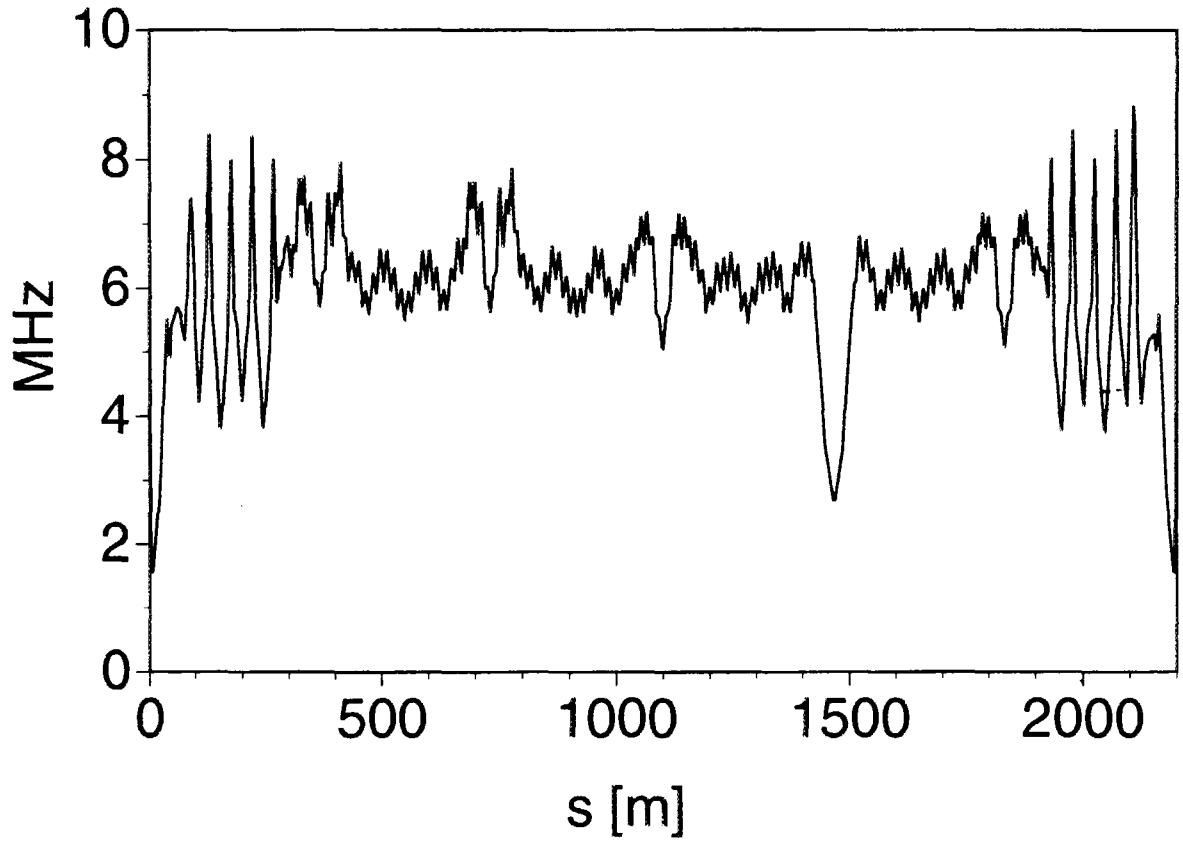

Fig. 9.

Saturation of the Ion Induced Transverse Blow-up Instability

S.A. HEIFETS

Stanford Linear Accelerator Center

Satnford University, Stanford, CA 94309

Introduction

In a recent paper[1], T. Raubenheimer and F. Zimmermann described a new, fast transverse instability caused by the interaction of a train of bunches with the residual gas. Ions produced by transversely offset bunches in the head of a train induce oscillations of the tail of the train. The ions may be cleared out by a gap after one revolution, but the memory remains in the train. Amplitude of oscillations keeps growing exponentially as $exp\sqrt{s/s_c}$ until the amplitude of a bunch centroid is on the order of the transverse rms σ of a bunch. The rise time s_c of the oscillations of a bunch centroid for the PEP-II HER was found to be a fraction of a millisecond, even taking into account the spread of ion frequencies[2].

Computer simulations[1][2]confirm the exponential growth. However, the results of the simulations show that the exponential regime holds only for a short period of time and then changes to a much slower growth. Initial growth is rapid; it would be difficult to observe it directly in experiments. From a practical point of view, the important questions are, what is the amplitude at which a transition to slow growth takes place and, secondly, what is the growth rate after that transition compared to the rate, which could be handled with a reasonable feedback system.

The exponential regime is limited by nonlinearity of the beam-ion interaction. As a result, exponential growth at large amplitudes is replaced by a linear dependence of the amplitude on time. The transition from exponential growth to a linear regime

* Work supported by DEpartment of Energy contract DE-AC03-76SF00515

depends on the initial conditions: exponential growth is noticeable only for very small initial amplitudes. An estimate of the growth rate at large amplitude is obtained and compared with computer simulations.

For completeness, the basic formulas of the original paper are re-derived.

Basic equations

First, we reproduce the basic equations of the paper [1]. Consider a train of bunches $n = 1, .., n_b$. The head of the n-th bunch is located at the position $z(s) = s - z_n$ of the ring at the moment $s = ct$ where $z_n = (n-1)s_b$ is the distance of the bunch from the head of the train.

The vertical motion of electrons of the n-th bunch is described by the equation

$$\frac{\partial^2 y(s, z_n)}{\partial s^2} + \omega_b^2 y(s, z_n) = \frac{r_e}{\gamma}\frac{\partial U}{\partial y}, \tag{1}$$

where ω_b is a betatron frequency (in cm^{-1}), and the potential U of the beam-ion interaction is

$$U(\vec{r}, s) = \int \frac{d\vec{r}'}{|\vec{r} - \vec{r}'|} n_i(\vec{r}', x). \tag{2}$$

The ion density $n_i(\vec{r}, s)$ is given by the initial density n_i^0;

$$n_i(\vec{r}, s) = \sum_k \int d\vec{r}' \delta[x - X_k(\vec{r}', s)]\delta[y - Y_k(\vec{r}', s)]\delta[z - z']n_i^0(\vec{r}'). \tag{3}$$

Here, $X_k(\vec{r}, s)$ and $Y_k(y', z, s)$ are trajectories of ions generated by the k-th bunch at the location z of the ring. The initial value y' for Y_k, $Y_k(y', z, s_k) = y'$, is equal to the offset $y' = y_b(s_k, z_k)$ of the k-th bunch at the location z of the ring at the moment $s_k < s$, $s_k = z + z_k$.

Ions are generated uniformly along the ring with the rate

$$\frac{dN_i}{dz} = 0.06(\frac{p}{\mathrm{torr}})(\frac{300K^o}{T})N_b \quad \mathrm{cm}^{-1}, \tag{4}$$

where p is the residual gas pressure and the ionization cross-section is assumed to be

2 Mbarn. Initial distribution of ions is defined by the density of the parent bunch

$$n_i^0(\vec{r}) = \frac{dN_i}{dz}\rho(x)\rho(y - y_b(z + z_k, z_k)), \tag{5}$$

where $\rho(x)$, $\rho(y)$ are Gaussian distributions with rms σ_x, σ_y, respectively. We assume a flat beam $\sigma_x >> \sigma_y$, and take $\sigma_{x,y}$ constant around the ring, and for all bunches. Therefore, the ion frequencies for ions with atomic number A,

$$\omega_{x,y}^2 = \frac{2N_b r_p}{A s_b \sigma_y \sigma_x}, \tag{6}$$

are also constant. The frequency spread in a nonlinear regime is produced automatically by nonlinearity of the motion.

For a flat beam we take $X_k(\vec{r}, s) = x\cos\psi_x$, $\psi_x = \omega_x(s - s_k)$, and $s_k = z + z_k$. Then

$$U(\vec{r}, s) = \sqrt{4\pi}\frac{dN_i}{dz}\hat{\rho}(x)\sum_k \int_0^\infty \frac{d\lambda}{\lambda^2}\int dy' e^{-\lambda^2[y - Y_k(y', z, s)]^2}\rho(y' - y_b(z + z_k, z_k)). \tag{7}$$

Here $\hat{\rho}(x)$ has rms $\sigma_x^2\cos^2\psi_x \simeq \sigma_x^2/2$. The equation for a bunch centroid is obtained by averaging Eq. (1) with the density $\rho_n(\vec{r}, s) = N_b\rho(x)\rho(y - y_b(s, z_n))\rho(z - (s - z_n))$ of the n-th bunch. The following relation simplifies the result

$$\int_0^\infty \frac{d\lambda}{[1 + 2\lambda^2\sigma_y^2]^{3/2}} e^{-\frac{\lambda^2 y^2}{1 + 2\lambda^2\sigma_y^2}} = \frac{1}{\sqrt{2}\sigma_y}\int_0^1 d\eta e^{-\frac{\eta^2 y^2}{2\sigma_y^2}}. \tag{8}$$

Averaging Eq. (7) gives

$$< \frac{\partial U(\vec{r}, s)}{\partial y} >= -\frac{2}{\sigma_x\sigma_y}\sqrt{\frac{2}{3}}\frac{dN_i}{dz}\sum_{k, z_k < z_n}\int dy'[y_b(s, z_n) - Y_k(y', s - z_n, s)]$$

$$\rho[y' - y_b(s - z_n + z_k, z_k)]\int_0^1 d\eta e^{-\frac{\eta^2}{2\sigma_y^2}[y_b(s, z_n) - Y_k(y', s - z_n, s)]^2}. \tag{9}$$

Here $y_b(s - z_n + z_k, z_k)$ is the offset of the k-th bunch at the moment $s_k = z + z_k$ when it generates ions at the same location $z = s - z_n$, where the n-th bunch is situated at the moment s.

Define the position $\hat{Y}_m(s, z_0)$ of the group of ions generated by the m-th bunch at the location z_0

$$\hat{Y}_m(s, z_0) \equiv Y_m(y_b(z_0 + z_m, z_m), z_0, s) \tag{10}$$

with the initial condition $\hat{Y}_m(z_0 + z_m, z_0) = y_b(z_0 + z_m, z_m)$ at $s = z_0 + z_m$. Equation (1) gives after averaging

$$\frac{\partial^2 y_b(s, z_n)}{\partial s^2} + \omega_b^2 y(s, z_n) = -\kappa s_b \sum_{k, z_k < z_n} [y_b(s, z_n) - \hat{Y}_k(s, s - z_n)] \int_0^1 d\eta e^{-\frac{\eta^2}{2\sigma_y^2}[y_b(s,z_n) - \hat{Y}_k(s, s-z_n)]^2} \tag{11}$$

Here

$$\kappa = \frac{4 r_e}{3\gamma s_b} \frac{dN_i}{ds} \frac{1}{\sigma_x \sigma_y}. \tag{12}$$

Note that parameter K of the paper[1] is $K = \kappa z_0$ where z_0 is the total length of the bunch train.

In the linear approximation $|y_b - Y_k| << \sigma_y$, we can take the dependence of the trajectory $Y_k(y, z, s)$ on the initial condition y in the form $Y_k(y, z, s) = y \cos \psi_y + Y_0(s)$ and obtain

$$< \frac{\partial U}{\partial y} >= -\frac{4}{3} \frac{1}{\sigma_x \sigma_y} \frac{dN_i}{dz} \sum_k [y_b(s, z_n) - \hat{Y}_k(s, s - z_n)]. \tag{13}$$

In another extreme case $\sigma_x >> |y_b - Y_k| >> \sigma_y$, Eqs. (8), and (9) give

$$< \frac{\partial U}{\partial y} >= -\frac{2}{\sigma_x} \sqrt{\frac{\pi}{3}} \frac{dN_i}{dz} \sum_k \mathrm{sign}[y_b(s, z_n) - Y_k(y_{nk}, s - z_n, s)]. \tag{14}$$

The force Eq. (11) depends on a sign of $(y_b - Y_k)$.

The motion of ions at the location z_0 can be considered similarly. The ion centroid is described by the equation

$$\frac{\partial^2 \hat{Y}_m(s, z_0)}{\partial s^2} = -\omega_y^2 e^{-\frac{x_m^2(s, z_0)}{2\sigma_x^2}} [\hat{Y}_m(s, z_0) - y_b(s, s - z_0)] \int_0^1 d\eta e^{-\frac{\eta^2 [\hat{Y}_m(s, z_0) - y_b(s, s - z_0)]^2}{2\sigma_y^2}}. \tag{15}$$

Equations (10), (11), and (15) can be generalized for the case when ions are not

cleared out after one turn. A centroid of ions, generated by the m-th bunch on the $l \geq 0$-th turn, is described by $\hat{Y}_m^l(s, z_0) \equiv Y_m(y_b(z_0 + z_m + lC, z_m), z_0, s)$ with the initial condition $\hat{Y}_m^l(z_0 + z_m + lC, z_0) = y_b(z_0 + z_m + lC, z_m)$ at $s = z_0 + z_m + lC$. Equations (11), (15) take the form

$$\frac{\partial^2 y_b(s,z_n)}{\partial s^2} + \omega_b^2 y(s,z_n) = -\kappa s_b \sum_{k,l} [y_b(s,z_n) - \hat{Y}_k^l(s, s_C - z_n)] \int_0^1 d\eta e^{-\frac{\eta^2}{2\sigma_y^2}[y_b(s,z_n) - \hat{Y}_k^l(s,s_C - z_n)]^2},$$

$$\frac{\partial^2 \hat{Y}_m^l(s,z_0)}{\partial s^2} = -\omega_y^2 e^{-\frac{x_m^2(s,z_0)}{2\sigma_x^2}} [\hat{Y}_m^l(s,z_0) - y_b(s,(s-z_0)_C)] \int_0^1 d\eta e^{-\frac{\eta^2[\hat{Y}_m^l(s,z_0) - y_b(s,(s-z_0)_C)]^2}{2\sigma_y^2}}.$$

Here C is the circumference of the ring, $s_C = s \bmod (C)$, and the sum over k is taken over bunches with $z_k < z_n$.

Linear approximation

Equations (11) and (15) give in the linear approximation $|y_b(s,z) - Y| << \sigma_y$ the system of equations

$$\frac{\partial^2 y_b(s,z_n)}{\partial s^2} + \omega_b^2 y(s,z_n) = -\kappa s_b \sum_{k, z_k < z_n} [y_b(s,z_n) - \hat{Y}_k(s, s - z_n)],$$

$$\frac{\partial^2 \hat{Y}_m(s,z)}{\partial s^2} = -\omega_y^2 [\hat{Y}_m(s,z) - y_b(s, s-z)]. \tag{17}$$

The second of Eqs. (17) has a solution

$$\hat{Y}_m(s,z) = y_b(z + z_m, z_m) \cos[\omega_y(s - z - z_m)] + Y_m^0(s,z), \tag{18}$$

$$Y_m^0(s,z) = \omega_y \int_{z+z_m}^{s} ds' y_b(s', s' - z) \sin[\omega_y(s - s')].$$

Equations (17) and (18) show that effect of the ions is equivalent to a transverse wakefield.

The solution was found in the original paper[1] in power series

$$y_b(s,z) = A_0 \sum_m y^{(m)}(s,z), \quad y^{(m)} = \frac{1}{(m!)^2}(\frac{\kappa\omega_y s z^2}{8\omega_b})^m \cos(\omega_b s - \omega_y z + \psi_0). \quad (19)$$

Indeed, substitution of the term $y^{(m)}(s,z)$ in the right hand side (RHS) of Eq. (17) gives the next term $y^{(m)}(s,z)$ provided the small terms of the order of $(\omega_y z/2m)^{-1}$, and $(\omega_b s/2m)^{-1}$ can be neglected. These conditions, compared to the original paper[1], include the additional factor m. From the expansion in Eq. (19), it is easy to see that significant $m \simeq \sqrt{\frac{\kappa\omega_y s z^2}{8\omega_b}}$ are large, and neglected terms are small provided

$$\sqrt{s/s_{eff}} << 1, \quad \frac{1}{s_{eff}} = \frac{\kappa}{2\omega_b\omega_y}, \quad z << \frac{2\omega_b^2}{\kappa}\sqrt{s/s_{eff}}. \quad (20)$$

Under these conditions, Eq. (18) gives the result[1]

$$y_b(s,z) = A_0 I_0(\omega_y z\sqrt{s/s_{eff}})\cos(\omega_b s - \omega_y z + \psi_0). \quad (21)$$

The solution grows exponentially as $exp[\omega_y z\sqrt{s/s_{eff}}]$. This expression depends only on two parameters: number of bunches in the train n_b, and characteristic time s_c

$$\frac{y_b}{a_0} \simeq e^{(n/n_b)\sqrt{s/s_c}}, \quad \frac{1}{s_c} = \frac{(\omega_y s_b n_b)^2}{s_{eff}}. \quad (22)$$

For larger $s >> s_{eff}$, the solution can be found in series

$$y_b(s,z) = \frac{A_0}{s}\sum_m \frac{1}{m!}(\frac{\kappa s z}{2\omega_b})^m \cos(\omega_b s - \omega_y z + \frac{m\pi}{2}) \quad (23)$$

giving oscillatory dependence on time

$$y_b(s,z) = A_0\frac{s_{eff}}{s}\cos(\omega_b s - \omega_y z + \frac{\kappa s z}{2\omega_b}). \quad (24)$$

This solution describes oscillations with the amplitude modulated in time s with frequency $2\omega_b/\kappa z$.

The PEP-II HER parameters are: $E = 9$ GeV, pressure 5 nTorr, $\sigma_x = 0.1$ cm, $\sigma_y = 0.02$ cm, bunch spacing $s_b = 1.24$ m, number of bunches $n_b = 1650$, $N_b = 8.3 \times 10^{10}$ (at the average beam current $I_b = 3$ A), and $\omega_b = 0.07\ m^{-1}$ (for $\nu_b = 23.5$). That gives $dN_i/ds = 24.9\ cm^{-1}$, $\omega_y = 0.96 \times 10^{-2}/\sqrt{A}\ cm^{-1}$, $\kappa = 2.1 \times 10^{-15}\ cm^{-3}$, $s_{eff} = 1.2 \times 10^9$ cm for $A = 28$. In this case z_{max} is larger than the ring circumference. Clearly, the regime shown in Eq. (24) can not be achieved, and the exponential growth of Eq. (22) can be stopped only by nonlinear effects.

The nonlinear regime

Exponential growth, as it was noticed in the original paper[1], tends to saturate at large amplitudes. Let us consider this regime in more details. Eq. (17) shows that Y_k grows faster than a bunch centroid y_b. Ions can be cleared out by a gap in the bunch train, but memory is retained in the beam, and the amplitude of ions is determined by the amplitude of bunch centroids. Motion becomes substantially nonlinear when the amplitude growth, Eq. (21), changes the ion frequency $\omega'(a/\sigma_y)^2 \simeq 1$ where the nonlinearity of ion oscillations $\omega' = \partial\omega_y/\partial(a/\sigma_y)^2$ on the order of $\omega' \simeq 0.1\omega_y$. This provides criterion for the time when transition to the nonlinear regime for the last n_b-th bunch takes place:

$$\sqrt{\frac{s}{s_c}} \equiv (\omega_y s_b n_b)\sqrt{\frac{s}{s_{eff}}} \simeq \ln(\frac{3\sigma_y}{a_0}). \tag{25}$$

Clearly, the exponential regime can be expected for $s >> s_c$ only if the initial amplitude a_0 is small.

In the substantially nonlinear regime when amplitudes of ions and electrons are large, $|y_b - \hat{Y}_k| \geq \sigma_y$, the equations of motion are

$$\frac{\partial^2 y_b(s,z_n)}{\partial s^2} + \omega_b^2 y_b(s,z_n) = -\sqrt{\frac{\pi}{2}}\kappa\sigma_y s_b \sum_k^{n-1} \mathrm{sign}[y_b(s,z_n) - \hat{Y}_k(y_b(s,s-z_n)], \tag{26}$$

$$\frac{\partial^2 \hat{Y}_m(s,z_0)}{\partial s^2} = -\sqrt{\frac{\pi}{2}}\sigma_y\omega_y^2 \mathrm{sign}[Y_m(s,z_0) - y_b(s,s-z_0)]. \tag{27}$$

The analysis of these equations is complicated. To achieve a qualitative result,

we proceed as follows. Take $y_b(s, z_m) = a(z_m)\cos\Phi(s, z_m)$ where, by analogy with the linear case,

$$\Phi(s, z_m) = \omega_b s - (\omega_b + \omega_y) z_m + \mu s. \tag{28}$$

Note, that

$$\Phi(s, s - z_0) = -\Psi(s, z_0) \equiv= -[\omega_y s - (\omega_b + \omega_y) z_0 - \mu s]. \tag{29}$$

Hence, $y_b(s, s - z_0) = a(s - z_0)\cos\Psi(s, z_0)$. The RHS of Eq. (27) is

$$-\sqrt{\frac{\pi}{2}}\sigma_y\omega_y^2 \mathrm{sign}[Y_m(s, z_0) - a(s - z_0)\cos\Psi(s, z_0)].$$

We assume

$$Y_m(s, z_0) = y_b(z_0 + z_m, z_m) + A_m(z_0)\cos[\Psi(s, z_0) + \xi_m]\,, \tag{30}$$

where the first term corresponds to the initial condition $Y_m(z_0 + z_m, z_0) = y_b(z_0 + z_m, z_m)$ for ions generated by the m-th bunch at location z_0 of the ring, and the second term describes oscillations of these ions induced by kicks of the following bunches. The argument of the *sign* function oscillates with s with frequency ω_y. The main Fourier harmonics of the *sign* function oscillates with the same frequency, confirming the choice of the solution shown in Eq. (29). From Eq. (27) it follows that $A_m \simeq \sigma_y$, but the phase ξ_m depends on the relation between amplitudes of different bunches.

Substitute now $Y_m(s, s - z_m)$ in Eq. (26) using

$$Y_m(s, s - z_m) = y_b(s, z_m) + \sigma_y\cos[\Phi(s, z_n) - \xi_m]. \tag{31}$$

The RHS of Eq. (26) takes the form

$$-\sqrt{\frac{\pi}{2}}\kappa\sigma_y s_b \sum_k^{n-1} \mathrm{sign}[a(z_n)\cos\Phi(s, z_n) - a(z_k)\cos\Phi(s, z_k) - \sigma_y\cos(\Phi(s, z_n) - \xi_m)]. \tag{32}$$

It oscillates with the frequency ω_b in the resonance with the betatron oscillations.

The solution of Eq. (26) grows linearly with time

$$y_b(s, z_n) = a_n \cos \Phi(s, z_n) - (\frac{\kappa \sigma_y s_b}{2\omega_b}) s d_n \sin \Phi(s, z_n) \tag{33}$$

where coefficients d_n depend again on the relation between the amplitudes of different terms in the sum of Eq. (32). The result, Eq. (33), can be written in the form Eq. (28) with the frequency shift $\mu = \kappa \sigma_y s_b/(2\omega_b)$, making analysis self-consistent. Note that the frequency shift μ kills resonance and stops amplitude growth but it happens only at very large numbers of turns.

Depending on the correlation of signs of different terms in Eq. (32), the amplitude squared is proportional to n or to n^2. Such uncertainty translates in the computer simulations to a non-monotonic growth of an amplitude for different bunches with the bunch number: the amplitudes of different bunches vary by several orders of magnitude and a bunch with a larger number does not necessarily have a larger amplitude. Assuming random signs of different terms in Eq. (32), we get the estimate for the time dependence of the amplitude of the n-th bunch when the amplitude is large

$$< [\frac{y_b(s, z_n)}{\sigma_y}]^2 > \simeq (\frac{s}{s_{eff}})^2 (\omega_y s_b)^2 n. \tag{34}$$

As discussed below, this estimate qualitatively agrees with numerical simulations, although it does not predict rather random variation of amplitude with time for individual bunches.

Because full scale modeling is time consuming, a simple code was used to model the instability based on Eqs. (17), (26), and (27). Equation (34) is compared below with the code to demonstrate that the estimate in Eq. (34) is consistent with Eqs. (17), (26), (27). Equation (34) is also compared with Raubenheimer's tracking simulations.

A train of bunches was modeled in the code as a train of macroparticles, a single macroparticle per bunch. Bunches generate a macroparticle representing ions at all locations around the ring separated by a bunch spacing. Ions are generated by all

bunches, which pass a given location and then are retained at this location for a specified number of turns, or until their amplitude is less than a certain aperture ($3 \times 10^3 \sigma_y$ was used in the simulations). The interaction between ions and bunches is described as a kick to ions and bunches proportional to the difference of the positions of the microparticles if the difference is smaller than σ_y, inversely proportional to the difference if the difference is larger than $10\sigma_y \simeq \sigma_x$, and as a constant kick dependent only on the sign of the difference in other cases. Variation of the ion frequencies around the ring and variation of the betatron frequencies of the individual bunches were optional.

The results of the simulations with this code are shown in Figs. 1-5. The train of $n_b = 80$ macroparticles moves in the 130 rf bucket long ring. Bunch spacing is $s_b = 0.42$ m, the ion frequency ω_y corresponds to $\omega_y s_b/c = 1.55$, the interaction is defined by $s_{eff} = 2.35 \times 10^5$ m, and characteristic time s_c, defined by $1/s_c = (\omega_y s_b n_b)^2/s_{eff}$, is $s_c = 15.3$ m. The initial amplitude is not zero only for the first bunch $y_1(0)/\sigma_y = 10^{-6}$.

Under this conditions, the linear theory predicts that the amplitude of the n-th bunch grows to $(a_n/\sigma_y)^2 = 0.1$ after $s = s_n = 2450(n_b/n)^2$ m. Fig. 1 shows the result of the simulations where all ions are cleared out after each turn and no frequency spread is included both for ions and bunches. The results qualitatively reproduce the main features of the exact simulations[1][2]. They give an exponential growth in agreement with linear theory, and show that exponential growth slows down at large amplitudes. The behavior predicted by Eq. (34) for the same bunches is superimposed with the results of the code in the lower part of Fig. 1. The curves obtained without any fitting confirm that the estimate Eq. (34) derived from Eqs. (26) and (27) agrees reasonably well with the code describing the same equations.

Fig. 2 is calculated with the same conditions but ions were retained in 10 turns rather than cleared out after the first turn. Results are similar but behavior of different bunches is much less systematic than in the first case. Quadratic dependence on s is seen more clearly if results are plotted in the usual (not semi-logarithmic) scale, Fig. 2b. Note that the amplitude of the first bunch grows because the ion are not

cleared out completelly by the gap. However, the amplitude of the first bunch remains smaller than that for the last bunch in the train by two orders of magnitude.

The effect of the frequency spread of ions was studied by G. Stupakov[2]. Fig. 3 shows the variation of the amplitude with time for the same parameters but ion frequency is varied periodically five times around the ring with 10% amplitude. The ions are cleared out in one turn.

Fig. 4 is calculated under the same conditions but betatron frequency is increased from bunch to bunch monotonically, increasing totally by 5% along the bunch train.

Fig. 5 compares Eq. (34) with the Raubenheimer tracking code. Parameters of the NLC damping ring were used: $E = 2GeV$, $n_b = 90$, $A = 28$, $N_b = 1.5 \times 10^{10}$, pressure 10^{-7} Torr, $s_b = 0.42$ m, $\beta_y = 8$ m, $\sigma_x = 42\mu m$, $\sigma_y = 7.7\mu m$. That gives $s_c = 0.82$ m, $s_{eff} = 1.3 \times 10^4$ m, and $\omega_y s_b = 1.4$. Agreement is reasonable.

Raubenheimer's numerical simulations for the ALS ring ($\omega_y s_b = 0.5$) give $s_{eff} = 1.7 \times 10^4$ m in good agreement with the linear theory for this machine. If this regime continued, the amplitude of the last bunch in the train of 150 bunches would grow to $y_b/\sigma_y \simeq 5 \times 10^9$ at $s = 1500$ m. The simulations show that this quantity is in the range of 0.1 to 10.0 for different bunches in the nonlinear regime after $s = 1500$ m. The estimate Eq. (34) for the last bunch is 0.3. Note that the range of the amplitudes for different bunches agrees with linear dependence on n in Eq. (34).

For parameters of PEP-II, $s_{eff} = 1.2 \times 10^7$ m, $\omega_y s_b = 0.22$, and $n_b = 1658$, equation (34) gives $(y_b/\sigma_y) = 7.5 \times 10^{-7}(s/m)\sqrt{n/n_b}$, or $y_b = \sigma$ in 4.5 msec for the last $n_b = 1650$ bunch. This rate is smaller than the PEP-II damping time but can be managed with the bunch-by-bunch feedback system.

We can estimate the amplitude, at which the transition from the exponential regime of Eq. (22) to the linear regime of Eq. (34) takes place by calculating s at which both formulas give the same result:

$$\sqrt{\frac{s}{s_{eff}}}(\omega_y s_b n) = \ln[(\frac{\sigma_y}{a_0})(\frac{s}{s_{eff}})(\omega_y s_b)\sqrt{n}]. \qquad (35)$$

The break point amplitude for the n-th bunch is

$$(\frac{y}{\sigma_y}) \simeq \frac{\ln^2(\sigma_y/a_0)}{4\omega_y s_b n^{3/2}}. \tag{36}$$

It is very small in the tail of the train, indicating that tail of bunches is always described by Eq. (34). In the head of the train, the break point amplitude can be large but time Eq. (35) in this case is large too, and growth can be stopped by a feedback system.

Conclusion

Ion-induced fast transverse instability is constrained by nonlinear effects. Nonlinear effects stop exponential growth of the amplitude at fractions of the rms bunch size. At large s the exponential growth described in the papers[1] [2] is replaced by the much slower linear growth of the amplitude. An estimate of the growth rate in this case is given by Eq. (34). The estimate is qualitatively consistent with numerical simulations. Instability at PEP-II can be controlled by the bunch-by-bunch feedback system with damping time of less than 4.5 ms.

Acknowledgement

I thank T. Raubenheimer for kindly providing me with the results of his simulations. I also thank A. Chao, F. Zimmermann, and G. Stupakov for discussions.

Figure Caption

Fig. 1 Comparison of the results of simulations (above) with Eq. (34). Lines are for different bunch numbers. All ions are cleared out after each turn and no frequency spread is included both for ions and bunches. Below: results of Eq. (34) are added, no additional parameters are used.

Fig. 2 The same as Fig. 1, but ions are retained for 10 turns. The same data are plotted in logarithmic (above) and linear (below) scales.

Fig. 3 Effect of ion frequency variation. The ions are cleared out in one turn.

Fig. 4 Betatron frequency variation is included.

Fig. 5 Comparison of Eq. (34) with the Raubenheimer's tracking code.

REFERENCES

1. T. Raubenheimer, F. Zimmermann. Interaction of a Charged Particle Beam with Residual Gas Ions or Electrons, SLAC, January, 1995

2. G. Stupakov, T. Raubenheimer, F. Zimmermann. Effect of Ion Decoherence on Fast Beam-Ion Instability, SLAC, January, 1995

Fig 1

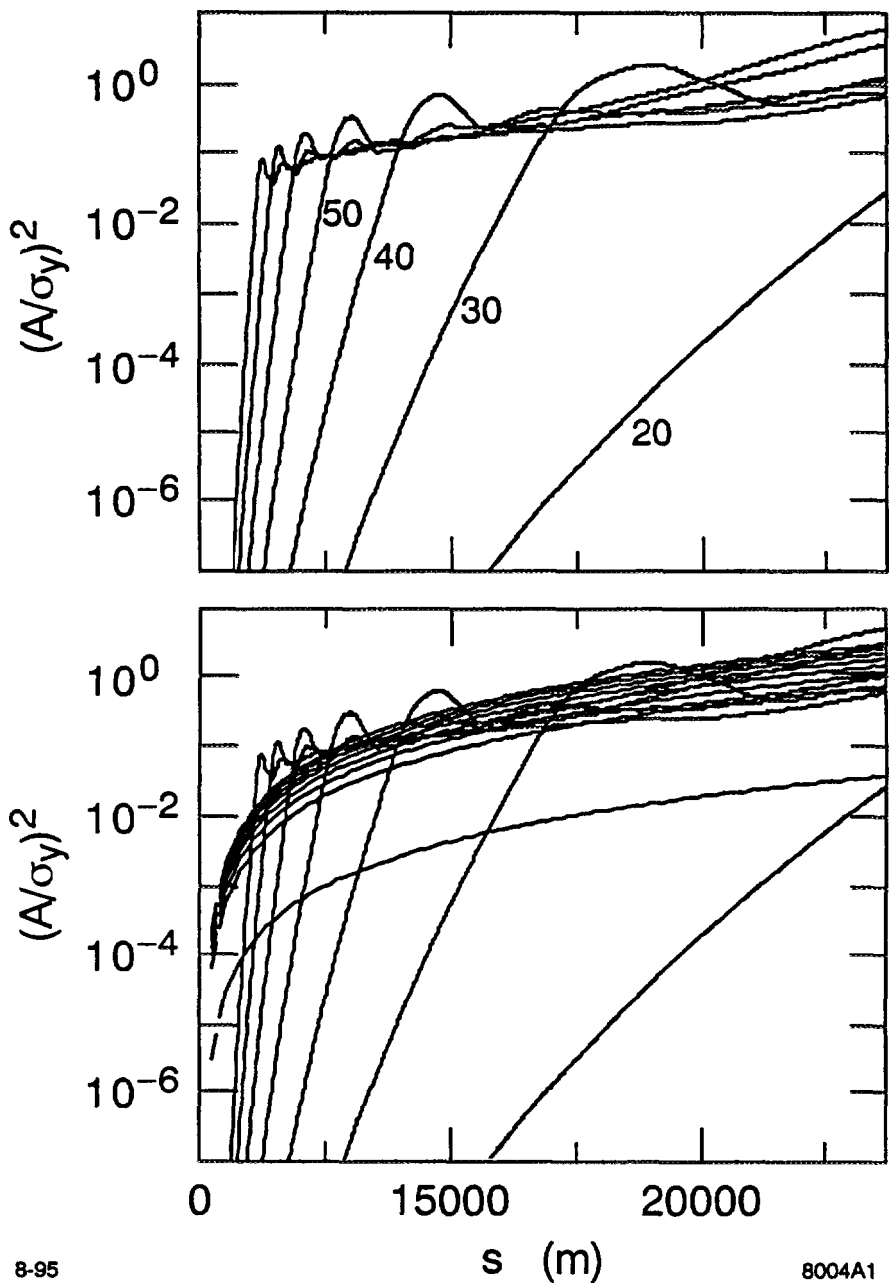
10^0
10^{-2}
10^{-4}
10^{-6}
$(A/\sigma_y)^2$
50
40
30
20
0
15000
20000
s (m)
8-95
8004A1

Fig 2

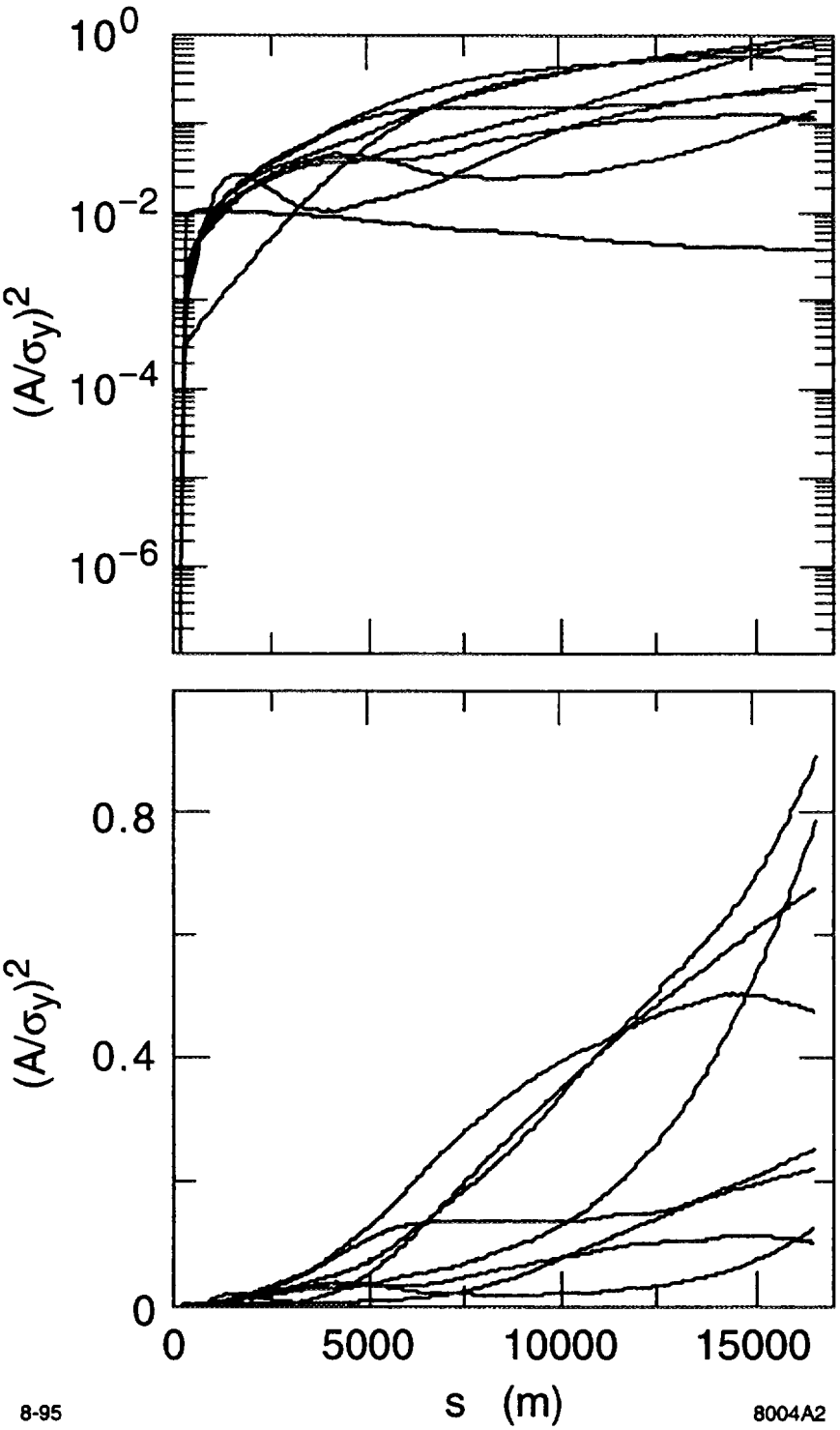
10^0
10^{-2}
10^{-4}
10^{-6}
$(A/\sigma_y)^2$
0.8
0.4
0
$(A/\sigma_y)^2$
0
5000
10000
15000
s (m)
8-95
8004A2

Fig. 3

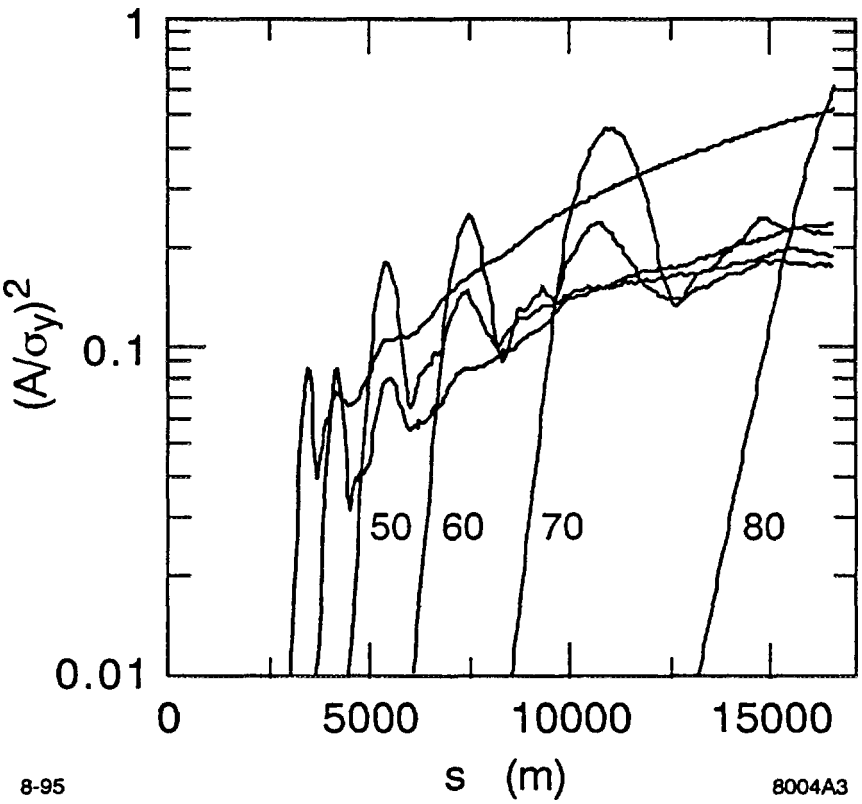

Fig 4

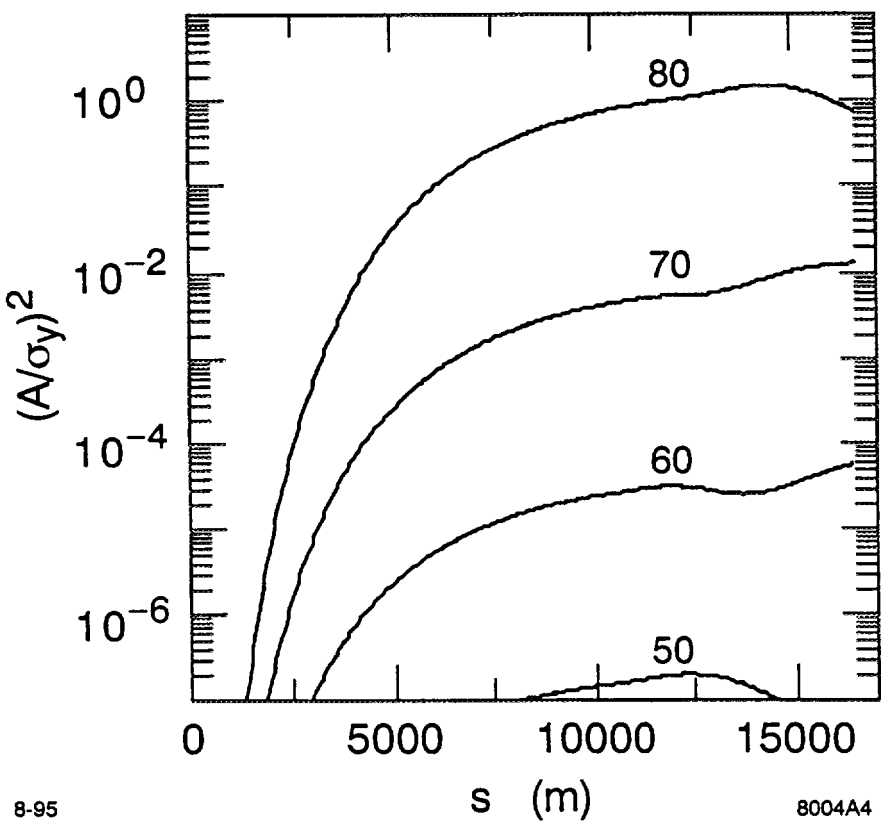
80
70
60
50
10^0
10^{-2}
10^{-4}
10^{-6}
$(A/\sigma_y)^2$
0
5000
10000
15000
s (m)
8-95
8004A4

Fig 5

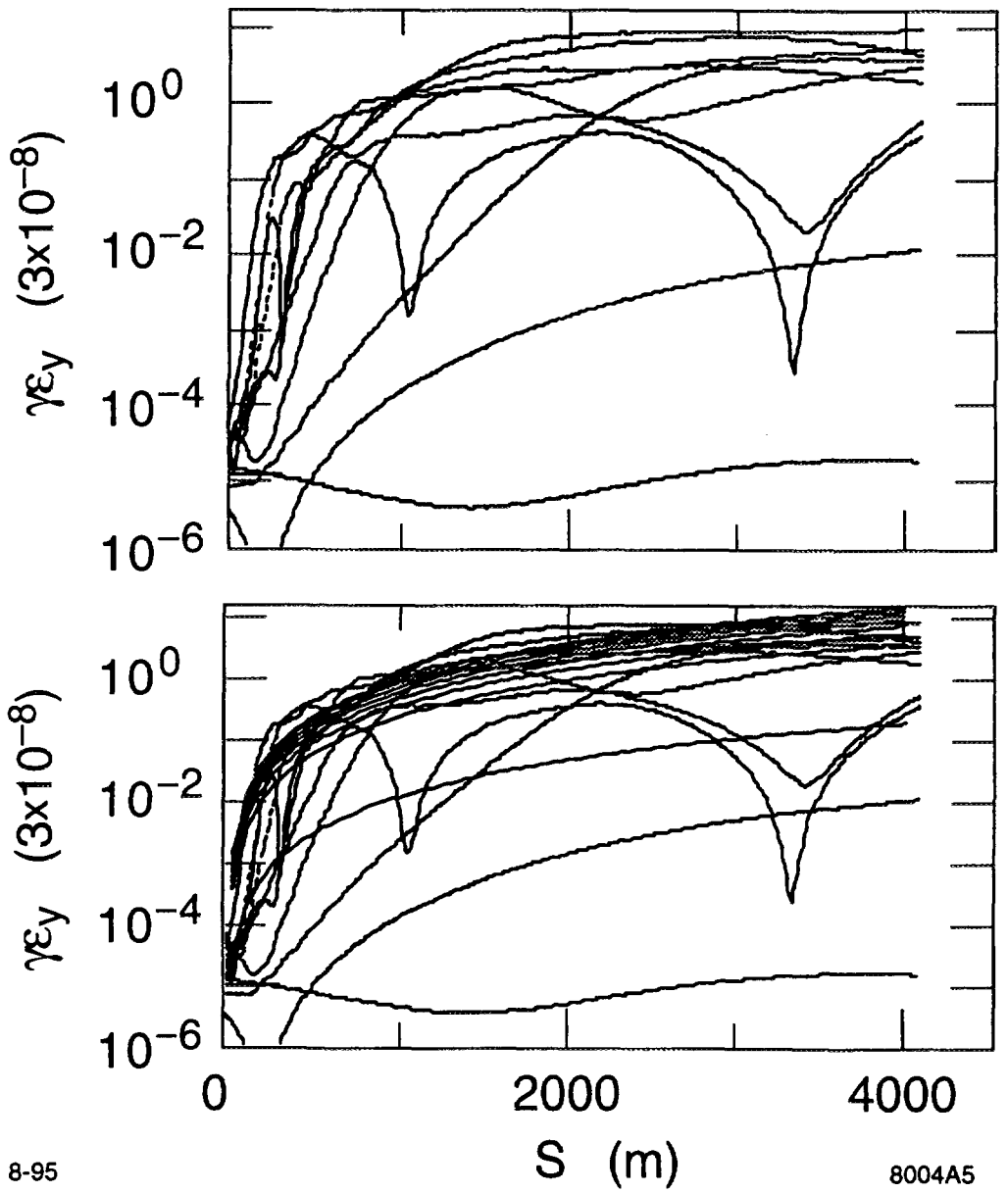
10^0
10^{-2}
10^{-4}
10^{-6}
$\gamma\varepsilon_y$ (3×10^{-8})
10^0
10^{-2}
10^{-4}
10^{-6}
$\gamma\varepsilon_y$ (3×10^{-8})
0
2000
4000
S (m)
8-95
8004A5

A coupled bunch instability due to beam-photoelectron interactions in KEKB-LER

Kazuhito OHMI

KEK, National Laboratory for High Energy Physics
Oho, Tsukuba, Ibaraki 305, Japan

1 Introduction

LER of KEKB is designed to storage the positron beam of $2.6A$ with multibunch operation. $N_b = 3.3 \times 10^{10}$ positrons are filled in a bunch and the bunch passes every $2ns$ through a beam chamber. In such a positron storage ring, a coupled bunch instability due to beam-photoelectron interactions[1] may become serious. In Photon Factory 2.5GeV storage ring, a coupled bunch instability has been observed in positron storage[2]. The instability was characterized by a low threshold current ($I_{th} = 15 \sim 20mA$) and a broad width of betatron sidebands. The instability has never observed in electron storage. Photoelectrons are produced when synchrotron photons emitted by positron beam hit the beam chamber. Most of the photoelectrons stay in the beam chamber during less than $0.1msec$. However a bunch produces a very huge number of photoelectrons, and the succesive bunches continue to supply them intermittently. The stationary distribution of photoelectron are formed like electron cloud. The positron beam passes through the photoelectron cloud. A coupled bunch instability is induced by the photoelectron cloud which mediates bunch to bunch coupling.

Let us consider the synchrotron radiation and photoelectron production quantitatively in the case of KEKB-LER. The number of photon emitted by a positron is expressed by,

$$N_\gamma = \frac{5\pi}{\sqrt{3}}\alpha\gamma, \tag{1}$$

where α and γ are the fine-structure constant and the Lorentz factor, respectively. Here, the bending radius is assumed to be a constant. In KEKB-LER, $\gamma = 6850$, so that $N = 453$ in a revolution. The chacteristic energy of the photon is $\sim 6keV$. The photoelectron conversion rate of the photon is assumed to be 0.02. The energy distribution is $5 \pm 15eV$[3]. Total number of photoelectron produced by a bunch is 3×10^{11} in a revolution. The conversion rate is measured by using photons with incidence perpendicularly on a metal surface. In the case of photons with a small angle of incidence, it is enhanced by several times or more. The other hand, all of photons would not move such as been simulated. Anyway there is some ambiguity for this value.

Table 1: Parameters of KEKB-LER

Beam energy	3.5GeV
e^+ in a bunch	3.3×10^{10}
beam size $(x/y)(m)$	$5.4 \times 10^{-4}/7.6 \times 10^{-5}$
RF frequency	508 MHz

In KEKB-LER, beam chambers have been designed to be cylindrical cupper pipe with a diameter of 9.6 cm. The same analysis as PF ring[1] has performed with those of KEKB-LER, see Table 1.

2 Photoelectron motion in the beam pipe

The photoelectrons produced at the chamber wall propagate to the beam position by an attractive force of positron beam. The photoelectrons are not trapped by the beam because of the light mass, if we consider the linear dynamics. However the time dependent nonlinear force from bunched beam may trap the photoelectrons for a short time. The trapping time will be far shorter than that of ion trapping in electron rings.

Now we consider a motion of photoelectrons produced by a bunch with a computer simulation technic. Each photoelectron, which started at beam chamber wall and interacted with the positron beam, was tracked. A cylindrical chamber with a diameter of $10cm$ was used as a model chamber. Fig.1 shows the motion of photoelectrons. The coulomb force by bunched beam with a gaussian distribution were considered. Though it would be better to consider a space charge effect of the photoelectrons, it did not dominate for the beam charge. The group of photoelectrons arrives at the beam position after interacting with the following 5 or 6 bunches. Because of the stochasticity of the time dependent force, a considerable rate of the photoelectrons were not absorbed into the chamber wall after twice of time arriving the beam center. After passing 100 bunches, 1.5% of initial photoelectrons was remained.

Photoelectrons are supplied continuously by bunches arriving one after another. A stationary distribution of photoelectrons are formed by an equilibrium of the supply and absorption. Since most of the photoelectrons are absorbed after passing the following 100 bunches, the stationary distribution is obtained by accumulating photoelectrons produced succesively. Fig.2 shows the stationary distribution. It is interesting to estimate how many photoelectrons in the beam chamber. Fig.3 shows the number of photoelectron accumulated in the beam chamber. There is about 15 times of the photoelectrons produced by a bunch.

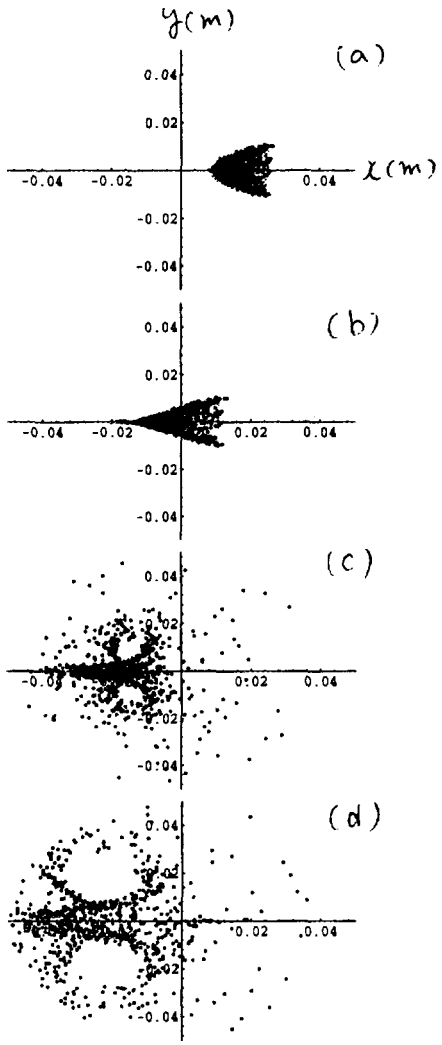

Figure 1: Motion of photoelectron produced by a bunch. (a) Distribution after passing 5 bunches, (b) 6 bunches, (c) 7 bunches, and (d) 8 bunches.

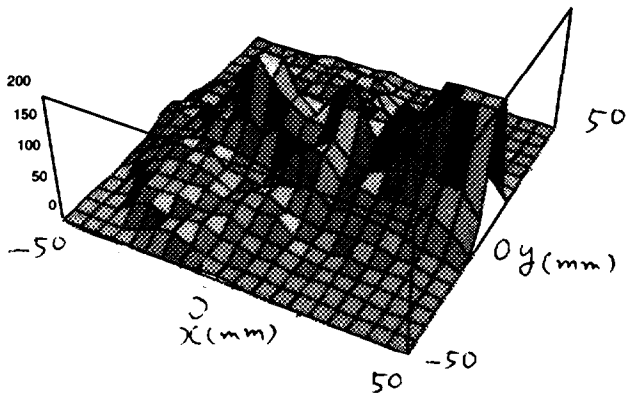

Figure 2: Stationary distribution of photoelectrons

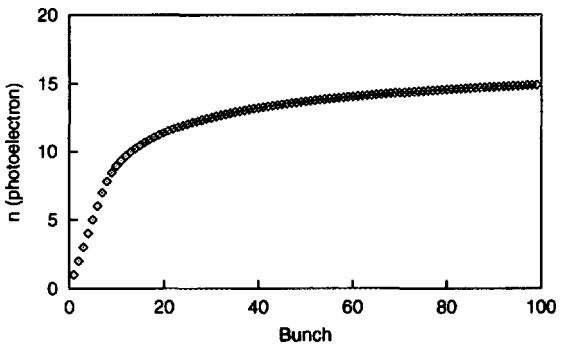

Figure 3: Number of photoelectron in the beam chamber. It is normalized by the number of photoelectron by a bunch.

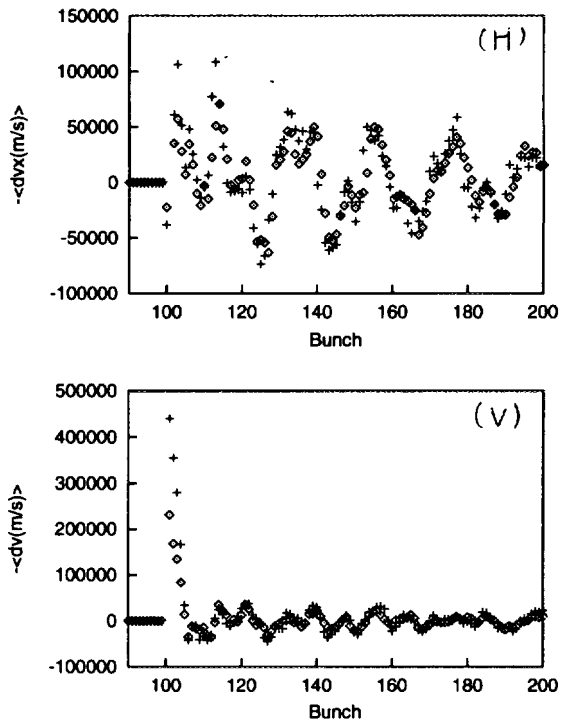

Figure 4: Horizontal and Vertical wake force. The wakes by $0.5mm$ and $1mm$ displacements are marked by tilt boxes and crosses, respectively

3 The coupled bunch instability due to photoelectrons

The positron beam passes through the stationary distribution of photoelectrons. Let us consider a loading bunch with a virtual displacement. If the loading bunch is shifted to the direction of positive-y, photo-electrons are attracted toward the new position. The loading bunch feels a kick in the negative-y direction from the stationary distribution. On the other hand, the following bunches feel kicks from a positively displaced distribution, and are kicked in the positive-y direction. We can interpret the momentum kick as being the wake force of the transverse dipole mode. The characteristics of the wake function is the same as that of an impedance problem, that is, it is negative near the loading bunch.

The wake force was obtained by doing above procesure with a computer. Fig.4 shows the wake force. The 100-th bunch is a loading bunch. The wake forces were calculated for the loading bunches with displacements of 0.5 mm and 1mm. The wake force is observed in following several bunches. The short-range feature results from the light mass of an electron. The vertical wake force kicks the following several bunches with good linearity.

We can observe two type of wake in the Fig.4. One is the short range wake which is shown in vertical and has good linearity. Another is that observed in horizontal and vertical. The horizontal wake did not show linear characteristics. In the vertical wake, linearity is not also good for backward of a dozen bunches. These, horizontal and vertical tail, are approximately equal in strength. As mension above, a portion of photoelectrons

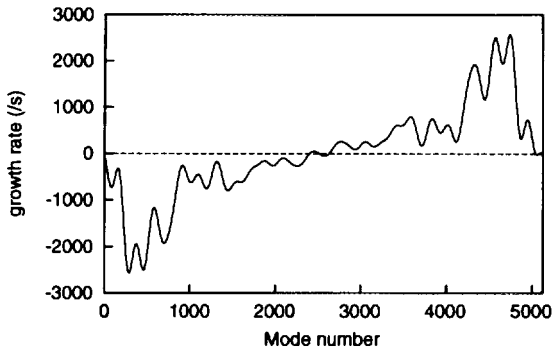

Figure 5: Growth rate of the vertical instability

are trapped in the beam chamber. The wake characteristics seems to be caused by the trapped electrons kicked by the loading bunch. The wake was satulated with the loading displacement of 0.5mm. The wake is anticipate to be sensitive for the boundary condition of chamber and self space charge of the photoelectrons. It may not enough to be estimated by this simulation. Now we consider only the linear wake.

We obtained a growth rate by the wake force. Fig.5 shows the growth rate. It is very high rate, $2500s^{-1}$. We should note that the growth rate depends linearly on the photoelectron conversion rate (0.02 is used here).

4 How to cure

We should consider how to cure the problem. We have some ideas as follows,

- Bunch to bunch feedback.
- Magnetic field.
- Bunch train.

The bunch to bunch feedback is expected to be $1msec$ (100 turn). The feedback is not enough to care the instability. Thus the problem is how the instability can be suppressed such as to care the feedback system. We consider to control magnetic fields so as to restrict the motion of electrons, because energy of photoelectrons are several eV near the surface of beam chamber. If photoelectrons come from horizontal direction, we can consider solenoid and vertical bending fields. Fig.6 shows the wake force when the magnetic fields is applied. The strength of wake was reduced remarkably. However it is not so easy to apply the magnetic field everywhere synchrotron radiation illuminate.

Another method is to operate with bunch trains. The wake force has a range of several bunches. Thus if we put a dozen of empty backets, most of the photoelectrons will absorbed into the beam chamber and first bunch of trains will be not affected by photoelectrons. However the photoelectron cloud is formed very rapidly. We should remember that photoelectrons produced by a bunch approach closely to following fifth or sixth bunch. Thus length of the bunch train will be limited by the formation of the cloud. In a preliminary calculation, if 20 bunches are joined, we are lucky.

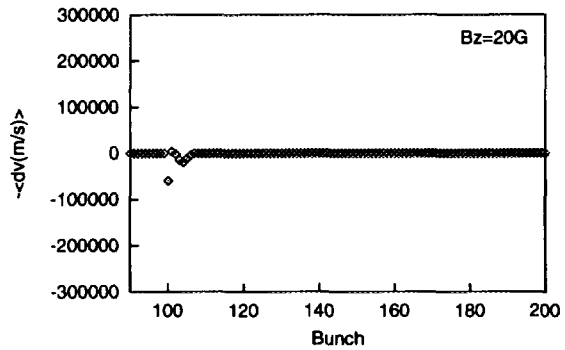

Figure 6: Wake force when applying solenoid fields of 20G.

5 Summary

The photoelectron instability may be serious for KEKB-LER. The growth rate exceeds damping rates of various mechanism: radiation, head-tail, and feedback.

Parpaps it is essential to remove the photoelectrons around the positron beam explicitely. If we apply magnetic fields of about $20G$, the growth rate will be reduced. Using bunch trains may cure the problem easily, though it will be not enough. In that case, the problem is how the luminosity is reduced by the limitation of the length of bunch train.

References

[1] K. Ohmi, Phys. Rev. Lett. 75, 1526 (1995).

[2] M. Isawa, Y. Sato and T. Toyomasu, Phys. Rev. Lett. 74, 5044 (1995).

[3] K. Kanazawa, private communications.

Study of an Instability of the PEP-II Positron Beam (Ohmi Effect and Multipactoring)*

S.A. HEIFETS

Stanford Linear Accelerator Center

Stanford University, Stanford, CA 94309

The transverse instability in the Photon Factory has been observed and described by Ohmi[1] as an instability of a positron beam in a storage ring induced by photoelectrons. (I would like to mention that W. Stoeffl also pointed out that photoelectrons may produce an effective wake-field somewhere in the middle of 1994). The photoelectrons are produced by synchrotron radiation in the beam pipe wall and accelerated by the transverse electric field of the beam. A transverse kick given by the photoelectrons to the trailing bunches depends on the off-set of the previous bunches. The situation is, in general, analogous to the beam break-up[2] induced by the regular transverse wakefields, and to the recently described ion-induced transverse instability of an electron beam[3].

The processes defining the density distribution of the photoelectrons are quite complicated. Detailed description of the instability requires computer simulations, as has been done in Ohmi's original paper. It is useful to have a simplified model of the instability to get a quick estimate of the growth rate of the instability and the relative importance of the parameters. The model described below uses parameters of the LER of the PEP-II B-factory[4].

The paper is organized in the following way. First, Ohmi effect induced by direct flow of primary photoelectrons is studied for the PEP-II parameters. The production rate and kinematics take into account the antechamber of the LER. We discuss the

* **Work supported by Department of Energy contract DE-AC03-76SF00515**

effect of the secondary emission of electrons in the AL chamber, where the yield is larger than one. Resonance multipactoring is considered, and then the average density of the secondary electrons is estimated taking into account the space-charge effect and the interaction with the beam. We show that in the extreme case there is a self-consistent regime similar to the regime of the space-charge dominated cathode. Finally, the rate of ion production by accumulated electrons and the possibility of the ion induced pressure instability is discussed.

Kinematics of the radiation

Consider a short dipole $l_d < \sqrt{2b\rho}$ with length l_d, and bending radius ρ. A photon emitted at the azimuth θ upstream from the end of the dipole, $0 < \theta < l_d/\rho$, propagates downstream into the beam pipe of the straight section, covering the distance $l_\gamma = \rho \tan\theta + s/\cos\theta$ before it hits the beam pipe wall. The photon hits the wall of the beam pipe with radius b at distance

$$s \simeq b/\theta - \rho\theta/2, \tag{1}$$

counting downstream from the end of the dipole. The distance l_γ is larger than the distance $l_e = \rho\theta + s$ passed by the parent electron to the same moment. The delay is $\Delta l = l_\gamma - l_e \simeq \rho\theta^3/12 + b\theta/2$. The maximum delay is for the photons emitted at the entrance to the dipole, $\theta = l_d/\rho$, $(\Delta l)_{\max} \simeq b\sqrt{b/2\rho}$. For the LER parameters, $l_d = 0.45$ m, $\rho = 13.75$m, $b = 4.5$cm, $\gamma = 6. \times 10^3$, the delay is small compared to the bunch length σ_l: the maximum delay is 1.3 mm, while $\sigma_l = 1$ cm. Neglecting the delay, we assume that the primary photon and the parent electron remain on the same azimuth during the life time of the photon.

The photons are radiated uniformly along the orbit within a dipole. The energy radiated per unit time and the solid angle $d\Omega$ in the frequency range $d\omega$ is given by the well known formula

$$\frac{dW}{d\omega} = \frac{e^2}{\rho}\frac{\omega^2}{6\pi^3\omega_0^2}[\epsilon^2 K_{2/3}^2(\frac{\omega}{3\omega_0}\epsilon^{3/2}) + \epsilon\sin^2\alpha K_{1/3}^2(\frac{\omega}{3\omega_0}\epsilon^{3/2})]d\Omega, \tag{2}$$

where ω_0 is the revolution frequency, $\epsilon = (1/\gamma)^2 + \alpha^2$, α is the radiation angle with the trajectory plane, and $d\Omega = \cos\alpha d\alpha d\theta$.

The number of photons per unit azimuth, and the total number of the radiated photons per dipole are respectively:

$$\frac{dN_\gamma^{tot}}{d\theta} = \frac{5\alpha_0\gamma}{2\sqrt{3}}, \quad N_\gamma^{tot} = \frac{5}{2\sqrt{3}}\alpha_0\gamma\theta_d. \tag{3}$$

The angle α defines the vertical displacement of a photon $y = l_\gamma\alpha$. Eq. (1) relates s and θ giving the distribution of photons $dn/dt = dW/h\omega$:

$$\frac{dn}{dt} = \frac{\alpha_0}{6\pi^3}\frac{\omega}{\omega_0}\frac{d\omega dy ds}{\rho(s^2+2b\rho)}[\sqrt{s^2+2b\rho} - s][\epsilon^2 K_{2/3}^2(\frac{\omega}{3\omega_0}\epsilon^{3/2}) + \epsilon\sin^2\alpha K_{1/3}^2(\frac{\omega}{3\omega_0}\epsilon^{3/2})] \tag{4}$$

where $\omega_0 = c/\rho$, $\alpha_0 = e^2/(hc) = 1/137$, and $\epsilon = (1/\gamma)^2 + y^2/(s^2+2b\rho)$.

Let us estimate the number of photons which strike the edges of the antechamber $|y| > h_g/2$, where $h_g = 1.5$ cm is the antechamber full height for PEP-II. In the most of the following, we ignore the photoelectrons produced in the antechamber, assuming that they loose memory on the offset of the parent bunch while drifting to the beam pipe. The photoelectrons that may be accelerated by the field of the beam and affect the beam stability are generated mostly on the edges of the slot of the antechamber. The electrons on the upper and lower decks of the slot may be pulled into the beam pipe by the field of the beam leaking inside of the slot, but their number is relatively small.

The maximum distance photons can travel in the beam pipe is limited by the bend of the beam pipe in the downstream dipoles, $s_{\max} < 9$ m. In this case, $\epsilon = y^2/(s^2+2b\rho)$, and number of photons radiated by a positron per one dipole is

$$\frac{d^2n}{dsdy} = \frac{\alpha_0}{3\pi^2}\frac{\omega d\omega}{\omega_0^2\sqrt{s^2+2b\rho}}(\frac{y^2}{s^2+2b\rho})^2[1-\frac{s}{\sqrt{s^2+2b\rho}}][K_{2/3}^2(\frac{\omega}{3\omega_0}\epsilon^{3/2})+K_{1/3}^2(\frac{\omega}{3\omega_0}\epsilon^{3/2})]. \tag{5}$$

Integration over frequencies gives

$$\frac{d^2n}{dsdy} = \frac{\alpha_0\sqrt{3}}{\pi\rho}[1-\frac{s}{\sqrt{s^2+2b\rho}}]\frac{\sqrt{s^2+2b\rho}}{y^2}. \tag{6}$$

At large $s^2 >> 2b\rho$,

$$n_\gamma(s,y) = \frac{d^2n}{dsdy} = \eta_\gamma \frac{b}{sy^2}, \tag{7}$$

where

$$\eta_\gamma = \frac{\alpha_0\sqrt{3}}{\pi} = 0.4 \times 10^{-2}. \tag{8}$$

This gives the number of photons hitting the edges of the antechamber downstream from a dipole

$$\frac{dN_\gamma}{ds} = \frac{4\alpha_0\sqrt{3}}{\pi}\frac{b}{sh_g}, \qquad N_\gamma = \frac{4\alpha_0\sqrt{3}}{\pi}\frac{b}{h_g}\ln(\frac{s_{\max}}{s_{\min}}). \tag{9}$$

The minimal distance $s_{\min}$ can be defined from the condition $(\omega/3\omega_0)y^3 < (s^2 + 2b\rho)^{3/2}$, otherwise the number of photons from Eq. (5) is exponentially small. The distance s cannot be too small because $y^2 > (h_g/2)^2$, and the photon energy should be large enough to produce a photoelectron: $h\omega > I_0$, where $I_0 \simeq 4.5$ eV is the work function of a beam pipe wall. This limits

$$s > s_{\min} = (h_g/2)[\frac{I_0}{3h\omega_0}]^{1/3}. \tag{10}$$

PEP-II parameters give $s_{\min} = 3.5$ m, larger than $\sqrt{2b\rho} = 1.1$ m.

Eq. (9) gives $N_\gamma = 0.045$ per positron per dipole. This is about 2.2% of the total number of photons given by Eq. (3) $N_\gamma^{tot} = 2.06$ for PEP-II parameters.

Kinematics of the photo-electrons

The average number of photoelectrons generated by N_b particles per bunch per unit length is

$$\frac{dN_e}{ds} = \eta_{e\gamma}\frac{N_\gamma}{(s_{\max} - s_{\min})}N_b \tag{11}$$

where the yield $\eta_{e\gamma}$ is the number of electrons per incident photon. This yield depends on the photon energy and the incident angle, which varies from 1.5 mrad at $s \simeq s_{\min}$ to 0.15 mrad at $s = s_{\max}$. Ohmi uses $\eta_{e\gamma} \simeq 0.1$ photo-electrons per photon. For the PEP-II parameters, $N_b = 8.3 \times 10^{10}$ at the beam current 3 A, $dN_e/ds = 6.8 \times 10^5$ cm^{-1}.

The initial photoelectrons have density $n_e(s,x,y,0) = \eta_{e\gamma} N_B n_\gamma(s,y)\delta(x-b)$ within the range $|y| > h_g/2$, $s_{\min} < s < s_{\max}$.

The photoelectrons have an initial energy on the order of a few eV-s. The transverse electric field of the parent bunch gives a kick to the photoelectrons

$$\Delta p(x) = \frac{2N_B e^2}{c}\frac{x}{x^2+y^2}, \qquad (\frac{v}{c})_{\max} = \frac{2N_B r_0}{b}, \tag{12}$$

where r_e is the electron classical radius. This corresponds to $(v/c)_{\max} = 1.0 \times 10^{-2}$, and energy $mv^2/2 = 26$ eV at 3A beam current.

This energy is large compared to the initial energy of photoelectrons coming out from the wall. Because the field lines are perpendicular to the wall, the photoelectrons get only horizontal kick from the parent bunch. The electrons are distributed vertically with the height on the order of $h_g = 1.5$ cm. An initial vertical velocity corresponding to the energy 1 eV would displace the electron vertically by the distance $2.5\,\text{mm} << h_g$ when the next bunch arrives for the PEP-II bunch spacing $s_b = 120$ cm. The actual displacement is even smaller due to $\cos\theta$ distribution of the initial photo-electrons. We may, therefore, neglect the initial energy of the photo-electrons so that the distribution of the photo-electrons over the horizontal velocity after the parent bunch passed by is

$$\rho(v) = \int d\rho(z)\,\delta[v_x(z) - v]\,. \tag{13}$$

Here, $\rho(z)$ is the longitudinal density of the bunch, and $v_x(z) = v_{\max}\int_{-\infty}^{z} dz'\rho(z')$ is the velocity of a photoelectron due to radiation of positrons at the location z within a bunch. In Eq. (13) we neglect the time delay between a photon and the parent positrons.

Integration in Eq. (13) gives a uniform distribution within the range $0 < v < v_{\max}$: $\rho(v) = (1/v_{\max})\Theta(v_{\max} - v)$. As a result, the distribution of the electrons in the horizontal direction at moment t after the parent bunch is also uniform within a

strip with length $\Delta x = v_{\max} t$:

$$n_e(s,x,y,t) = \eta_\gamma \eta_{e\gamma} \frac{N_b}{\Delta x(t)} \frac{b}{s(y-y_c^l)^2}. \tag{14}$$

The density is nonzero in the range $|y| > h_g/2$, $s_{\min} < s < s_{\max}$. Here we modified Eq.(8), introducing the offset y_c^l of the parent bunch centroid. The vertical distribution remains unchanged.

At the moment $t_1 = s_b/c$, when the next bunch comes to the same azimuth s, $\Delta x = v_{\max} s_b/c$. For PEP-II parameters at 3 A current, $\Delta x = 1.28$ cm, $\Delta x << b$. The density in this moment is independent on N_b. The maximum average density at $|y| = h_g/2$ is $n_{\max} = 3.6. \times 10^5$ cm^{-3} at PEP-II parameters. Later the strip is stretched because the kick is larger for the particles at the end of the strip that is closer to the beam. At the arrival of the next bunch, the strip is 2.2 cm long and the head of the strip is at a distance $x = 3.47$ cm from the wall, close to the beam. When the next bunch comes, the head of the strip is 0.25 cm away from the opposite wall and the bunch is 5.3 cm long. The centroid of the strip moves vertically from a position above beam line to the position below it before it hits the wall.

The head of another strip of electrons produced by the next bunch coincides with the tail of the strip of the previous bunch. The beam makes a continuous ribbon of photoelectrons flowing from the wall toward the beam with varying density due to the stretching of each strip.

Effect of the photoelectrons

Consider for the sake of simplicity the 1-D case, $y = y_c = 0$.

The photoelectrons give a kick to the positrons $dp_y/ds = -(\partial/\partial y)e^2 U$, where $U(s,x,y)$ is the potential defined by the density Eq. (14), properly modified in time

$$\Delta U(s,x,y) = -4\pi n_e(s,x,y). \tag{15}$$

Taking into account the interaction of a bunch only with the group of photoelectrons closest to the beam, we get the equation of betatron oscillations in the vertical plane

$x = 0$

$$\frac{d^2y}{ds^2} + k_\beta^2 y = \frac{r_e}{\gamma}\frac{\partial U(s,0,y)}{\partial y}, \tag{16}$$

where $k_\beta = \nu_y/R_0$ is defined by the vertical betatron tune ν_y and the average radius of the machine R_0.

Considering the potential of a strip of electrons with the length Δx and the centroid at x_c, we can estimate

$$\frac{\partial U(s,0,y)}{\partial y} = 2\int dx'dy' n_e(x',y')\frac{y-y'}{(x'-x_c)^2+(y-y')^2}, \tag{17}$$

where n_e is given by Eq. (14).The integration over y' is in the limits $|y'| > h_g/2$

The equation of motion takes the form

$$\frac{d^2y}{ds^2} + k_\beta^2 y = \frac{\Lambda}{s}J(y,y_c^l), \tag{18}$$

where $\Lambda = \eta_\gamma \eta_{e\gamma} N_b b r_e/\gamma$. The RHS of Eq. (18) is nonzero in the range $s_{\min} < s < s_{\max}$ after each dipole, and

$$J(y,y_c^l) = \frac{2}{\Delta x}\int \frac{dx'dy'}{(y'-y_c^l)^2}\frac{y-y'}{(x'-x_c)^2+(y-y')^2}. \tag{19}$$

Consider expansion of the RHS of Eq. (18) in y and y_c^l. The term driving the instability is proportional to the offset y_c^l. Other terms give a negligible small correction to the betatron tune and orbit distortion. The driving term is

$$J = \frac{8\pi}{\Delta x h_g^2} y_c^l \tag{20}$$

in the case $\Delta x >> x_c$, and $\Delta x \simeq h_g$, and J is smaller than this for large $x_c >> h_g/2$, $x_c \simeq \Delta x$ by a factor $\Delta x h_g/(\pi x_c^2)$.

The offset of the accelerating bunch affects the density distribution and is suppressed by a factor $\pi h_g/8b << 1$. Equations (18), and (20) give

$$\frac{d^2y}{ds^2} + k_\beta^2 y = -\lambda y_c^l, \tag{21}$$

where the averaged λ is

$$\lambda = 8\pi\eta_\gamma\eta_{e\gamma}\frac{N_b r_e b}{\gamma(s_{\max} - s_{\min})h_g^2\Delta x}\ln\frac{s_{\max}}{s_{\min}}. \tag{22}$$

The vertical component of the kicks changes the width of the distribution and the vertical offset of the centroid of the group of photoelectrons simultaneously without changing this result.

Oscillations of the first bunch in a train of bunches with the amplitude A_1, $y_1(s) = A_0 e^{ik_\beta s}$, excite oscillations of the following bunches with the amplitude of the n-th bunch growing with the distance s as

$$y_{n+1} \propto \frac{A_1}{n!}(\frac{\lambda s}{2k_\beta})^n. \tag{23}$$

The amplitude of the n-th bunch

$$A_{n+1} \propto \frac{A_1}{\sqrt{n}} e^{n\ln[e\lambda s/(2nk_\beta)]} \tag{24}$$

starts growing at $s > s_n = 2nk_\beta/(e\lambda)$, $e = 2.718...$ Consider the worst situation of a 3 A beam bunch, when the head of the strip is only 1 cm away from the beam and $\Delta x = 2.2$ cm. Although at a lower current this distance can decrease, the reduction of N_b does not make the situation worse.

For the PEP-II parameters, $\lambda = 0.6\times10^{-6}\ m^{-2}$ for $\eta_{e\gamma} = 0.1$, and average current 3 A. The amplitude of the second bunch becomes equal to the amplitude of the first bunch after 100 turns, or 0.73 msec and then propagates to the tail of the beam with the same rate from bunch to bunch.

Effect of the background electrons and multipactoring

The instability described above is due to interaction with a single group of photoelectrons.

The interaction with other groups of photoelectrons or with electrons existing in the beam pipe may give a similar effect. Such "background" electrons is the media interacting with the beam and the electron density defines the beam instability. The background electrons may be generated by different mechanisms: inelastic collisions of the positron beam with the residual gas, photoeffect on the residual gas, diffusion of photoelectrons from the antechamber, generation of electrons by the scattered synchrotron radiation, by secondary electron emission, etc.

The secondary electrons may be accelerated by the transverse field of the beam to large energies and, hitting the wall, produce new electrons. The number of fast electrons can be enhanced at certain currents when secondary electrons are produced at the moment when another bunch is passing by. Such a beam induced multipactoring may lead to a substantial increase in the electron density, provided that the yield η_{ee} of the secondary electrons is more than one.

The interaction with the background electrons is the main concern in the dipoles where the magnetic field prevents the photoelectron from drifting toward the beam, because the Larmor radius of such electrons is of the order of 20 μm. The electrons move primarily in the vertical plane, because the longitudinal cross-field drift and the drift caused by the space charge are slow. The multipactoring of the background electrons in the dipoles may lead to large electron densities. It is worthwhile noting that instability of the KEK Photon Factory probably is the result of some processes in the dipoles.

The average number of photoelectrons per unit length from Eq. (11) generated by the primary synchrotron radiation of a bunch with $N_b = 8.3 \times 10^{10}$ positrons is $dN_{e\gamma}/ds = 6.8 \times 10^5$ cm^{-1}, and the initial density in a stripe of photoelectrons $n_{\max} = 3.6 \times 10^5$ cm^{-3}. The density of a stripe which centroid moved to the beam, is smaller, about $2. \times 10^5$ cm^{-3}. The question here is whether the density of the background electrons can be much larger. In a steady state regime, one

could expect the equilibrium electron density given by the condition of neutrality: $n = N_B/(\pi b^2 s_b) = 1.5 \times 10^7 \mathrm{cm}^{-3}$. However, the background electrons are not in equilibrium, and the answer may depend on such details as the energy dependence of the yield of the secondary electrons.

Fig. 1 shows dependence of the yield η_{ee} on the energy of the incident electron for Al oxide and the distribution of the secondary electrons. The distribution at large initial energy $E_0 >> E^{\eta}_{\min}$ has two maxima. The high energy peak is at $E \simeq E_0$ and corresponds to a backscattered incident electron. The width of the first maxima describing real secondary electrons is about 5 eV. Fig. 2 shows the yield for the different materials.

The kick from the transverse electric field of a bunch changes the velocity of an electron located at distance r from the beam by $v(r)$, Eq. (12), and electrons hitting the wall can produce secondary electrons, if $r/b = (N_b r_0/b)\sqrt{2mc^2/E^{\eta}_{\min}}$. This condition is easy to satisfy: $r/b = 0.7$ for the PEP-II parameters at 3A current.

As mentioned above, the motion of an electron may be quite complicated, an electron can be kicked several times by bunches before it reaches a wall. At the high N_b corresponding to the 3 A current for PEP-II, an electron experiences on average three kicks before it reaches the wall. At lower currents, the situation is even more complex: the number of kicks increases, seeFig. 3, an electron can come back to the wall where it started, and, in general, motion becomes quite stochastic, see Fig. 4. Neglecting the effect of the space charge, it is easy to show that electrons at large distances from the beam are indeed unstable. The coordinate and impulse of an electron are changed from bunch-to-bunch as

$$x \to \hat{x} = x + \frac{s_b}{mc}\hat{p}_x; \quad p_x \to \hat{p}_x = p_x - \frac{2N_b e^2 x}{c(x^2+\sigma_t^2)}. \tag{25}$$

Here, σ_t is the transverse rms bunch size. The electron is stable if the trace $|SpM| < 2$ where M is the matrix transforming Δx, Δp_x to $\hat{\Delta} x$, $\hat{\Delta} p_x$. Calculations give

$$\frac{1}{2}SpM = 1 + \frac{N_b r_e s_b}{2}\frac{x^2-\sigma_t^2}{(x^2+\sigma_t^2)^2}, \tag{26}$$

which is larger than one for $|x| > |\sigma_t|$. Hence, the motion is random, and electron

trajectories tend to cover all phase space at large distances.

It seems that if multipactoring occurs, fast electrons may multiply to large densities and become dangerous for beam stability. The process stops, however, due to the finite energy spread E_0 of the secondary electrons. This results from both the initial distribution in energy of the secondary electrons (see Figs. 1, 2), and from the difference in the kick gained from a bunch with a finite bunch length σ_l.

As a result of the initial spread in velocity Δv, the primary group of electrons is extended by $\Delta x = \Delta v s_b/c$ at the time when the interaction with the next bunch occurs. Interaction with the bunch transforms Δx into additional spread in velocities and, as result, in the difference in time Δt when electrons hit the wall. The effective yield of secondary electrons is $\eta_{\rm eff} = \eta \Delta t/(\sigma/c)$. Estimate gives

$$\frac{\eta_{eff}}{\eta} = \frac{N_b r_0 \sigma_l}{2 b s_b} \sqrt{\frac{2mc^2}{E_0}}. \tag{27}$$

For PEP-II parameters, the ratio is of the order of 10^{-2} at 3 A current, and even smaller for smaller N_b. This result agrees with what can be expected from a stochastic behavior of electron trajectories at low currents. Hence, the resonance multipactoring does not lead to a large electron density. Effect of the secondary electrons is considered below. The space-charge effect changes the dynamics of the background electrons and has to be taken into account in the estimate of the equilibrium density.

Fig. 5 shows the variation of the electron density with time for the 1-D problem. The result was obtained by tracking photoelectrons taking into account the space-charge effect, interaction with the beam, and the secondary electron emission at the walls.

The equilibrium density of the background electrons

Let us estimate the steady-state density of the background electrons. The density depends in the self-consistent way on the average space charge of electrons and on the yield of the secondary electrons from the walls.

The problem is quite complicate and consideration is restricted to the 1-D problem for particles within the range $0 < x < 2b$, $|y| < h_g/2$ with the density $n(x, v, t)$ being independent on the longitudinal and vertical y coordinates.

The dimensionless variables are used

$$z = \frac{x}{2b}, \quad u = \frac{s_b v}{2bc}, \quad \tau = \frac{ct}{s_b}. \tag{28}$$

The equations of motion in this units are

$$\frac{dz}{d\tau} = u, \quad \frac{du}{d\tau} = F_t(z, \tau), \quad 0 < z < 1, \tag{29}$$

where the total force F_t includes periodic kicks from the beam with the period $\tau = 1$ and the space-charge force $F(z)$, given by the Poisson equation

$$F_t = \beta F(z, \tau) - \frac{\alpha}{2z - 1}\delta_1(\tau), \quad \alpha = \frac{N_b r_0 s_b}{b^2}, \quad \beta = 4\pi r_0 s_b^2 \tag{30}$$

$$F_t = -\frac{\partial U(z)}{\partial z}, \quad \frac{\partial F(z)}{\partial z} = n(z), \tag{31}$$

$$F(z) = \int_0^z z' dz' n(z') - \int_z^1 dz'(1 - z')n(z'). \tag{32}$$

Here $n(z, \tau) = \int dun(u, z, \tau)$ is the density with the usual dimension cm^{-3} defined in such a way that $n(x, t) = n(z, \tau)$ for corresponding z and x. The total number of particles is $n_{\mathrm{tot}} = \int n(x)dx = 2b \int n(z)dz$. We use the Vlasov equation:

$$\frac{\partial n(z, u, \tau)}{\partial \tau} + u\frac{\partial n(z, u, \tau)}{\partial z} + F_t\frac{\partial n(z, u, \tau)}{\partial u} =$$

$$[Q_0\delta(\tau) + \eta_0 J_+^\eta]\Phi(-u)\delta(1-z) - un(u, 1)\delta(1-z)\Theta(u) + [\eta_0 J_-^\eta \Phi(u) + un(u, 0)\Theta(-u)]\delta(z). \tag{33}$$

where we neglected collisions between the electons, but included the interaction of electrons with the beam and the average effect of the space charge. The source terms

in the RHS include the term proportional to the flux dN_e/ds of photoelectrons per unit length of the beam pipe per bunch:

$$Q_0 = \frac{1}{2bh_g}(\frac{dN_e}{ds}). \tag{34}$$

Other terms describe particles loss at the wall and the secondary emission of the electrons. For Al, the maximum yield $\eta_0 = 2.6$ corresponds to the energy 400 eV of the incident electron, rolling off to $\eta = 1$ at $E_{\min} = 50$ eV and $E_{\max} = 2.6$ keV. Eq. (33) uses notation

$$J_+^\eta = \int_{u_{\min}}^{u_{\max}} udun(u,z); \quad J_-^\eta = -\int_{-u_{\max}}^{-u_{\min}} udun(u,z) \tag{35}$$

for the number of incident electrons able to produce the secondary electrons, where

$$u_{\min} = (\frac{s_b}{b})\sqrt{\frac{E_{\min}}{2mc^2}}. \tag{36}$$

The distribution of the secondary electrons is described here by the function $\Phi(u)$, which is non zero only for $u > 0$, and normalized to one, $\int_0^\infty du\Phi(u) = 1$. The distribution may be characterized by momentums

$$u_0 = \int_0^\infty udu\Phi(u), \quad \hat{u}_0^2 = \int_0^\infty u^2 du\Phi(u). \tag{37}$$

$\Phi(u)$ has a sharp maximum at the energy of few eV. We will neglect another peak with the energy close to the energy of the incident electron with a small yield.

The equilibrium density can be obtained by deriving a set of equations for the momentums of $n(u,z,\tau)$. Let us define momentums

$$J^+(z) = \int_0^\infty udun(u,z), \quad J^-(z) = -\int_{-\infty}^0 udun(u,z),$$

$$n(z)T^{+}(z) = \int_0^{\infty} u^2 dun(u,z), \quad n(z)T^{-}(z) = \int_{-\infty}^{0} u^2 dun(u,z). \tag{38}$$

Both $J^{\pm} > 0$ and the total current $J(z) = n(z)v(z)$ is $J(z) = J^{+} - J^{-}$. Similarly, $T(z) = T^{+}(z) + T^{-}(z)$. To close the system of equations, we assume that the third momentums can be approximated as

$$\int_0^{\infty} u^3 dun(u,z) \simeq J^{+}(z)T^{+}(z), \quad \int_{-\infty}^{0} u^3 dun(u,z) = -J^{-}(z)T^{-}(z). \tag{39}$$

Integrating Eq. (2-5) over du, udu, and u^2du gives the system of equations

$$\frac{\partial n(z,\tau)}{\partial \tau} + \frac{\partial J(z,\tau)}{\partial z} = 0, \tag{40}$$

$$\frac{\partial J}{\partial \tau} + \frac{\partial n(z,\tau)T}{\partial z} - F_t n = 0, \tag{41}$$

$$\frac{\partial n(z,\tau)T}{\partial \tau} + \frac{\partial J(z,\tau)T}{\partial z} - 2F_t J = 0, \tag{42}$$

and the boundary conditions:

$$J^{-}(1) = [Q_0\delta(\tau) + \eta_0 J_{+}^{\eta}], \quad J^{+}(0) = \eta_0 J_{-}^{\eta}. \tag{43}$$

$$T^{-}(1)n(1) = u_0[Q_0\delta(\tau) + \eta_0 J_{+}^{\eta}], \quad T^{+}(0)n(0) = u_0\eta_0 J_{-}^{\eta}, \tag{44}$$

$$T(1)J(1) = -\hat{u}_0^2[Q_0\delta(\tau) + \eta_0 J_{+}^{\eta}] + T^{+}(1)J^{+}(1),$$

$$T(0)J(0) = \hat{u}_0^2\eta_0 J_{-}^{\eta} - J^{-}(0)T^{-}(0). \tag{45}$$

Averaging in time over the period $\tau = 1$ changes this equation only by replacing $\delta(\tau) \to 1$ and taking away terms with derivatives over τ.

After averaging, Eq. (40) gives $J(z) = J_0 = \text{const}$. Eq. (42) then gives the energy conservation

$$\frac{T(z)}{2} + U(z) = \text{const} = \frac{T(0)}{2} = \frac{T(1)}{2} \tag{46}$$

where $U(z)$ is defined by Eq. (34) with the conditions $U(0) = U(1) = 0$. Eqs. (41), (42) give together

$$n^2 T = \text{const} = A^2 = n(0)^2 T(0) = n(1)^2 T(1) \tag{47},$$

and the remaining equation defines the density

$$\frac{\partial}{\partial z}\frac{A^2}{n} = F_t(z) n(z). \tag{48}$$

It follows from Eqs. (46), (47) that $T(0) = T(1)$, $n(0) = n(1)$.

Define $J^{\pm}$ and $T^{\pm}$ from Eqs. (45). This gives

$$T(0) = \hat{u}_0^2 + \frac{u_0}{n(0)}[\eta_0 J_-^\eta - J_0], \quad T(1) = \hat{u}_0^2 + \frac{u_0}{n(1)}[Q_0 + \eta_0 J_+^\eta + J_0]. \tag{49}$$

Condition $T(0) = T(1)$ defines J_0:

$$2J_0 = -[Q_0 + \eta_0(J_+^\eta + J_-^\eta)]. \tag{50}$$

Hence,

$$T(1) = \hat{u}_0^2 + \frac{u_0}{2n(1)}[Q_0 + \eta_0(J_+^\eta + J_-^\eta)]. \tag{51}$$

By definitions,

$$T(1) = \frac{1}{n(1)} \int u^2 du n(1, u) = (\overline{u})^2 + \overline{(u - \overline{u})^2}. \tag{52}$$

Identify $\overline{(u - \overline{u})^2} = \hat{u}_0^2$, $\overline{u} = u_0$, then, the boundary conditions are

$$n(0) = n(1), \qquad 2n(1)u_0 = Q_0 + \eta_0(J_+^\eta + J_-^\eta). \tag{53}$$

We now need to define the current J^η of high energy particles going toward the wall. This cannot be done from the steady-state equations: particles in the steady

state move in an effective potential, and they return to the wall with exactly the same energy they leave the wall. To define J^η, we go to the basic equation of motion (31). A kick from a bunch has to increase the energy of a particle to the the range from $E_{\min}$ to $E_{\max}$. This means that a particle has to be at the distances from a bunch in the range

$$u_{\min} < \frac{\alpha}{(2z-1)} < u_{\max} \tag{54}$$

where $u_{\min}$, $u_{\max}$ are defined by Eq. (36). If $u_{\min}$ is large compared to the velocity u of a particle before kick, then

$$J^\eta = \int dz' n(z', \tau) \tag{55}$$

where the integral is taken over the range Eq. (54). The minimum distance from the beam here is $\Delta z = \alpha/(2u_{\max})$ and has to be replaced by the dimensionless transverse rms bunch size $\sigma_x/2b$ if $\Delta z < \sigma_x/2b$.

The minimum distance from the beam here is $\Delta z = \alpha/(2u_{\max})$ and has to be replaced by the dimensionless transverse rms bunch size $\sigma_x/2b$ if $\Delta z < \sigma_x/2b$.

Taking another derivative over z in Eq. (48), we get

$$\frac{\partial}{\partial z}\frac{1}{n}\frac{\partial}{\partial z}\frac{1}{n} = \frac{\beta}{A^2}n + \frac{2\alpha}{A^2}\frac{1}{(2z-1)^2}\,. \tag{56}$$

The first term in the RHS describes the space-charge effect. It is small compared to the second term describing the average field of the bunch for the densities $n < 2\alpha/\beta$, or $n < 5. \times 10^6$ cm^{-3} for PEP-II at 3 A current.

Neglecting the space-charge term, we get the solution

$$n(z) = \frac{Q_0}{u_0}[1 + \frac{\alpha}{2u_0^2}\ln|\frac{1}{2z-1}|]^{-1/2} \tag{57}$$

where, for simplicity we put $\hat{u}_0^2 = u_0^2$.

The density Eq. (57) is of the order of $n \simeq Q_0/2u_0$, or $n = 4.0 \times 10^5$ for PEP-II at 3 A current. That is larger than $n_{\max}$ of the initial density of a strip, but decreases logarithmically at the beam position $z = 1/2$ due to the interaction with the beam.

At very large densities, the RHS of Eq. (56) is dominated by the space-charge term. Neglecting the second term, we get the solution similar to the problem of the space-charge dominated current from a cathode:

$$n(z) = (\frac{2}{9\beta})^{1/3} |\frac{A}{z - 1/2}|^{2/3}. \tag{58}$$

This solution should be matched with the solution Eq. (57), which is always correct in the close vicinity to the bunch.

Result of the numeric integration of Eq. (56) are shown in Fig. 6. The equilibrium density is maximum at the wall and is much larger than the density of the photo-electrons, $n \simeq 5. \times 10^7$ cm^{-3}.

The equation was solved numerically for the variable $y(z) = n(1)/n(0)$. The solution depends on two parameters α, u_0, for different values of the parameter $\hat{\beta} = \beta n(1)$. After the solution of the equation with the boundary conditions $y(0) = y(1) = 1$ was found by the shooting method, the integrals $\hat{J}^\eta = J^\eta/n(1)$ can be defined. Then, the boundary condition Eq. (53) defines the solution $n(z) = \hat{\beta}/[\beta y(z)]$, which corresponds to

$$\eta_0(\hat{\beta}) = \frac{u_0}{\hat{J}^\eta}[1 - \frac{\beta Q_0}{2u_0\hat{\beta}}]. \tag{59}$$

The quasi-equlibrium solution for given Q_0 exists only for certain range of $\eta_0 > 0$ as it can be seen from Eq. (59). Outside the range, the solution is unstable what corresponds to the avalanch of the secondary electrons.

The self-consistent regime is described here approximately using averaging in time. If η_0 is two small, the bunch-to-bunch modulation of the density become large and all electrons can go to the wall within before another bunch arrives. The minimal η_0 can be obtained from the first relation Eq. (55) estimating the current to the wall J^+ as $J^+ = \int_{z_{\max}}^1 dz n(z)$.

Effect of Ions

The inelastic collisions in the residual gas with pressure p have a typical cross-section $\sigma_c \simeq 2$ Mbarn and, at normal temperature, generate electrons with the rate $dN_e/ds = 0.06\,(p/\text{torr})\ \text{cm}^{-1}$ per positron. The photoeffect on the residual gas gives rate comparable with the rate of inelastic collisions. For a pressure $p = 5$ ntor (the density of the residual gas at normal temperature $n_g = 1.5 \times 10^8\ \text{cm}^{-3}$) this rate is 2×10^4 smaller than the rate of photoelectron production.

Let us consider therefore the rate of ionization of the residual gas by the photo- and background electrons. The potential problem here is the induced de-gasing from the wall, which may produce pressure instability.

The photoelectrons hitting the walls do not cause the problem. They are produced with the rate

$$\frac{d^2N_e}{dsdt} = (\frac{dN_e}{ds})\frac{I_b}{eN_b} \tag{60}$$

where I_b is the average beam current. This rate is very high,of the order of 10^{14} $\text{cm}^{-1}\text{sec}^{-1}$, and the electrons can produce neutrals hitting the walls. However, the yield of neutrals per electron is smaller than that for ions. More than that, this effect is independent of pressure and, hence, does not lead to the run-away increase of the pressure of the residual gas, although more pumping may be required. Similarly, in the case of the formation of the equilibrium plasma, the flux of ions to the wall is equal to the flux of the photoelectrons in the beam pipe. This flux is large, but again does not depend on the residual gas density n_g.

Photoelectrons can also ionize residual atoms, which, hitting the wall, produce more neutrals. This process increases effective yield of the neutrals produced by ions at the walls and reduces the threshold of the pressure build-up. The cross section of the ionization of the residual gas is of the order of $\sigma_i \simeq 10^{-16}\ \text{cm}^2$ at low energy. The rate of ion production per electron moving from wall-to-wall is then

$$\frac{d^2N_{ie}}{dsdt} = 2bn_g\sigma_i(\frac{dN_e}{ds})\frac{I_b}{eN_b}. \tag{61}$$

Comparing this yield with the rate of ions produced in the inelastic collisions of the

beam with the residual gas

$$\frac{d^2N_i}{dsdt} = n_g\sigma_c\frac{I_b}{e}, \tag{62}$$

we see that the rate in Eq. (61) is small, only few percent of the rate in Eq. (62), even with the relatively low σ_c.

The rate of ions produced by the background electrons with density n_e may be higher. An electron produces an ion within the ionisation length $l = (n_g\sigma_i)^{-1}$, and if the average velocity of the electrons is v, they produce

$$\frac{d^2N_i}{dsdt} = n_g n_e \sigma_i 4abv \tag{63}$$

ions per unit length of the beam pipe with the dimensions $a \times b$. This rate is $d^2N_i/dsdt = 2.0 \times 10^7$ cm^{-1}sec^{-1} for $n_e = 10^5$ cm^{-3}, $v/c = 10^{-2}$, and $b = 2a = 5$ cm. This has to be compared with the rate from Eq. (63) $d^2N_i/dsdt = 6.0 \times 10^9$ cm^{-1}sec^{-1}.

Thus, the rate of the ion production by the electrons is small compared to the rate of ion production by the beam.

Finally, ions may, in their turn, affect the density of the background electrons. The ionization of the residual gas may produce more than enough ions to make a neutral plasma, which would change the space charge effect and the dynamics of the background electrons. The Debye length at the plasma density $n = 10^7$ cm^{-3} and the temperature of the order of $E_{\min} = 50$ eV is of the order of 1.6 cm. Plasma with these parameters may affect the condition of the equilibrium. However, the ionization rate is relatively low: the cross section $\sigma \simeq 10^{-16}$ cm^2 corresponds at this density to ionization length $3. \times 10^7$ cm or to the ionization time 20 msec at the electron velocity $v/c = 5 \times 10^{-3}$. This time is much larger than the revolution period 7 μsec, but the ion density can increase up to 10^4 cm^{-3}. The 100 m gap in the bunch train will clear electrons, and their space charge drags ions to the wall. However, the gap in the PEP-II positron ring is partially filled, and ions can survive and be accumulated to make the low-density neutral plasma.

The plasma oscillations at such density have the wavelength $2\pi/\sqrt{4\pi r_0 n}$ of the order of 100 m, too large to affect the beam.

Conclusion

The production rate and dynamics of the photoelectrons are studied for the PEP-II parameters. The growth rate of the transverse instability driven by the primary photoelectrons is of the order of 0.7 msec for the PEP-II parameters. This is comparable with the rate of instability driven by ions in the HER: the large flux of the primary photoelectrons is compensated by the low density and small number of interacting bunches.

The multipactoring at resonance currents cannot produce large electron density due to the final energy spread caused by the finite bunch length and the intrinsic energy spread of the secondary electrons.

Production of the secondary electrons may lead to large average densities. This effect is studied in the 1-D model, taking into account the space-charge effect, interaction with the beam, and production of the photoelectrons.

The ions can be produced in electron collisions with the residual gas with density of the order of the electron density. They may not be cleared out by a partially filled gap. While going to the wall, the ions can increase the rate of production of neutral atoms and increase pressure of the residual gas.

Acknowledgment

I am very thankful to W. Stoeffl, J. Seemann, G. Lambertson, M. Zisman, A. Chao, and M. Zolotorev for useful discussions.

Figure Captions.

1. The yield of the secondary electrons: dependence on the energy of the incident electron (below, from R. Kollath, Phys. Z. 38, p. 202, 1937), and the energy spectrum of the secondary electrons (above, from J. R. Brinsmade, Phys. Rev. 30, p.494, 1927).

2. Dependence of the yield of the secondary electrons on initial energy for different materials, LBL Engineering Manual.

3. Dependence of number of kicks an electron receives travelling from wall to wall on current.

4. Examples of the trajectories in the phase plane for three different location around the ring (i.e. for different transverse rms σ_t) at $I = 0.015$ A.

5. Dependence of the average density on time in the 1-D model including both effects of the photoelectrons and of the secondary emission. $dN_e/ds = 6.8 \times 10^5$, $\eta_0 = 2.6$. Time in units s_b/c.

6. Density profile for the same case as in Fig. 5.

REFERENCES

1. K. Ohmi, Beam and Photoelectron Interactions in Positron Storage Rings, KEK Preprint 94-198, February 1995

2. A. Chao, B. Richter, and Y. Yao, Beam Emittance Growth Caused by Transverse Deflecting Fields in a Linear Accelerator, Nucl. Instr. and Methods 178, 1980, 1-8

3. T. O. Raubenheimer and F. Zimmermann, Interaction of a Charged Particle Beam with Residual Gas Ions or Electrons, unpublished, SLAC, 1994.

4. PEP-II, An Asymmetric B factory, SLAC- 418, June 1993.

Fig 1

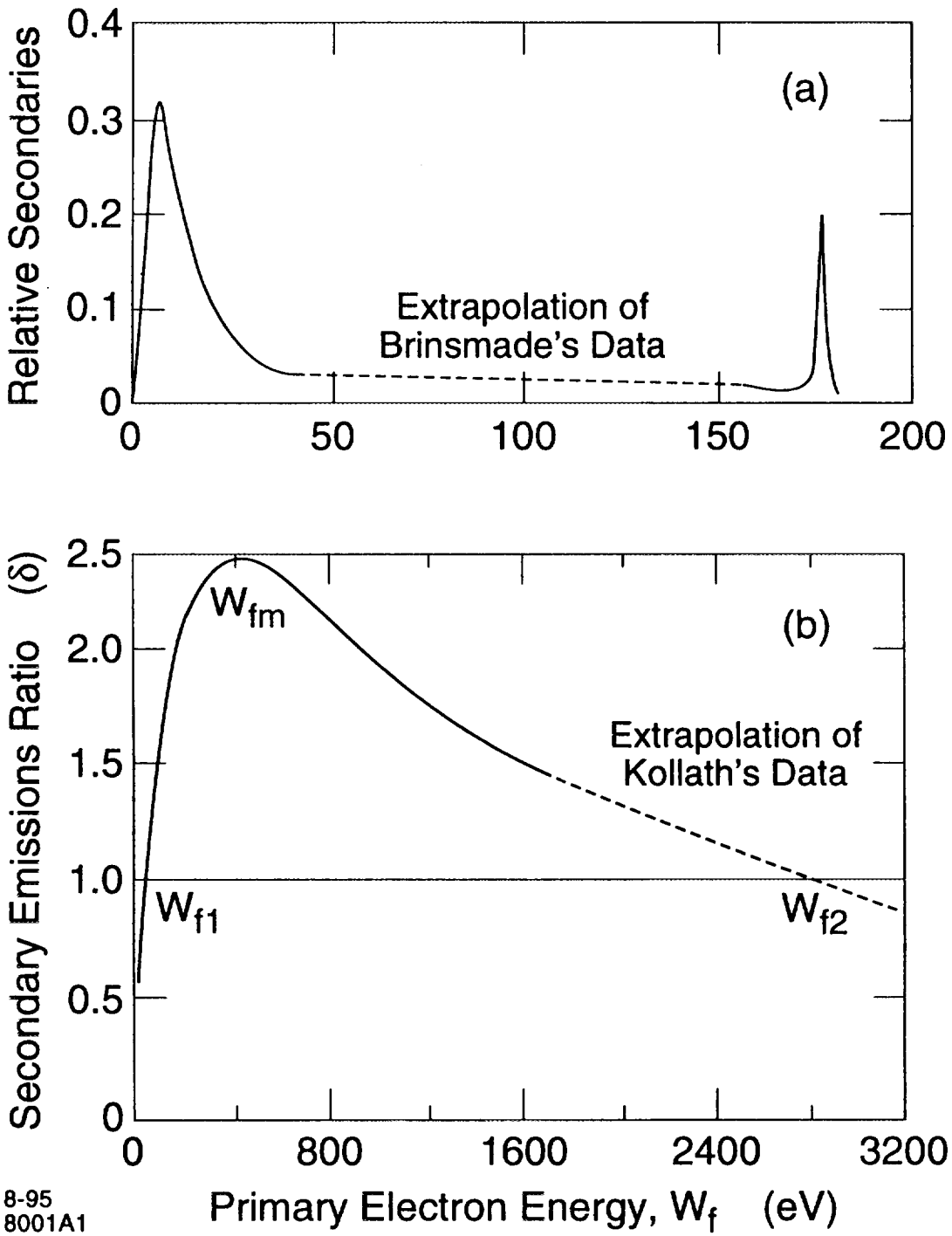
Relative Secondaries
0.4
0.3
0.2
0.1
0
(a)
Extrapolation of
Brinsmade's Data
0
50
100
150
200
Secondary Emissions Ratio (δ)
2.5
2.0
1.5
1.0
0.5
0
W_{fm}
(b)
Extrapolation of
Kollath's Data
W_{f1}
W_{f2}
0
800
1600
2400
3200
8-95
8001A1
Primary Electron Energy, W_f (eV)

Fig 2.

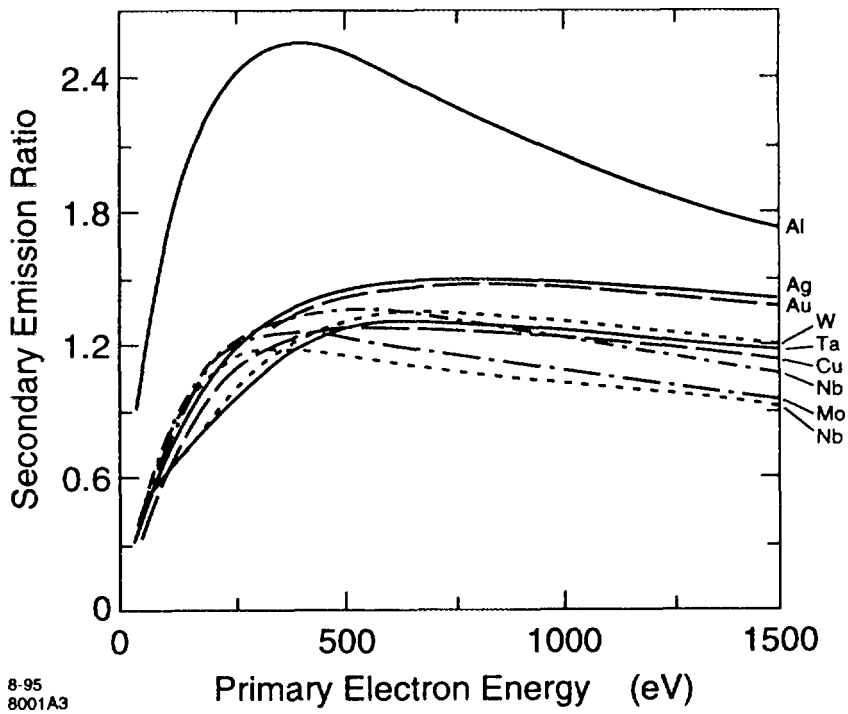
Secondary Emission Ratio
2.4
1.8
1.2
0.6
0
0
500
1000
1500
Primary Electron Energy (eV)
Al
Ag
Au
W
Ta
Cu
Nb
Mo
Nb
8-95
8001A3

Fig. 3

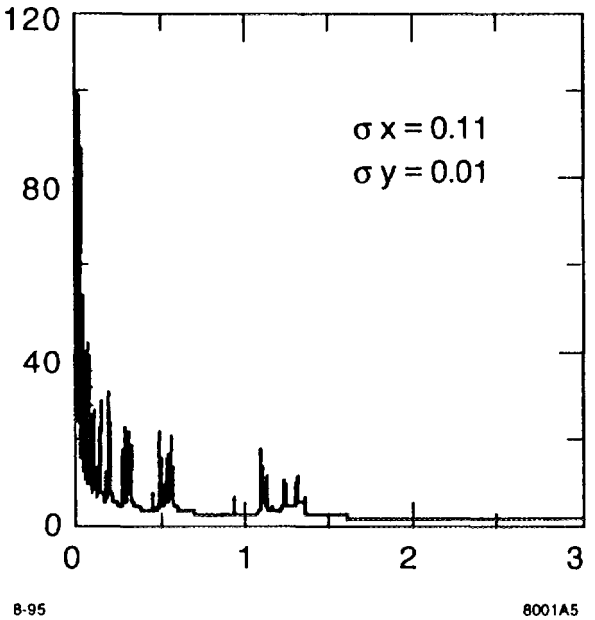

Fig.4

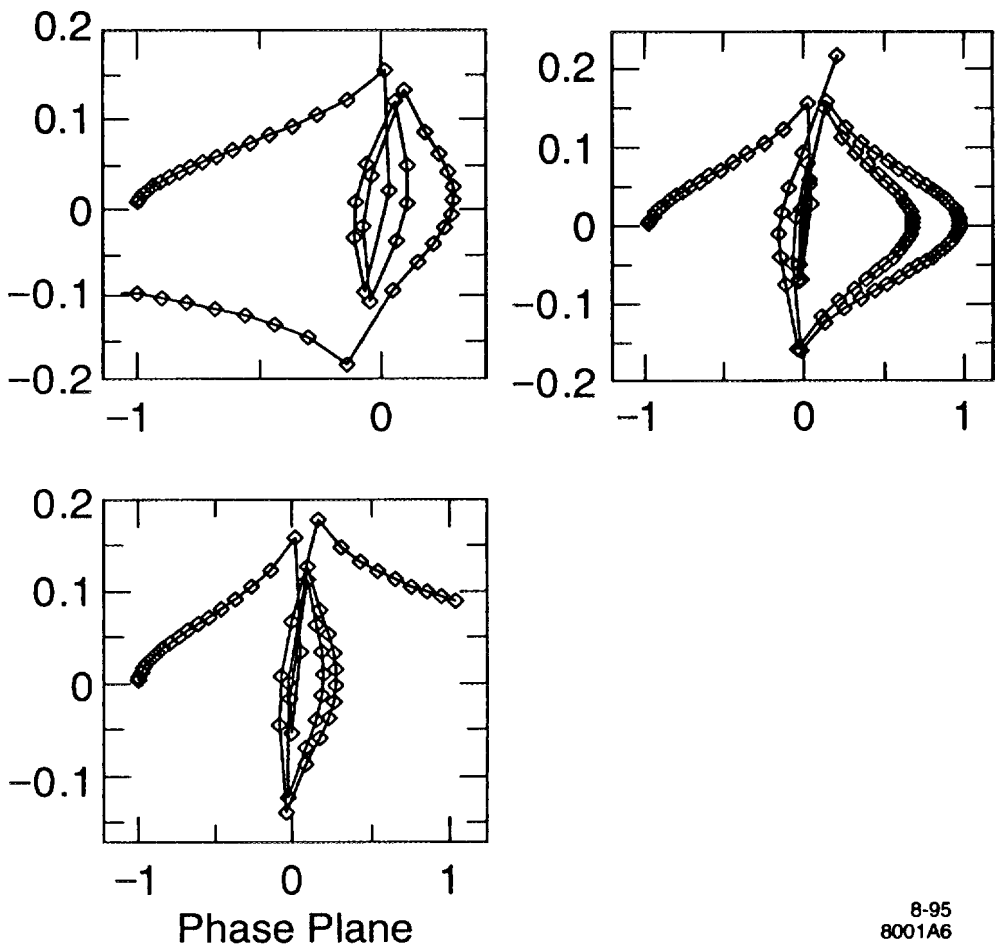

8-95
8001A6

Fig. 5

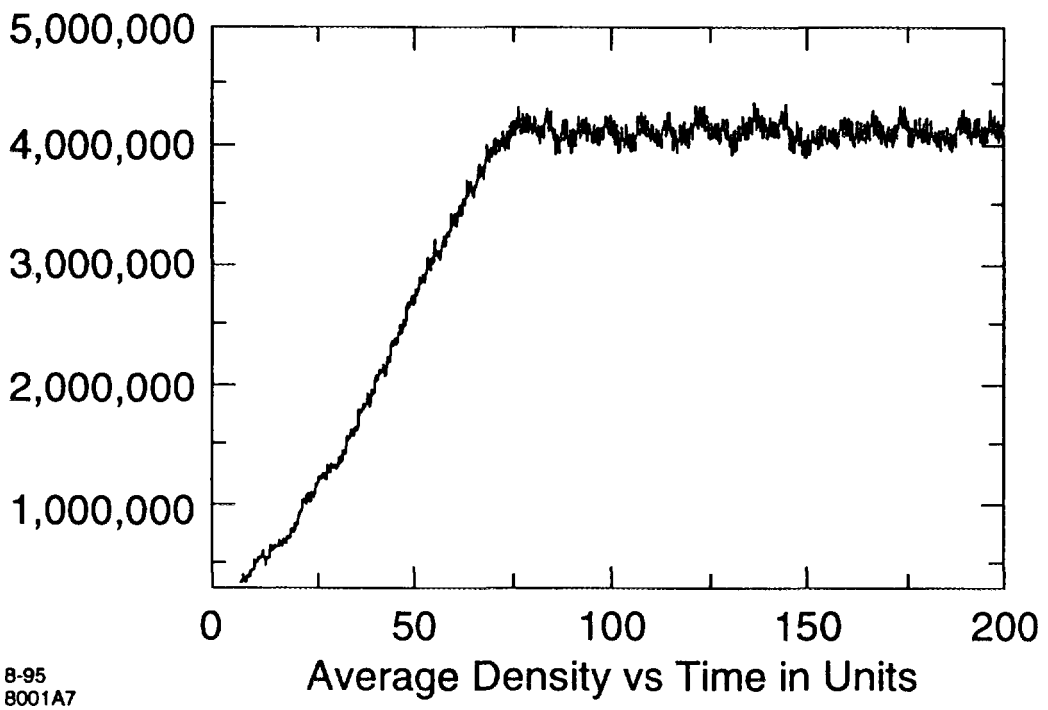

8-95
8001A7

Fig. 6

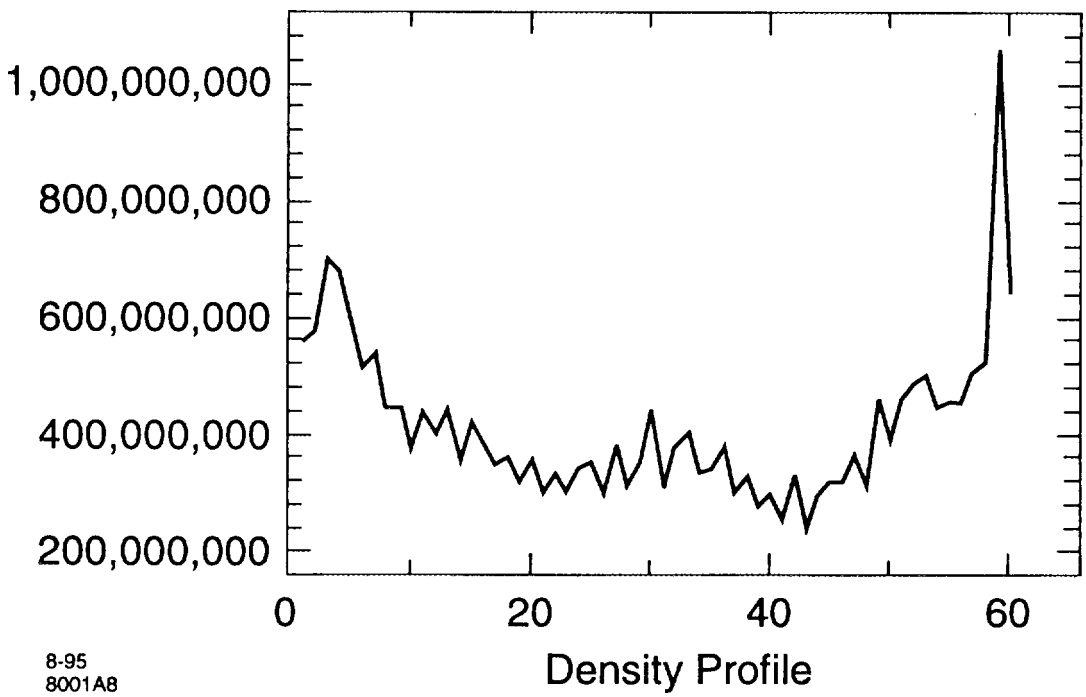
1,000,000,000
800,000,000
600,000,000
400,000,000
200,000,000
0
20
40
60
Density Profile
8-95
8001A8

Distributed Ion Pump Related Transverse Instability in CESR[1]

J.T. Rogers and T. Holmquist[2]
Laboratory of Nuclear Studies, Cornell University, Ithaca, NY 14853 USA

An anomalous damping or growth of transverse coupled bunch modes is observed in the Cornell Electron Storage Ring (CESR). The growth rates and tune shifts of these modes are a highly nonlinear function of current. Unlike an instability produced by the coupling impedance of the vacuum chamber, the magnitude of the growth rate first increases, then declines, as the beam current is increased. The effect is known to be related to the operation of the distributed ion pumps, as it disappears when the pumps are not powered. We review the observations of this effect, and show that it can be explained by the presence of electrons trapped in the CESR chamber by the field of the dipole magnets and the electrostatic leakage field of the distributed ion pumps. Photoelectrons are introduced into the chamber by synchrotron radiation and can be captured in or ejected from the chamber by the passage of the beam. The transverse position of the beam thus modulates the trapped photoelectron charge density, which in turn deflects the beam, creating growth or damping and a tune shift for each coupled bunch mode. Predictions of the dependence of growth rate and tune shift on bunch current and bunch pattern by a numerical model of this process are in approximate agreement with observations.

1 Distributed ion pumps

CESR contains both lumped ion pumps and distributed ion pumps (DIPs). Within the length of each bending magnet, the CESR vacuum chamber contains two DIPs, shown in cross section in Fig. 1. The pump anodes are operated at 7.4 kV.

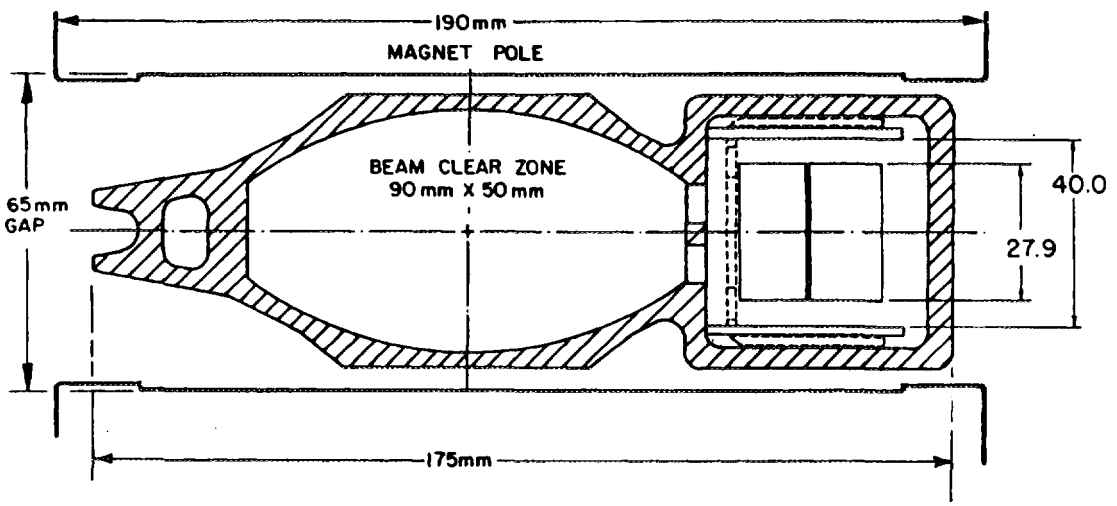

Figure 1: Cross-section of the CESR vacuum chamber inside the bending magnets. The distributed ion pump is in the chamber on the right. A small number of DIPs (those within the hard bend magnets) have copper shields (dotted outline).

A series of slots, shown in Fig. 2, allows gas to flow from the beam chamber to the pump chamber. These slots also allow electromagnetic fields to penetrate from one part of the chamber to the other. The coupling of the bunch current to the DIP anode has been simulated on the bench by sending a nearly Gaussian pulse

[1]This work has been supported by the National Science Foundation.
[2]Reporting for the CESR Operations Group.

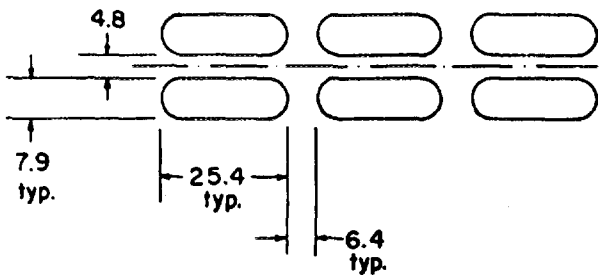

Figure 2: The pattern of pumping slots between the beam chamber and pump chamber.

down a thin conductor placed along the beam chamber axis. The measured coupling amplitude for a current pulse with $\sigma_L = 2.7$ cm is 2×10^{-4} [1]. The slots also allow the DC electric field produced by the DIP anode to leak into the beam chamber. A numerical computation of the leakage field [2] shows that at the center of the beam chamber the dipole and quadrupole components of the electric field are 320 V/m and -2.1×10^4 V/m^2, respectively. Significant higher-order multipole fields are also present. The direct influence of the dipole and quadrupole leakage fields on the orbit and tune of the beam have been observed [2]. Distributed ion pumps in the CESR hard bend magnets have additional copper shields with offset slots, shown as the dotted outline in Fig. 1, which are intended to prevent scattered synchrotron radiation from entering the DIP. These shield the beam chamber from the DIP field.

In the center of each bending magnet, between the two DIPs, there is a circular port in the partition between the beam chamber and the pump chamber which may also electromagnetically couple the two chambers. The effect of this port has not been investigated to date.

2 Anomalous instability

An anomalous transverse coupled bunch instability ("anomalous antidamping") is observed in CESR [3]. Unlike an instability caused by the coupling impedance of the vacuum chamber, the growth rates and tune shifts are strongly nonlinear functions of beam current. The absolute value of the growth rate is largest at the intermediate currents encountered during CESR injection, and becomes dramatically smaller at higher currents. Thus the anomalous instability is troublesome during positron injection from a state where the is no current in the machine. During colliding beam operation, the instability is suppressed, probably by Landau damping from the beam-beam force. The instability occurs for electrons as well as positrons, but is not as severe or reproducible for electrons as it is for positrons. The growth rates are very reproducible for positrons, over periods of years, and do not depend on the residual gas pressure. All of the data presented here have been taken with positrons in CESR.

The anomalous instability is much stronger in the horizontal plane than in the vertical plane. Coupled bunch modes at positive frequencies are damped; those at negative frequencies are antidamped (tend to grow). The absolute values of both the growth rate and tune shift are largest for the lowest frequency mode and decrease with mode frequency.

The current at which the absolute value of the growth rate reaches its maximum value has a mild dependence on the number of bunches, unless the bunches are closely spaced, as shown in Table 1. The instability "sees" two bunches which are spaced by 28 ns or less as a single bunch, and bunches spaced by 280 ns or more as separate. The growth rate is dramatically reduced when a gap is present in the bunch pattern.

Table 1: Bunch current at maximum $|\alpha|$

Number of trains	Bunches per train	Minimum bunch spacing	Bunch current at $\|\alpha\|_{max}$
1	1	2562 ns	7 ± 1 mA
3	1	854 ns	7 ± 1 mA
7	1	364 ns	5 ± 1 mA
9	1	280 ns	4 ± 0.5 mA
9	2	28 ns	2.2 ± 0.3 mA

The anomalous instability is present only when the distributed ion pumps are powered [4]. It disappears quickly when the DIPs are turned off, with a time constant consistent with the discharge of the power supply filter capacitors. There should be no rapid change in the residual gas pressure because of the continued gettering of the DIPs. The instability reappears immediately when the pumps are turned on. The growth rate is proportional to the number of DIPs (without copper shields) powered [4, 5]. The DIPs with shields have no detectable effect on the beam.

We have measured the growth rate of the $f_0 - f_h = 171$ kHz coupled bunch mode (which has the largest growth rate) as a function of bunch current and DIP anode voltage [5]. For this measurement, several CESR DIP power supply chassis were modified so that their output voltage could be varied continuously. We made measurements with eight and 35 DIPs under voltage control. The growth rate per DIP was found to be very nearly the same for eight and 35 pumps powered. At the full 7.4 kV anode voltage the growth rate per DIP was found to be the same for eight, 35, or all 141 unshielded pumps powered. Figure 3 shows the growth rate vs. bunch current for seven values of the anode voltage. We used the present CESR bunch pattern of 9 trains of 2 positron bunches with a bunch spacing of 28 ns. Figure 4 shows the growth rate per pump plotted as a function of anode voltage for eight values of the bunch current. Note that the growth rate is approximately linear with DIP anode voltage.

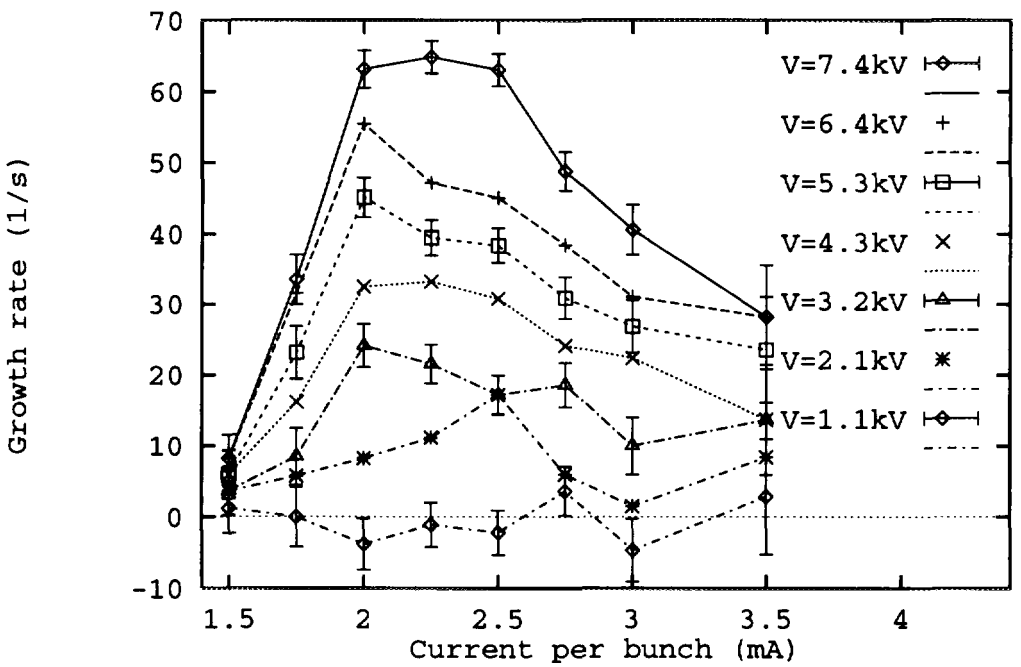

Figure 3: Growth rate of the $f_0 - f_h$ mode vs. positron bunch current for distributed ion pump anode voltages from +1.1 to +7.4 kV. Eight DIPs were powered. The background growth rate with these eight pumps turned off has been subtracted. Error bars on alternate sets of data points have been omitted for clarity.

3 Photoelectron trapping

We present the hypothesis that slow electrons trapped in the CESR beam chamber are responsible for the anomalous instability. These electrons are produced through photoemission by synchrotron radiation striking the beam chamber walls and are trapped in the combined dipole magnetic field and electrostatic leakage field from the distributed ion pumps, shown in Fig. 5. The passage of the beam can capture or eject some of these photoelectrons. In this way the transverse position of the beam modulates the trapped charge density, which in turn produces a time-dependent force on the beam.

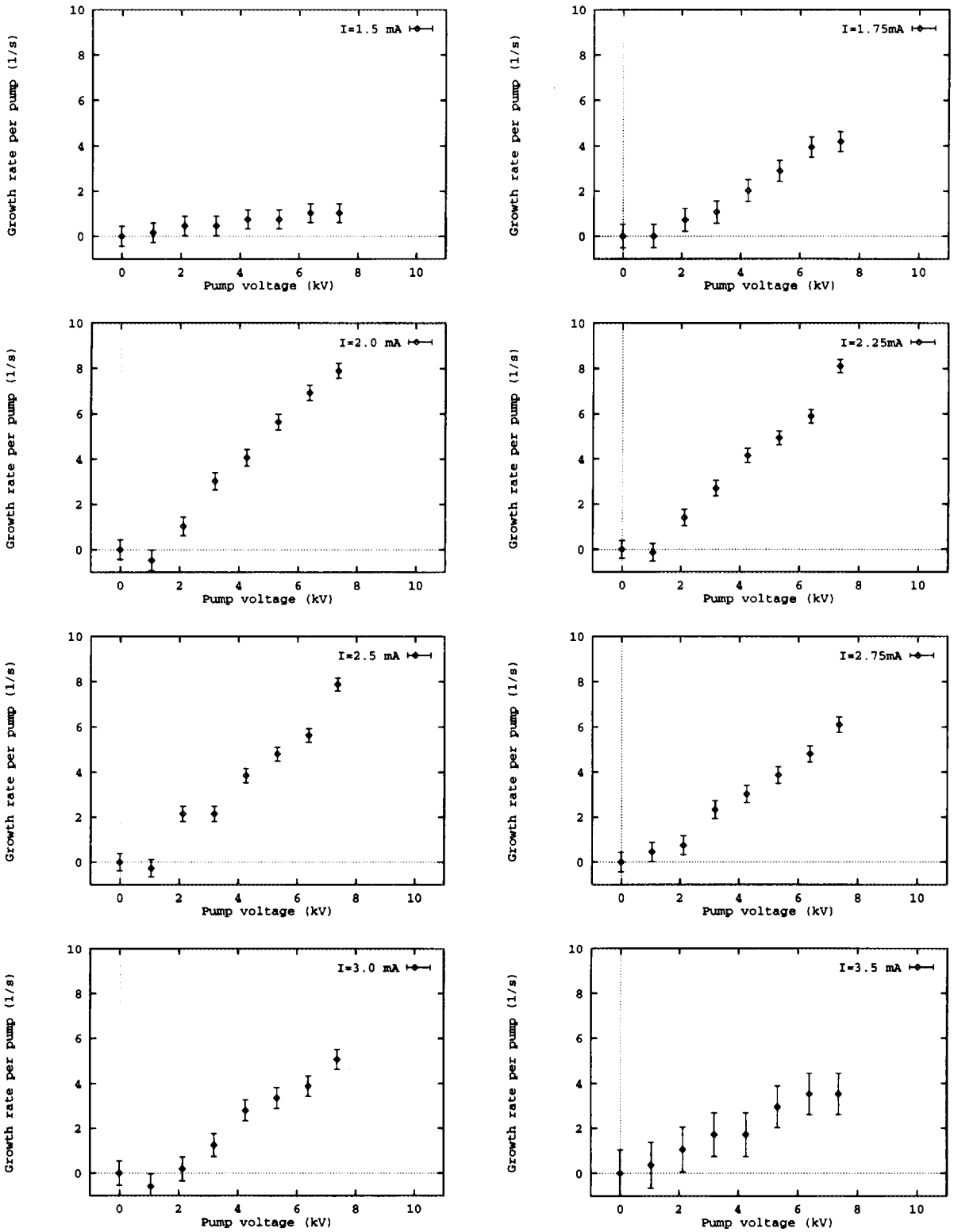

Figure 4: Growth rate per pump of the $f_0 - f_h$ mode vs. DIP anode voltage for positron currents from 1.5 to 3.5 mA per bunch. Eight DIPs were powered. The background growth rate with these eight pumps turned off has been subtracted. These are the data of Fig. 3, divided by the number of DIPs powered.

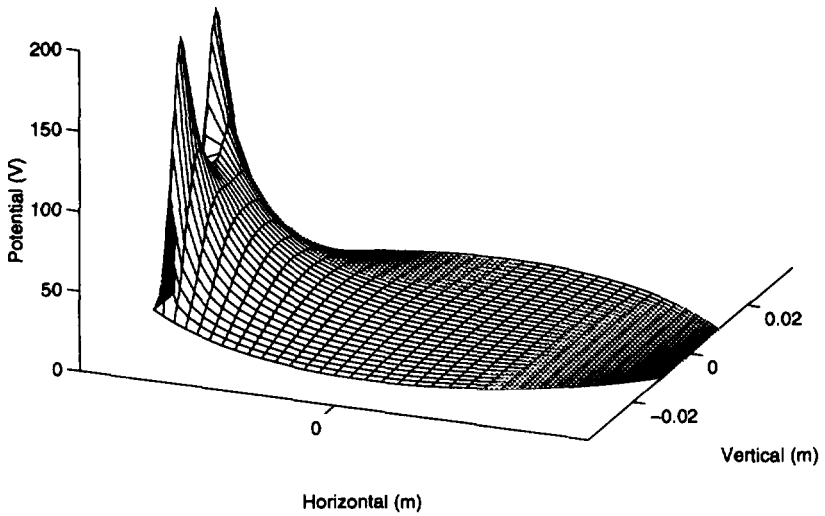

Figure 5: Potential inside the CESR vacuum chamber due to the DIP leakage field.

Slow photoelectrons in the CESR chamber will be confined to very small orbits in the horizontal plane by the 0.2 T magnetic field of the CESR dipoles. The quadrupole component of the leakage field from the DIP slots confines the electrons vertically. Positive ions are expelled by this field. The combination of the magnetic and electric fields acts as a Penning trap for electrons, much like the ion pump itself. Because of the horizontal dipole component of the pump leakage field, the trapped electrons undergo an $\mathbf{E}\times\mathbf{B}$ drift down the length of the magnet, with a velocity of the order of 1.6×10^3 m/s. Thus a trapped electron is lost from the 6.5 m long magnets in about 2 ms. Electrons are removed by interactions with the beam on a far shorter time scale, so their drift velocity may be neglected. The cyclotron frequency of the trapped electrons is 5.6 GHz, so their cyclotron motion is unimportant at the frequencies of the coupled bunch modes. The vertical motion, with frequencies of the order of 10 MHz or less, dominates the dynamics.

4 Simulation of photoelectron trapping

A numerical model of photoelectron trapping was produced to calculate the coupled bunch growth and tune shift. In this model, we calculate the trajectories of electron macroparticles moving under the influence of the electric field of the distributed ion pumps, a bunched positron beam, and the space charge of the other photoelectrons. Only vertical motion of the electrons is allowed because of the strong dipole magnetic field.

Electron macroparticle velocities and positions and the electric field in the chamber are updated each time step of 0.5 ns. If the trajectory of the macroparticle has taken it outside the chamber boundaries, it is removed. Secondary emission is modeled by injecting one or more macroparticles, depending on the secondary emission efficiency, which is a function of the incident macroparticle energy. During the beam passage, smaller time steps are used. In each of these small time steps, several photoelectron macroparticles are injected with a uniform distribution of velocities from zero to v_{max}, and all velocities, positions, and the electric field are updated.

The oval shape of the CESR beam chamber is represented by a non-cartesian computational grid. While the vertical coordinate is linear, the horizontal coordinate is curvilinear, thus matching the profile of the chamber. Simulation results presented in this article were accomplished with a 17x17 grid, with the exception of the DIP potential and electron charge density plots, where a 33x33 grid was used.

There is considerable uncertainty in the value of the photoemission rate for the aluminum vacuum chamber. We have used a value which nearly reproduces the measured current dependence of the instability growth rate. This value is consistent with an extrapolation of the photoemission rate measured at DCI [7] to CESR parameters. The simulation physical parameters are summarized in Table 2.

Table 2: Simulation physical constants

Q_x	Fractional horizontal tune	≈ 0.5
T_0	Revolution period	2.562 μs
$\overline{\beta}_x$	Average β in dipole magnets	19 m
p	Beam momentum	5.3 GeV/c
L_{slot}	Total pump slot length	408 m
R_{pe}	Photoemission rate	0.4 m^{-1}
v_{max}	Maximum photoelectron velocity	$8 \times 10^5 m/s$

5 Simulation results

5.1 Time dependence of trapped charge density

Figures 6, 7, and 8 show the magnitude of the trapped electron charge density for the present CESR bunch pattern of 9 trains of 2 bunches, with bunches in a train separated by 28 ns. In these figures, the pumping slots are to the left, and the beam is in the center of the chamber at the origin of the coordinate system. The simulation has been run long enough for the charge density to reach an equilibrium. Figure 6 shows the charge density immediately before the passage of the first bunch in a train. Figure 7 shows the charge density 10 ns after the passage of the bunch. The newly emitted photoelectrons are evident as bands at the top and bottom of the chamber. The space charge in this band is sufficient to drive the lagging electrons back into the chamber wall. The acceleration of the new photoelectrons by the DIP leakage field is significant on the left side of the chamber. At the extreme left, the photoelectrons have already crossed the chamber and have been lost.Figure 8 shows the charge density immediately before the passage of the second bunch in the train. Most of the new photoelectrons on the right side of the chamber will be driven to larger amplitudes by the positron bunch and be lost, while those on the left will be kicked to smaller amplitudes and be trapped.

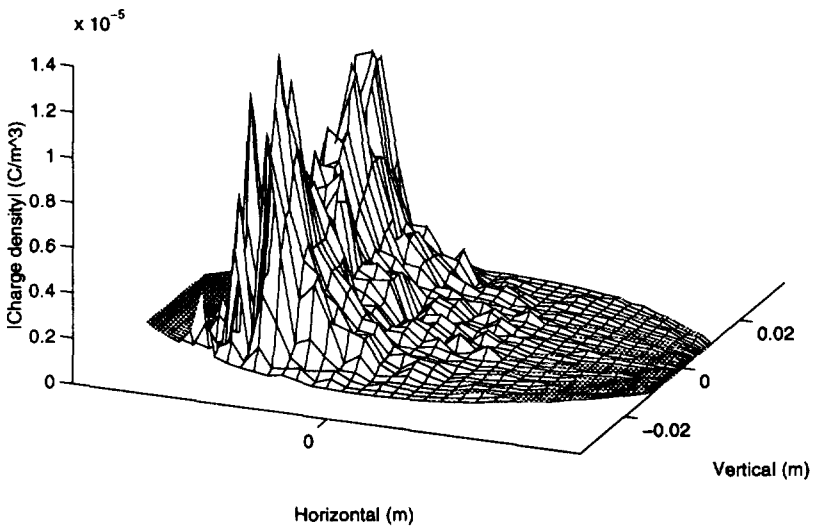

Figure 6: Magnitude of the trapped electron charge density just before the passage of the first positron bunch in a CESR bunch train.

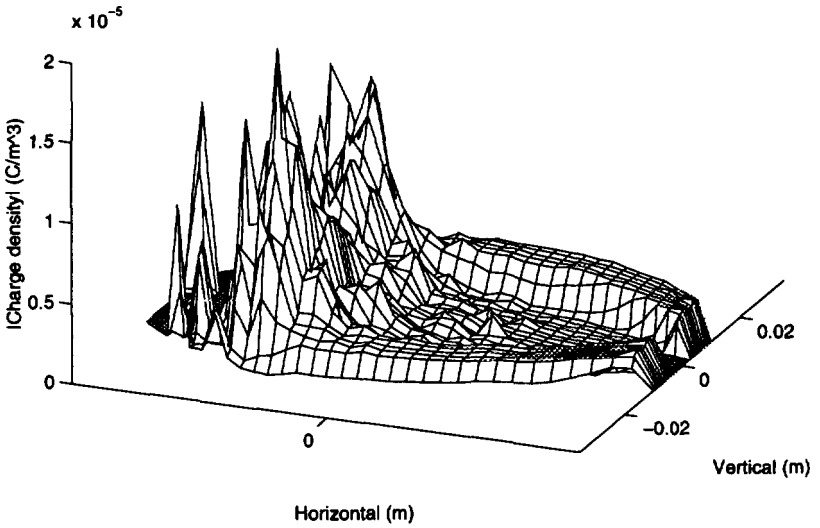

Figure 7: Charge density 10 ns after the passage of the first bunch in a train.

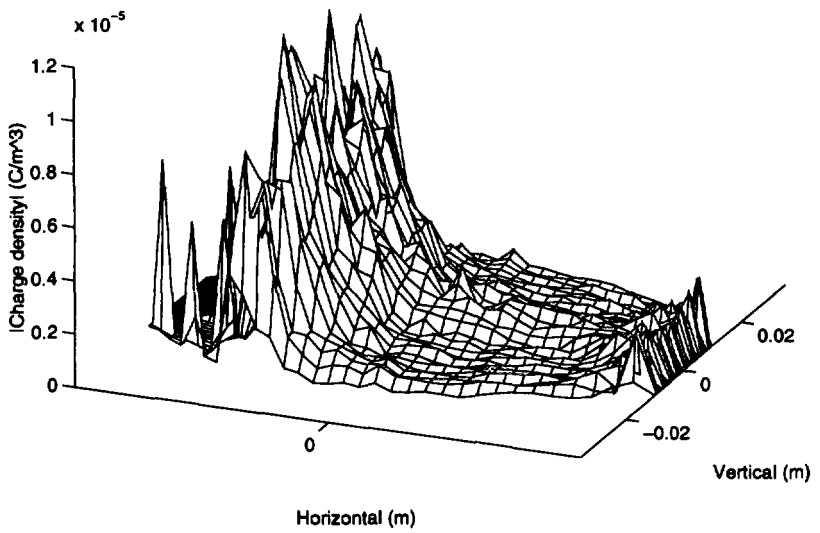

Figure 8: Charge density just before the passage of the second bunch in a train, 28 ns later than Fig. 6.

Trapping also occurs on time scales longer than the average transit time of the electrons across the chamber. The space charge of the newly emitted photoelectrons slows the electrons emitted later during the bunch passage, trapping them on low amplitude trajectories.

Although secondary emission is included in this calculation, it has been found to have a negligible effect on the trapped charge density.

5.2 Current dependence of growth rate and tune shift

In the simulation the beam was moved horizontally at the tune frequency with an amplitude of 5 mm. The force on the beam at that frequency was used to calculate the growth rate and tune shift of the lowest frequency coupled bunch mode. The growth rate and tune shift for the 9 train × 2 bunch pattern are shown in Fig. 9. The current dependence of the calculated growth rate is similar to that experimentally observed (Fig. 3), but the magnitude is 2.5 times smaller. The reason for this discrepancy is not known.

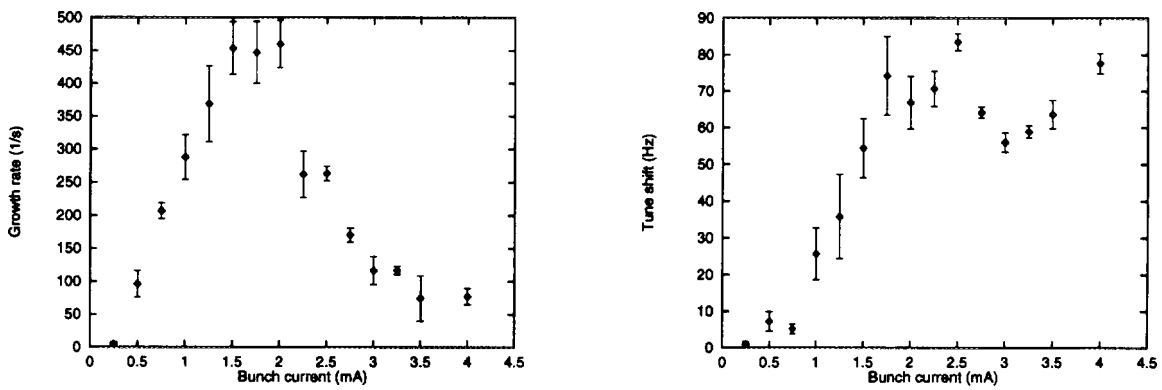

Figure 9: Growth rate and tune shift of the lowest frequency coupled bunch mode.

5.3 Variation of bunch pattern

Because the transit time of the photoelectrons across the chamber is shorter than the bunch train spacing in CESR but longer than the bunch spacing in B-factories, the behavior of the photoelectrons in B-factories with closely spaced bunches may be very different than that observed in CESR. Figure 10 shows the calculated photoelectron charge density in the CESR chamber just before the positron bunch arrival, when the bunch spacing and charge are varied over a wide range. CESR operates in the upper right corner of this diagram if trains of bunches are considered to be nearly equivalent to single bunches. With the DIP field present (left figure), charge is trapped. When the DIP field is turned off (right), charge is not trapped and the instability is absent. However, there is a large charge density present for bunch intervals characteristic of B-factories even in the absence of a DIP leakage field.

Figure 11 shows regions of bunch spacing and charge where the electron density is primarily due to electrons which can move freely in the vertical direction (white) and due to trapping assisted by the DIP leakage field (gray). Secondary emission has a negligible effect on the electron density everywhere in this space.

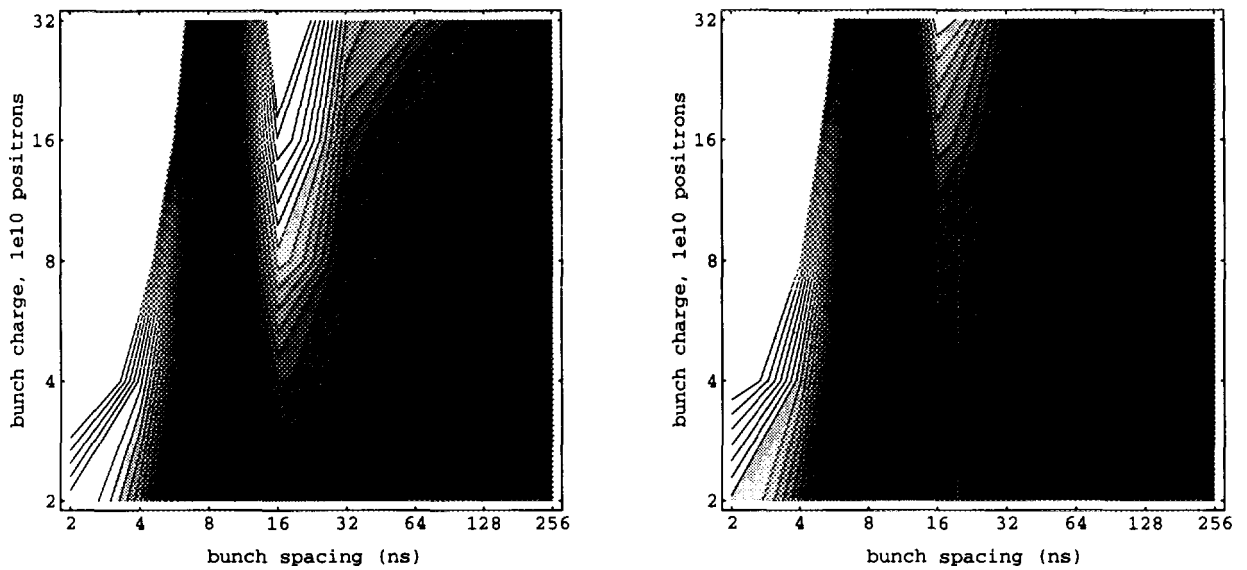

Figure 10: Calculated photoelectron charge density in the CESR beam chamber just before a bunch arrival as a function of e^+ bunch spacing and charge. Left: DIP leakage field included. Right: no leakage field from DIPs.

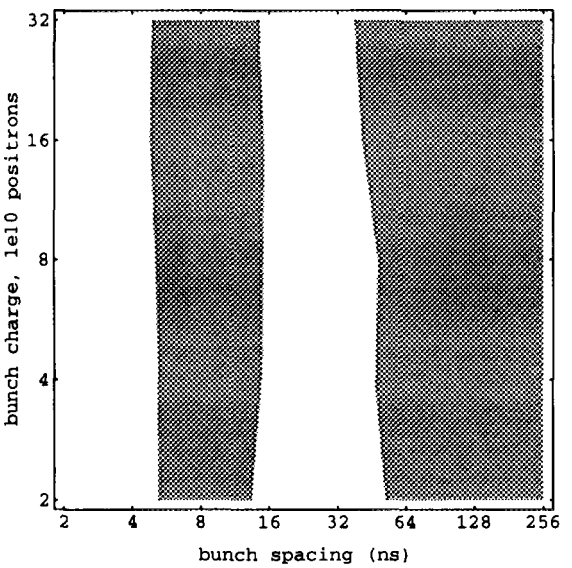

Figure 11: Regions where vertically free or trapped photoelectrons dominate. The shaded areas represent regions where trapping assisted by the DIP leakage field is responsible for most of the photoelectron density.

6 Cures

The are several ways in which the effects of the anomalous instability can be suppressed. Transverse feedback has been successfully used to stabilize the beam against this instability [8, 9]. The presence of a gap in the bunch pattern has been used during positron injection to reduce the growth rate. One half of the bunch pattern, consisting of adjacent bunches, are filled past the most unstable current level, after which the remainder are filled. This method is no longer used because the present feedback system suffices to stabilize the beam. Because the growth rate is proportional to the DIP anode voltage, we are currently modifying the DIP power supplies to produce a variable voltage which can be remotely controlled. We have found that the DIP pumping rate is approximately constant with voltage from 1.8 kV to the normal operating voltage of 7.4 kV at the present CESR chamber pressure [10].

The shields installed in the hard bend pump chambers completely suppress the anomalous instability. It is possible to fit similar shields into all of the CESR DIPs, although this is the most costly and time-consuming solution. It has been observed that the $m = 1$ vertical head-tail mode is stabilized by the operation of the distributed ion pumps [4]. We note that the peak of the frequency spectrum for this mode occurs at approximately 2.4 GHz, with substantial spectral density at the 5.6 GHz cyclotron frequency of the trapped photoelectrons. The photoelectrons may be damping this mode by absorbing energy from the head-tail mode before being lost by collision with the chamber. We may want to retain the effect in a controlled way. The combination of reduced DIP anode voltage and transverse feedback is expected to be more than sufficient to stabilize any bunch pattern planned for the CESR upgrade.

7 Conclusions

We believe the anomalous instability in CESR can be explained by the trapping of photoelectrons by the combination of the magnetic field of the bending magnets and the electrostatic leakage field of the distributed ion pumps. The photoelectron trapping model successfully describes the qualitative features of the observed instability. Secondary emission is found to have a negligible effect in our numerical simulation. For the closely spaced bunches of B-factories a high density of photoelectrons is present in the chamber even in the absence of the DIP leakage field. By a combination of reduced DIP anode voltage and transverse feedback, we can adequately suppress the instability in CESR.

The authors wish to acknowledge the work done by the many members of the CESR Operations Group in characterizing this instability. We particularly wish to thank M. Billing, D. Sagan, and D. Hartill of CESR, and K. Ohmi, S. Heifets, and J. Byrd for helpful discussions.

References

[1] M.G. Billing, private communication.

[2] D. Sagan and J.J. Welch, Cornell LNS report CBN 92-1 (1992).

[3] L.E. Sakazaki, R.M. Littauer, R.H. Siemann, and R.M. Talman, IEEE Trans. Nucl. Sci. **32** (1985) 2353-2355; L.E. Sakazaki, Ph.D. thesis, Cornell Univ. (1985).

[4] R. Littauer, Cornell LNS report CLNS 88/847 (1988).

[5] D.L. Hartill, T. Holmquist, J.T. Rogers, and D.C. Sagan, Cornell LNS report CBN 95-3 (1995).

[6] J.T. Rogers, Cornell LNS report CBN 95-2 (1995).

[7] O. Groebner, *et al.*, J. Vac. Sci. Technol. **A7**, (1989) 223.

[8] R. Littauer, Cornell LNS report CON 87-19 (1987).

[9] J.T. Rogers, *et al.*, "Fast Digital Transverse Feedback System for Bunch Train Operation in CESR", these proceedings.

[10] Y. Li, Cornell LNS unpublished report (1995).

Transverse mode coupling instability for leptons in the CERN SPS

T. Linnecar, E.N. Shaposhnikova

CERN, Geneva, Switzerland

Abstract

The intensity of leptons accelerated in the SPS machine is limited by a vertical transverse instability. The results of measurements of the thresholds for this transverse instability are compared with theoretical predictions for different broad band impedance models of the SPS. The threshold intensities found for the transverse instability and the position of the losses in the cycle enable the parameters of the broadband resonant impedance to be specified.

Contents

1 Introduction

The fast transverse single bunch instability was first observed in PETRA, [1]. Subsequently similar effects were seen in several other machines. The phenomena was explained in Ref.[2] by the coupling of head-tail modes, their natural mode frequencies shifting with increasing beam current due to the interaction with the machine impedance.

It was predicted in Ref.[3], with the help of empirical rules, that this instability would occur with the lepton beams that would be present when the SPS was used as the LEP injector. Theoretical approaches based on the numerical solution of an infinite matrix equation derived from the Vlasov equation, [4]-[6], gave an estimation of the maximum lepton intensity which could be injected without losses into the SPS. The assumed transverse shunt impedances were $Z_t = 18M\Omega/m$ and $Z_t = 47.7M\Omega/m$ for a broad-band resonator having quality factor 1 and resonant frequency $1.3GHz$.

Following all these predictions fast losses of the lepton beam were indeed observed during the first injection tests into the SPS in 1987. The results of measurements made at this time allowed a further estimate of the transverse impedance ($Z_t = 23M\Omega/m$) assuming the broad-band model with $Q = 1$ and $f_{res} = 1.35GHz$, [7]. On the other hand, it was shown in Refs.[7]-[9], that the experimental results at injection could be better explained using another impedance model with $Q = 6$ (and $Z_t = 102M\Omega/m$), a model that had been suggested for the SPS in Ref.[10].

Both analytical estimations and the results of simulation, [8],[9],[11], implied that the threshold of the transverse instability should increase during the cycle so that the maximum intensity per bunch that could be injected into LEP would be defined by the limitations in the SPS at $3.5GeV$. However the first tests, using different injection schemes, [11], where acceleration to $18GeV$ was achieved, indicated that a transverse instability occurred during acceleration at about $12GeV$ leading to strong losses. Experimentally it was found that this could be alleviated by increasing the longitudinal emittance with RF shaking.

From the time that the SPS started its operational life as a lepton injector the magnetic field cycle has remained effectively unchanged but the RF system has continued to evolve. These changes in the RF hardware and the ways in which the systems are used have modified the beam parameters and behaviour during acceleration. The original design for the acceleration system operated at $200MHz$. Subsequently a $100MHz$ RF system, which had been designed and installed to permit the transfer of long bunches from the CPS in $p\bar{p}$ operation, was brought into service for the same purpose for the lepton beams to increase the threshold for instabilities at injection, [12]. More recently, a $352MHz$ superconducting system has been installed. These latter cavities are used to provide extra accelerating voltage later in the cycle when the bunch length has become sufficiently short.

At the moment the experimental situation is as follows. If no artificial blow up of the lepton bunches is provided during the cycle the intensity of the lepton beam in the SPS is limited by losses in the middle of the cycle. The interesting peculiarity observed with this "high energy" instability is that it is restricted both in the time when losses occur (approximately from $170ms$ till $270ms$ after injection, or from $6GeV$ to $13GeV$) and in the intensities for which they occur (from 1.4×10^{10} to 1.9×10^{10}). At injection the operational bunch of length $\sigma_z = 30cm$ and relative energy spread $\sigma_E/E = 10^{-3}$ is stable up to an intensity of 2.1×10^{10}. Above this intensity the bunch suffers first from the transverse mode coupling instability and then, above 3.5×10^{10}, from the longitudinal microwave instability. The microwave instability has not been observed at higher energies.

The purpose of the present work is to attempt to explain the facts which have been observed, in order to be able to predict the behaviour of the beam with future possible changes of the parameters of the RF systems, or of the magnetic field cycle, and to provide information on the ways in which these limitations may be overcome or avoided. At the same time more information about the impedances and impedance models applicable to the SPS is of immense value for predicting the behaviour of very intense proton beams in the SPS, such as those to be used for LHC injection.

The complete analysis of the threshold for the transverse mode coupling, TMC, instability during the acceleration cycle requires:

- knowledge of the beam parameters during the cycle (by measurement or by simulation);
- the choice of the correct impedance model;
- the application of a theory of transverse mode coupling instability which works both for long (injection) and for short (top energy) bunches;
- estimations of the influence of other collective effects on the threshold.

These various subjects are discussed in the paper together with recent experimental results. For more technical details on the measurement methods see Ref.[13].

2 Machine conditions and experimental description

In normal operation each lepton cycle in the SPS is used to accelerate four electron or positron bunches from $3.5GeV$ to $20GeV$. Chromaticity is positive in both planes ($\sim +0.2$) and the tunes are set to nominally 0.61 horizontally and 0.58 vertically. The octupoles are off, the natural octupole strength in the machine is approximately $3m^{-3}$.

For the studies presented here the machine was operated with only one bunch, the selection being made by switching off the last three injection kicker pulses. This was necessary since not all of the measurement techniques at our disposal are capable of distinguishing between the various bunches. At the same time we eliminate the possibility of coupled bunch

effects. One possible area in which the latter may be important is the longitudinal phase plane due to the presence of the RF phase loop. This loop, which is installed to damp out injection errors and maintain phase stability at low energies where the leptons are not naturally damped, is locked on to one bunch only - the master bunch. The $n = 0$ dipole mode is damped in this way but if higher modes exist ,e.g. $n = 1$, then the master bunch may have a smaller longitudinal emittance compared to the others as it is the only one locked strongly to the RF. The selection of one bunch implies the master bunch. The other machine parameters were unchanged from the operational values.

The various measurement possibilities at our disposal were as follows, [14],[15]:

1) Intensity measurement of each bunch individually along the cycle;

2) Bunch length measurements:

a) bunch profile at fixed time, based on a sampling technique, where the profile is made typically of 100 points taken at the revolution frequency,

b) continuous bunch length along the cycle for each bunch separately. This measurement is based on the acquisition of the amplitude of two frequency components in the bunch spectrum which together give an estimation of the bunch length;

3) Vertical, horizontal and longitudinal wideband monitors. The transverse stripline monitors and the longitudinal wall-current monitor have a flat transfer impedance over a wide frequency range and are used in

a) instability identification,

b) growth rate measurements,

c) spectral analysis.

3 Threshold calculations

To calculate the threshold for the transverse mode coupling instability we used the code MOSES, [16], which searches for solutions of Sacherer's integral equation with mode coupling included.

After expansion of the perturbed distribution function in both azimuthal (modes m), and radial (modes k) coordinates in longitudinal phase space, using orthogonal functions with coefficients $a_k^{(m)}$, the matrix eigenvalue equation for coherent frequencies Ω has the form, [6],

$$(\lambda - m)\, a_k^{(m)} = \sum_{n=-\infty}^{\infty} \sum_{l=0}^{\infty} M_{nl}^{mk}\, a_l^{(n)}, \tag{1}$$

where $\lambda = \frac{\Omega - \omega_\beta}{\omega_s}$, ω_β and ω_s are betatron and synchrotron frequencies.

The matrix elements are given by

$$M_{nl}^{mk} = -iK \sum_{p=-\infty}^{\infty} Z_{\perp}(p')\, i^{m-n}\, I_{mk}(p_{\xi}) I_{nl}(p_{\xi}). \tag{2}$$

Here $p_{\xi} = p' - \xi/\alpha$, $p' = p + \Omega/\omega_{rev}$, p is an integer, ω_{rev} is the revolution frequency, ξ is the chromaticity, α is the momentum compaction factor and $Z_{\perp}$ is the transverse impedance function. For the case where the impedance model is represented by a resonator,

$$Z_{\perp}(\omega) = \frac{\omega_{res}}{\omega} \frac{Z_t}{1 + jQ(\frac{\omega}{\omega_{res}} - \frac{\omega_{res}}{\omega})}, \tag{3}$$

where Z_t is the transverse impedance and ω_{res} is the resonant frequency.

For the Gaussian bunch the intensity parameter K has the form

$$K = \frac{\beta_z \omega_{rev}^2 N e^2}{8\pi^2 E_s \omega_s}, \tag{4}$$

where β_z is the beta-function, N is the number of particles per bunch and the bunch spectrum functions are

$$I_{mk}(p_{\xi})^2 = \frac{1}{(|m|+k)!k!} x^{|m|+2k} e^{-2x}, \tag{5}$$

where $x = (p_{\xi}\sigma_z)^2/(2R^2)$, σ_z is the bunch length corresponding to one σ_E in energy distribution, R is the machine radius.

The appearance of an imaginary part in the solutions of eq.(1) for the coherent frequencies Ω with increasing intensity gives the threshold intensity N_{th}. It occurs when the adjacent mode frequencies, shifted from their unperturbed values, merge together.

Parameter K shows how results scale with different parameters. In fact if the summation over p in eq.(2) is approximated by an integration we can write (for zero chromaticity)

$$N_{th} \sim \frac{E_s \nu_s}{e^2 \beta_z Z_t \omega_{res}} F(\sigma_t \omega_{res}, Q), \tag{6}$$

where the function $F(\sigma_t\omega_{res}, Q)$ can be defined from numerical calculations. The dependence of the threshold on the bunch length $\sigma_t = \sigma_z/c$, resonant frequency ω_{res} and Q is given by the relative positioning in the frequency domain of the machine impedance and bunch spectrum functions.

The position of the maximum of the bunch spectrum function I_{mk} with modes m and k is

$$f_{max} = p f_{rev} = (|m| + 2k)^{1/2} \frac{c}{\sigma_z} \tag{7}$$

In Figs.1, 2 we show the spectrum calculated for the longest and shortest bunches used at present in the SPS, together with the impedance function as given by the two broadband models discussed in the Introduction. These models have the same centre frequency for the

broadband resonator $f_{res} = 1.3GHz$ but differing quality factors, $Q = 1$ and $Q = 6$. It is seen that the beam spectrum for short bunches samples the whole impedance function, whether high or low Q, whereas the longer bunches with energy concentrated at lower frequencies are affected more strongly by the resistive part of the impedance of the lower Q model. So the measurements of thresholds for long and short bunches can give information about the Q of the model. However, as follows from equation (6) for a fixed value of Q we can define the resonant frequency only if the function $F(\sigma_t\omega_{res})$ is not simply proportional to $\sigma_t\omega_{res}$.

Note that the position of the maximum of the spectrum function is defined only by the value of $q \equiv |m| + 2k$. The amplitudes of modes which have their maximum at the same position (the same q) are larger for the modes with the lower azimuthal modes m but higher radial modes k (see Fig.2). In other words we cannot ignore the contribution of the higher radial modes at least up to $k \sim |m|/2$ if coupling of mode m is important.

The general criterion that we used for the choice of the azimuthal and radial modes that should be included in the calculation is to increase them until the results no longer change significantly. Usually there were a few unshifted azimuthal modes on either side of modes which are strongly shifted or coupled.

Following these rules the dependence of threshold intensity on bunch length at injection into the SPS was calculated by MOSES for a synchrotron tune $\nu_s = 0.008$ and the impedance model defined by: $Z_t = 23M\Omega/m$, $Q = 1$, $f_{res} = 1.3GHz$. Results are given in Fig.3. We do not take into account Landau damping resulting from betatron tune spread or synchrotron frequency spread.

As shown in this Figure, for short bunches (with bunch length $\sigma_z < 10cm$) the threshold intensity is defined by the coupling of azimuthal modes (0,-1). With increasing bunch length the coupling which defines the threshold shifts to the modes (-2,-3) and then (-4,-5) passing through shorter regions where coupling between modes (-1,-2) and (-3,-4) can be important. It seems that the coupling between the pairs of modes (0,-1), (-2,-3), (-4,-5), and so on, is more significant than the other pairs.

In the same Figure we show with dotted lines the thresholds for the coupling of lower azimuthal modes while they still exist. Nonetheless these have an order of magnitude smaller growth rate (which also decreases with increasing bunch length) than the dominant modes which are shown with a solid line. Dominance is determined by comparison with the synchrotron period. We expect that during the acceleration cycle when conditions are changing rapidly only instabilities with fast growth rates have time to develop.

Note that with increasing synchrotron frequency not only the threshold increases, (due to the intensity parameter K), but also the growth rate, $Im(\Omega - \omega_\beta)/\omega_s$.

The azimuthal modes used in calculations by MOSES for long bunches were in the range (2,-8). The results for the dominant modes did not change significantly with any further

increase of the azimuthal mode numbers involved in the range available in the code. The number of radial modes k taken for calculation increased with the increasing maximum azimuthal mode number used in the calculations (up to 7 for longer bunches). Note that results can be very different when only a small number of higher radial modes is included in the calculations. Usually in this case it is impossible to determine the dominant modes. As an example, some results from MOSES are given in Figs.4,5. In these figures the bunch length, energy and number of azimuthal modes m is the same but the maximum number of radial modes k included is different.

Several positive azimuthal modes should be included in the calculations even when the threshold is apparently defined by the coupling of modes with large negative numbers. This is explained by the strong shift of the $m = 0$ mode which influences the negative modes and is itself influenced by the positive modes. As also pointed out in Ref.[6], after several modes have coupled and decoupled they can no longer be considered pure.

4 Beam parameters in the cycle

The bunch parameters which we need to know for the calculation of the instability threshold at a given energy are the synchrotron oscillation frequency and the bunch length.

If collective effects are ignored then the bunch parameters are defined by the magnetic cycle together with the RF voltage program, (see Fig.6), and the initial conditions. The most recent cycle uses the three RF systems ($100MHz$, $200MHz$ and $352MHz$), which switch on one after the other during the cycle (while the bunch becomes shorter).

The behaviour of the beam changes significantly during the cycle. At injection and during the early part of the cycle while the energy is still low the radiation losses are very small, there is little natural damping and the long bunches behave like protons. Later on, the radiation becomes more and more important, the damping time becomes shorter until at top energy this process defines the bunch parameters. The previous history of the bunch becomes almost irrelevant.

The bunch length can, in principle, be either measured or calculated. However to use the profile measurement implies that the loss point is known in advance. The alternative technique providing the continuous bunch length is very sensitive to calibration errors in the region of instability, i.e. where the bunches are short. Hence to know the bunch length at the loss point we are obliged to use calculation. The synchrotron frequency is also calculated and shown in Fig.7.

We assume that during the acceleration cycle the longitudinal emittance is changing

according to the equation, (see also Ref.[17]):

$$\frac{1}{\varepsilon}\frac{d\varepsilon}{dt} = \frac{2}{\tau(t)}\left(\frac{\sigma_{E0}^2(t)}{\sigma_E^2(t)} - 1\right), \tag{8}$$

which takes into account radiation damping and quantum excitation. Here τ is the damping time, σ_{E0} is the equilibrium energy spread, σ_E is the current energy spread of the beam and ε is the longitudinal emittance corresponding to one σ_E of the Gaussian distribution. The equilibrium energy spread varies with energy as E_s^2 and $\tau \sim E_s^{-3}$.

The emittance found by the numerical solution of this equation along the acceleration cycle was used in a code which calculates the bunch parameters (including bunch length and synchrotron frequency) for a given emittance ε matched to the bucket in multiharmonic RF system.

The comparison between the calculated bunch length and measurements given by both the continuous bunch length measurement, taken from the photo in Fig.8, and some profile measurements is shown in Fig.9.

5 TMC instability at high energies

5.1 Experimental results

The "high energy" instability, i.e. that which occurs between $6GeV$ and $13GeV$, is seen operationally as a sharp loss of bunch intensity. A typical picture of the loss pattern as seen on two bunches is reproduced in Fig.10. The other curve in this photo corresponds to the peak detected microwave signal from the vertical wideband monitor. As the photo shows this loss can occur in any given cycle on one or more of the four bunches at independent times. It was checked that the instability is not a function of the number of bunches in the machine.

Observation of the various signals from the wideband monitors shows that the losses coincide with strong vertical signals in the $1GHz$ range with growth rates typically less than a few ms, see Fig.11.

Injecting only a single bunch we recorded the time of the losses together with the intensity of the beam just before the loss. It is clear that the instability start time is earlier than the loss, but with the typical growth rates that are observed, it is not much earlier.

The results of the measurements corresponding to the cycle shown in Fig.6 are shown in Fig.12. The clustering of experimental points is obvious. The time of the instability is limited to between $170ms$ and $270ms$ while the intensity range is restricted to between 1.5×10^{10} to 1.8×10^{10} particles per bunch. At injection, intensities above 2.1×10^{10} were unstable. For this set of measurements bunches with intensities between 1.8×10^{10} and

2.1×10^{10} suffered losses around $100ms$ for reasons other than the TMC instability. The measurements shown were taken on two different occasions, the sets being shown by crosses and circles.

5.2 Calculation results

To estimate the threshold intensity we used MOSES with the beam parameters calculated along the cycle. The results were obtained for different broadband impedance models of the SPS.

The resonant model is defined by the parameters f_{res}, Q and Z_t. Note that there are an infinite number of impedance models which can fit the measurements at some particular point but by considering the variation of threshold intensity with bunch parameters we can try and restrict the number of models. As a first step we fixed the resonant frequency assuming $1.3GHz$ as has been suggested before.

In Fig.12 we see the TMC threshold as calculated from MOSES for the two impedance models, mentioned earlier, with $Q = 1$ and $Q = 6$, scaled using Z_t to give a good fit around the observed results. For these models this implies $Q = 1$, $Z_t = 23M\Omega/m$ or $Q = 6$, $Z_t = 102M\Omega/m$. The last value coincides with the one suggested in Ref.[9] to fit the results of measurements of instabilities at injection for $16cm$ long bunches. The calculated thresholds for both impedance models go through a minimum at around $240ms$ and the experimental points cluster in this dip.[1]

To explain the fact that there is a maximum intensity observed as well as an earliest time we have to look more closely at the behaviour of the two curves at earlier times. As we go back towards injection the $Q = 6$ model supposes that the threshold increases continuously. Therefore for higher and higher intensities the loss point should move back continuously towards injection. This is not so for the $Q = 1$ model . Here the threshold goes through a peak at 100ms before decreasing towards injection. If this model is correct then as the intensity increases the loss point will move back to $150ms$ and then jump to injection. Higher intensities are lost at injection and we will never see in this cycle a beam loss between injection and $150ms$. Since this is what we observe, there is a strong indication that a low Q model is more close to reality. We repeated the calculations with $Q = 2$ and the shunt impedance defined by high energy measurements and found that for these values a higher threshold is predicted at injection than that observed.

[1]The points near $170ms$ belong to the range of bunch lengths, see Figs.3,9, where the threshold is given either by coupling between modes (0,-1) or modes (-1,-2) and is very sensitive to small changes in bunch length. Note also that points marked as crosses belong to the set where accurate bunch-length measurements are absent, but we have some indications that the bunches in this set were more stable after injection and hence shorter at later times.

The different behaviour of the TMC threshold with the model chosen also shows that observations at earlier times in the cycle, where the bunches are longer, will allow the SPS impedance model to be further refined.

Taking $Q = 1$ we now consider varying the resonant frequency. In Fig.13 the thresholds for $f_{res} = 1.5GHz$, $1.7GHz$ and $2GHz$ are shown and can be compared with the results for $1.3GHz$, (see Fig.12). As expected from previous arguments we see that thresholds for long bunches are insensitive to the choice of resonant frequency which is not the case for short bunches. As the resonant frequency increases the dip centred at $235ms$ decreases in amplitude while another appears at $320ms$. For resonant frequencies around $2GHz$ losses should occur at this time in the cycle. For $f_{res} = 1.7GHz$ we have two dips separated by a small barrier. With the dispersion in bunch length observed during the measurements, for f_{res} more than $1.6GHz$ we would expect losses in the second dip which were never observed. For $f_{res} \sim 1.5GHz$, the barrier is re-established. If f_{res} is decreased further it is difficult to explain the really narrow region of losses observed in the last set of measurements. Note that the thresholds calculated correspond to the minimum bunch lengths along the cycle for this set.

From all the measurements we conclude that the resonant frequency lies in the range $1.3GHz$ to $\sim 1.6GHz$.

Applying the commonly used analytical formulae, which supposes that $F(\sigma_t\omega_{res}, Q) \sim (\sigma_t\omega_{res})$ in eq.(6), gives the curve shown as a dashed line in Fig.14 for $\sigma_z > 10cm$. This result, normalised at injection, suggests that the beam becomes more and more stable along the cycle, in contradiction to measurements. The long bunch approximation is normally applied for $\sigma_z >> \sigma_{z0} = c/(2\pi f_{res})$. For $f_{res} = 1.3GHz$, $\sigma_{z0} = 3.7cm$. In our case this approximation works for $\sigma_z > 20cm$.

A linear approximation,

$$N_{th} = 4 \times 10^{10} E_s \nu_s (\sigma_z - 6.5), \tag{9}$$

where E_s is in GeV and σ_z in cm, obtained from the dependence of threshold on bunch length over the restricted range $10cm$ to $30cm$ in Fig.3 can predict the main characteristics of the threshold behaviour in the first part of the cycle, This expression is normalised at injection and is shown as a dotted line in Fig.14.

6 Instabilities at injection

6.1 Measurements

The parameters of the injected beam into the SPS are well defined due to the fast damping times on the flat top in the CPS. Measurements of fast instabilities at injection, much faster than the synchrotron period, have the advantage that the beam parameters can be considered to be constant.

For the injection measurements the CPS provided injected bunches of different length, energy spread and intensity. The range of bunch lengths available was from $15cm$ to $30cm$ with a relative energy spread of 10^{-3}. For the shorter bunches a relative energy spread of 0.7×10^{-3} was also available. The intensity could be varied from 10^9 to 3×10^{10} leptons/bunch. Information on the numerical values for the bunch shape parameters was given by the CPS, the intensity was measured at injection into the SPS.

We worked with a single injected bunch captured in a $100MHz$ bucket, the $200MHz$ system being switched off rather than counterphased to zero voltage. We observed the filtered microwave signals from the vertical and longitudinal monitors, simultaneously with the bunch current signal. Sometimes we also used the peak detected longitudinal wideband signal which gives information on the instantaneous peak density and hence bunch shape changes. In all cases we confirmed that there were no horizontal signals present.

Typical results for different strengths of transverse and longitudinal instabilities are given in Fig.15. In general instabilities are present in both planes but their signatures make it possible to disentangle them. Longitudinal instabilities lead to emittance increase but rarely loss, whereas step losses occur with the TMC instability usually after several revolution periods. At the same time the relative strength of the two wideband signals is a good indication of the dominant instability.

The synchrotron tune is an important parameter; to confirm the voltage measurement we also observed the oscillation of bunch form at twice the synchrotron frequency as given by the peak detector.

The TMC measurements are given in Fig.16, where beam intensity is plotted against bunch length.

6.2 TMC instability calculations

It is obvious from the measurements that the threshold increases with bunch length. Unfortunately the number of experimental points available do not allow the relationship between the two to be determined accurately. The threshold is not sensitive to resonant frequency for the range of bunch lengths available at injection but is much more affected by changes in

Q. Using MOSES the dependence of the threshold on bunch length for impedance models with $f_{res} = 1.3GHz$ and with different values of Q was found (see Fig.16). These models, as defined by the high energy measurements, all fit well at short bunch lengths but can be distinguished as expected by their behaviour at long bunch lengths. The $Q = 1$ model gives the best fit. The $Q = 2$ model, even with the limited number of experimental points is already seen to give too high a threshold for the longest bunch.

We note that the calculated curve is certainly not linear and is not even smooth but is rather made of several segments with breakpoints. It has previously been shown that these breakpoints come from the choice of the dominant mode coupling pair. The measurements confirm the choices made, particularly in the region $20cm - 25cm$, for the $Q = 1$ model.

7 Discussion of results

These results on the TMC instability found on the present operational cycle can be used to analyse previous or future cycles.

For example, we have analysed the cycle used initially in the SPS for lepton acceleration when only the 200MHz system was available. The injected beam had a bunch length of σ_z=16cm and a relative energy spread of σ_E/E=0.7 $\times$ 10^{-3}. The TMC threshold for this cycle is also shown in Fig.12 as a dotted line. Intensities higher than 10^{10} will be unstable. In practice not more than 0.8 $\times$ 10^{10} particles were ever accelerated on this cycle with these bunch parameters. Note that the losses which were observed at energy $12GeV$ correspond to the minimum of the calculated threshold (around $250ms$). Comparing these results with that produced for the present cycle, shows the gain obtained by the addition of the $100MHz$ system and the effect of the $352MHz$ system.

One possible way to avoid the high energy limitations in the present cycle is to increase the emittance. RF shaking, (modulation of the RF amplitude with a signal at twice the synchrotron frequency), has already been used for this purpose. Another possibility is the use of wigglers. We have calculated the effect that a wiggler of the Robinson type with the same parameters as those used at present in the CPS, [18], would have on the threshold when placed in a region of high dispersion ($2.9m$) in the SPS. The result is a 20% increase in bunch length and threshold intensity in the region of minimum threshold.

We note that we have also used MOSES to check the results of the calculations in Ref.[19], where a direct observation of the shift of mode 0 with intensity was made. The value for the inductive impedance obtained with this method remains a factor of two higher than we find from threshold measurements. However these measurements are in contradiction with later tune-shift measurements, [20], where the value $Z_t = 26.76M\Omega/m$ was found.

To obtain more precision in the values for the parameters of the impedance model more

stable bunch lengths combined with finer intensity changes are required.

8 Conclusions

Recent experimental data on the transverse mode coupling instability seen in the SPS both at high and low energies, and for short and long bunches, can be explained using an impedance model defined by a broadband resonator centred at a frequency f_{res} between $1.3GHz$ and $1.6GHz$, with quality factor Q close to 1, and $Z_t/Q = 23M\Omega/m$. With the assumptions that have been made the accuracy on the last figure is around 10%.

The large variation in bunch length during the lepton acceleration cycle in the SPS, (more than a factor 10), and hence the large change in bunch spectrum, provides an effective means of determining the parameters of the impedance model applicable to the SPS. The fact that we have losses for short and long bunch regimes allows the determination of Z_t and Q whereas the time of the losses or the position of the minimum threshold at high energies gives f_{res}.

The numerical calculations have been made with the code MOSES. With increasing bunch length, the range of azimuthal modes and the number of higher radial modes required for convergence of the results produced by MOSES, also grows. Higher radial modes play an important role. For long bunches, $\sigma_z > 20cm$, we have taken the threshold intensity to be determined by the mode coupling with the dominant growth rate.

Acknowledgements

We thank the following people for their help. Y.H.Chin made a new, fast version of MOSES available to us. The experiments at injection relied on the expertise of J-P.Riunaud in the CPS who also supplied information on wigglers. The choice of optimum position for wigglers in the SPS was made by W.Herr. D.Boussard and B.Zotter proof-read the paper and made helpful comments leading to additions and changes in the final version.

References

[1] PETRA-Project Group, IEEE-Trans., NS26, 2970 (1979).

[2] R.D.Kohaupt, report DESY 80-22 (1980).

[3] J.Gareyte, CERN LEP Note 356 (1982).

[4] B.Zotter, CERN LEP Note 418 (1982).

[5] G.Besnier, D.Brandt, B.Zotter, CERN LEP-TH/84-11 (1984).

[6] Y.H.Chin, CERN/SPS/85-2 (DI-MST) (1985).

[7] D.Brandt and J.Gareyte, CERN SPS/88-17 (AMS) (1988).

[8] D.Brandt, CERN SPS/AMS/Note/88-7 (1988).

[9] D.Brandt, CERN SPS/AMS/Note/88-15 (1988).

[10] L.Vos, CERN SPS/86-21 (MS) (1986).

[11] D.Brandt et al., CERN SPS/89-6 (AMS) (1989).

[12] D.Boussard, CERN SPS/ARF/Note/DB/gw/83-83 (1983).

[13] T.Linnecar and E.N.Shaposhnikova, CERN/SL/93-43 (RFS) (1993).

[14] T.Linnecar, CERN SPS/ARF/78-17 (1978).

[15] T.Linnecar and D.Stellfeld, CERN SL/RFS/Note/90-3 (1990).

[16] Y.H.Chin, CERN/LEP-TH/88-05 (1988).

[17] Y.Baconnier et al, CERN/PS/PSR/83-6 (1983).

[18] Y.Baconnier et al, NIM A234, 244-252 (1985).

[19] T.Linnecar and W.Scandale, CERN SPS/DI-MST/ME-84-12 (1984).

[20] D.Brandt et al, CERN SPS/AMS/Note/88-14 (1988).

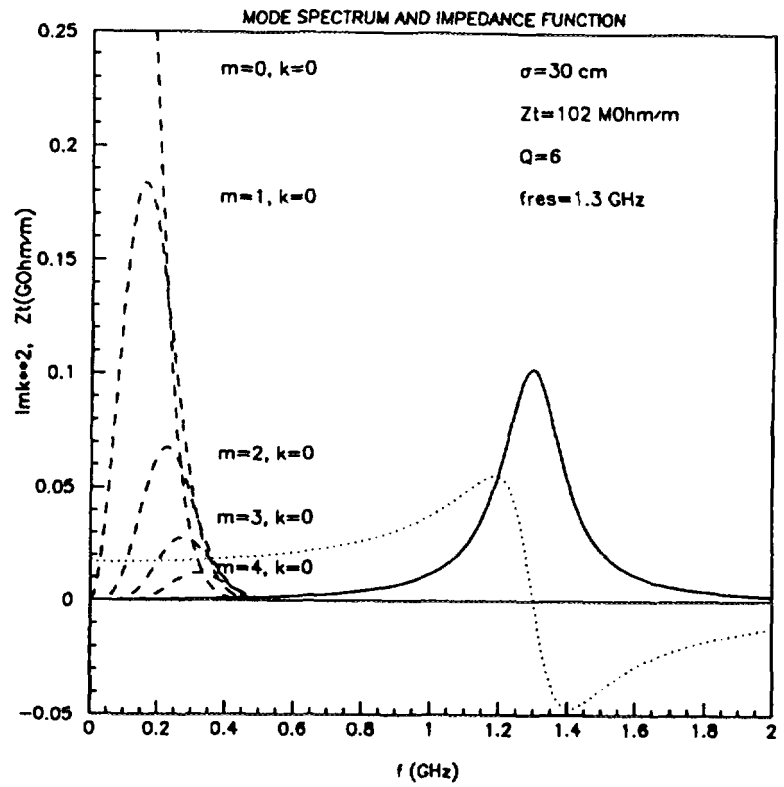

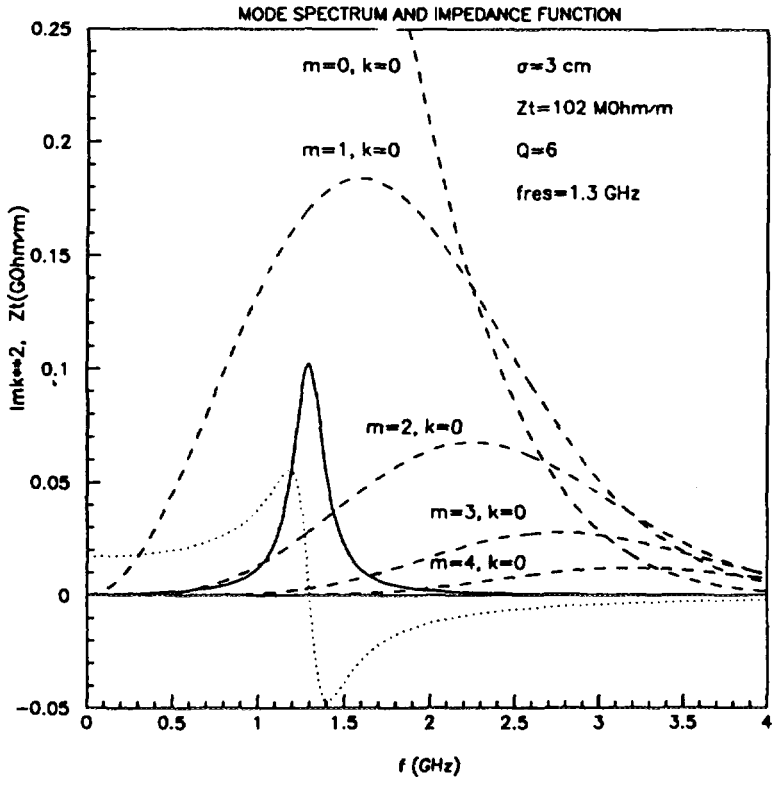

Figure 1: Long (a) and short (b) bunch spectra and impedance function for the $Q = 6$ model.

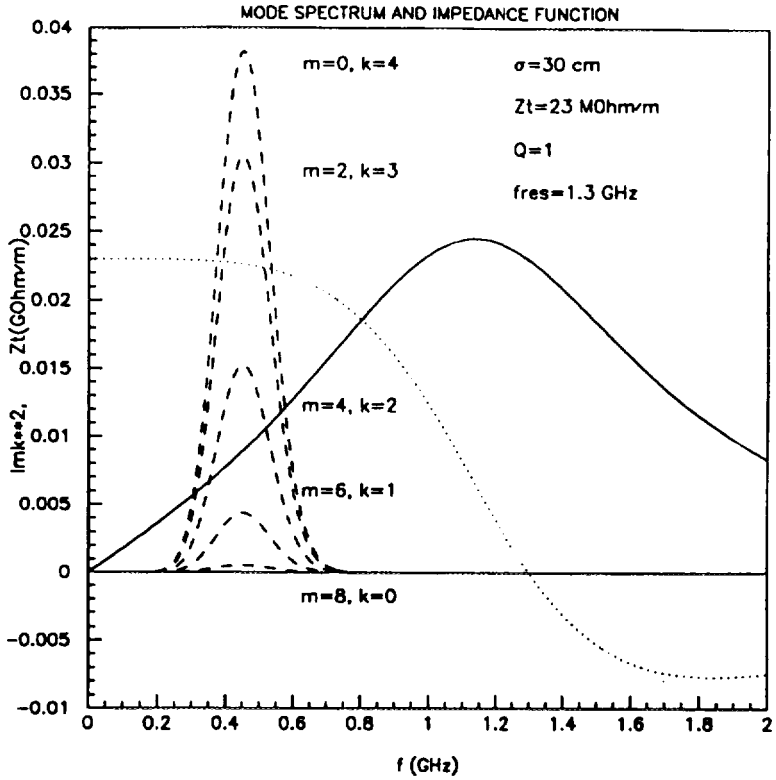

Figure 2: Bunch spectra for the modes with $q = |m| + 2k = 8$ and impedance function for the $Q = 1$ model.

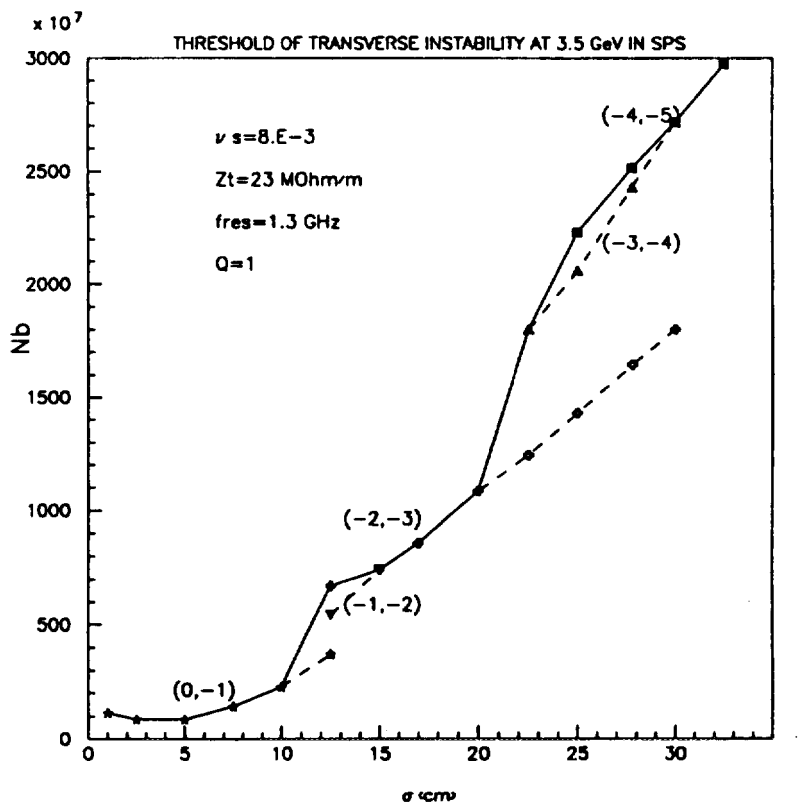

Figure 3: Threshold calculated at injection in the SPS as a function of the bunch length.

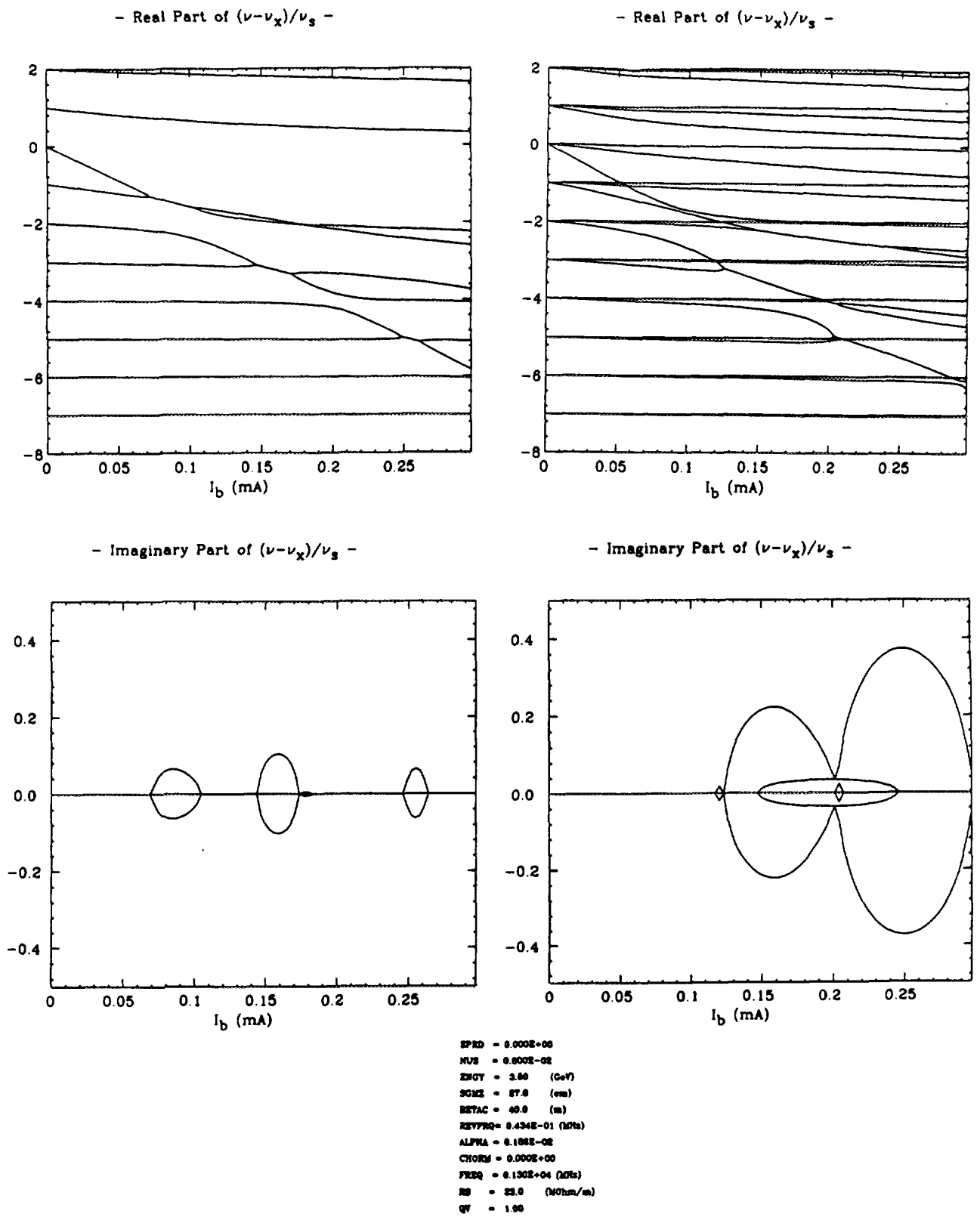

Figure 4: Real and imaginary parts of frequency shift as a function of intensity for the number of higher radial modes $k = 0$, left, and $k = 2$, right.

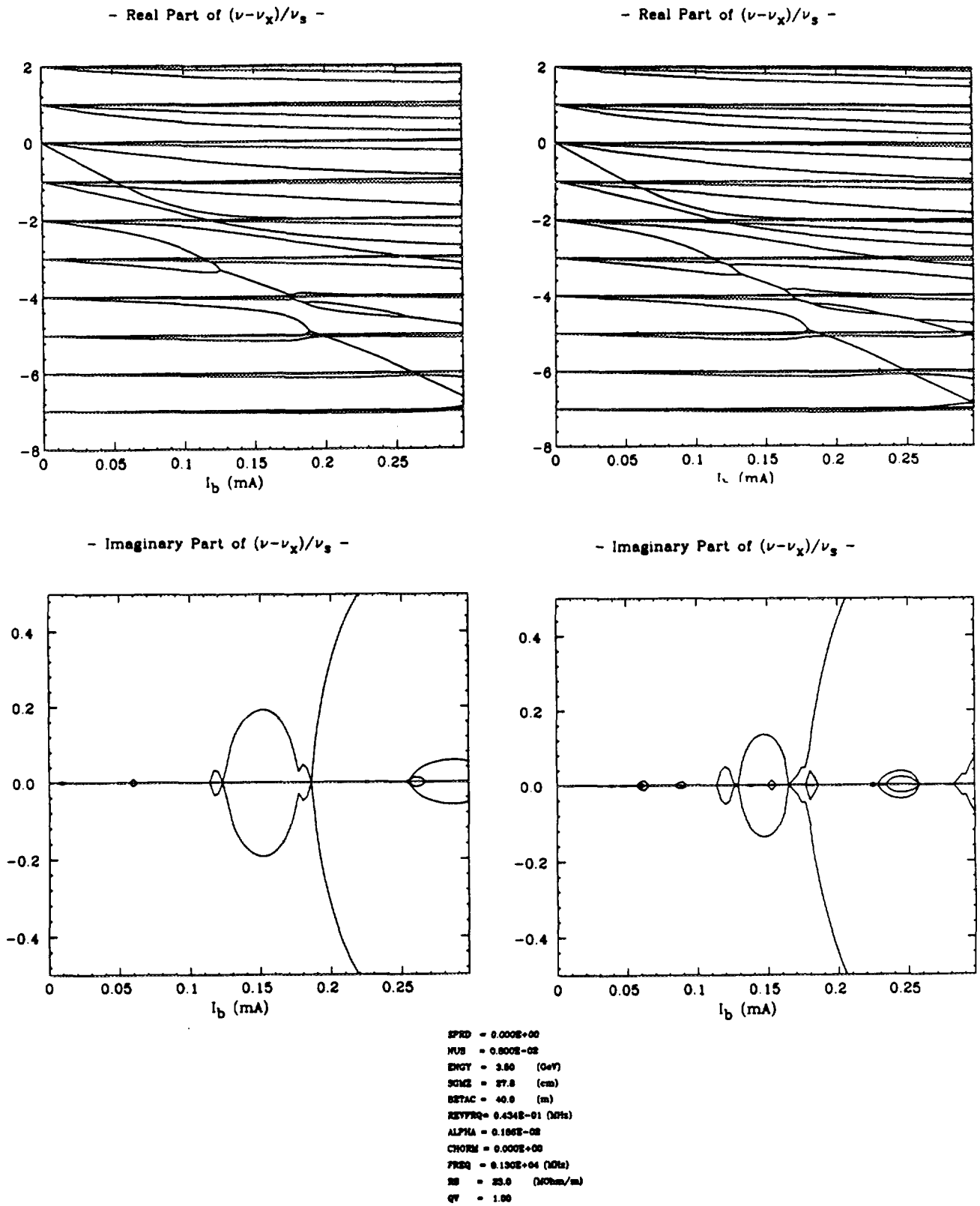

Figure 5: Real and imaginary parts of frequency shift as a function of intensity for the number of higher radial modes $k = 4$, left, and $k = 6$, right.

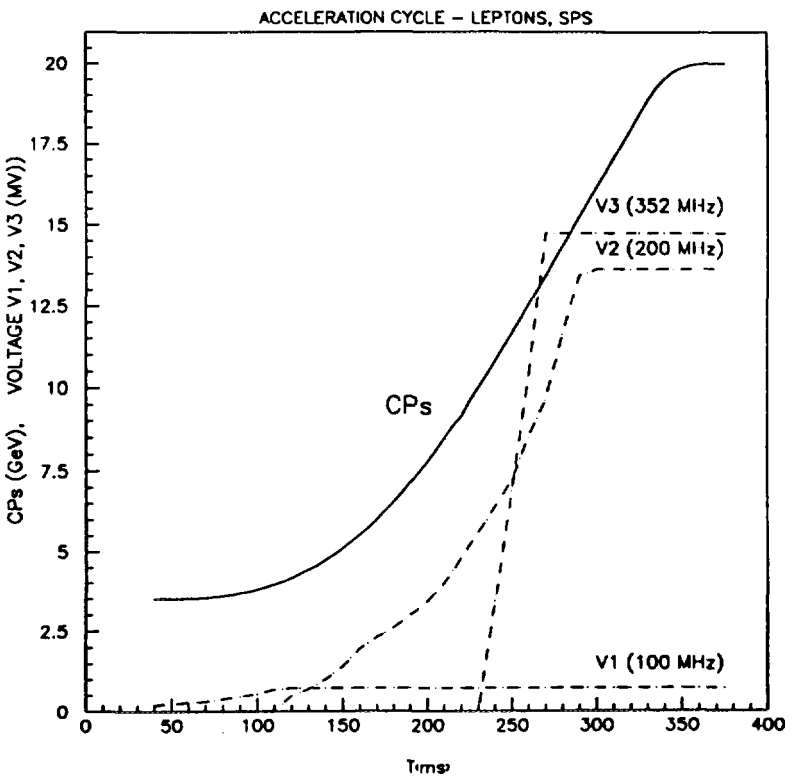

Figure 6: Energy and voltage programs through the cycle.

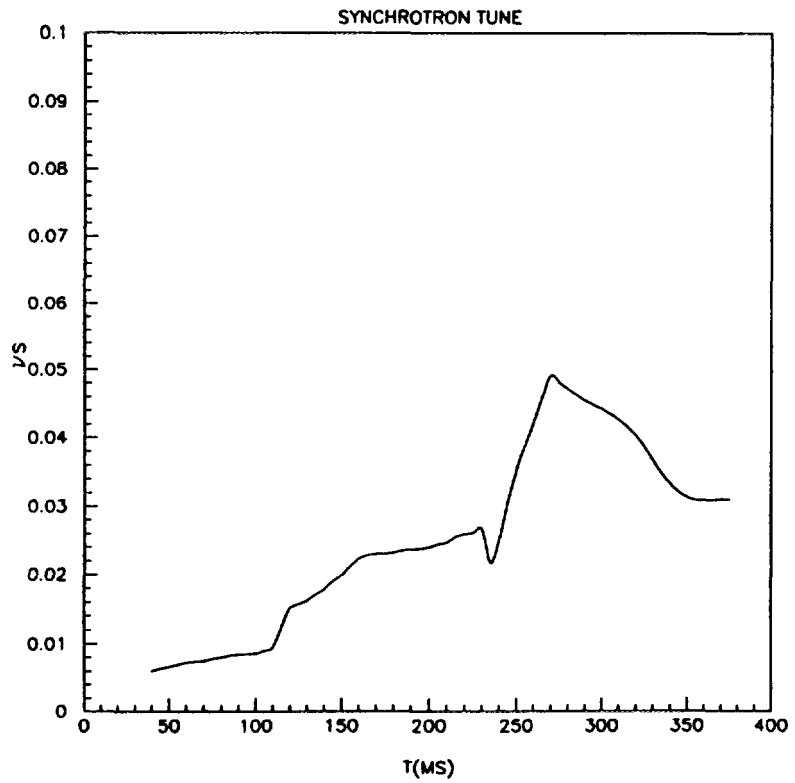

Figure 7: Synchrotron frequency along cycle.

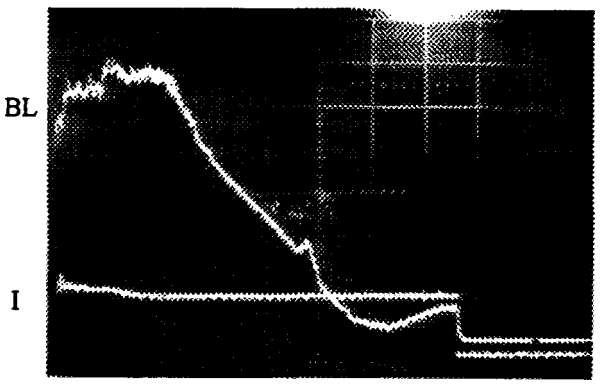

Figure 8: Photo of continuous bunch length measurement (BL) together with intensity signal (I). Time scale 50 ms/division.

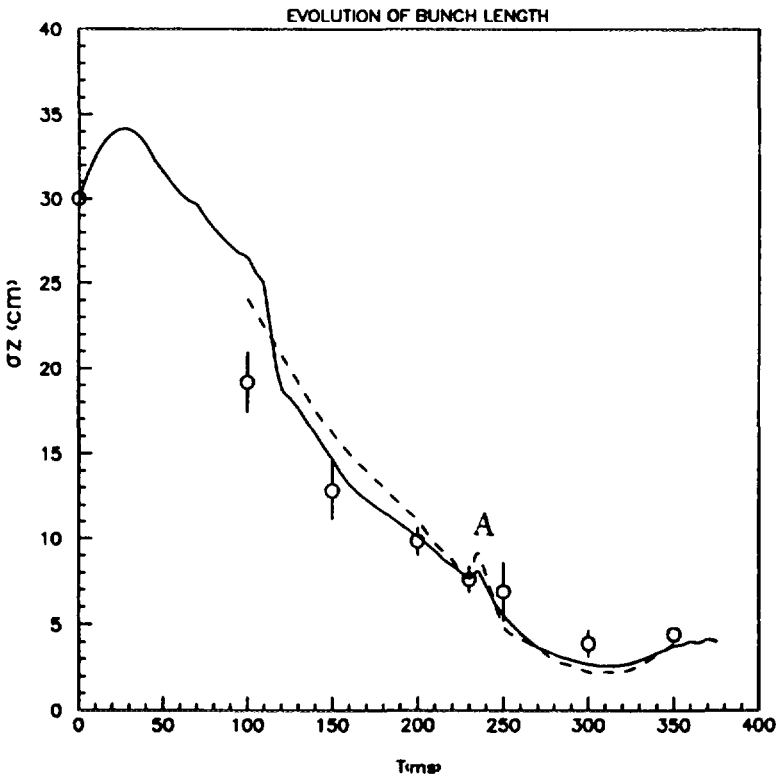

Figure 9: Calculated and measured bunch length evolution. Dashed line corresponds to the continuous bunch length measurement, circles are from profile measurements.

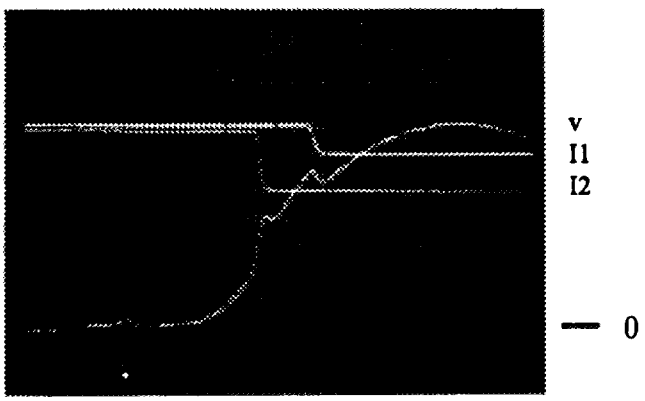

Figure 10: Intensity loss seen on two bunches (I1,I2) together with filtered vertical signal (V). Time scale 20 ms/division.

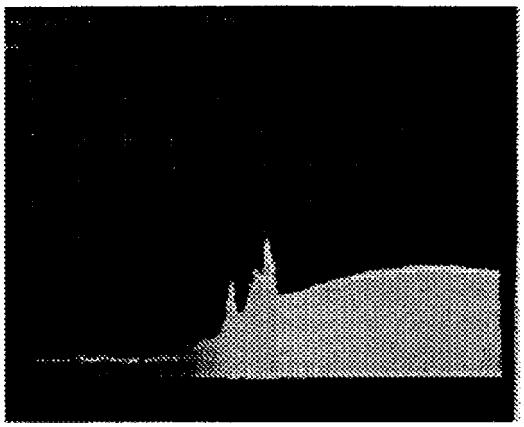

(V)

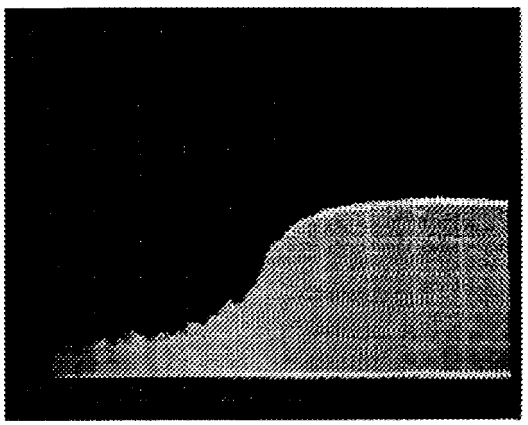

(L)

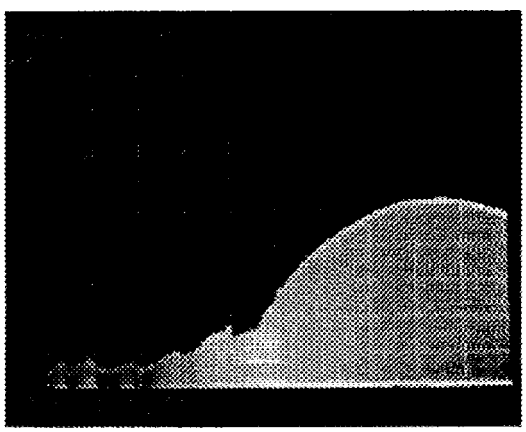

(H)

Figure 11: Signals coincident with beam loss as seen on vertical (V), longitudinal (L) and horizontal (H) monitors. Time scale 20 ms/division, vertical scale 10db/div.

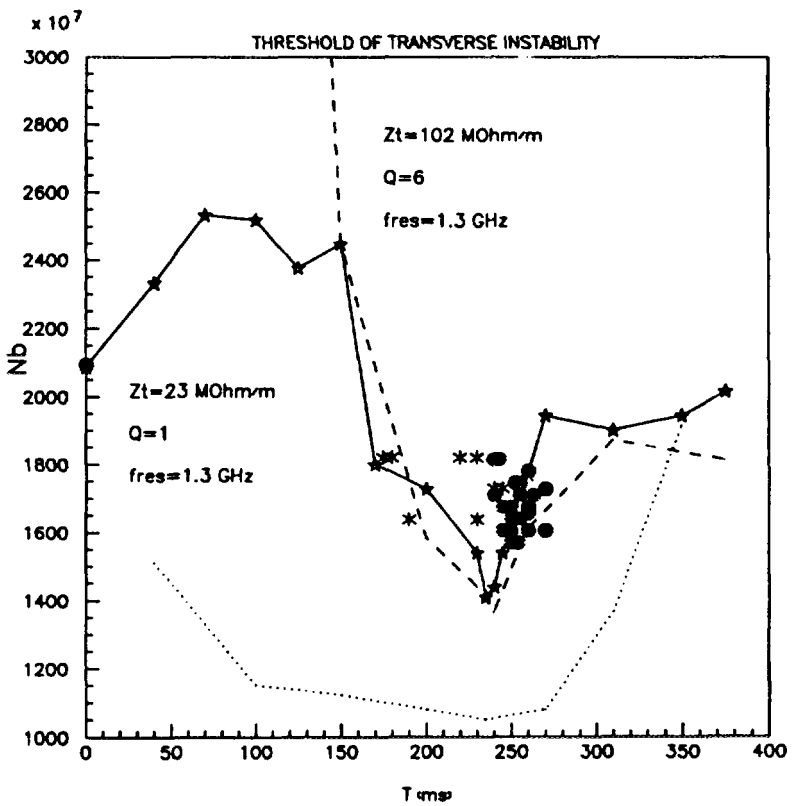

Figure 12: Measurements of beam losses due to transverse instability during the cycle (filled circles and crosses) and calculated thresholds for $Q = 1$ (solid line) and $Q = 6$ (dashed line) models for the present cycle. TMC threshold for old $200MHz$ cycle with $Q = 1$ impedance model (dotted line).

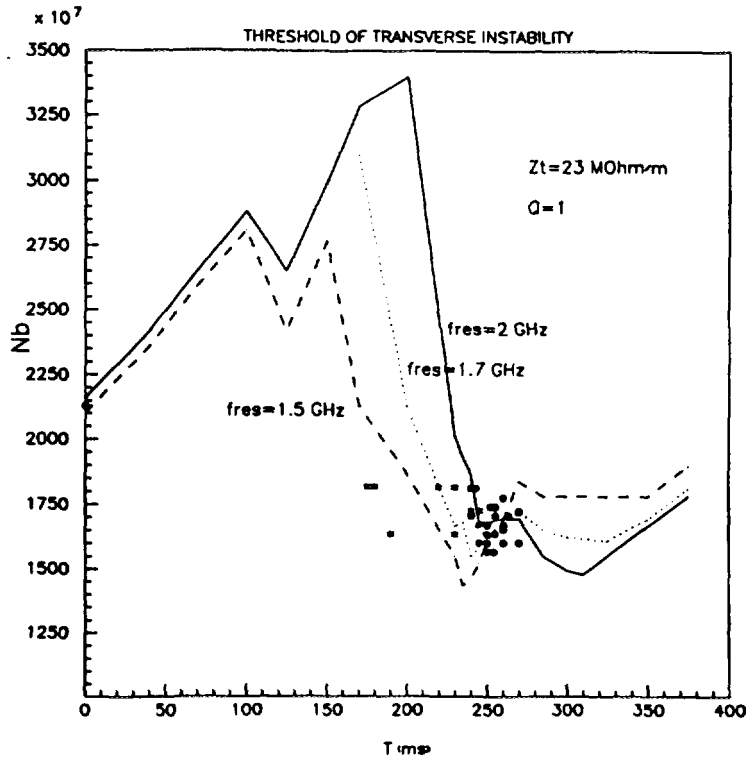

Figure 13: TMC threshold for $f_{res} = 1.5GHz$ (dashed line), $1.7GHz$ (dotted line) and $2GHz$ (solid line) together with measurements (filled circles and crosses).

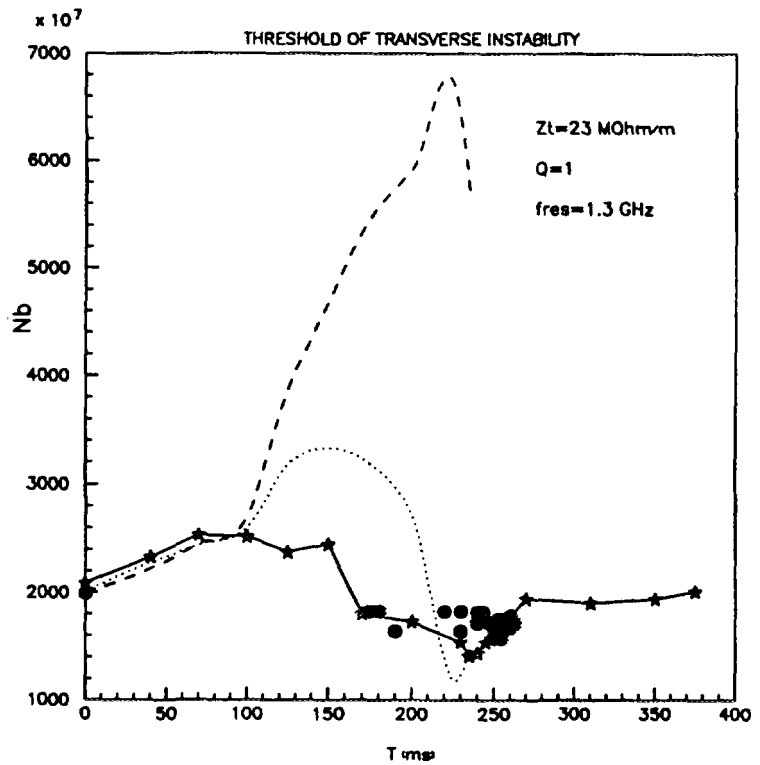

Figure 14: Thresholds obtained by MOSES (solid line), with a linear approximation for bunch length dependence (dashed line), and a linear fit to MOSES output at injection (dotted line).

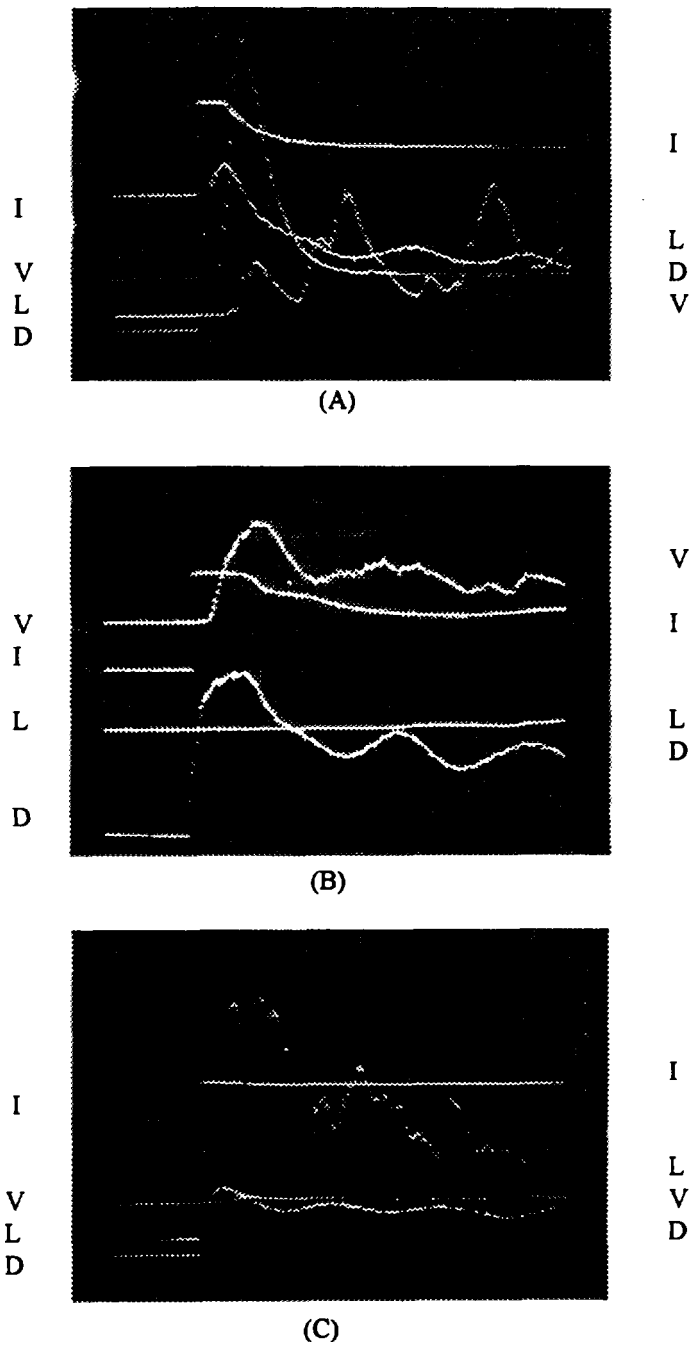

Figure 15: Photos of injection signals: intensity (I), vertical (V), longitudinal (L), peak bunch density (D). (A) is with both instabilities present, (B) with transverse dominant and (C) with microwave dominant. Time scale 0.5 ms/division.

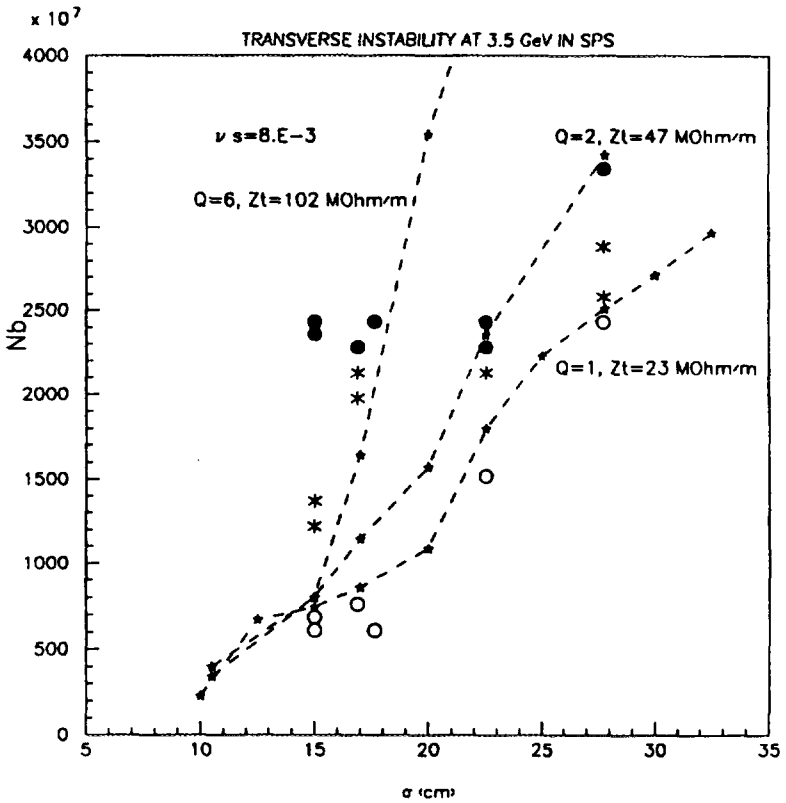

Figure 16: TMC threshold measurements at injection showing the cases of strong (filled circles) and weak (crosses) instability and no instability (empty circles). Calculated thresholds for three different impedance models with $f_{res} = 1.3GHz$.

Transverse Multibunch Modes for Non-Rigid Bunches, Including Mode Coupling *

J. Scott Berg and Ronald D. Ruth
Stanford Linear Accelerator Center, Stanford University, Stanford, CA 94309

Abstract

A method for computing transverse multibunch growth rates and frequency shifts in rings, which has been described previously [1, 2], is applied to the PEP-II B factory. The method allows multibunch modes with different internal-bunch oscillation modes to couple to one another, similar to single-bunch mode coupling. Including coupling between the multibunch modes gives effects similar to those seen in single-bunch mode coupling. These effects occur at currents that are lower than the single-bunch mode coupling threshold.

1 Physical Motivation

Instability due to transverse mode coupling cannot occur unless two requirements are met. First, there must be a mechanism for the rigid ($m = 0$) motion to drive the head-tail ($m = 1$) motion, or vice-versa (only considering coupling between these two modes). In the case of a single bunch, this driving comes about because the head of the bunch sees no wakefield, whereas the tail of the bunch sees the wakefield of the entire bunch. The second requirement is that the frequencies of the two types of motion must be similar so that one mode can resonantly drive the other. In the case of a single bunch, this comes about because the average transverse wake in the bunch usually acts as an effective defocussing force on the bunch centroid, reducing the oscillation frequency of the $m = 0$ mode to the point where it eventually equals the frequency of one of the $m = 1$ modes.

Now consider multibunch modes. A transverse multibunch mode is a mode where each bunch in the train executes identical types of oscillations: for example, rigid oscillations ($m = 0$), or head-tail oscillations ($m = 1$). Calculations up to this point have typically treated these multibunch modes as uncoupled. This paper shows that important effects are missed when coupling between these modes is ignored.

One expects some coupling between the multibunch modes for the reasons outlined in the first paragraph. Consider an $m = 0$ multibunch oscillation. Such an oscillation will induce a wakefield, which in general has a nonzero slope in most places. This nonzero slope means that each bunch sees a different wakefield at the head and the tail. Thus, an $m = 0$ multibunch oscillation can drive an $m = 1$ multibunch oscillation. If the current is high enough and/or the bunches are close enough together so that the wakefields extend from one bunch to the next, the difference in wake seen across one bunch due to previous bunches can be significant, even compared to the difference in wake seen across the bunch due to its own wakefield. This can occur even when the wavelength of the wakefield in question is much longer than the length of the bunch. B factories such as PEP-II at SLAC [3] operate at high currents with a large number of bunches, and thus one might expect this driving to be significant.

A broadband impedance corresponds to a wakefield that is short range; the wakefields do not typically extend from one bunch to the next. Therefore, when only a broadband impedance exists, mode coupling is adequately described by looking at a single bunch. But for narrow-band impedances, such as cavity higher order modes, which correspond to wakefields that extend over long distances, a bunch can create wakefields that are visible to several bunches behind it. Thus, these narrow-band impedances can easily be the mechanism through which the $m = 0$ and $m = 1$ multibunch modes drive one another. The decay time for the cavity higher order modes in the PEP-II B factory is much longer than the time between bunches [3, 4], and thus this driving can be significant.

*Work supported by Department of Energy contract DE–AC03–76SF00515.

Since these narrow-band impedances couple the various bunches together, they also may cause frequency shifts and growth rates in the multibunch modes that are comparable to the synchrotron frequency. Thus, there are multibunch modes whose frequencies are shifted in such a way that the corresponding $m = 0$ and $m = 1$ multibunch mode frequencies coincide at currents that are smaller than the current at which the two modes coincided if only a single bunch was considered. Multibunch mode coupling is therefore expected to give sharp increases in growth rates at currents that are lower than the corresponding current at which single-bunch mode coupling occurs.

2 Basic Formalism

Stability of the beam is determined as follows:

- Start with equally spaced bunches, each bunch having an identical Gaussian bunch distribution.
- Consider small perturbations about that distribution; use the Vlasov equation to obtain an eigenvalue equation for the oscillation frequency of these perturbations.
- If that oscillation eigenvalue has a positive imaginary part, the beam is unstable.

After much manipulation, the resulting eigenvalue equation becomes [1]

$$\phi_m(\Omega) = \sum_{n=0}^{\infty} K_{m+n}(\Omega + p\omega_0) F_n(\Omega) \phi_n(\Omega) \tag{1}$$

$$F_n(\Omega) = \frac{1}{2^n n!} \sum_{k=0}^{n} \binom{n}{k} \frac{[\omega_y - (n-2k)\omega_z]^2}{\Omega^2 - [\omega_y - (n-2k)\omega_z]^2} \tag{2}$$

$$K_k(\omega) = -i \frac{r_0 c^2 \beta_y N M}{\gamma_0 L^2 \omega_y} \sum_{\alpha} \left(\frac{\sigma_\ell}{\beta_0 c} \right)^k (\omega + M\alpha\omega_0)^k Z_\perp(\omega + M\alpha\omega_0) e^{-\sigma_\ell^2 (\omega + M\alpha\omega_0)^2 / \beta_0^2 c^2}, \tag{3}$$

where ω_0 is the angular revolution frequency of the ring, ω_y is the betatron frequency, ω_z is the synchrotron frequency, r_0 is the classical radius of the electron (or the corresponding value for whatever type of particle the beam consists of), c is the speed of light, β_y is the average β function, N is the number of particles in a bunch, M is the number of bunches, γ_0 is the nominal beam energy divided by the rest-mass energy of the particle, L is the length around the ring, σ_ℓ is the bunch length, $\beta_0 c$ is the nominal particle velocity, and $Z_\perp$ is the transverse impedance. The coherent frequency in the bunch frame is Ω, and it will have a positive imaginary part if the beam is unstable. p is an integer index describing the multibunch mode number; it can take on the values $0 \ldots M-1$. A feedback system is modelled by adding an additional term to K_k with $Z_\perp(q\omega_0 + \Omega)$ replaced by $Z_{\mathrm{FB}}(q\omega_0 + \Omega) e^{-2\pi i q \Delta s / L}$, where Z_{FB} is the Fourier transform of the feedback response, and Δs is the distance between the pickup and kicker. Here q is the combination $p + M\alpha$ in equations (1–3). See [1] for more details.

3 Impedance Model Used for PEP-II

A computer program was written that computes the multibunch mode eigenfrequencies as described in [1, 2]; the program is able to use an arbitrary impedance. The transverse impedance used is a sum of several terms, each corresponding to a different source of impedance. Terms for the resistive wall, an inductive part, high-frequency tails for the cavities, and cavity higher order modes are used.

3.1 Resistive Wall

The resistive-wall impedance can be taken directly from [4]. It is given by the formula

$$Z_\perp^{\mathrm{RW}}(\omega) = -i\sqrt{2} \frac{R_{\mathrm{RW}}}{\sqrt{-i\omega/\omega_0}}, \tag{4}$$

where ω_0 is the angular revolution frequency. R_{RW} is 1.175 MΩ/m horizontally, and 1.61 MΩ/m vertically.

3.2 Inductive

Many devices, such as bellows, BPM's, and slots, give an impedance that is primarily inductive. The inductive part is obtained by scaling the longitudinal inductive impedance of 83.3 nH [4] by $2c/\omega b^2$ [5], where b is a characteristic size of the beam pipe. Worst-case values are obtained by performing this scaling with $b = 2.5$ cm (the vertical size of the beam pipe in the bends [3]).

The impedance will not be constant for all frequencies; it is expected to begin to roll off at high frequencies. Since the average behavior at high frequencies is expected to be similar to that of a cavity, a high frequency roll-off of $\omega^{-3/2}$ is used [6]. On average, the roll-off is estimated to be around 10 GHz [6]. Thus, the model

$$Z_{\perp}^{\mathrm{Ind}}(\omega) = \frac{-iL}{(1 - i\omega/\omega_C)^{3/2}} \tag{5}$$

is used, with $L = 83.3$ nH, and $\omega_C = 10$ GHz.

An improvement on this model would be to consider the loss factor from these "inductive" elements as well. The choice of the cutoff also needs further study [7].

3.3 Cavity Tails

It is well known that the longitudinal impedance of a single cavity rolls off at high frequency as $\omega^{-1/2}$ [8]. A simple model with the appropriate high-frequency roll-off is

$$Z_{\parallel}^{\mathrm{Tail}}(\omega) = iA\left[\left(1 + \frac{\omega}{\omega_0 + i\alpha}\right)^{-1/2} - \left(1 - \frac{\omega}{\omega_0 - i\alpha}\right)^{-1/2}\right]. \tag{6}$$

This model is fit to a model of the cavity run through ABCI for $m = 1$ [4, 9] with the known higher order modes removed. The parameters are found to be $A = 45.1344$ kΩ/m, $\omega_0 = 2.4$ GHz, and $\alpha = 1.34722$ GHz [7]. This model for the longitudinal impedance is then turned into a transverse impedance using the Panofsky-Wentzel theorem [5].

Since the cavities are localized, the impedance must be multiplied by the ratio of the average β function at the cavities to the average β function used in equation (3) (typically the average β function of the ring) [1, 10, 11, 12]. For the PEP-II LER, these values are 12.0066 m and 18.5074 m respectively in the vertical direction [13].

3.4 Cavity Higher Order Modes

The transverse cavity higher order modes can be obtained directly from [4]. Each mode is considered to be a single resonator of the form [5]

$$Z_{\perp}^{\mathrm{Res}}(x\omega_R) = \frac{Z_{\mathrm{eff}}}{x + iQ(1 - x^2)}. \tag{7}$$

As for the cavity tails, the impedance must be multiplied by the ratio of the average β function at the cavities to the average β function used in the formulas.

3.5 Other Sources Not Included

Potentially large resonances due to beam position monitors and the interaction region chamber have not been included in this calculation. A preliminary estimate indicates that these resonances will probably have only a small effect, but enough that they should be included in the calculation.

4 Results for PEP-II

The impedance model from section 3 was used to compute multibunch modes as described in [1, 2]. The computations shown here are for the vertical direction in the low-energy ring, which typically gives the worst case results. Table 1 gives the relevant parameters. The operating current assumed in this calculation is 3.159 A, not 3 A, because the higher current is the total beam current that gets the single-bunch current

betatron tune	ν_y, ν_β	37.64
synchrotron tune	ν_s	.03362246
bunch length	σ_ℓ	1 cm
circumference	L	2199.318 m
average β function	$\langle\beta_y\rangle$	18.5074 m
average β function at cavities	$\langle\beta_y\rangle_{\rm CAV}$	12.0066 m
energy	E	2.5 GeV
operating current	I	3 A
number of cavities	$N_{\rm CAV}$	24
r.f. frequency	$f_{\rm RF}$	476 MHz
harmonic number	h	3492
number of bunches	k_B	1658
number of bunch buckets	M	1746
vertical damping time	τ_y	.0576 s

TABLE 1: Parameters for the PEP-II B factory low-energy ring that are used in the calculations here [3, 13]. Note that energy, current, and number of cavities are worst-case values.

right. This current gives the worst-case values for growth rates for multibunch modes when coupling is ignored [14]. Also, getting the single-bunch current right gives the correct results for single-bunch mode coupling. The combination of these two effects would cause one to expect that getting the single-bunch current right will give the worst-case growth rates for multibunch mode coupling as well.

Only the $m = 0$ and $m = 1$ modes are computed in this calculation. Since many of the impedances used have potentially significant contributions at high frequencies, it would be useful to also include terms for higher m (see equation (3) and [15, 16, 17]).

First, for the purposes of comparison, one can examine the results for single-bunch mode coupling, shown in Fig. 1. The single-bunch mode coupling threshold is approximately 14.5 A (8.3 mA per bunch). The behavior of single-bunch mode coupling will determine the average behavior for multibunch mode coupling.

Next, one can compute the frequencies of the multibunch modes. Frequencies for multibunch modes when coupling is not considered are shown in Fig. 2. Narrow-band impedances cause the various multibunch modes to have different frequency shifts; these frequency shifts are approximately centered about the frequency shift due to broadband impedances only, which is what would be seen for only a single bunch. The modes with the largest downward shifts can have the frequencies of their corresponding $m = 0$ and $m = 1$ modes coincide as low as 10 A in this case, much lower than where single-bunch mode coupling occurred. Since there is no coupling between the $m = 0$ and $m = 1$ modes, the frequencies shift almost exactly linearly with current.

If coupling between the $m = 0$ and $m = 1$ multibunch modes is included, the picture of the frequency shifts appears very similar (Fig. 3). The mode frequencies now shift nonlinearly with current, and the frequencies for many modes coincide at even lower currents than if coupling is ignored.

Now consider the growth rates of the multibunch modes. The $m = 0$ modes without mode coupling are shown in Fig. 4. The growth rates increase linearly with current, and are thus nonzero even for small currents. The largest growth rates are significantly larger than growth rates that result from single-bunch mode coupling. Fig. 5 shows the $m = 0$ modes with coupling. Now the growth rates no longer increase linearly with current. Growth rates increase sharply near the single-bunch mode coupling threshold for modes that had low growth rates when coupling wasn't considered. These are modes which don't see any of the narrow-band resonances, and thus involve little bunch-to-bunch coupling; their behavior therefore imitates single-bunch mode coupling. Modes that had high growth rates when mode coupling wasn't considered are affected only slightly by mode coupling because their growth rates were much larger than the characteristic growth rates from mode coupling (see Fig. 1).

The $m = 1$ modes without coupling are shown in Fig. 6. Since coupling is ignored, the growth rates increase linearly with current. The growth rates are much smaller than growth rates that occur once single-bunch mode coupling occurs. Thus, when coupling of the $m = 1$ modes with the $m = 0$ modes is considered, a significant increase in growth rates due to multibunch mode coupling is found, as shown in Fig. 7. Growth rates start to increase sharply at currents close to where the frequencies of the $m = 0$ and $m = 1$ multibunch modes coincided (see Fig. 3). This current is significantly lower than the threshold current for single-bunch

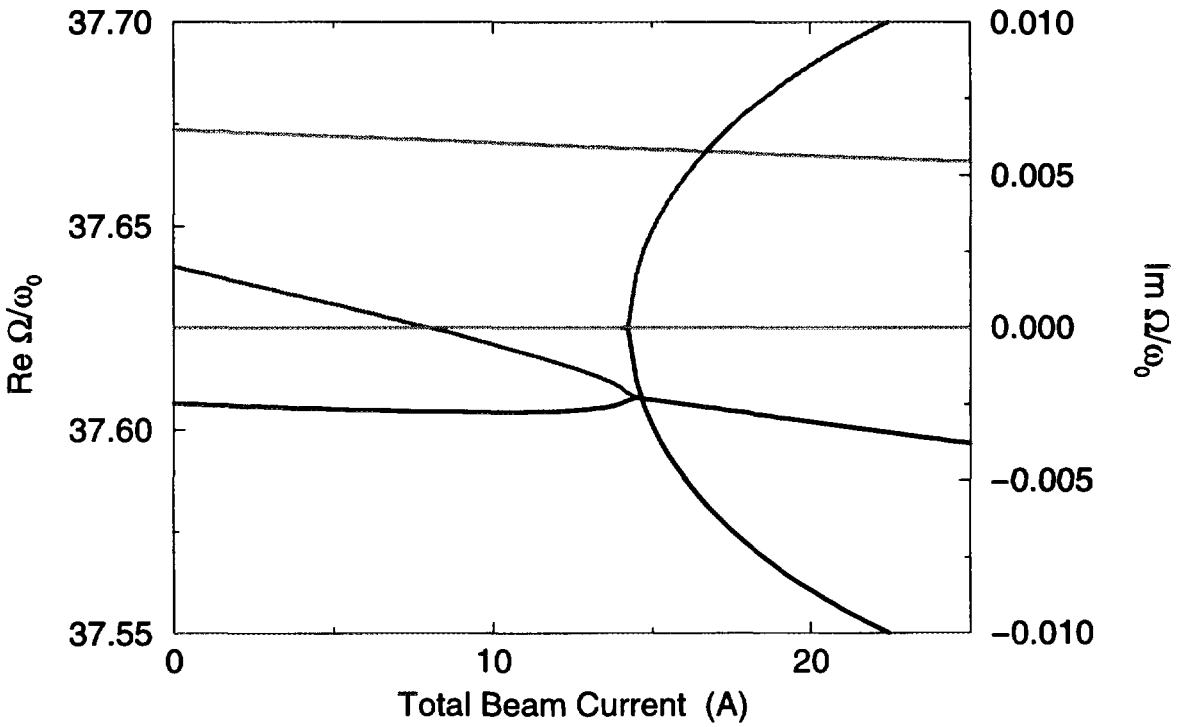

FIGURE 1: Single-bunch mode coupling, plotted versus total beam current for 1746 bunches. Real and imaginary parts of frequencies are shown on the same graph. Real frequencies shift with increasing current until two frequencies coincide. Those frequencies continue to be identical for higher currents. Imaginary parts are zero until the real parts coincide. The imaginary parts then have a nonzero value for higher currents. Note that real and imaginary parts that correspond to the same mode have the same line style.

mode coupling.

Multibunch mode coupling also has an effect at currents below where the mode frequencies coincide. This is because the finite growth rates of the multibunch modes effectively broaden the frequency of a multibunch mode, and thus coupling can occur at currents lower than the current where the real parts of the frequencies are equal. This effect can be seen in Fig. 8. The modes grow nonlinearly with current even at currents much lower than 10 A, which was the lowest current where the mode frequencies coincided (see Fig. 3). This effect can be seen more clearly when looking at the multibunch modes plotted for a fixed current. Fig. 9 shows these modes without coupling, whereas Fig. 10 shows these modes with coupling. These figures are plotted for 3.159 A, well below the 10 A where mode frequencies coincide. Without coupling, the $m = 1$ modes are nearly degenerate. When coupling is added, the growth rates of the $m = 1$ modes change significantly.

A feedback system in PEP-II is designed to damp the transverse rigid motion of the bunches. Such a system operates at relatively low frequencies. Thus, it fails to damp the $m = 1$ growth rates that result from multibunch mode coupling, as shown in Fig. 11.

The main problems that are seen from this analysis of PEP-II are $m = 1$ modes that have growth rates significantly above radiation damping, as can be seen in Fig. 10. These growth rates are primarily caused by cavity higher order modes at 1435 MHz and 1674 MHz. Some Landau damping [18, 19, 20, 21, 22, 23] is expected, but it is not expected to be large enough to damp these modes. Others are studying ways to damp these modes in the cavities.

5 Estimate of Mode Coupling Threshold

The sharp rise in growth rate for multibunch mode coupling occurs about when the real parts of the frequencies of the modes coincide. One can make a first approximation that the main change in the frequencies

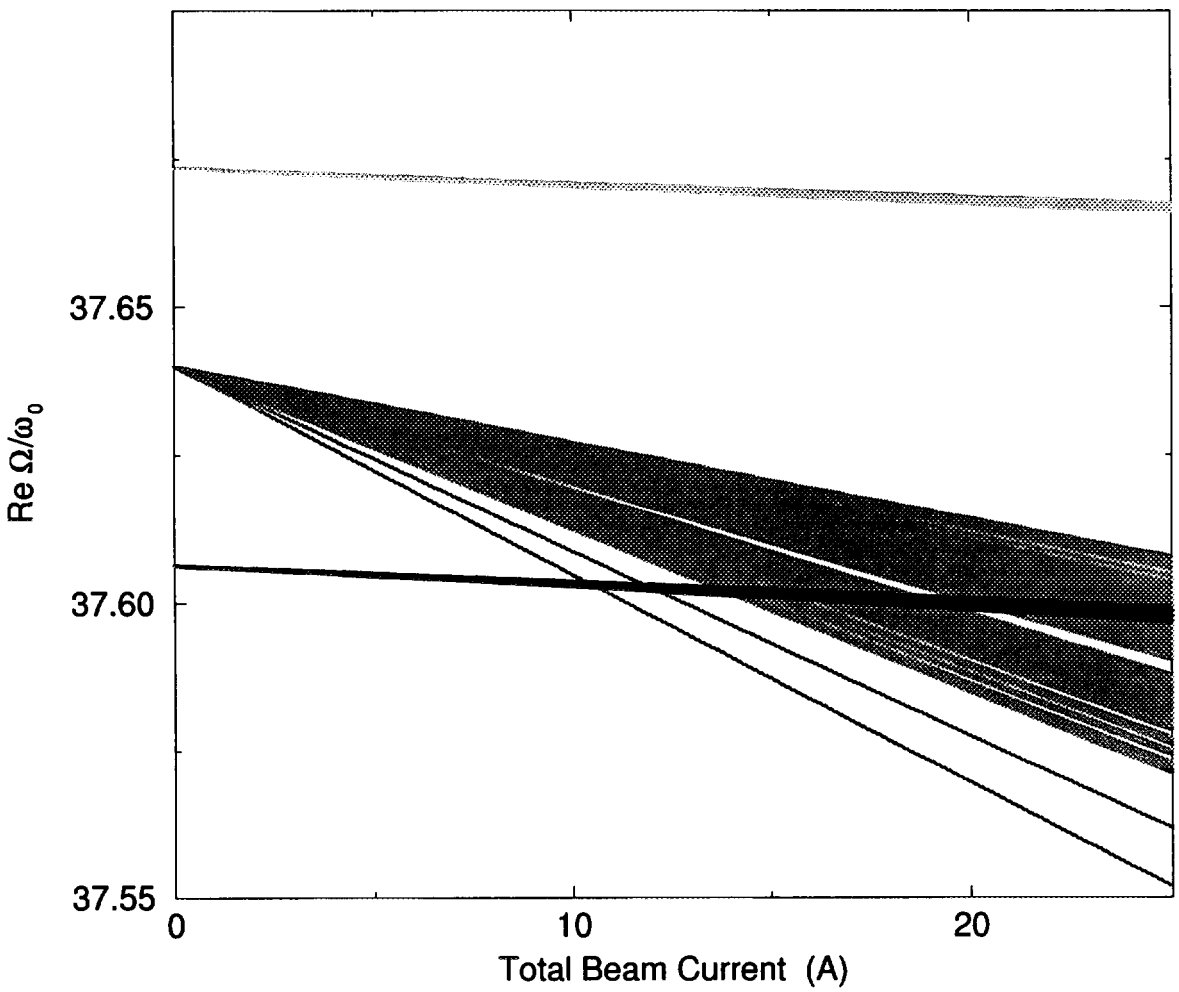

FIGURE 2: Multibunch mode frequencies, without coupling. Shown are three "fans" of 1746 lines each. Each line is the frequency of a single multibunch mode plotted versus current. The upper and lower fans contain the $m = 1$ modes, while the middle fan contains the $m = 0$ modes.

of the modes is in the shift in the $m = 0$ mode, ignoring coupling [10, 24]. Thus, once the frequency shift of the $m = 0$ mode is equal to $-\omega_s$, instability is expected.

Using equations (1–3) to compute the frequency shift of the $m = 0$ mode, the threshold current is approximately

$$I_{\rm th} = -4\pi\nu_s\beta_0^2\frac{E/e}{\beta_y Z_{\rm eff}} \tag{8}$$

$$Z_{\rm eff} = \sum_\alpha Im\left\{Z_\perp\left(\Omega + (p_0 + M\alpha)\omega_0\right)\right\} e^{-\sigma_t^2[\Omega+(p_0+M\alpha)\omega_0]^2/\beta_0^2c^2}. \tag{9}$$

The contribution to $Z_{\rm eff}$ can be separated into a piece due to broadband impedances, and a piece due to narrow-band impedances.

The piece due to broadband impedances is assumed to vary slowly, even over the scale of the bunch frequency $M\omega_0$. Thus, $Z_{\rm eff}$ can be approximated as an integral

$$Z_{\rm eff}^{\rm BB} \approx \frac{1}{M\omega_0}\int Im\left\{Z_\perp(\omega)\right\} e^{-\sigma_t^2\omega^2/\beta_0^2c^2} d\omega. \tag{10}$$

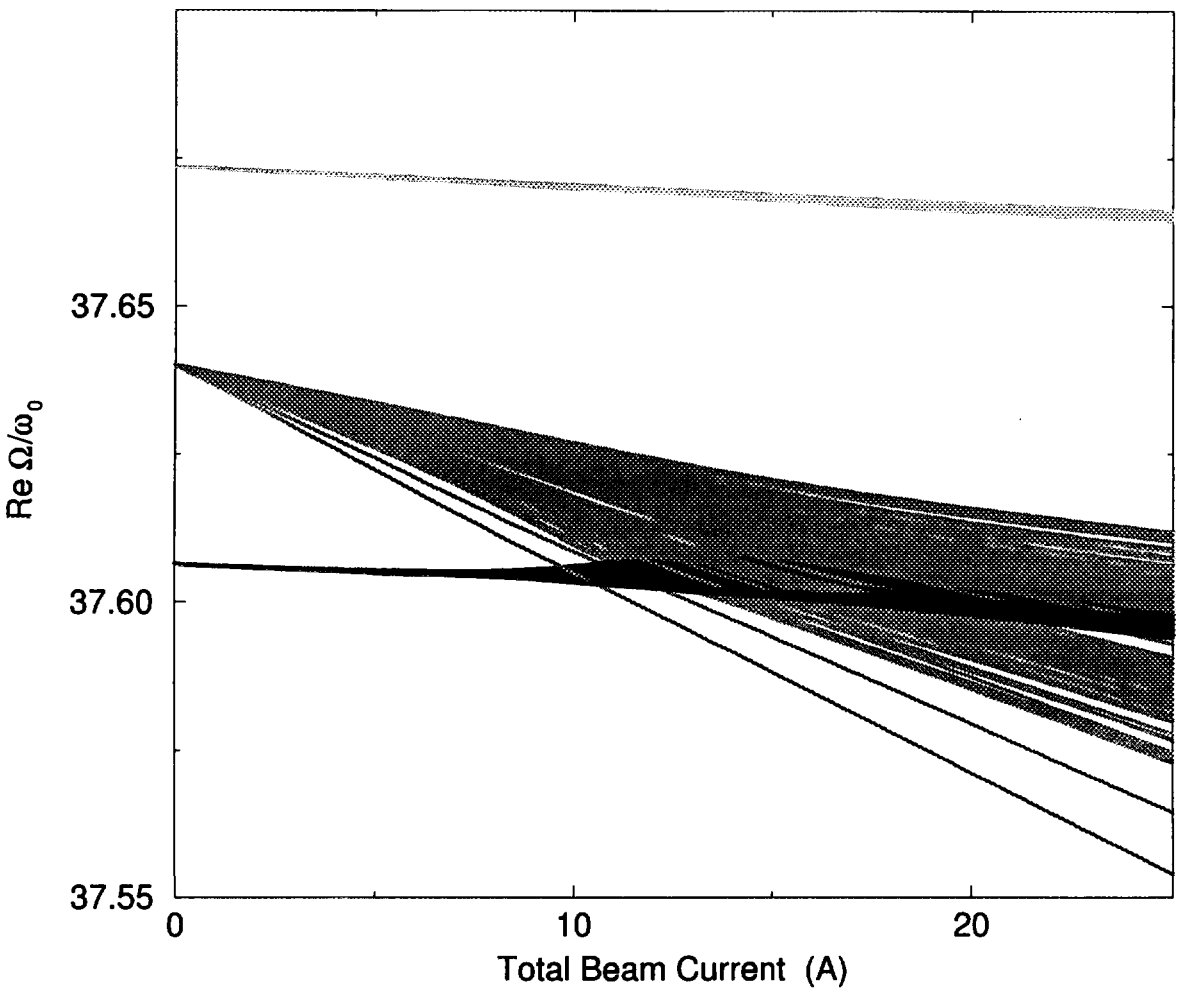

FIGURE 3: Multibunch mode frequencies, with coupling. Compare with Fig. 2.

Note that the $1/M$ dependence makes the threshold current per bunch independent of the number of bunches, as expected. If the broadband impedance is assumed to be constant over the bunch spectrum, this simplifies to

$$Z_{\text{eff}}^{\text{BB}} \approx \frac{L}{2\sqrt{\pi}M\sigma_\ell} Im\{Z_\perp\} \tag{11}$$

If the main contribution to the impedance is from a scaled inductance of 83.3 nH as in section 3.2 (ignoring the roll-off), Eqs. (8) and (11) predict a Z_{eff} of 2.84 MΩ/m, and therefore a mode coupling threshold of approximately 20.1 A. This result compares favorably to the actual threshold of 14.5 A, especially considering that many other sources of impedance have been ignored.

The contribution to Z_{eff} from narrow-band impedances can be computed by taking the peak of the narrow-band impedance. In most cases, it is only necessary to take a single term. However, if impedances are separated by a multiple of the bunch frequency, then they must be added together. The largest narrow-band impedance in PEP-II is the peak of the resistive wall, which is at 2.68 MΩ/m. Adding this to the Z_{eff} from the broadband impedance gives a mode coupling threshold of 10.33 A. This threshold agrees very well with where the mode coupling is beginning to have its strongest increase (see Figs. 3 and 7).

These estimates must be considered approximate, not only because other sources of frequency shift (from the coupling term, for instance) have been ignored, but also because mode coupling doesn't give a sharp threshold in the multibunch case; the effect occurs even at currents lower than where the frequencies coincide.

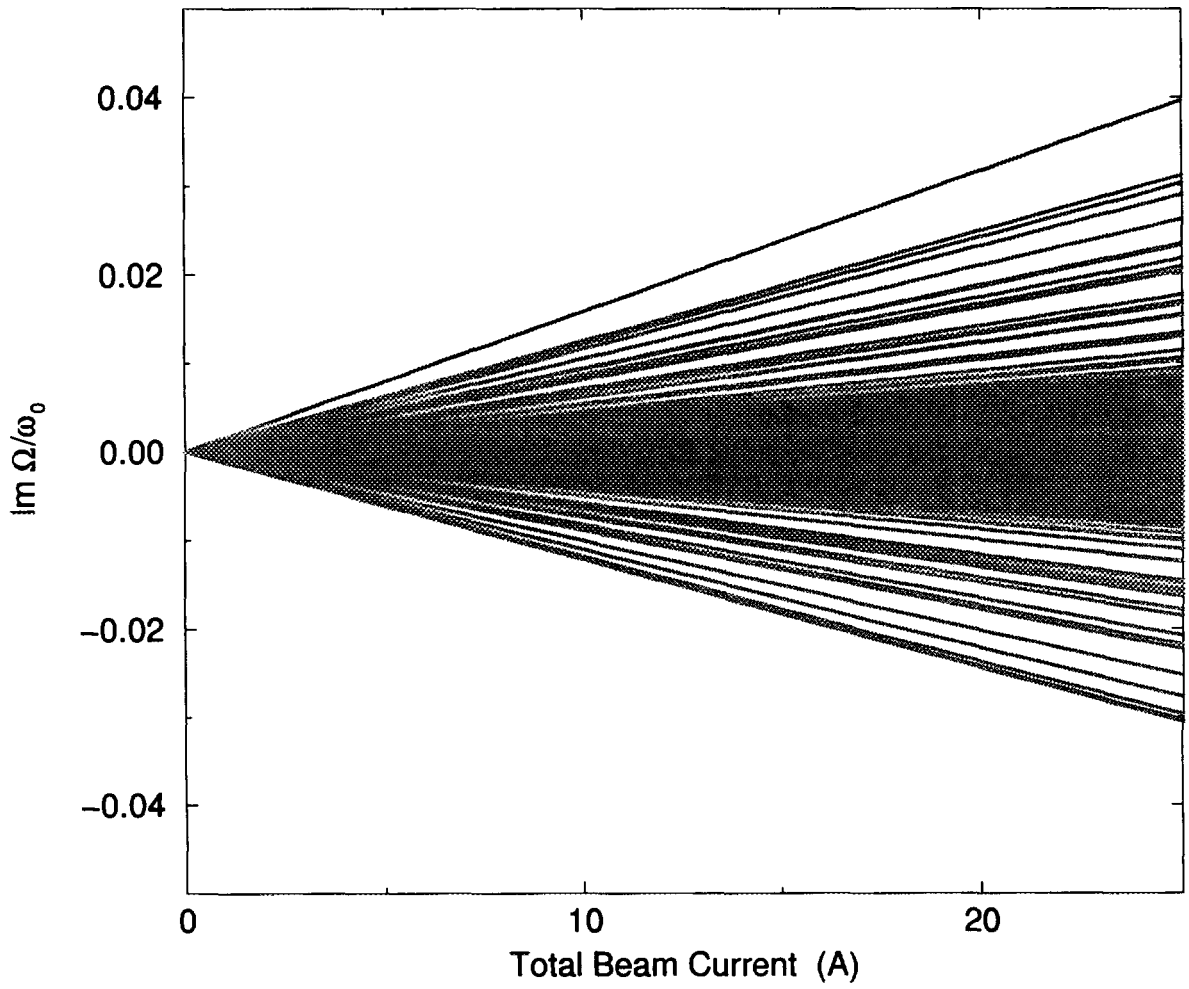

FIGURE 4: Multibunch $m = 0$ growth rates, no coupling. All 1746 modes are shown.

6 Conclusions

Multibunch mode coupling can cause significant increases in the growth rates of multibunch modes. The strongest effects are seen in $m = 1$ multibunch modes. The effect occurs at currents that are lower than the current where mode coupling would occur if only a single bunch were considered. The effect can be significant even well below the current where the frequencies of the multibunch modes coincide, although its strength increases rapidly at that current.

While this effect is fairly small in PEP-II, it is also clear that this machine is pushing the boundary of the importance of multibunch mode coupling.

References

[1] J. S. Berg and R. D. Ruth. "Transverse instabilities for multiple nonrigid bunches in a storage ring." SLAC-PUB-95-6829, Stanford Linear Accelerator Center, Stanford, CA (1995). To appear in Phys. Rev. E.

[2] J. S. Berg and R. D. Ruth. "Transverse Multibunch Instabilities for Non-Rigid Bunches." SLAC-PUB-95-6830, Stanford Linear Accelerator Center, Stanford, CA (1995). Presented at the 16th IEEE Particle

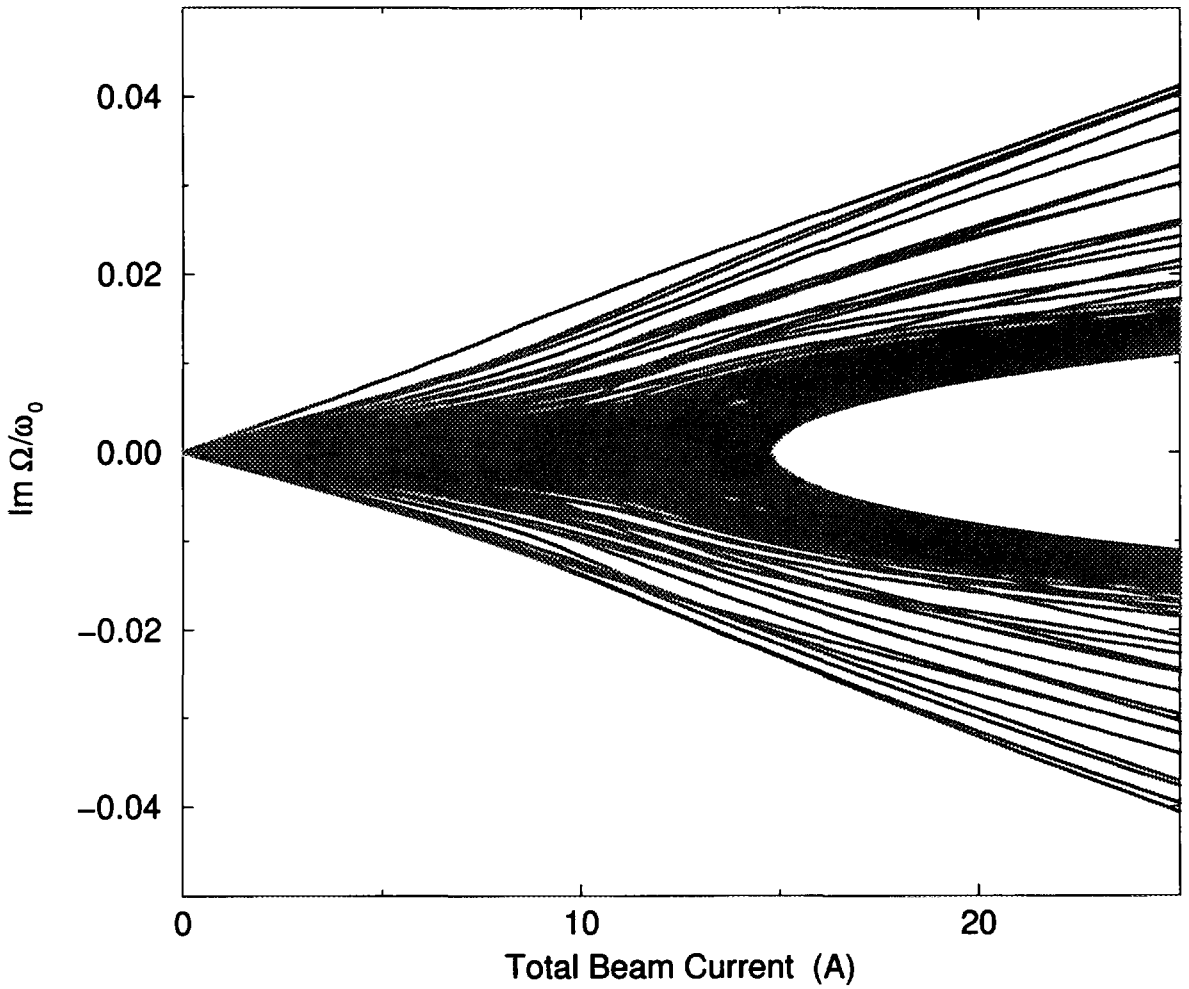

FIGURE 5: Multibunch $m = 0$ growth rates, with coupling.

Accelerator Conference (PAC95) and International Conference on High-Energy Accelerators, Dallas, Texas, May 1-5, 1995.

[3] "PEP-II An Asymmetric *B* Factory, Conceptual Design Report." SLAC-418, LBL-PUB-5379, CALT-68-1869, UCRL-ID-114055, UC-IIRPA-93-01 (1993).

[4] S. Heifets, et al. "Impedance Study for the PEP-II *B*-factory." SLAC/AP-99, Stanford Linear Accelerator Center, Stanford, CA (1995).

[5] A. W. Chao. *Physics of Collective Beam Instabilities in High Energy Accelerators.* John Wiley & Sons, Inc., New York (1993).

[6] S. Heifets. Private communication.

[7] J. S. Berg. "Observations Involving Broadband Impedance Modelling." In these proceedings.

[8] S. A. Heifets and S. A. Kheifets. "High-frequency Limit of the Longitudinal Impedance of an Array of Cavities." Phys. Rev. D, **39**(3), 960–970 (1989).

[9] Y. H. Chin. "User's Guide for ABCI Version 8.8 (Azimuthal Beam Cavity Interaction)." LBL-35258, Lawrence Berkeley Laboratory, Berkeley, CA (1994).

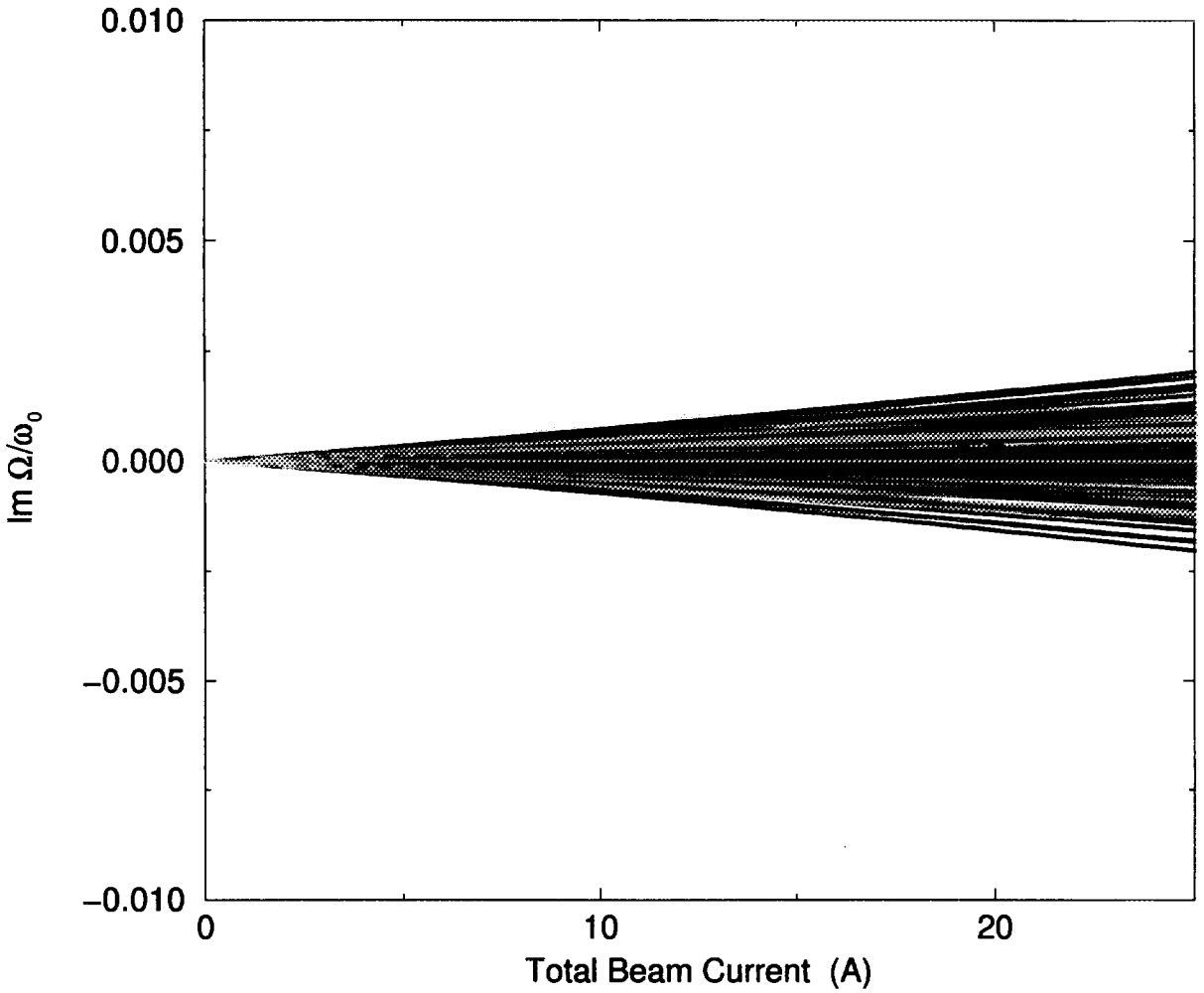

FIGURE 6: Multibunch $m = 1$ growth rates, no coupling. The 3492 mode lines correspond to two sets of 1746 $m = 1$ modes.

[10] K. Satoh and Y. Chin. "Transverse Mode Coupling in a Bunched Beam." Nucl. Instrum. and Methods, **207**, 309–320 (1983).

[11] Y. H. Chin. "Coherent Synchro-Betatron Resonances Driven by Localized Wake Fields." CERN-SPS/85-33, CERN, Geneva, Switzerland (1985).

[12] T. Suzuki. "Transverse Mode Coupling Instability Due to Piecewise Constant Impedances." CERN-LEP-TH/87-55, CERN, Geneva, Switzerland (1987).

[13] Y. Cai. Private communication.

[14] R. D. Kohaupt. "On Multi-bunch Instabilities for Fractionally Filled Rings." DESY-85-139, DESY, Hamburg, Germany (1985).

[15] T. Linnecar and E. N. Shaposhnikova. "Analysis of the Transverse Mode Coupling Instability of the Leptons in the SPS." CERN/SL/93-43 (RFS), CERN, Geneva, Switzerland (1993).

[16] T. P. R. Linnecar and E. N. Shaposhnikova. "The Transverse Mode Coupling Instability and Broadband Impedance Model of the CERN SPS." In V. Suller and C. Petit-Jean-Genaz, editors, *Fourth European Particle Accelerator Conference*, Vol. 2, pp. 1093–1095, Singapore (1994). World Scientific.

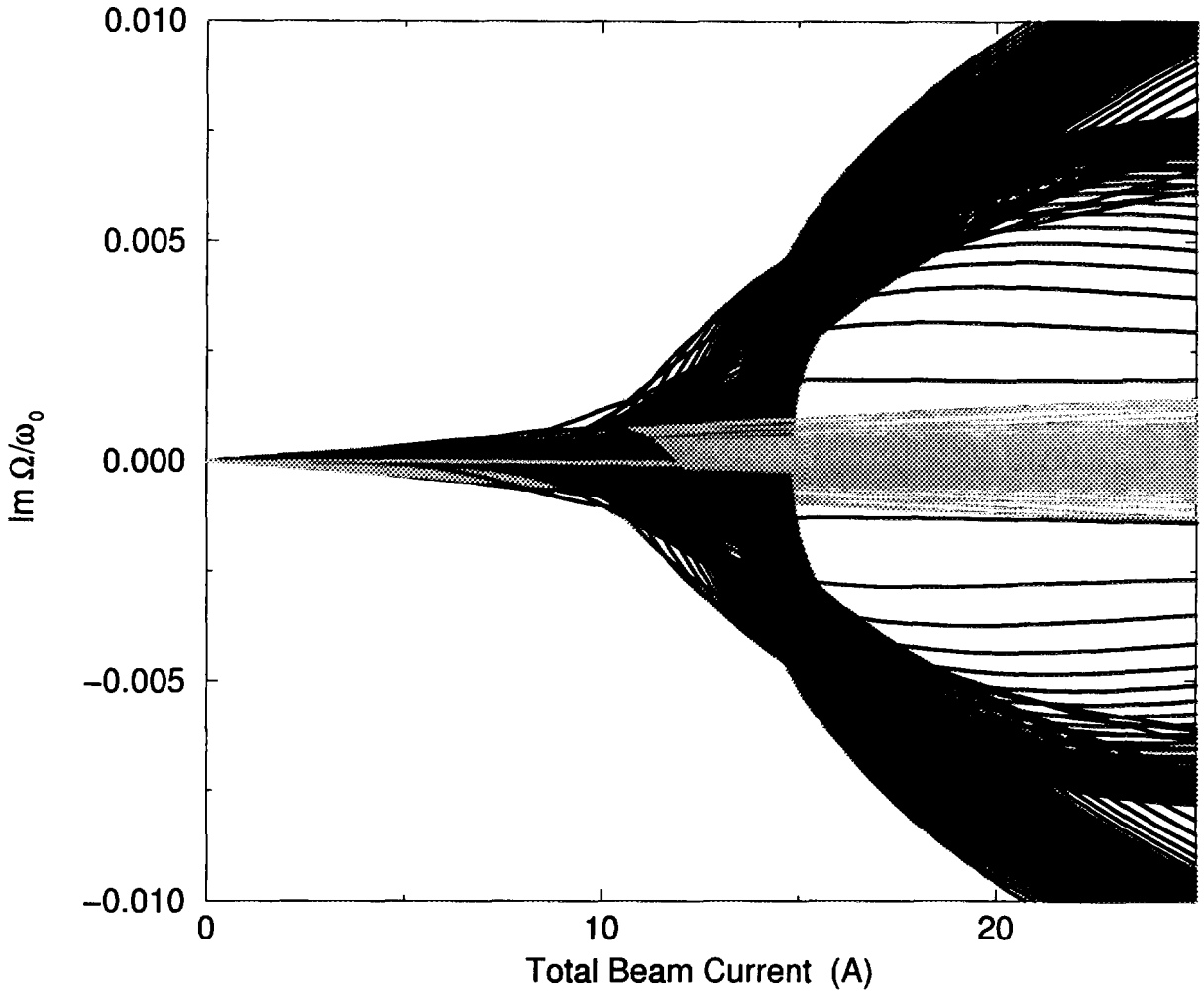

FIGURE 7: Multibunch $m = 1$ growth rates, with coupling. Lighter shaded lines are $\nu_\beta + \nu_s$ lines, darker lines are $\nu_\beta - \nu_s$ lines.

[17] T. Linnecar and E. N. Shaposhnikova. "Transverse Mode Coupling Instability of the Leptons in the CERN SPS." In these proceedings.

[18] H. G. Hereward. "Landau Damping by Non-linearity." CERN/MPS/DL 69-11, CERN, Geneva, Switzerland (1969).

[19] Y. Chin, K. Satoh, and K. Yokoya. "Instability of a Bunched Beam with Synchrotron-frequency Spread." Part. Accel., **13**, 45–66 (1983).

[20] Y. H. Chin. "Hamiltonian Formulation for Transverse Bunched Beam Instabilities in the Presence of Betatron Tune Spread." CERN SPS/85-9, CERN, Geneva, Switzerland (1985).

[21] Y. H. Chin and K. Yokoya. "Landau Damping of a Multi-bunch Instability due to Bunch-to-bunch Tune Spread." DESY 86-097, DESY, Hamburg, Germany (1986).

[22] M. S. Zisman, S. Chattopadhyay, and J. J. Bisognano. "ZAP User's Manual." LBL-21270 and UC-28, Lawrence Berkeley Laboratory, Berkeley, CA (1986).

[23] K. A. Thompson and R. D. Ruth. "Transverse Couplied-bunch Instabilities in Damping Rings of High-energy Linear Colliders." Phys. Rev. D, **43**(9), 3049–3062 (1991).

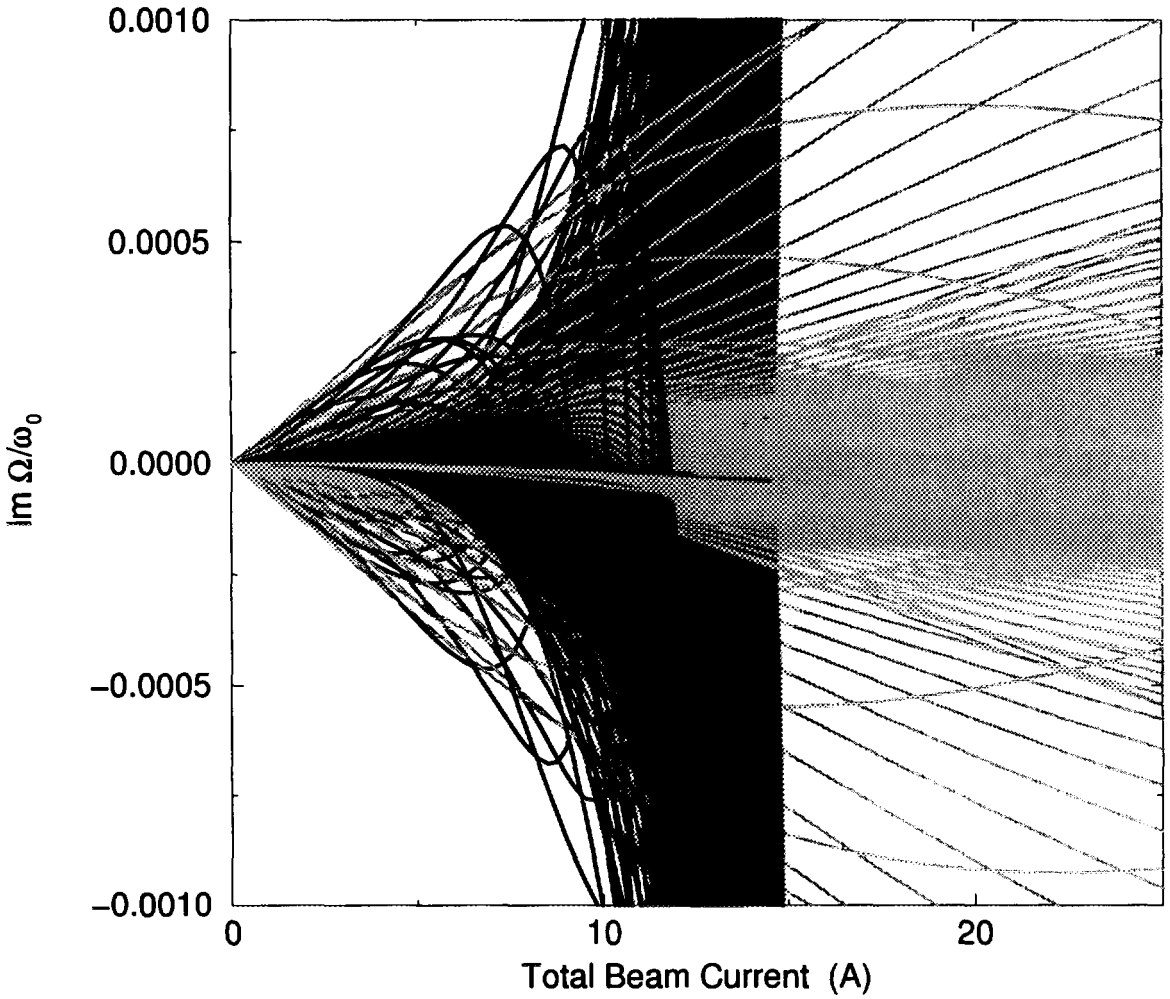

FIGURE 8: Multibunch $m = 1$ growth rates, with coupling. Vertical scale blown up a factor of 10 from Fig. 7.

[24] B. Zotter. "Limitations of Bunch-current in LEP by Transverse Mode-coupling." IEEE Trans. Nucl. Sci., **NS-30**(4), 2519–2521 (1983).

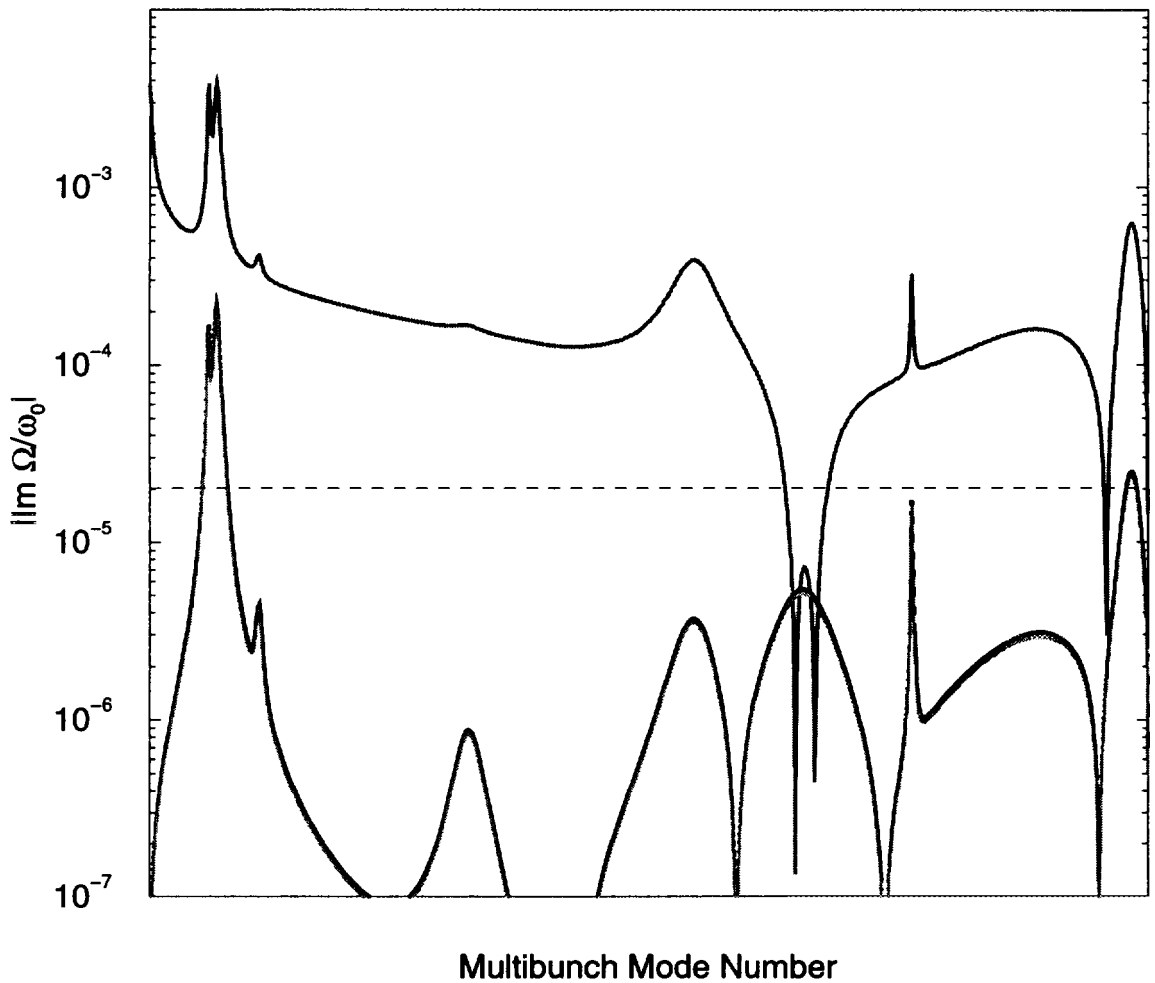

FIGURE 9: Multibunch modes at 3.159 A total beam current. Coupling is ignored. Note that the two $m = 1$ modes are nearly degenerate. The horizontal axis is the frequency offset of the mode. The lines are actually 873 points connected by lines.

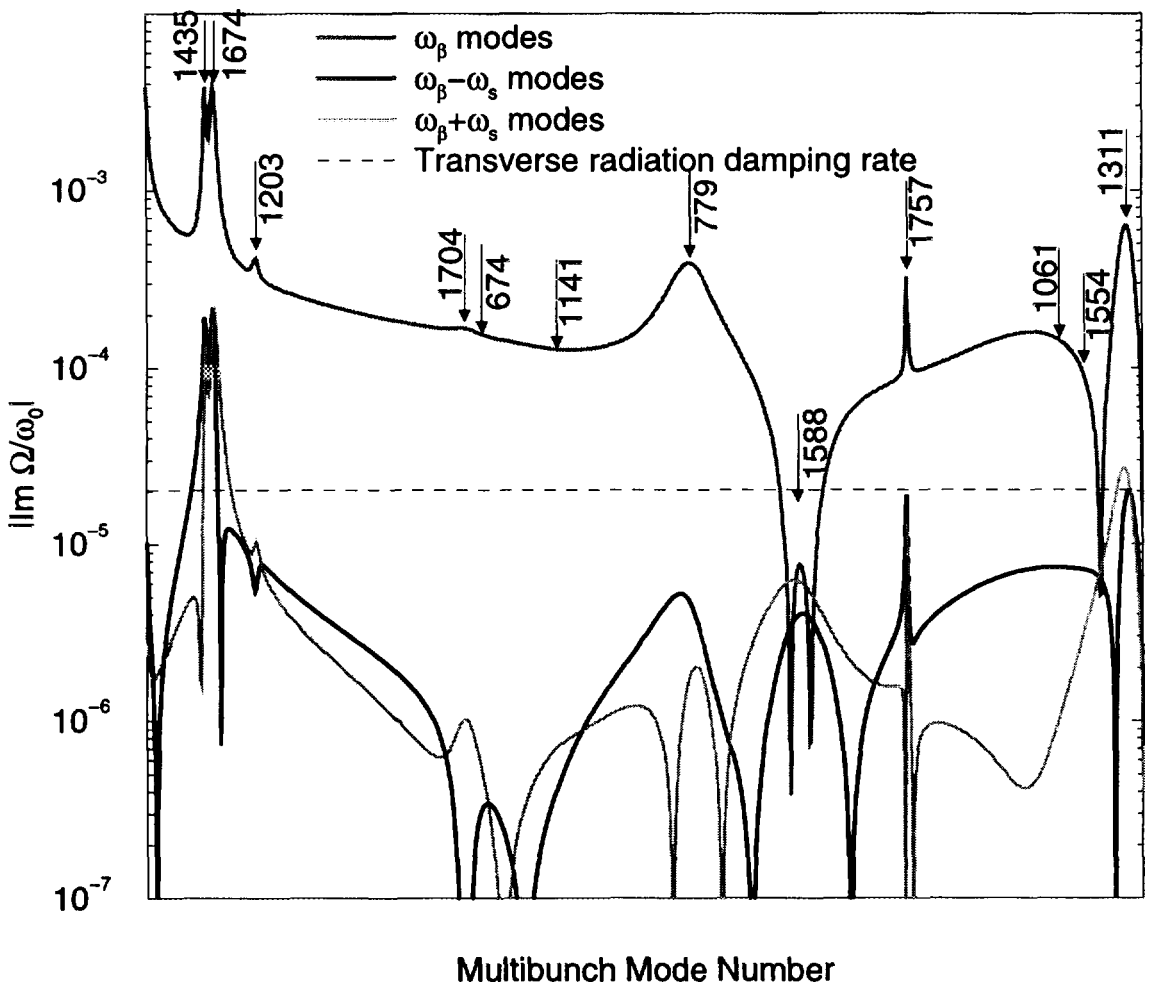

FIGURE 10: Multibunch modes at 3.159 A total beam current, with coupling. Arrows are numbered with the frequencies (in MHz) of the cavity higher order modes. The horizontal axis is the frequency offset of the mode. The large peak corresponding to the 1435 MHz cavity mode is enhanced nontrivially by multibunch mode coupling.

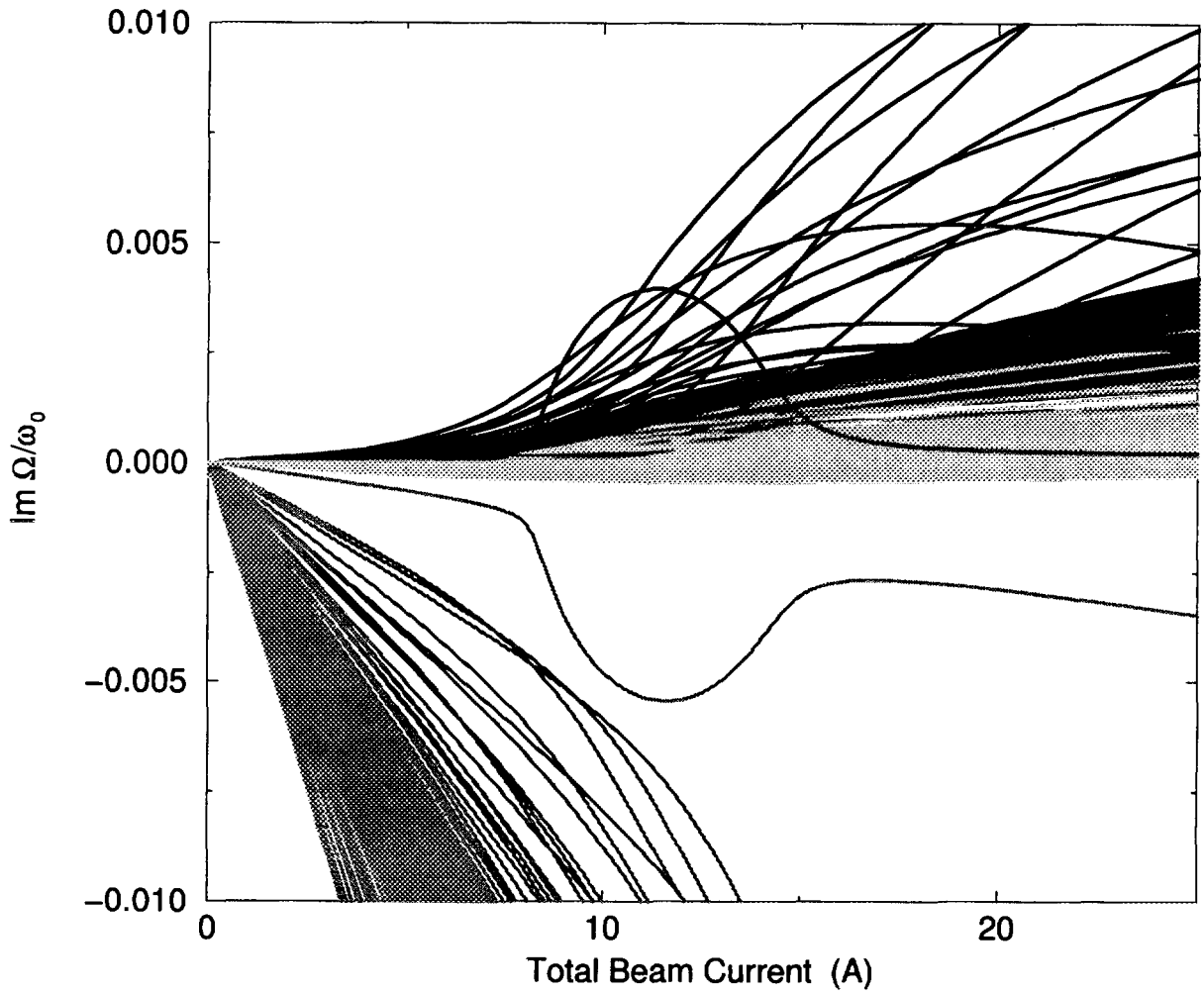

FIGURE 11: Multibunch growth rates, with feedback. The feedback is modelled as a Gaussian response about zero frequency with standard deviation of 125 MHz. Lower lines are $m = 0$ growth rates, upper lines are $m = 1$.

Simple Model with Damping of the Mode-Coupling Instability

D.V. Pestrikov
Budker Institute for Nuclear Physics,
630090 Novosibirsk, Russian Federation

Abstract

In this paper we use a simple model to study the suppression of the transverse mode-coupling instability. Two possibilities are considered. One is due to the damping of particular synchrobetatron modes, and another – due to Landau damping, caused by the nonlinearity of betatron oscillations.

1 Introduction

Presumably after paper [1] the transverse mode-coupling instability was recognized as a universal phenomenon that can limit the bunch intensity in large storage rings. As is known, this instability occurs due to merging of frequencies of the bunch synchrobetatron modes and thus, it can take place even for reactive coupling of the beam with its surroundings. In contrast to the head-tail instability, whose increments for very short bunches linearly decrease with a decrease in the bunch length, the increments of the mode-coupling instability may have weaker dependences on the bunch length, so that this instability will dominate for short bunches (see, for instance, in Ref.[2]). The last circumstance can be very important for operation of future electron-positron factories, where the bunch lengths (σ_s) must be comparable, or less than the β-function at the interaction point (typically, in the range $\sigma_s \leq 1$ cm).

If the beam interacts with a non-resonant environment, the description of the mode-coupling instability generally demands solution of an infinite system of the coupled integral equations. In many cases, an expansion of unknown eigenfunctions in some orthogonal polynomials is employed in order to replace initial system by an equivalent system of algebraic equations. Approximate solution of these equations enables then the calculation of instability increments and stability criteria of modes. Typically, these are calculated ignoring the effect of the frequency spreads in the beam and corresponding Landau damping of modes.

In this paper we study the suppression of the synchrobetatron mode-coupling instability due to the damping of particular modes as well as due to Landau damping. In colliders the necessary frequency spread in the beams can be enhanced by the non-linearity of the

beam-beam interaction. In order to focus on the properties of the mode-coupling instability below we perform the calculations for a simplified solvable model, suggested in Ref.[3].

2 General Equations

We assume that incoherent oscillations of particles in the bunch are described by usual equations (see, for example, in Ref.[4])

$$z = \sqrt{\frac{2IR}{p\nu_z}}\cos\psi_z, \quad p_z = \frac{p}{R}\frac{dz}{d\theta}, \tag{2.1}$$

$$\theta = \omega_0 t + \varphi\cos\psi_s, \quad \dot{\psi}_z = \omega_z = \omega_0\nu_z, \quad \dot{\psi}_s = \omega_s = \omega_0\nu_s.$$

Here, $2\pi R$ is the closed orbit perimeter, p is the particle momentum, ω_0 is the revolution frequency of the synchronous particle. We consider the modes, when the bunch executes the dipole vertical betatron coherent oscillations and assume that the bunch wake fields decay much faster than the particle revolution period in the ring ($2\pi/\omega_0$). Then, a solution of the linearized Vlasov equation

$$f(I,\psi_z,\varphi,\psi_s,t) = \rho(\varphi)f_0(I) + \delta f(I,\psi_z,\varphi,\psi_s,t),$$

$$\delta f = \frac{\sqrt{I}(\partial f_0/\partial I)}{\omega - m_z\omega_z - m_s\omega_s}\sum_{m_z=\pm1}\sum_{m_s=-\infty}^{\infty}\chi_m(\varphi)e^{im_z\psi_z + m_s\psi_s - i\omega t}$$

results in the following infinite system of coupled equations for synchrobetatron modes of the bunch (see, for example, in Ref.[5])

$$\chi_m = \rho(\varphi)\sum_{m_s'=-\infty}^{\infty}F(\omega - m_s'\omega_s)\int_0^{\infty}d\varphi'\varphi' K_{m_s,m_s'}(\varphi,\varphi')\chi_{m_s'}(\varphi'),$$

$$K_{m_s,m_s'}(\varphi,\varphi') = \int_{-\infty}^{\infty}dn\Omega_m(\omega_{mn})J_{m_s}(n_1\varphi)J_{m_s'}(n_1\varphi'), \quad n_1 = n + m_z\frac{d\omega_z}{d\omega_0}, \tag{2.2}$$

$$F(\omega) = -\int_0^{\infty}dI\frac{I\partial f_0/\partial I}{\omega - \omega_z(I)}, \quad \mathrm{Im}\omega > 0.$$

Here, $\rho(\varphi)$ is the beam distribution in amplitudes of synchrotron oscillations of particles, f_0 is the distribution function in amplitudes of betatron oscillations. If we assume the interaction with localized wake fields, the value $\Omega_m(\omega_{mn})$ is expressed in terms of the so-called transverse coupling impedance of the electrodes, surrounding the beam

$$\Omega_m(\omega_{mn}) = -m_z\frac{Ne^2\omega_0}{4\pi p\nu_z}Z_\perp(\omega_{mn}), \quad \omega_{mn} = m_z\omega_z + n\omega_0, \quad m_z = \pm1. \tag{2.3}$$

In order to simplify the studying of phenomena related to the coupling of synchrotron coherent modes we consider the model [3], where

$$\rho(\varphi) = \delta(\varphi_0^2 - \varphi^2), \quad \Omega_m(n) = \frac{i\Omega_m}{\pi(n + i\Delta)}, \tag{2.4}$$

and the ring chromaticity is zero ($d\nu_z/d\omega_s = 0$). In such a model we have

$$\chi_m(\varphi) = C_m \delta(\varphi_0^2 - \varphi^2), \tag{2.5}$$

so that the system of integral equations in (2.2) is replaced by the infinite system of algebraic equations for amplitudes C_m

$$C_m = \frac{i\Omega_m}{\pi} \sum_{m_s'=-\infty}^{\infty} C_{m'} F(\omega - m_s'\omega_s) \int_{-\infty}^{\infty} \frac{dn}{n + i\Delta} J_{m_s}(n\varphi_0) J_{m_s'}(n\varphi_0). \tag{2.6}$$

Using

$$\lim_{\Delta \to 0} \frac{1}{n + i\Delta} = \mathcal{P}\frac{1}{n} - i\pi\delta(n),$$

where $\mathcal{P}$ means the calculation of the Cauchy principal value of integrals,

$$J_{2p}(n) = J_{2p}(-n), \quad J_{2p}(n) = J_{-2p}(n),$$

$$J_{2p+1}(n) = -J_{2p+1}(-n), \quad J_{-2p-1}(n) = -J_{2p+1}(n),$$

and that

$$\int_0^{\infty} \frac{dn}{n} J_{2p}(n) J_{2k+1}(n) = \frac{(-1)^{k-p} 2}{\pi[(2k+1)^2 - 4p^2]}.$$

we rewrite Eqs(2.6) in the following form

$$C_0[1 - wF(x)] = \frac{4iw}{\pi^2} \sum_{k=0}^{\infty} \frac{C_{2k+1}}{(2k+1)^2} [F(x - 2k - 1) + F(x + 2k + 1)],$$

$$C_{2k+1} = \frac{4iw}{\pi^2} \frac{C_0 F(x)}{(2k+1)^2} + \frac{4iw}{\pi^2} \sum_{p=1}^{\infty} \frac{C_{2p}}{(2k+1)^2 - 4p^2} [F(x - 2p) + F(x + 2p)], \tag{2.7}$$

$$C_{2p} = \frac{4iw}{\pi^2} \sum_{k=0}^{\infty} \frac{C_{2k+1}}{(2k+1)^2 - 4p^2} [F(x - 2k - 1) + F(x + 2k + 1)],$$

$$C_{-2k-1} = -C_{2k+1}, \quad C_{-2p} = C_{2p}.$$

Here,

$$x = \frac{\Delta\omega_m}{\omega_s}, \quad w = \frac{\Omega_m}{\omega_s}.$$

If we neglect in these equations the mode-coupling ($|\Omega_m| \ll \omega_s$) and Landau damping, the eigenvalues of the problem read

$$x_{m_s} = \begin{cases} w, & m_s = 0, \\ m_s, & m_s \neq 0, \end{cases} \tag{2.8}$$

This solution clarifies the sense of the value Ω_m as the coherent frequency shift of the betatron mode. If we take into account in Eqs(2.7) Landau damping and ignore the mode-coupling, the dispersion equation for betatron mode reads

$$1 = -\Omega_m \int_0^\infty dI \frac{I\partial f_0/\partial I}{\omega - \omega_z(I)}, \quad \mathrm{Im}\omega > 0, \tag{2.9}$$

3 Monochromatic modes

If we neglect Landau damping (taking, for instance, $d\omega_z/dI = 0$ and, therefore, $F(\omega) = 1/(\omega - m_z\omega_z)$, then Eqs(2.7) can be solved more or less easily [3]. The result is expressed in terms of some dispersion equation, which enables the calculation of eigenfrequencies and stability criteria for modes without Landau damping. In this case, the instability occurs due to subsequent merging of the betatron ($\omega \simeq m_z\omega_z$) and some of neighbor synchrobetatron mods ($\omega \simeq m_z\omega_z \pm \omega_s$). This general solution has maybe more academic than a practical worth. A simplified stability criterion without Landau damping can be calculated assuming $|w| < 1$ and taking into account the coupling of the closest neighbor modes only. If we take, for example, $\Omega_m > 0$, the simplified equations describing the coupling of the betatron and of the first synchrobetatron mode read

$$\begin{aligned} (x - w)C_0 &= i\frac{4w}{\pi^2}C_1, \\ (x - 1)C_1 &= i\frac{4w}{\pi^2}C_0. \end{aligned} \tag{3.10}$$

According to Eqs (3.10) the eigenfrequencies of the coupled modes can be found as the roots of the following dispersion equation

$$(x - w)(x - 1) = -\frac{16w^2}{\pi^4}, \tag{3.11}$$

which read

$$x_{1,2} = \frac{1 + w}{2} \pm \sqrt{\frac{(1 - w)^2}{4} - \frac{16w^2}{\pi^4}}. \tag{3.12}$$

This expression shows that both modes will be stable provided that

$$(1 - w)^2 - \frac{64w^2}{\pi^4} \geq 0. \tag{3.13}$$

Above the threshold current, which can be calculated from this condition, the frequencies of the coupled modes merge (see in Fig.1) and one of the eigensolutions becomes unstable. The stability condition generally does not depend on the sign of Ω_m. If $\Omega_m > 0$, unstable are the betatron and the first synchrobetatron modes; if $\Omega_m < 0$, unstable are the betatron and the -1st synchrobetatron modes. In both cases the instability occurs, when

$$|w| > \frac{1}{1 + 8/\pi^2} \approx 0.552. \tag{3.14}$$

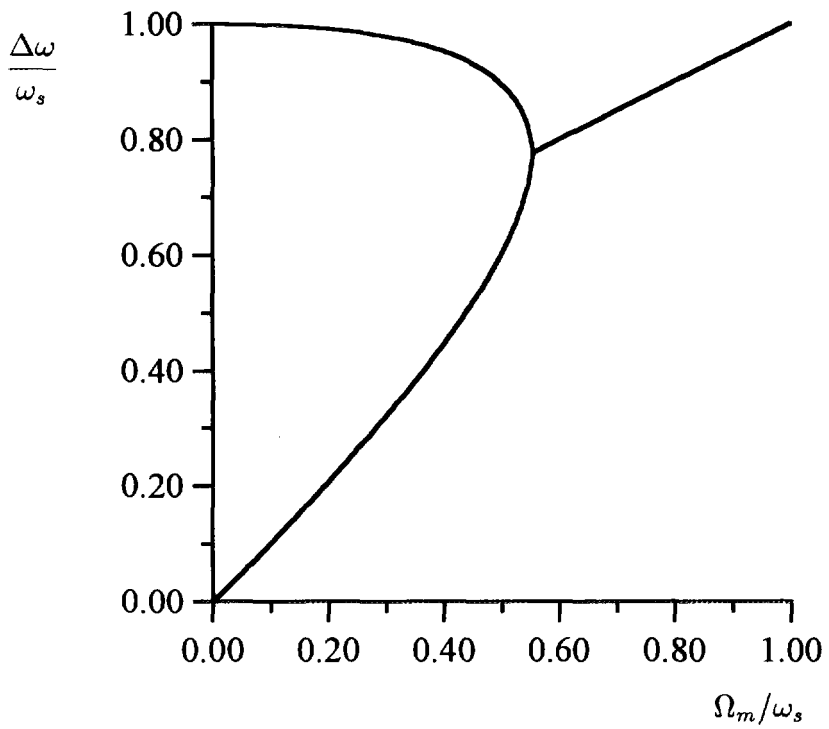

Figure 1: Dependences of coherent frequency shifts of the betatron and of the first synchrobetatron modes on the bunch current (Ω_m).

Let us now consider the damping of this instability due to damping of the coupled modes. That can be the synchrotron radiation damping, or the damping of coherent oscillations due to interaction with special system, affecting particular modes of the bunch. If we denote as Δ_1 and Δ_0 the frequency shifts of the coupled modes, then unstable modes obey the 'resonant condition' of the sum-type resonance:

$$\omega_s = \Delta_1 + \Delta_0.$$

For this reason, the coupling-mode instability can be suppressed only in the case, when both coupled modes are damped. As was shown in [6] this is a generic property of such kind of the coupled-mode instability. Here, we can illustrate this fact using the following simple calculations. Let λ_0 be the decrement of the betatron mode, while λ_1 - of the first synchrobetatron mode. Then, Eq.(3.11) can be rewritten as

$$(x - w + i\lambda_0)(x - 1 + i\lambda_1) = -\frac{16w^2}{\pi^4}. \tag{3.15}$$

The roots of this equation are

$$x_{1,2} = \frac{1 + w - i\Lambda_+}{2} \pm \sqrt{\frac{(1 - w - i\Lambda_-)^2}{4} - \frac{16w^2}{\pi^4}}, \tag{3.16}$$

where $\Lambda_\pm = \lambda_1 \pm \lambda_0$. Eq.(3.16) results in the following expressions for the decrements of modes

$$-\mathrm{Im}x = \frac{\Lambda_+}{2} \pm \sqrt{\frac{1}{2}\left[\sqrt{X^2 + \frac{\Lambda_-^2(1-w)^2}{4}} - X\right]}, \tag{3.17}$$

$$X = \frac{(1-w)^2 - \Lambda_-^2}{4} - \frac{16w^2}{\pi^4}.$$

If $\Lambda_+ > 0$, both decrements will be positive and, therefore, both modes will be stable, when

$$\frac{\Lambda_+}{2} \geq \sqrt{\frac{1}{2}\left[\sqrt{X^2 + \frac{\Lambda_-^2(1-w)^2}{4}} - X\right]}.$$

After simple calculations this condition can be rewritten as

$$(1-w)^2 \frac{\lambda_0\lambda_1}{\Lambda_+^2} + \lambda_0\lambda_1 - \frac{16w^2}{\pi^4} \geq 0. \tag{3.18}$$

With obvious substitutions this stability condition exactly coincides with that, obtained in Ref.[6] for sum-type resonant instability. In both cases, if one of the decrements is equal to zero ($\lambda_0\lambda_1 = 0$), stability condition never holds. This proves the fact that the mode-coupling instability can be stabilized only in the case, when both modes are damped.

4 Landau damping

Let us now consider the effect of Landau damping on the mode-coupling instability. It is described by Eqs.(2.7). In case of interest these equations cannot be solved directly like it was done in Ref.[3]. For this reason, below we focus on approximate dispersion equations and their solutions. These approximate equations are obtained solving Eqs(2.7) taking into account the coupling of limited amount of modes. If we want to calculate the stability criterion, we can trace the variation in the positions of the roots of the dispersion equation, when the beam current is increased from a value below threshold. This means that again we can take into account the coupling of the betatron and of the nearest synchrobetatron modes. The amount of coupled modes generally depends on the ratio of the frequency of synchrotron oscillations to the frequency spread in the beam ($\delta\omega$). In the region, where $\omega_s \gg \delta\omega$, stability condition can be found taking into account the coupling of the betatron with two first synchrobetatron modes. However, if we want to consider cases, when the frequency of synchrotron oscillations is comparable to the frequency spread in the beam, amount of coupled modes in equations to be solved must be increased. In any case, if we cut Eqs(2.7) at some $m = M$, these equations get the form

$$\sum_{m=0}^{M} Q_{m,m'}(x) C_{m'} = 0,$$

so that the dispersion equation reads

$$\Phi(x) = \det(\mathbf{Q}(x)) = 0. \tag{4.19}$$

For a given dispersion equation the stability conditions of modes can be calculated using the so-called Nyquist stability criterion. As is known, for a dispersion equations of the form of Eq.(4.19) this criterion is based on the calculation of the phase advance of the function $\Phi(x)$, when x varies slightly above the real axes. If the beam distribution function

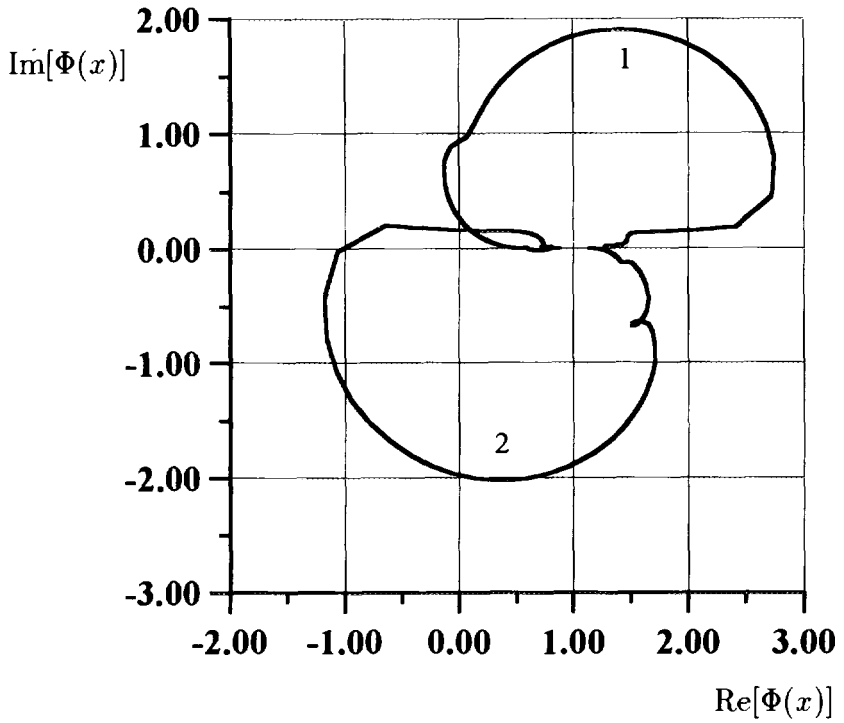

Figure 2: Hodographs of $\Phi(x)$ for the dispersion equation (4.19). 1: $\omega_s = 3 \times \delta\omega_z$, $\Omega_m = 1.7 \times \delta\omega_z$; 2: $\omega_s = 3 \times \delta\omega_z$, $\Omega_m = -1.7 \times \delta\omega_z$.

is a nonsingular function of I, both F and Φ are also nonsingular functions in the upper half-plane of the complex variable x. For this reason and since

$$\lim_{|x|\to\infty} \Phi(x) = 1,$$

the number of the roots of the dispersion equation in the upper half-plane of the complex variable x is equal to the mentioned phase advance of Φ divided by 2π (see, for instance, in Ref.[7]). Since $\Phi(x)$ maps the real axes x into some closed curve in the plane of the complex variable Φ (the so-called hodograph of Φ), the Nyquist criterion states that modes are stable, if the hodograph of Φ does not encircle the origin.

In this paper for the sake of simplicity we calculate hodographs of Eq.(4.19) assuming that ω_z is a linear function of I

$$\omega_z = \omega_{z0} + \kappa I,$$

and that f_0 is an exponential function

$$f_0 = \exp(-I/I_0)/I_0.$$

Then,

$$\begin{aligned} F(x) &= \int_0^\infty du \frac{ue^{-u}}{x - zu + i\Delta}, \quad z = \frac{\delta\omega_z}{\omega_s}, \quad \delta\omega_z = \kappa I_0, \\ &= ve^{-v}[\mathrm{Ei}(v) - i\pi\theta(v)] - 1, \quad v = x/z, \end{aligned} \tag{4.20}$$

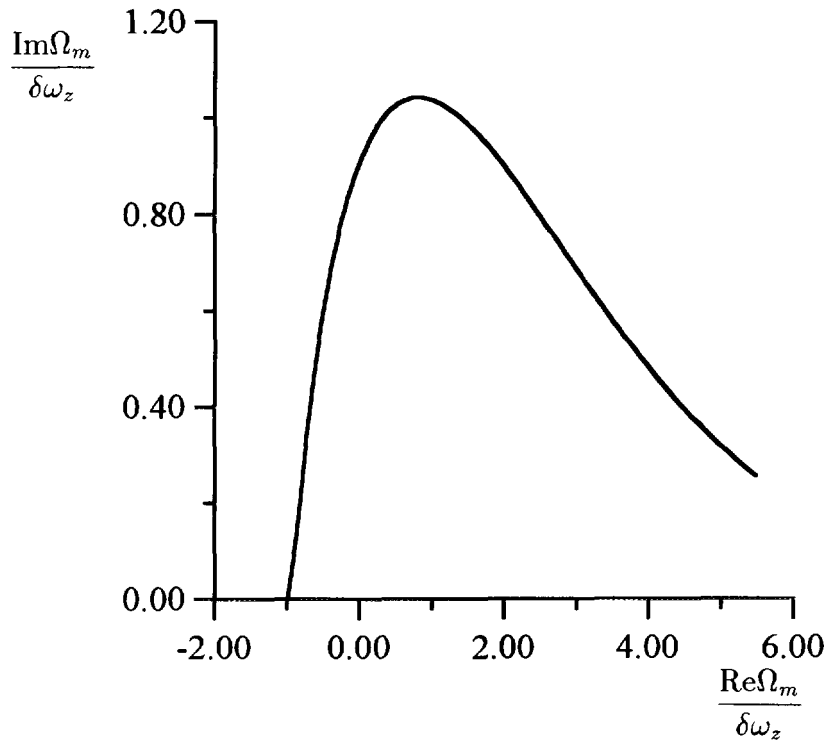

Figure 3: Stability diagram for uncoupled dipole betatron oscillations.

where $\mathrm{Ei}(x)$ is the exponential integral function

$$\mathrm{Ei}(x) = -\int_{-x}^{\infty} dt \frac{e^{-t}}{t},$$

and

$$\theta(x) = \begin{cases} 1, & x > 1, \\ 0, & x < 0\,. \end{cases}$$

Two of these hodographs are shown as examples in Fig.2. Hodograph 1 in this figure does not encircle the origin and therefore, corresponds to stable oscillation. This case agrees with the threshold in Eq.(3.14). On the contrary, hodograph 2 in Fig.2 corresponds to unstable oscillations. The difference in behavior of modes for positive and negative Ω_m is due to effect of the frequency spread in the beam. Analogous behavior shows the so-called stability diagram of modes with dipole betatron oscillations, calculated for modes without coupling (Fig.3, see, for example in [5] for more detail). Inspecting the behavior of various hodographs one can plot the stability diagram for the dispersion equation Eq.(4.19). Such a plot (see in Fig.4) indicates the mentioned nonsymmetry of the stability diagram relative to the sign of Ω_m and a tendency to an increase in the width of the stability band (in Ω_m), in the regions, where $\omega_s \gg \delta\omega_z$ and $\omega_s \ll \delta\omega_z$ (in both cases $\Omega_m > 0$). For high synchrotron frequencies stability condition asymptotically tends to that, given in Eq.(3.14). An increase in the width of the stability band at low synchrotron frequencies is in general agreement with the behavior of the stability diagram, shown in Fig.3. However, for very low synchrotron frequencies ($\omega_s \ll \delta\omega_z$) an instability becomes fast relative to synchrotron oscillations of particles and, for this reason, the eigenvalue

analysis of the beam stability becomes less important than the beam break-up behavior of coherent oscillations of the bunch (see, for example, in Refs.[3, 5]).

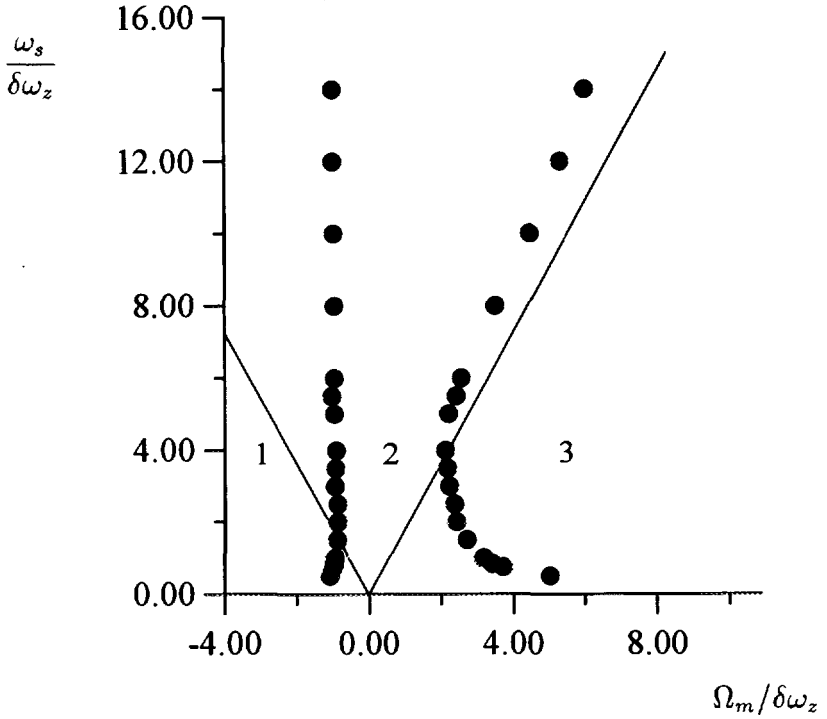

Figure 4: Stability diagram for the mode-coupling instability (dots: Eq.(4.19)). The solid line presents the stability diagram, corresponding to stability condition in Eq.(3.14). Oscillations are unstable in the regions 1 and 3.

The instability of the coupled betatron and first synchrobetatron modes in the region $\omega_s \gg \delta\omega_z$ and $-1 < w < 0$ can be illustrated by the following simple calculations. For these parameters the eigenfrequencies can be found using equation similar to Eq.(3.11)

$$\begin{aligned} 1 &= wF(x) - \frac{16w^2}{\pi^4}F(x)[F(x+1)+F(x-1)], \\ &= w_{eff}F(x), \quad w_{eff} = w\Big(1 - \frac{16w}{\pi^4}[F(x+1)+F(x-1)]\Big). \end{aligned} \tag{4.21}$$

If we take also $|\Omega_m| \gg \delta\omega_z$, we may expect that increments of unstable modes are small compared to the frequency shifts. Accordingly, we write

$$F(x) \simeq \frac{1}{x} - i\pi\Lambda(x), \quad \Lambda(x) = \frac{xe^{-x/z}}{z}\theta(x).$$

Using for the roots of Eq.(4.21) the form $x = x_0 + i\delta$, we can find the frequency shifts x_0 from unperturbed dispersion equation

$$1 - \frac{w}{x_0} + \frac{32w^2}{\pi^4}\frac{1}{x_0^2 - 1} = 0$$

If w is negative, only the roots with $x_0 < 0$ must be inspected. For these roots, the calculation of δ in the first approximation of the perturbation theory results in

$$\delta = -\frac{16|w|}{\pi^4 z} \frac{x_0(1+x_0)\exp\left(-\dfrac{1+x_0}{z}\right)}{1+\dfrac{16|w|}{\pi^4}\dfrac{x_0^2}{(1-x_0^2)^2}}. \tag{4.22}$$

This expression is always positive, which corresponds to unstable oscillations. Note, however, that below the threshold, given in Eq.(3.14), and in the region, where $z \ll 1$ and $|w| \gg 1$, the increments of these instabilities are exponentially small. Accordingly, we may state that in real cases, the left border of the stability diagram for the mode-coupling instability is very sensitive to 'residual' damping of coherent oscillations. That can be, for example, the synchrotron radiation damping, or single-mode damping like a combination of the effect of the so-called fast damping of betatron oscillations [8, 9, 5] and of the head-tail damping of the synchrobetatron modes.

In any case, these calculations show that, apart from an increase in the frequency of synchrotron oscillations, the stability of the coupled synchrobetatron modes can be improved due to Landau damping, provided that $\Omega_m > 0$. If $\Omega_m < 0$, for beam currents below threshold, given in Eq.(3.14) the position of the stability diagram strongly depends on the additional damping of coherent oscillations.

References

[1] R.D. Kohaupt. DESY Report 80/22, 1980.

[2] Working Group Reports to Proc. of the Fourth Advanced ICFA Beam Dynamics Workshop on Collective Effects in Short Bunches. KEK, Japan, 1990.

[3] D.V. Pestrikov. Part. Acc. **41**, (1993), p.13.

[4] A.A. Kolomensky, A.N. Lebedev. Theory of Cyclic Particle Accelerators. Willey, New York, 1962.

[5] N.S. Dikansky, D.V. Pestrikov. Physics of Intense Beams and Storage Rings. AIP PRESS, New York, 1994.

[6] Ya.S. Derbenev, N.S. Dikansky. In Proc. of All Union Part. Acc. Conf., Moscow, (1970), v. 2, p. 391.

[7] V.I. Smirnov. Course of Higher Mathematic. v. 3, Moscow, Fizmatgiz, 1958.

[8] V.L. Auslender, N.S. Dikansky, et al. Atomnaya Energia, **22**, (1967), p. 198.

[9] N.S. Dikansky, M.M. Karliner, et al. Atomnaya Energia, **22**, (1967), p. 188.

POTENTIAL-WELL DISTORTION AND MODE-MIXING INSTABILITY IN PROTON MACHINES

King-Yuen Ng

Fermi National Accelerator Laboratory, P.O. Box 500, Batavia, IL 60510*

Abstract

In proton machines, potential-well distortion leads to small amount of bunch lengthening with minimal head-tail asymmetry. Longitudinal mode-mixing instability occurs at higher azimuthal modes. When the driving resonance is of broad-band, the threshold corresponds to the Boussard-modified Keil-Schnell criterion for microwave instability. [1] When the driving resonance is narrower than the bunch spectrum, the threshold corresponds to a similar criterion derived before. [2] The thresholds are higher when the machine operates below transition.

I. INTRODUCTION

Proton bunches are very much different from electron bunches. First, electron bunches have a length roughly equal to or shorter than the radius of the beam pipe, whereas proton bunches are usually very much longer. Second, the momentum spread of the electron bunches is determined by the heavy synchrotron radiation. Protons do not radiate and behave quite differently in the longitudinal phase space, with the bunch area conserved instead. These differences lead to different results in potential-well distortion and mode mixing. [3]

II. DISTORTION ASYMMETRY

As an example, the bunches in the Fermilab Main Ring have a typical full length of $\sim$ 60 cm or $\tau_L \sim 2$ ns. The spectrum has a half width of $\sim \tau_L^{-1} = 0.5$ GHz. Therefore, the static bunch profile is hardly affected by the resistive part of the broad-band impedance which is centered at $1.5 \sim 4$ GHz. As a result, the inductive part of the broad-band will only lead to a symmetric broadening (shortening) of the bunch above (below) transition. This conjecture can be tested by means of the Haïssinski equation [4]. Strictly speaking, the Haïssinski equation does not apply to proton bunches where the bunch area is conserved and the momentum spread is not a fixed Gaussian. Nevertheless, it should give us an idea of the amount of asymmetric head-tail distortion. Adapting the Main Ring bunch at $E = 150$ GeV to a longitudinal Gaussian profile, we take the bunch area as $A = 6\pi\sigma_\tau\sigma_E = 0.15$ eV-sec, where σ_τ and σ_E are the rms bunch length in time and rms energy spread. With a

*Operated by the Universities Research Association, Inc., under contract with the U.S. Department of Energy.

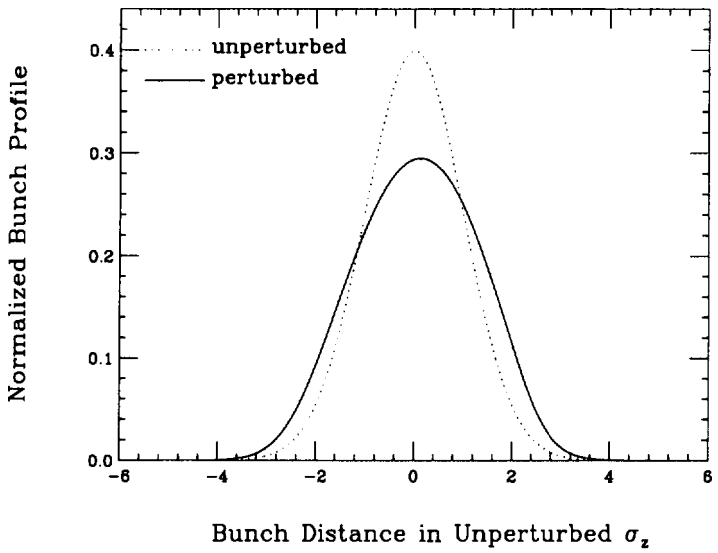

Fig. 1. An estimate of potential-well distortion of a Main Ring bunch from the solution of Haïssinski equation. Note that the head-tail asymmetry is very small.

revolution frequency of $f_0 = \omega_0/2\pi = 47.7$ kHz, a phase-slip parameter of $\eta = 0.0028$, and an unperturbed synchrotron tune of $\nu_{s0} = \omega_{s0}/\omega_0 = 0.00361$, we obtain an unperturbed rms bunch length of $\sigma_\tau = \sqrt{\frac{\eta A}{6\pi\omega_{s0}E\beta^2}} = 0.37$ ns or 11 cm. This profile is plotted as dashes in Fig. 1. At present, the Main Ring bunch has an intensity of $N = 4.5 \times 10^{10}$ protons and the Main Injector under construction has a designed intensity of $N = 6.0 \times 10^{10}$. The broad-band impedance of the Main Ring is believed to be $Z/n \approx 5$ to 10 Ω and the cut-off frequency is $\sim$ 4 GHz, while the broad-band impedance of the Main Injector is $Z/n \lesssim 1$ Ω. Here, we take as illustration $N(Z/n) = 60 \times 10^{10}$ Ω with the broad-band impedance centered at 2 GHz. The self-consistent Haïssinski equation is then solved and the impedance-distorted bunch profile is plotted as solid in Fig. 1. We can see that the asymmetry in the distortion is indeed extremely small.

III. POTENTIAL-WELL LENGTHENING

When the small asymmetry in the potential-well distortion is neglected, we can considered the driving impedance to be pure inductive. The wake potential is the derivative of the δ-function. For a parabolic bunch, the wake force will be linear and can be superimposed onto the linearized rf force easily. The potential-well distorted bunch will therefore remain parabolic. For this reason, the distribution in longitudinal phase space should be, [5]

$$\psi(\tau,\delta) = \frac{3\eta cN}{2\pi\omega_{s0}\hat{\tau}_0^3}\sqrt{\hat{\tau}_0^2 - \frac{1}{\kappa}\left(\frac{\eta}{\omega_{s0}}\delta\right)^2 - \kappa\tau^2}\,, \tag{3.1}$$

where we have used as conjugate variables: τ, the time of arrival with respect to the synchronous particle, and $-\eta\delta/\omega_{s0}$ where δ is the momentum spread. The independent "time"

variable is s, the distance along the ring. The original half length of the bunch $\hat{\tau}_0$ has been lengthened to $\hat{\tau}_0/\sqrt{\kappa}$, whereas the momentum spread δ is shortened by $\sqrt{\kappa}$, so that the bunch area remains the same. Throughout this paper, the particles are considered to be ultra-relativistic, so that their longitudinal velocities are taken to be c, the velocity of light. With the addition of the inductive wake potential, the Hamiltonian is modified to

$$H = \frac{\eta^2}{2\omega_{s0}c}\delta^2 + \frac{\omega_{s0}}{2c}(1 - D\kappa^{3/2})\tau^2 \ , \tag{3.2}$$

where

$$D = \frac{3e^2N\eta}{4\pi\omega_{s0}^2 E\hat{\tau}_0^3}\left.\frac{Z}{n}\right|_{\rm ind} \ . \tag{3.3}$$

The incoherent synchrotron angular frequency is therefore $\omega_s = \omega_{s0}(1 - D\kappa^{3/2})^{1/2}$. Since the distribution $\psi(\tau, \delta)$ must be a function of the Hamiltonian, to conform with Eq. (3.1), we have

$$\psi(\tau, \delta) = \frac{3\eta cN}{2\pi\omega_{s0}\hat{\tau}_0^3}\sqrt{\hat{\tau}_0^2 - \frac{2c}{\kappa\omega_{s0}}H} \ , \tag{3.4}$$

with the constraint

$$\kappa^2 = 1 - D\kappa^{3/2} \ . \tag{3.5}$$

Again, consider a 150 GeV Main Ring bunch with $N = 4.5 \times 10^{10}$ of bunch area 0.15 eV-sec and an inductive impedance of $Z/n|_{\rm ind} \approx 20 \times 10^{10}$ Ohms. Then $D = 0.204$, indicating that the bunch has been lengthened by $\kappa^{-1/2} = 1.05$ and the momentum spread flattened by 5%. This implies that we cannot infer the momentum spread naively through the relation $\hat{\delta} = \omega_{s0}\tau_L/\eta$ by measuring the bunch length and the synchrotron frequency, because the answer will be $\sim 10\%$ too large, giving a wrong idea about the amount of Landau damping. Instead, the momentum spread should be measured from Schottky signals or inferred through dispersion from the measurement of the transverse profile of the bunch using a flying wire.

IV. MODE-MIXING

The coherent bunch modes will be shifted by the impedance of the vacuum chamber. As the current increases, two modes will collide to give an instability. It was illustrated in Sec. II that the potential-well distortion has very little head-tail asymmetry, indicating that radial modes will not be important and will be neglected. However, we do want to keep the effect of the potential-well modification; therefore, the perturbed ω_s will be used in below. In fact, going from the coordinates (τ, δ) to the polar coordinates (r, ϕ), where

$$\begin{cases} \tau &= r\cos\phi \ , \\ -\dfrac{\eta}{\omega_s}\delta &= r\sin\phi \ , \end{cases} \tag{4.1}$$

the potential-well lengthening of the bunch discussed in Sec. III has been included already.

The shifts of the synchrotron side-bands can be derived using Vlasov equation. Here, we follow the Sacherer's approach. [6] The bunch profile of the i-th coherent mode can be written as

$$\rho^{(i)}(\tau) = \sum_k \alpha_k^{(i)} \lambda_k(\tau) \ , \tag{4.2}$$

where $\lambda_k(\tau)$ denotes a set of normalized orthogonal profile functions with k nodes between $-\frac{1}{2}\tau_L$ and $+\frac{1}{2}\tau_L$, with τ_L denoting the total length of the bunch. It can be shown that (see Appendix) $\alpha_m^{(i)}$ satisfies the equations

$$\sum_k [(\Omega^{(i)} - m\omega_s)\delta_{mk} - M_{mk}]\alpha_k^{(i)} \ , \tag{4.3}$$

for all m's. In other words, $(\alpha_1^{(i)}, \alpha_2^{(i)}, \cdots)$ is the i-th eigenvector corresponding to the eigenvalue $\Omega = \Omega^{(i)}$. In the above, the coupling matrix is given by

$$M_{mk} = -\frac{i\omega_s \omega_0 I_b}{3B_0^3 h V_T \cos\varphi_s} \frac{m}{m+1} \frac{\sum_n h_{mk}(\omega') Z(\omega')/\omega'}{\sum_n h_{mm}(\omega')} \tag{4.4}$$

where $\omega' = n\omega_0 + \Omega$, V_T is the potential-well modified rf voltage, which is related to the unperturbed rf voltage V_0 by $V_T/V_0 = (\omega_s/\omega_{s0})^2$, φ_s is the synchronous phase, h is the rf harmonic, I_b is the average bunch current, $B_0 = \tau_L f_0$ is the bunching factor, and $h_{mk}(\omega') = \tilde{\lambda}_m^*(\omega')\tilde{\lambda}_k(\omega')$ are the overlap of the spectral functions $\tilde{\lambda}_m(\omega')$, which are Fourier transforms of the profile functions $\lambda_m(\tau)$ introduced in Eq. (4.2).

The profile functions $\lambda_m(\tau)$ should be eigenstates for each corresponding azimuthal mode m, when the bunch intensity is small and no mixing occurs. Here, we choose them as the sinusoidal densities introduced by Sacherer. [7]

$$\lambda_m(\tau) = \begin{cases} \dfrac{\pi}{2\tau_L} \cos \dfrac{(m+1)\pi\tau}{\tau_L} & m \text{ even} \\ \\ \dfrac{\pi}{2\tau_L} \sin \dfrac{(m+1)\pi\tau}{\tau_L} & m \text{ odd} \end{cases} \tag{4.5}$$

The spectral functions are therefore

$$\tilde{\lambda}_m(x) = \begin{cases} i^m \dfrac{m+1}{2\pi} \dfrac{\cos \pi x/2}{x^2 - (m+1)^2} & m \text{ even} \\ \\ i^m \dfrac{m+1}{2\pi} \dfrac{\sin \pi x/2}{x^2 - (m+1)^2} & m \text{ odd} \end{cases} \tag{4.6}$$

where a dimensionless frequency parameter $x = \omega\tau_L/\pi$ has been introduced, so that, with the exception of $m = 0$, the spectrum for the mth mode peaks at $x \approx m + 1$ and has a full width of $\Delta x \approx 2$, as illustrated in Fig. 2. The revolution angular frequency is therefore given by $x_0 = \omega_0\tau_L/\pi$. We also introduce a dimensionless current parameter

$$\epsilon = -\frac{I_b R_s/n_r}{3B_0^3 h V_0 \cos\varphi_s} \ , \tag{4.7}$$

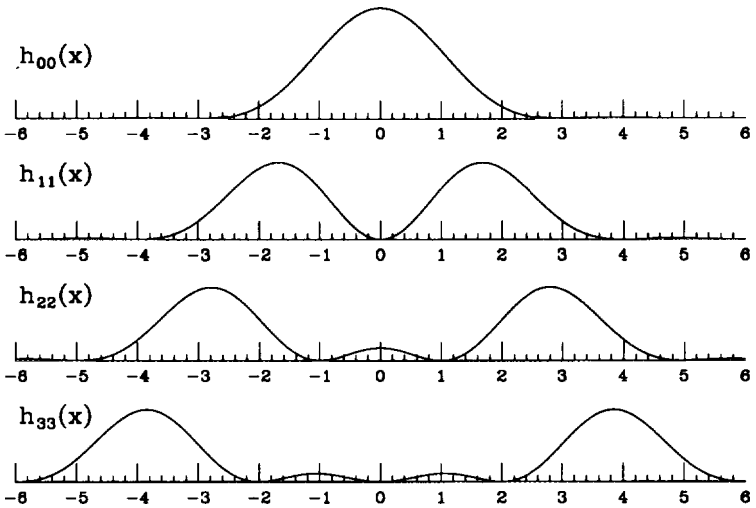

Fig. 2. Some of the power spectra $h_{mm}(x)$ of the sinusoidal modes introduced by Sacherer.

which is positive above transition. Unlike the first factor on the right-hand side of Eq. (4.4), ϵ is proportional to $I_b R_s$ linearly, where R_s is the shunt impedance of the driving resonant impedance centered at $n_r f_0$ or at $x_r = 2n_r f_0 \tau_L$.

For a broad-band impedance the argument $\omega' = n\omega_0 + \Omega$ in the coupling matrix M_{mk} can be replaced by $\omega = n\omega_0$. Then $Z(\omega)$ and $\tilde{\lambda}_m(\omega)$ possess definite symmetries. It is easy to see that all matrix elements are real. We can also see that modes m and k are coupled through $\mathcal{R}e\, Z$ when $m - k$ is odd, and through $\mathcal{I}m\, Z$ when $m - k$ is even. For each individual mode m, the shift in coherent frequency is due to the diagonal element M_{mm} driven by $\mathcal{I}m\, Z$. Above transition ($\eta > 0$ or $\cos\varphi_s < 0$), the inductive impedance shifts the frequency upward, while the capacitive impedance shifts the frequency downward. These shifts can cause two modes to cross each other, but produce no instability because the shifts are real. Instability is contributed by the non-diagonal elements. For two adjacent modes to merge into one and produce instability, the driving force is the real part of the impedance.

Let us continue with the example of the Fermilab Main Ring which has a broad-band impedance centered at $x_r = 7.5$ or $f_r \sim 1.88$ GHz and quality factor $Q \approx 1$. The eigen frequencies obtained from solving Eq. (4.3) are plotted in Fig. 3 versus the current parameter ϵ. We find mode 6 peaks at the inductive part of the resonant impedance and is therefore shifted upward. Mode 7 peaks at the capacitive part of the impedance and is shifted downward. The real part of the resonant peak merges the two modes into one at $\epsilon = 0.94$, after which the bunch becomes unstable. Note that the ordinate of Fig. 3 is normalized with respect to the unperturbed synchrotron frequency ω_{s0}, and an adjustment for the incoherent tune shift

$$\omega_s - \omega_{s0} = \frac{3}{2\pi^2} \frac{\omega_{s0} I_b (Z/n)_{\text{ind}}}{B_0^3 h V_0 \cos\varphi_s} \tag{4.8}$$

has been made. This correction pushes all coherent modes downward. When the current is

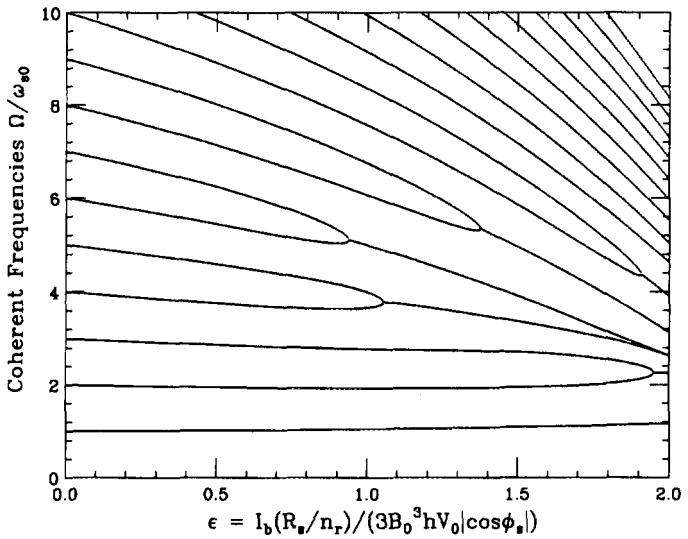

Fig. 3. Coupling of modes $m = 6$ and 7 in the presence of a resonance at $x_r = 7.5$ and $Q = 1$ above transition.

small, the rigid dipole mode $m = 1$ is not shifted at all. This is to be expected because the center of the rigid bunch cannot see any modification of the rf potential due to the bunch itself.

We vary Q and compute the threshold ϵ_{th} in each case. The result is plotted in Fig. 4 versus $z = \Delta f_r \tau_L = x_r/4Q$, where $\Delta f_r = f_r/2Q$ is the HWHM of the resonance. Physically z denotes the ratio of the FWHM of the resonance to roughly the full width of the spectrum of the bunch. Also plotted are threshold curves for resonances centered at different frequencies from $x_r = 3.5$ to 10.5. Note that all the threshold curves fall roughly on top of each other, and approach a minimum threshold of $\epsilon_{th} \approx 0.92$ when z reaches ~ 0.6. The latter has the physical meaning of the resonance peak just wide enough to cover only two coupling modes. A smaller z implies that the resonance peak is too narrow and interacts with only parts of the two mode spectra, thus giving a higher instability threshold. A larger z means that the resonance will cover more than two mode spectra. For $x_r = 7.5$ say, modes 6 and 7 will then be pulled and pushed also by the other modes as well so that some cancellation will occur, and one may expect the threshold for their collision to be higher also. However, Eq. (4.4) reveals that the coupling comes in not through $\mathcal{R}e\, Z(\omega)$ but through $\mathcal{R}e\, Z(\omega)/\omega$, whose peak value becomes larger and the peak frequency smaller when the quality factor Q is small, although the zero of $\mathcal{I}m\, Z(\omega)/\omega$ remains unchanged. Figure 5 shows such a plot with $x_r = 7.5$ and $Q = 0.2$, where the peak of $\mathcal{R}e\, Z(\omega)/\omega$ increases from ~ 1 to 2.6 and the position of the peak shifts to $x = 1.6$. Figure 6 shows the enhancement of $\mathcal{R}e\, Z(\omega)/\omega$ and its frequency position as the quality factor decreases from 100 to 0.001. For this reason, when Q is small enough, the lower modes start to collide first. For the case of the resonant broad-band centered at $x_r = 7.5$ and $Q = 0.2$ (or $z = 9.4$), Fig. 7 shows that modes 1 and

2 start to merge first. Thus, the threshold for large z remains small, which is very much different from what Sacherer stated in his paper.

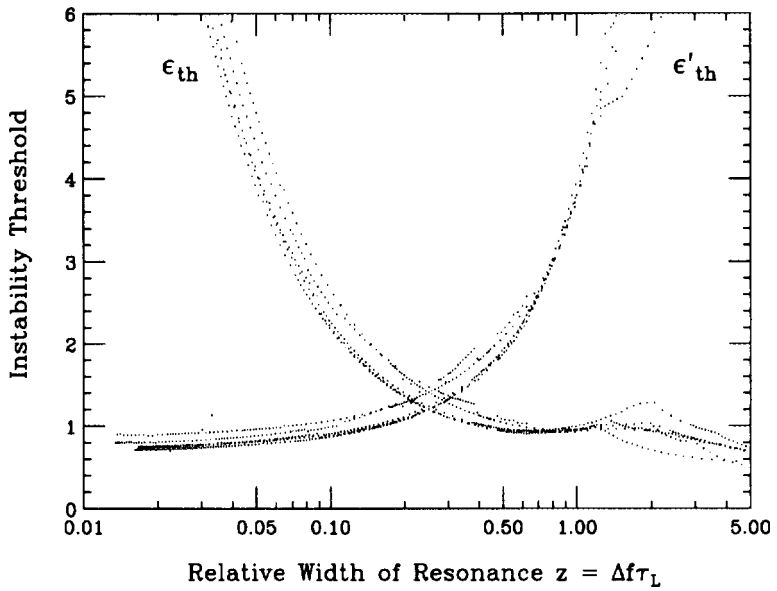

Fig. 4. Instability thresholds ϵ_{th} and ϵ'_{th} for various widths of the resonance impedance located at $x_r = 3.5$ to 11.5.

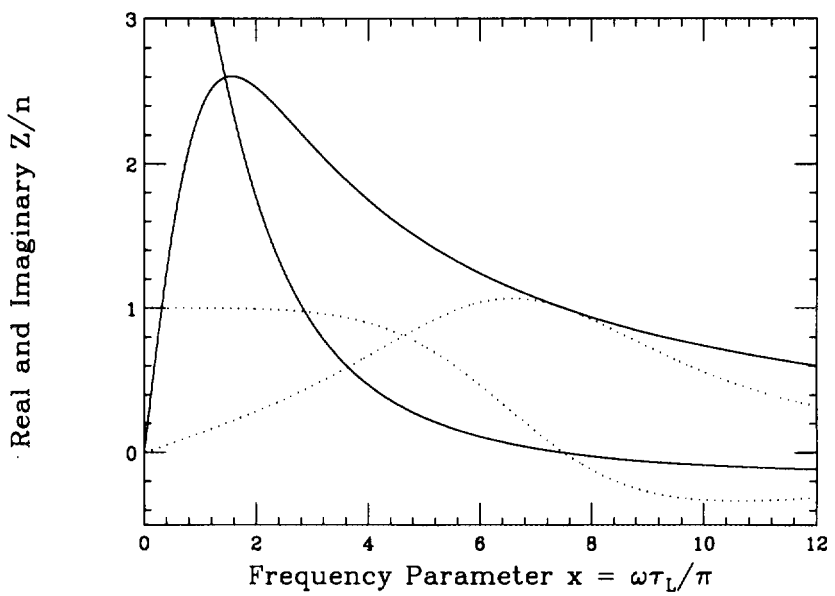

Fig. 5. Comparison of $\mathcal{R}e\, Z/n$ and $\mathcal{I}m\, Z/n$ centered at $x_r = 7.5$ for $Q = 1$ (dots) and $Q = 0.2$ (solid). Note that when the resonance becomes broader, the contributions of Z/n move towards lower frequencies.

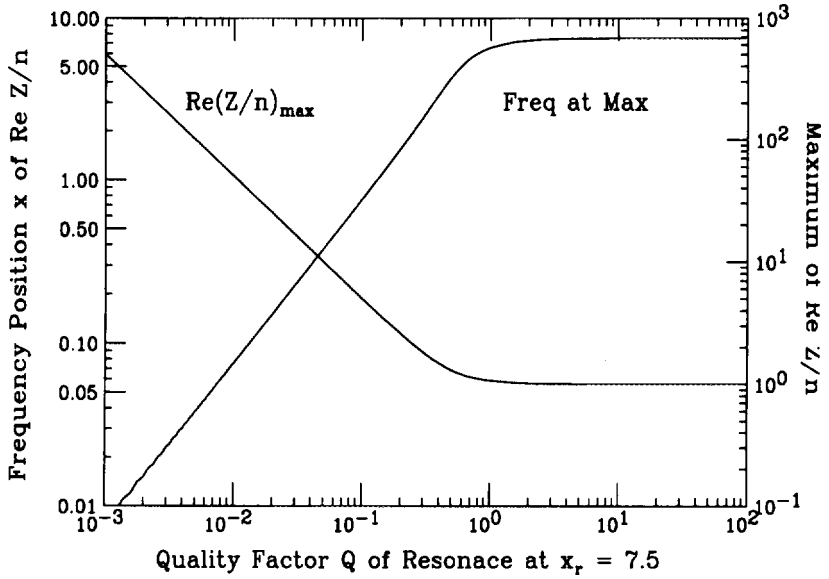

Fig. 6. Enhancement of $(\mathcal{R}eZ/n)_{\max}$ (normalized to R_s) and its frequency position x as the quality factor Q of the resonance centered at $x_r = 7.5$ decreases.

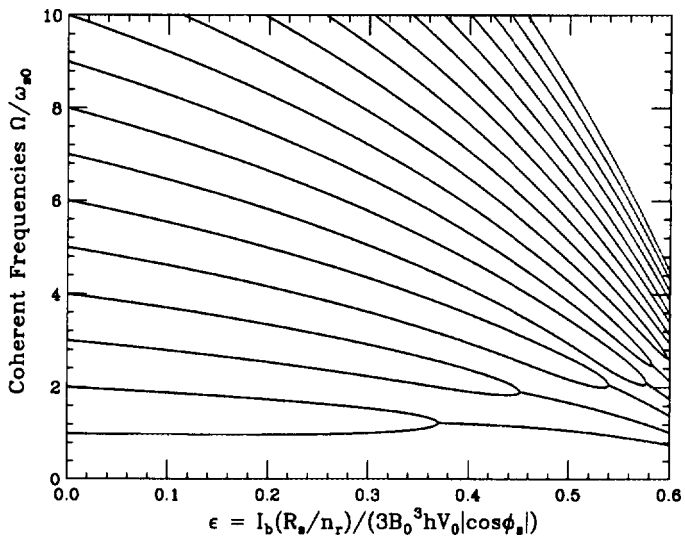

Fig. 7. Mode coupling starts at the lowest modes when the driving resonance is much wider than the bunch spectrum. Here $x_r = 7.5$, $Q = 0.2$, $\tau_L = 2$ ns, or $z = 9.4$.

V. MICROWAVE INSTABILITY DRIVEN BY BROAD RESONANCES

Microwave instability can occur when the resonance is much wider than the bunch spectrum. When this happens, many coherent modes are excited. We see that modes 6 and 7 merge first in Fig. 3 when $Q = 1$ but modes 1 and 2 merge first in Fig. 7 when $Q = 0.2$. In between, when $Q \sim 0.45$, we find that modes 2 and 3, 4 and 5, 6 and 7 start to merge at nearly the same threshold of $\epsilon_{th} \approx 0.75$. Therefore, we can conclude that the threshold

at the $z \gg 1$ end is the threshold of microwave instability. This threshold condition can be easily rewritten in terms of the energy spread $(\Delta E)_{\rm FWHM} = \frac{3}{2}(\Delta E)_{\rm full}$ and bunch peak current $I_p = \pi I_b/(2\tau_L f_0)$ of the sinusoidal profile as

$$\frac{R_s}{n_r} = \frac{27}{16}\epsilon_{th}\frac{\eta(E/e)}{I_p}\left(\frac{\Delta E}{E}\right)^2_{\rm FWHM} , \tag{5.1}$$

which is the familiar Boussard-modified Keil-Schnell criterion [1] of microwave instability driven by a broad resonance. The form factor for this type of cosine bunch shape should be close to unity, which is close to $\frac{27}{16}\epsilon_{th} = 1.3$ obtained here. The equivalence of mode-coupling and microwave instability had been pointed out by Sacherer [6] and Laclare. [8]

The threshold ϵ_{th} can also be estimated. When the resonant impedance $\mathcal{R}e\, Z$ is just wide enough to cover two adjacent modes m and $m' = m + 1$, and the excitation is one with $x_r = \frac{1}{2}(m + 3)$ nodes along the bunch, the coupling matrix can be truncated to include only these two modes. The coupling matrix of Eq. (4.5) can be rewritten as

$$M_{mm'} = \epsilon A_{mm'} , \tag{5.2}$$

or

$$A_{mm'} = \frac{i\sum_n h_{mk}(n)[n_r\hat{Z}(n)/n]}{\sum_n h_{mm}(n)} , \tag{5.3}$$

where $\hat{Z}(n) = Z(n)/R_s$. In above, the factor $\frac{m}{m+1}$ as well as the difference between ω_s and ω_{s0} have been neglected. The eigen equation (4.3) now becomes

$$\begin{vmatrix} \frac{\Omega}{\omega_{s0}} - m - \epsilon A_{mm} & \epsilon A_{mm'} \\ \epsilon A_{m'm} & \frac{\Omega}{\omega_{s0}} - m' - \epsilon A_{m'm'} \end{vmatrix} = 0 , \tag{5.4}$$

from which we obtain, with $A_{mm'}A_{m'm} = -|A_{m'm}|^2$,

$$\Omega = \tfrac{1}{2}\omega_{s0}\left[(\nu_m + \nu_{m'}) \pm \sqrt{(\nu_{m'} - \nu_m)^2 - 4\epsilon^2|A_{mm'}|^2}\right] , \tag{5.5}$$

where $\nu_k = k + \epsilon A_{kk}$, $k = m$ or m'. The threshold of instability ϵ_{th} is therefore given by

$$|\epsilon_{th}A_{mm'}| = \tfrac{1}{2}|\epsilon_{th}(A_{m'm'} - A_{mm}) + 1| . \tag{5.6}$$

The matrix elements A_{mm}, $A_{m'm'}$, and $A_{mm'}$ have been computed numerically for any two adjacent m, m', with the resonance peak centered at $x_r = \frac{1}{2}(m + 3)$. The result is actually very close to $\epsilon_{th} = 0.92$ and depends on m very weakly. It can also be estimated easily. We first neglect A_{mm} and $A_{m'm'}$, and get $|\epsilon_{th}A_{mm'}| \approx \frac{1}{2}$. We can approximate the resonance $\mathcal{R}e\, Z(x)/x$ by a rectangular box of height R_s/x_r and width wide enough to contain the two coupling adjacent spectra, as illustrated in Fig. 8. Each spectral function $\tilde{\lambda}_m(x)$ can also be approximated by a rectangular box of total width $\Delta x = 2$. Since the two spectra are adjacent, the overlap is $\Delta x = 1$. Therefore, we obtain $|\sum_n \tilde{\lambda}^*_m(n)\tilde{\lambda}_{m'}(n)| \approx \frac{1}{2}\sum_n \tilde{\lambda}^*_m(n)\tilde{\lambda}_m(n)$ or $|A_{mm'}| \approx \frac{1}{2}$; thus $\epsilon_{th} \approx 1$. We can now include A_{mm} and $A_{m'm'}$ by further approximating $\mathcal{I}m\, Z(x)/x$ by R_s/x_r when $x < x_r$ and $-R_s/x_r$ when $x > x_r$. We obtain $A_{mm} \approx -A_{m'm'} \approx \frac{1}{2}$, which is an overestimate, and $\epsilon_{th} = \frac{1}{2}$. Therefore, $\frac{1}{2} < \epsilon_{th} < 1$.

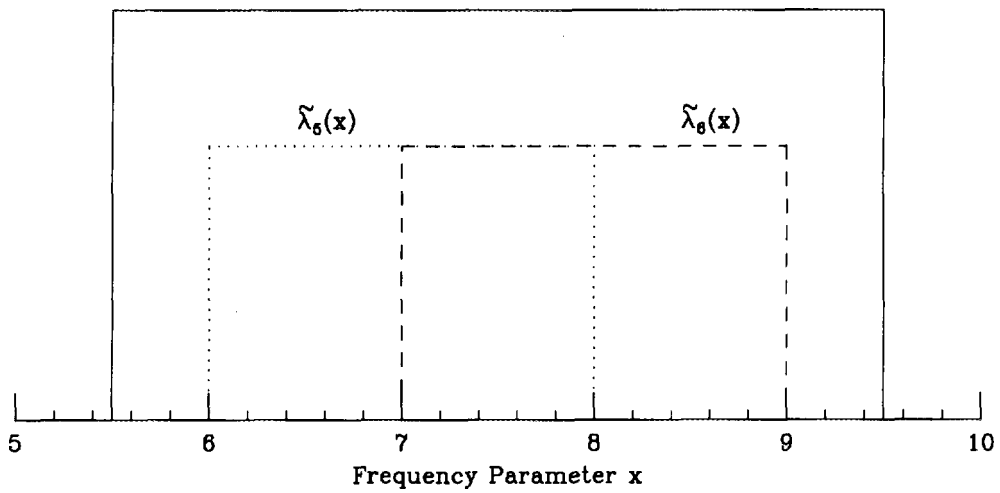

Fig. 8. An estimate of the nondiagonal coupling matrix elements by rectangularizing $\mathcal{R}e\, Z$ and the adjacent coupling spectral modes.

VI. MICROWAVE INSTABILITY DRIVEN BY NARROW RESONANCES

When the resonance is much narrower than the width of the bunch spectrum, we have $z \ll 1$. Then, the summation over frequency in Eq. (3.2) can be approximated by

$$\sum_n \frac{x_r Z(n)}{n} h_{mm'}(n) \approx \frac{\pi R_s x_r}{Q} \tilde{\lambda}_m^* \tilde{\lambda}_{m'}|_{x=x_r} \ . \tag{6.1}$$

Since the area under the narrow resonance is concerned here, a new dimensionless current parameter

$$\epsilon' = -\frac{2I_b(R_s/Q)}{3B_0^2 h V \cos\phi_s} \tag{6.2}$$

is required. This new threshold ϵ'_{th} is now plotted versus z in Fig. 4. For small z, we obtain $\epsilon'_{th} \approx 0.75$ which is almost independent of x_r. Again, this threshold can be computed numerically using the truncated 2×2 coupling matrix, or estimated by approximating the spectral functions by rectangular curves. When it is cast into the form

$$\frac{R_s}{Q} = \frac{27}{16\pi} \epsilon'_{th} \frac{\eta(E/e)}{I_b} \left(\frac{\Delta E}{E}\right)^2_{\text{FWHM}} \ , \tag{6.3}$$

it is just the criterion of microwave instability driven by an impedance resonance that is narrower than the bunch spectrum. [2] The form factor is 0.41, which agrees very well with $\frac{27}{16\pi}\epsilon'_{th} \approx 0.40$. This may be a more appropriate microwave instability threshold for electron machines, since electron bunches are short.

We have computed the mode-mixing for our former Main Ring bunch when the driving resonant impedance is narrow with a $Q = 100$. The result in Fig. 9 gives a threshold of

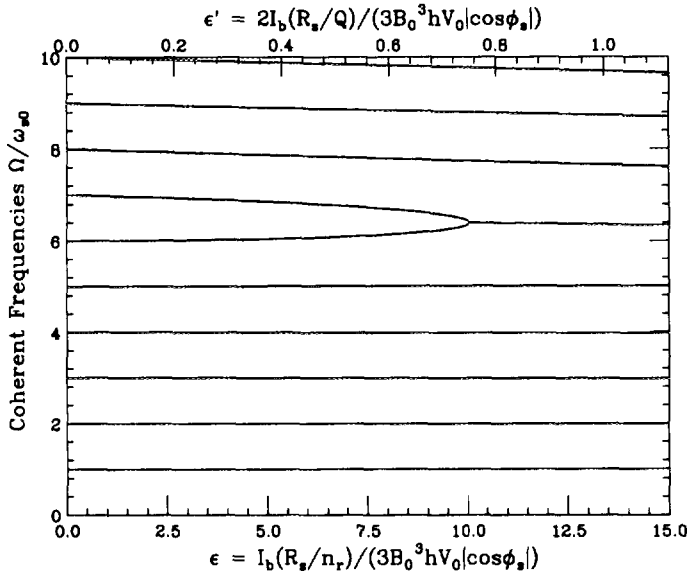

Fig. 9. Coupling of modes $m = 6$ and 7 in the presence of a narrow resonance at $x_r = 7.5$ and $Q = 100$ above transition.

$\epsilon_{th} = 10.0$ (or $\epsilon'_{th} = 0.75$), which is much larger than that for the broad-band impedance. This increase in threshold has been explained in Sec. IV, and is a result of the fact that the narrow resonance interacts with only a small part of the overlapping spectra. We also see that, as ϵ increases, the coherent frequencies here do not shift so much lower than the situations in Figs. 3 and 7. This is because the resonances there are rather broad and their contributions move towards lower frequencies (Fig. 5).

VII. GOING BELOW TRANSITION

Figure 3 shows that the coherent frequencies tend to cluster together when the current ϵ increases. This is because we are above transition, $\cos\varphi_s < 0$. Looking into the diagonal elements of Eq. (4.4), modes with $m < x_r - 1$ ($> x_r - 1$) sample the inductive (capacitive) part of the impedance and are shifted upward (downward). Below transition, the shifts will be in the opposite direction; i.e., diverging outward with increasing $|\epsilon|$. Mathematically, $(\nu_{m'} - \nu_m)^2$ inside the square root of Eq. (5.5) becomes larger. However, this does not mean that there will be no instability. This is because the off-diagonal elements $\epsilon A_{mm'}$ that are responsible for mode merging contribute as squares and therefore do not change sign. In fact, from Eq. (5.5), we obtain the threshold

$$|\epsilon_{th}| = \frac{1}{2|A_{mm'}| - |A_{m'm'} - A_{mm}|} \tag{7.1}$$

below transition, and

$$\epsilon_{th} = \frac{1}{2|A_{mm'}| + |A_{m'm'} - A_{mm}|} \tag{7.2}$$

above transition. It is now clear why the threshold below transition is much higher than the threshold above transition. We tried to reverse the sign of $\cos\varphi_s$ in the example of Fig. 3 to obtain Fig. 10 and found $|\epsilon_{th}|$ actually increases from 0.94 to 1.88. This is also true for narrow resonances; Fig. 9 becomes Fig. 11 below transition with $|\epsilon'_{th}|$ increases from 0.75 to 1.8. This conclusion is in sharp contradiction to the statement of Laclare [8] that "below transition mode coupling cannot lead to instability."

The above discussion leads to the conjecture that a bunch in a machine with a negative momentum-compaction factor [9] will be more stable. This idea had been pointed out by Fang et al [10] in obtaining shorter electron bunches for colliders.

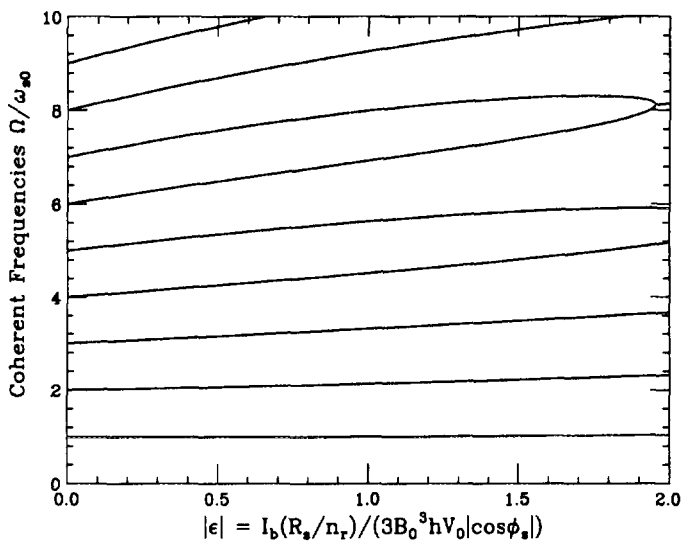

Fig. 10. The situation of Fig. 3 below transition. Note the increase in threshold $|\epsilon_{th}|$.

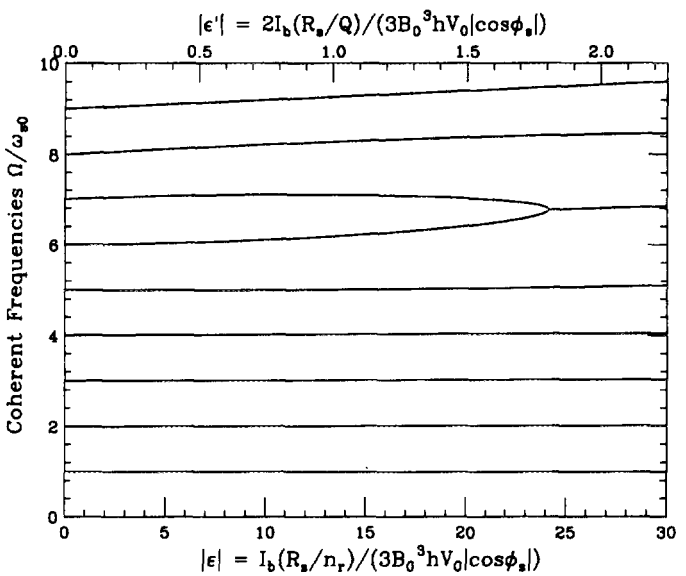

Fig. 11. The situation of Fig. 9 below transition. Note the increase in threshold $|\epsilon'_{th}|$.

VIII. CONCLUSIONS

We have explored the effects of potential-well distortion and mode mixing for proton bunches. Applications have been made to the Main Ring bunches and the future Main Injector bunches. Due to the long length of a proton bunch, the spectrum of its profile sees mostly only the inductive part of the broad-band coupling impedance. As a result, potential-well distortion only amounts to the lengthening of the bunch with very little head-tail asymmetry. A Main Ring bunch will be lengthened by $\sim 5\%$. The higher-order modes, however, can see the peak of the real part of the impedance, which will drive adjacent modes to merge together to produce instability. When the resonant impedance is much wider than the spectrum of the bunch, this mode-mixing threshold is equivalent to the threshold of the Boussard-modified Keil-Schnell criterion of microwave instability. When the resonant impedance is much narrower than the spectrum of the bunch, such as in electron machines, the mode-mixing threshold is equivalent to the threshold of microwave instability driven by narrow resonances. For short electron bunches, usually it is modes 1 and 2 that collide first as the bunch intensity increases. For proton bunches, however, higher modes start to collide first unless the impedance is extremely broad. This is because the proton bunch usually has a length equal to many cut-off wavelengths of the vacuum chamber. We have also discussed the situation when the machine operates below transition and found that the threshold will be pushed to a larger value and thus becoming more stable.

The complete equivalence of mode-coupling instability and microwave instability has not been established here. For example, we have not addressed the microwave instability driven by a pure space-charge impedance above transition. If we carry out an analysis similar to that in Sec. V, we find that coupling occurs only between modes m and m' with $|m-m'| = 2, 4, \cdots$. Then, a coupling element and its conjugate gives $A_{mm'}A_{m'm} = |A_{m'm}|^2$ instead, or the discriminant in Eq. (5.5) will be positive definite. In other words, there will not be any instability, contrary to the negative-mass instability observed just after transition. This and other issues will be examined further and reported elsewhere.

APPENDIX

In this Appendix, we derive the equation for coupled bunch modes of (4.3). The Vlasov Equation with canonical variables

$$\begin{cases} q = \tau \\ p = -\frac{\eta}{\omega_s}\delta \ , \end{cases} \tag{A.1}$$

is given by

$$\frac{\partial\psi}{\partial s} + \frac{\partial\psi}{\partial q}q' + \frac{\partial\psi}{\partial p}p' = 0 \ , \tag{A.2}$$

where the 'prime' denotes derivative with respect to s, the distance along the ring. The distribution function ψ is written as unperturbed part ψ_0 plus a perturbed part ψ_1 having a coherent frequency Ω:

$$\psi(r,\phi) = \psi_0(r) + \psi_1(r,\phi)e^{-i\Omega s/c} \ , \tag{A.3}$$

where the polar coordinates defined in Eq. (4.1) has been used. When the effect of the wake potential is included, the Hamiltonian equations are

$$q' = -\frac{\nu_s}{R}r\sin\phi \ , \tag{A.4}$$

and

$$p' = -\frac{\nu_s}{R}r\cos\phi + \frac{e^2\eta}{2\pi RE\nu_s}\sum_n \tilde{\rho}_1(\omega')Z(\omega')e^{i\omega'\tau - i\Omega s/c} \ , \tag{A.5}$$

where $\omega' = n\omega_0 + \Omega$ and the spectrum of the perturbed linear distribution is defined as

$$\tilde{\rho}_1(\omega) = \frac{1}{2\pi}\int d\tau d\delta \, e^{-i\omega\tau}\psi_1(\tau,\delta) \ . \tag{A.6}$$

The perturbed distribution is now expanded into azimuthal harmonics in the longitudinal phase space

$$\psi_1(r,\phi) = \sum_m \alpha_m R_m(r)e^{im\phi} \ . \tag{A.7}$$

Multiplying by $e^{-im\phi}$ and integrating over ϕ, the Vlasov equation becomes

$$(\Omega - m\omega_s)\alpha_m R_m(r) = \frac{i^{m-1}me^2\eta}{2\pi RE\nu_s}\frac{\psi_0'}{r}\sum_n \tilde{\rho}_1(\omega')J_m(\omega' r)\frac{Z(\omega')}{\omega'} \ , \tag{A.8}$$

where $\psi_0' = d\psi_0/dr$. Changing the variables from (τ,δ) to (r,ϕ) and substituting Eq. (A.7), the perturbed spectrum of Eq. (A.6) can be simplified to

$$\tilde{\rho}_1(\omega) = \sum_m \alpha_m \tilde{\lambda}_m(\omega) \ , \tag{A.9}$$

where

$$\tilde{\lambda}_m(\omega) = \frac{i^{-m}\omega_s}{\eta}\int_0^\infty dr \, rR_m(r)J_m(\omega r) \tag{A.10}$$

is the Fourier transform of the perturbed bunch linear density corresponding to azimuthal harmonic m. At low bunch intensity, for each m, the various radial modes can be denoted by $R_{mq}(r)$ with $q = 1, 2, \cdots$. Since we are going to neglect radial modes, we only include the "most coherent" one with $q = m$. Then, $\tilde{\lambda}_m(\omega)$ peaks at $\omega \approx (m+1)\pi/\tau_L$, and the corresponding perturbed linear density $\lambda_m(\tau)$ has m nodes. Relation (A.10) can also be inverted to read

$$R_m(r) = \frac{i^m \eta}{\omega_s} \int_0^\infty d\omega\, \omega \tilde{\lambda}_m(\omega) J_m(\omega r) \ . \tag{A.11}$$

Using Eq. (A.10), the Vlasov equation can be transformed from Eq. (A.8) to

$$(\Omega - m\omega_s)\alpha_m \int_0^\infty dr\, |R_m(r)|^2 \frac{r^2}{\psi_0'} = -\frac{ime^2\eta^2}{2\pi\nu_s^2 E} \sum_n \tilde{\rho}_1(\omega') \frac{Z(\omega')}{\omega'} \tilde{\lambda}_m^*(\omega') \ . \tag{A.12}$$

Substituting the harmonic expansion of $\tilde{\rho}_1$, we arrive at the eigen-equation

$$(\Omega - m\omega_s)\alpha_m = \sum_k \left[-\frac{ime^2\eta^2}{2\pi\nu_s^2 E} \frac{\sum_n \tilde{\lambda}_k(\omega') \frac{Z(\omega')}{\omega'} \tilde{\lambda}_m^*(\omega')}{\int_0^\infty dr\, |R_m(r)|^2 \frac{r^2}{\psi_0'}} \right] \alpha_k \ , \tag{A.13}$$

which is of the same form as Eq. (4.3).

Finally, we need to compute the integral in the denominator of Eq. (A.13). We can write

$$\int_0^\infty dr\, |R_m(r)|^2 \frac{r^2}{\psi_0'} = \langle \frac{r}{\psi_0'} \rangle \int_0^\infty dr\, r |R_m(r)|^2 \ , \tag{A.14}$$

where $\langle r/\psi_0' \rangle$ denotes some characteristic value of r/ψ_0'. Since ψ_0 is normalized to $\eta N/\omega_s$ and depends on τ_L only, we must have

$$\langle \frac{r}{\psi_0'} \rangle \propto -\frac{\omega_s \tau_L^4}{\eta N} \ . \tag{A.15}$$

The integral on the right side of Eq. (A.14) can now be performed with the aid of Eq. (A.11) to give

$$\int_0^\infty dr\, r |R_m(r)|^2 \ = \frac{\eta^2}{\omega_s^2} \int_0^\infty d\omega\, \omega |\tilde{\lambda}_m(\omega)|^2 \ . \tag{A.16}$$

We next make use of the fact the $\tilde{\lambda}_m(\omega)$ has definite symmetry and peaks at $\omega \sim (m+1)\pi/\tau_L$. Then,

$$\int_0^\infty d\omega\, \omega |\tilde{\lambda}_m(\omega)|^2 \approx \frac{(m+1)\pi\omega_0}{2\tau_L} \sum_{n=-\infty}^{\infty} |\tilde{\lambda}_m(\omega')|^2 \ , \tag{A.17}$$

Combining Eqs. (A.14) to (A.17), eigen-equation (A.13) takes the form

$$(\Omega - m\omega_s)\alpha_m = -F \sum_k \left[\frac{imI_b\omega_s\omega_0}{3(m+1)B_0^3 h V_T \cos\varphi_s} \frac{\sum_n \tilde{\lambda}_k(\omega') \frac{Z(\omega')}{\omega'} \tilde{\lambda}_m^*(\omega')}{\sum_n |\tilde{\lambda}_k(\omega')|^2} \right] \alpha_k \ , \tag{A.18}$$

where F is a form factor which is of $\mathcal{O}(1)$, depending on the form of the unperturbed distribution $\psi_0(r)$. For example, if we choose

$$\psi_0(r) = \frac{32\eta N}{\pi\omega_s\tau_L^4}\left(\frac{\tau_L^2}{4} - r^2\right) , \tag{A.19}$$

so that

$$\frac{\psi_0'}{r} = -\frac{64\eta N}{\pi\omega_s\tau_L^4} \tag{A.20}$$

is no longer r-dependent, we obtain $F = 96/\pi^4 = 0.986$.

References

[1] D. Boussard, CERN/LAB II/RF/75-2 (1975); E. Keil and W. Schnell, CERN/ISR/TH/RF/69-48 (1969)

[2] K.Y. Ng, Proc. 1986 Summer Study on Phys. of SSC, ed. R. Donalson and J. Marx, 1986, p.590.

[3] K.Y. Ng, Proc. 1995 Particle Accelerator Conference, Dallas, Texas, May 1-5, 1995.

[4] J. Haïssinski, Nuovo Cimento **B18**, 72 (1973).

[5] A.W. Chao, *Physics of Collective Beam Instabilities in High Energy Accelerators,* Wiley, p.284.

[6] F.J. Sacherer, IEEE Trans. Nucl. Sc. **24**, No.3, 1393 (1977).

[7] F.J. Sacherer, CERN Internal Report CERN/SI-BR/72-5.

[8] J.L. Laclare, CERN Accel. School, Queen's College, Oxford, England, 1985, p.264.

[9] S.Y. Lee, K.Y. Ng, and D. Trbojevic, Phys. Rev. **E48**, 3040 (1993).

[10] S.X. Fang, K. Oide, Y. Yokoya, B. Chen, and J.Q. Wang, KEK Preprint 94-190, 1995.

Bunch Lengthening with Bifurcation in Electron Storage Rings

Eun-San Kim
Department of Accelerator Science, The Graduate University for Advanced Studies
1-1 Oho, Tsukuba, Ibaraki, 305, Japan
Kohji Hirata *
National Laboratory for High Energy Physics (KEK), 1-1 Oho, Tsukuba, Ibaraki, 305, Japan

Abstract

The mapping which shows equilibrium particle distribution in shychrotron phase space for electron storage rings is discussed with respect to some localized constant wake function based on the Gaussian approximation. This mapping shows multi-periodic states as well as double bifurcation in dynamical states of the equilibrium bunch length. When moving around parameter space, the system shows a transition/bifurcation which is not always reversible. These results derived by mapping are confirmed by multiparticle tracking.

1 Introduction

Electromagnetic interaction beteween charged particles and the surrounding takes place a wake force. This wake force affects the distribution of particles in a beam. Usually, wake force is averaged over one turn, and is distributed uniformly throughout the ring. However, wake sources are actually highly localized. Thus, assumptions which averaged wake force distributes uniformly in the ring might make the behavior of the system unrealistic in some cases. To study such position-dependent wake forces it seems to be reasonable to start with a single wake source in the ring.

In Ref.(1), using the Gaussian approximation, equilibrium particle distribution was investigated by the model using a localized wake, which was assumed to be a step function. It was shown that bunch length in the asymptotic state could then have a cusp-catastrophe behavior. Here, we extend the study to a wider range of parameters. We will show that a system in the equilibrium state exhibits another remarkable dynamical feature, that is, states with multi-periodicity. These states can be also coexisted in some cases. It illustrates new types of bunch lengthening. The asymptotic state can bifurcate as we vary parameters. This process does not always show reversible.

Section 2 describes the model. Section 3. consider the dynamical states of equilibrium particle distribution for constant wake function. To check these results, based on the

*Also Department of Accelerator Science, The Graduate University for Advanced Studies

Gaussian approximation, in Sec.4 we compare them with those of multiparticle tracking. Section 5 is devoted to discussions and conclusions.

2 The Model

Let us assume that there is only one localized wake source in the ring. An extension to uniformly distributed wake source is easily obtained by introducing many sources periodically and increasing the periodicity to infinity, as shown in Ref.(1). More realsitic cases in which the wake function varies from position to position in the ring can also be studied by a straightforward extension of the present formalism. We consider the dynamics of the particle distribution in longitudinal phase space. It is convenient to introduce normalized synchrotron variables,

$$x_1 = \frac{\text{longitudinal displacement}}{\sigma_l}, \quad x_2 = \frac{\text{energy deviation}}{\sigma_E}$$

where σ_l is the nominal bunch length and σ_E is the nominal energy spread. Here, "nominal" means "zero current". $x_1 > 0$ corresponds to the rear part of the bunch.

After one turn in the ring the motion of a particle can be represented by

$$\begin{pmatrix} x_1' \\ x_2' \end{pmatrix} = U \begin{pmatrix} x_1 \\ \Lambda x_2 + (1-\Lambda^2)^{1/2}\hat{r} - \phi(x_1), \end{pmatrix} \tag{1}$$

where $\Lambda = \exp[-2/T_e]$, T_e being the synchrotron damping time divided by the revolution time, ν the sychrotron tune and $\hat{r}$ a Gaussian random varible with $< \hat{r} > = 0$ and $< \hat{r}^2 > = 1$. U is the rotation matrix of the synchrotron oscillation,

$$U = \begin{pmatrix} \cos 2\pi\nu & \sin 2\pi\nu \\ -\sin 2\pi\nu & \cos 2\pi\nu \end{pmatrix} \tag{2}$$

The wake force is

$$\phi(x_1) = \int_0^\infty \rho(x_1 - u) W(u) du, \tag{3}$$

where $\rho(x)$ is the longitudinal charge density, which is normalized to unity. Here, $W(u)$ is the longitudinal wake function multiplied by eQ/σ_E, where e is the electron charge and Q the total charge in a bunch.

We consider constant wake function in order to dertermine the effects of the wake source on the distribution of particles in the beam: where $W(u)=a\Theta(u)$ (Θ being the unit step function). Since the constant wake is assumed to vanish at a short distance behind the particles which produce it, we can neglect the multiturn effects. Because particles in the front of a bunch lose energy due to wake fields, we note here that the signs of a in the wake function has to be positive.

Since it is not realistic to observe individual particles, we are more interested in some statistical quantities, such as

$$\bar{x}_i =< x_i >, \qquad \sigma_{ij} =< (x_i - \bar{x}_i)(x_j - \bar{x}_j) > . \tag{4}$$

and so on, where i, j are 1 or 2, which are the moments of the phase space distribution $\Psi(x_1, x_2)$. Since we assume that the distribution function in phase space always remains Gaussian, we need to consider only the first and second order moments.

Then, each mapping can be described by these moments:

1) Radiation

$$\bar{x}_1' = \bar{x}_1, \qquad \bar{x}_2' = \Lambda \bar{x}_2 \tag{5}$$

$$\sigma_{11}' = \sigma_{11}, \qquad \sigma_{12}' = \Lambda \sigma_{12}, \qquad \sigma_{22}' = \Lambda^2 \sigma_{22} + (1 - \Lambda^2) \tag{6}$$

2) Wake

$$\bar{x}_1' = \bar{x}_1, \qquad \bar{x}_2' = \bar{x}_2 - < \phi > \tag{7}$$

$$\sigma_{11}' = \sigma_{11}, \qquad \sigma_{12}' = \sigma_{12} - < (x_1 - \bar{x}_1)\phi > \tag{8}$$

$$\sigma_{22}' = \sigma_{22} - 2 < (x_2 - \bar{x}_2)\phi > + < \phi^2 > - < \phi >^2, \tag{9}$$

where <> denotes the average over all of the particles.

3) Synchrotron Oscillation

$$\bar{x}_i' = \sum_j U_{ij} \bar{x}_j, \qquad \sigma_{ij}' = \sum_{h,k=1}^{2} U_{ih} \sigma_{hk} U_{jk} \tag{10}$$

We always approximate Ψ as

$$\Psi(x_1, x_2) = \frac{1}{2\pi\sqrt{det\sigma}} \exp[-\frac{1}{2} \sum_{ij} \sigma_{i,j}^{-1} (x_i - \bar{x}_i)(x_j - \bar{x}_j)]. \tag{11}$$

We thus obtain the mapping for the wake as follows:

$$\bar{x}_1' = \bar{x}_1, \qquad \bar{x}_2' = \bar{x}_2 - a/2, \tag{12}$$

$$\sigma_{11}' = \sigma_{11}, \qquad \sigma_{12}' = \sigma_{12} - a\frac{\sqrt{\sigma_{11}}}{2\sqrt{\pi}}, \qquad \sigma_{22}' = \sigma_{22} - a\frac{\sigma_{12}}{\sqrt{\pi\sigma_{11}}} + a^2/12 \tag{13}$$

We note that the mappings for $\bar{x}_i$ and σ_{ij} are not related to each other. This fact is due to the Gaussian distribution approximation.

Then $\bar{x}_i$ falls into a period one fixed point:

$$\bar{x}_1^{\infty} = -\frac{a}{2\tan(2\pi\nu)} \frac{1}{1+\Lambda}, \qquad \bar{x}_2^{\infty} = \frac{a}{2} \frac{1}{1+\Lambda} \tag{14}$$

Note that if $\phi = 0$, we have $\bar{x}_i^{\infty} = 0$ and $\sigma_{ij} = \delta_{ij}$ after many turns.

We can estimate typical values of a, the wake force strength. We consider the TRISTAN at 8 GeV (Ref.4) as an example. We can compare our model with the energy loss by the wake effect per turn (the loss parameter). The loss parameter per turn is 37.8 MeV for I=5 mA. Setting the nominal energy spread to 3.49 MeV, we obtain a=21.6.

3 Constant wake function

Let us write the map as S, which is a composition of maps of the radiation, wake and oscillation. The mappings can then be described as $S(\sigma) = \sigma'''$,

$$\sigma_{ij} \overset{Radiation}{\longrightarrow} \sigma'_{ij} \overset{Wake}{\longrightarrow} \sigma''_{ij} \overset{Oscillation}{\longrightarrow} \sigma'''_{ij}.$$

If there is a point on the map such that $\sigma_1 = S(\sigma_1)$, σ_1 is called the period-1 fixed point. If it is stable, it might determine the stationary state of the system. Similarly, the period-2 fixed point is defined as: $\sigma_1 = S(\sigma_2)$, $\sigma_2 = S(\sigma_1)$ and $\sigma_1 \neq \sigma_2$. If σ_1 and σ_2 are stable points, they constitute alternating pairs of successive turns in the equilibrium state. We can also define period-n states in similar way.

In Ref.(1) it was shown that the equilibrium state was divided into three dynamical states when the synchrotron tune ν is 0.2; in the first state only the period-1 solution is stable; in the second state only period-2 solution is stable; and in the third state the system chooses one of them according to the initial condition. The parameter space which illustrates these three dynamical states is shown in Fig.1.(a). When we slowly move the system along the path from A to G in Fig.1.(a), it shows a period-doubling bifurcation at D, and remains as period-2 until F. It then becomes the period-1 state at F and remains so until G. The situations are shown in Fig.1.(c). Conversely, when we start from G it shows period-doubling bifurcation at F, and remains as period-2 until B. It then becomes the period-1 state at B and remains so until A, as shown in Fig.1.(d). This feature can be illustrated as in Fig.1.(b). Here, we can see that the system shows hysteresis in parameter space C of Fig.1.(a). We can also see that the transitions are continuous at F and discontinuous at B and D.

On the contrary, for ν=0.01 the equilibrium states are more complicated, presenting the coexistence of states with period-2,3,4, period-1,3,4, period-2,3, period-1,3 and period-1,4 in addition to the period-1 state and the period-2 state as shown in Fig.2.(a). Fig.2.(b) shows the initial values for the σ_{11} and σ_{22} conditions which result in the equilibrium period-2 state, period-3 state and period-4 state. We obtained these conditions under the assumption that σ_{12}=0. According to the initial σ_{11} and σ_{22}, the system can have quite a different equilibrium periodic state. The properties of the transitions of these multi-periodic states are depicted in Fig.2.(c). To observe the behavior of the system at F of Fig.2.(c), we move the system slowly from I, where it is at period-4 state, to A. The system changes to the period-3 state or period-2 state as T_e decreases. It depends on whether the system exists any fixed point among 4-fixed points at F. From these facts we can see that there exists a range of parameter values for which two or three dynamical states coexist for a constant wake function. The transition behaviors of the system show continuous or discontinuous bifurcations. It is then shown that continuous bifurcation only occurs at H. The dynamical process is reversible when we move the system slowly between the period-1 state and the period-2 state and returns to its starting point.

We can summarize these facts as follows; As the synchrotron tune is decreased to values less than ν=0.23, in addition to the period-1 and the period-2 states, the period-3 and the period-4 states become stable states in the some parameter space.

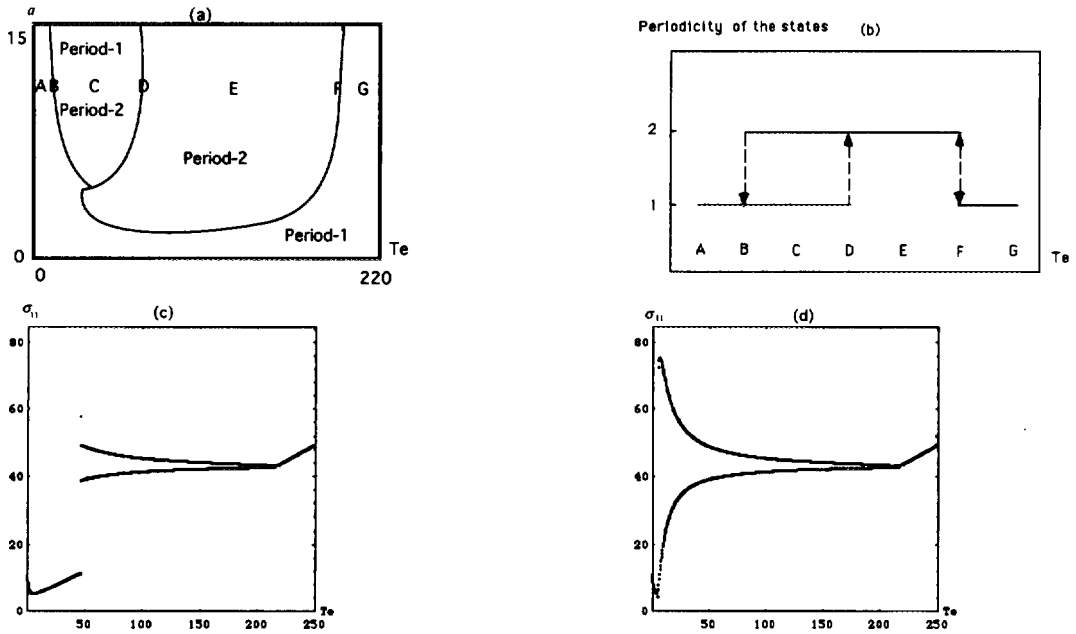

Figure 1: (a) the parameter space for ν=0.2 (b) shows the properties of the transitions. Here, arrow indicates that the transition occurs along the path in given periodic state. (c) and (d) Equilibrium value of σ_{11} when we slowly move the system from A to G and from G to A, respectively.

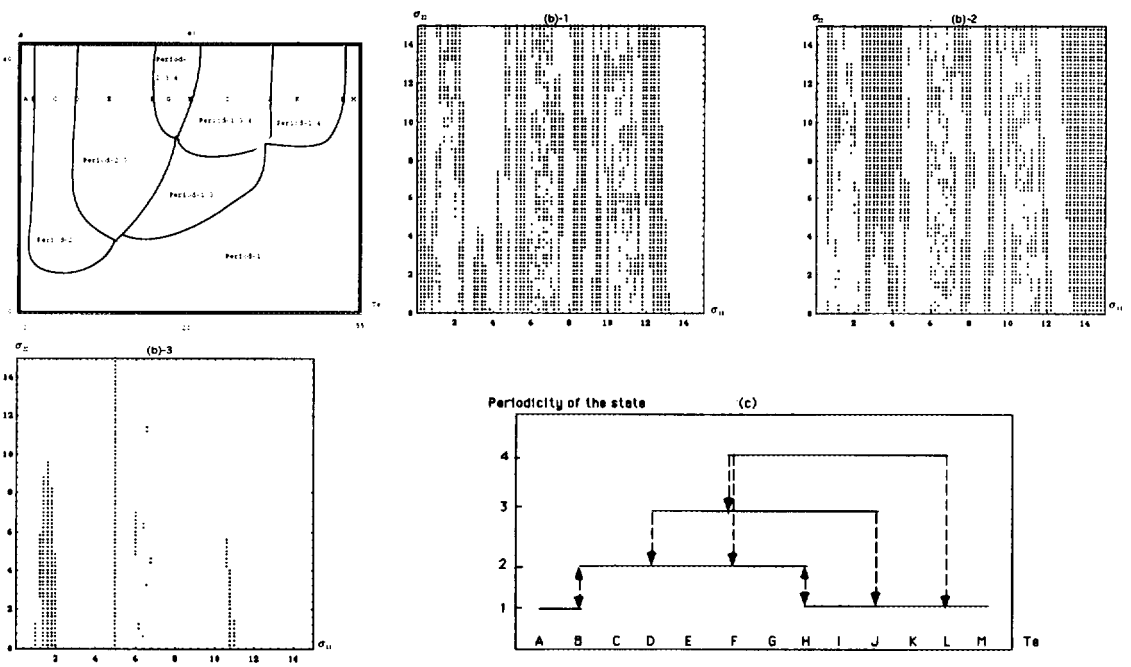

Figure 2: (a) The parameter spaces for ν=0.01. The dots in (b)-1,2,3 represent the initial σ_{11} and σ_{22} which show the equilibrium period-2, period-3 and period-4 states, respectively. The parameters are T_e=20, a=45. The (c) shows properties of the transitions among these states. Arrow indicates that the transition occurs along the path in given periodic state.

4 The MultiParticle Trakcing

We discuss the reliability of the the model presented above, because the model is based on the Gaussian approximation in the distribution of particles. We thus need a comparison with the multiparticle tracking in order to see whether features obtained from the model only come from the results of the simplification in the distribution functions. We apply the Eq.(1) to the phase-space coordinates of an ensemble of 10000 particles. The stochastic variable $\hat{r}$ is given by a Gaussian random generator. We observe the dynamical states of the distribution of particles for the constant wake function by multiparticle tracking.

We tracked 10000 particles and 20000 turns in the ring according to the map represented by Eq.(1). The initial particle coordinates in synchrotron phase space are given by the Gaussian random. We use a sorting routine in order to calculate the wake force acting on each particle. That is, the wake force ϕ that a given particle experiences from wake field can be obtained by the total number of particles preceding it. The parameter space which illustrates results of the multiparticle tracking for ν=0.01 is shown in Fig.3.(a). It is shown that the equilibrium states in the multiparticle tracking present the coexistence of states with period-1,4, period-2,4, period-2,3,4 and period-1,2,4, in addition to the states of the period-1 and period-2. But coexistence of states of period-1,3, period-1,3,4 and period-2,3 which were shown in moment mapping didnot appear in multiparticle tracking. The properties of the transitions of these multi-periodic states are depicted in Fig.3.(b). When we slowly move the system along the path from A to H in Fig.3.(a), it shows a period-doubling bifurcation at B and remains as period-2 state until F. It becomes the period-1 state at F and remains so until H. When we conversely move the path, we get same features. Here, we can see that the system shows cusp catastrophe at B and F of Fig.3.(a). The dynamical process is reversible when we move the system slowly between the period-1 state and the period-2 state and returns to its starting point. But the transitions between other states show irreversible. These properties show the same results with those of moment mapping.

Synchrotron phase-space distributions of the multiparticle tracking corresponding to these periodic states are shown in Figs.(3)-(7). Let us investigate the properties of the transition among the periodic states in multiparticle tracking as we change the T_e and a. The period-4 state after 20000 turns with the parameter T_e=31, a=40 and ν=0.01 are shown in Fig.4. Besides the core of the bunch distribution one can observe two islands. These two islands are rotated around the core per turn and the original distribution is appeared after four turns. When a and T_e in Fig.4 are decreased, the period-4 state changes to uncomplete period-4 state, as disappearing one island, and at last changes to the period-2 state which the other island is also disappeared. The period-2 state with parameter T_e=12, a=40 and ν=0.01 is shown in Fig.5 and the asymptotic states show the same distributions per two turns. We can also see the fact that, as the a decreases, the period-4 state in larger T_e than Fig.4 changes to the period-1 state on the dashed line of Fig.3.(a) by way of the uncomplete period-4 state. On the other hand, uncomplete period-4 states under dashed line of Fig.3.(a) donot change to the period-2 state, even though a is increased. This is because uncomplete period-4 states under dashed line of Fig.3.(a) also exist in the above the dashed line. However, uncomplete period-4 states with core and one island only exist above the dashed line of Fig.3.(a).

We can guess from these facts that uncomplete period-4 states of the several types can be existed according to the space parameters. This property did not be observed in moment mapping with Gaussian approximation. The period-3 state is shown in Fig.6. Transition from the period-4 state to the period-3 state which was shown in moment mapping doesnot occur in the moment mapping. It is due to the fact that there is no coexistence state of the period-2,3 in the parameter space.

One remarkable point is that uncomplete period-4 states under the dashed line of Fig.3.(a) also change to the period-2 state, as the T_e and a decrease, in the parameter space that uncomplete period-3 state and the period-3 state exist. The period-3 state is composed of two parts of the different distribution per turns, but uncomplete period-3 state shows two parts of the same distribution per turns. However, uncomplete period-4 and the period-4 states in the parameter space that the states of period-2,3,4 exist do not change to the period-2 state when T_e and a is increased. This shows different property of transition from the period-4 state of the moment mapping. Fig.7 is the period-1 state which is shown when a in Fig.3 is decreased.

In result, the comparison of results of multiparticle tracking with those of the moment mapping show agreements in facts that properties of the period-doubling and coexistences of the multiperiodic states exist for the constant wake function. When moving around parameter space, the system shows a transition/bifurcatioin which is not always reversible. These features are also shown in analysis of moment mapping and multiparticle tracking.

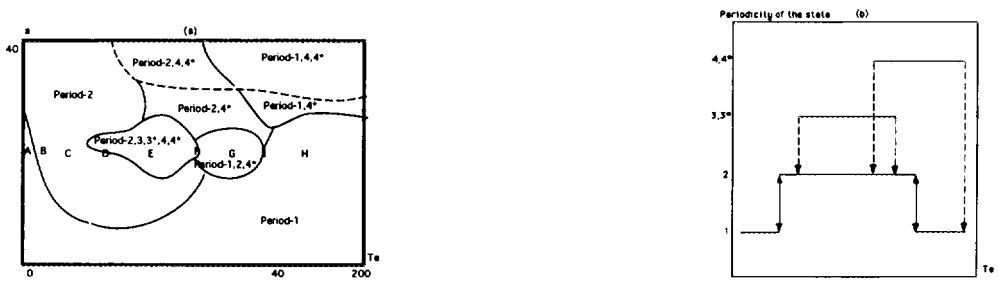

Figure 3: (a) The parameter spaces of multiparticle tracking for ν=0.01. Here 3* and 4* indicate uncomplete period-3 and period-4 states. (b) shows properties of the transitions among states in multiparticle tracking. arrow indicates that the transition occurs along the path in given periodic state.

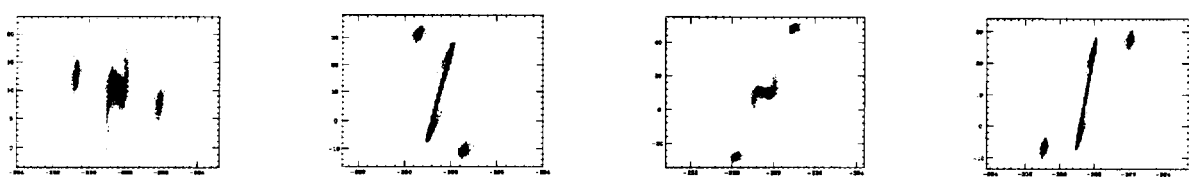

Figure 4: Phase space distribution for the period-4 state from multiparticle tracking. The distribution of the bunch shows core and two islands which rotates around the core per turns. The equilibrium state shows same distribution per four turns. The parameters are ν=0.01, T_e=31, a=40,10000 particles and 20000 turns.

Figure 5: Phase space distribution for the period-2 state from multiparticle tracking. The equilibrium state shows same distribution per two turns. The parameters are ν=0.01, T_e=12, a=40, 10000 particles and 20000 turns.

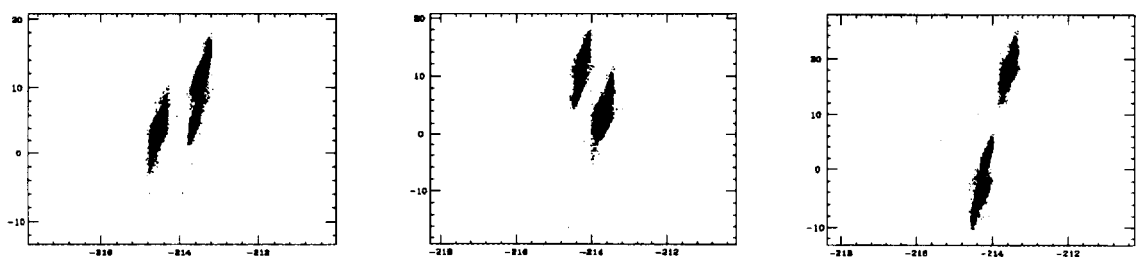

Figure 6: Phase space distribution for the period-3 state from multiparticle tracking. The equilibrium state shows same distribution per three turns. The parameters are ν=0.01, T_e=29, a=26, 10000 particles and 20000 turns.

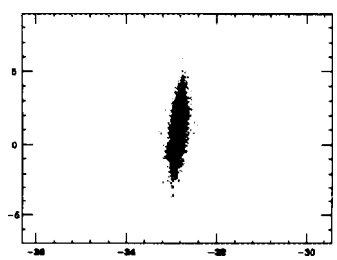

Figure 7: Phase space distribution for the period-1 state from multiparticle tracking. This period-1 state is obtained as a is decreased in Fig.7. The parameters are ν=0.01, T_e=31, a=4, 10000 particles and 20000 turns.

5 Discussions

5.1 Summary

We showed an analytic study of a moment mapping in order to see the equilibrium distribution in synchrotron phase space for electron storage rings. It is assumed that there is one localized and constant wake source. The results of a moment mapping were compared by the multiparticletracking.

In moment mapping the distributions of particles in a beam show three dynamical states for ν=0.2: the states where the period-1 state is stable; the period-2 state is stable; both the period-1 and the period-2 states are stable. We have showed in moment mapping that there is parameter spaces where the states of period-2,3,4, period-1,3,4, period-2,3 and period-1,3 coexist as stable states for ν=0.01. In multiparticle tracking we also confirmed coexistences of the multi-periodic states, such as period-2,3,4,period-1,2,4, period-1,4 and period-2,4 for $\nu = 0.01$.

Here, it is remarkable that these periodic states show continuous or discontinuous bifurcation to another periodic states under some conditions. The transitions between these states then show reversible and irreversible processes, which are also shown in multiparticle tracking. In moment tracking we assumed Gaussian approximation in the particle distribution in synchrotron phase space. This Gaussian distribution could not explain the presence of the islands in phase space which are shown by multiparticle tracking. These islands in synchrotron phase space show the deviations from the Gaussian approximation. In result, double bifurcation and coexistences of the multi-periodic states which are derived by moment mapping are confirmed by results of multiparticle tracking.

5.2 Conclusions

We showed equilibrium particle distribution and their stability for a localized constant wake force with the Gaussian approximation in electron storage rings. Depending on the parameters, such as the synchrotron tune, the wake force strength and the damping time, model calculation shows double bifurcation and coexistences of the multi-periodic states in a distribution of particles in a beam. These facts are also confirmed by multiparticle tracking. In the multiparticle tracking it is sometimes difficult to decide the exact threshold for the transition between two states. Despite the simplification of the Gaussian approximation, within these limitations, in result the model showed good agreement with multiparticle-tracking results. What we can argue from this point of view is that we can explain to some degrees the dynamical states of the system with Gaussian approximation.

References

[1] K. Hirata, S. Petracca and F. Ruggiero, Phys. Rev. Lett.**66**, 1693 (1991).

[2] K. Hirata, Part. Accel. **22**, 57 (1987).

[3] A. W. Chao, Physics of Collective Beam Instabilities in High Energy Accelerators (John Wiley and Sons, 1993)

[4] K.Satoh, private communication

A Simulation Study of the Sawtooth Behavior

ALEX CHAO
Stanford Linear Accelerator Center, Stanford, CA 94309, USA

The fact that bunch lengthening sometimes occurs with a sawtooth behavior has received some attention recently.[1-6] Various possible mechanisms which might explain the sawtooth behavior have been suggested. In particular, in Ref.6, Baartman and D'Yachkov proposed a mechanism that involves an interplay of synchrotron oscillation, potential well distortion (which at some moment of bunch oscillation creates a double-humped longitudinal beam distribution), quantum diffusion, and radiation damping and performed computer simulations to demonstrate this mechanism. Although this BD mechanism is not the only possible explanation of a sawtooth behavior, this note is an attempt to follow up on this trend of thought by yet another simulation study, and to draw a few tentative conclusions from this study.

The collective effect is presumably caused by some wake function $W(z)$. We assume the wake function is short-ranged and only single-turn wake needs to be considered. To enhance the BD mechanism in our simulation, a wake function model has been chosen which (a) has a range approximately equal to a few times the natural bunch length σ_z, and (b) flips sign once in this range (to make it easier to produce a second hump in potential well). In fact, we have chosen a wake function $W(z) = W_0$ when $0 < z < z_0$ and $-W_0$ when $z_0 < z < 2z_0$. Of course, $W(z) = 0$ when $z < 0$. With such a choice of wake function, a second beam distribution hump, if formed, would be approximately at a distance $\sim z_0$ behind the first hump. One expects that when $z_0 \gg \sigma_z$, the quantum diffusion (needed to transport particles from one hump to the other) is too slow to give a clear sawtooth behavior. One also expects that when $z_0 \ll \sigma_z$, the diffusion is too fast and only a chaotic behavior appears. In the simulation, parameters W_0 and z_0 are varied.

In our simulation for a damping ring, we launch a beam whose injected longitudinal emittance has rms sizes of $5\sigma_\delta$ and $5\sigma_z$. The damping time in the simulation has been chosen to be 400 turns, synchrotron oscillation tune is 0.0137. We track 1200 particles typically for 20,000 turns. We also took $\sigma_z = 5$ mm and $\sigma_\delta = 0.001$.

Figure 1 is a summary of our simulation study. The unit of W_0 is not specified. When W_0 and z_0 are varied, we found three regions in the (W_0, z_0) space. Region H is when a stable Haissinski state[7] is found. In a significant portion of the H region, the equilibrium beam distribution is double-humped (thanks to the choice of the wake function model). The S region is when there is observed a sawtooth behavior, while the C region is when the beam behaves chaotically.

Figures 2(a) to (f) show some of the simulation details for the three cases represented by the three dots in Fig.1: (a,b) $W_0 = 0.8, z_0 = 15$ mm; (c,d) $W_0 = 1, z_0 = 12$ mm; (e,f) $W_0 = 1.5, z_0 = 10$ mm. (a), (c) and (e) show the instantaneous rms bunch length as a function of the number of turns after injection. (b), (d) and (f) similarly

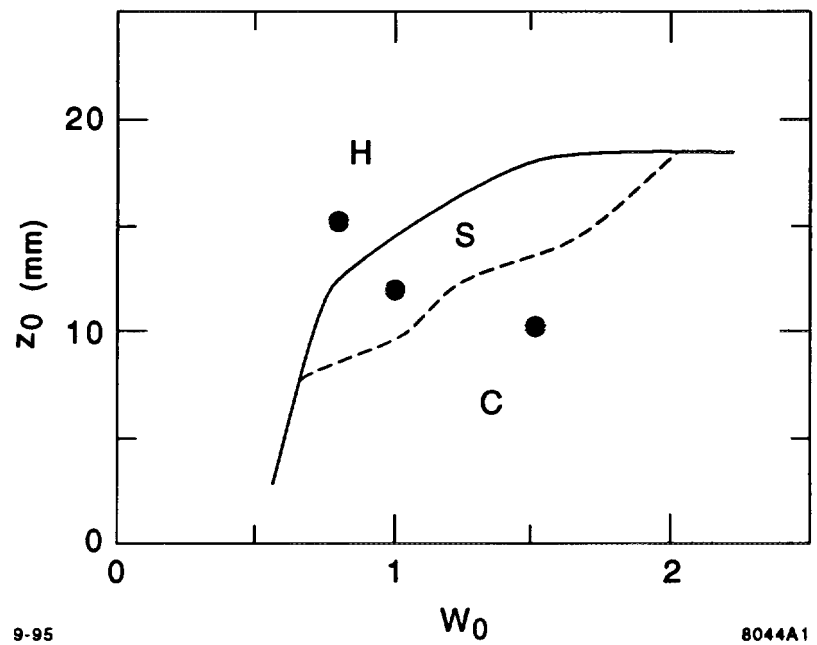

Fig. 1. Behavior of an injected beam in the (W_0, z_0) space.

show the instantaneous rms energy spread. The Haissinski steady state (a,b), the sawtooth behavior (c,d), and the chaotic behavior (e,f) are apparent. Note that in the Haissinski state, the energy spread damps down to the unperturbed value $\sigma_\delta = 0.001$, as it should, although the z-distribution of the beam has acquired distinct double humps and has an rms different from the unperturbed value.

In a separate study, a case with $W_0 = 2, z_0 = 20$ mm is first shown in Fig.3(a,b), which exhibits a chaotic behavior. (Here we used 10000 turns tracking.) When the injected beam emittance is changed from $5\sigma_z \times 5\sigma_\delta$ to $\sigma_z \times \sigma_\delta$ under otherwise the same conditions, we obtained Fig.3(c,d), which is a Haissinski state. This indicates the fact that how the beam behaves depends on the initial conditions of how the beam is injected.

Some tentative conclusions are given below:

(1) We reconfirmed the existence of the BD mechanism.

(2) However, because no double-humped distribution and no large-scale bunch shape oscillation have been observed in streak camera experiments, it seems unlikely that the BD mechanism alone is responsible for what was observed at the SLC Damping Ring.

(3) The threshold for the sawtooth behavior is not the same as the threshold when the Haissinski solution develops a second hump. It is possible to have a stable double-humped Haissinski distribution which is stable against sawtooth behavior as well as the microwave instability. This observation may be in conflict with some phenomenological models of the bunch lengthening effect.

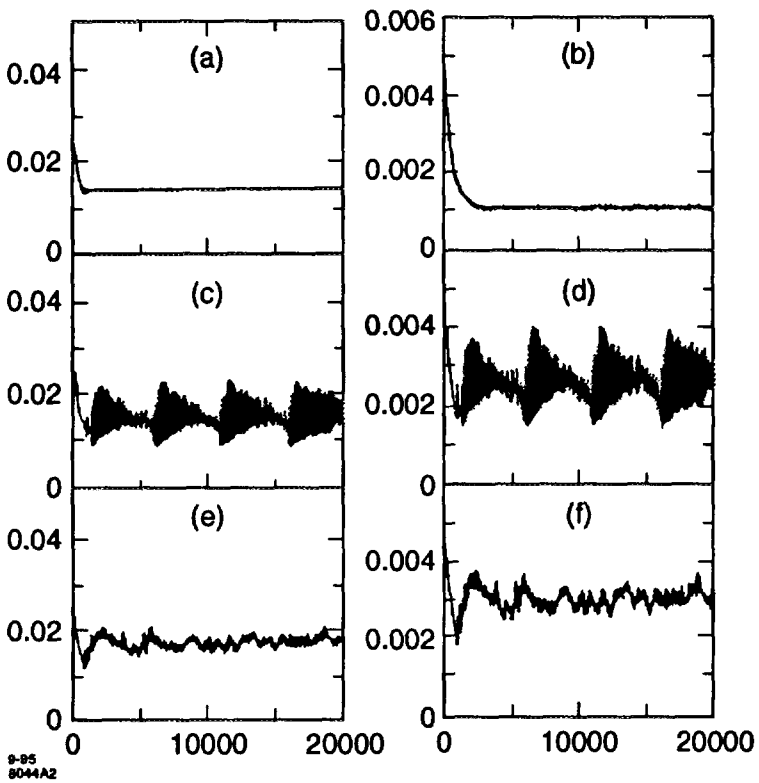

Fig. 2. Examples of beam behavior (a,b) Haissinski steady state, (c,d) sawtooth behavior, and (e,f) chaotic behavior.

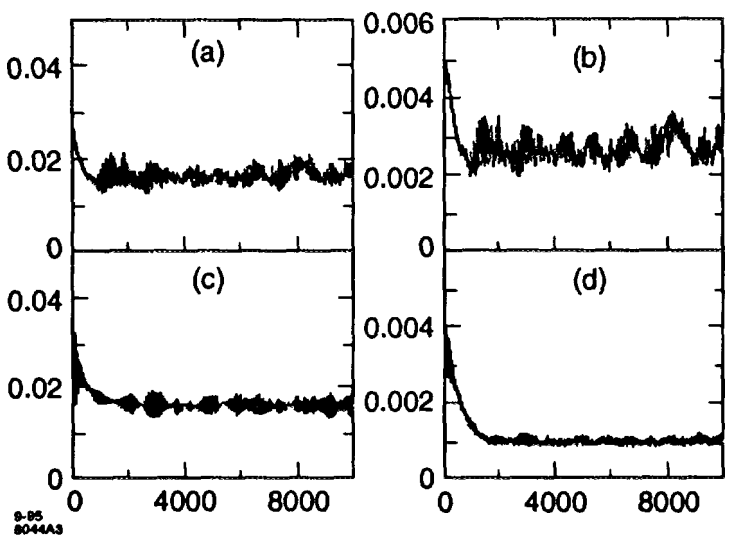

Fig. 3. Beam behavior also depends on the injected beam emittance. In case $W_0 = 2, z_0 = 20$ mm, the beam exhibits (a,b) chaotic behavior when injected with a large emittance, and (c,d) Haissinski state when injected with a small emittance.

(4) Another question arises as to whether the threshold for the sawtooth behavior is the same as the threshold of a microwave instability. More specifically, does the solid curve in Fig.1 coincide with the microwave instability threshold. This question seems to deserve a closer study and is yet to be completed.

(5) The existence and the stability of the Haissinski distribution does not guarantee a stable beam in a damping ring. The beam, injected with a much larger emittance, may choose to stay in a sawtooth state before it damps down to the Haissinski state, even when the Haissinski state is stable. This issue should receive some attention in the design of damping rings because the beam may not always reach the damped state as one might assume.

I would like to thank K. Bane, D. Brandt, J. Gareyte, S. Heifets, R. Holtzapple, K. Oide, R. Ruth, R. Siemann, G. Stupakov for several helpful discussions.

1. References

1. P. Krejcik, et al., Proc. IEEE Part. Accel. Conf., Washington D.C., 1993, p.3240.
2. K. Bane, et al., to appear in Proc. IEEE Part. Accel. Conf., Dallas, 1995.
3. K.L.F. Bane and K. Oide, to appear in Proc. IEEE Part. Accel. Conf., Dallas, 1995.
4. Yongho Chin and Kaoru Yokoya, Nucl. Instr. Meth. in Phys. Res. 226 (1984) 223.
5. Kaoru Yokoya, Proc. Tamura symposium
6. R. Baartman and D'Yachkov, to appear in Proc. IEEE Part. Accel. Conf., Dallas, 1995.
7. J. Haissinski, Nuovo Cimento 18B, 72 (1973).

Bunch motion in the presence of the self-induced voltage due to a reactive impedance with RF off

E.Shaposhnikova

CERN, Geneva, Switzerland

Abstract

Analytic self-consistent solutions have been found for the nonlinear Vlasov equation describing different types of behaviour with time of an intense bunch under the influence of voltage induced due to a reactive part of broad band impedance. The problem is solved for the particular type of the initial distribution function in longitudinal phase space which is elliptic and corresponds to parabolic line density.

This paper is devoted to the consideration of the effects in the machine with RF off. In this case the induced voltage is changing with time and can significantly affect bunch motion. The same method applied in the case with RF on allows the time dependent effects of potential well distortion to be analysed.

Numerical estimations for the CERN SPS show that effect of induced voltage is important for beam manipulations with RF off. Measurements of the change in the rate of debunching with intensity can be used to estimate the value of the reactive impedance.

Contents

1 Introduction

It is well known that voltage induced due to the interaction of high intensity long bunches with the low frequency reactive part of the broad band impedance can produce significant potential well distortion when RF is on. Measurements of the resulting bunch-lengthening (or shortening) allow the value of the low frequency part of the impedance to be estimated.

The purpose of the present work is to evaluate the possible effect of the induced voltage on the motion of the intense single bunch when RF is off. Without the focusing effect of the external RF system this bunch normally starts to spread out or debunch. Then the induced voltage which affects the bunch motion is also changing with time.

Debunching is often one of the manipulations with the beam in the machine. Smooth changing of bunch parameters during debunching is also used to measure momentum spread in the bunch and as a method to investigate beam instabilities. However it was noticed already in [1] that measurements of microwave instability threshold during debunching don't give accurate results due to the influence of induced voltage on the variation of beam parameters. Debunching was recently used during studies of the microwave instability threshold for the proton beam in the SPS, [2]. The rate of debunching measured from the decay of the peak line density signal was found to be significantly different from the expected value. It was suggested, [3], that this fast debunching can also be explained by the defocusing effect of induced voltage.

Below the problem is examined in the following way. To introduce convenient definitions we start with the trivial case of the debunching of a low intensity bunch. In the next chapter we consider first the main equations describing the motion of a dense bunch with RF off but in the presence of induced voltage which is changing with time during debunching. With a special choice of the initial distribution function (elliptic in phase space with parabolic line density) this nonlinear problem has exact self-consistent solutions. These solutions, depending on the parameters of the system, describe different kinds of bunch behaviour which are analysed. A defocusing type of induced voltage makes debunching faster in comparison with the zero intensity case. With a focusing induced voltage, increase of intensity first slows down debunching, and then starting from some critical intensity leads to oscillations of the line density. From the exact solutions some simplified expressions are obtained for the variation of beam parameters during the initial part of debunching and these are used later for preliminary numerical estimations of the effect in the SPS. We show the possibility of estimating the low frequency part of the impedance from the measured decay of peak line density during debunching. Finally the variation of microwave instability threshold during debunching is also discussed.

The same method can be used to analyse the effect of induced voltage on the evolution

of the bunch injected into machine with RF on.

2 Bunch motion with RF off in the low intensity case

Let us start first by considering the debunching of the single bunch in the machine with RF off and when any intensity effects are ignored.

In general at the beginning of debunching the initial distribution function of the bunch is the function of the Hamiltonian H_0 of the system with RF on in the same machine or in the injector:

$$F = F(H_0). \tag{1}$$

If bunches are sufficiently short compared with the RF period, the Hamiltonian of the particle in the single RF system can be written in the form

$$H_0 = \dot{\theta}_0^2 + \Omega^2\theta_0^2, \tag{2}$$

where Ω is the frequency of linear synchrotron oscillations in the RF system where the bunch was created. Here θ_0 and $\dot{\theta}_0$ are initial values of

$$\theta \quad \text{and} \quad \dot{\theta} = \frac{d\theta}{dt},$$

a pair of conjugate coordinates we shall use to define the position of the single particle in the longitudinal phase space: θ is an azimuthal coordinate measured from the position of the synchronous particle $\theta = 0$ (when RF was on) and $\dot{\theta}$ is connected with momentum deviation $\Delta p = p - p_s$ from the synchronous value p_s by the expression

$$\dot{\theta} = \omega_0\eta\frac{\Delta p}{p_s}. \tag{3}$$

Here $f_0 = \omega_0/(2\pi)$ is the revolution frequency and $\eta = 1/\gamma_t^2 - 1/\gamma^2$.

Distribution function (1) after integration over $\dot{\theta}_0$ gives the initial line density (at $t = 0$):

$$\lambda_0 = \lambda(\theta_0) = \int_{-\dot{\theta}_l}^{\dot{\theta}_l} F(\dot{\theta}_0^2 + \Omega^2\theta_0^2)d\dot{\theta}_0, \tag{4}$$

where the limits of integration are functions of θ_0

$$\dot{\theta}_l = (H_m - \Omega^2\theta_0^2)^{1/2} \tag{5}$$

with

$$H_m = \Omega^2\theta_m^2 = \dot{\theta}_m^2. \tag{6}$$

Above θ_m and $\dot{\theta}_m$ are the maximum values of θ_0 and $\dot{\theta}_0$ in the bunch.

From the normalisation condition we also have

$$N = \int_{-\theta_m}^{\theta_m} \lambda(\theta) d\theta, \tag{7}$$

where N is the number of particles in the bunch.

Single particle motion when RF is off and any intensity effects are ignored is governed by the equation:

$$\frac{d^2\theta}{dt^2} = 0. \tag{8}$$

The solution of this equation for the particle with initial coordinates $(\theta_0, \dot{\theta}_0)$ has the form:

$$\theta = \theta_0 + \dot{\theta}_0 t, \tag{9}$$

$$\dot{\theta} = \dot{\theta}_0. \tag{10}$$

According to Liouville's theorem phase space density doesn't change with time along the particle trajectories. To calculate line density during the debunching process we can then substitute the solutions (9)-(10), rewritten in the form

$$\theta_0 = \theta - \dot{\theta} t, \tag{11}$$

$$\dot{\theta}_0 = \dot{\theta}, \tag{12}$$

into the initial distribution function (1), and integrate it over $\dot{\theta}$. For the Hamiltonian (2) we have

$$H_0 = \dot{\theta}_0^2 + \Omega^2 \theta_0^2 = q^2 \left[\dot{\theta} - \frac{\Omega^2 \theta t}{q^2} \right]^2 + \Omega^2 \frac{\theta^2}{q^2}, \tag{13}$$

where

$$q = q(t) = (1 + \Omega^2 t^2)^{1/2}. \tag{14}$$

The line density can be written as

$$\lambda(\theta, t) = \frac{1}{q} \int_{-\dot{\Theta}_l}^{\dot{\Theta}_l} F_0 \left(\dot{\Theta}^2 + \Omega^2 \frac{\theta^2}{q^2} \right) d\dot{\Theta}, \tag{15}$$

where the integration variable $\dot{\Theta}$ is defined by

$$\dot{\Theta} = q \left(\dot{\theta} - \frac{\Omega^2 \theta t}{q^2} \right), \tag{16}$$

and the integration limits are:

$$\dot{\Theta}_l = \left(H_m - \Omega^2 \frac{\theta^2}{q^2} \right)^{1/2} = \dot{\theta}_m \left(1 - \frac{\theta^2}{\theta_m^2 q^2} \right)^{1/2}. \tag{17}$$

The expression for line density (15) should be compared with the expression for the initial line density (4). As a result the line density during debunching can be written in the form

$$\lambda(\theta,t) = \frac{1}{q}\lambda_0\left(\frac{\theta}{q}\right). \tag{18}$$

As can be checked easily it satisfies the normalisation condition (7).

Momentum spread along the bunch during debunching can be found from expressions (3) and (13).

A useful characteristic of the debunching rate is the time constant

$$t_d = 1/\Omega. \tag{19}$$

This is the time at which the peak line density is reduced by $\sqrt{2}$ from the initial value. If $t \ll t_d$ the line density doesn't change significantly, and for $t \gg t_d$ the decrease in line density is inversely proportional to time.

As we can see, for low intensity bunches the decay of peak line density during debunching

$$\lambda_p = \frac{\lambda_{p0}}{(1+\Omega^2 t^2)^{1/2}}. \tag{20}$$

is independent of the form of the initial distribution function assuming that it is the function of the Hamiltonian for the short bunch in the single RF system with peak value at $\theta = 0$.

3 Bunch motion with RF off in the high intensity case

3.1 Main equations

Here we consider the situation when an intense bunch created in the single RF system is injected at the moment $t = 0$ into the machine with RF off.

The equations of motion for the particles under these conditions become

$$\frac{d\theta}{dt} = \omega_0\eta\frac{\Delta p}{p_s}, \tag{21}$$

$$\frac{d(\Delta p)}{dt} = \frac{e}{2\pi R}V_e(\theta,t), \tag{22}$$

where R is the average radius of the machine. The voltage V_e induced by the interaction of the bunch with the low frequency reactive part of the broad band impedance can be presented in the form:

$$V_e(\theta,t) = -L\frac{dI(\theta,t)}{dt} = -Le\omega_0^2\frac{\partial\lambda(\theta,t)}{\partial\theta}, \tag{23}$$

where $I(\theta,t)$ is the bunch current and L is the effective inductance of the machine connected with the reactive part of the longitudinal coupling impedance by the relation $\omega_0 L = \mathrm{ImZ/n}$. In expression (23) we neglect derivatives $\frac{\partial\lambda(\theta,t)}{\partial t}$ describing the slow dependence of $\lambda(\theta,t)$ on time during debunching.

Equations (21)-(22) are nonlinear since the induced voltage V_e is defined by the derivative of the line density the variation of which with time depends upon the induced voltage. To find a self consistent solution to the system of equations (21)-(22) is equivalent to solving the nonlinear Vlasov equation for distribution function $F = F(\theta,\dot{\theta},t)$

$$\frac{\partial F}{\partial t} + \dot{\theta}\frac{\partial F}{\partial \theta} + \frac{\omega_0 \eta e V_e(\theta,t)}{2\pi R p_s}\frac{\partial F}{\partial \dot{\theta}} = 0. \tag{24}$$

By analogy with the low intensity case, we can try to find the distribution function at the moment t from the initial distribution function

$$F(\theta,\dot{\theta},t) = F_0\left(\theta_0(\theta,\dot{\theta},t), \dot{\theta}_0(\theta,\dot{\theta},t), 0\right), \tag{25}$$

if initial coordinates θ_0 and $\dot{\theta}_0$ are defined as functions of coordinates θ, $\dot{\theta}$ and t.

In general, there are no regular methods which would allow us to find solutions to nonlinear problem of this type. However, in this particular case it turns out that analytic solutions can be obtained with a special choice for the initial distribution function. Let us consider the case where, at the moment $t = 0$, the bunch has an elliptical distribution function in longitudinal phase space

$$F = \mathcal{F}_0\left(1 - \frac{H_0}{H_m}\right)^{1/2} = \mathcal{F}_0\left(1 - \frac{\theta_0^2}{\theta_m^2} - \frac{\dot{\theta}_0^2}{\dot{\theta}_m^2}\right)^{1/2}, \quad H_0 < H_m. \tag{26}$$

This distribution function corresponds to a bunch with parabolic line density

$$\lambda(\theta_0) = \lambda_{p0}\left(1 - \frac{\theta_0^2}{\theta_m^2}\right), \tag{27}$$

where $\lambda_{p0} = \mathcal{F}_0\dot{\theta}_m\pi/2$ and from the normalisation condition we have also $\lambda_{p0} = 3N/(4\theta_m)$.

According to (18), the line density of low intensity bunches with this type of particle distribution would change with time during debunching as

$$\lambda(\theta,t) = \frac{\lambda_{p0}}{q(t)}\left[1 - \frac{\theta^2}{q^2(t)\theta_m^2}\right], \tag{28}$$

where function $q(t)$ is defined by expression (14).

For the chosen distribution function the induced voltage can be written at the beginning of debunching ($t = 0$) as

$$V_e(\theta,0) = V_0\,\theta, \tag{29}$$

where we define

$$V_0 = \frac{3Ne\omega_0}{2\theta_m^3}\frac{\mathrm{Im}Z}{n}. \tag{30}$$

Before describing the nonlinear solution let us first introduce some preliminary considerations which may suggest the form in which we can look for the self-consistent solution in the following section.

If we would try to find an approximate solution for this problem by iteration we can use first the zero intensity solution (28) to calculate the induced voltage during debunching. Then the equation of particle motion giving the next approximation is

$$\frac{d^2\theta}{dt^2} - \frac{\epsilon\,\theta}{q^3(t)} = 0, \tag{31}$$

where the parameter

$$\epsilon = \frac{\omega_0^2\eta e V_0}{2\pi\beta^2 E_s} \tag{32}$$

has the dimensions of frequency squared and can be written also as

$$\epsilon = \mathrm{sgn}(\eta \mathrm{Im}Z)\,\Omega_\epsilon^2. \tag{33}$$

Differential equation (31) is linear in θ with a time dependent coefficient. The general solution for the equations of this type can be written in the form

$$\theta = \theta_0 f_1(t) + \dot{\theta}_0 f_2(t), \tag{34}$$

where $f_1(t)$ and $f_2(t)$ are the fundamental solutions [1] with Wronskian $W = f_1\dot{f}_2 - \dot{f}_1 f_2 = const.$

The next step is to express the initial coordinates as functions of θ, $\dot{\theta}$ and t and substitute them in the initial distribution function (26). As a result for the next iteration one obtains the equation

$$\frac{d^2\theta}{dt^2} - \frac{\epsilon\,\theta}{q_1^3(t)} = 0, \tag{35}$$

where $q_1(t) = (f_1^2 + \Omega^2 f_2^2)^{1/2}$. As we can see this equation repeats the form of equation (31) but with a different time dependent coefficient. This suggests that if our iteration proccess converges we can search for a closed form solution of the same type as presented by expressions (34) and (35). This is done in the next section.

Note that equation (31) shows the well known fact that if the low frequency part of the coupling impedance of the machine is inductive ($\mathrm{Im}Z > 0$) then the induced voltage has a defocusing effect above transition ($\eta > 0$) and focusing below transition.

[1] We were not able to find analytical expressions for functions f_1, f_2.

3.2 Nonlinear solution

Using the definitions introduced above the nonlinear self-consistent system of equations governing the particle motion during debunching finally can be presented in the form

$$\frac{d^2\theta}{dt^2} + \frac{\epsilon\theta_m^2}{2\lambda_{p0}}\frac{\partial\lambda}{\partial\theta} = 0, \tag{36}$$

$$\lambda(\theta,t) = \mathcal{F}_0 \int_{\dot\theta_1}^{\dot\theta_2} \left[1 - \frac{\theta_0^2(\theta,\dot\theta,t)}{\theta_m^2} - \frac{\dot\theta_0^2(\theta,\dot\theta,t)}{\dot\theta_m^2}\right]^{1/2} d\dot\theta, \tag{37}$$

where $\dot\theta_1 = \dot\theta_1(\theta,t)$ and $\dot\theta_2 = \dot\theta_2(\theta,t)$ are solutions of equation

$$1 - \frac{\theta_0^2(\theta,\dot\theta,t)}{\theta_m^2} - \frac{\dot\theta_0^2(\theta,\dot\theta,t)}{\dot\theta_m^2} = 0. \tag{38}$$

Suppose that for the particle with initial coordinates $(\theta_0,\dot\theta_0)$ the system of equations (36)-(37) has a solution which can be written in the following form

$$\theta(t) = \theta_0\, y_1(t) + \dot\theta_0\, y_2(t), \tag{39}$$

$$\dot\theta(t) = \theta_0\, \dot y_1(t) + \dot\theta_0\, \dot y_2(t), \tag{40}$$

where y_1 and y_2 are unknown functions of time with initial conditions:

$$y_1(0) = 1, \quad y_2(0) = 0, \tag{41}$$

$$\dot y_1(0) = 0, \quad \dot y_2(0) = 1. \tag{42}$$

The Wronskian of this system is

$$W = y_1\dot y_2 - \dot y_1 y_2. \tag{43}$$

Suppose that

$$W = const \tag{44}$$

then from initial conditions (41)-(42) it follows that $W = 1$.

This assumption allows us to use the same method as used above in the low intensity case, and express the initial coordinates as functions of coordinates θ and $\dot\theta$ at the moment t

$$\theta_0 = \theta\,\dot y_2 - \dot\theta\, y_2, \tag{45}$$

$$\dot\theta_0 = -\theta\,\dot y_1 + \dot\theta\, y_1. \tag{46}$$

Substitution of the expressions (45)-(46) into the initial distribution function (26) makes it possible to find the distribution function at the moment t

$$F = \mathcal{F}_0 \left[1 - \frac{(\theta\dot y_2 - \dot\theta y_2)^2}{\theta_m^2} - \frac{(\dot\theta y_1 - \theta\dot y_1)^2}{\dot\theta_m^2}\right]^{1/2}. \tag{47}$$

Then the line density (37), after integration over $\dot{\theta}$ of the above expression and using condition (44) becomes

$$\lambda(\theta,t)=\int_{\dot{\theta}_1}^{\dot{\theta}_2}F(\theta,\dot{\theta},t)d\dot{\theta}=\frac{\lambda_{p0}}{r}\left[1-\frac{\theta^2}{r^2\theta_m^2}\right], \tag{48}$$

where we define

$$r=r(t)=(y_1^2+\Omega^2y_2^2)^{1/2}. \tag{49}$$

The derivative of the line density can also be find

$$\frac{\partial\lambda}{\partial\theta}=-\frac{\lambda_{p0}2\theta}{r^3\theta_m^2}. \tag{50}$$

Now our main differential equation (36) can be rewritten either in the form

$$\frac{d^2\theta}{dt^2}-\frac{\epsilon\theta}{r^3}=0 \tag{51}$$

or as a system of equations for y_1 and y_2

$$\frac{d^2y_1}{dt^2}-\frac{\epsilon y_1}{(y_1^2+\Omega^2y_2^2)^{3/2}}=0, \tag{52}$$

$$\frac{d^2y_2}{dt^2}-\frac{\epsilon y_2}{(y_1^2+\Omega^2y_2^2)^{3/2}}=0. \tag{53}$$

It is interesting to note that this last system of equations is also known to describe the motion of a body in the $(y_1,\Omega y_2)$ plane under the influence of gravitation with attractive force for $\epsilon<0$ and repulsive for $\epsilon>0$.

Let us introduce new variables $r(t)$ and $\xi(t)$ according to the following formulae

$$y_1=r\cos\xi,\quad y_2=\frac{r}{\Omega}\sin\xi. \tag{54}$$

Then equations (52) - (53), using these new variables, can be transformed into the form:

$$r\ddot{\xi}+2\dot{r}\dot{\xi} = 0, \tag{55}$$

$$\ddot{r}-r\dot{\xi}^2-\frac{\epsilon}{r^2} = 0. \tag{56}$$

This system of nonlinear equations has as first integrals of motion

$$r^2\dot{\xi} = C_1, \tag{57}$$

$$\dot{r}^2+\frac{C_1^2}{r^2}+\frac{2\epsilon}{r} = C_2, \tag{58}$$

Using again gravitation terminology one can say that the first expression corresponds to the second law of Kepler (law of areas) and the second equation describes conservation of energy

in the system. Constants C_1 and C_2 are defined by the initial conditions (41)-(42) which now have the form

$$r(0) = 1, \quad \xi(0) = 0, \tag{59}$$

$$\dot{r}(0) = 0, \quad \dot{\xi}(0) = \Omega. \tag{60}$$

Thus for C_1 and C_2 we get

$$C_1 = \Omega, \tag{61}$$

$$C_2 = \Omega^2 + 2\epsilon. \tag{62}$$

We must check now that the Wronskian (43) of the system satisfies our initial assumption (44) that it is constant and equal to one. Indeed using variables $r(t)$ and $\xi(t)$ and the expressions(57), (61) we obtain

$$W = \frac{r^2\dot{\xi}}{\Omega} = \frac{C_1}{\Omega} = 1. \tag{63}$$

Note, that the solutions found above for $y_1(t)$ and $y_2((t)$ define, in fact, from expression (47) a distribution function which is a time dependent solution of the nonlinear Vlasov equation (24). However this method only works due to the special choice of initial distribution function, with which the induced voltage is proportional to θ.

3.3 Analysis of solutions

3.3.1 Exact solutions

The integrals of motion found in the previous section allow us to rewrite expression (58) in the form

$$\frac{\dot{r}^2}{2} + U(r) = 0, \tag{64}$$

where

$$U(r) = -\frac{\Omega^2(r-1)(ar+1)}{2r^2} \tag{65}$$

and constant

$$a = \frac{C_2}{C_1^2} = 1 + 2\frac{\epsilon}{\Omega^2} = 1 + 2\mathrm{sgn}(\eta \mathrm{Im}Z)\frac{\Omega_\epsilon^2}{\Omega^2}. \tag{66}$$

This equation can be interpreted as the equation of motion of some particle with the coordinate r in the potential $U(r)$. In reality, according to expression (48), $r(t)$ is a positive defined function which describes the variation with time of bunch length τ

$$\frac{\tau(t)}{\tau(0)} = r(t) \tag{67}$$

or of peak line density

$$\frac{\lambda_p(t)}{\lambda_{p0}} = \frac{1}{r(t)} \tag{68}$$

with the initial condition

$$r(0) = 1. \tag{69}$$

Increasing of r with time means decreasing of peak line intensity - or debunching.

The solution of equation (64) can be written in the following form:

$$\Omega t = \pm \int_1^r \frac{r dr}{\sqrt{\rho(r)}}, \tag{70}$$

where we use the definition

$$\rho(r) = (r-1)(ar+1). \tag{71}$$

If the solution $r(t)$ is known, then the function $\xi(t)$ can be found from (57)-(58) and is defined by the expression:

$$\xi = \pm \int_1^r \frac{dr}{r\sqrt{\rho(r)}}. \tag{72}$$

After integration, we have:

$$r[(\Omega^2 + \epsilon)\cos\xi - \epsilon] = \Omega^2. \tag{73}$$

Depending on the shape of the effective potential $U(r)$ (or value of parameter a) solutions of equation (64) have different character. Let us consider them.

$\boldsymbol{a = 1}$. If any intensity effects are absent then parameters $\epsilon = 0$ and $a = 1$, and as follows from (65) the potential has the shape

$$U(r) = \frac{\Omega^2}{2}\left(\frac{1}{r^2} - 1\right). \tag{74}$$

This potential is shown in Fig.1. Expression (70) gives in this case the solution (14) already found in Chapter 1 for the low intensity case:

$$r(t) \equiv q(t) = (1 + \Omega^2 t^2)^{1/2}. \tag{75}$$

The behaviour of the normalised peak line density $\lambda_p(t)/\lambda_{p0} = 1/r$ for $\epsilon = 0$ (and $a = 1$) is shown in Fig.2.

For cases where the intensity effects are considered and therefore $\epsilon \neq 0$ there are two main types of solutions of equation (64) which correspond to infinite and finite (periodic) motion. We analyse them below.

$\boldsymbol{a > 0}$. The integral (70) gives the solution

$$\Omega t = \frac{\sqrt{\rho(r)}}{a} + \frac{a-1}{2a^{3/2}} \ln \frac{|2\sqrt{a\rho(r)} + 2ar + 1 - a|}{1+a}, \tag{76}$$

where $\rho(r)$ is defined by expression (71). Motion in this case is only infinite, which means continuous debunching ($r \to \infty$ with $t \to \infty$). However the character of the debunching is different depending on the value of a. If $a > 1$ the induced voltage has a defocusing effect and debunching is faster compared to the low intensity case. For $a < 1$ debunching is slowed down by the focusing effect of the induced voltage. These two situations are shown in Figs.1-2 together with the low intensity case $a = 1$.

$\boldsymbol{a = 0}$. This value of parameter a corresponds to the point of bifurcation where the character of the solution is changing. From (70) we can find

$$\Omega t = \frac{2}{3}(r-1)^{3/2} + 2(r-1)^{1/2}. \tag{77}$$

This solution is presented in Figs.1-4.

$\boldsymbol{a < 0}$. This case can only occur for a focusing type of induced voltage ($\eta \mathrm{Im}Z < 0$) and $\Omega_\epsilon^2 > \Omega^2/2$. The potential $U(r)$ has the shape of a potential well and the solutions describe oscillations of peak line density with time.

If $\boldsymbol{-1 < a < 0}$ then the solution found from (70) has the form

$$\Omega t = \frac{\sqrt{\rho(r)}}{a} + \frac{1-a}{2a|a|^{1/2}}\left[\arcsin\frac{2ar+1-a}{|1+a|} - \frac{\pi}{2}\right], \tag{78}$$

where $a \neq -1$. In this case oscillations begin with the line density decreasing (which appears for some time as if it is debunching). Oscillation amplitude is defined by the inequality

$$|a| \leq \frac{1}{r} \leq 1. \tag{79}$$

The effective potential well is shown in Fig.3 for $a = -0.3$ together with the $a = 0$ case for comparison. The corresponding behaviour of bunch line density is presented in Fig.4.

The period of the oscillations of the line density is

$$T = \frac{\pi}{\Omega}\frac{(1-a)}{|a|^{3/2}} = \frac{2\pi\Omega_\epsilon^2}{(2\Omega_\epsilon^2 - \Omega^2)^{3/2}}. \tag{80}$$

As can be seen from this expression a bunch with an intensity such that $\Omega_\epsilon^2/\Omega^2 = 1/2$ ($a = 0$) has an infinitely large oscillation period and continuously debunches.

The period and amplitude of the line density oscillations decrease (compare Fig.5 with Fig.4) with growing absolute value of parameter a (which can be for example due to increasing intensity or impedance). As a result at $a \sim -1$, the period $T \sim (2\pi)/\Omega$ but with oscillation amplitude close to zero.

$\boldsymbol{a = -1}$. This case corresponds to the equilibrium situation when the bunch at the moment $t = 0$ is in the minimum of the potential well $U(r)$ with solution $r = 1$ not changing with time (see Fig.6). With this value of a, $\Omega_\epsilon^2 = \Omega^2$ and the initial bunch is matched to the waveform created by the induced voltage.

For $\boldsymbol{a < -1}$ the amplitude of peak line density oscillations starts to grow with increasing absolute value of parameter a:

$$1 \leq \frac{1}{r} \leq |a| \tag{81}$$

Oscillations now start at $t = 0$ with the peak line density increasing and have a period also defined by expression (80). The solution found from (70) has the form

$$\Omega t = \frac{\sqrt{\rho(r)}}{|a|} + \frac{1-a}{2|a|^{3/2}} \left[\arcsin \frac{2ar + 1 - a}{|1+a|} + \frac{\pi}{2} \right], \tag{82}$$

where also $a \neq -1$.

The effective potential well is shown in Fig.6 for $a = -1.3$. Corresponding behaviour of bunch line density is presented in Fig.7.

3.3.2 Approximate solutions

To estimate these effects it is useful to have simplified expressions to describe the variation of beam parameters during debunching ($a > 0$).

As follows from (65), at the beginning of debunching, when $r \sim 1$, we can obtain an approximate solution by replacing Ω^2 by $(\Omega^2 + \epsilon)$ in the formula (14) and then

$$r(t) \simeq [1 + (\Omega^2 + \epsilon)t^2]^{1/2}. \tag{83}$$

According to the assumption made to obtain this expression it is valid only at the start of debunching for times $t \ll 1/(\Omega^2 + \epsilon)^{1/2}$.

For $r \gg 1$ i.e. when the initial distribution is strongly debunched, the asymptotic solution can be again obtained from (65) by using the same formula (14) with $\Omega^2 \rightarrow (\Omega^2 + 2\epsilon)$:

$$r(t) \simeq [1 + (\Omega^2 + 2\epsilon)t^2]^{1/2}. \tag{84}$$

Both these approximations are shown together with the exact solution in Fig.8 for $a = 3$. As can be seen the exact solution lies between these two limits.

For a rough estimation of the time constant for the debunching of the intense beam at the beginning of the process ($t \ll 1/\Omega_\epsilon$ and $t \ll 1/\Omega$) we can use the following approximate formula

$$t_{de} \simeq 1/\sqrt{\Omega^2 + \epsilon}. \tag{85}$$

As can be seen a change in debunching rate due to intensity effects can be used to estimate the inductive part of the broad band impedance if the parameters of initial bunch are known.

However it is interesting to note that if the initial bunch was created in the same machine and later allowed to debunch, then the measured time t_{de} in first approximation is defined

only by the external voltage and doesn't depend on intensity. Indeed due to potential well distortion the matched bunch has dimensions defined by

$$\dot{\theta}_m/\theta_m = \Omega = \sqrt{\omega_s^2 - \epsilon},$$

where ω_s is the frequency of synchrotron oscillations with RF on. In this situation the measured debunching time will be

$$t_{de} \simeq 1/\omega_s.$$

3.4 Numerical estimations for the SPS

3.4.1 Defocusing effect

Let us start first with the analysis of the case which we had during the MD study, [2]. The injected bunches of 5-10ns were created in the low frequency RF system (10MHz) of the PS and can be considered there as "short" bunches. For the SPS, the spectrum of these 5-10ns long bunches is situated in the inductive part of the broad band impedance with resonant frequency of 1.3GHz. Previous measurements and estimations show that the space charge impedance of the SPS at 26GeV is much less than this inductive impedance.

Machine parameters were: $E_s = 26\text{GeV}, \gamma_t = 23.4$. For this situation we can expect that the induced voltage has a defocusing character which makes debunching faster. For the 5ns long bunch with emittance $\varepsilon_L = 0.2\text{eVs}$ we have

$$\Omega = \frac{\dot{\theta}_m}{\theta_m} = \frac{2\eta}{\tau}\frac{\Delta p_m}{p_s} = 0.21 \times 10^3 \text{s}^{-1},$$

which should give a debunching time constant in the low intensity case

$$t_d = 1/\Omega = 5\text{ms}.$$

For an intensity $N = 5 \times 10^{10}$ and the inductive part of the broad band impedance ImZ/n = 20Ω, we obtain from expression (32)

$$\Omega_\epsilon = 0.22 \times 10^3 \text{s}^{-1}.$$

This gives a value $a \simeq 3$. Supposing that the initial bunch was close to parabolic then we can calculate the decay of peak line density. This is shown in Fig.8 as a solid line together with the low intensity case, $a = 1$, for comparison. The debunching time constant, which measurement can provide, is

$$t_{de} \simeq 1/\sqrt{\Omega^2 + \Omega_\epsilon^2} = 3.3\text{ms}.$$

For 10ns long bunches with the same emittance $\varepsilon_L = 0.2eVs$ and intensity $N = 5 \times 10^{10}$ we can compare the values of

$$\Omega = 51.5\mathrm{s}^{-1} \quad \text{and} \quad \Omega_\epsilon = 56.6\mathrm{s}^{-1}.$$

Related to these values are the debunching time constants in the low and high intensity cases,

$$t_d = 19.5\mathrm{ms} \qquad \mathrm{t_{de}} \simeq 13.1\mathrm{ms}.$$

In this case parameter $a = 3.4$.

For both sets of measurements, with "short" and "long" bunches, we can observe a significant effect of the induced voltage on the debunching process. Moreover, accurate measurements of the decay of peak line density during debunching in this situation can give important information about the low frequency part of the coupling impedance of the machine.

3.4.2 Focusing effect

The interaction of the bunch with the inductive part of the impedance below transition, or with the capacitive above leads to a focusing effect which we would expect to slow down the debunching of the intense beam. The debunching time constant (at the beginning of the process) becomes

$$t_{de} = 1/\sqrt{\Omega^2 - \Omega_\epsilon^2}. \tag{86}$$

Let us estimate the possible effect in the SPS in the present fixed target mode of operation with machine parameters $E_s = 14\mathrm{GeV}, \gamma_t = 23.4$. Then for high intensity bunches with parameters $\tau = 5\mathrm{ns}, \varepsilon_\mathrm{L} = 0.1\mathrm{eVs}, \mathrm{N} = 5 \times 10^{10}$, available from the PS for recent MD studies at 14 GeV, and using again the value ImZ/n = 20Ω we obtain

$$\Omega = 0.95 \times 10^3 s^{-1} \quad \text{and} \quad \Omega_\epsilon = 0.68 \times 10^3 s^{-1}.$$

In this case $a = 0.025$. For bunches with a line density close to parabolic the corresponding decay of peak line density is described by the curve shown in Fig.2 for $a = 0$. From the previous analysis of different types of possible solutions in this system, at slightly higher intensities we could expect to observe rebunching.

4 Microwave instability threshold during debunching

The threshold of the microwave instability can be defined from the Boussard criterion. For a parabolic line density it has a form, [4]:

$$\frac{|Z_L|}{n} \leq F^* \frac{E_s|\eta|\beta^2}{eI(\theta)} \left[\frac{\Delta\hat{p}(\theta)}{p}\right]^2, \tag{87}$$

where formfactor $F^* = 0.7\pi 3/2 = 1.05\pi$. Here $\pm\Delta\hat{p}$ is the maximum momentum spread in the bunch at the position θ and I is the local current. During debunching both $\Delta\hat{p}$ and I become not only functions of coordinate θ but also of time. By analogy with the case when RF is on, [5], for the type of particle distribution in phase space chosen, the ratio

$$P = \frac{(\Delta\hat{p})^2}{I}$$

does not depend on coordinate θ and is constant along the bunch even during debunching.

The variation of line density is described by formula (48). The change of maximum momentum spread during debunching can be also calculated

$$\Delta\hat{p}(\theta,t) = \frac{\Delta p_m}{r(t)} \left[1 - \frac{\theta^2}{r^2(t)\theta_m^2}\right]^{1/2}, \tag{88}$$

where $\pm\Delta p_m$ is the maximum momentum spread in the bunch at $t = 0$. As a result we have

$$\frac{P(t)}{P(0)} = \frac{1}{r(t)}. \tag{89}$$

If the effect of induced voltage on the changing of bunch parameters during debunching is ignored then the function $r(t)$ is simply replaced by $q(t) = (1 + \Omega^2 t^2)^{1/2}$.

Using the expressions for Ω and Ω_ϵ, criterion (87) can be rewritten in our definitions as

$$\Omega_\epsilon^2 < \frac{\Omega^2}{r(t)} \frac{|\mathrm{Im}Z|}{|Z_L|}. \tag{90}$$

From the analysis of this expression we can make a few conclusions:

(1) If debunching is used as a method to determine the microwave instability threshold from criterion (87) it is necessary to take into account the effect of induced voltage on the bunch parameters variation. Otherwise (as was noticed first in [1], see also [2]) measurements do not give consistent results.

(2) Measurements of the peak line density variation during debunching give simultaneously information about function $P(t)$, which can be used to define the threshold intensity for microwave instability.

(3) Possible deviations of the value of the debunching time constant of an intense beam t_{de} from the low intensity value t_d should lie within some limits defined by the microwave instability.

5 Conclusions

Analytic solutions of the nonlinear Vlasov equation describing different types of behaviour with time have been found for an intense bunch, with an initial elliptic distribution function, under the effect of of self induced voltage in the machine with RF off.

Voltage induced due to the interaction of the beam with the low frequency part of the coupling impedance of the machine, as in the case with RF on, can have a significant effect on processes when RF is off. Measurements of the change in the rate of debunching with intensity can be used to estimate the value of the impedance supposing that the initial particle distribution in phase space is close to elliptic.

If debunching is used as a method to determine instability thresholds it is necessary to take into account the effect of induced voltage on the variation of the bunch parameters.

Acknowledgements

The author would like to thank T.Linnecar for many usefull discussions of this work, and D.Boussard, A.Hofmann and B.Zotter for reading the manuscript and valuable comments.

References

[1] P.Bramham et al., Longitudinal instabilities of bunched beams in the ISR, IEEE Trans. Nucl. Sci. NS-24, N3, 1490 (1977).

[2] T.Linnecar, E.Shaposhnikova, Measurements of the microwave instability in the SPS, CERN SL MD Note 164, SPS (1995).

[3] D.Boussard (private communication).

[4] D.Boussard, Observation of microwave longitudinal instabilities in the CPS, CERN LABII/RF/Int./75-2 (1975).

[5] A.Hofmann, F.Pedersen, Bunches with local elliptic energy distributions, IEEE Trans. Nucl. Sci., Vol. NS-26, No.3, 3526 (1979).

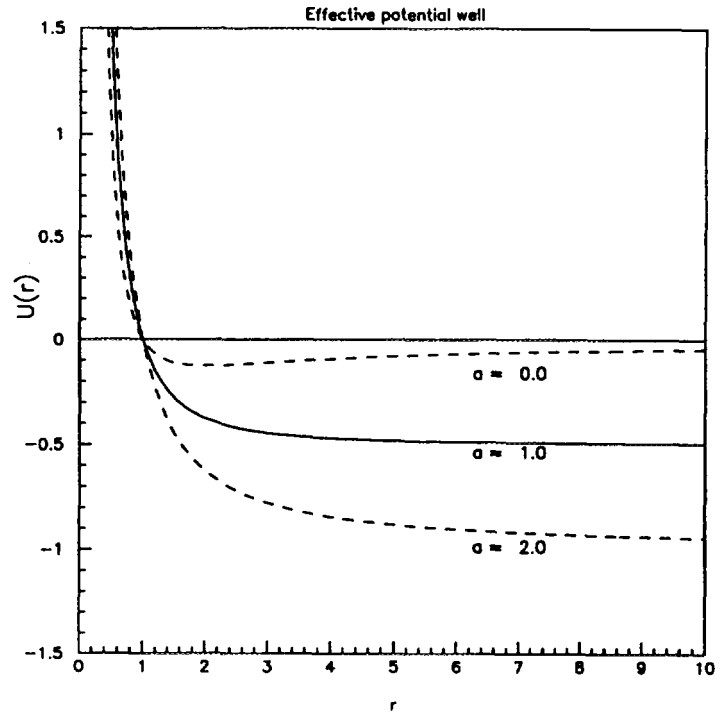

Figure 1: Effective potential $U(r)$ describing debunching in low intensity case, $a = 1$, and high intensity case with different types of induced voltage: defocusing, $a = 2$, and focusing, $a = 0$.

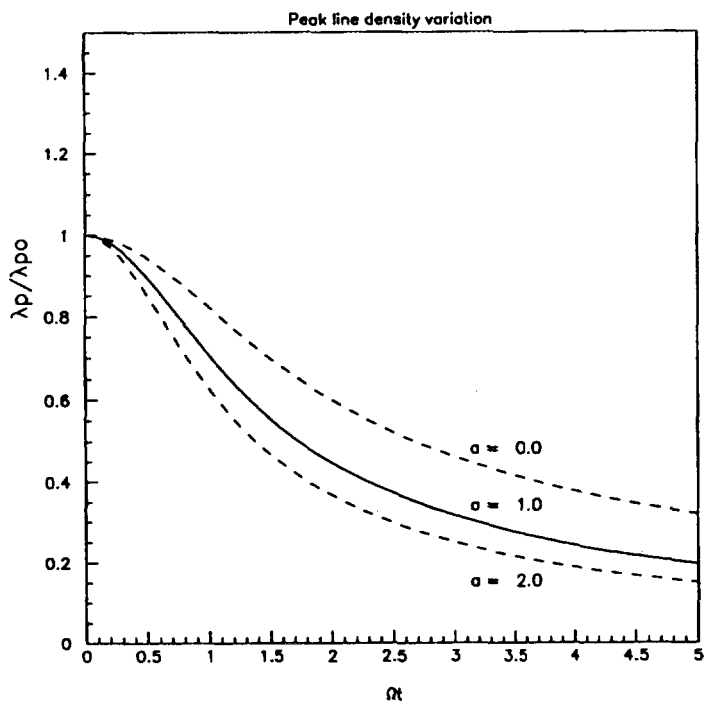

Figure 2: Variation of normalised peak line density $1/r$ during debunching for low intensity case, $a = 1$, and high intensity case with defocusing, $a = 2$, and focusing, $a = 0$, type of induced voltage.

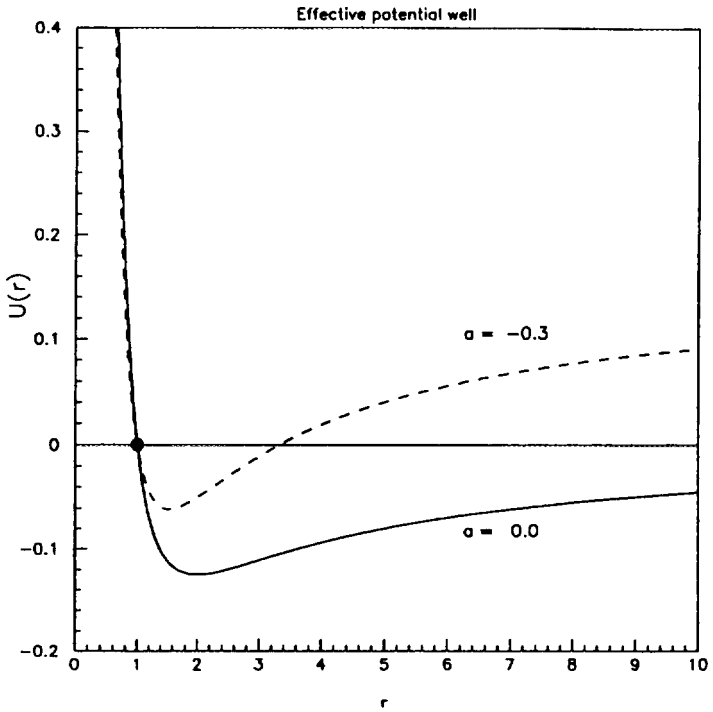

Figure 3: Effective potential well $U(r)$ describing oscillations of line density for focusing type of induced voltage.

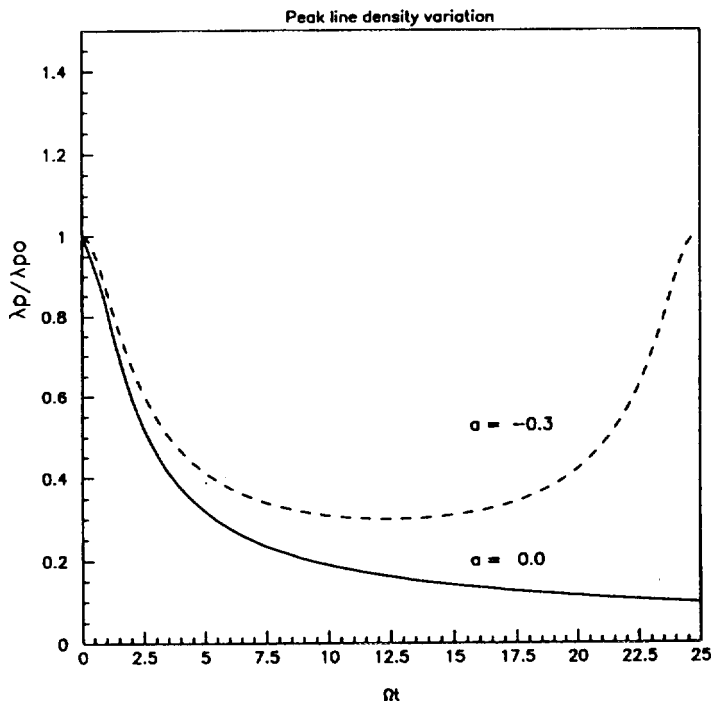

Figure 4: Variation of normalised peak line density $1/r$ for focusing type of induced voltage, $a = -0.3$ and $a = 0$.

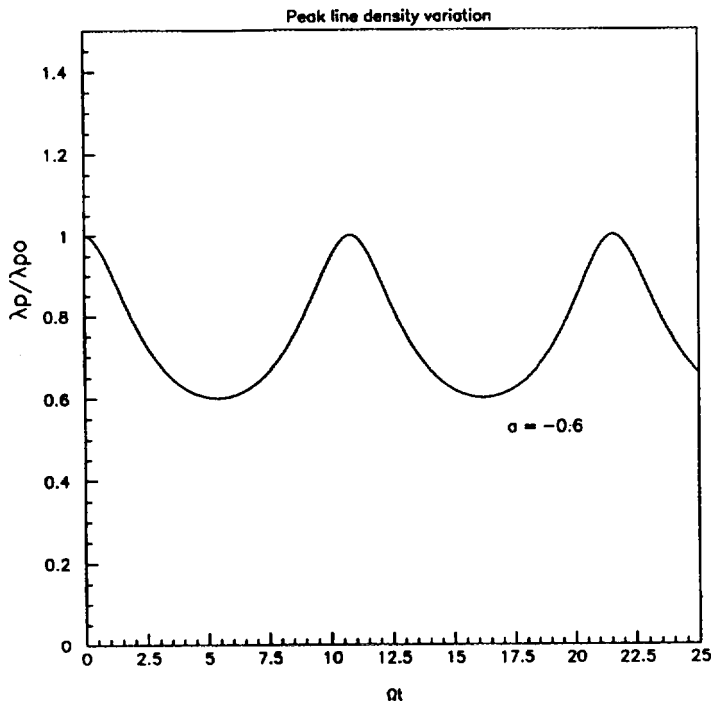

Figure 5: Variation of normalised peak line density $1/r$ for focusing type of induced voltage, $a = -0.6$.

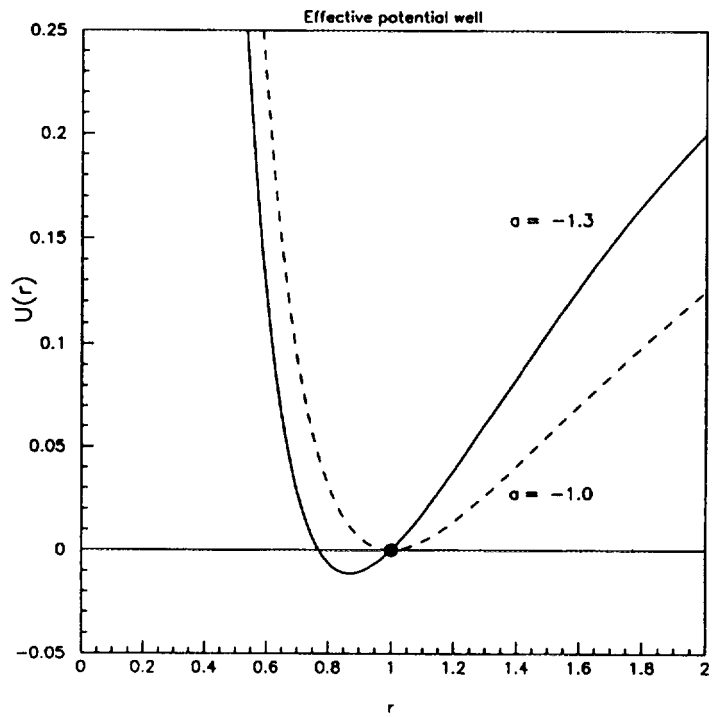

Figure 6: Effective potential well for equilibrium solution, $a = -1$, and oscillation of line density, $a = -1.3$.

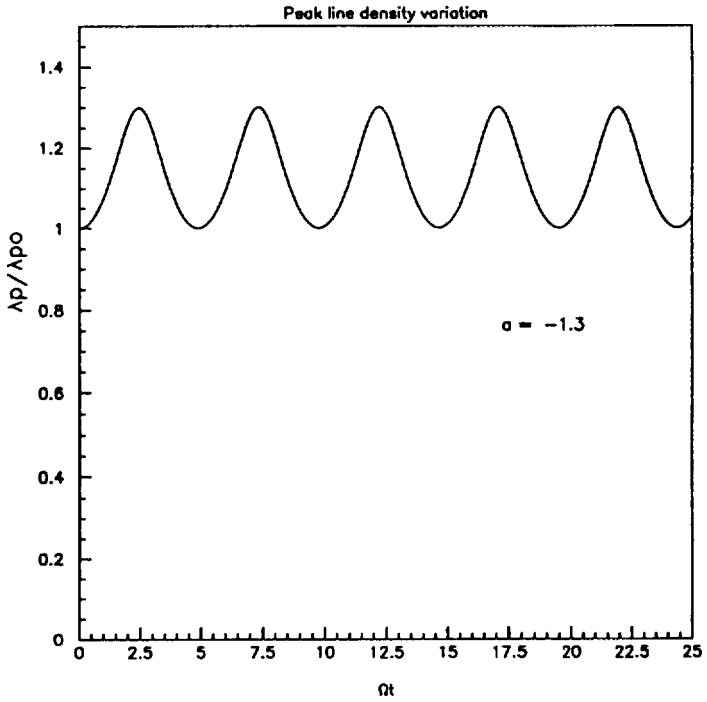

Figure 7: Variation of normalised peak line density $1/r$ for focusing type of induced voltage, $a = -1.3$.

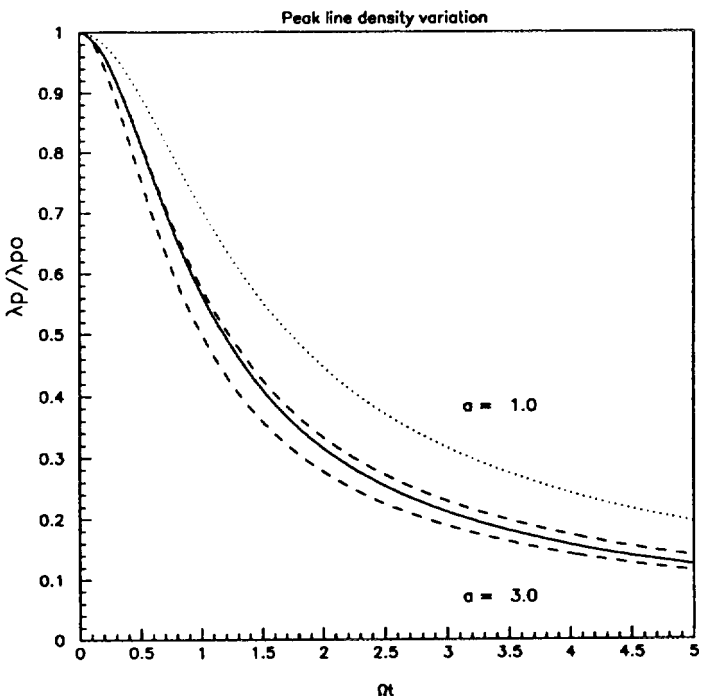

Figure 8: Exact (solid line) and approximate (dashed lines) solutions for peak line density variation during debunching of intense beam for defocusing type of induced voltage, $a = 3$, together with exact solution for low intensity case, $a = 1$, (dotted line)

RF - FEEDBACK WORKING GROUP

RF Feedback for KEKB

Eizi Ezura, Shin-ichi Yoshimoto and Kazunori Akai
KEK, National Laboratory for High Energy Physics
1-1, Oho, Tsukuba-shi, Ibaraki-ken, 305, Japan

Abstract

This paper describes the present status of the RF feedback development for the KEK B-Factory (KEKB). A preliminary experiment concerning the RF feedback using a parallel comb-filter was performed through a choke-mode cavity and a klystron. The RF feedback has been tested using the beam of the TRISTAN Main Ring, and has proved to be effective in damping the beam instability.

I. Introduction

One of the most serious problems in B-factory accelerators is how to deal with severe longitudinal coupled-bunch instabilities caused by the accelerating mode of heavily detuned RF cavities. These instabilities can be avoided if the cavity detuning required to compensate for the reactive beam loading can be significantly reduced. For KEKB, a three-cavity accelerating system (ARES [1]~[5]) and a superconducting cavity (SCC [6][7]) are now being developed [8]. Each type of cavity has a large stored energy which contributes to reducing the detuning of the cavity [9]. Another possible way to cope with the instability problem is to develop an RF feedback system which can reduce the effective cavity impedance responsible for the coupled-bunch instabilities. As a backup scheme for the ARES and SCC, we are developing an RF feedback system using a parallel comb-filter.

II. Requirements

The type of cavity which we use determines the necessary loop gain of the RF feedback. Table 1 gives the expected growth time of the instability and the necessary impedance reduction rate for the ARES, the SCC and the CMC (choke-mode cavity), which is an accelerating cavity of the ARES [10]. The expected damping time due to longitudinal bunch-by-bunch feedback is also shown in the table together with the longitudinal radiation-damping time. If we use the ARES, RF feedback is not necessary in both rings, while the SCC requires RF feedback in LER. If we use the CMC, a very sophisticated RF feedback system is necessary to reduce the cavity impedance to less than 1/100.

The design goal of the feedback is to reduce the effective cavity impedance to the extent that even the CMC can be used as the KEKB accelerating structure. Fig. 1 shows the calculated growth rates of the longitudinal coupled-bunch instabilities due to the accelerating mode when the CMC's are used in LER (a) and HER (b). The parameters used in the calculations are listed in Table 2. The RF feedback must reduce the growth rates, at least down to a level which can be damped by the bunch-by-bunch feedback system. This means that the RF feedback must have a loop gain of at least 40 dB, and must handle more than six modes. Since the revolution frequency

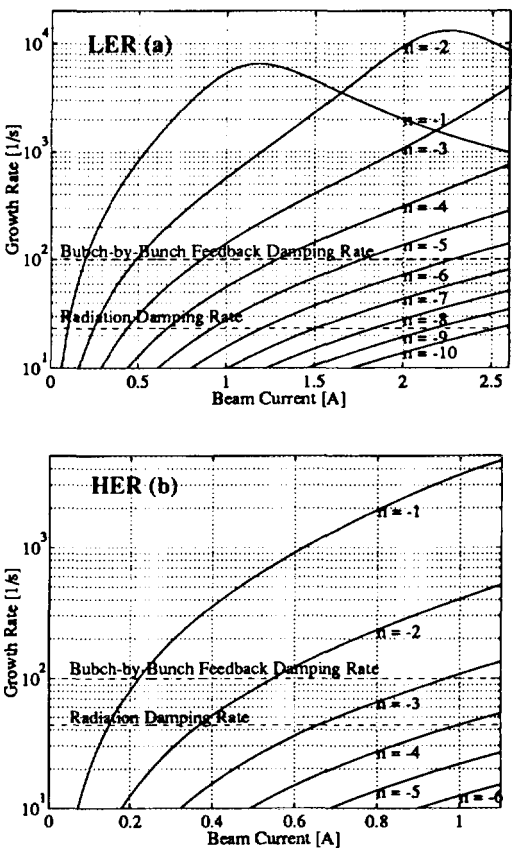

Fig. 1. Calculated growth rates of the longitudinal coupled-bunch instabilities caused by the accelerating mode of the choke-mode cavities in LER (a) and in HER (b).

Table 1
Expected growth time of the instability and the necessary impedance reduction rate for three types of cavities.

	expected growth time		Re[Z] must be reduced to
	LER	HER	
ARES	$30 \sim 50$ ms	$100 \sim 180$ ms	1/1
SCC	$0.3 \sim 14$ ms	$23 \sim 54$ ms	$\approx 1/20$
CMC	$0.05 \sim 0.2$ ms	$0.1 \sim 0.3$ ms	$\approx 1/100$
Bunch-feedback damping time	10 ms		
Radiation damping time (without (with) wigglers)	43 (23) ms	23 ms	

Table 2
Parameters used in the instability calculations.

		LER	HER	
Type of cavity		CMC (accelerating cavity of ARES)		
Total cavity voltage	V_c	8.6	15.7	MV
Number of cells	N_c	20	32	
Cavity voltage/cell	$V_c/cell$	0.43	0.49	MW
Shunt impedance/cell	R_{sh}	5.3		MΩ
Unloaded Q	Q_0	35000		
R/Q		147		Ω
Maximum frequency detuning	Δf	−232	−82	kHz
Synchrotron frequency	f_s	1.7	1.6	kHz
Energy loss/turn	U_0	0.81	3.5	MeV

is about 100 kHz, the frequency range to be covered is more than 600 kHz in LER.

III. Principles of the system

For economical reasons, all of the TRISTAN RF components, except for the cavities, will be reused for KEKB. Its disadvantage from the viewpoint of RF feedback, however, is a long group delay, which comes from a rather narrow-band klystron as well as long distances among the components to form the feedback loop. The cables, waveguides and wideband amplifiers cause an almost constant group delay of about 1 μs, while the klystron causes a frequency-dependent group delay of about 0.6 μs at maximum. This group delay limits the half bandwidth of the loop to around 80 kHz for a 45° stability phase margin [11], while the necessary bandwidth is 600 kHz, as mentioned above.

D. Boussard has pioneered an RF feedback scheme which overcomes the delay limitations by using a comb-filter combined with a one-turn delay [12]. It has a large loop gain only in the vicinity of the frequencies $f_{rf} \pm n f_{rev}$, and is effective when the group delay is almost frequency-independent. One way to compensate for the frequency-dependent group delay is to add a phase equalizer in the feedback path [13]~[16]. The other way is to adjust the phase only at the synchrotron sidebands of the revolution harmonics, where the impedance must be reduced [17]. This is realized by using a parallel comb-filter, an array of resonators, each phase of which is properly shifted so as to compensate for the phase difference among the sideband frequencies.

A block diagram of the RF feedback system using the parallel comb-filter is shown in Fig. 2. A sample of the cavity field is down-converted to the baseband frequency, then filtered and adjusted in phase (and in amplitude, if necessary) by the parallel comb-filter. After being up-converted to the RF frequency, it is fed back to the RF signal path to the cavity. The feedback is done only in the lower side of the RF frequency, because all of the unstable modes due to the accelerating mode are there. A frequency converter which also serves as a single-sideband filter is used to eliminate the upper sideband of the RF frequency. The parallel comb-filter can be easily and accurately adapted to any kind of group-delay properties of the loop. It will also be able to automatically track the cavity phase which changes with the beam current

through a change in the detuning frequency. For this purpose, however, it will be necessary to store the necessary phase compensations of each channel as a function of the beam current and the cavity voltage, and to remove them properly for use.

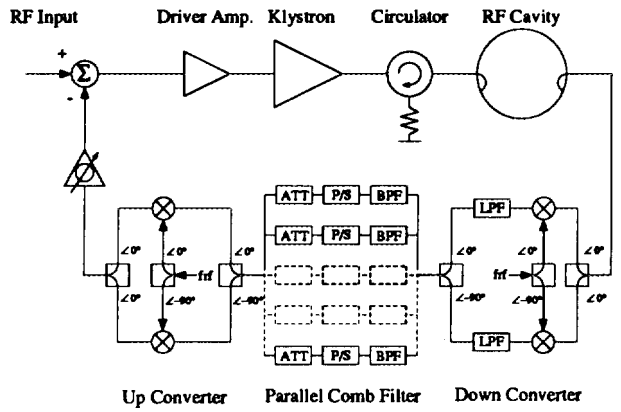

Fig. 2. Block diagram of the RF-cavity feedback system using a parallel comb-filter.

A bunch signal from a button electrode can also be used as an instability signal source; that is, it can be fed into the down-converter shown in Fig. 2 instead of the cavity pick-up signal. In this system (system B) the frequency-dependent cavity phase, which must be compensated in the system using a cavity signal (system A), is no longer a problem. This is because the phase of the feedback voltage does not depend on the cavity tuning, while that of system A does. Another advantage of system B is that when an RF station trips or is shut off, and, consequently, its RF feedback is no longer available, the RF feedback of other stations can compensate for any loss of the damping rate. Since a single feedback system may not be enough to obtain a loop gain of more than 40 dB, combining systems A and B may be an appropriate option. In this case, however, the cavity cannot act as a kicker, or, the feedback system cannot compensate for a loss of the other station's damping rate, because system A always works to reduce the cavity voltage to zero.

Another beam-loading effect appearing in B-factory machines, other than the longitudinal coupled-bunch instabilities due to detuned cavities, is the presence of bunch-phase modulation due to gaps in the bunch-train [18]. The bunch-phase modulation can be greatly reduced by canceling the beam-induced voltages at the revolution harmonics, with either the RF feedback or the RF feedforward technique [18][19]. It, however, requires a large peak klystron power [18][19]. Therefore, it is better to keep the RF feedback inactive around the revolution harmonics by forming notches there [18]. The bunch-phase modulation in HER will be compensated for by providing a partially filled bunch-gap in LER, whose filling factor is adjusted so as to give the same gap transient as that in HER [18]~[21]. Another cure for the bunch-gap effect is to properly modulate the amplitude and phase of the RF drive in order to counteract the modulations appearing on the cavity [18].

Fig. 3 shows the transfer functions of a 6-channel parallel comb-filter with a zero phase shift and an IIR digital comb-filter with a 1-turn delay. For a comparison, the 3 dB bandwidth of both filters is taken to be the same value. Both transfer functions are almost identical if the filter bandwidth is much smaller than the revolution frequency, and if the parallel comb-filter has infinite channels. The slight difference shown in the figure comes from the fact that the parallel comb-filter has only six channels.

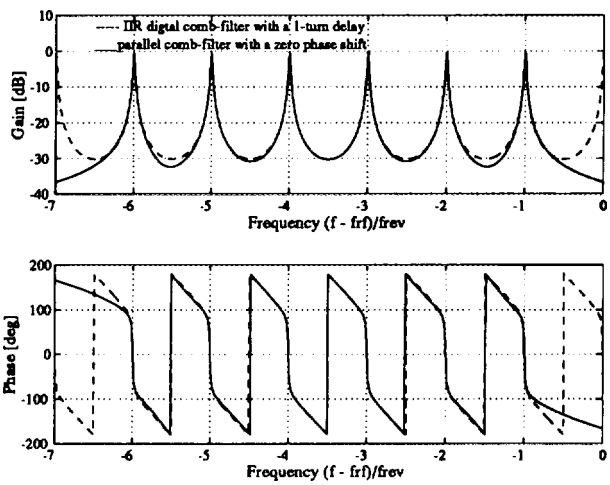

Fig. 3. Transfer functions of a 6-channel parallel comb-filter with a zero phase shift (solid line) and an IIR digital comb-filter with a 1-turn delay (broken line).

Although the direct RF feedback, in our case, does not have a sufficient bandwidth to cure the coupled-bunch instabilities (as stated above), it will be a powerful measure to reduce the beam-loading effects on the cavity operating in the accelerating mode.

IV. RF feedback experiment

A. Experimental setup

We have carried out a preliminary experiment concerning the RF feedback using a prototype parallel comb-filter. Fig. 4 shows the experimental setup, which includes a parallel comb-filter, a 1.2-MW klystron and a choke-mode cavity. The cable length was adjusted so as to give a total constant group-delay of 1 μs, which is comparable to that of the KEKB RF system. The detuning frequency and the loaded Q of the cavity were adjusted to the values used in the instability calculation for LER shown

in Fig. 1(a). Fig. 5 shows the transfer function of the klystron used in the experiment. The 3 dB bandwidth is about 800 kHz and the maximum group delay is about 500 ns. In this experiment, only a very low RF power was fed into the cavity, though the klystron was operated at an RF power of 200 ~ 300 kW. A network analyzer was used to measure the open and closed-loop transfer functions over a 1 MHz frequency range.

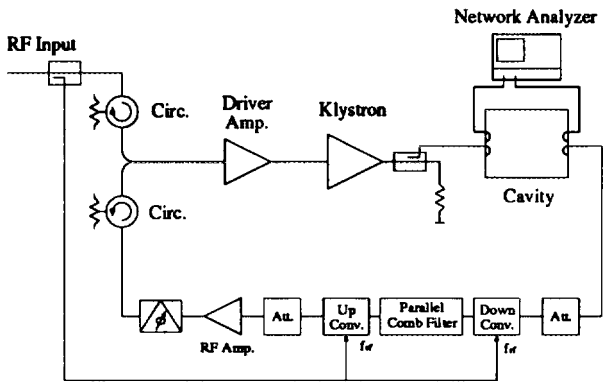

Fig. 4. Block diagram of the experimental RF-cavity feedback loop, which includes a parallel comb-filter, a choke mode cavity and a klystron.

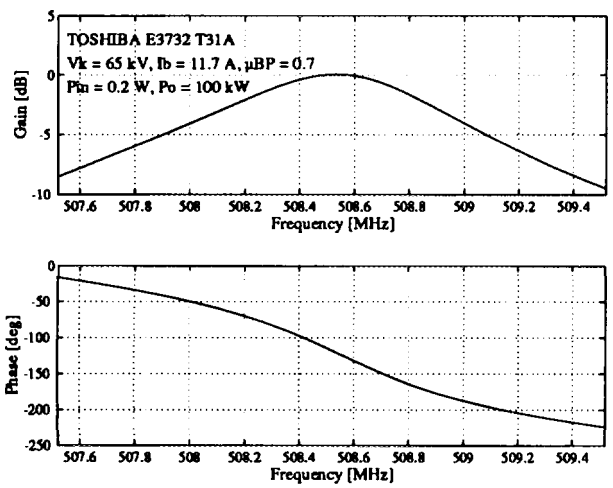

Fig. 5. Measured transfer function of the klystron which was used in the feedback experiment.

The parallel comb-filter comprises five individual LC resonators arranged at 100 kHz intervals; each resonator has a 2 kHz 3 db-bandwidth. Fig. 6 shows the circuit configuration of a channel in the comb-filter. In order to increase the Q value of the resonator, the apparent resistance of the coil is reduced by adding a negative resistance generated by the positive feedback. The center frequency of the resonator has a temperature coefficient of about $1 \times 10^{-4}/°C$. The phase shifter uses variable capacitance diodes to control the phase, and covers the range over ±200°. The analogue multiplier is used to control the amplitude over a range of 0 ~ 100%. Both the phase shifter and the attenuator are controlled either by a dial at the panel or by an external voltage.

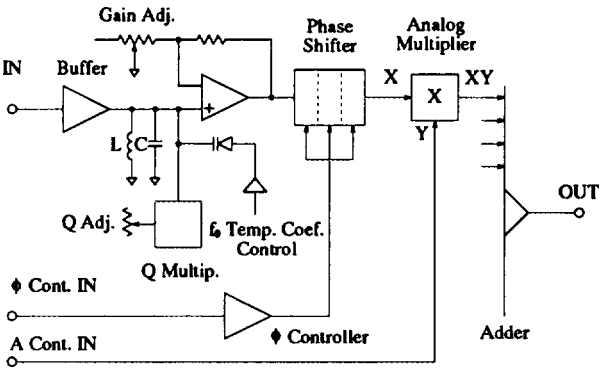

Fig. 6. Circuit configuration of a channel in the prototype comb-filter.

B. *Results of measurement*

Fig. 7 shows the measured open-loop response of the amplitude and phase as a function of the normalized frequency $((f - f_{rf})/f_{rev})$. The center frequency of each resonator was set to $nf_{rev} + f_s$, where f_s is 7 kHz, because the comb-filter had been made on the basis of the old KEKB design. Although the phase response was adjusted to zero at each frequency by the phase shifter, the amplitude response was kept unchanged. The maximum loop gain was 29.8 dB with a 0° phase margin and 25.2 dB with a 45° phase margin over a 1 MHz bandwidth. The single-sideband filter rejected the unwanted upper side of the RF fre-

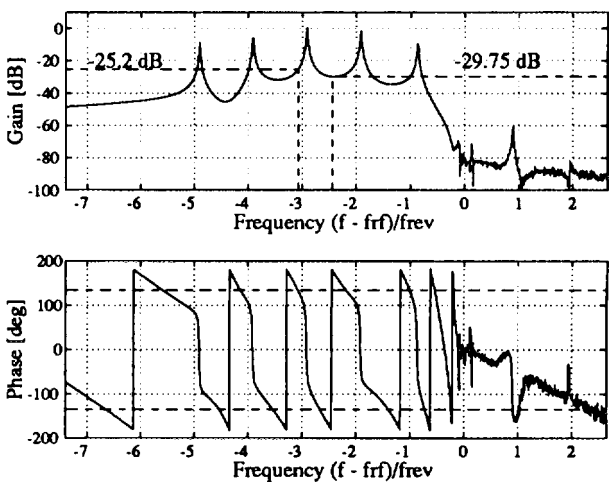

Fig. 7. Measured open-loop response of the feedback system as a function of the normalized frequency $(f - f_{rf})/f_{rev}$.

Table 3
Measured real part of the cavity impedance and the corresponding growth time of the instability, with or without feedback.

Mode	without feedback			with feedback		
	$\mathrm{Re}\{Z_+\}$ [kΩ]	$\mathrm{Re}\{Z_-\}$ [kΩ]	Growth time [ms]	$\mathrm{Re}\{Z_+\}$ [kΩ]	$\mathrm{Re}\{Z_-\}$ [kΩ]	Growth time [ms]
+7	1.70	6.84	−5.85	1.70	4.42	−11.07
+6	2.13	10.94	−3.40	2.13	11.86	−3.08
+5	2.74	20.07	−1.73	2.74	42.11	−0.76
+4	3.65	46.52	−0.70	3.65	97.79	−0.32
+3	5.10	156.10	−0.20	5.10	262.89	−0.12
+2	7.61	219.44	−0.14	7.61	38.78	−0.96
+1	12.51	62.73	−0.60	12.51	51.87	−0.76
0	48.04	49.32	−46.71	48.04	49.32	−46.71
-1	60.36	12.76	0.63	11.27	12.76	−20.16
-2	211.46	7.73	0.15	17.23	7.73	3.15
-3	163.33	5.16	0.19	10.63	5.16	5.48
-4	48.18	3.69	0.67	6.08	3.69	12.55
-5	20.56	2.76	1.68	3.43	2.76	45.18
-6	11.14	2.15	3.33	13.23	2.15	2.70
-7	6.94	1.71	5.75	4.72	1.71	10.00

quency by about 60 dB, as shown in the top of Fig. 7.

The measured closed-loop response is shown in Fig. 8. The top figure shows the normalized magnitude (broken line) and the real part (solid line) of the effective cavity impedance, with or without feedback; the bottom figure shows the phase of the cavity. With the feedback, the real part of the impedance was reduced by 16 dB to 24 dB at five sideband frequencies. The measured values are in good agreement with the calculated ones, which were obtained using the measured parameters of the loop components.

The results of the measurements are summarized in Table 3, which gives the measured real part of the cavity impedances at the upper and lower sidebands of the −7 to +7 modes, as well as the corresponding growth time of the coupled-bunch instability, with or without feedback. In LER, the growth time of six modes from −1 to −6 was faster than 10 ms, as shown in Fig. 1(a); however, in this experiment, only five modes were treated, because of limitations of available comb-filter channels. With feedback the growth times of the −1 and −5 modes became much slower than 10 ms, and that of the −4 mode was marginal, while those of the −2 and −3 modes were still much faster. To stabilize all of the modes, the loop gain must be improved by more than 10 dB, which will be possible by reducing the bandwidth of the filter to less than 1 kHz.

Although the feedback was intended only for the −1 to −5 modes, it affects the impedance of the −6

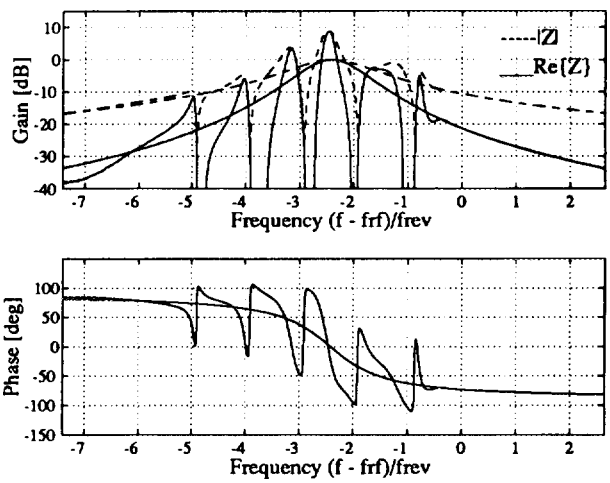

Fig. 8. Measured closed-loop response of the feedback system as a function of the normalized frequency $(f - f_{rf})/f_{rev}$.

mode while slightly decreasing its growth time. A more serious consequence of the feedback was that it also reduced the impedances at the lower sidebands of the +1 and +2 modes. In this experiment, these two modes were still kept in the damping state due to the large synchrotron frequency (f_s) of 7 kHz. However, both the +1 and +2 modes would be unstable if f_s is less than 2 kHz, as is the case with the new lattice design. The impedance reduction at these frequencies can be controlled to some extent by narrowing the bandwidth of the filter and by adjusting

the phase of the relevant channels. As a more effective cure, we are planning to provide notches at these lower sideband frequencies.

V. Beam Test of RF Feedback in TRISTAN MR

The purpose of the beam test was to confirm that a coupled-bunch instability caused by the cavity impedance could really be eliminated by reducing it by means of RF feedback. A beam test was made in the TRISTAN Main Ring (MR), whose tunnel will be reused for KEKB; its RF frequency is about the same as that of KEKB. Under usual operation, the MR beam is stable, owing to a much lower beam intensity than that of KEKB. One RF station was

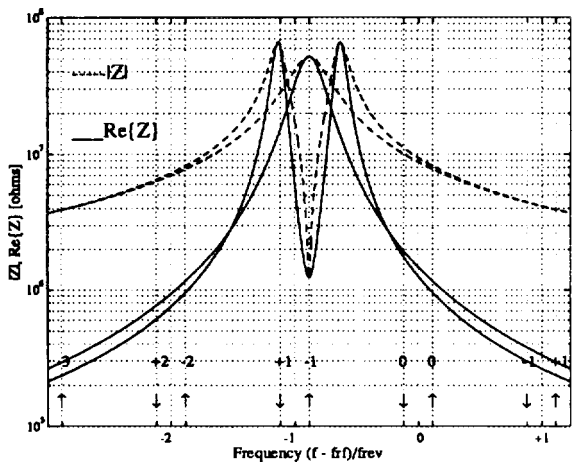

Fig. 9. Magnitude and the real part of the cavity impedance for detuned thirty six cells, with or without RF feedback.

Table 4
Machine parameters during the beam test.

e^- beam energy		8	GeV
e^- beam current		6	mA
Number of bunch		4	
RF frequency	f_{rf}	508.6	MHz
Revolution frequency	f_{rev}	100	kHz
Synchrotron frequency	f_s	11.6	kHz
Detuning frequency	Δf	−87.7	kHz
Shunt impedance of 36 cells		239	MΩ
Coupling factor	β	1.3	
Growth time of −1 mode		6.5	ms
Radiation damping time	τ_{rad}	20	ms

therefore put out of operation, and its idling cavities were substantially detuned to make the beam unstable. An RF station has two accelerating units, each comprising a pair of nine APS (alternating periodic structure) cells [22]. A total of thirty six cells were detuned by 88 kHz ($= f_{rev} - f_s$) in order to set the resonant frequency of the cavities to the upper synchrotron sideband of the −1 mode. Fig. 9 shows the magnitude and real part of the cavity impedance for detuned thirty six cells, with or without RF feedback. The growth time of the −1 mode, estimated from the machine parameters given in Table 4, is 6.5 ms, while the radiation damping time is 20 ms. The growth times of the other modes are much slower than 20 ms.

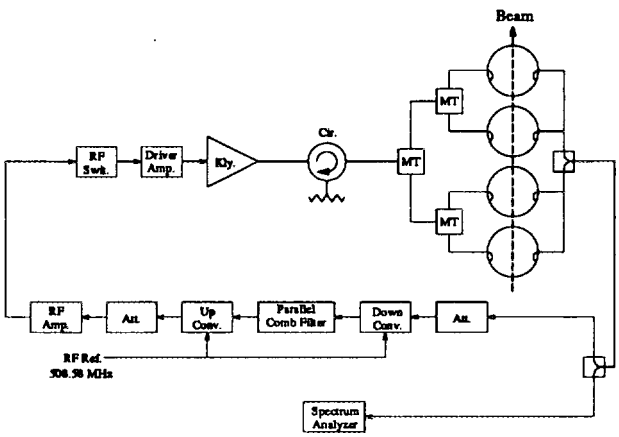

Fig. 10. Block diagram of the RF feedback system used in the beam test.

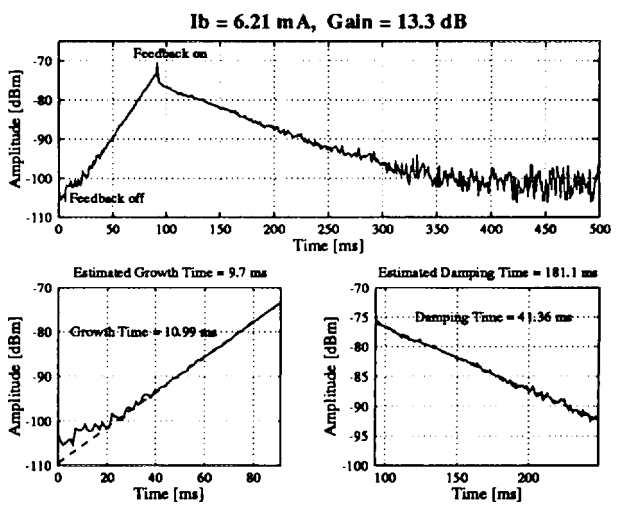

Fig. 11. Measured amplitude of the -1 mode oscillation versus time.

Fig. 10 shows a block diagram of the RF feedback system used in the experiment. Since only the −1 mode could be unstable, only one channel of the parallel comb-filter was used. The RF switch was used to open and close the feedback loop. In order to detect the growth and damping of the coupled-bunch

oscillations a spectrum analyzer was used in a zero-scan mode.

Fig. 11 shows an example of the measured amplitude versus the time of the -1 mode oscillation. The amplitude began to increase exponentially when the feedback loop was opened at 0 ms, and turned to decrease when the loop was closed at about 90 ms. This figure clearly shows the effectiveness of the RF feedback. The bottom figures show expanded views of the amplitude behavior just after the loop off and on. A more detailed report of the beam test will appear soon elsewhere [23].

VI. Summary

A. Purpose and Requirements

- An RF feedback system will be prepared as a backup scheme for the ARES and SCC, to prevent coupled-bunch instabilities caused by the accelerating mode of detuned cavities.
- If the choke-mode cavities are used, the effective cavity impedance must be reduced by a factor of 100 to make the growth time slower than 10 ms, the expected damping time of the bunch-by-bunch feedback system. In LER, six modes must be damped and the necessary frequency range is more than 600 kHz.

B. Feedback System

- In the parallel comb-filter (an array of resonators), each resonator is tuned at $nf_{rev} + f_s$, and used to compensate for any group delay of the feedback loop.
- To make the system simple, feedback is done only in the lower side of the RF frequency by eliminating the upper side with a single-sideband filter.
- As an instability-signal source, both a cavity signal and a bunch signal will be prepared. The combination of two feedback systems, one using the cavity signal and the other the bunch signal, may be a promising option to reduce the cavity impedance to less than 1/100.
- Picked-up voltages at the revolution harmonics will be eliminated by providing notches in order to avoid any increase in the peak klystron power.
- In KEKB, a direct RF feedback will not be used to cure the instabilities because of its narrow bandwidth. It will be used only around the RF frequency to reduce the beam-loading effects during operation in the accelerating mode.

C. Feedback Experiment

- A preliminary experiment of the parallel comb-filter feedback has been carried out through the choke-mode cavity and the klystron.
- The real part of the cavity impedance was reduced by 16 dB to 24 dB at five frequencies, 100 kHz apart from each other. The loop gain must be improved by more than 10 dB to stabilize all of the six modes in LER.
- Some measure is required to avoid excitation of the $+1$ and $+2$ modes for a synchrotron frequency less than 2 kHz.

D. Beam Test

- The RF feedback system has been tested using the beam of the TRISTAN Main Ring.
- The coupled-bunch instability of the -1 mode was excited by intentionally detuning the RF cavities; it was then successfully damped by reducing their impedances with the RF feedback.

REFERENCES

[1] T. Kageyama et al., "Design of a Prototype of RF Cavity for the KEK B-Factory(KEKB)", Proc. 4th European Particle Accelerator Conf., Vol.3 of 3, p. 2098, 1994.

[2] Y. Yamazaki et al., "A Three-Cavity System which suppresses the Coupled-bunch Instability associated with the Accelerating Mode", Particle Accelerators, Vol. 44, p.107 (1994).

[3] Y. Yamazaki et el., "An Accelerator resonantly coupled with an Energy Storage (ARES) for the KEKB", presented at 1995 IEEE PAC and Int. Conf. High Energy Accelerators, Dallas, Texas, 1995.

[4] N. Akasaka et al., "RF Characteristics of ARES cold Models", contributed to 1995 IEEE PAC and Int. Conf. High Energy Accelerators, Dallas, Texas, 1995.

[5] T. Kageyama et al., "ARES : Accelerating Cavity Resonantly coupled with Energy Storage", presented at this Workshop.

[6] K. Asano et al., "Stable Performance of Superconducting Cavities for KEKB", contributed to 1995 IEEE PAC and Int. Conf. High Energy Accelerators, Dallas, Texas, 1995.

[7] S. Mitsunobu et al., "A Prototype Superconducting Cavity for KEK B-Factory", contributed to 1995 IEEE PAC and Int. Conf. High Energy Accelerators, Dallas, Texas, 1995.

[8] "KEKB Accelerator Design Report", to be published as a KEK Report.

[9] T. Shintake, "Proposal of an Accelerating RF-Cavity coupled with an Energy Storage Cavity for Heavy Beam Loading Accelerators", Particle Accelerators, Vol. 44, p.131 (1994).

[10] T. Kageyama et al., "Development of a HOM-Damped Cavity for the KEK B-Factory (KEKB)", contributed to 1995 IEEE PAC and

Int. Conf. High Energy Accelerators, Dallas, Texas, 1995.

[11] D. Boussard, "Control of Cavities with Heavy Beam Loading", IEEE Trans. Nucl. Sci. Vol. NS-32, No.5, p.1852 (1985).

[12] D. Boussard et al., "Reduction of the Apparant Impedance of Wide Band Accelerating Cavities by RF Feedback", IEEE Trans. Nucl. Sci. Vol. NS-30, No.4, p.2239 (1983).

[13] P. Corredoura, "Klystron Equalization for RF Feedback", Proc. Int. Work Shop on B-Factories : Accelerators and Experiments, Tsukuba, p.159, 1992. , and also SLAC-PUB 6049, 1993.

[14] P. Corredoura et al., "RF Feedback Development for the PEP-II B-Factory", Proc. 4th European Particle Accelerator Conf., Vol.3 of 3, p. 1954, 1994., and also SLAC-PUB-6534 June 1994.

[15] R. Tighe, "RF Feedback Simulation Results for PEP-II", contributed to 1995 IEEE PAC and Int. Conf. High Energy Accelerators, Dallas, Texas, 1995.

[16] R. Tighe, "PEP-II RF Feedback System Simulation", presented at this Workshop.

[17] S. Yoshimoto et al., "Experiment of the RF Feedback using a Parallel Comb Filter", contributed to 1995 IEEE PAC and Int. Conf. High Energy Accelerators, Dallas, Texas, 1995.

[18] F. Pedersen, "RF Cavity Feedback", Proc. B Factories - The State of the Art in Accelerators, Detectors and Physics, SLAC-400, p.192, 1992.

[19] K. Akai et al, "Simulation of Influence of a Bunch Gap in TRISTAN-II", Proc. 4th European Particle Accelerator Conf., Vol.2 of 3, p. 1141, 1994.

[20] K. Akai et al., "Design of the KEKB RF System", contributed to 1995 IEEE PAC and Int. Conf. High Energy Accelerators, Dallas, Texas, 1995.

[21] K. Akai, "Coupled-Bunch Instabilities caused by the Cavities for KEKB", presented at this Workshop.

[22] T. Higo et al., "RF Cavity for TRISTAN Main Ring", Proc. 1987 IEEE Particle Accelerator Conf. Vol. 3 of 3, p. 1945, 1987.

[23] S. Yoshimoto et al., "Beam Test of the RF feedback for KEKB in TRISTAN MR", to be presented at 10th Symp. Accelerator Science and Technology, Oct.25 $\sim$ 27, 1995, Hitachinaka, Japan.

PEP-II RF Feedback System Simulation

Richard Tighe
SLAC

A model containing the fundamental impedance of the PEP-II cavity along with the longitudinal beam dynamics and RF feedback system components is in use. It is prepared in a format allowing time-domain as well as frequency-domain analysis and full graphics capability.

Matlab and Simulink are control system design and analysis programs (widely available) with many built-in tools. The model allows the use of compiled C-code modules for compute intensive portions.

We desire to represent as nearly as possible the components of the feedback system including all delays, sample rates and applicable nonlinearities.

Components

Cavity

A baseband representation of the total number of cavities of the ring. Baseband: A DC input representing the klystron RF input leads to a DC value representing the cavity voltage. Modulations to the cavity are made within a small (10 MHz) bandwidth around the center frequency. Forward and reflected power signals are recorded.

Beam

Longitudinal dynamics with enough macro bunches (36) to simulate coupled-bunch motion throughout the range excited by the cavity and feedback. Includes ion clearing gap.

Two macro-bunches are left empty in HER to represent the ion clearing gap (2/36 = 5.56%). Two bunches are partially filled in the LER for transient matching.

Direct RF Feedback

Reduces the cavity impedance seen by the beam.

Comb Filter Feedback

Periodic structure applying gain at the synchrotron sidebands; one-turn delay. Further reduces the impedance seen by the beam. Sample rate: 10MHz, same as in hardware.

Group delay equalizer

Mitigates the effects of the in-band and out-of-band delay differences.

Delays

Signal delays in system prevent the application of unlimited gain. Loop delay including waveguide, cable, klystron, and feedback components is approximately 550ns.

Saturating Klystron

Contains group delay and bandwidth behavior.
Saturation characteristics of klystron. AM gain decreases when running into saturation.
The klystron operating point is nominally set to 90% of saturated power (95% of saturated voltage) in order to compromise between operating efficiency and feedback headroom.

Longitudinal (Bunch-by-Bunch) Feedback

Two aspects: Implemented as additional term in beam dynamics akin to radiation damping; also connection from B-by-B system to RF feedback system.

Adaptive Feedforward

A profile corresponding to 20MHz samples is generated by sampling the klystron drive signal over many turns, averaging, and modifying the feedforward values in order to produce a more constant klystron output. The feedforward signal adapts slowly and will not interfere with the operation of the feedback loops. An RF reference is generated to allow gap induced cavity transients to occur without feedback intervention. This reduces power fluctuation in the presence of gap transients to less than 2%.

Analysis and Predictions

Gain, phase, delay setting
Analytic frequency-domain representation used to determine gains, phases, margins. The phase margin of the combined direct and comb feedback loops is set to 45°.

Modal impedance based on system
Expected modal impedance may be calculated based on linear system components.

Performance

Presently takes 3min/1ms of beam time on a SPARC 10.

Operation

The model runs with full current at startup. The assumption is that the B-Factory will be free of large injection transients due to the gradual injection scheme. Slow loops (tuner and gap voltage) are preset and disabled.

Uses:

System stability with linear and nonlinear operation
Klystron saturation and gap transients. The effect of the nonlinear klystron saturation is what largely requires the use of time-domain simulations.
Adaptive Gap Voltage program to follow gap transient.

System parameter variation:
Klystron delay and bandwidth were varied to validate the klystron purchase specification.

Forward and reflected power information
Tracking of reflected voltage in waveguide ahead of cavity allowed testing worst-case trip scenarios (beam dump, klystron trip) confirming best window placement.

Test bed for additional components

Summary:

System has shown stable operation for PEP-II nominal HER and LER configurations.

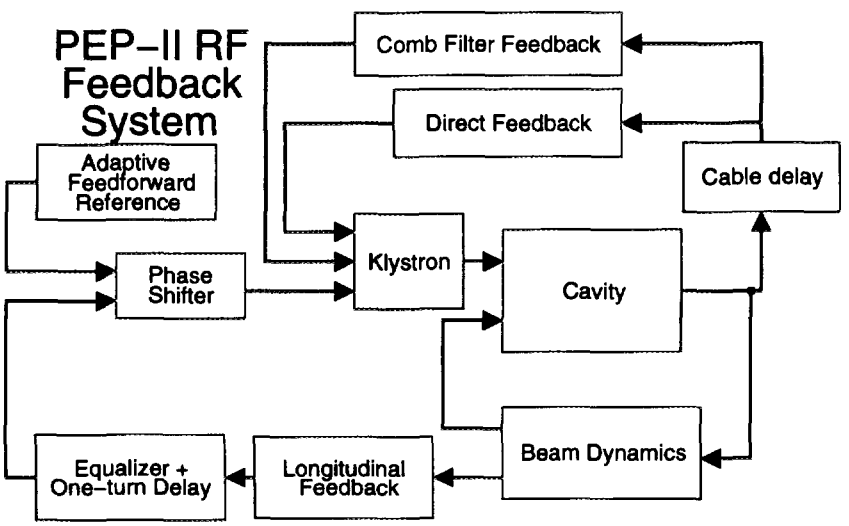

System Block Diagram

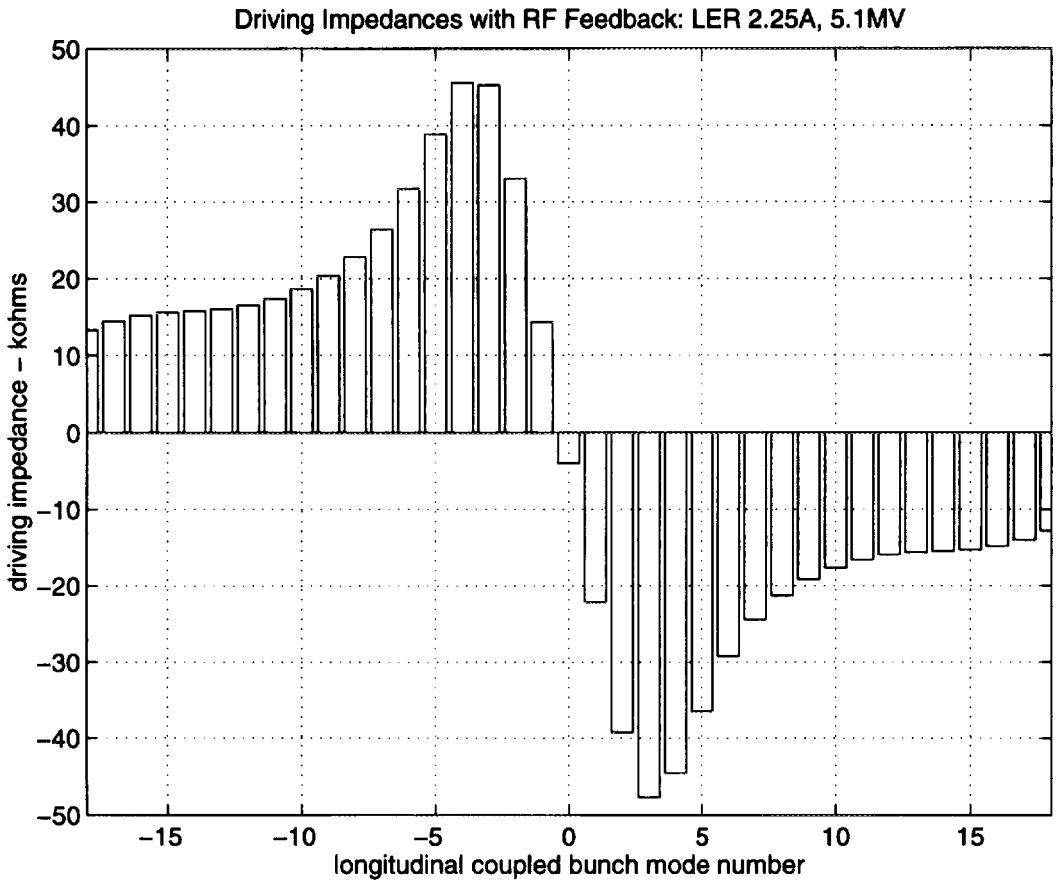

From a linear impedance calculation the coupled-bunch driving impedances for the modes affected by the RF cavity fundamental and feedback may be found.

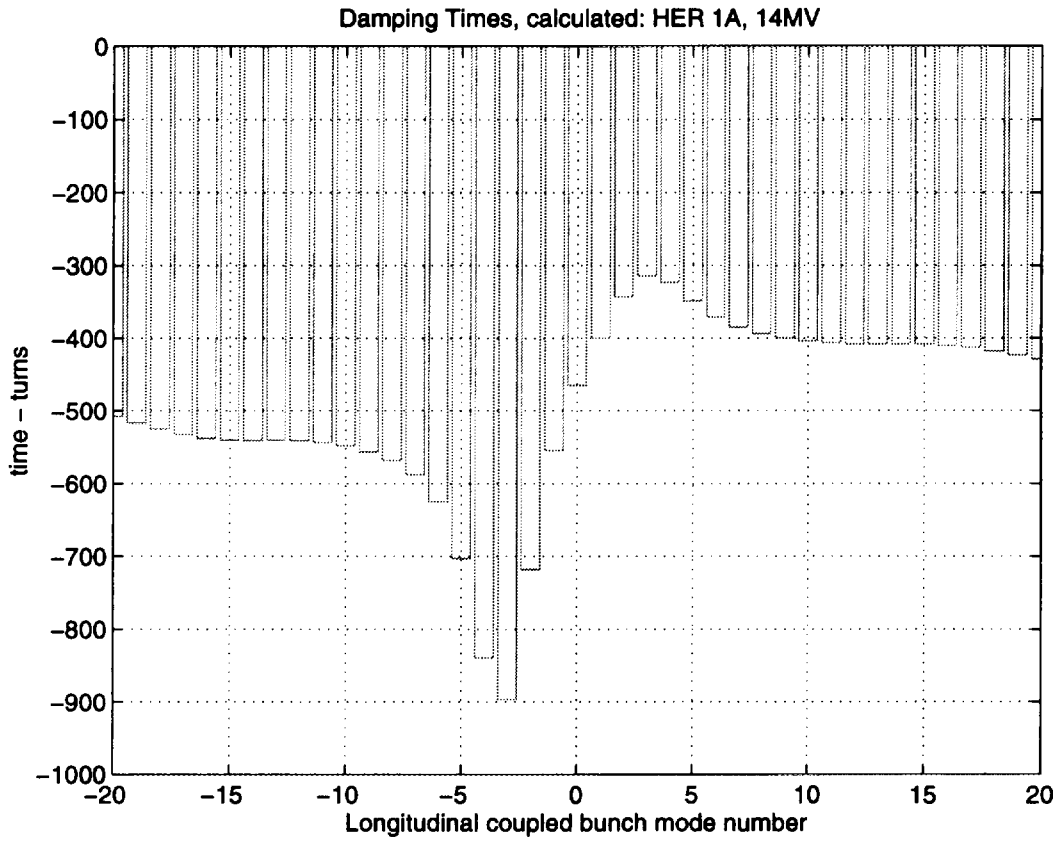

The results of the linear driving impedance calculation is converted to expected growth rates for a given configuration.

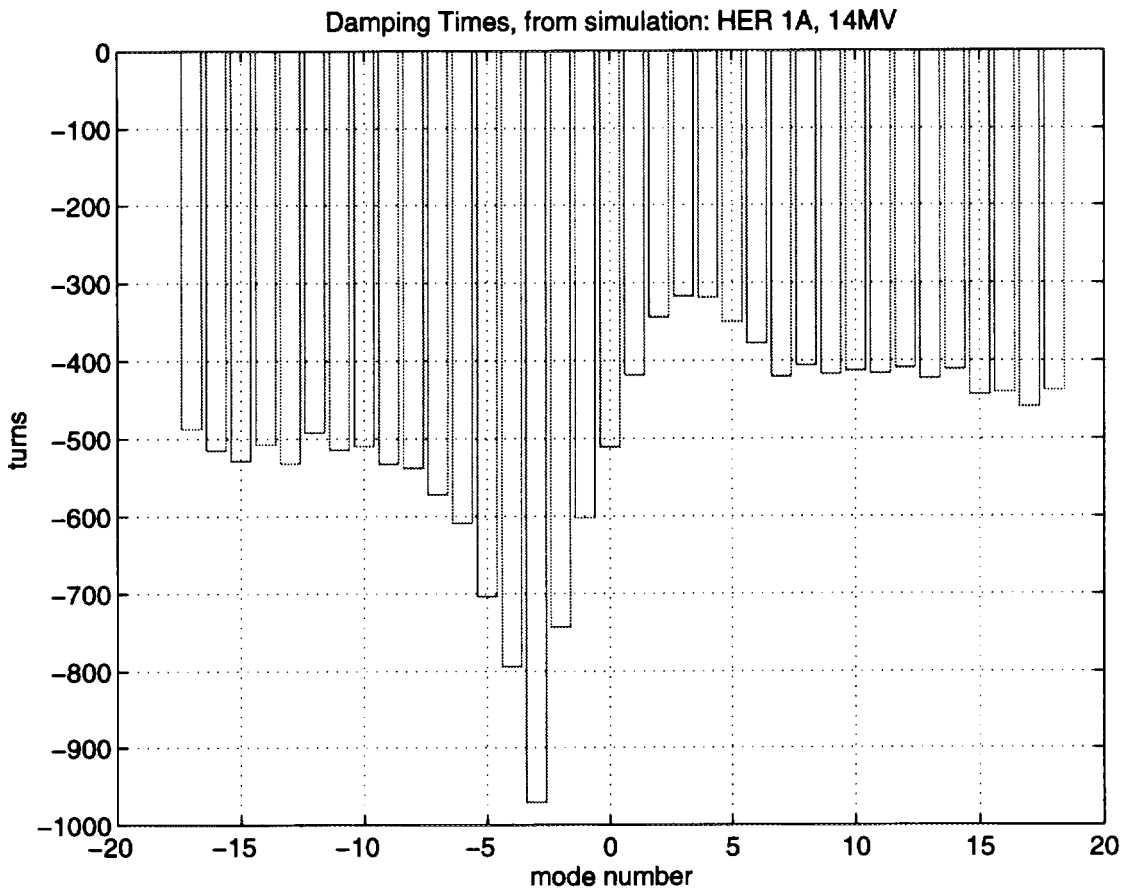

The results of the linear time-domain simulation give good agreement with the expected values. This allows us to proceed and add the saturation effect.

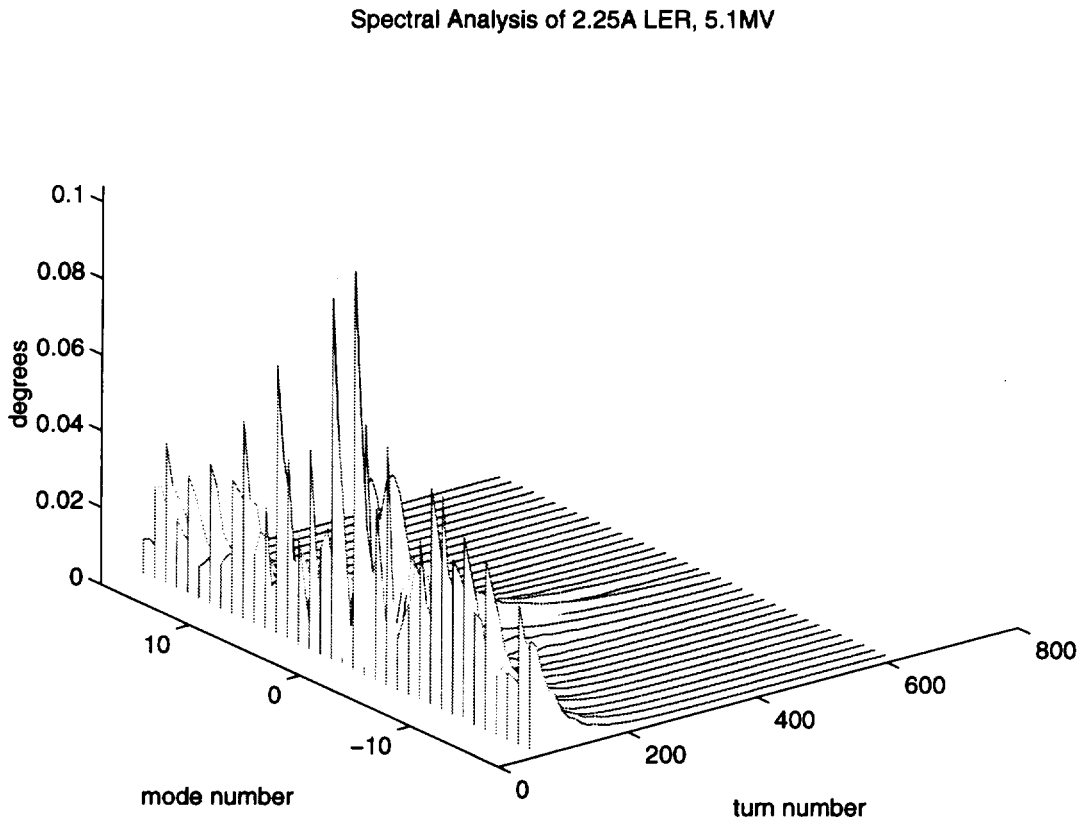

After completing the simulation, the bunch signals are converted to their modal components. Here we see all modes damping within 500 turns. In fact, the slowest mode to damp has a damping time of 150 turns. The radiation damping time is 3500 turns.

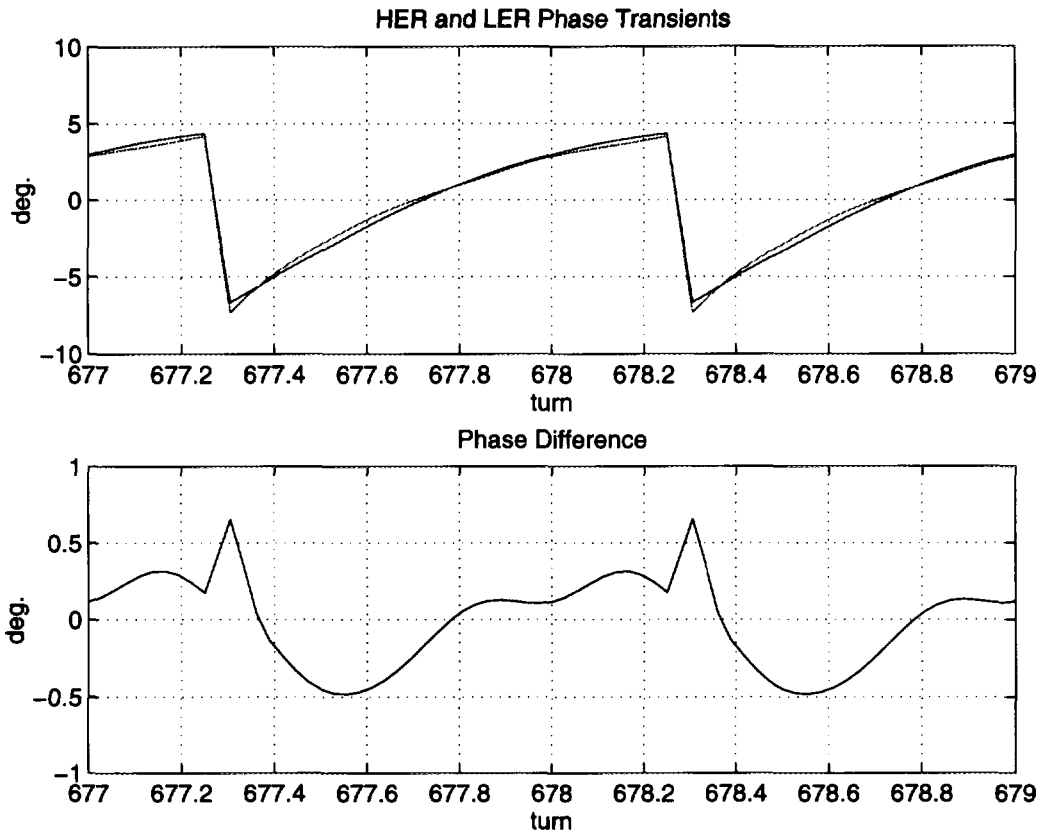

The gap induced transients in the two rings must be matched to prevent excessive collision point variation. Here the transients from the two rings are matched to within 0.6° (0.1 σ_z). Fine tuning of the simulation parameters is possible to reduce this further. Theoretically, the transients may be perfectly matched (assuming equal cavity coupling in the two rings)

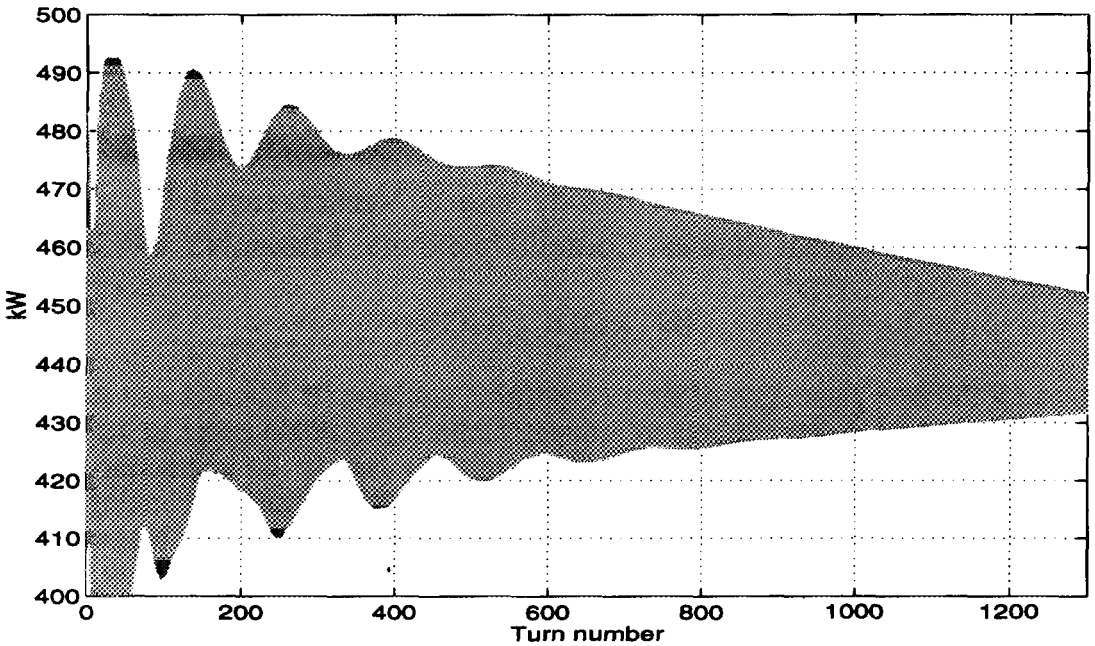

Forward Power Envelope During Adaptation

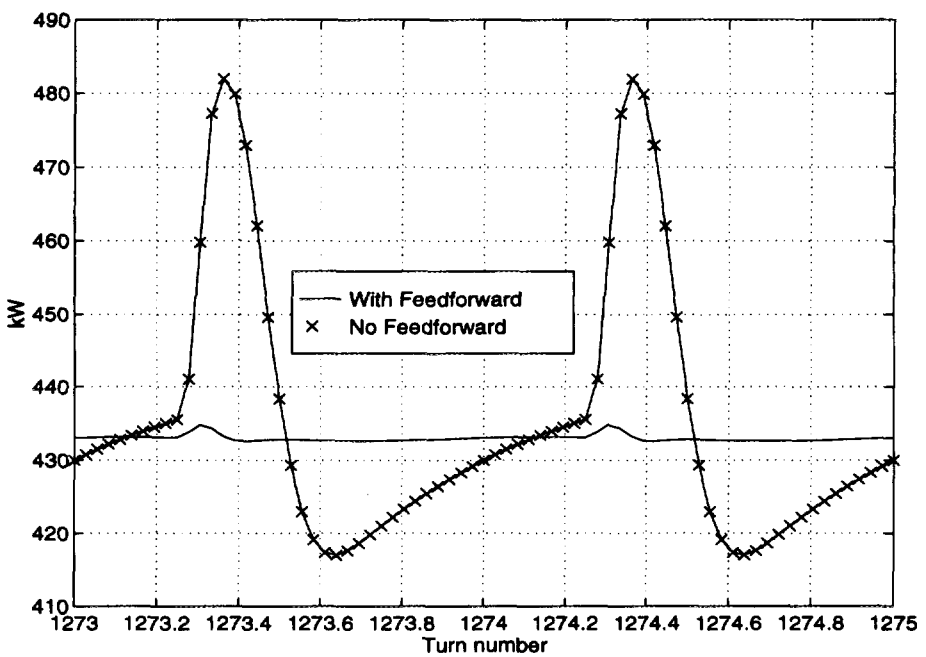

Forward Power Variation, with and without Feedforward.

The Interaction between a Beam and a Superconducting Cavity Module: Measurements in CESR and CESR-Phase III Goals*

S. Belomestnykh †, G. Flynn‡, W. Hartung, J. Kirchgessner, D. Moffat, H. Muller, H. Padamsee, M. Pisharody, and V. Veshcherevich †
Laboratory of Nuclear Studies, Cornell University, Ithaca, NY 14853 USA

INTRODUCTION

Plans for the next generation of electron-positron colliders (B-factories and B-factory-like machines) call for high beam currents to produce luminosities of the order of 10^{33}. To store these high currents in a machine, special attention must be paid to the interaction of the beam with discontinuities in the surrounding vacuum chamber. RF cavities are among the biggest perturbations in accelerator vacuum chambers and are therefore among the biggest sources of beam instabilities. Accelerating structures for new machines are being designed to have smaller impedance to reduce the beam-cavity interaction. Several new designs for both normal and superconducting cavities are now being considered at various laboratories [1].

The phased luminosity upgrade program for CESR calls for a total current of 1A in two beams [2]. The existing normal conducting copper cavities are to be replaced with superconducting niobium cavities. Quality factors of less than 100 are required for the dangerous cavity higher-order modes (HOMs) [3, 4].

Figure 1 shows a schematic of the entire module which includes the cavity, a 24 cm round beam pipe, a fluted beam pipe, two ferrite HOM loads, sliding joints, gate valves, and tapers to the CESR beam pipe.

The beam tubes were designed so that all of the HOMs propagate out of the cavity and are damped by the ferrite HOM loads, which are located outside the cryostat and which are an integral part of the beam tube.

Prototypes for the cavity, input coupler, cryostat, and HOM loads were subjected to a beam test in CESR in August 1994. Figures 2 - 4 show photographs of the HOM load, cavity, and cryostat being installed in CESR. A superconducting (SRF) cavity was installed in addition to the four five-cell normal conducting (NRF) cavities. The results of the test have been reported at the PAC'95 conference [5-7]. In this paper we review the results from the perspective of the CESR Phase III upgrade plan.

SYSTEM PERFORMANCE

The performance of the SRF system as a whole and cavity in particular was quite good. Below we briefly review some important results achieved in the beam test.

---

* Work supported by National Science Foundation, with supplementary support from the US-Japan Collaboration.

† Visitor from Budker Institute of Nuclear Physics, 630090 Novosibirsk, Russia

‡ Visitor from LURE, 91405 Orsay, France

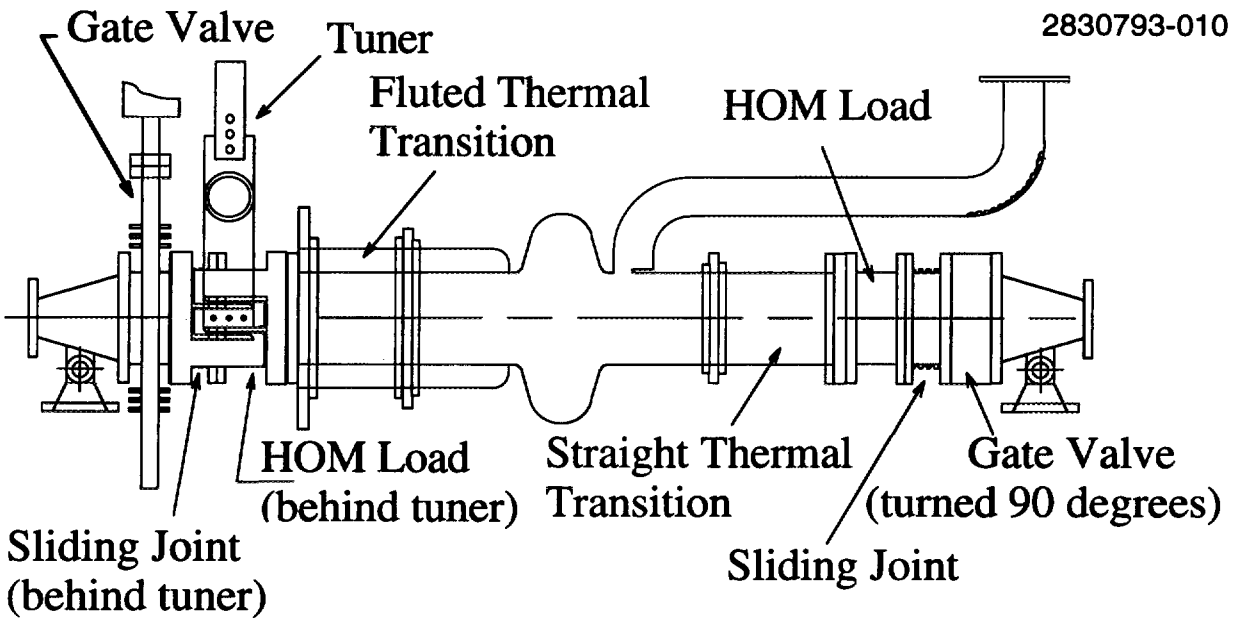

Figure 1. Schematic of the SRF cavity module.

Accelerating Gradients

Before the beam test, the niobium cavity was tested in a vertical cryostat up to an accelerating gradient of 10 MV/m [8]. The cavity was then tested in its horizontal cryostat with high RF power (without beam). After processing to 6 MV/m CW, it was installed in CESR.

Throughout most of the test, we kept the accelerating gradient of the cavity at 4.5 MV/m. A special run was dedicated to investigation of the behavior of our system at higher gradients. At 5 MV/m, the cavity was run stably for 1/2 hour with 100 - 110 mA beam current.

The cavity could only be operated for short periods above 5 MV/m, because of increased dissipation due to field emission, which caused the cryostat pressure to increase steadily. The pressure increase required tuner motion to maintain the correct cavity frequency; eventually the tuner ran into its safety stop. Nevertheless, we were able to run the cavity for few minutes with beam currents between 95 and 120 mA and a cavity gradient of up to 6 MV/m. A gradient of 6 MV/m is our goal for Phase III.

Beam Current

The maximum current for the test was 220 mA (in 27 bunches, distributed into 9 trains of 3 bunches with $1.3 \cdot 10^{11}$ particles per bunch). The current limit was set not by the performance of the cavity but by the heating of other CESR components. The maximum single-bunch current was 44 mA ($7 \cdot 10^{11}$ particles), with the limit again set by heating of other CESR components. Note that the product of the number of bunches times the square of the single bunch current was nearly the same as for the 220 mA, 27 bunch case. We are a factor of 6 below the CESR-Phase III goal, which calls for a beam current of 500 mA in 45 bunches (9 trains of 5 bunches) for each beam.

RF Power

A special experiment was dedicated to delivering the maximum RF power to the beam. The relative phase between the NRF and SRF cavities was adjusted so that the bunches went through the SRF cavity at the peak of the SRF voltage. The NRF cavities provided longitudinal

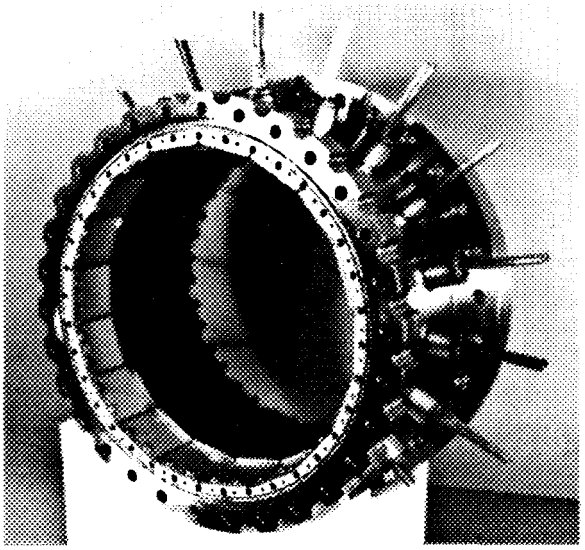

Figure 2. "Porcupine" HOM load near the end of construction.

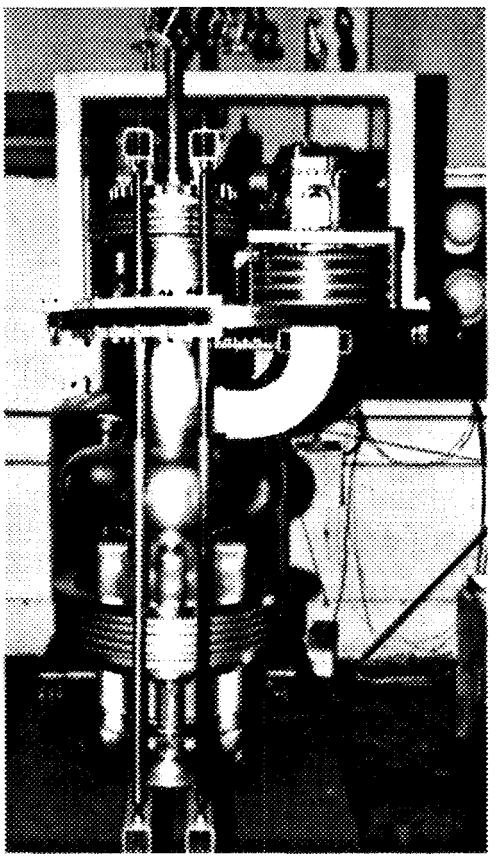

Figure 3. Niobium cavity being prepared for assembly into horizontal cryostat.

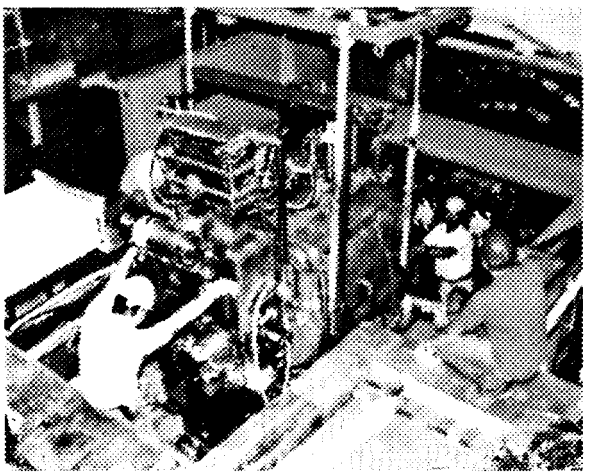

Figure 4. Cryostat being installed in CESR.

beam stability and extracted the excess power delivered to the beam from the SRF cavity.

The maximum power delivered to the beam by the SRF cavity was 155 kW, a factor of 2 above the world record set by the SRF cavity tested in TRISTAN-AR at 2 MV/m [9], but still a factor of 2 less than the Phase III goal. Vacuum bursts and arc trips near the RF window prevented us from going higher. We hope that new planar waveguide RF window, recently tested at LNS [10], will allow us to reach the Phase III requirement.

BEAM-CAVITY INTERACTION MEASUREMENTS

Studies of the beam-cavity interaction were conducted with a variety of bunch configurations: single bunch, 9 bunches per beam, and 9 trains of 2 or 3 bunches per train. We used a high energy lattice for most of the experiments; a low energy lattice was also used to

Table 1. Selected Parameters of the CESR Storage Ring

Parameter	High Energy Lattice	Low Energy Lattice
Ring circumference	768.4 m	
Revolution frequency	390.15 kHz	
RF Frequency	499.78 MHz	
Beam energy	5.265 GeV	4.400 GeV
SR energy loss per turn	1.0105 MeV	0.4928 MeV
Momentum compaction	0.01142	0.00926
RMS energy spread	$6.122 \cdot 10^{-4}$	$5.116 \cdot 10^{-4}$

measure the loss factor vs. bunch length. Some machine parameters for these optics are given in Table 1.

Power Dissipated in the HOM Loads and Loss Factor

We measured the temperature of the input and output cooling water for each HOM load, along with the water flow rate. The values yield the power transferred to the water from the ferrite:

$$P = \sum_{i=1}^{2} v_f^i \, C \rho \, (T_{out}^i - T_{in}^i),$$

where P is the power transferred to the cooling water from the two HOM loads; v_f is the water flow rate; C is the specific heat capacity of the water; ρ is the water density; T_{out} and T_{in} are the output and input temperatures of the cooling water.

This power should be approximately equal to the power lost by the beam due to its interaction with the cavity structure below the cutoff frequencies of the beam pipes because (i) in our HOM load design [6], other heat transfer mechanisms (conduction through the copper plate to the stainless steel shell, and heat radiation) should not give a significant contribution relative to the water cooling, and (ii) the HOMs with resonant frequencies below the cutoff frequencies of the nearby beam pipes (2.2 GHz and 3.4 GHz) are trapped inside the accelerating structure, so all their energy should be dissipated in the lossy material of the HOM loads.

We used the two lattices to obtain bunch lengths between 10 and 25 mm. Uniformly-filled bunches were used. Most measurements were done with one or 9 bunches. For uniformly-filled bunches, the loss factor is given by

$$k = \frac{N P f_{rev}}{I_o^2},$$

where I_o is the average beam current; f_{rev} is the revolution frequency; N is the number of bunches.

We do not have a bunch length monitor for CESR, but previous measurements [11, 12] indicate that there is no bunch lengthening in the storage ring; so we can calculate the bunch length via

$$\sigma_l = \frac{\alpha c}{\Omega_s} \cdot \frac{\sigma_E}{E_o},$$

$$\Omega_s^2 = \omega_{rev}^2 \cdot \frac{\alpha h e \sqrt{V_{RF}^2 - (U_o/e + U_{coh}/e)^2}}{2\pi E_o},$$

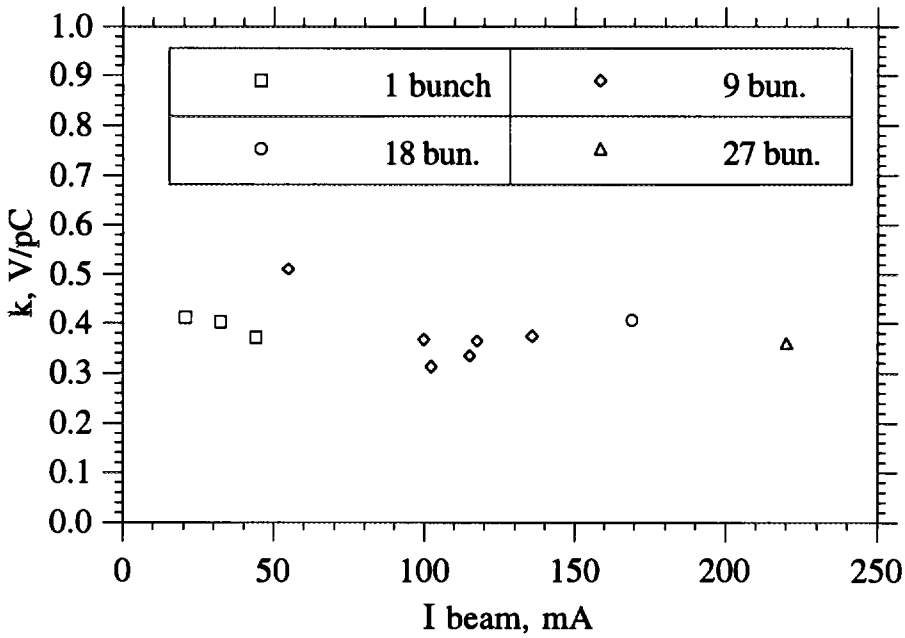

Figure 5. The loss factor of the SRF cavity vs. total beam current.

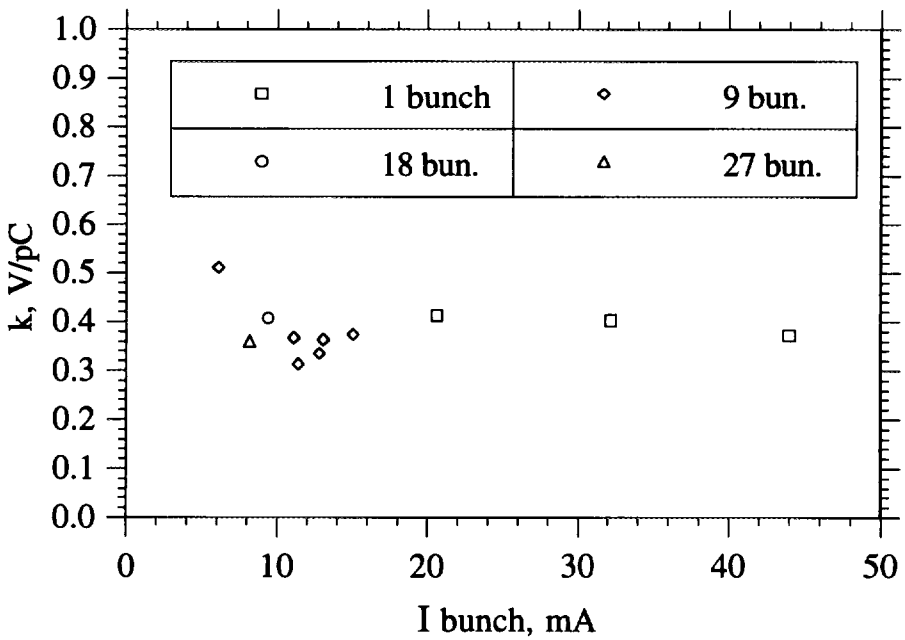

Figure 6. The loss factor of the SRF cavity vs. current per bunch.

where α is the momentum compaction factor; c is the speed of light; Ω_s is the synchrotron frequency; σ_E is the energy spread; h is the RF harmonic number, E_o is the beam energy; V_{RF} is the RF voltage; U_o is the energy loss per turn due to synchrotron radiation; and U_{coh} is the coherent energy loss per turn due to the total loss factor of the ring.

To verify that we do not have bunch lengthening, the loss factor was plotted as function of beam current for the same machine optics (high energy lattice) and RF voltage (Figures 5 and 6).

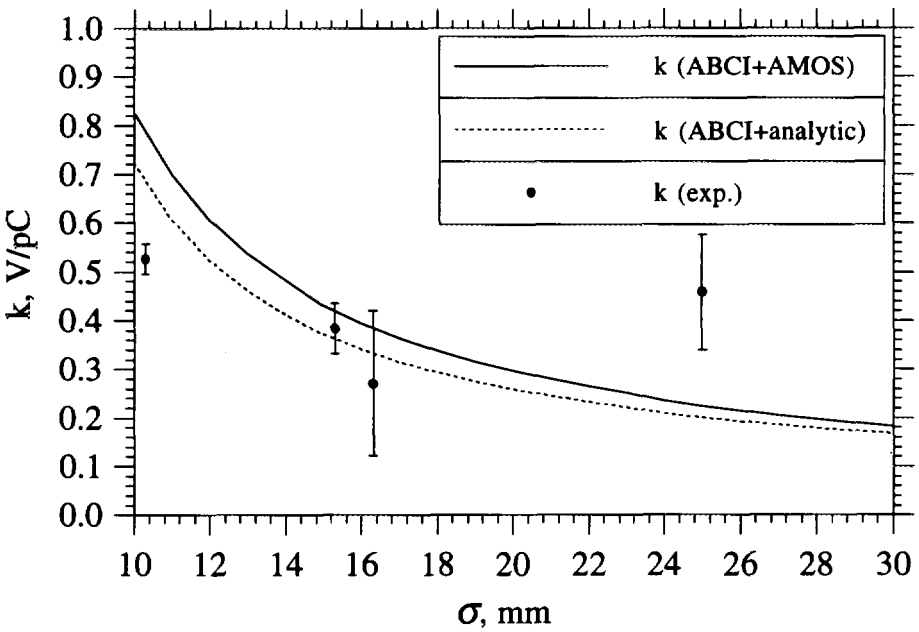

Figure 7. The loss factor of the SRF cavity assembly (experimental data and prediction).

The theoretical bunch length σ_l is equal to 15.3 mm for these measurements. One can see that the loss factor does not depend on current, i.e. there is no evidence of bunch lengthening.

The experimental results for the loss factor versus bunch length are compared with the predictions [6] in Figure 7. One can see that there is some disagreement for the shortest bunch length. That disagreement may be due to propagation of some portion of the HOM power into the beam pipes for frequencies above cutoff. There is also a big disagreement for the 25 mm bunch length. That data point was obtained with the low-energy lattice, using only the SRF voltage (with the NRF system switched off and the NRF cavities detuned). Unfortunately, the accelerating voltage was not high enough to allow us make measurements with high beam current: the total current was limited to 29 mA in 9 bunches due to the poor life time. The signal was therefore small, and this data point may have a big systematic error.

The maximum HOM power extracted by the two HOM loads was 2 kW, which is about 10 times less than needed for CESR-III. In a separate high power test of an HOM load, however, we reached a dissipated power of 14 kW (per load) [6] which is higher than the Phase III goal.

Sampling the Wake Potential with Two Bunches

An elegant method of the wake potential sampling, proposed recently by A. Temnykh [13], was used in the beam test: with two bunches of equal current, placed close to each other, we can measure the power loss due to some impedance. By varying the distance between the bunches, we can obtain information about the time structure of the wake potential. Also, we can calculate the loss factor and wake potentials for the two-bunch case using computer codes like ABCI [14] and AMOS [15] and compare these calculations with the measured values.

Using the definition of loss factor given above, we see that the loss factor for two bunches will be equal to the loss factor of a single bunch if the wake potential decays completely before the arrival of the second bunch, or if the HOMs with high *R/Q*s are all detuned far enough from harmonics of one half the RF frequency (so that the wake fields are not close to being completely in phase or completely out of phase).

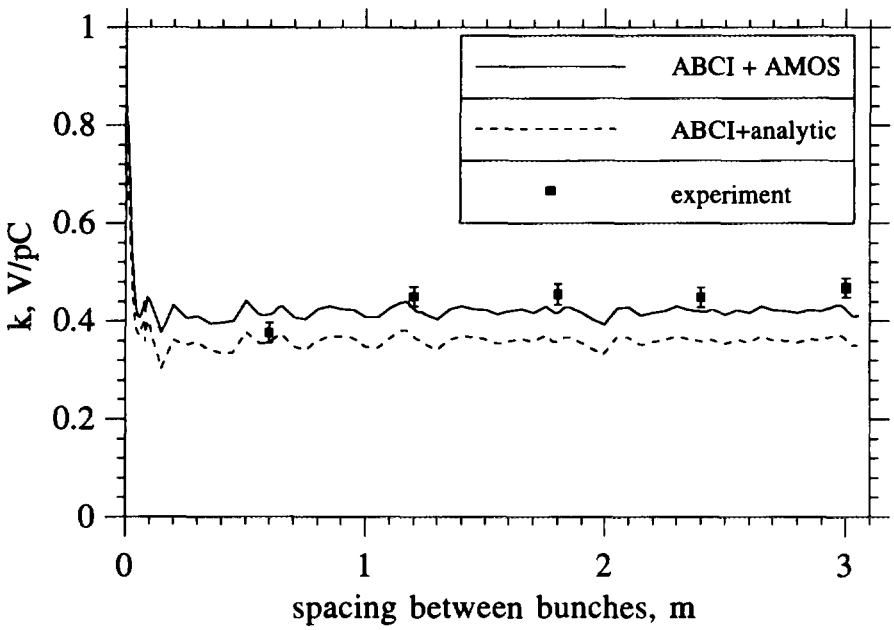

Figure 8. The loss factor of the SRF cavity assembly sampled by two bunches (experimental data and prediction).

The minimum spacing between two bunches is equal to the wavelength of the RF system, i.e. 60 cm for CESR. We measured the power dissipation in the HOM loads of the cavity module calorimetrically and varied the bunch spacing from 1 to 5 buckets. The measurements were done with a beam energy of 5.3 GeV and three different total beam currents: 10, 20, and 30 mA. Figure 8 shows the measured loss factor in comparison with ABCI and AMOS calculations. The agreement is very good.

Total Loss Factor of the Ring

Higher mode losses in CESR have been studied by M. Billing [16]. Scaling laws for the loss factor of different components in the vacuum chamber are in good agreement with experimental data; we used them to predict the total loss factor of the machine under the conditions of our test. Both the predictions and the separate calorimetric measurements of the loss factor of the superconducting cavity module show that the loss factor of the SRF cavity is much less than the total CESR loss factor. Nevertheless we measured the total loss factor of the machine before and after installation of the SRF cavity, to make sure that there were no gross errors in the calorimetric measurements. The predicted and measured total CESR loss factors are shown in the Fig. 9.

Dipole Loss Factor

We tried to measure the dipole component of the cavity loss factor by displacing a 120 mA (in 9 bunches) beam (with a bunch length of about 15 mm) horizontally and vertically by ±10 mm in the SRF cavity. According to calculations, the monopole component of the loss factor is 0.43 V/pC, and the dipole component is 0.006 V/pC for a 10 mm beam displacement. The cooling water ΔT was about 3.5°C for each HOM load. That means that the contribution from the dipole component should be of order 0.05°C. The resolution of our calorimetry is 0.03°C, and the noise level is of the same order. No changes in the cooling water ΔT were seen in excess of the resolution and noise level of the measurement.

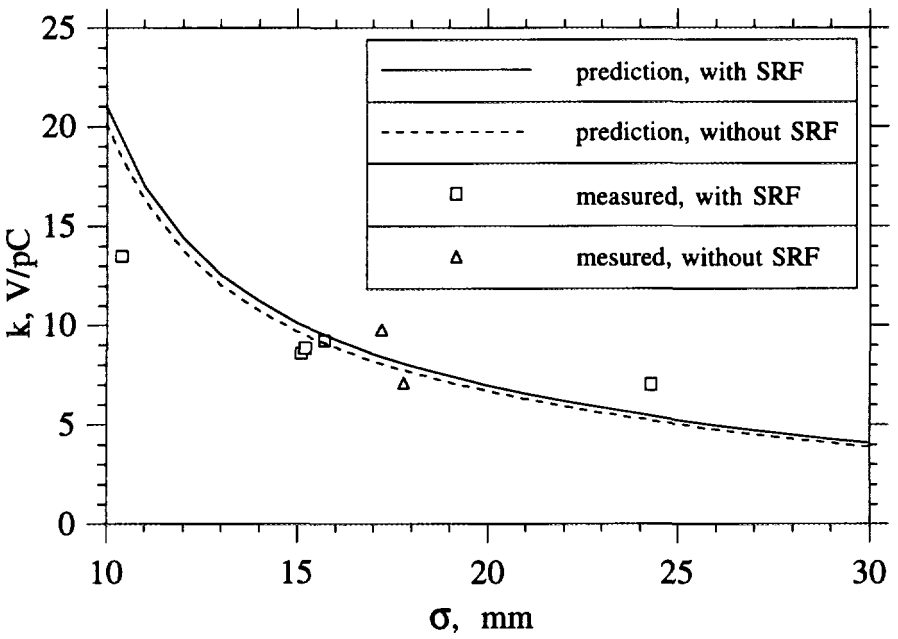

Figure 9. The total CESR loss factor (experimental data and prediction).

Sweeping HOM Frequencies with the Tuner and HOM Spectra

Using the cavity's fundamental mode frequency tuner, we changed the HOM frequencies to investigate the influence of the HOMs on the beam dynamics and to look for any unexpectedly dangerous (high $R/Q*Q$) HOMs. In these tests, the RF power for the SRF cavity was switched off and the fundamental mode frequency remained detuned. While scanning the tuner position, we were able to maintain a 100 mA beam, and there were no beam instabilities. We continuously monitored the HOM power deposited by the beam. The loss factor was calculated from the power dissipation in the HOM loads. The dependence of the loss factor on tuner position is shown in Figure 10. The small variation of the loss factor shows that there was no resonant excitation of HOMs as their frequencies changed. In addition, we measured the tunes and damping times of coupled bunch modes with a nine bunch beam, using a spectrum analyzer, for two positions of the tuner. The technique of these measurements is the same as described in [17]. No significant changes in damping times or tunes were observed between the two tuner positions: all changes were within the repeatability of the measurements.

We searched for dangerous HOMs by exciting the cavity via a single-bunch beam of 30 mA and varying the transverse displacement of the beam. The HOM spectra were observed and recorded using a spectrum analyzer.

We used results from URMEL [18] and CLANS [19] (for monopole HOMs) calculations [20] and measurements on a copper model of the cavity [21] to compare with the beam test measurements. Unfortunately we were not very successful in our attempts to match up the HOMs, though we can say that, for monopole HOMs, Q-factors are of order of 100, and for dipole and quadrupole HOMs, Q-factors are typically less than 1000. This is consistent with previous measurements. No resonant excitation of HOMs or beam instabilities were observed.

Synchrotron Radiation Heating

The position of the SRF cavity in CESR was such that dipole magnets were located < 1 m away from one side; on the other side, the closest magnet was >15 m away. Most of the tests were carried out with a positron beam, so as not to irradiate the cavity region with an excessive

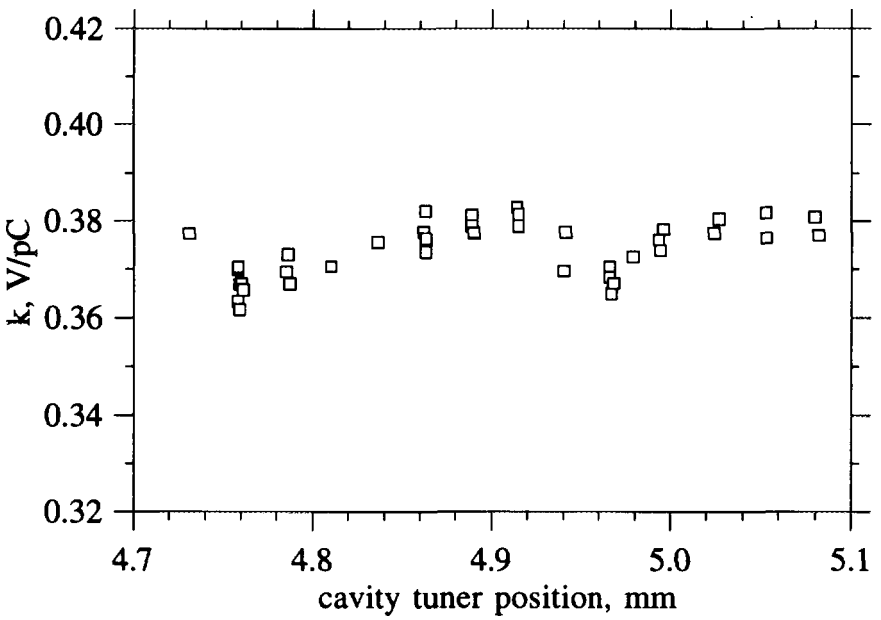

Figure 10. Dependence of the cavity loss factor on the cavity tuner position.

dose of synchrotron radiation (SR) from the nearby bending magnet. Near the end of the test, however, a 57 mA electron beam (in 9 bunches) was also run through the cavity, to see how the cavity performed in the presence of a severe SR dose. With 100 W of synchrotron radiation power incident on the stainless steel taper, its temperature increased to 100°C and the vacuum degraded from $6 \cdot 10^{-9}$ to $6 \cdot 10^{-8}$ torr. The cavity operated stably in the presence of this large SR dose and there was no increase in cryogenic losses. In order to reduce the temperature rise and vacuum degradation, we plan to add water cooling and SR masks to the tapers.

CONCLUSIONS

The calorimetry and RF power results agree with predictions up to their respective uncertainties. The results of wake potential sampling suggest that the wake fields of the SRF cavity will not limit the performance of CESR in bunch train operation. No beam instabilities or dangerous HOMs were encountered while sweeping the HOM frequencies using the cavity tuner or while exciting multipole HOMs by displacing the beam off axis.

The next step in the RF system upgrade for CESR-III will be to replace one of the NRF cavities with an SRF cavity in a new cryostat for a long-term test, which is scheduled to begin in late summer of 1996.

ACKNOWLEDGEMENTS

We would like to thank our colleagues P. Barnes and J. Sears for valuable assistance in many stages of the preparations for the beam test as well as during beam test itself; R. Ehrlich and E. Nordberg, who were responsible for the refrigerator and cryogenic distribution system; R. Kaplan and J. Reilly for their extremely useful help with the RF system operation. Our special

thanks to Prof. D. Rubin, Prof. M. Tigner, M. Billing, and D. Rice for their help and guidance throughout the beam test. We appreciate S. Peck's design of a special low energy lattice for the beam test. Also, we are pleased to thank S. Henderson for calculation of SR power and B. Vakoc for help with numerous computer calculations. We acknowledge the valuable contribution of E. Chojnacki during the test of the new RF window. Finally, we wish to thank all of the Laboratory staff, and the CESR operations staff in particular, who helped to make the beam test possible.

REFERENCES

[1] J. Kirchgessner, "Review of the Development of RF Cavities for High Currents", *presented at the 1995 Particle Accelerator Conference, Dallas, TX* (to be published)

[2] D. Rubin, "CESR Status and Plans", *presented at the 1995 Particle Accelerator Conference, Dallas, TX* (to be published)

[3] H. Padamsee, et al., "Accelerating Cavity Development for the Cornell B-Factory, CESR-B", *Conference Record of the 1991 Particle Accelerator Conference,* Vol. 2, pp. 786-788, San Francisco, CA, May 1991

[4] H. Padamsee, et al., "Design Challenges for High Current Storage Rings", *Particle Accelerators,* 1992, Vol. 40, pp. 17-41

[5] H. Padamsee, et al., "Beam Test of a Superconducting Cavity for the CESR Luminosity Upgrade", *presented at the 1995 Particle Accelerator Conference, Dallas, TX* (to be published)

[6] S. Belomestnykh, et al., "Comparison of the Predicted and Measured Loss Factor of the Superconducting Cavity Assembly for the CESR Upgrade", *presented at the 1995 Particle Accelerator Conference, Dallas, TX* (to be published), also *Cornell LNS Report SRF 950406-04* (1995)

[7] S. Belomestnykh et al., "Wake fields and HOMs Studies of a Superconducting Cavity Module with the CESR Beam", *presented at the 1995 Particle Accelerator Conference, Dallas, TX* (to be published)

[8] D. Moffat, et al., "Preparation and Testing of a Superconducting Cavity for CESR-B", *Proceedings of the 1993 Particle Accelerator Conference,* Vol. 2, pp. 763-765, Washington, D.C., May 1993

[9] K. Akai, et al., "Beam Tests and Operation of Superconducting Cavities", *Proceedings of the 4th Workshop on RF Superconductivity,* KEK Report 89-21, Vol. 1, pp. 189-206, KEK, Tsukuba, Japan, August 1989

[10] M. Pisharody, et al., "Planar Waveguide Window for the CESR Upgrade", *presented at the 1995 Particle Accelerator Conference, Dallas, TX* (to be published)

[11] E. B. Blum, et al., "Bunch Length Measurements in CESR Using an X-Ray Sensitive Photoconducting Detector", *Nuclear Instruments and Methods,* 1983, Vol. 207, pp. 321-324

[12] Z. Greenwald, et al., "Bunch Length Measurement Using Beam Spectrum", *Conference Record of the 1991 Particle Accelerator Conference,* Vol. 2, pp. 1246-1248, San Francisco, CA, May 1991

[13] A. Temnykh, "Wake function study using two spaced bunches", *Cornell LNS Report CBN 95-11* (1995)

[14] Y. H. Chin, "Advances and Applications of ABCI", *Proceedings of the 1993 Particle Accelerator Conference,* Vol. 2, pp. 3414-3416, Washington, D.C., May 1993

[15] J. DeFord, et al., "The AMOS (Azimuthal Mode Simulator) Code", *Proceedings of the 1989 IEEE Particle Accelerator Conference,* Vol. 2, pp. 1181-1183, Chicago, IL, March 1989

[16] M. Billing, "Higher Mode Power Loss Limitations for Beam Currents in CESR", *Cornell LNS Report CBN 84-15* (1984)

[17] M. Billing, et al., "Measurements of Vacuum Chamber Impedance Effects on the Stored Beam at CESR", *presented at the 1995 Particle Accelerator Conference, Dallas, TX* (to be published)

[18] U. Laustroer, et al., "URMEL and URMEL-T User Guide (Modal Analysis of Cylindrically Symmetric Cavities; Evaluation of RF-Fields in Waveguides)", *DESY M-87-03* (1987)

[19] D. G. Myakishev, V. P. Yakovlev, "The New Possibilities of SuperLANS Code for Evaluation of Axisymmetric Cavities", *presented at the 1995 Particle Accelerator Conference, Dallas, TX* (to be published)

[20] B. Vakoc, "HOM Spectra and Dissipated Power Density Profiles for the SRF cavity with a Ferrite HOM Load: Calculations with CLANS and Analysis", *Cornell LNS Report SRF 950811-11* (1985)

[21] V. Veshcherevich, et al., "Higher Order Modes Damping in CESR B Cavity", *Proceedings of B Factories: The State of the Art in Accelerators, Detectors and Physics,* SLAC-400/CONF-9204126, pp. 177-180, Stanford, CA, April 1992

Measurement of the Interaction Between a Beam and a Beam Line Higher-Order Mode Absorber in a Storage Ring*

W. Hartung, P. Barnes, S. Belomestnykh, M. Billing, R. Chiang, E. Chojnacki, J. Kirchgessner, D. Moffat, H. Padamsee, M. Pisharody, D. Rubin, & M. Tigner
Laboratory of Nuclear Studies, Cornell University, Ithaca, New York 14853

"Underneath this chilly gray October sky,
We can make believe the SSC is still alive;
We've shootin' for the Higgs,
An' smilin' Hazel's drivin' by." [1]

I. INTRODUCTION

A phased luminosity upgrade of the CESR e^+e^- storage ring has been initiated [2]. The upgrade program calls for the eventual installation of superconducting cavities with strongly damped higher-order modes (HOMs). The cavity is designed to allow all HOMs to propagate into the beam pipe, so that they may be damped by a layer of microwave-absorbing ferrite. RF measurements with a full-size copper cavity and loads made of TT2-111R ferrite[1] indicate that the design gives adequate HOM damping [3]. The coupling impedance of the ferrite loads and the consequences for beam stability in a high-current ring have been predicted [7]. Prototypes for the cavity, cryostat, and HOM loads were subjected to a beam test in CESR [4, 5, 6]. To further test our understanding of the beam-ferrite interaction, beam measurements were done in CESR in December 1994 on a ferrite load of magnified coupling impedance. This test is described herein.

II. LOAD FABRICATION

We designed a test structure with a beam tube diameter 2.5 times smaller and a ferrite-bearing length 6 times larger than an actual "porcupine" HOM load [6]. The predicted coupling impedance of this test structure is $\sim$ 2 times the predicted monopole impedance and $\sim$ 10 times the predicted dipole impedance of the 8 porcupine loads to be installed in CESR. The structure was split into three units, with sections of straight beam tube (with pumping ports) between them. Each unit consisted of a copper tube with 40 TT2-111R ferrite tiles soldered to the inside and water cooling on the outside (Fig. 1), incorporating features from both the original full-size HOM load [8] and the redesigned porcupine HOM load [6]. A total of four ion pumps, each rated at 140 L/s, were adjacent to the ferrite sections during the vacuum bake and the beam test.

A prototype unit with only 10 tiles was made first for evaluation in a high power density RF test with a 500 MHz klystron. For this test, the ferrite-lined tube became the outer conductor of a coaxial line, with a short placed to produce relatively uniform dissipation in the ferrite. An average surface power density of 15 W/cm^2 was reached without visible damage to any of the tiles. The maximum (measured) tile surface temperature was 96°C.

*Work supported by the National Science Foundation, with supplementary support from U. S.-Japan collaboration.

[1] A product of Trans-Tech, Inc.

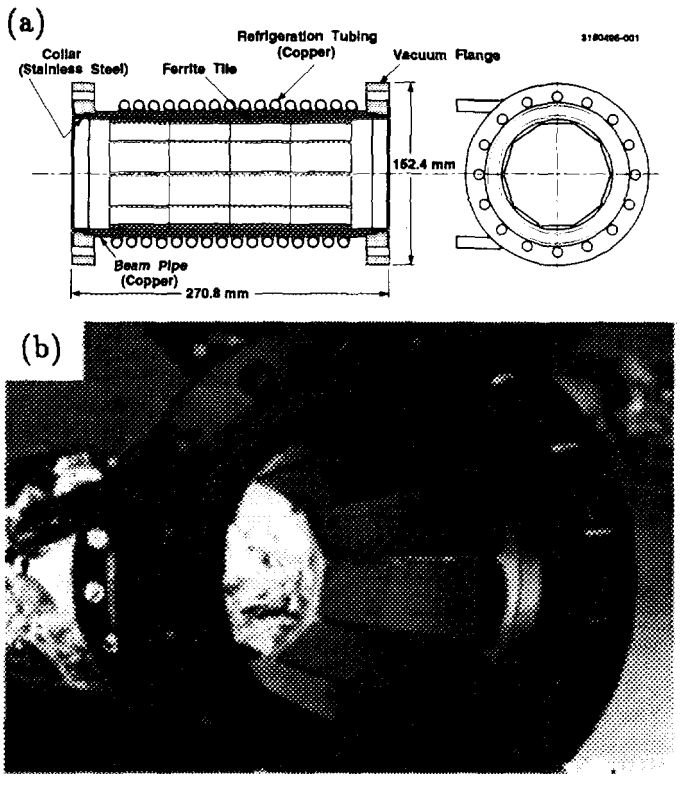

Figure 1. (a) Drawing and (b) photograph of one unit of the ferrite structure. The ID of the Cu tube is 92.1 mm; the ferrite tiles are $50.8 \times 25.4 \times 3.175\,\mathrm{mm}^3$ before radiusing.

III. BEAM TEST RESULTS

The beam measurements on the ferrite section were done over several days, interleaved with machine start-up activities following a down period. Some measurements were done with 9 bunches, in addition to the 1- and 2-bunch measurements discussed herein. Positrons were used almost exclusively, because we did not have complete masking for direct synchrotron radiation from the electron beam. The predictions mentioned in this section are based on the same type of coupling impedance calculations as was done for the HOM loads, *i.e.* using the AMOS program [9] and an analytic approximation [7]. In the calculations, we assumed an axisymmetric geometry with a 3.175 mm layer of ferrite, and did not split the ferrite into three sections.

A. Calorimetric Measurements

The power dissipation in each unit was obtained calorimetrically via the flow rate, inlet temperature, and outlet temperature of the cooling water (the volume flow rate of water was $\sim$ 50 mL/s per unit for most of the test). The monopole loss factor $k_0^{\parallel}$ of the ferrite units can be obtained directly from the total power dissipation P_d and total beam

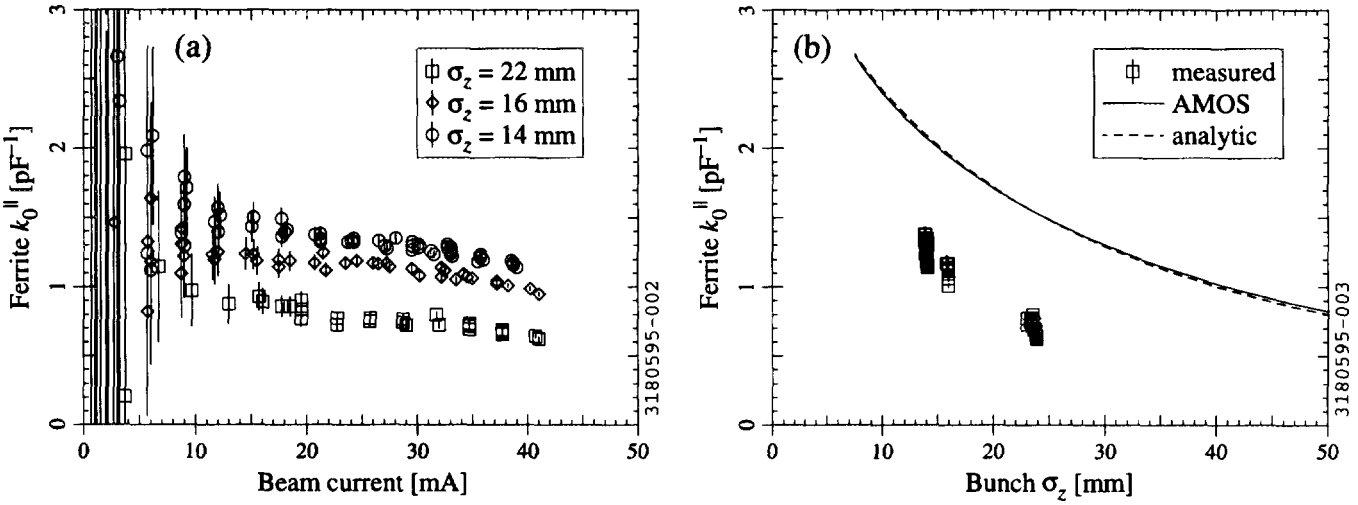

Figure 2. Calorimetrically measured single-bunch loss factor (summed over all 3 units) of the ferrite section as a function of (a) beam current, and (b) bunch length (with predictions). The RF voltage was adjusted to vary the bunch length. Noisy low-current points ($I < 20$ mA) are omitted in (b).

current I. The measured $k_0^{\parallel}$ as a function of I is shown in Fig. 2a for a single bunch. The noise in the data at low I is due to the poor resolution of the small ΔT values. At higher I, a slight decrease in the measured $k_0^{\parallel}$ as function of I is visible. Possible explanations for this effect include (i) systematic error in the calorimetry, (ii) non-linearity in the ferrite response to the RF field, or (iii) the ferrite properties' temperature dependence.

Fig. 2b shows the single-bunch data plotted as a function of the longitudinal bunch size σ_z, calculated from the measured synchrotron frequency f_s (we did not have any means to measure the bunch length directly), along with the predicted $k_0^{\parallel}$. It can be seen that, inasmuch as f_s is a reliable indicator of the bunch length, the decrease in $k_0^{\parallel}$ with I cannot be explained as being due to changes in σ_z as a function of I. The measured $k_0^{\parallel}$ is smaller than predicted by about a factor of 2, perhaps because of the afore-mentioned idealisations in the model.

We used the Temnykh method [10] to sample the wake field: with two bunches of equal charge (I_b = current per bunch = 20 mA for each), we measured the power dissipation in the ferrite as a function of the spacing Δz between the bunches. In terms of a power loss factor

$$P_0^{\parallel} \equiv \frac{P_d f_0}{N_b I_b^2} ,$$

where N_b = number of bunches and f_0 = revolution frequency, we should have[2] $P_0^{\parallel} = k_0^{\parallel}$ if the wake fields have vanished by the time the second bunch arrives and $P_0^{\parallel} \to 2k_0^{\parallel}$ as $\Delta z \to 0$. The results are shown in Fig. 3, along with a prediction obtained by integrating the calculated coupling impedance with the appropriate form factor. The measurement suggests that the ferrite section's wake fields endure longer than predicted; for $\Delta z >$ one RF bucket, however, the measurements and predictions seem to agree that the wake field has decayed to zero.

[2] we are (justifiably, we think) treating the single-bunch $k_0^{\parallel}$ and the single-pass $k_0^{\parallel}$ as synonymous.

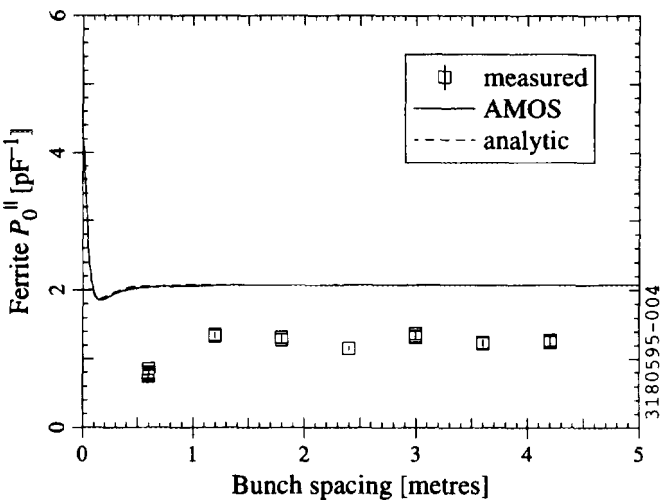

Figure 3. Calorimetrically measured and predicted 2-bunch power loss factor of the ferrite as a function of spacing, with σ_z = 14 mm (from f_s). Because the RF frequency is 500 MHz, the smallest measurable Δz is 0.6 m.

We used magnetic and electrostatic elements to produce a transverse displacement of the beam in the ferrite chamber and its vicinity. The measured calorimetric single-bunch loss factor as a function of displacement is shown in Fig. 4, along with a prediction based on the calculated monopole and dipole loss factors. Though the measurement suggests that there is some dependence on displacement, the signal-to-noise ratio is not very favourable.

B. RF Power Measurements

It is possible to infer the total loss factor of a storage ring by applying the appropriate book-keeping methods to the cavity RF power and synchrotron radiation power [11]. We applied this technique with and without the ferrite in order to get an independent measure of the power loss due to the

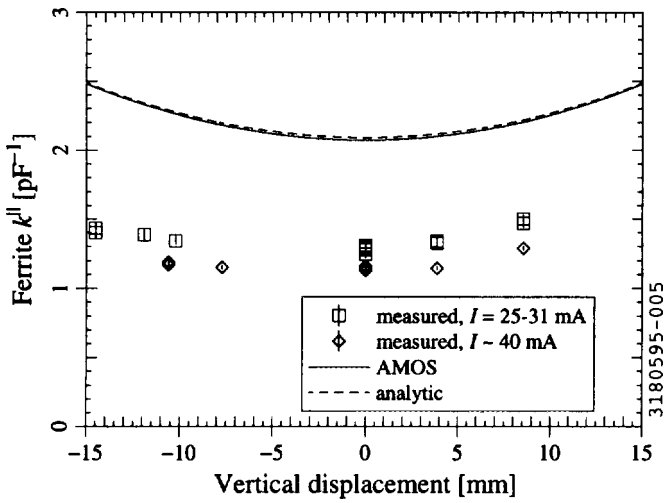

Figure 4. Calorimetrically measured and predicted loss factor of the ferrite section as a function of the vertical displacement of the beam, with $\sigma_z = 14$ mm (from f_s).

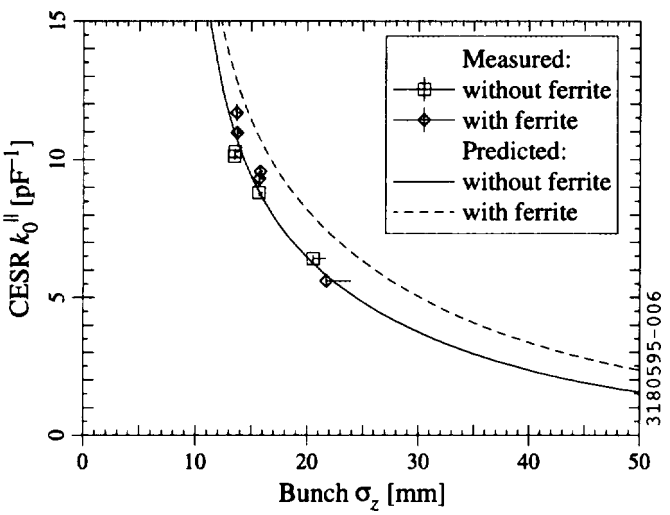

Figure 5. Measured and predicted single-bunch loss factor of CESR, with and without ferrite present.

ferrite. The results are compared in Fig. 5. The predicted $k_0^{\parallel}$ of CESR shown in Fig. 5 was obtained from scaling laws for various machine elements [12] (updated to account for recent modifications). The total $k_0^{\parallel}$ measurement gave less accuracy than the calorimetric measurement, but the results do not overtly contradict each other.

C. Tune Shift And Damping Rate Measurements

According to theory, the total ring impedance should produce shifts in the frequencies and damping rates of coupled-bunch modes. In the "effective impedance" approximation, the shift in the frequency f and damping rate α should be proportional to I. We used established techniques [13] to measure the lowest-order single-bunch transverse mode frequencies (*i.e.* the horizontal and vertical betatron frequencies) and corresponding α's as a function of I, with and without ferrite. We did the measurements with the CESR distributed ion pumps turned off, in order to eliminate anomalous growth effects [13]. We believe that measured differences in slope ($\Delta f' = 0$ to 13 kHz/A and $\Delta\alpha' = -4$ to -6 ms^{-1}A^{-1}) are below the reproducibility threshold of the measurement.

IV. LOAD PERFORMANCE

The maximum (total) power dissipation in the ferrite was was 5.8 kW according to calorimetry (average power density = 3.8 W/cm^2); this was obtained with $I = 142$ mA in 9 bunches. At this current, the pressure gauges read ≤ 30 pbar, although pressures as high as 50 pbar were recorded (at lower I) during an earlier "beam processing" shift. Several vacuum "spikes" occurred in the course of the test, with the pressure rising to 100–200 pbar or higher. Prior to installation, the pressure in the ferrite assembly reached 1 pbar at 17°C after a vacuum bake-out to 150°C.

A brief inspection of the ferrite chamber after removal from CESR revealed that one corner of one tile had broken off; it was found lying on the bottom of one of the ferrite sections. The piece appeared to have been unsoldered except along one edge. The remaining tiles have not yet been closely inspected for cracks.

V. CONCLUSION

CESR beam measurements with a ferrite-lined section of magnified impedance indicate that the loss factor is a factor of ~ 2 smaller than predicted; the measured wake field endures longer than predicted, but is not visible for $\Delta z \geq 4.2$ m, which is planned for CESR. The signal-to-background ratio made it difficult to pick out effects from the ferrite via measurements on the beam only. We are working on predictions which model the actual load geometry more closely.

We wish to thank all of the Laboratory staff who helped to make this beam test possible.

VI. REFERENCES

[1] C. Blonde, "Tomorrow, Wendy (remix)," in *Songs of the DOE: A Benefit Compilation*, Polymer Records, New York, 1995.
[2] D. Rubin, these proceedings.
[3] V. Veshcherevich *et al.*, *Proceedings of B Factories: The State of the Art in Accelerators, Detectors, and Physics*, SLAC-400/CONF-9204126, p. 177.
[4] H. Padamsee, *et al.*, these proceedings.
[5] S. Belomestnykh, *et al.*, "Wakefields and HOMs Studies...," these proceedings.
[6] S. Belomestnykh, *et al.*, "Comparison of the Predicted and Measured Loss Factor...," these proceedings.
[7] W. Hartung *et al.*, *Proceedings of the 1993 Particle Accelerator Conference*, p. 3450.
[8] D. Moffat *et al.*, ibid., p. 977.
[9] J. DeFord *et al.*, *Proceedings of the 1989 IEEE Particle Accelerator Conference*, p. 1181.
[10] A. Temnykh, Cornell LNS Report CON95-06 (1995).
[11] D. Rice, *et al.*, *IEEE Trans.* **NS-28**, p. 2446 (1981).
[12] M. Billing, Cornell LNS Report CBN84-15 (1984).
[13] M. Billing, *et al.*, these proceedings.

KEKB Bunch Feedback Systems

M. Tobiyama and E. Kikutani
National Laboratory for High Energy Physics, 1-1 Oho, Tsukuba 305, Japan

Abstract

Design and the present status of the bunch by bunch feedback systems for KEKB rings are shown. The detection of the bunch oscillation are made with the phase detection for longitudinal plane, the AM/PM method for transverse plane. Two GHz component of the bunch signal which is extracted with an analog FIR filter is used for the detection. Hardware two-tap FIR filter systems to shift the phase of the oscillation by 90° will be used for the longitudinal signal processing. The same system will be used with no filtering but with only digital delay for transverse system. The cantidate for the kicker and the required maximum power are also estimated.

I. Introduction

The rings of KEKB are designed to accumulate many bunches with huge beam current, which will cause many strong coupled bunch instabilities both in transverse and longitudinal planes. Even with the special care for the reduction of the sources of the instabilities, impedance of some dangerous modes may remain high. Studies on the acceleration cavities indicate that growth times of the multi-bunch instabilities at KEKB will be of the order of a few ms to 10 ms. The transverse instabilities will be generally stronger than the longitudinal ones. Therefore the method to analyze and suppress the instabilities have the key to achieve the designed quality of the rings. The goal of the feedback systems have been set to achieve the damping time of one ms for the transverse and 10 ms for the longitudinal planes.

We are now developing beam feedback systems with the bunch-by-bunch scheme and making experiments using TRISTAN accumulation ring (TRISTAN-AR). In our feedback systems, we detect the individual bunch oscillations separately, shift the phase of the signal by 90°, then kick the bunch to damp the oscillation. In this paper, we show the present status of R & D of feedback systems very briefly. Detailed discussions for each part of the systems and the results of R & Ds are written elsewhere[1],[3],[2],[4],[5]. Related parameters of the KEKB accelerators are listed in Table 1.

The key technique in the signal processing for the feedback system is to store the information of bunch orbit deviations for at least one full revolution period of the ring. At KEKB this is achieved by a pure hardware digital filter system, which can work in a very high-frequency environment. The reasons for adapting the digital delay technique are as follows:

- A digital system is more flexible than an analog delay with optical fiber cables and other devices.
- Static components can be easily eliminated with a simple digital filter. In the longitudinal plane, the synchronous phases of bunches can vary because of the huge beam loading on the cavities introduced by the bunch gap. The elimination of the DC offset for an individual bunch is essential for saving the (very expensive) power to send to the kickers.
- It is easier to adjust phase and delay with digital systems. This helps the rapid start-up of the system as well as the efficient maintenance.

II. Bunch detection systems

The feedback systems of KEKB consist of three parts: the bunch detection part, the signal processing part and the kicker part. Figure 1 and 2 show the block diagram of the longitudinal system and transverse system, respectively. The design of each of the three parts are described in the followings.

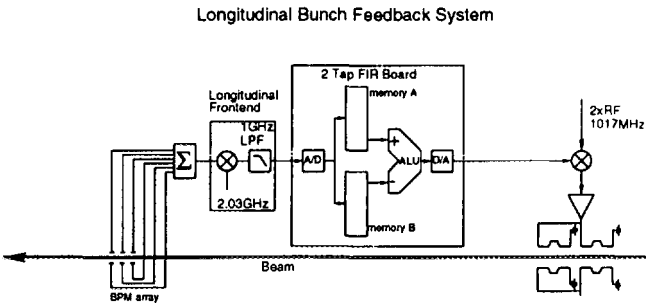

Figure. 1. Block diagram of the longitudinal feedback system.

A. *Longitudinal detection*

The longitudinal position (timing) of a bunch is converted into the phase difference between the pickup signal and a timing-reference signal, which is generated by multiplying the accelerating RF signal, as shown in Fig. 3. Hereafter, we call the frequency of the reference signal as the 'detection

Ring		LER	HER	
Energy	E	3.5	8	GeV
Circumference	C	3016.26		m
Beam current	I	2.6	1.1	A
RF frequency	f_{RF}	508.887		MHz
Harmonic number	h	5120		
Particles/bunch	N	3.3×10^{10}	1.4×10^{10}	
Synchrotron tune	ν_s	$0.01 \sim 0.02$		
Betatron tune	ν_x/ν_y	45.52/45.08	47.52/43.08	

Table I
Main parameters of KEKB.

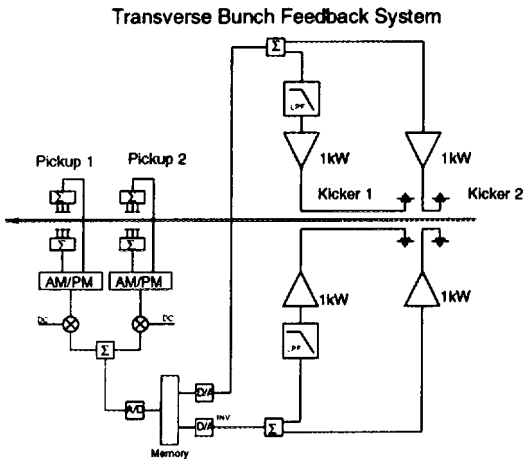

Figure. 2. Block diagram of the transverse feedback systems.

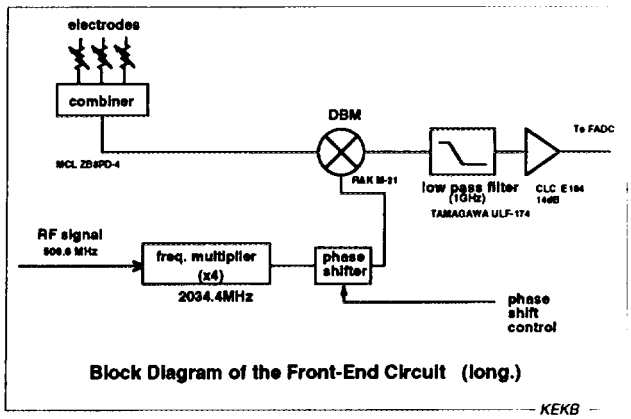

Figure. 3. Front-end circuit for longitudinal detection system.

frequency'. It is chosen to be 4 times of the RF frequency, about $4 \times f_{rf} = 2$ GHz. The pickup signal is created by combining 3 pulses from 3 longitudinally aligned pickup electrodes with a power combiner. The timing differences of these pulses should be adjusted so that the combined signal contains the detection frequency component.

Since the output of this circuit is proportional to the bunch current, the feedback gain will be proportional to the bunch current. However, this gain variation is not considered a major problem, since the growth rates of the instabilities are also proportional to the bunch current.

B. Transverse detection

The transverse position of a bunch is detected by the AM/PM method. Figure 4 shows the block diagram of the circuit. Similar to the longitudinal one, the transverse signal is created by combining 3 pulses from three pairs of pickup electrodes. We will use two sets of detection system placed with the distance of about 90° of the betatron phase.

The detection frequency used in the AM/PM circuit is chosen to be 2 GHz. This frequency is not sufficient for the 2 ns bunch separation. We will try to increase the frequency up to 2.5 GHz.

The DC offset of the detection signal, that is the residual closed orbit distortions, may be much larger than that of the dynamic range of the ADC. We plan to apply an analog DC suppression feedback circuit in the front-end circuit.

III. Signal Processing

A. 2-Tap FIR filter for longitudinal system

The functions of the longitudinal signal processing part are: (1) create the signal delay, and (2) eliminate the static (DC) component.

These functions are realized by a simple 2-tap finite impulse response (FIR) filter. In general, the

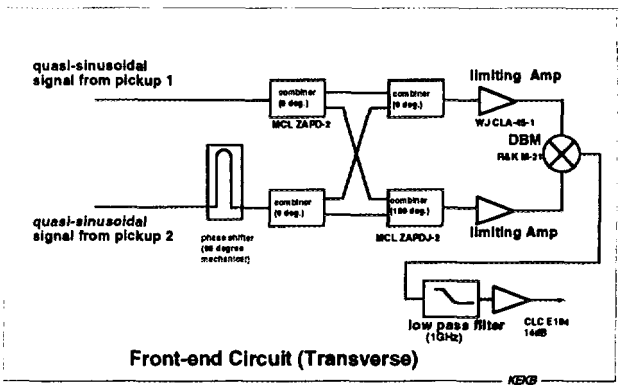

Figure. 4. Front-end circuit for transverse detection system.

relation between the inputs (x_i) and the output (y) of an FIR filter is expressed by

$$y = \sum_{j=1} a_j x_j,$$

where a_j's are called the filter coefficients. The 2-tap filter are the simplest ones among these FIR filters, and they will be employed in the KEKB feedback systems. The output of the filter is a very simple function of the inputs, which can be written as:

$$y = a(x_k - x_j),$$

so the two coefficients have the same magnitude with opposite signs. This ensures that the gain of the filter is zero in the limit of the frequency near zero. This also means that the calculations required in the operation of the digital filter involves only subtraction operations and not multiplication's. Consequently, the required hardware of the filter calculation is much simplified.

As the synchrotron tune is much smaller than unity, in our case about 0.01, we will use the peak gain mode of the filter, in which the positions of two taps should be separated by a half of the full period of the oscillation. By choosing the taps at the 1/4 (-90°) and 3/4 period (-270°) relative to the timing of applying correction kicks to the beam, the phase shift of 90° is performed.

In the transverse plane, we will not use the two-tap filter. Only the function of the digital delay will be used.

B. Processor board

The heart of the signal processing part, which executes the filter calculation, is the digital filter complex. It consists of the memory and simple arithmetic units. Since the digital filter complex is a relatively low-speed device, two auxiliary devices, that is fast data demultiplexers (FDMUX) and fast data multiplexers (FMUX) will be implemented to connect them with very fast devices such as FADC and DAC. Figure 5 shows a block diagram of the system.

The digital filter complex consists of 32 identical units, each of which treats the data of 160 bunches (5210/32=160). The memory in one unit are aligned in two series. Each series is used for one of the two taps. Capacity of one memory series is 16 k bytes, and it can store the data for 100 turns for each bunch. There is one arithmetic logic unit (ALU) in one unit and it executes the subtraction of data from two series of memories. Additionally, there are a bit-shifter to change the gain of the filter up to 20 dB. The digital filter complex will be assembled with wired logic's or custom LSIs. It will be able to process all the data within the one period of revolution of the KEKB rings.

For the practical use it must be made possible to rearrange the tap positioning easily and quickly, when the working point of an accelerator is changed. For this purpose this circuit is equipped with a tap pointers which can be modified with a relatively slow logic circuit. Detailed design of the board is written in Ref. [5].

IV. Power amplifiers and kickers

A. Longitudinal system

The kicker for the bunch feedback system must support a wide-band operation while keeping the reasonable shunt impedance. At KEKB the bandwidth of the kicker required for the bunch by bunch feedback is 255 MHz.

The required voltage of the longitudinal system is given as

$$V_{turn} = 2\frac{1}{\tau_e} T_0 (\Delta E/e)$$

where τ_e is the damping time of the feedback system. If we require the damping time of 10 ms with $\Delta E/e$=0.1%, the required voltage for HER is 16 kV and 7 kV for LER.

The R & D for the KEKB longitudinal kicker has been centered on the wideband device, which is based on series stripline structure(the series drift tube type), originally proposed by G. Lambertson[6]. A combination of the beam pipe and the inner electrodes creates a coaxial structure of the characteristic impedance of 25Ω. RF power fed by power amplifiers propagates as the TEM wave along the structure. The frequency of the carrier is 1 GHz ($=2 \times f_{RF}$). We plan to use quadrature phase shift keying technique with the frequency of 1.27 GHz to escape from the beam loading. If we expect the effective shunt impedance of the kicker as about 80 %

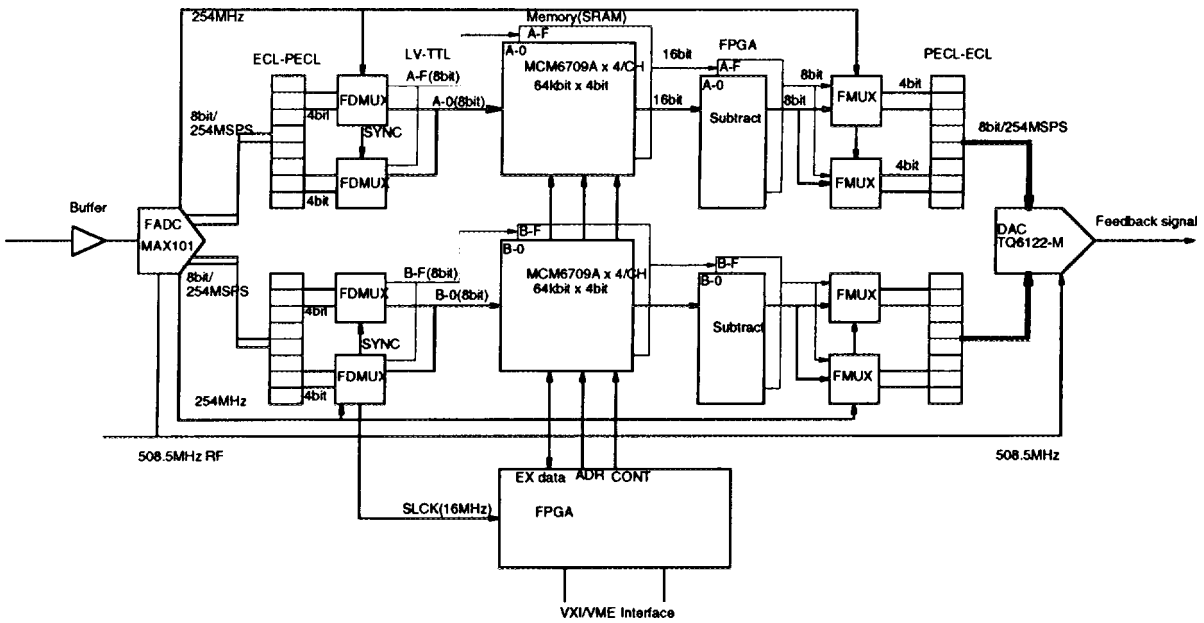

Figure. 5. Block diagram of the filter board.

of the ideal case, that is somehow optimistic assumption though, we can calculate the required number of the cell-structures of the kicker. In HER, we will need 12 × 2 cells kicker ($\sim$ 3 m in length) with the $R_{sh} \sim 46\text{k}\Omega$. The required maximum total power will be about 6 kW. In LER, we will need 8 × 2 cells kicker ($\sim$ 2 m in length) with the $R_{sh} \sim 20\text{k}\Omega$. The required power will be about 3 kW.

Another candidate for our longitudinal kicker is a very low-Q resonator with radial-line inputs. This kicker has the structure of higher-order-mode free and has relatively higher shunt impedance. In this case the bandwidth is limited about 180 MHz so it may be fairly difficult to use it for 2 ns bunch spacing of operation.

B. Transverse system

The damping time of the transverse feedback system is expressed as

$$V_{turn} = 2\frac{1}{\tau}T_0(E/e)\frac{1}{\sqrt{\beta_m\beta_k}}x_{max}$$

where β_m and β_k is the betatron function at the monitor and the kicker, respectively. If we need the damping time of 1 ms at maximum amplitude of 1 mm, the required voltage is 16 kV for HER, 7 kV for LER if we assume $\beta_k = \beta_m = 10$ m.

We will use standard strip-line kickers. Though the shunt impedance of at very low frequency of a kicker is proportional to the square of the length, the shunt impedance at higher frequency reduces very rapidly with the length. The length of the wideband kicker we have chosen is 30 cm, the shunt impedance of which is about 8 kΩ at the lowest frequency, 3.5 kΩ at 250 MHz. To gain the damping time of 1 ms at the saturation amplitude of 0.1 mm at 250 MHz, we need 730 W at HER, 140 W at LER.

Estimated modes for the instabilities that have rapid growth time are localized around the lower frequencies, that is from 1 kHz to 20 MHz. It is therefore effective to prepare a very long stripline kicker to suppress such instabilities other than the wideband one. We will use a 3 m-long kicker for HER, a 1.2 m kicker for LER. The expected shunt impedance at the lowest frequency are 200 kΩ and 100 kΩ, respectively. To gain the damping time of 1 ms at the saturation amplitude of 1 mm, we need 1.2 kW for HER, 500 W for LER.

V. Schedule

We are now fabricating the first set of a prototype of full speed (509 MHz) two-tap FIR board with 1 Mb memory[5]. It is scheduled in completion in the end of this October. We will close the feedback loop for longitudinal plane with the board and measure the characteristics of the feedback system, such as the damping time or stability criterion. Other two sets of the prototype board will be completed by the

end of this fiscal year. By using the three boards, we will try to close the feedback loops for both longitudinal and transverse planes. Based on the same high speed technique, we will also make a transient memory board with 40 Mb memory, that can store bunch oscillation data of full bunch of TRISTAN-AR about 65 k turns. It will be used to study the fast ion-trapping effect in the next year.

The first set of the transverse wideband kicker, the length of which 30 cm, has successfully been installed in TRISTAN-AR in this September. With coming four sets of power amplifiers of 200 W each, we expect the transverse damping time of about 0.5 ms at the saturation amplitude of 1 mm. In the high beam current study of TRISTAN-AR scheduled on the next year, we hope to study the beam behavior of time domain with the feedback systems.

References

[1] E. Kikutani, T. Kasuga, Y. Minagawa, T. Obina, M. Tobiyama and L. Ma, in proceedings of the 4th European Particle Accelerator Conference, London, UK (1994) p.1613.

[2] E. Kikutani, T. Kasuga, Y. Minagawa, T. Obina and M. Tobiyama, in proceedings of the 1995 IEEE Particle Accelerator Conference, Dallas Texas. U.S.A./ KEK Preprint 95-20.

[3] E. Kikutani, T. Obina, T. Kasuga, Y. Minagawa, M. Tobiayma and L. Ma, AIP Conference Proceedings 333, p.363,1995.

[4] M. Tobiyama, E. Kikutani and Y. Minagawa, in proceedings of the 10th Symposium on Accelerator Science and Technology, Hitachinaka, Japan (1995)/ KEK Preprint 95-103.

[5] M. Tobiyama, E. Kikutani, T. Taniguchi and S. Kurokawa, in proceedings of the 10th Symposium on Accelerator Science and Technology, Hitachinaka, Japan (1995)/ KEK Preprint 95-104.

[6] J. N. Corlett, J. Johnson, G. Johnson, G. Lambertson, F. Voelker, in proceedings of the 4th European Particle Accelerator Conference, London, UK (1994).

Fast Digital Transverse Feedback System for Bunch Train Operation in CESR

J.T. Rogers, M.G. Billing, J.A. Dobbins, C.R. Dunnam, D.L. Hartill, T. Holmquist, B.D. McDaniel, T.A. Pelaia, M. Pisharody, J.P. Sikora, and C.R. Strohman
Laboratory of Nuclear Studies, Cornell University, Ithaca, NY 14853 USA

We have developed a time domain transverse feedback system with the high bandwidth needed to control transverse instabilities when the CESR e^+e^- collider is filled with trains of closely spaced bunches. This system is based on parallel digital processors and a stripline driver. It is capable of acting on arbitrary patterns of bunches having a minimum spacing of 14 ns. Several simplifying features have been introduced. A single shorted stripline kicker driven by one power amplifier is used to control both counter-rotating beams. The desired feedback phase is achieved by sampling the bunch position at a single location on two independently selectable beam revolutions. The system adapts to changes in the betatron tune, bunch pattern, or desired damping rate through the loading of new parameters into the digital processors via the CESR control system. The feedback system also functions as a fast gated bunch current monitor. Both vertical and horizontal loops are now used in CESR operation. The measured betatron damping rates with the transverse feedback system in operation are in agreement with the analytical prediction and a computer simulation developed in connection with this work.

1 Introduction

The Cornell Electron Storage Ring (CESR) is being upgraded to allow collisions of short trains of electron and positron bunches [1]. CESR is now operating with nine trains of two bunches each. We plan to operate with nine trains of as many as five bunches in the near future. A transverse coupled bunch instability [2] in CESR requires the use of active feedback. Before the present work, a time-domain horizontal feedback system based on a coaxial cable delay line and ferrite kicker magnet was used to stabilize the beam [3]. The use of bunch trains requires a redesigned transverse feedback system with higher bandwidth.

We chose to build a time domain feedback system because of the large number of coupled bunch modes that need to be damped. The minimum bunch spacing compatible with efficient injection fixes its sampling rate at 71.4 MHz. We further required that the feedback system accomodate a dynamic beam motion of ± 3 mm and arbitrary changes in tune, produce an error signal normalized to beam current, and provide a damping rate of 1000 s^{-1}.

Transverse feedback damping operates by sensing the beam position and applying a deflection to the beam proportional to its sensed position after its betatron phase has advanced by $\pi/2 + n\pi$. Because of signal processing delays the deflection cannot be applied to the beam on the same turn as the position is sensed. The error signal must be delayed by at least one turn. The 2.56 μs revolution period of CESR implies a delay-bandwidth product of approximately 500 for the error signal. It is difficult to achieve this product by purely analog means, so we chose to delay the error signal digitally, and to implement the current normalization and other signal processing functions digitally as well.

2 Signal Processing

We require four independent feedback loops, for electrons and positrons in the vertical and horizontal directions. Figure 1 is a block diagram of one digital feedback loop. The beam position signal is derived from the button electrodes used by the CESR orbit measurement system. The signals from opposite pairs of electrodes are summed in hybrid combiners. The remainder of the signal processing is done outside the CESR tunnel for access to the electronics during storage ring operation.

Each receiver channel for the beam signal contains a GaAs SPDT switch that serves as a fast gate, a diode rectifier which traps the signal as a charge on a capacitor, and an FET switch which discharges the capacitor before the next time the GaAs switch closes. Five parallel channels are are needed (a sixth is left unused) because of the limited sampling rate of a commercially available 10 bit ADC.

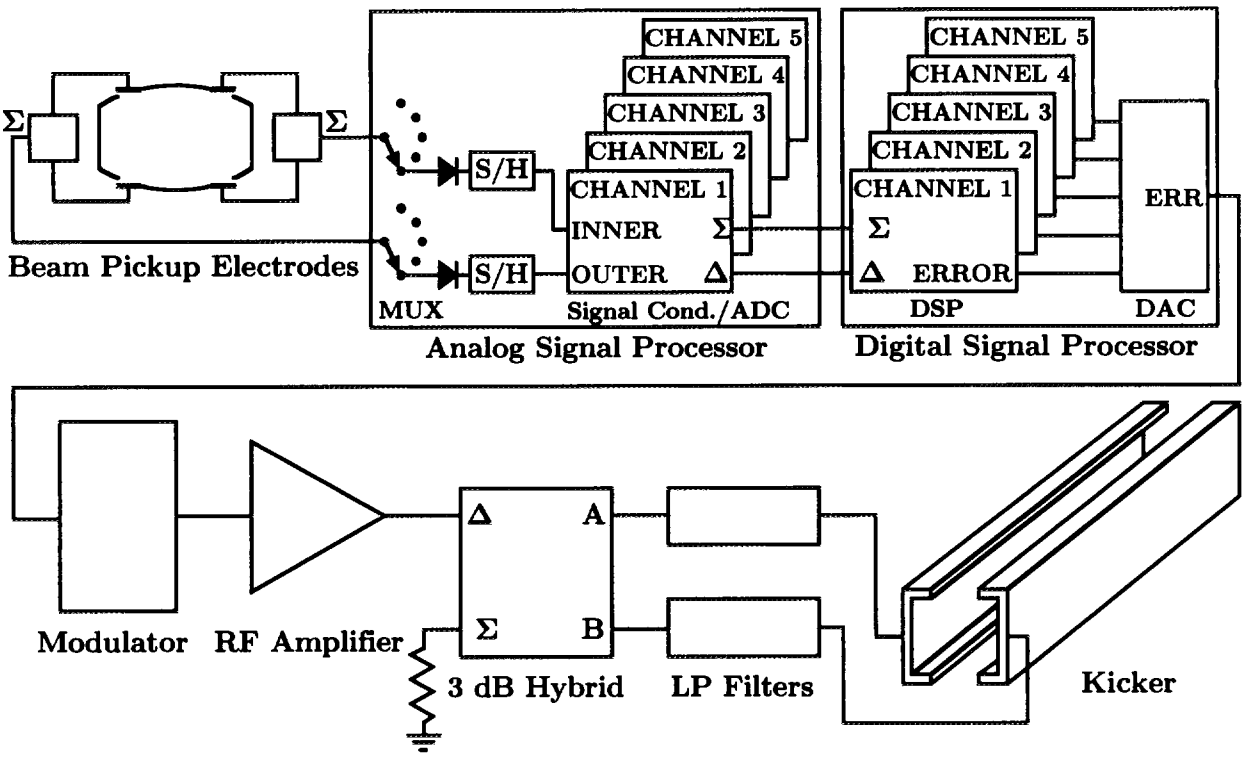

Figure 1: Block diagram of one digital feedback loop.

The remainder of the signal processing occurs in five parallel channels. The sum and difference of the receiver signals from opposite pairs of electrodes are formed by a pair of operational amplifiers. These contain information about the bunch current and the product of the bunch current and beam displacement, respectively. These sum and difference signals are then digitized by a pair of 10 bit ADCs. Figure 2 is a block diagram of one digital signal processor channel.

The position of the beam is reconstructed from the digitized sum and difference signals. The eight most significant bits of the sum word and the 10 bits of the difference word form an 18 bit address for a lookup table that stores a 12 bit beam position word. The contents of the lookup table can be tailored to produce a damping rate that is any desired function of bunch current. It can also be used to compensate the position nonlinearity of the button electrodes, although we have not made use of this feature.

We delay the position word by an integer number of turns in FIFO memory and subtract it from the current position. The resulting number is the 10 bit error word, which is insensitive to static displacements and has a partially suppressed response to low frequency motions such as synchrotron oscillations. Another FIFO memory is used to delay the error word by an integer number of turns before it is used to deflect the beam, with the number of turns chosen to provide the correct $\pi/2 + n\pi$ betatron phase advance. Both of these delays are established in software and can be easily modified to accomodate changes in the storage ring optics, tunes, or feedback hardware location. A 10 bit DAC common to all five channels converts the error word to a voltage. The digital signal processor also contains FIFO memory, 512 words deep, that stores the bunch current and charge information for diagnostic purposes.

The digital signal processor is constructed of cards which plug into a VME backplane. Four feedback loops are needed for the horizontal and vertical stabilization of the electron and positron beams. For each of these loops a motherboard is used to provide the internal timing signals and data paths. Each motherboard holds five daughterboards, each of which performs the signal processing functions described above. Each daughterboard in turn holds a board which contains the analog sum and difference circuits and the associated pair of ADCs. Figure 3 is a photograph of the feedback motherboard assembly containing the five daughterboards and ADC boards. A microprocessor in the VME crate runs the program which is used to enable or disable channels, load the lookup tables, and initialize the system so that it starts in a well-defined state. This program also calculates the current in each bunch by scaling and averaging the data from the 10 bit sum word. This current measurement is used in the CESR control room display and the

automated injection procedure. An Xbus to VME interface is used for communication between the control system and the feedback microprocessor. External signals from the CESR ultrafast timing system are used by the feedback processor to generate its own internal timing.

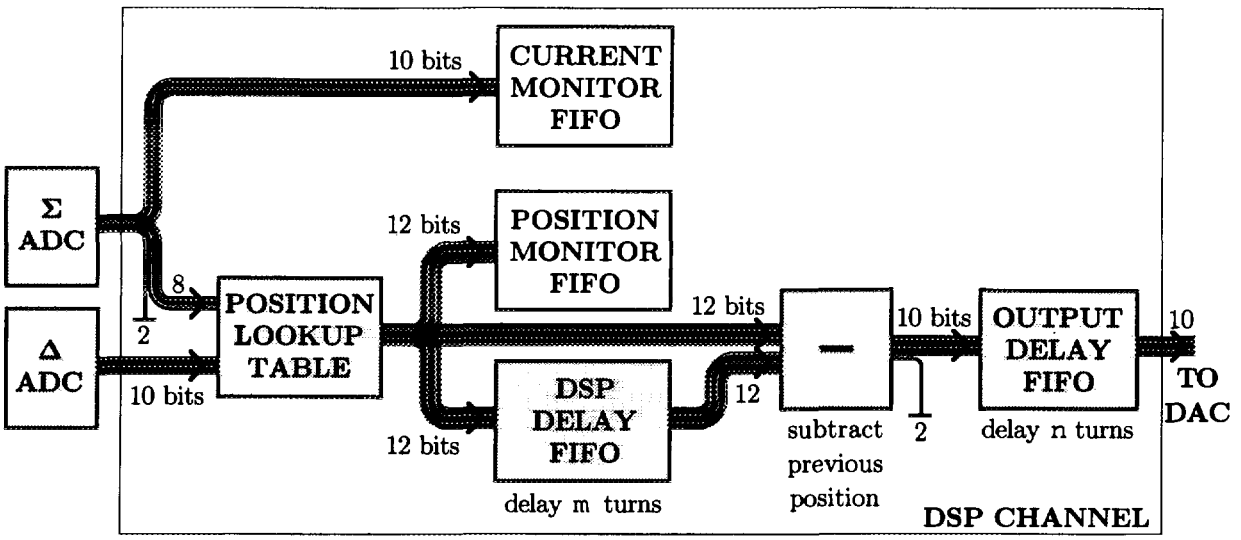

Figure 2: Block diagram of a digital signal processor channel.

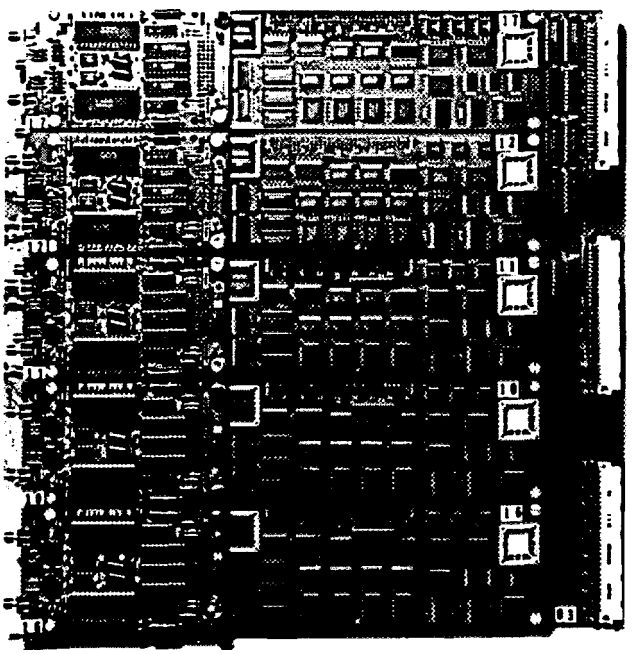

Figure 3: Feedback motherboard with five digital processor daughterboards. Each daughterboard holds an ADC board at its left.

3 RF Electronics

To drive the stripline kicker, we require a wideband RF amplifier with a flat phase response, the ability to drive a shorted line stably, and tolerance for some beam induced power returning to its output. After a survey of commercially available amplifiers, we chose a 200 W amplifier with a 0.25 to 150 MHz band[1].

[1]Model 3200L, ENI, Rochester, NY, USA.

Because the lowest transverse mode frequencies fall below this amplifier's range, we upconvert the DAC output in a modulator. A trigger supplied by the digital feedback motherboard generates a 14 ns long bipolar pulse within the modulator. This bipolar pulse is then multiplied by the DAC output in a double balanced mixer. The modulator output is used to drive the power amplifier. There is some ringing in the mixer, so an improved modulator based on a fast four quadrant multiplier has been designed. A prototype of this modulator does not display this ringing and has improved frequency response.

A 180° 3 dB hybrid[2] located at the stripline kicker splits the amplifier output into a differential drive for the kicker. The hybrid is protected from the beam induced power from the stripline by matched low-pass filters. To avoid high frequency resonances in the striplines, the filters need to be purely resistive. They are implemented as water-cooled ferrite-loaded coaxial lines.

4 Stripline Kickers

We use stripline kickers because of their high bandwidth. Each kicker contains two electrodes which act as 50 Ω transmission lines. Each electrode is shorted at one end, which spoils the directionality of the kicker, and allows the use of a single kicker driven by a single RF amplifier for both e^+ and e^- beams. The transverse deflection, voltage induced by the beam at the kicker terminals, and the beam impedance of the shorted kicker are the same as those of a kicker with striplines terminated in their own characteristic impedance [4].

The stripline electrodes are formed from OFHC copper sheet, and have a lip on each side to improve field uniformity and mechanical rigidity. Two flat copper ground electrodes are placed in the midplane between the stripline electrodes. These have the effect of conducting a substantial fraction of the beam image current, which reduces the longitudinal coupling of the kickers to the beam, and hence their beam impedance, while leaving the intended transverse coupling unaffected. The stripline and ground plane electrodes are cooled by water flowing in 5/16 in. O.D. copper tubing welded along their length.

The stripline electrodes and ground plane electrodes are assembled on one of the endplates of the kicker vacuum chamber [5]. This endplate also contains the cooling water tubes and one type HN RF vacuum feedthrough for each stripline electrode. Ceramic spacers maintain a vacuum gap between the end of the stripline electrode and an extension of the beam pipe into the kicker chamber. This gap is designed to produce a 10 pF shunt capacitance to prevent arcing in the RF feedthroughs and external RF components when CESR is operated with high bunch currents. This shunt capacitance is the limitation on the bandwidth of the kicker. The edges of the gap have been rounded to prevent high surface fields.

At the other end of the kicker the stripline and ground plane electrodes are welded into a square frame which is surrounded by beryllium copper spring finger contacts. During assembly this frame slides into a square ground contact on the other chamber end flange. The assembly process and a detail of the gap and feedthroughs are shown in Fig. 4.

The aperture between the electrodes is larger than the the wide axis of CESR beampipe so that synchrotron radiation does not intercept the electrodes. Stainless steel transitions from the square opening of the kicker chamber to the approximately elliptical beampipe are provided with water-cooled copper absorbers to intercept the synchrotron radiation at a grazing angle. The stainless steel vacuum chamber has its own ion pump.

The higher order mode loss factor was measured on the bench by launching a pulse on a thin center conductor running down the axis of an RF prototype of the kicker. The loss factor for a gaussian bunch with $\sigma_L = 2.7$ cm is $k = 0.018$ V/pC. The higher order mode power leaving the kicker RF terminals in the presence of beam is half the total power corresponding to the above value of k, suggesting that the other half of the power is dissipated in the kicker chamber or radiated down the beam pipe.

5 Operation

All four loops of the digital transverse feedback system have been in operation since November, 1994. It is routinely used to stabilize bunch trains in high energy physics operation. Table 1 summarizes the digital feedback parameters.

[2]Model H3099, Werlatone, Inc., Brewster, NY, USA.

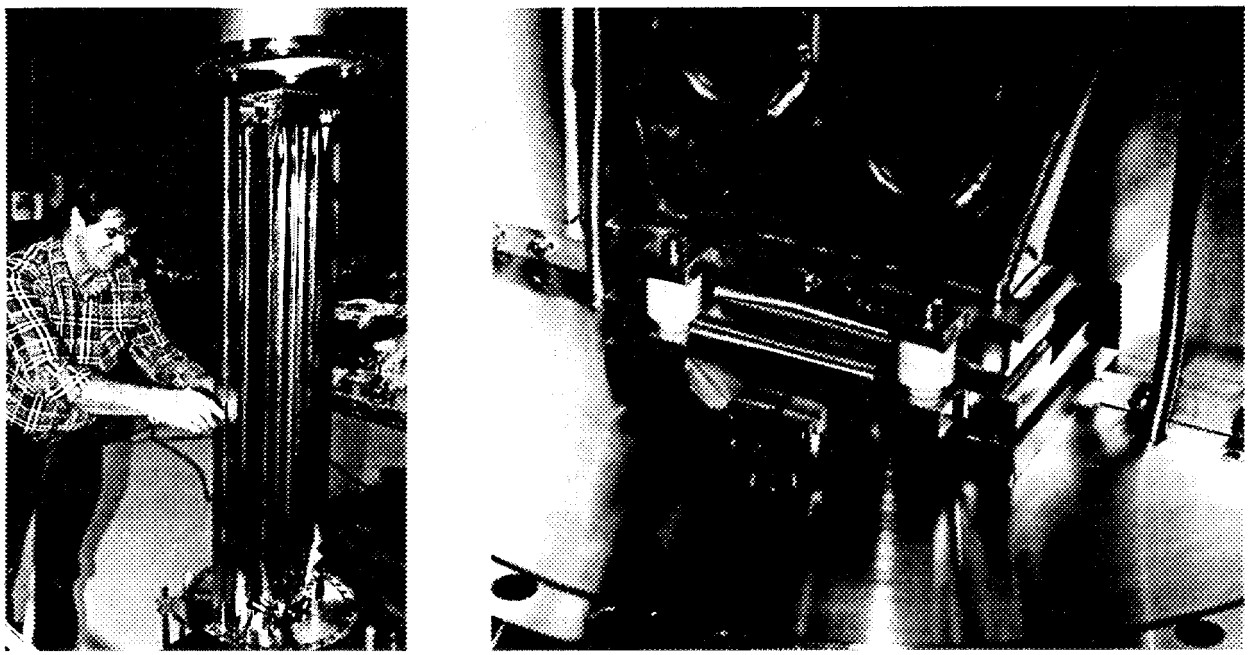

Figure 4: Stripline kicker during assembly. The photograph on the right shows the RF feedthroughs in the endplate, the alumina spacers that maintain the gap between the stripline electrode and ground, and the ground plane electrodes (visible to the far left and right).

Table 1: Feedback parameters in current operation

L	Stripline electrode length	116 cm
w	Stripline electrode width	17.5 cm
b	Stripline electrode gap	12.0 cm
Z_C	Stripline impedance	50 Ω
k	Stripline HOM loss factor	0.018 V/pC
V_{peak}	Maximum amplifier voltage	143 V
p	Beam momentum	5.3 GeV/c
β_x,β_y	Beta function at kicker	25.6, 18.2 m
x_{max},y_{max}	Dynamic range referenced to pickup	5, 5 mm
α_x,α_y	Measured damping rate	2.4, 0.58 ms^{-1}

The dominant horizontal instability in CESR, which is related to the operation of the distributed ion pumps[2], has a maximum growth rate at 2.5 mA/bunch when CESR is filled with nine trains of two bunches each. This is approximately one fourth of the typical operating current. For this reason the current normalization is essential to the succesful use of this feedback system. The lookup tables are programmed to make the damping rate proportional to current up to 2 mA/bunch and constant above that current. By damping the vertical motion of the beam we have been able to lower the vertical chromaticity, thus eliminating an $m = -1$ vertical head-tail instability. The digital phase adjustment has also proven successful. When it is properly selected, the tune shift produced by the feedback system is small to be measured (less than 50 Hz). In open loop tests the shorted stripline kickers produced the calculated deflection for both e^+ and e^- beams, and the measured damping rate agrees with the calculated rate. Figure 5 shows a control room display of the amplitude of the $f_0 - f_h$ (182 kHz) horizontal coupled bunch mode as a function of time. The horizontal feedback has been momentarily gated off, then on again, restoring rapid damping of the instability.

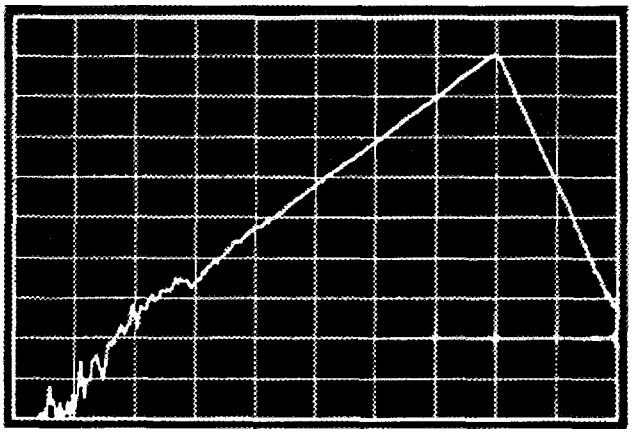

Figure 5: Amplitude of horizontal betatron motion vs. time. The feedback has been gated off during the first 8 divisions, then on again. The vertical scale is 5 dB/div. and the horizontal scale is 2.56 ms/div.

Acknowledgments

The authors wish to thank M. Tigner, N. Kazarinov, D. Rubin, and the members of the CESR operations group for invaluable discussions. We gratefully acknowledge the efforts of the LNS technicians, machinists, and operators. Special thanks are due R. Meller for many useful suggestions and for providing the fast timing system. This work has been supported by the National Science Foundation.

References

[1] D. Rice, *Proc. 1993 Particle Accelerator Conf.*, 1978 (1993).

[2] L.E. Sakazaki, *et al., IEEE Trans. Nucl. Sci.* **32** 2353 (1985).

[3] R. Littauer, Cornell LNS note CON 87-19 (1987).

[4] J.T. Rogers, Cornell LNS note CBN 95-4 (1995).

[5] B. McDaniel, Cornell LNS note CBN 93-2 (1993).

A WAVEGUIDE OVERLOADED CAVITY AS LONGITUDINAL KICKER FOR THE DAΦNE BUNCH-BY-BUNCH FEEDBACK SYSTEM

A. Gallo, R. Boni, A. Ghigo, F. Marcellini, M. Serio, M. Zobov

INFN-Laboratori Nazionali di Frascati
P.O. Box 13, I-00044 Frascati (Roma), Italy

1. Introduction

The multibunch operation of DAΦNE, and in general of any "factory" machine, calls for a very efficient feedback system to damp the coupled-bunch longitudinal instabilities. A collaboration program among SLAC, LBL and LNF labs on this subject[1] led to the development of a time domain, digital system based on digital signal processors (DSP) that has been already successfully tested at ALS.

The feedback chain ends with the longitudinal kicker, an electromagnetic structure capable of transfering the proper energy correction to each bunch.

The kicker design has to be optimised mainly with respect to the following parameters: the shunt impedance (i.e. the ratio between the square of the kick voltage and the peak forward power at input), the bandwidth ($f_{RF}/2$ required at least to damp any coupled-bunch mode) and the content of High Order Modes that can further excite coupled-bunch instabilities.

A stripline based design has been already proposed and adopted for ALS[2]; it consists of a pair of coaxial (with respect to the vacuum vessel) quarter-wavelength electrodes series connected through a half-wavelength delay line. Even though this solution can meet our impedance and bandwidth specifications, we have learned from experience on a prototype that proper tuning and matching is not simple and requires several iterations; moreover such kind of structures shows a worrisome content of undamped HOMs.

Therefore, we have explored the possibility of using an "overdamped" RF cavity as longitudinal kicker, in the same fashion as the DAΦNE main ring cavity[3] except that in this case the waveguide coupling has been enhanced and extended to the fundamental mode to enlarge its bandwidth. The strong waveguide coupling leads also to a remarkable damping of all the cavity HOMs.

Since the modeling of this structure is simpler than that of a stripline based kicker, the field solutions are easier to calculate, so that in this case we can rely on a design based on 3D simulations performed with the Hewlett-Packard code HFSS[4].

The result of the design simulation together with some encouraging preliminary measurement performed on a prototype built at LNF are presented and discussed in this paper.

2. Design of the overdamped cavity

A cut view of the final geometry of the overdamped cavity proposed as longitudinal kicker is shown in Fig. 1. The very large bandwidth required has been obtained by strongly loading a pill-box cavity with special ridged waveguides followed by broadband transitions to 7/8" standard coaxial. Ceramic feedthroughs allow in-air connections to the driving amplifiers (input ports) and dummy loads (output ports). The waveguides are placed on both cavity sides symmetrically with respect to the field distribution of the operating mode. Due to this symmetry it turns out that, if the ports on one side are driven in phase with balanced levels and the ports on the opposite side are connected to dummy loads, the system in principle is perfectly matched at its central frequency, i.e. no power is reflected at that frequency by the input ports.

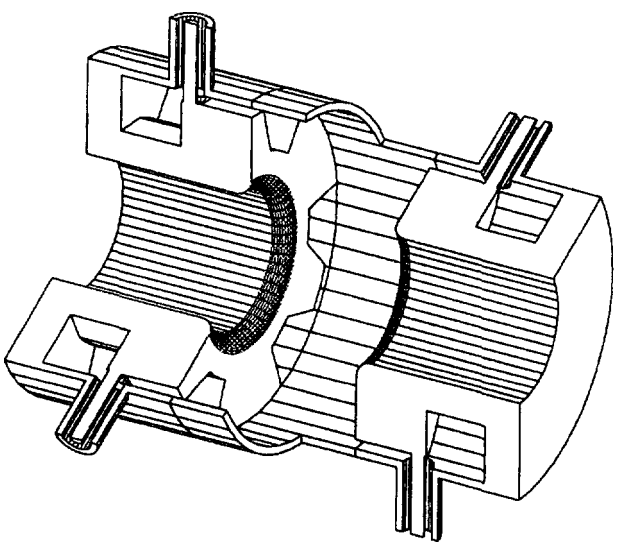

Fig. 1: Kicker cavity cutview.

Moreover the cavity, being broadband, does not need to be tuned nor cooled, since almost all the power is dissipated in the external loads.

The idea of using an RF cavity as longitudinal kicker is based on some simple considerations. When all the RF buckets are filled, all possible coupled bunch modes are present in a frequency span between nf_{RF} and $(n+1/2)f_{RF}$, with n any integer. Therefore, without an *a-priori* knowledge of the position of the most dangerous HOMs, the minimum bandwidth requirement for the longitudinal kicker is $f_{BW}=f_{RF}/2$, as long as the response is centered onto $f_c=(n+1/4)f_{RF}$ [3]. A center frequency $f_c = 3.25\ f_{RF} \approx 1197$ MHz has been chosen so that the resulting loaded quality factor of the cavity has to be set to about $Q_L = f_c / f_{BW} \approx 6.5$. Therefore, if the damping waveguides are symmetrically placed with respect to the fundamental mode field distribution and half of them are used as input ports while the remaining as matched terminations, the external Q values are given by:

$$Q_{ext\,inp} \approx Q_{ext\,out} \approx 2Q_L \approx 13 \qquad (1)$$

The R/Q factor of a pill-box cavity resonating at around 1.2 GHz with stay-clear apertures of 88 mm is limited to about 60 Ω. The kicker shunt impedance R_s has a peak value given by:

$$R_s = V_k^2/2P_{in} \approx (R/Q)\, Q_{ext\,out} \approx 780\ \Omega \qquad (2)$$

This means that the attainable shunt impedance is about twice the value of a two-electrodes stripline module[2], while no HOMs are likely to remain undamped in this structure.

The cavity design has been based on the pill-box cavity profile sketched in Fig. 2. The pill-box modes up to the beam pipe cutoff computed by the 2D code URMEL [5] are shown in Tab. 1. The Q values reported refer to copper cavity walls. Due to the large size of the stay-clear apertures, there was very little margin for the optimisation of the R/Q factor, so that we accepted to base the design on a simple pill-box shape instead of a more complex nosecone geometry.

Tab. 1: Summary of the pill-box modes as given by the code URMEL.

Mode	0-EM-1	0-MM-1	0-EM-2	1-EM-1	1-MM-1
f [MHz]	1227.06	2421.81	2663.60	1729.00	1750.29
Q	22318	20533	41260	23645	25101
R/Q [Ω]	54.696	5.129	0.132	17.979	2.888

As a second step, the shape of the loading waveguides has been defined. The waveguide cross-section and the pill-box side view are shown in Fig. 3. It is a single ridged like waveguide with 6 mm gap to lower the TE10 cutoff frequency down to 690 MHz. As described in the following, a low cutoff frequency makes the conversion of the TE10 waveguide mode to the coaxial TEM mode in a wide frequency range easier.

The cross-section area of each waveguide covers about 11% of the available surface of the pill-box side and up to 4 waveguides can be applied on each cavity side. Actually, only 3 waveguides per side are enough to get a Q_L value lower than 6.5 and a bandwidth larger than $f_{RF}/2$, as shown in the following.

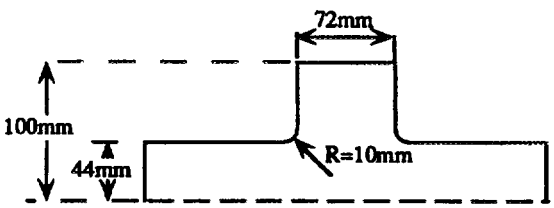

Fig. 2: Pill-box profile.

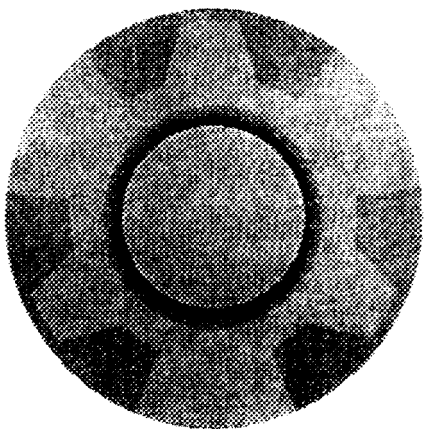

Fig. 3: Waveguides cross-section on cavity wall.

Once the shape of the damping waveguides had been defined, we designed the waveguide-to-coaxial transition with the same criteria adopted for the main ring cavity [6].

A sketch of the transition cut-view is shown in Fig. 4. The waveguide ridge is truncated with a round section where the coaxial inner conductor is connected; a short-circuited waveguide section behind the coaxial insertion (the so called "back cavity") helps in centering the transition frequency response.

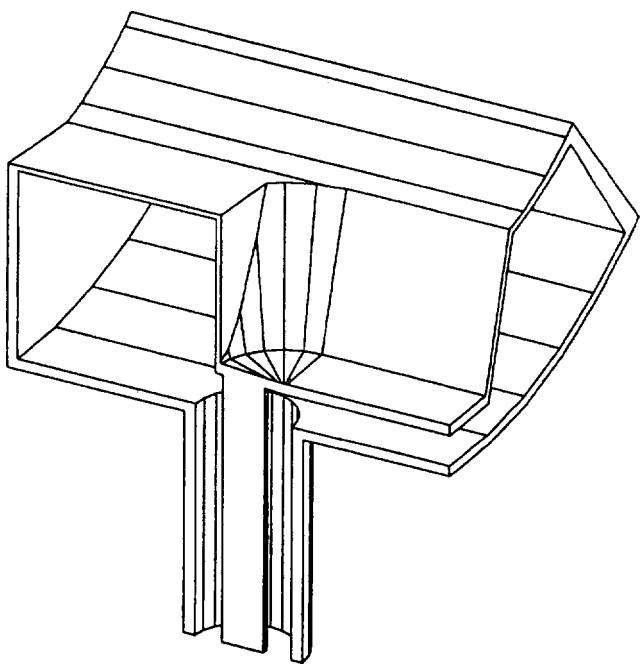

Fig. 4: Broadband transition sketch (section view).

The coaxial size is the standard 50 Ω 7/8" which can withstand more than 1 kW power flow. Moreover, we can use for this coaxial standard the broadband ceramic feedthrough already developed for the transitions of the main ring cavity [7].

The reflection frequency response of the transition computed with HFSS is shown in Fig. 5. The S_{11} value is lower than 0.25 along the entire frequency band up to the beam pipe cut-off; the low cut-off frequency of the TE10 mode of the waveguide (≈ 690 MHz) is crucial to get a good wave transmission in the low frequency band.

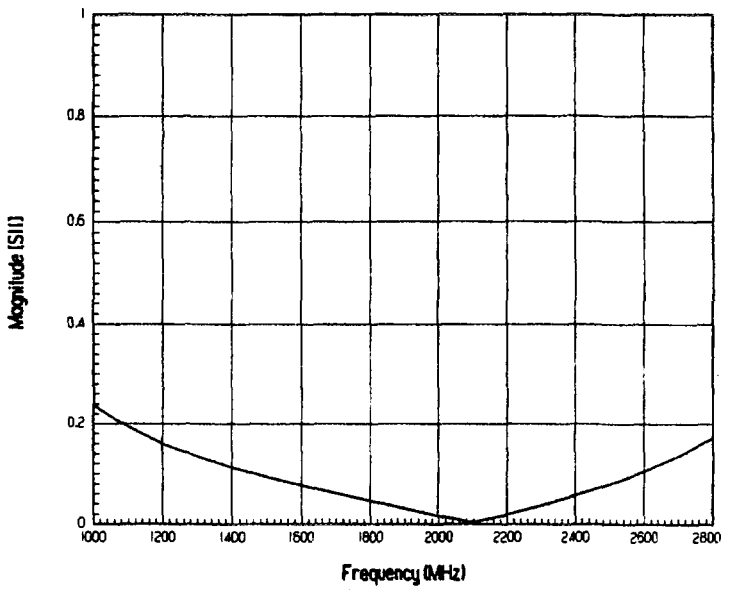

Fig. 5: Transition frequency response (HFSS simulation).

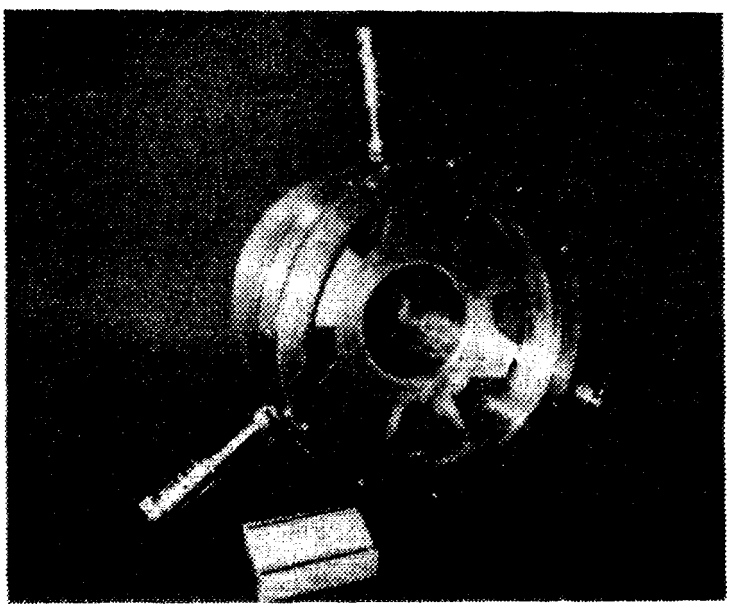

Fig. 6: Kicker cavity prototype.

The kicker geometry shown in Fig. 1 is tha assembly of the pill-box cavity with three equally spaced broadband transitions of the kind sketched in Fig. 4. per side.

3. The overdamped cavity prototype

A full scale aluminium prototype of the kicker cavity has been manufactured at LNF in order to get an experimental proof of the computer simulation results. A picture of the inside view half of the prototype structure is shown in Fig. 6. The prototype is only suitable for low-power, in-air measurements.

4. Computer simulations and experimental results

4.1 Frequency response

The transmission coefficient S_{21} from the three input ports to the three output ports for the cavity fundamental mode is shown in Fig. 7. The solid line represents the computed response and has a peak at about 1215 MHz and a bandwidth as large as 220 MHz.

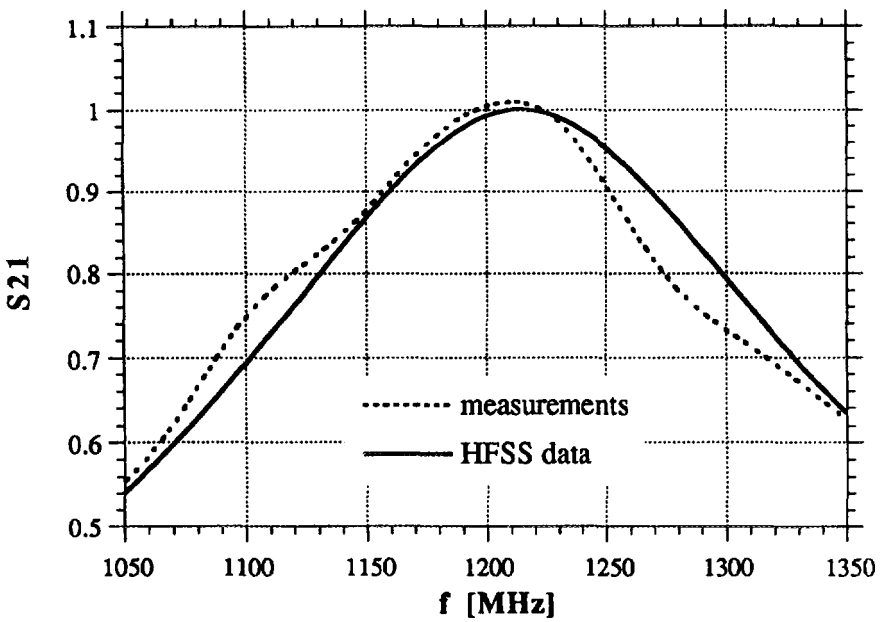

Fig. 7: Kicker frequency response.

The measured transmission coefficient is represented by the dashed line showing approximately the same bandwidth around a center frequency of about 1209 MHz. The shape of the measured frequency response appears to be a little distorted. This is probably due to the mechanical imperfections of the prototype since the response has been found to be very sensitive to any mechanical or electrical difference among the six input/output channels.

The computed and measured frequency response of the two dipole modes 1EM1 and 1MM1 is shown in Fig. 8. The 1EM1 mode is strongly damped ($Q_L \approx$ 16 in both simulations and measurements). The resulting peak transverse impedance $R_\perp$(1EM1) is about 300 Ω while the "actual" transverse impedance, that takes into account the beam spectrum roll-off and the form factor corresponding to a 3 cm bunch length, is reduced to about 125 Ω.

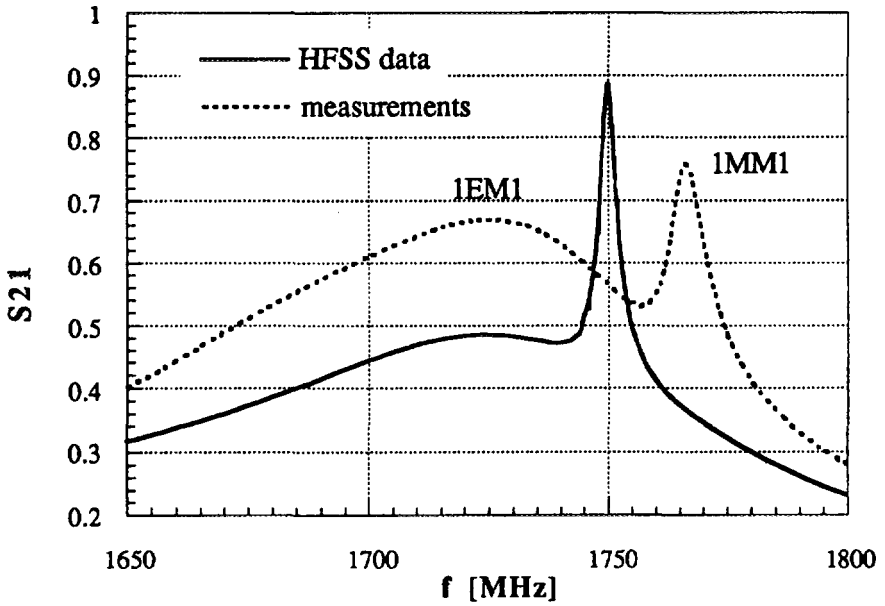

Fig. 8: Dipolar modes frequency response.

The 1MM1 dipole is less damped than the 1EM1. The simulations give a Q_L value of about 500 corresponding to 1400 Ω and 550 Ω of peak and "actual" impedances respectively. In this case the measured Q_L seems to be a factor 3 lower than the computed value and the impedance values should scale accordingly by the same factor. However, the contribution of this mode to the machine transverse instability (rise time $\tau_T \geq 4.5$ msec in full coupling and 30 bunches) is at most comparable to the contribution of the first dipole modes of the DAΦNE main ring cavity, that are considered not dangerous for the transverse dynamics [8].

The 0MM1 monopole mode, mentioned in Tab. 1, looks extremely damped in the HFSS simulations ($Q_L \approx$ 10) while it is not clearly detectable and measurable from prototype port-to-port transmission measurements.

The investigation of the 0EM2 monopole mode reported in Tab. 2 has been considered meaningless since its resonant frequency is too close to the beam pipe cut-off.

4.2 Shunt impedance calculation and measurements

The most important figure of merit of the kicker is the shunt impedance R_s defined as:

$$R_s = \frac{|V_g|^2}{2\,P_{fw}} \tag{3}$$

where V_g is the kicker gap voltage and P_{fw} is the forward power at kicker input. The only straightforward way to compute the shunt impedance is to post-process the field solution given by the 3D simulator. In fact, the gap voltage V_g may be obtained by integrating the longitudinal E-field on the beam axis including in the integration the transit time factor.

What one can get from the HFSS field solution is the value of the fields at the solution frequency and at the desired phase. The longitudinal E-field on the beam axis computed by HFSS at 1.2 GHz and 1W forward input power is shown in Fig. 9 at 0 and $\pi/2$ phases.

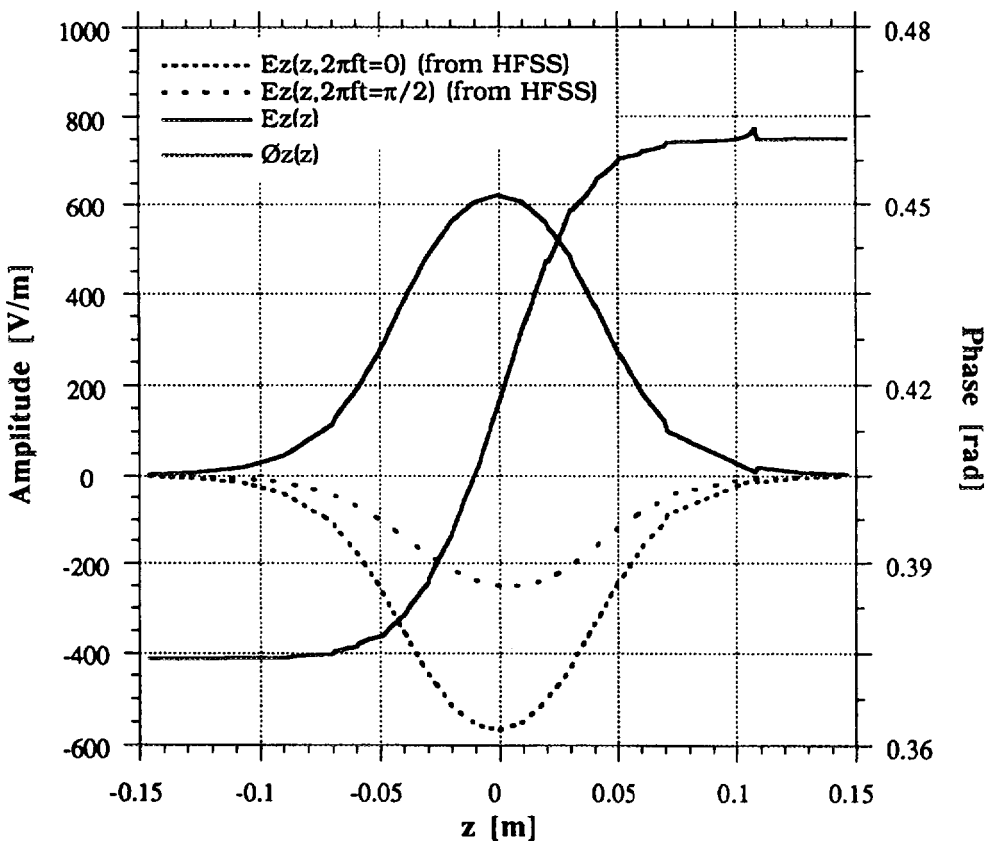

Fig. 9: Longitudinal E-field on beam axis.

In order to compute the shunt impedance R_s it is convenient to represent the longitudinal E-field as a phasor, namely:

$$E_z(z,t) = \mathrm{Re}\left\{E_z(z)\, e^{j[\omega t - \phi_z(z)]}\right\} \tag{4}$$

where the two functions $E_z(z)$ and $\phi_z(z)$ can be obtained from the field solutions according to:

$$\begin{aligned} E_z(z) &= \sqrt{E_z^2(z,\ \omega t=0) + E_z^2(z,\ \omega t=\pi/2)} \\ \phi_z(z) &= \mathrm{Atan}\left[\frac{E_z(z,\ \omega t=\pi/2)}{E_z(z,\ \omega t=0)}\right] \end{aligned} \tag{5}$$

Once the functions $E_z(z)$ and $\phi_z(z)$ have been computed at a certain frequency, the gap voltage as a complex phasor is given by:

$$V_g(\omega) = \int_{-L/2}^{L/2} E_z(z)\, e^{j[\omega z/c - \phi_z(z)]}\, dz \tag{6}$$

where L is the cavity length and the term $\omega z/c$ in the exponential accounts for the transit time effect.

The amplitude and phase of the phasor $V_g(\omega)$ is plotted in Fig. 10 for 7 different frequencies, while the shunt impedance $R_s(\omega)$, given by eq. (3), is shown in Fig. 11. The impedance peak value is about 750 Ω, in good agreement with the rough estimate (2).

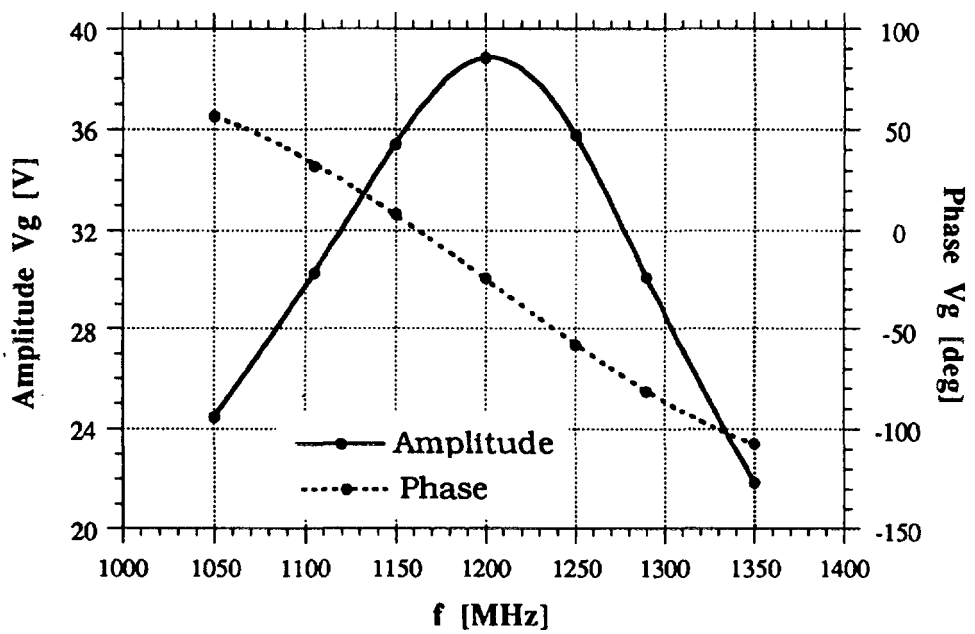

Fig. 10: Gap voltage (P_{in}=1W).

It is interesting to remark that the impedance peak value occurs at about 1.2 GHz, i.e. 15 MHz below the transmission peak response, and that the high frequency portion of the plot decreases more rapidly than the low frequency one. Both effects are due to the fact that, since we are considering a wide frequency band, the transit time factor is no longer a constant but decreases linearly with frequency.

The shunt impedance of the cavity prototype has been measured with the wire method. A 3 mm diameter copper wire has been inserted in the cavity along the beam axis and connected to a 50 Ω line through a resistive matching network. The coaxial wire-beam tube system is a Z_0'=203 Ω transmission line and the matching network task is to adapt it to the 50 Ω input/output ports. The longitudinal beam impedance Z(ω), defined as the complex ratio between the cavity gap voltage and the beam current, can be calculated [9] with some approximation, according to:

$$Z(\omega) \approx 2\, Z_0' \left(\frac{1}{S_{21}} - 1 \right) \tag{7}$$

where S_{21} is the complex transmission coefficient between the 2 wire ports measured by a Network Analyzer accurately calibrated to take into account the cable and matching network attenuations, as well as the linear phase advance due to the electrical length of the device.

The quality of the matching is crucial to eliminate or reduce spurious resonances in the frequency response arising from the TEM wave reflections at the step transition between the 50 Ω and 203 Ω coaxial lines.

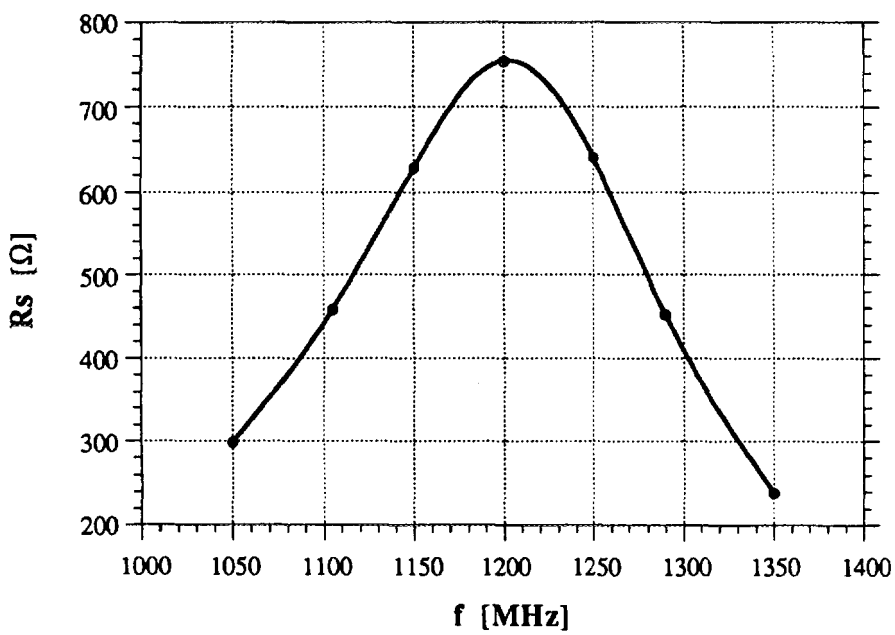

Fig. 11: Kicker shunt impedance.

The reflection coefficient measured at the step transition with and without the resistive matching network is shown in Fig. 12 (solid and dashed line respectively). The dashed line shows a return loss value of about -4 dB all over the measurement bandwidth, corresponding to a 50 Ω line terminated with a 200 Ω resistor. The solid line, i.e. the matched case, shows a substantially lower return loss value increasing with frequency and limited to about -17 dB in the measurement bandwidth (1 + 1.5 GHz).

The amplitude and phase of the transmission coefficient S_{21} measured with the already mentioned calibration factors is shown in Fig. 13. The amplitude minimum, corresponding to the peak power absorption of the device and therefore to the impedance peak value, is located at about 1325 MHz. This means that the wire perturbs the field distribution and shifts the resonant frequency by about +125 MHz.

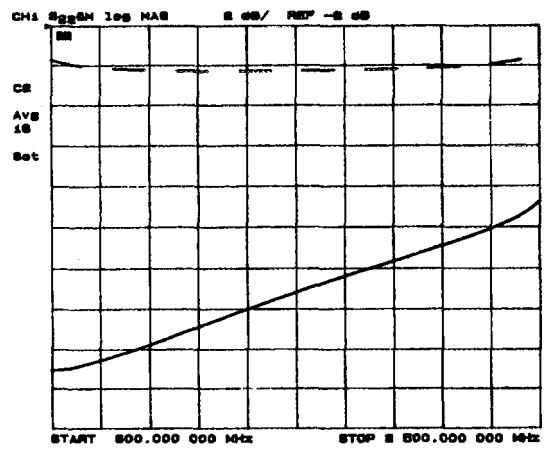

Fig. 12: Matching network effect on step transition return loss.

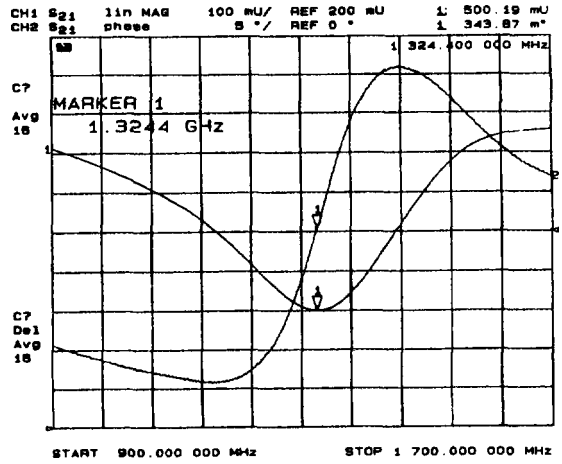

Fig. 13: Wire measurement transmission response.

By applying the simple formula (7) on the data taken with the measurement of Fig. 13 the longitudinal beam impedance shown in Fig. 14 has been obtained. Both real and imaginary parts of the impedance can be very well fitted with by an R-L-C lumped resonator.

The shunt impedance, as defined in (3), turns out to be twice the value of the real part of the beam impedance. In Fig. 15 the dashed line represents the shunt impedance obtained from the wire measurements, while the solid line is a HFSS simulation of the wire measurement. The measurement and simulation curves are in rather good agreement and show a similar frequency shift value (+125 and +160 MHz respectively) and a peak value of 800 Ω and 720 Ω respectively that confirm the data of the Fig. 11 plot. However, by reducing the wire diameter in the simulations, a lower shift value and a higher impedance have been obtained, in better agreement with the experimental results.

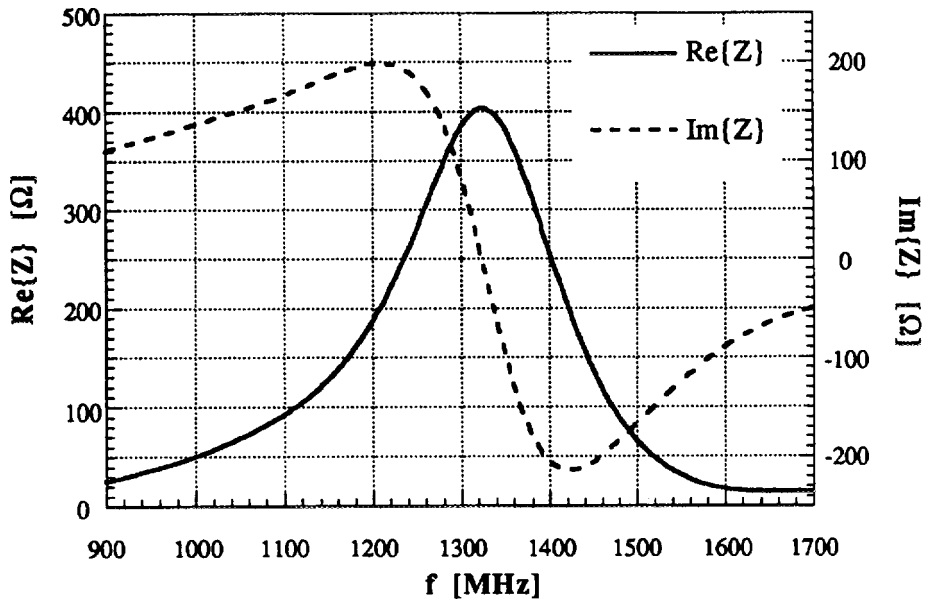

Fig. 14: Beam coupling impedance measured on the kicker prototype.

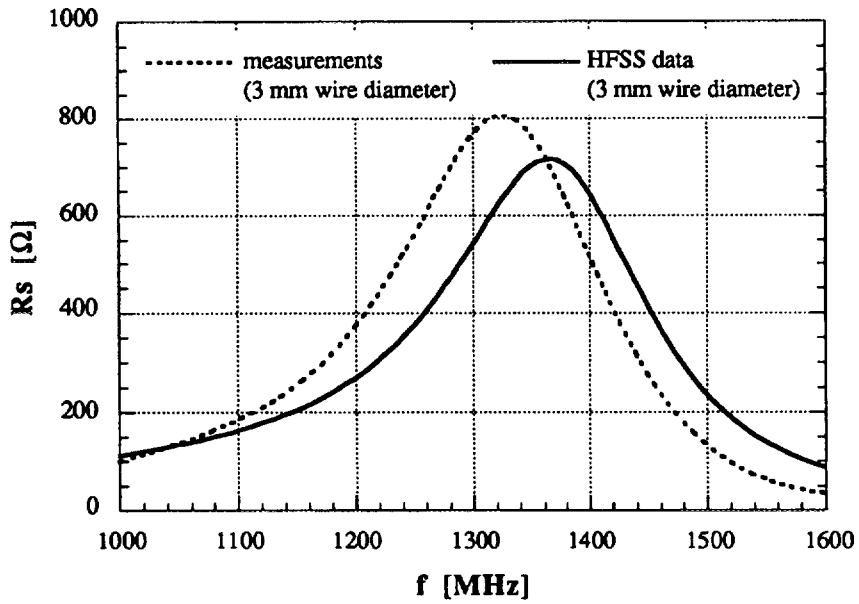

Fig. 15: Kicker shunt impedance obtained with the wire method.

The contribution of the basic pill box of Fig. 2 to the machine broadband impedance has been estimated by means of the ABCI code [10]. The longitudinal and transverse loss factors k_l and k_T of the device for a 3 cm bunch length are ≈0.12 V/pC and ≈3.5 V/pC m respectively. With respect to a two-electrode stripline module, the k_l value is comparable while the k_T value is about 50% lower. It must be pointed out, however, that such a module can only provide half of the kicker cavity shunt impedance.

5. Power considerations

According to simulations, DAΦNE operation will require a maximum longitudinal kick voltage of ≈400 V with 30 bunches and 1600 V with 120 bunches in order to damp an initial offset of 100 psec, a prudent estimate of the maximum injection error of the last bunch. A 200 W input power with a single kicker cavity per ring will be enough for the 30 bunch operation while 2 kickers per ring fed with 600 W each will be eventually required for the 120 bunch operation [11].

On the other hand, the beam current interacts with the device beam impedance, and the power released by the beam can be much higher than the incoming power from the feedback system. The plot of the kicker beam impedance real part and various configurations of the beam current spectrum are shown in Fig. 16. The total power P_b released by the beam for a certain current spectrum configuration is simply by:

$$P_b = \sum_n \frac{1}{2} \mathrm{Re}\,[Z(\omega_n)]\, I_n^2 \qquad (8)$$

so that the resulting power rates are reported in Tab. 2. The beam spectra shown in Fig. 16 include the effect of the roll-off due to the 3 cm DAΦNE bunch length.

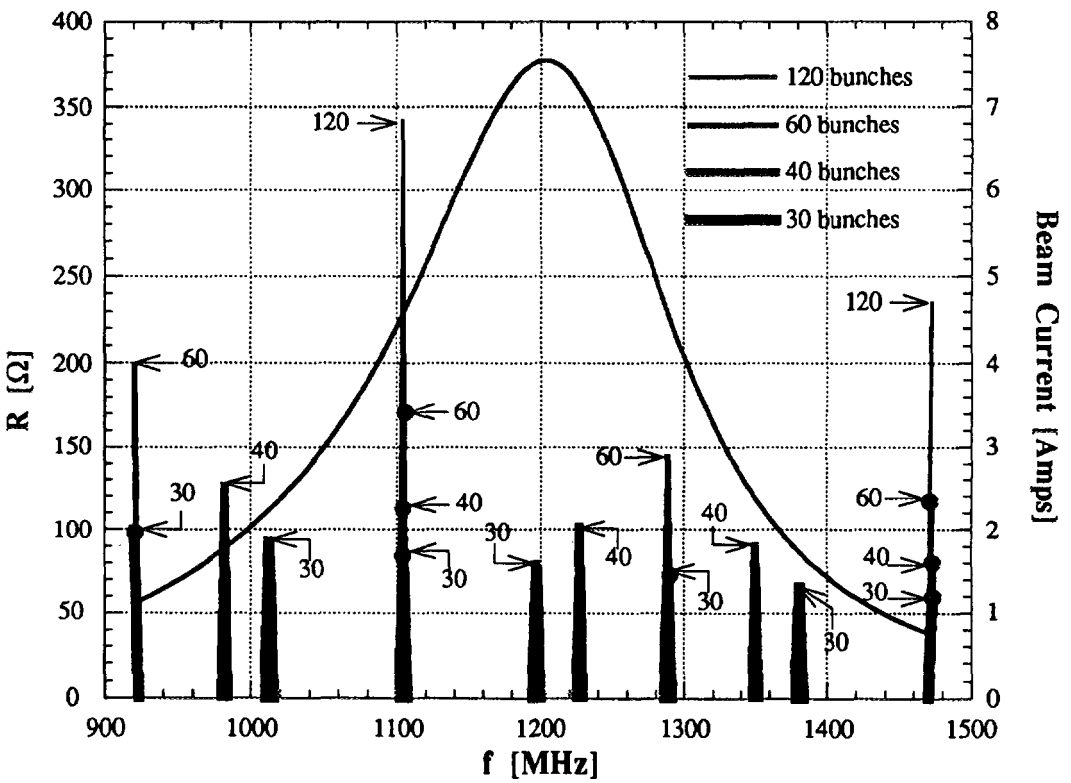

Fig. 16: Beam spectrum and cavity coupling impedance.

Tab. 2: Power released to the cavity by various DAΦNE beam configurations.

Number of regularly spaced bunches	30	40	60	120
Total Power [W]	2500	3200	4800	9600
Power per guide [W]	420	530	800	1600

Being mainly a standing wave structure, the cavity kicker is not a directional device and upstream and downstream ports are almost equally coupled to the beam. Therefore, unlike the case of the stripline based kicker, in the cavity the beam power reaches indifferently the input and output ports, and the longitudinal feedback power amplifiers must be protected with ferrite circulators against the backward power which can be one order of magnitude higher than the forward level. A preliminary market investigation has proven that a custom ferrite circulator covering a band wider than the 1÷1.4 GHz range at a power rate of 1.5 kW with an isolation higher than 18 dB can be certainly developed [12].

Conclusions

A cavity kicker for the DAΦNE bunch-by-bunch longitudinal feedback system based on a pill-box loaded by six waveguides has been designed and a full-scale aluminium prototype has been fabricated at LNF. Both simulations and measurements have shown a peak shunt impedance of about 750 Ω and a bandwidth of about 220 MHz. The large shunt impedance allows to economise on the costly feedback power. Moreover the damping waveguides drastically reduce the device HOM longitudinal and transverse impedances.

The feedback signal can enter the cavity from the coaxial ports attached to the waveguides so that no special input coupler is required. Due to the large bandwidth and low internal dissipation, neither tuning nor cooling is necessary.

The mechanical specifications and drawings of the vacuum compatible cavity have been finalised and an order for two pieces (one per ring) will be placed soon.

One cavity per ring will be sufficient to operate the machine up to 30 bunches while a second device per ring together with a feedback power improvement will be necessary to reach the ultimate current.

Acknowledgments

The authors wish to thank M. Migliorati, L. Palumbo and B. Spataro for the continuous opinion exchange on the subject.

Thanks also to D. Boussard and all the DAΦNE machine reviewers who have revised a preliminary version of this work.

Thanks to S. Quaglia for his help in the computer acquisition of the RF measurements.

The authors are especially in debt with T. Tranquilli who worked hard to mechanically design and fabricate a very good kicker prototype in a very short time. Thanks also to P. Baldini and M. Scampati who helped him in many ways.

References

[1] J. D. Fox et al., "Operation and Performance of a Longitudinal Damping System Using Parallel Digital Signal Processing", in Proceedings of the 4th EPAC, London, 1994, p. 1619.

[2] J. N. Corlett et al., "Longitudinal and Transverse Feedback Kickers for the ALS", in Proceedings of the 4th EPAC, London, 1994, p. 1625.

[3] A. Gallo et al., "Simulations of the Bunch-by-Bunch Feedback Operation with a Broadband RF Cavity as Longitudinal Kicker", DAΦNE Technical Note G-31, Frascati, April 29, 1995.

[4] Hewlett-Packard Co, "HFSS, The High Frequency Structure Simulator HP85180A™".

[5] T. Weiland, NIM 216 (1983), pp. 329-348.

[6] R. Boni et al., "A Broadband Waveguide to Coaxial Transition for High Order Mode Dam-ping in Particle Accelerator RF Cavities", Particle Accelerator, Vol. 45, 4 (1994), p. 195.

[7] R. Boni et al., "Update of the Broadband Waveguide to 50 Ω Coaxial Transition for Parasitic Mode Damping in the DAΦNE RF Cavities", in Proceedings of the 4th EPAC, London, 1994, p. 2004.

[8] M. Migliorati, private communication.

[9] H. Hahn and F. Pedersen, "On Coaxial Wire Measurements of the Longitudinal Coupling Impedance", BNL-50870, UC-28, April 1978.

[10] Y.H. Chin, "User's Guide for ABCI Version 8.8 (Azimuthal Beam Cavity Interaction)", LBL-35258, UC-414, February 1994.

[11] G. Vignola and the DAΦNE Project Team, "DAΦNE Status and Plans", in Proceedings of Particle Accelerator Conference, Dallas TX, May 1-5, 1995, in preparation.

[12] Advanced Ferrite Technology Co, Spinnerei 44, 71522 Backnang (FRG), private communication.

SUMMARY SESSION

Summary of the Impedance Working Group

Bruno Zotter *

CERN, Geneva 23, Switzerland

Abstract

Impedance issues are important for B-factories because of the very high beam currents required to achieve the desired luminosities. A number of critical objects which are unavoidable inside the vacuum chamber of such machines require not only careful design, but sometimes special RF shielding to reduce the induced voltages and energy loss to an acceptable level. Bellows shielding, holes in screens for distributed pump chambers, beam position monitors, interaction region masks and absorbers for superconducting cavities were discussed in some detail, as well as some analytic impedance models. Feedback kickers were discussed in a joint session with the RF working group. Threshold currents were the subject of the instability working group and are not reported here.

1 Introduction

The workshop on "Collective Effects in B-factory Accelerators" (CEIBA 95) was organized at the Tsukuba Conference Center, Japan, from 12 to 17 June 1995 by S.Kurokawa and Y.Chin from KEK. Three working groups were formed on Impedances, Instabilities, and RF (in the order of presentation of the summaries on the last day). However, the first 2 mornings were reserved for plenary sessions, with reports on impedance and instability issues for the two B-factories projects KEK-B (Japan) and PEP-II (USA), the Phi-factory DAPHNE in Italy, as well as a number of related machines such as SPRING-8 (Japan), SOLEIL (France), or LHC and LEP (CERN), and a joint session of all working groups was held to discuss two recently uncovered instability mechanisms: the "transient-ion instability" which might become important for dense electron bunches such as required for B-factories, and the "photo-electron instability" which could similarly limit dense positron bunches.

Five half-day sessions were reserved for discussions in the working groups, and well over 20 individual papers were presented in the one on impedances. We treated one topic per session: pumping slots, bellows shielding, BPMs, IR chambers, and others (absorbers, impedance models, feedback kickers). Between 15 and 25 participants were usually present for these discussions on impedance issues, out of a total of 70 - 80 workshop participants.

2 Pumping Slots

The KEK-B vacuum chamber is separated from the distributed ion pump (DIP) chamber by a screen with rectangular slots (4 by 100 mm). K. Kanazawa (KEK) presented

* Talk given at the workshop on collective effects in B-factories CEIBA 95, Tsukuba, Japan, July 1995

3 possible solutions to reduce the EM fields penetration through the slots: (1) two equally thick walls with slots perpendicular to each other, (2) a slotted wall of double thickness and a thin plate with square holes, and (3) a slotted wall and a wall with square holes of equal thickness. In the discussion it was pointed out that a slotted wall of simple thickness, with the thin plate with square holes, should be quite sufficient to shield against both TM and TE fields.

For the PEP-II DIP screen, "hidden slots" were described by Cho Ng (SLAC). Long grooves (4 m long, 4mm wide) penetrate the screen halfway. The grooves are parallel to the beam, but off-axis in order to avoid a direct path for ions - or dust - from the pumps. A large number of small circular holes (3 mm diameter) are situated on the rear side of the grooves. The narrow groove presents a low impedance to the beam and damps TM modes, while the holes damp also TE modes which might be excited by mode conversion or turbulent bunches. The design has been modelled with MAFIA (K.Ko), and trapped modes have been identified and analyzed. This design was judged quite satisfactory, but somewhat of an overkill considering the small contribution of the DIP screen to the total impedance budget.

S. Kurennoy (U.Maryland) presented an analysis of impedances and loss factors of slots and holes. The results can be expressed in compact form using the electric and magnetic polarizabilities. Long slots, parallel to the beam axis, have in general lower impedances than round holes for equal areas, in particular if the corners are rounded. The cutoff frequency for TM modes is given by the slot width. However, if TE modes are excited, they can penetrate slots down to lower frequencies with wavelengths given by the slot length. The question of tolerances for relative tilt between beam and slot was raised and should be investigated.

The impedance of arrays of holes was discussed by G.Stupakov (SLAC), since a very large number of the rather small holes are needed for vacuum reasons. Many "trapped modes" can appear just below the cutoff frequencies of each waveguide mode in the beam pipe. In order to avoid quadratic power addition of them, it was recommended to use "hidden holes" as in PEP-II, or to cover the holes with finer grid meshes to reduce field penetration. For the LHC beam screen ("liner"), randomized lengths and distances between holes were proposed to avoid such resonant buildup.

3 Bellows Shielding

Y.Suetsugu presented the design of the RF bellows shields for KEK-B. Similar to the CERN design with long Be-Cu fingers sliding on an oval SS tube, they have replaced the single spiral spring by many short spring fingers, one for each contact finger. In this way, the force on each finger can be adjusted, and made equal everywhere. The fingers are silver coated, and the SS tube plated with rhodium to reduce abrasion. A model has been tested in the lab to determine the best contact force - at 200 g the mechanical resistance was too high and rapid abrasion of the fingers was found. For forces below 50 g, the electrical resistance went up due to bad contacts, and a force of around 100 g was chosen as optimal. A model was successfully tested in TRISTAN.

S.Heifets described the PEP-II bellows shielding. Due to the octogonal cross section of the vacuum chamber, the RF shielding is done by 4 flat slotted sheets made of "Glibcop", which has a better conductivity than Be-Cu. The fingers are rather short and supposed to be sufficiently stiff not to require additional springs. Rather wide slots are left between the sheets, and concern about coupling to the volume behind was voiced. Also the contact may deteriorate when the fingers become hot.

The design for SPRING-8 was presented by T.Nakamura. Somewhat longer fingers made of 1 mm thick Be-Cu are expected to exert enough contact force without additional springs. An earlier "buckling tube" design without sliding contacts - essentially a single convolution inner bellows - has been abandoned except for a few radiation absorbers which are shielded by a thin, slotted constriction in the vacuum chamber.

The present RF shielding of bellows in DAPHNE, presented by M.Zobov, is based on the requirement that sliding contacts should be avoided because of the very high beam currents needed in Phi-factories. The shield consists of a number of parallel zigzag vanes which permit compression and should stretch almost flat during operation. Some concern was expressed about wall currents flowing at an angle to the beam due to residual zigzag. It was recommended that the design should be tested before installation.

4 Beam Position Monitors (BPMs)

Three talks were given on the "damped" beam position monitors which are developed for KEK-B. T.Shintake presented the basic ideas to damp the TE110 resonance: a small diameter button to increase its resonant frequency, and an asymmetrically cut stem of the button to suppress it. A MAFIA calculation of the asymmetric button by T.Obino, essentially agreed with these predictions. However, measurements of the quality factor on a model by N.Akasaka failed to show a reduction when excited directly with antennas. These results are rather recent and still need more study to be fully understood.

Measurements of the button BPMs for PEP-II were presented by J.Corlett (LBL). Using a coax wire technique the TE11 resonance was found to be dominant. The button diameter was therefore reduced from 20 to 15 mm, and different asymmetric cuts were tested: suppression was better with cuts perpendicular to the beam motion. Simulations of the BPMs for the high-energy ring with MAFIA were reported by Cho Ng. The suppression of the TE11 resonance with cuts and with shorts was investigated. Trapped modes were found to create rather long-range wakes. The power loss in the ceramic holding the electrode was found to be small (1 W), but the total loss quite large (100 W for 3 A beam current). S. Kurennoy showed that the broad-band part of the impedance can be estimated simply using the analytic expression with the polarizabilities of a annular gap.

5 IR Chambers and Masks

Y. Chin reported computations of the synchrotron radiation masks on both sides of the Be chamber in the interaction region, consisting of annular irises cut on one side. The code ABCI for rotationally symmetric structures was extended to 3-D (MASK30) in order to calculate the fields. Over 200 W of power was found to be generated between the masks, but most of it is expected to leak out and will be absorbed somewhere in the IR chamber. This chamber is limited on both sides by crotches which radiate up to 20 kW of power, and an estimated 0.5 % (100 W) could be absorbed on the Be chamber.

A similar IR chamber for PEP-II was described by S.Heifets. Estimates of the power generated in the Be pipe are much lower, since the masks are tapered. While up to 25 kW could be generated upstream, less than 0.1 % (20 W) are expected to be absorbed in the Be tube, which is water-cooled and can stand up to 200 W. However,

trapped modes, in particular if they are in resonance with the bunch spacing, could create up to 400 W and exceed the power rating.

6 Other Impedances

T.Tajima described a beam test in TRISTAN of Ferrite absorbers for KEK-B SC cavities. These are produced from micron size powder directly on the vacuum chamber wall by a "HIP" (Hot Isostatic Press) process involving high temperatures and pressures lasting several hours. For short bunches, the measured loss is somewhat higher than computed with ABCI, indicating that the bunch shape is not quite Gaussian, but has tails. No arcing was seen, but the beam current in TRISTAN was too small to expect it.

Ferrite tiles soldered to water cooled Cu plates for SC cavities in CESR were described by W.Hartung from Cornell. Calorimetric tests of HOM losses showed no change with bunch length, while the total loss factor of the ring varies by a factor 2 for rms lengths between 11 and 25 mm. The loss was also smaller than expected, possible explanations like loss into beam pipes, edge effects and gaps were found to be too small to explain this discrepancy completely.

2 Contributions were concerned with analytic impedance models:

S. Petracca (University of Salerno) explained her approach to compute the impedance of multi-layer coaxial pipes for LHC. Using a novel perturbation technique, based on Debye potentials and the reciprocity theorem, the impedance of a complex structure can be expressed by that of a simpler one plus 2 integral terms. The first one describes small geometric deviations, e.g. rounded edges of a square LHC liner, and the second one the finite resistivity of the material, e.g. a copper-clad SS wall. Applications of this approach to the B-factory problems are foreseen in the weeks following the workshop.

J.Scott-Berg (SLAC) introduced a transverse impedance model which has the correct asymptotic inverse 3/2 power dependence not only for real, but also for complex frequencies. The validity of this assumption was questioned by the audience. The model fulfills the Kramers-Kronig relations between real and imaginary parts of any impedance, and can be fitted to computed cavity impedances after subtracting the strongest resonances.

7 General Conclusions

A lot of work has already been done on optimizing the impedances of components for the B-factories, but some questions remain which need more study:

- The penetration of TM/TE fields through slots, in particular when they are not parallel to the beam motion, such as caused by closed-orbit (tilt tolerances).
- Bellows shielding with sliding contacts may be limited in the maximum current they can handle, and solutions with fixed contacts should be studied. The zigzag vanes proposed for Daphne may cause problems due to induced transverse currents, while the "buckling tube" proposed some time ago for Spring8 - although abandoned - may still be a valid alternative.
- The large power generated in the IR chambers between the crotches needs to be absorbed to avoid damage to the central Be tube. Such absorbers could be made of Ferrites, which should have good thermal contact to the cooled walls, such as are under development for SC cavities. But they also have to be located where they do not shadow the experiments.

• A comparison of shielding against direct synchrotron radiation by masking (KEK-B) and by chamber offset (PEP-II) should be made, as these solutions have both certain advantages and disadvantages.

• Damping of the TE110 resonance in BPMs by asymmetrically cut stems - although predicted by theory and modelling, was not found in experiment. This should be understood, and possible alternative designs investigated.

I add some general remarks on the use of computer modelling for field and loss calculations, a topic also discussed by K. Ko in a plenary talk:

• There is now widespread use of FTDT (Finite Difference Time Domain) codes both in 2-D (TBCI, T3, ABCI) and 3-D (MAFIA, MASK30) - but all of these codes approximate inclined boundaries by "staircases". This leads to slow convergence with decreasing mesh size for small taper angles. This is avoided in the code XWAKE (Harfoush-Jurgens, FNAL) which can approximate even curved boundaries. Now it is available only for axially symmetric (m=0) modes, but the m=1 part is nearly ready, as has been recently announced at the PAC95 in Dallas.

• Finite element codes - which permit triangular meshes - have mostly been used only in the frequency domain, except in the time domain codes PRIAM (2-D) and ANTIGONE (3-D) which have been developed recently (Lemeur, LAL-Orsay). These codes still need to be tested thoroughly.

• Pure frequency domain codes (SUPERFISH, URMEL) are useful for narrow-band impedances, but do not handle correctly "open boundaries". Impedances can also be obtained by Fourier transforming wake potentials of short bunches, but care must be taken to use long enough wakes and proper windowing techniques to get correct results.

With these limitations of numerical codes, analytic estimates and perturbation approaches are still often a valid alternative to get first estimates and scaling laws.

In conclusion, I would like to emphasize that all critical issues concerning impedances in B-factories are actively being worked on, in excellent collaboration between hardware designers and accelerator physicists.

WORKING GROUP ON COLLECTIVE EFFECTS SUMMARY

Jacques Gareyte

CERN, Geneva 23, Switzerland

Abstract

This report is a summary of a selection of the contributed papers presented and of the discussions held in the Working Group on Collective Effects at the CEIBA 95 Workshop. B factories need increased beam currents compared to previous machines. Therefore a large and concerted effort is developing to better understand the intricacies of the well established theories of "classical" instabilities, and in parallel to explore possibilities for new potentially dangerous mechanisms. Whereas in the domain of "classical" instabilities current progress increases our confidence that necessary beam parameters can be achieved, other destabilizing mechanisms due to ions or photoelectrons seem to pose problems and require further work.

1 Introduction

The theory of beam instabilities is now a mature field and the calculation of coupling impedances, which is a most necessary ingredient to apply the theory, is a well mastered subject. However, past experience has shown that any increase in beam intensity or density usually reveals new, unthought–of phenomena.

With the B factory projects, we make a considerable leap forward as far as beam intensity is concerned, and I take no risk in predicting a lot of fun to the physicists who will have to commission these machines.

At present we are in the design phase and we must of course do our best to anticipate problems and propose solutions: this was the aim of our working group on Collective Effects. We heard a large number of presentations by 17 of the participants. Others contributed full time or part time to the discussions.

Two recently uncovered instability mechanisms were discussed in a joint session of the three working groups. These are a transient ion instability which might affect long trains of dense electron bunches, and an instability induced by photoelectrons which might affect trains of dense positron bunches. Discussions on these very important subjects were extended in the working group sessions. Another set of interesting communications concerned progress made recently in the understanding of mode coupling effects in the transverse as well as in the longitudinal directions of motion. We heard other talks on "multiperiodicity, limit cycle and chaos in bunch lenghtening with localized impedance" (E.S. Kim), "simulation and understanding of sawtooth effects in SLC damping ring" (A. Chao), " a simple model with damping of the mode coupling instability" (N. Dikansky), "on saturation of a longitudinal instability" (J. Byrd), "physical understanding of microwave instability by simple analytical

model" (S.X. Fang), and "debunching in proton rings" (E. Shaposhnikova). Although they also reveal recent and interesting progress, these last talks will not be summarized here, as they seem to be less focused on the urgent preocupations of B factory designers. They can be found in the proceedings.

2 Ion Effects

K. Yokoya (KEK B), G. Stupakov (PEP II) ans S. Heifets (saturation effects) introduced the subject by their comprehensive presentations.

Ion induced instabilities are well known to plague storage rings for negatively charged particles (electrons and antiprotons). As a matter of fact the first electron-electron storage ring, the Princeton-Stanford machine, saw clearly in 1962-64 the effects of ions being accumulated in the potential well of the electron beam. In this machine it did not create an instability, on the contrary it allowed to store ten times more beam current than without ions. The reason was that ions created a large tune spread which stabilized the beam against the resistive-wall instability. In other machines a beam-ions instability was observed for instance in the CERN antiproton accumulator. The cure is to leave a gap in the beam to prevent accumulation or to shake the beam at a frequency close to the ions bouncing frequency.

Modern large high-energy storage rings have a small number of widely spaced bunches, and are not prone to ions effects.

In B factories on the contrary there are many dense, closely spaced bunches. A large number of ions are created at each bunch passage, and a sufficient fraction of them may remain long enough inside the beam enveloppe to create problems: a small initial transverse displacement of an electron bunch produces a deflection of the ion cloud which in turn influences subsequent bunches. The perturbation may resonantly grow along the bunch train to attain large amplitudes at the end of the train after a few revolutions around the machine. There is no need for long-term ion accumulation and there is no need for a closed loop interaction around the ring as in classical coupled-bunch instabilities. This is more reminiscent of multibunch beam break-up in Linacs.

First calculations gave frighteningly small growth times both for PEP II and KEK B, of the order of a few turns. However many effects have to be considered which may considerably reduce the growth rate of this instability. For instance the fact that the beam is flat introduces a spread in the vertical bouncing frequencies of ions which see different electron densities according to the horizontal position at which they are created. The change of beta functions around the ring and the existence of different ion species also create a spread of frequencies which reduces the growth rate. Also the growth rate calculated at vanishingly small amplitude is not sustained at amplitudes of the order of a R.M.S. beam size: there is a saturation effect. Even taking this into account present calculations give growth times of the order of 100 turns, which is still cause for concern.

Following a suggestion by D. Brandt, G. Stupakov applied the theory developped at SLAC to the ESRF operating with a large number of bunches. With a partial pressure of CO of 10^{-9} Torr he estimated the growth time to be of the order of one turn, whereas this instability is not observed in reality. If this is confirmed, it could imply that something important has been left out in the theory.

Clearly further work is needed to better understand this potential instability.

The effectiveness of a feedback system in damping the ion instability was discussed. There is no much doubt that provided the growth time is long enough (say a few tens of turns) a feedback system can suppress the dipole bunch motion. However it was pointed out that in this kind of two-beam instability, the quadrupole collective motion is potentially not much weaker than the dipole one. Collective quadrupole modes have been observed in the CERN AA (antiproton -ions) and in LEP (electron-positron beam-beam). It is suggested to study the possibility of higher order modes in simulation by artificially blocking the dipole motion.

The working group further recommends that experimental studies be carried out on existing machines, with the ESRF and the Taiwan light source as possible suitable candidates. One should try to see the effect, possibly by increasing the residual gaz pressure, and then observe its spectrum (ion frequencies?), compare with positron beams, and try to cure it through feedback and beam shaking. A proposal to get rid of the ions is to have small regularly spaced holes in the beam, in order to resonantly excite the motion of the ions (J. Seeman).

3 Photoelectron effects

An instability affecting only positrons was recently discovered in the KEK Photon Factory. This seems to be a new phenomenon and is currently explained by an interaction of the positron beam with a cloud of photoelectrons present in the vicinity of the beam in the vacuum chamber.

M. Isawa made a very interesting presentation of the main features of the Photon Factory instability, K. Ohmi described the theory proposed to explain this and its implications for KEK B, and G. Lambertson reported on the work done on this subject in the framework of PEP II studies.

The instability seen in the Photon Factory affects the vertical beam oscillations during the accumulation of a multibunch positron beam. It appears at a low threshold (one tenth of maximum current) and its signature is a broad spectrum of betatron sidebands spanning about half the 500 MHz total range between RF lines. J. Byrd showed the results of measurements carried out on CESR (Cornell) which display symptoms very similar to those. The classical transverse coupling impedance which should be invoked to explain the Photon Factory instability is unphysically large and anyway this should affect equally the electrons, which is not the case.

Therefore the explanation put forward by K. Ohmi seems convincing: a large number of photoelectrons are created on the inner surface of the vacuum chamber. In the portion of the beam pipe outside bending magnets these electrons are transversely accelerated towards the beam by the electric field of the positrons. Simulations, at KEK as well as at LBL show that indeed an important cloud of electrons can accumulate in this way in the chamber. Wether multipacting on the walls could increase further the electron density is being debated.

After the passage of a certain number of bunches at the head of the train, there are enough electrons in the vicinity of the beam to affect the oscillation of the following bunches. As we have seen with ions, a displaced particle bunch then perturbs the charge distribution, leaving behind a wake which in turn deflects following bunches. Simulation predicts a wide band spectrum of betatron frequencies, in good agreement with observations at the Photon Factory.

It was discussed wether this instability could be cured by a fast feedback system, or wether one could prevent the photoelectrons from drifting towards the beam by applying a modest vertical or solenoidal magnetic field in the straight sections of the machine.

The working group recommends to pursue theoretical investigations and to carry out experiments on existing machines (CESR and BEPC seem to be suitable candidates). One could vary γ to change the photon flux, vary the radial beam position to detect any influence of the distance of the beam to the electron emitting wall. Changing Q or Q' should have no effect. It would be interesting to record the modes spectrum, try to shake the beam or make small longitudinal holes to reduce the electron density, and last but not least compare with an electron beam. Influence of applying magnetic fields in the straight sections should also be tested.

J. Rogers described an instability observed in CESR on the positron beam which was recently explained by electrons being trapped along the electric field lines leaking out of the ion pumps inside the bending magnets. In some respects this is reminiscent of the phenomenon discussed above. Clearly the occurence of trapping fields generated by pumps or other items can be easily avoided in B factories. But it was conjectured by S. Heifets that the field lines of the dense beam itself could as well trap electrons inside bending magnets. Photons scattered in the vacuum chamber could generate electrons at the right place with the required energy.

4 Transverse Mode Coupling

The Transverse Mode Coupling of dense single bunches has been thorougly investigated. It is the main performance limitation of LEP and of its injector the SPS. The two following reports show that further progress is being made in this area.

E. Shaposhnikova presented a study which shows that it is possible to predict the T.M.C. threshold with a high degree of accuracy, provided one takes into account a sufficient number of high order radial modes for each head-tail mode involved in the coupling process.

J. Scott Berg showed that coupling between head-tail single bunch modes can influence coupled bunch instabilities in the case of the B factories intense multibunch. beams. Long range or medium range wake fields couple bunches together. This leads to multibunch instabilities where usually the rigid mode m =0 of individual bunches is involved. This kind of instability can be damped by feedback. However the same long or medium range wake fields produce also a large tune shift of certain coupled bunch modes so that m=0 and m=-1 head-tail modes merge at a lower value of the beam current than they would in the case of single bunches. Provided that a wakefield component exists at a sufficiently high frequency to couple modes m=0 and m=-1, the mode coupling instability can then occur at a lower threshold.

The threshold for this phenomenon calculated for PEP II parameters is higher than the design current. However, the important question is wether all modes will be damped in this situation in presence of feedback; simulations show that this might not be the case, and therefore this phenomenon has to be considered seriously.

5 Bunch Lengthening and Longitudinal Mode Coupling

Mode Coupling has been first proposed by Sacherer in 1977 to explain turbulent bunch lengthening. Whereas the same concept has been easy to apply in the transverse case, progress in understanding its detailed mechanism in the longitudinal case has been very slow. The main reason is probably that potential well deformation occuring in parallel considerably complicates the dynamics.

The apporach of Oide and Yokoya now sheds more light on the subject. A strong microwave instability occurs, as predicted by Sacherer, when two azimuthal modes couple. But a weaker instability can manifest itself at lower threshold, which can be described as coupling of radial modes pertaining to the same azimuthal mode, as a consequence of potential well deformation.

K. Oide presented results of simulations for the KEK Low Energy Ring. In the regime of radial mode coupling a very strong synchrotron damping of the collective motion (orders of magnitude larger than single particle damping) suppresses turbulent bunch lenghtening. This surprising result was discussed in the working group but no obvious explanation could be found. Disregarding this strong damping the threshold for microwave instability is just above the design current.

K. Bane analysed in the light of the Oide-Yokoya technique the situation of the SLC damping ring before and after the effort undertaken to reduce its coupling impedance. Befofe, a strong bunch lengthening was observed accompanied at large bunch current by turbulence and a "sawtooth" variation of the bunch length.

Oide's programme reveals in this situation a strong instability due to coupling of quadrupole and sextupole modes. After the reduction of the impedance (which affected the inductive part but not much the resistive part) bunch lengthening was reduced but surprisingly turbulence now occured at a lower bunch current. Oide's programme in this situation indeed predicts instability at lower current through radial mode coupling inside the quadrupole azimuthal mode.

Other interesting developments in the domain of bunch lengthening and longitudinal mode coupling were presented by S.X. Fang and K.Y.Ng. They show that the rather intuitive argument according to which below transition ($\alpha<0$) bunch lengthening should be diminished and mode coupling should occur at a higher current is indeed borne out by detailed calculations in the case of realistic coupling impedances. Bunch lengthening is reduced below transition because the interaction with the wake fields tend to increase the bunch density towards the tail of the bunch, so that the main part of the wake then develops behind the bunch. The reverse is true for $\alpha>0$, the head is dense and its wake strongly perturbs the tail. Mode coupling is pushed to larger currents below transition because low order modes tend to be pulled apart whilst the reverse occurs above transition.

6 Conclusion

Steady progress is being made in the understanding of "classical" instabilities. With a good knowledge of the coupling impedances, thresholds and growth rates can be predicted with sufficient accuracy. The design of B factories poses challenging problems in this area, but there is evidence that solutions exist.

However as we enter a new domain of beam intensity and density, we can expect new

phenomena to appear. In this workshop the cases of ion induced instabilities (for the electron ring) and electron induced instabilities (for the positron ring) have been discussed at length. They seem to be potentially dangerous but we are at present far from mastering these subjects in sufficient detail.

Further theoretical and experimental work is urgently needed.

LIST OF PARTICIPANTS

Kazunori Akai

KEK
Oho 1-1, Tsukuba-shi
Ibaraki-ken
JAPAN
"akai@kekvax.kek.jp"

Nobumasa Akasaka

KEK
Oho 1-1, Tsukuba-shi
Ibaraki-ken
JAPAN
"akasaka@kekvax.kek.jp"

Kiyomitsu Asano

KEK
Oho 1-1, Tsukuba-shi
Ibaraki-ken
JAPAN
"asano@kekvax.kek.jp"

Karl L. Bane

SLAC
MS#26, P.O. Box 4349
Stanford, CA 94309
U.S.A.
"kbane@slac.stanford.edu"

Joseph Scott Berg

SLAC
MS#26, P.O. Box 4349
Stanford, CA 94309
U.S.A.
"alhy@slac.stanford.edu"

Alex W. Chao

SLAC
MS#26, P.O. Box 4349
Stanford, CA 94309
U.S.A.
"achao@slac.stanford.edu"

Daniel Brandt

CERN
SL-Division
CH-1211,Geneva 23
SWIZERLAND
"brandt@cernvm.cern.ch"

John Byrd

LBL-AFRD
MS#71-259, 1 Cyclotron Road
Berkeley, CA 94720
U.S.A.
"jmbyrd@lbl.gov"

Yong Ho Chin

KEK
Oho 1-1, Tsukuba-shi
Ibaraki-ken
JAPAN
"yongho@kekvax.kek.jp"

Jinhyuk Choi

POSTECH-PAL
Hyojia San 31, Pohang
Kyungbuk
KOREA
"jchoi@vision.postech.ac.kr"

John Corlett

LBL-AFRD
MS#71-259, 1 Cyclotron Road
Berkeley, CA 94720
U.S.A.
"jnc@bc1.lbl.gov"

Nikolai Dikansky

Institute of Nuclear Physics

Novosibirsk, 630090
RUSSIA
"lisman@inp.nsk.su"

Eiji Ezura

KEK
Oho 1-1, Tsukuba-shi
Ibaraki-ken
JAPAN
"ezura@kekvax.kek.jp"

Gerard Flynn

LAL'Orsay LURE
Centre Universitaire Paris-Sud
91405 Orsay
FRANCE
"flynn@dvx.lal.in2p3.fr"

John D. Fox

SLAC
MS#33 P.O. Box 4349
Stanford, CA 94309
U.S.A.
"jdfox@unixhub.slac.stanford.edu"

Takaaki Furuya

KEK
Oho 1-1, Tsukuba-shi
Ibaraki-ken
JAPAN
"furuya@kekvax.kek.jp"

Jacques Gareyte

CERN
SL Division
CH-1211, Geneva 23
SWIZERLAND
"jga@cernvm.cern.ch"

Walter Hartung

Cornell Univ.
124 Newman Lab. of Nuclear Studies
Ithaca, NY 14853
U.S.A
"whh@lns62.lns.cornell.edu"

Samuel Heifets

SLAC
MS#26, P.O. Box 4349
Stanford, CA 94309
U.S.A.
"heifets@slac.stanford.edu"

Shigenori Hiramatsu

KEK
Oho 1-1, Tsukuba-shi
Ibaraki-ken
JAPAN
"hiramatu@kekvax.kek.jp"

Koji Hirata

KEK
Oho 1-1, Tsukuba-shi
Ibaraki-ken
JAPAN
"hirata@kekvax.kek.jp"

Takao Ieiri

KEK
Oho 1-1, Tsukuba-shi
Ibaraki-ken
JAPAN
"ieirit@kekvax.kek.jp"

Yoshiro Irie

KEK
Oho 1-1, Tsukuba-shi
Ibaraki-ken
JAPAN
"iriey@kekvax.kek.jp"

Masaaki Isawa

KEK
Oho 1-1, Tsukuba-shi
Ibaraki-ken
JAPAN
"isawa@kekvax.kek.jp"

Yoshihiro Ishi

Mitsubishi

JAPAN
"ishi@kekvax.kek.jp"

Jiuqing Wang

KEK/IHEP
BEPC NL

P.R. CHINA
"wangjq@bepc3.ihep.ac.cn"

Tatsuya Kageyama

KEK
Oho 1-1, Tsukuba-shi
Ibaraki-ken
JAPAN
"kageyama@kekvax.kek.jp"

Susumu Kamada

KEK
Oho 1-1, Tsukuba-shi
Ibaraki-ken
JAPAN
"kamada@kekvax.kek.jp"

Ken-ichi Kanazawa

KEK
Oho 1-1, Tsukuba-shi
Ibaraki-ken
JAPAN
"kanazawa@kekvax.kek.jp"

Mitsuo Kikuchi

KEK
Oho 1-1, Tsukuba-shi
Ibaraki-ken
JAPAN
"kikuchim@kekvax.kek.jp"

Eiji Kikutani

KEK
Oho 1-1, Tsukuba-shi
Ibaraki-ken
JAPAN
"kikutani@kekvax.kek.jp"

Eun San Kim

KEK
Oho 1-1, Tsukuba-shi
Ibaraki-ken
JAPAN
"eskim@kekvax.kek.jp"

Yoshitaka Kimura

KEK
Oho 1-1, Tsukuba-shi
Ibaraki-ken
JAPAN
"kimura@kekvax.kek.jp"

Jun-ichi Kishiro

KEK
Oho 1-1, Tsukuba-shi
Ibaraki-ken
JAPAN
"kishiro@kekvax.kek.jp"

Kwok Ko

SLAC
2575 Sandhill Rd.
Menlo Park, CA 94309
U.S.A.
"kwok@slac.stanford.edu"

Kiyomo Koba

KEK
Oho 1-1, Tsukuba-shi
Ibaraki-ken
JAPAN
koba@kekvax.kek.jp

Raj Kumar

Utsunomiya Univ.
Dept. of Electrical & Electronic Engineering
2753 Ishi-machi, Utsunomiya-shi, Tochigi-
JAPAN
"kumar@cc.utsunomiya-u.ac.jp"

Sergey Kurennoy

Univ. of Maryland
Physics Department
College Park, MD 20742
U.S.A
"kurennoy@quark.umd.edu"

Shin-ichi Kurokawa

KEK
Oho 1-1, Tsukuba-shi
Ibaraki-ken
JAPAN
"kurokawa@kekvax.kek.jp"

Glen R. Lambertson

LBL-AFRD
MS#71-259, 1 Cyclotron Road
Berkeley, CA 94720
U.S.A.
"lambertson@lbl.gov"

De-Kang Liu

KEK/IHEP
Oho 1-1, Tsukuba-shi
Ibaraki-ken
P.R. CHINA
"liudk@kekvax.kek.jp"

Shinji Machida

KEK
Oho 1-1, Tsukuba-shi
Ibaraki-ken
JAPAN
"machida@kekvax.kek.jp"

Yasuyuki Minagawa

KEK
Oho 1-1, Tsukuba-shi
Ibaraki-ken
JAPAN
"minagawa@kekvax.kek.jp"

Toshiyuki Mitsuhashi

KEK
Oho 1-1, Tsukuba-shi
Ibaraki-ken
JAPAN
"mitsuhas@kekvax.kek.jp"

Shinji Mitsunobu

KEK
Oho 1-1, Tsukuba-shi
Ibaraki-ken
JAPAN
"mitunobu@kekvax.kek.jp"

Hajime Mizuno

KEK
Oho 1-1, Tsukuba-shi
Ibaraki-ken
JAPAN
"mizuno@kekvax.kek.jp"

Yoshiharu Mori

Univ. of Tokyo INS
3-2-1 Midori-cho, Tanashi-shi
Tokyo 188
JAPAN
"moriy@kekvax.kek.jp"

Takeshi Nakamura

JASRI SPring-8
Beam Dynamics Group Accelerator
Kamigori Ako-gun, Hyogo 678-12
JAPAN
"nakamura@sp8sun.spring8.or.jp"

Cho-K. Ng

SLAC
P.O. Box 4349
Stanford, CA 94309
U.S.A.
"cho@slac.stanford.edu"

King Yuen Ng

Fermilab.
MS#345, P.O. Box 500
Batavia, IL 60510
U.S.A.
"ng@calvin.fnal.gov"

Takashi Obina

KEK
Oho 1-1, Tsukuba-shi
Ibaraki-ken
JAPAN
"obina@kekvax.kek.jp"

Kazuhito Ohmi

KEK
Oho 1-1, Tsukuba-shi
Ibaraki-ken
JAPAN
"ohmi@kekvax.kek.jp"

Katsunobu Oide

KEK
Oho 1-1, Tsukuba-shi
Ibaraki-ken
JAPAN
"oide@kekvax.kek.jp"

Flemming Pedersen

CERN
SL-Division
CH-1211,Geneva 23
SWIZERLAND
"pedersen@ps.msm.cern.ch"

Guoxi Pei

KEK/IHEP
Oho 1-1, Tsukuba-shi
Ibaraki-ken
P.R. CHINA
"guoxi@kekvax.kek.jp"

Stefania Petracca

Univ. of Salerno
Dept. Fisica teorica E.S.M.S.A.
Via S.Allennde 84081, Batonissi (SA)
ITALY
"petracca@vaxsa.dia.unisa.it"

Joseph Rogers

Cornell Univ.
124 Newman Lab. of Nuclear Studies
Ithaca, NY 14853
U.S.A
"jtr1@cornell.edu"

Shogo Sakanaka

KEK
Oho 1-1, Tsukuba-shi
Ibaraki-ken
JAPAN
"sakanaka@kekvax.kek.jp"

Kotaro Satoh

KEK
Oho 1-1, Tsukuba-shi
Ibaraki-ken
JAPAN
"satok@kekvax.kek.jp"

John T. Seeman

SLAC
MS#17, P.O. Box 4349
Stanford, CA 94309
U.S.A.
"seeman@slac.stanford.edu"

Elena Shaposhniko

CERN
SL-Division
CH-1211,Geneva 23
SWIZERLAND
"elenas@cernvm.cem.ch"

Tsumoru Shintake

KEK
Oho 1-1, Tsukuba-shi
Ibaraki-ken
JAPAN
"shintake@kekvax.kek.jp"

Katsuhiro Shinto

KEK
Oho 1-1, Tsukuba-shi
Ibaraki-ken
JAPAN
shinto@kekvax.kek.jp

Gennady Stupakov

SLAC
MS#26, P.O. Box 4349
Stanford, CA 94309
U.S.A.
"stupakov@slac.stanford.edu"

Yusuke Suetsugu

KEK
Oho 1-1, Tsukuba-shi
Ibaraki-kenIbaraki-ken
JAPAN
"suetsugu@jpnkekvx"

Hirotaka Sugawara

KEK
1-1 Oho, Tsukuba-shi
Ibaraki-ken 305
JAPAN
"sugawara@director.kek.jp"

Toshio Suzuki

KEK
Oho 1-1, Tsukuba-shi
Ibaraki-ken
JAPAN
"toshio@jpnkekvx"

Tsuyoshi Tajima

KEK
Oho 1-1, Tsukuba-shi
Ibaraki-ken
JAPAN
"tajimat@kekvax.kek.jp"

Takeshi Takahashi

KEK
Oho 1-1, Tsukuba-shi
Ibaraki-ken
JAPAN
"takahash@kekvax.kek.jp"

Masaru Takao

JASRI SPring-8
Beam Dynamics Group Accelerator
Kamigori Ako-gun, Hyogo 678-12
JAPAN
"takao@sp8sun.spring8.or.jp"

Koji Takata

KEK
Oho 1-1, Tsukuba-shi
Ibaraki-ken
JAPAN
"takata@kekvax.kek.jp"

Masaki Tejima

KEK
Oho 1-1, Tsukuba-shi
Ibaraki-ken
JAPAN
"tejima@kekvax.kek.jp"

Nobuhiro Terunuma

KEK
Oho 1-1, Tsukuba-shi
Ibaraki-ken
JAPAN
"terunuma@kekvax.kek.jp"

Richard Tighe

SLAC
MS#33, P.O. Box 4349
Stanford, CA 94309
U.S.A.
"rtighe@slac.stanford.edu"

Makoto Tobiyama

KEK
Oho 1-1, Tsukuba-shi
Ibaraki-ken
JAPAN
"tobiyama@kekvax.kek.jp"

Takeshi Toyama

KEK
Oho 1-1, Tsukuba-shi
Ibaraki-ken
JAPAN
"toyama@kekvax.kek.jp"

Fang Shou Xian

KEK/IHEP
Oho 1-1, Tsukuba-shi
Ibaraki-ken
P.R. CHINA
"fangsx@kekvax.kek.jp"

Yoshishige Yamazaki

KEK
Oho 1-1, Tsukuba-shi
Ibaraki-ken
JAPAN
"yoshishi@kekvax.kek.jp"

Kaoru Yokoya

KEK
Oho 1-1, Tsukuba-shi
Ibaraki-ken
JAPAN
"yokoya@kekvax.kek.jp"

Shin-ichi Yoshimoto

KEK
Oho 1-1, Tsukuba-shi
Ibaraki-ken
JAPAN
"yosimoto@kekvax.kek.jp"

Xiaolong Zhang

KEK
Oho 1-1, Tsukuba-shi
Ibaraki-ken
JAPAN
"

Feng-qing Zhang

staff
Oho 1-1, Tsukuba-shi
Ibaraki-ken
JAPAN
zhangfq@kekvax.kek.jp

Xiong Xu Zhong

IHEP
The Storage Division of BEPC, P.O. Box
Beijing, 100039
P.R. CHINA
"xuzx@bepc3.ihep.ac.cn"

Feng Zhou

IHEP
P.O. Box 918-9
Beijing, 100039
P.R. CHINA
"zhouf©bepc3.ihep.ac.cn"

Mikhail Zobov

LNF INFN
Divione Acceleratori, Instuto Nazionale di
C.P. 13-00044 Frascati (Rome)
ITALY
"mikhail@irmlnf.bitnet"

Bruno Zotter

CERN
SL-Division
CH-1211,Geneva 23
SWIZERLAND
"zotter@cernvm.cern.ch"